

## **Rechargeable Lithium Batteries**

## **Related titles**

*Solid oxide fuel cell technology*

(ISBN 978-1-84569-628-3)

*Polymer electrolyte membrane and direct methanol fuel cell technology*

*Volume 1: Fundamentals and performance of low temperature fuel cells*

(ISBN 978-1-84569-773-0)

*Polymer electrolyte membrane and direct methanol fuel cell technology*

*Volume 2: In situ characterization techniques for low temperature fuel cells*

(ISBN 978-1-84569-774-7)

Woodhead Publishing Series in Energy:  
Number 81

# Rechargeable Lithium Batteries

From Fundamentals to Applications

*Edited by*

*Alejandro A. Franco*



AMSTERDAM • BOSTON • CAMBRIDGE • HEIDELBERG  
LONDON • NEW YORK • OXFORD • PARIS • SAN DIEGO  
SAN FRANCISCO • SINGAPORE • SYDNEY • TOKYO

Woodhead Publishing is an imprint of Elsevier



Woodhead Publishing is an imprint of Elsevier  
80 High Street, Sawston, Cambridge, CB22 3HJ, UK  
225 Wyman Street, Waltham, MA 02451, USA  
Langford Lane, Kidlington, OX5 1GB, UK

Copyright © 2015 Elsevier Ltd. All rights reserved.

No part of this publication may be reproduced, stored in a retrieval system or transmitted in any form or by any means electronic, mechanical, photocopying, recording or otherwise without the prior written permission of the publisher.

Permissions may be sought directly from Elsevier's Science & Technology Rights Department in Oxford, UK: phone (+44) (0) 1865 843830; fax (+44) (0) 1865 853333; email: [permissions@elsevier.com](mailto:permissions@elsevier.com). Alternatively you can submit your request online by visiting the Elsevier website at <http://elsevier.com/locate/permissions>, and selecting Obtaining permission to use Elsevier material.

### Notice

No responsibility is assumed by the publisher for any injury and/or damage to persons or property as a matter of products liability, negligence or otherwise, or from any use or operation of any methods, products, instructions or ideas contained in the material herein. Because of rapid advances in the medical sciences, in particular, independent verification of diagnoses and drug dosages should be made.

### British Library Cataloguing-in-Publication Data

A catalogue record for this book is available from the British Library

### Library of Congress Control Number: 2015932579

ISBN 978-1-78242-090-3 (print)

ISBN 978-1-78242-098-9 (online)

For information on all Woodhead Publishing publications  
visit our website at <http://store.elsevier.com/>

Typeset by SPi Global

[www.spi-global.com](http://www.spi-global.com)

Printed and bound in the United Kingdom



Working together  
to grow libraries in  
developing countries

[www.elsevier.com](http://www.elsevier.com) • [www.bookaid.org](http://www.bookaid.org)

# List of contributors

**G.B. Appetecchi** ENEA, Agency for New Technologies, Energy and Sustainable Economic Development, Rome, Italy

**N. Azimi** Argonne National Laboratory, Argonne, IL, USA

**M. Bini** Section of Physical Chemistry, University of Pavia, Pavia, Italy

**D. Capsoni** Section of Physical Chemistry, University of Pavia, Pavia, Italy

**H. Cheng** School of Chemical Engineering & Advanced Materials, Newcastle University, Newcastle upon Tyne, UK

**M.J. Cleland** University of Ottawa Heart Institute, Ottawa, ON, Canada

**Th. Coosemans** Vrije Universiteit Brussel, Brussels, Belgium

**M.W. Ellis** Institute for Critical Technology and Applied Science (ICTAS), Virginia Tech, Blacksburg, VA, USA

**S. Ferrari** Section of Physical Chemistry, University of Pavia, Pavia, Italy

**Y. Firouz** Vrije Universiteit Brussel, Brussels, Belgium

**J.S. Forner** Vrije Universiteit Brussel, Brussels, Belgium

**J. Graetz** HRL Laboratories, LLC, Malibu, CA, USA

**H. Gualous** Université de Caen Basse Normandie, Cherbourg-Octeville, France

**J. Hou** Institute for Critical Technology and Applied Science (ICTAS), Virginia Tech, Blacksburg, VA, USA

**X. Jie** Global Research Center for Environment and Energy based on Nanomaterials Science (GREEN), National Institute for Materials Science (NIMS), Tsukuba, Japan

**C.M. Julien** Sorbonne Universités, Paris, France; PHENIX-Laboratoire de Physicochimie des Electrolytes et Nanosystèmes Interfaciaux, Paris, France

**P. Kaghazchi** Freie Universität Berlin, Berlin, Germany

**T. Kallio** Aalto University, Espoo, Finland

**Y. Kim** University of Michigan, Ann Arbor, MI, USA

**F. Liu** University of Texas, Arlington, TX, USA

**A. Mauger** Sorbonne Universités, Paris, France; IMPMC-Institut de Minéralogie, de Physique des Matériaux, et de Cosmochimie, Paris, France

**M. Messagie** Vrije Universiteit Brussel, Brussels, Belgium

**M. Montanino** ENEA, Agency for New Technologies, Energy and Sustainable Economic Development, Portici, Italy

**R.B. Moore** Institute for Critical Technology and Applied Science (ICTAS), Virginia Tech, Blacksburg, VA, USA

**P.P. Mukherjee** Texas A&M University, College Station, TX, USA

**P. Mustarelli** Section of Physical Chemistry, University of Pavia, Pavia, Italy

**L. Oliveira** Vrije Universiteit Brussel, Brussels, Belgium

**N. Omar** Vrije Universiteit Brussel, Brussels, Belgium

**S. Passerini** Helmholtz Institute Ulm, Karlsruhe Institute of Technology, Ulm, Germany

**E. Quararone** Section of Physical Chemistry, University of Pavia, Pavia, Italy

**S. Rangaraju** Vrije Universiteit Brussel, Brussels, Belgium

**M.H. Rivas** Vrije Universiteit Brussel, Brussels, Belgium

**J. Salminen** VTT Technical Research Centre of Finland, Espoo, Finland

**K. Scott** School of Chemical Engineering & Advanced Materials, Newcastle University, Newcastle upon Tyne, UK

**A.G. Stefanopoulou** University of Michigan, Ann Arbor, MI, USA

**J.M. Timmermans** Vrije Universiteit Brussel, Brussels, Belgium

---

**K. Uosaki** Global Research Center for Environment and Energy based on Nanomaterials Science (GREEN), National Institute for Materials Science (NIMS), Tsukuba, Japan; International Center for Materials Nanoarchitectonics (WPI-MANA), National Institute for Materials Science (NIMS), Tsukuba, Japan

**P. Van den Bossche** Vrije Universiteit Brussel, Brussels, Belgium

**J. Van Mierlo** Vrije Universiteit Brussel, Brussels, Belgium

**C. Villevieille** Paul Scherrer Institute, Villigen PSI, Switzerland

**W.Q. Walker** National Aeronautics and Space Administration (NASA), Houston, TX, USA

**Z. Xue** Argonne National Laboratory, Argonne, IL, USA

**K. Zaghib** Energy Storage and Conversion, Research Institute of Hydro-Québec, Varennes, QC, Canada

**S.S. Zhang** U.S. Army Research Laboratory, Adelphi, MD, USA

**Z. Zhang** Argonne National Laboratory, Argonne, IL, USA

# Woodhead Publishing Series in Energy

- 1 **Generating power at high efficiency: Combined cycle technology for sustainable energy production**  
*Edited by Eric Jeffs*
- 2 **Advanced separation techniques for nuclear fuel reprocessing and radioactive waste treatment**  
*Edited by Kenneth L. Nash and Gregg J. Lumetta*
- 3 **Bioalcohol production: Biochemical conversion of lignocellulosic biomass**  
*Edited by Keith W. Waldron*
- 4 **Understanding and mitigating ageing in nuclear power plants: Materials and operational aspects of plant life management (PLiM)**  
*Edited by Philip G. Tipping*
- 5 **Advanced power plant materials, design and technology**  
*Edited by Dermot Roddy*
- 6 **Stand-alone and hybrid wind energy systems: Technology, energy storage and applications**  
*Edited by John K. Kaldellis*
- 7 **Biodiesel science and technology: From soil to oil**  
*Edited by Jan C. J. Bart, Natale Palmeri and Stefano Cavallaro*
- 8 **Developments and innovation in carbon dioxide (CO<sub>2</sub>) capture and storage technology**  
**Volume 1: Carbon dioxide (CO<sub>2</sub>) capture, transport and industrial applications**  
*Edited by M. Mercedes Maroto-Valer*
- 9 **Geological repository systems for safe disposal of spent nuclear fuels and radioactive waste**  
*Edited by Joonhong Ahn and Michael J. Apted*
- 10 **Wind energy systems: Optimising design and construction for safe and reliable operation**  
*Edited by John D. Sørensen and Jens N. Sørensen*
- 11 **Solid oxide fuel cell technology: Principles, performance and operations**  
*Edited by Kevin Huang and John Bannister Goodenough*
- 12 **Handbook of advanced radioactive waste conditioning technologies**  
*Edited by Michael I. Ojovan*
- 13 **Membranes for clean and renewable power applications**  
*Edited by Annarosa Gugliuzza and Angelo Basile*
- 14 **Materials for energy efficiency and thermal comfort in buildings**  
*Edited by Matthew R. Hall*
- 15 **Handbook of biofuels production: Processes and technologies**  
*Edited by Rafael Luque, Juan Campelo and James Clark*

16 **Developments and innovation in carbon dioxide (CO<sub>2</sub>) capture and storage technology**  
**Volume 2: Carbon dioxide (CO<sub>2</sub>) storage and utilisation**  
*Edited by M. Mercedes Maroto-Valer*

17 **Oxy-fuel combustion for power generation and carbon dioxide (CO<sub>2</sub>) capture**  
*Edited by Ligang Zheng*

18 **Small and micro combined heat and power (CHP) systems: Advanced design, performance, materials and applications**  
*Edited by Robert Beith*

19 **Advances in clean hydrocarbon fuel processing: Science and technology**  
*Edited by M. Rashid Khan*

20 **Modern gas turbine systems: High efficiency, low emission, fuel flexible power generation**  
*Edited by Peter Jansohn*

21 **Concentrating solar power technology: Principles, developments and applications**  
*Edited by Keith Lovegrove and Wes Stein*

22 **Nuclear corrosion science and engineering**  
*Edited by Damien Féron*

23 **Power plant life management and performance improvement**  
*Edited by John E. Oakey*

24 **Electrical drives for direct drive renewable energy systems**  
*Edited by Markus Mueller and Henk Polinder*

25 **Advanced membrane science and technology for sustainable energy and environmental applications**  
*Edited by Angelo Basile and Suzana Pereira Nunes*

26 **Irradiation embrittlement of reactor pressure vessels (RPVs) in nuclear power plants**  
*Edited by Naoki Soneda*

27 **High temperature superconductors (HTS) for energy applications**  
*Edited by Ziad Melhem*

28 **Infrastructure and methodologies for the justification of nuclear power programmes**  
*Edited by Agustín Alonso*

29 **Waste to energy conversion technology**  
*Edited by Naomi B. Klinghoffer and Marco J. Castaldi*

30 **Polymer electrolyte membrane and direct methanol fuel cell technology Volume 1: Fundamentals and performance of low temperature fuel cells**  
*Edited by Christoph Hartnig and Christina Roth*

31 **Polymer electrolyte membrane and direct methanol fuel cell technology Volume 2: In situ characterization techniques for low temperature fuel cells**  
*Edited by Christoph Hartnig and Christina Roth*

32 **Combined cycle systems for near-zero emission power generation**  
*Edited by Ashok D. Rao*

33 **Modern earth buildings: Materials, engineering, construction and applications**  
*Edited by Matthew R. Hall, Rick Lindsay and Meror Krayenhoff*

34 **Metropolitan sustainability: Understanding and improving the urban environment**  
*Edited by Frank Zeman*

35 **Functional materials for sustainable energy applications**  
*Edited by John A. Kilner, Stephen J. Skinner, Stuart J. C. Irvine and Peter P. Edwards*

36 **Nuclear decommissioning: Planning, execution and international experience**  
*Edited by Michele Laraia*

37 **Nuclear fuel cycle science and engineering**  
*Edited by Ian Crossland*

38 **Electricity transmission, distribution and storage systems**  
*Edited by Ziad Melhem*

39 **Advances in biodiesel production: Processes and technologies**  
*Edited by Rafael Luque and Juan A. Melero*

40 **Biomass combustion science, technology and engineering**  
*Edited by Lasse Rosendahl*

41 **Ultra-supercritical coal power plants: Materials, technologies and optimisation**  
*Edited by Dongke Zhang*

42 **Radionuclide behaviour in the natural environment: Science, implications and lessons for the nuclear industry**  
*Edited by Christophe Poinsot and Horst Geckeis*

43 **Calcium and chemical looping technology for power generation and carbon dioxide (CO<sub>2</sub>) capture: Solid oxygen- and CO<sub>2</sub>-carriers**  
*Paul Fennell and E. J. Anthony*

44 **Materials' ageing and degradation in light water reactors: Mechanisms, and management**  
*Edited by K. L. Murty*

45 **Structural alloys for power plants: Operational challenges and high-temperature materials**  
*Edited by Amir Shirzadi and Susan Jackson*

46 **Biolubricants: Science and technology**  
*Jan C. J. Bart, Emanuele Gucciardi and Stefano Cavallaro*

47 **Advances in wind turbine blade design and materials**  
*Edited by Povl Brøndsted and Rogier P. L. Nijssen*

48 **Radioactive waste management and contaminated site clean-up: Processes, technologies and international experience**  
*Edited by William E. Lee, Michael I. Ojovan, Carol M. Jantzen*

49 **Probabilistic safety assessment for optimum nuclear power plant life management (PLiM): Theory and application of reliability analysis methods for major power plant components**  
*Gennadij V. Arkadov, Alexander F. Getman and Andrei N. Rodionov*

50 **The coal handbook: Towards cleaner production Volume 1: Coal production**  
*Edited by Dave Osborne*

51 **The coal handbook: Towards cleaner production Volume 2: Coal utilisation**  
*Edited by Dave Osborne*

52 **The biogas handbook: Science, production and applications**  
*Edited by Arthur Wellinger, Jerry Murphy and David Baxter*

53 **Advances in biorefineries: Biomass and waste supply chain exploitation**  
*Edited by Keith Waldron*

54 **Geological storage of carbon dioxide (CO<sub>2</sub>): Geoscience, technologies, environmental aspects and legal frameworks**  
*Edited by Jon Gluyas and Simon Mathias*

55 **Handbook of membrane reactors Volume 1: Fundamental materials science, design and optimisation**  
*Edited by Angelo Basile*

56 **Handbook of membrane reactors Volume 2: Reactor types and industrial applications**  
*Edited by Angelo Basile*

57 **Alternative fuels and advanced vehicle technologies for improved environmental performance: Towards zero carbon transportation**  
*Edited by Richard Folkson*

58 **Handbook of microalgal bioprocess engineering**  
*Christopher Lan and Bei Wang*

59 **Fluidized bed technologies for near-zero emission combustion and gasification**  
*Edited by Fabrizio Scala*

60 **Managing nuclear projects: A comprehensive management resource**  
*Edited by Jas Devgun*

61 **Handbook of Process Integration (PI): Minimisation of energy and water use, waste and emissions**  
*Edited by Jiří J. Klemeš*

62 **Coal power plant materials and life assessment**  
*Edited by Ahmed Shibli*

63 **Advances in hydrogen production, storage and distribution**  
*Edited by Ahmed Basile and Adolfo Iulianelli*

64 **Handbook of small modular nuclear reactors**  
*Edited by Mario D. Carelli and Dan T. Ingersoll*

65 **Superconductors in the power grid: Materials and applications**  
*Edited by Christopher Rey*

66 **Advances in thermal energy storage systems: Methods and applications**  
*Edited by Luisa F. Cabeza*

67 **Advances in batteries for medium and large-scale energy storage**  
*Edited by Chris Menictas, Maria Skyllas-Kazacos and Tuti Mariana Lim*

68 **Palladium membrane technology for hydrogen production, carbon capture and other applications**  
*Edited by Aggelos Doukelis, Kyriakos Panopoulos, Antonios Koumanakos and Emmanouil Kakaras*

69 **Gasification for synthetic fuel production: Fundamentals, processes and applications**  
*Edited by Rafael Luque and James G. Speight*

70 **Renewable heating and cooling: Technologies and applications**  
*Edited by Gerhard Stryi-Hipp*

71 **Environmental remediation and restoration of contaminated nuclear and NORM sites**  
*Edited by Leo van Velzen*

72 **Eco-friendly innovation in electricity networks**  
*Edited by Jean-Luc Bessede*

73 **The 2011 Fukushima nuclear power plant accident: How and why it happened**  
*Yotaro Hatamura, Seiji Abe, Masao Fuchigami and Naoto Kasahara. Translated by Kenji Iino*

74 **Lignocellulose biorefinery engineering: Principles and applications**  
*Hongzhang Chen*

75 **Advances in membrane technologies for water treatment: Materials, processes and applications**  
*Edited by Angelo Basile, Alfredo Cassano and Navin Rastogi*

76 **Membrane reactors for energy applications and basic chemical production**  
*Edited by Angelo Basile, Luisa Di Paola, Faisal Hai and Vincenzo Piemonte*

77 **Pervaporation, vapour permeation and membrane distillation: Principles and applications**  
*Edited by Angelo Basile, Alberto Figoli and Mohamed Khayet*

---

- 78 **Safe and secure transport and storage of radioactive materials**  
*Edited by Ken Sorenson*
- 79 **Reprocessing and recycling of spent nuclear fuel**  
*Edited by Robin Taylor*
- 80 **Advances in battery technologies for electric vehicles**  
*Edited by Bruno Scrosati, Juergen Garche and Werner Tillmetz*
- 81 **Rechargeable lithium batteries: From fundamentals to applications**  
*Edited by Alejandro A. Franco*
- 82 **Calcium and chemical looping technology for power generation and carbon dioxide (CO<sub>2</sub>) capture**  
*Edited by Paul Fennell and Ben Anthony*
- 83 **Compendium of hydrogen energy Volume 1: Hydrogen production and purification**  
*Edited by Velu Subramani, Angelo Basile and T. Nejat Veziroglu*
- 84 **Compendium of hydrogen energy Volume 2: Hydrogen storage, transmission, transportation and infrastructure**  
*Edited by Ram Gupta, Angelo Basile and T. Nejat Veziroglu*
- 85 **Compendium of hydrogen energy Volume 3: Hydrogen energy conversion**  
*Edited by Frano Barbir, Angelo Basile and T. Nejat Veziroglu*
- 86 **Compendium of hydrogen energy Volume 4: Hydrogen use, safety and the hydrogen economy**  
*Edited by Michael Ball, Angelo Basile and T. Nejat Veziroglu*
- 87 **Advanced district heating and cooling (DHC) systems**  
*Edited by Robin Wiltshire*

# Preface

Challenges facing humanity today include climate change, the depletion of fossil resources, and the rapid growth of the demand for energy. These challenges drive our societies in an increasing desire to transition away from traditional fossil fuel-based energy sources and toward more renewable sources of energy, which, in general, are inherently intermittent in supply.

Within the spectrum of power devices suitable in a sustainable world, electrochemical devices for electrical energy storage, so-called batteries, are called to play a significant role. These efficient and environmentally benign technologies have great potential to become cost competitive in numerous application domains and can even make possible the emergence of revolutionary technologies for our day-by-day life. For instance, lithium ion batteries (LIBs) have contributed to the commercial success of portable electronics.

LIBs may soon dominate the electric transportation market as well because of their distinctive advantages, including their high energy density and low maintenance requirements: LIBs are among the favorite choices of electric vehicle manufacturers and are currently being used in the demonstration and deployment phase. Alternative concepts such as lithium air and lithium sulfur batteries are also the subject of increasing interest and intensive research due to their theoretical high energy densities. Additionally, the goal of creating smart grids for large-scale energy management has triggered impressive efforts to develop redox flow batteries and other similar energy-storage devices.

These efforts are set to grow exponentially in the next few years. However, one can see that breakthroughs are still needed regarding battery performance, durability, and safety so that modern, new batteries can widely and positively impact our economy.

Actually, batteries are multiscale and multiphysics systems involving different functional materials. Their design and optimization should arise from the evaluation and analysis of their numerous interfaces, microstructural features, components, and cell architectures. The rate-determining processes during their charge and discharge capabilities arise from a delicate compromise between electrochemical, charge transport, thermal, and mechanical phenomena, which strongly depend on the end-user application conditions. Moreover, the formulation and fabrication process of the composite electrodes has to be rationally designed to ensure an optimal three-dimensional ionic and electronic percolation, while minimizing the amounts of electrolyte/electronic conductor, both acting as inert materials. Hence, the optimization of the composite electrodes' formulation is the only way to achieve high-energy density batteries. The relation between the materials fabrication processes and the real-life performance of the cells is clearly a field that merits more significant research efforts.

This complexity, appearing at multiple levels, translates to the need for experimental techniques and modeling methods spanning multiple scales, multidisciplinary R&D approaches by combining materials science with electrochemical engineering, and even applied mathematics and informatics for the *in silico* design of materials, components and cells. Only a multifaceted approach with close cooperation between academics and industry can guarantee successful outcomes.

This book intends to provide a comprehensive overview of the fundamentals and practical aspects of present and future rechargeable battery technologies, with particular emphasis on LIBs and some emerging energy-storage technologies, such as lithium air batteries. The book has several illustrative chapters about state-of-the-art and emerging characterization techniques, modeling and analysis methods, materials, cells and applications.

More generally, this book should be seen as a “snapshot” of one specific technology at this specific time.

Indeed, technological “quantum jumps” are strongly expected in our electricity-based economy, such as happened during the discovery of the nanosciences and the ability to manipulate individual atoms and molecules in the 1980s. The impressive developments in computational sciences and artificial intelligence will surely play a crucial role in supporting innovative characterization techniques. These innovative approaches will allow researchers to link the chemical/microstructural properties of materials and components with their macroscopic efficiency. In combination with dedicated experiments, these approaches can potentially generate tremendous progress in designing and optimizing the next-generation cells.

But future technological “quantum jumps” should be also expected from the possible invention of devices able to directly use other forms of energy that are available in the universe, forms that we know exist (e.g., photons, neutrinos, etc.) and forms that we do not yet know the nature of or have just speculated about from our current knowledge of fundamental physics (e.g., dark energy). Electricity is only one form of energy available, and we have used it only since the end of the nineteenth century. Furthermore, history teaches us that energy forms can be used to make practical things without knowing the nature or fully understanding the fundamentals of those energy forms. This affirmation is not unrealistic: Volta described the first electric battery in 1800, almost 100 years before electrons were discovered (credited to Thomson, in 1897).

Last but not least, I address my sincere thanks to all chapter authors of this book for their great dedication and valuable contributions. I hope readers will enjoy this text. Welcome to an infinitesimally small piece of the whole energy story.

*Prof. Alejandro A. Franco  
Laboratoire de Réactivité et Chimie des Solides,  
Université de Picardie Jules Verne, Amiens, France*

# Rechargeable lithium batteries: key scientific and technological challenges

1

*M. Bini, D. Capsoni, S. Ferrari, E. Quartarone, P. Mustarelli*  
Section of Physical Chemistry, University of Pavia, Pavia, Italy

## 1.1 Introduction

At present, lithium-based batteries (LBs) are by far the most important storage systems available on the market. At the same time, however, they are still under massive development, chiefly because their use has been gradually extended from portable electronics (PEs; laptops, smartphones, camcorders, etc.), to more demanding sectors such as automotive and smart grids. It is important to state immediately that “lithium storage” is a very complex world including several chemistries characterized by largely uneven Technology Readiness Levels (TRLs), which, in turn, may also vary depending on the emitting agency. Just as an example, Table 1.1 reports the TRL scale recently adopted by EU Program Horizon 2020. Even in the frame of a given chemistry, moreover, TRLs will change depending on the application and related specs. In this chapter, we will treat three main chemistries (or chemistry families): lithium-ion, lithium–air (lithium–oxygen), and lithium–sulfur.

Lithium-ion rechargeable batteries (LIBs) are indeed the most common energy sources for today’s PEs and their use is mature, as the practically attainable specific energy density of the order of  $10^2$  Wh kg $^{-1}$  is enough to fulfill the main requirements of this market. Here the TRL is 9, which means “competitive manufacturing,” and only incremental work should be expected in the near future. But simply moving toward the electric car (EV), the performances of even the most advanced Li-ion technology (lithium iron phosphate) are indeed not enough to satisfy the market requirements, which point to 300–400 Wh kg $^{-1}$  with output power density of about  $2 \times 10^3$  W kg $^{-1}$ .

Lithium–air batteries (Li–air, both aqueous and nonaqueous) were proposed a few years ago as a possible solution for very high-energy-density applications such as in automotive [1]. As a matter of fact, the maximum theoretical energy density values are of the order of 3.5 kWh kg $^{-1}$  [2], which is lower than that of a gasoline engine by no more than a factor of three. However, many relevant practical problems must be solved (e.g., charging overpotential, side reactions, pore clogging, etc.) before these devices can be considered as industrially available [3]. A TRL of 4 (technology validated in lab) can be estimated at present, with a time-to-market of about 10–15 years. Although several relevant technological differences hold depending on the oxidant

**Table 1.1 TRL scale adopted in Horizon 2020 Work Program 2014–2015**

TRL 1	Basic principles observed
TRL 2	Technology concept formulated
TRL 3	Experimental proof of concept
TRL 4	Technology validated in lab
TRL 5	Technology validated in relevant environment (industrially relevant environment in the case of key enabling technologies)
TRL 6	Technology demonstrated in relevant environment (industrially relevant environment in the case of key enabling technologies)
TRL 7	System prototype demonstration in operational environment
TRL 8	System complete and qualified
TRL 9	Actual system proven in operational environment (competitive manufacturing in the case of key enabling technologies; or in space)

(air vs. oxygen), in the following we will not discriminate between them and use indifferently the terms Li–air and Li–O<sub>2</sub>.

Lithium–sulfur (Li–S) batteries were already patented in 1962 [4], but many relevant technological challenges, including low rate capability due to the insulating nature of Li<sub>2</sub>S, and fast capacity fading due to the formation of soluble polysulfides, have curbed their development up to now [2]. Moreover, the theoretical specific energy density is about 2.5 kWh kg<sup>−1</sup>; i.e., 30% lower than that of Li–air. Nevertheless, this chemistry is considered even more promising than the Li–air one, chiefly thanks to the expected help provided by nanotechnology in designing nanostructured materials and architectures that could overcome the problems related to the use of the bulk counterparts both in electrolyte and cathode development [5]. Here, a TRL value of 5 (technology validated in relevant environment) may be assumed at present. Sion Power developed a prototype able to deliver 350 Wh kg<sup>−1</sup>, a good value but still lower by a factor of about seven with respect to the theoretical expected one [2].

To achieve significant progress beyond commercial LB technology (i.e., LIB), various key factors must be taken into account, including energy and power density, the ability to work under severe thermal conditions, charging speed, and inherent safety of the battery cells including crash and abuse conditions. Even the aging of the new chemistries must be fully understood, in order to achieve a longer battery lifetime under safe conditions. Moreover, the future batteries must be competitive as far as cost is concerned. Finally, in the frame of a responsible research and innovation (RR&I) approach [6], which is one of the “pillars” of the European Union (EU) Horizon 2020 Program, batteries have also to be produced in an environmental friendly way, considering the availability of raw materials and the overall recycling potential, as well as a sound life cycle assessment.

## 1.2 Current market position of rechargeable lithium batteries, chiefly as far as concerns the portable electronics

The global battery market is expected to reach \$74 billion (US) in 2015. The rechargeable sector is likely to dominate the global market in 2015 with 82.6% of total revenues, with most of this from LIBs [7]. The remaining part will be covered by residual nickel-cadmium, and nickel–metal hydride chemistries. By limiting the attention to lithium batteries, roughly 90% of production in 2010 was devoted to PEs, whereas this fraction is expected to be about 60% in 2015, with automotive worth 30% and industry 10%.

Indeed, LIBs are the technology of choice for delivering power to PE devices. In contrast, at present they are not yet the ultimate choice for grid applications, chiefly because of cost and capacity performances. Other electrochemical storage systems seem competitive, at least in the short term, including lead–acid, sodium–sulfur, and vanadium redox flow batteries [8]. The first LIB generation (Sony Corporation, 1991) was produced in a standardized format, the well-known 18650 cylindrical cell. The increase in performances of the 18650 cell is reported in Figure 1.1. It is clear that only incremental improvements may be expected in the near future. At the same time, however, the demand for battery geometries with increasing energy content and for high power in reduced volume has been leading the development of alternative LIB technologies, the most important of them being the prismatic one. At present, the worldwide market is offering both standardized and nonstandardized cylindrical and prismatic batteries. In particular, prismatic ones are requested by OEMs who are developing new products and concepts in a context where size, autonomy, life cycle, and functionality must be optimized. As a matter of fact, the integration of a prismatic battery inside the

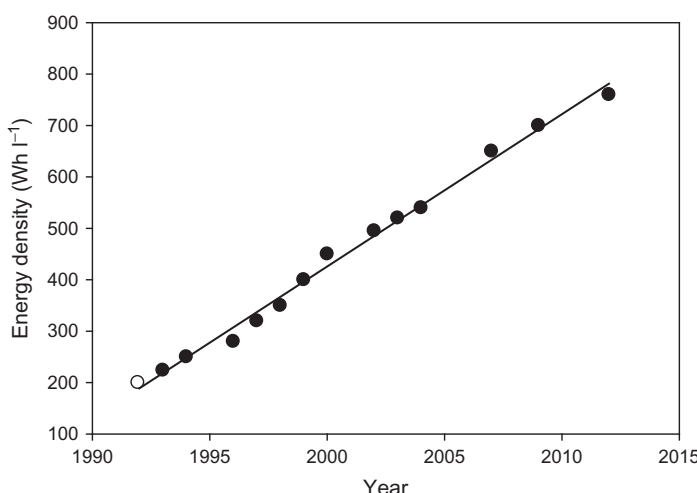


**Figure 1.1** Energy density trend of 18650 Li-ion cell.

equipment offers the advantage of saving the battery housing, because the equipment casing will protect the battery against external impacts while providing for user safety. This means that equipment will be smaller and/or that the practical capacity can increase without increasing the LIB dimensions. In turn, the higher available capacity and the miniaturization of electronics are leading to the development of more advanced electronic products' functionalities. In addition, the evolution of cycling performances of rechargeable batteries is allowing the OEM to envisage a service life that is even longer than the equipment service life itself, with no further need to replace the battery. The more recent developments point to the fabrication of flexible LIBs as a promising power source in several emerging technological fields including roll-up displays, conformable active radio-frequency identification tags, touch screens, wearable sensors, and implantable medical devices. Recently, LG commercialized the G Flex cell phone, powered by a 3500 mAh Li polymer battery [9].

## 1.3 Major fundamental and technological challenges in the development of rechargeable lithium batteries

### 1.3.1 Sources and availability of materials for lithium batteries

Since late 1990s, when the concept of the electric vehicle (EV) came out with the idea of using new promising LIBs as energy storage systems, the necessity to assess the past, present, and future trends of the lithium (Li) market, sources, and availability became an issue, especially in view of the evolution in the transportation sector from the current hybrid electric vehicles (HEV) to all electric ones. For Li-ion batteries, the typical compounds used for cathode are lithium-transition metals oxides (layered compounds, spinels) and salts (phosphates, orthosilicates, and fluorosulfates), and it is recognized that the abundance of the nonlithium elements (Mn, Fe, Co, Ni, Si, P, etc.) does not represent a limiting factor. These elements are available in larger amounts than Li, and their use in batteries requires a relatively low fraction of the total demand of these metals. The same considerations are valid also for the graphite anode.

For the Li-air and Li–S, no limits are obviously envisioned for air, but also for S, which is the 17th richest element in the earth's crust and is easily extracted in several allotrophic forms [10]. The case of lithium is different: in fact, it is expected that the growing EV diffusion will make this the main Li market during the twenty-first century [11]. The critical point of this development is surely related to lithium abundance on the earth, its extraction and availability, but it also strictly depends on less trivial parameters. In fact, it is not simply the quantity of resources that is relevant, but even its flow rate into society may be a much more difficult constraint, as in the past transient events have disrupted heavily concentrated material supply chains [12].

The main lithium resources are minerals, chiefly pegmatites and related magmatic deposits, evaporating brines, and a growing group of unusual deposits including both rocks and brines. Among pegmatites, the main lithium-containing mineral is spodumene ( $\text{LiAlSi}_2\text{O}_6$ ). Although widespread, amblygonite ( $\text{LiAlPO}_4(\text{F},\text{OH})$ ) is economically less

relevant, whereas petalite ( $\text{LiAlSi}_4\text{O}_{10}$ ), eucryptite ( $\text{LiAlSiO}_4$ ), and lepidolite ( $\text{KLi}_2\text{AlSi}_4\text{O}_{10}\text{F}_2$ ) are less common. Brines are obtained from basins containing lacustrine evaporates produced by high rates of evaporation relative to precipitation. Where these resources are present on the earth is also an important issue. The location of major lithium pegmatite and brines is shown in [Figure 1.2](#).

It can be seen that the distribution of lithium sources is not homogeneous. The main pegmatite mines are located in North and South America, Asia, and South Africa, whereas brines mainly reside in the Central Andes and China, with smaller deposits in the western United States and North Africa. Concerning lithium abundance, recent studies seem to agree that lithium sources are enough to satisfy market needs, which are estimated to be of the order 20 Mt for the present century. In fact, an amount of 21.6 Mt of Li comes from the brine deposits, 3.9 Mt from pegmatite, and 3.4 Mt from hectorite and jadarite ones. Another 2 Mt of lithium has been estimated from oilfield and geothermal brines. Therefore, a total of about 31 Mt of lithium is available.

This outlook on lithium resources, independently of the exact source, is encouraging and, at the same time, challenging. In fact, there is a rather large amount of minerals and also of lithium in the minerals, even though not yet productive, but it is also necessary to invest in the exploration and development to find new deposits, thus converting resources into reserves.

Whereas the overall lithium amount is expected to satisfy the PHEV-EV requirements until 2100 [13], the extraction of lithium is suspected to have significant environmental and social impact, especially due to water pollution and depletion. In addition, toxic chemicals are needed to process lithium. The release of such chemicals through leaching, spills, or air emissions can harm communities, ecosystems and food production [14]. A 2008 report claimed that mass production of lithium carbonate is not environmentally sound and LIB propulsion is incompatible with the notion of “Green Car” [15].



**Figure 1.2** Location of the major pegmatite (square) and brines (cross) deposits.  
Reprinted from Ref. [11] with permission of Elsevier.

### 1.3.2 Critical issues in terms of cost/performance, durability, safety, and overall life cycle

As stated in [Section 1.1](#), LIBs found large application as the primary power source in PEs. Notwithstanding their broad diffusion, to achieve a step change in LIBs performance to satisfy the demands of grid storage and transportation, breakthroughs with existing energy and power constraints are needed. Anyway, at present, LBs seem the only sustainable and promising technology able to reach the energy density required for automotive (EV) and, at least in perspective, also for storing intermittent renewable energies like solar and wind. A schematic representation of Li-ion, Li-air, and Li-S batteries is shown in [Figure 1.3](#).

LIBs commercialized so far are the result of the relevant knowledge in intercalation chemistry achieved since the 1970s. The positive electrode (cathode) is a lithium-containing material able to reversibly intercalate–deintercalate the Li ions; the negative one (anode) is made of graphite, and the electrolyte is generally based on organic solvents containing a proper lithium salt [16]. The electrochemical process can be summarized by the discharge reaction reported in [Figure 1.3](#). During charge/discharge,  $\text{Li}^+$  ions shuttle between the two electrodes, giving rise to intercalation/deintercalation processes.

The critical issues that should be addressed in a Li-ion cell are cost, safety, lifetime, and durability; to solve these problems, relevant advances in each battery component are necessary. Cathode materials should be chemically and structurally stable during the intercalation–deintercalation process; be low-cost, safe, and environmentally friendly; and should possess good electronic and ionic conductivity, work at high voltage, and have high theoretical capacity [17]. With this in mind, the first choice for a commercial battery was the  $\text{LiCoO}_2$  layered compound (theoretical capacity of  $140 \text{ mAh g}^{-1}$ ; cell voltage  $\sim 4 \text{ V}$ ) [18]. This cathode satisfied the request for good conductivity and structure stability, but it had high cost, high toxicity, safety concerns, and only about 50% of its theoretical capacity was available. Therefore, other cathode materials were considered, in particular the spinel  $\text{LiMn}_2\text{O}_4$  [19,20] and the olivine-type  $\text{LiFePO}_4$  [21,22]. Although both these materials are low cost, environmentally friendly, and safe, a severe capacity fade at elevated temperature and a limited energy made the  $\text{LiMn}_2\text{O}_4$  spinel not

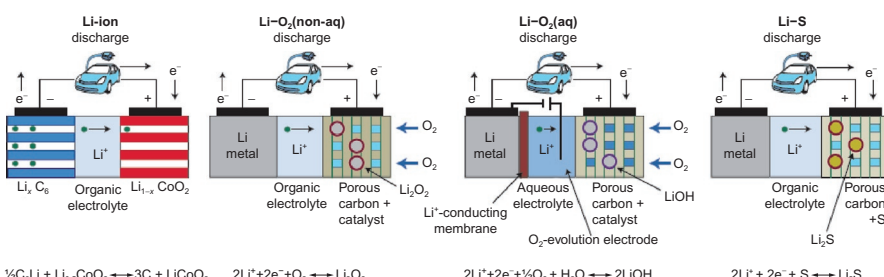


**Figure 1.3** Schematic cell design of the three main families of LBs.  
Reproduced from Ref. [2] with permission of Nature Publishing Group.

so commercially attractive, whereas the poor electronic and ionic conductivity of  $\text{LiFePO}_4$  still remain major issues for this compound [23,24]. To obtain a performance improvement of these cathode materials, a set of approaches can be used, such as fabrication of nanoparticles, so increasing the  $\text{Li}^+$  diffusion, carbon coating that improves the electronic conductivity [25,26] and, in particular for the spinel case, doping with different transition metal ions (e.g., Ni and Co) ([17] and references therein) to obtain structural stability. The use of doping ions with an oxidation state lower than +3 and/or the use of lithium excess imply the increase of the mean oxidation state of Mn from +3.5 to at least +3.6, thus suppressing the Mn Jahn–Teller distortion [27]. Moreover, the Mn substitution in the spinel structure produces interesting compounds (e.g.,  $\text{LiNi}_{0.5}\text{Mn}_{1.5}\text{O}_4$ ), working at a voltage of about 5 V, with energy densities higher than 500  $\text{Wh kg}^{-1}$ , which can be obtained at an industrial scale [17].

The most recently investigated cathode materials for Li-ion batteries are  $\text{Li}_2\text{MSiO}_4$  ( $\text{M}=\text{Fe, Mn}$ ) compounds with a theoretical capacity of about 330  $\text{mAh g}^{-1}$  for the reversible extraction/insertion of two  $\text{Li}^+$  ions per formula unit [28,29]. Anyway, relevant limiting factors such as the low electronic conductivity, the rich polymorphism, difficulties in extracting the second Li ion, and impurity phases formation during the synthesis [27,30,31] hinder the advent on the market of these orthosilicates. At present,  $\text{LiFePO}_4$  seems the most interesting cathode for Li-ions cells in terms of cost/performances and safety. Besides,  $\text{LiNi}_{1/3}\text{Mn}_{1/3}\text{Co}_{1/3}\text{O}_2$  (NMC) was shown to be an attractive alternative to  $\text{LiCoO}_2$  as high-energy-density material (volumetric energy density 2.87  $\text{Wh cm}^{-3}$  vs. 2.95  $\text{Wh cm}^{-3}$ ), with excellent thermal stability in the charged state, and is now commercialized. Recently, the research has also focused on lithium-rich systems such as  $(1-x)\text{LiMO}_2 \cdot x\text{Li}_2\text{MnO}_3$  ( $\text{M}=\text{Ni, Co}$ ) that charged above 4.5 V versus  $\text{Li}/\text{Li}^+$  and can deliver up to 250  $\text{mAh g}^{-1}$  [32].

Concerning the anode, graphite represents a good compromise to increase the cell energy while avoiding the use of lithium metal. In any case, the main drawbacks are related to the thermal stability (possible thermal runaway at moderate temperatures) and lithium plating, followed by dendrite formation [23,27]. A solution is offered by alternative anode materials; e.g., metals that can reversibly alloy with lithium such as Si, Sn, Sb, and Ge. Particularly interesting are the Si-based anodes, which could deliver up to about 3500  $\text{mAh g}^{-1}$ , depending on the alloy composition. However, practical applications of Si anodes are limited by their very huge volume variation during charge–discharge. Several Si architectures and nanocomposites have been proposed to overcome this problem [23,33].

Along with conventional intercalation materials, the attention is now moving beyond classical intercalation reactions toward materials that can store lithium through conversion reactions, such as various metal oxides, sulfides, and fluorides [34]. As an example, the conversion of  $\text{Fe}_2\text{O}_3$  is associated with a very large capacity (1007  $\text{mAh g}^{-1}$ ) but, in general, the improvement of electrode kinetics and reversibility will require many research efforts to bring these transition metal binary phases into use.

Also, the choice of the electrolyte is not trivial: it should possess low flammability, high diffusion of  $\text{Li}^+$  ions, and chemical and electrochemical stability at about 5 V. Despite the important advantage of the high ionic conductivity at ambient temperature offered by liquid electrolytes based on organic solvents, their flammability poses

serious risks for the safety of the battery. Good alternatives could be polymer electrolytes [35] for specific applications above ambient temperature, and gel polymer electrolytes that can offer improved conductivity with respect to the polymeric ones [36]. Concerning safety, the ionic liquids are very appealing [37], despite their high cost and high viscosity that limit  $\text{Li}^+$  ions diffusion and wettability of the electrodes [38].

Modern LIBs can store about four times the energy of the first Sony cell, but they are nearing their limit and, although superior to any other commercial rechargeable batteries for energy storage, cannot achieve long driving ranges such as 500 miles on a tank of gas [39]. Moreover, to start cutting down the use of gasoline (its resources are limited, it generates  $\text{CO}_2$  and other pollutants, and its price can only increase in the future) looking beyond Li-ion by exploring new chemistries is mandatory [18]. Li–sulfur and Li– $\text{O}_2$ /air batteries offer the promise of high theoretical specific energy and a gravimetric energy density similar to that of gasoline; moreover, their low weight is surely an added value. As already stated, the Li–S battery was first proposed in the early 1960s, whereas the first reported demonstration of a nonaqueous Li– $\text{O}_2$  cell dates back to 1996 [40]. Although Li–air and Li–S share the same anode and have active cathode components, there are important differences related to the different chemistry of  $\text{O}_2$  and S.

The electrochemical reactions in the Li–air cells are complex and not yet completely addressed [41]. The main processes are summarized in Figure 1.3 and strictly depend on the electrolyte that can be nonaqueous or aqueous [1]. In the second case, we need to distinguish between alkaline and acidic media, the former being the most investigated.

Focusing attention on the Li–air cells with nonaqueous electrolyte, many issues must be addressed for cathode, anode, and electrolyte. The cathode is typically constituted by a porous carbon to allow the diffusion of  $\text{O}_2$ , which is the other reactant with lithium in the electrochemical process. Recently, TiC [42] and porous gold [43] electrodes were investigated by Bruce and coworkers. Different configurations of the cathode were proposed to minimize the problems associated with the oxygen reduction reaction (ORR) and the oxygen evolution reaction (OER) [44,45]. In fact, the carbon material should have the following:

- (i) High surface area, to allow a good contact with  $\text{O}_2$ , its easy diffusion, and guarantee a good electrolyte permeation.
- (ii) Proper porosity and pore size distribution. This is an important feature because, if the pores are large, much of the volume of the electrode may be inactive; if they are too small, the reaction product (insoluble  $\text{Li}_2\text{O}_2$  and  $\text{Li}_2\text{O}$ ) may clog the pores. So, a narrow pore size distribution in the range of 10–100 nm is desirable [46]. In this framework, multiscale modeling is becoming a helpful tool [47,48].
- (iii) A  $\text{O}_2$ -selective membrane, to prevent the contact of battery components with  $\text{CO}_2$  and  $\text{H}_2\text{O}$  from the atmosphere, allow a proper flow of oxygen, and retard the evaporation of the organic solvents out of the cell [49].
- (iv) A proper binder with enough chemical and electrochemical stability to avoid parasitic reactions that limit the performance of the battery.

The high overpotential associated with the ORR and OER, due to the sluggish kinetics of these reactions, is a major problem of this technology that could be solved by means of proper catalysts. Different metals (Pt, Au, Ru, Pd) and oxides catalyst with a proper

particle size and distribution (loading) on the carbon were tested and seemed to improve the cyclability of the cells [44].

In Li–air batteries, the anode is typically lithium metal. Whereas it contributes to obtain very high energy density, it suffers from some of the following problems [3]:

- (i) Dendrite formation that is detrimental for the correct functioning of the cell.
- (ii) Low cycling efficiency.
- (iii) Possible corrosion and consumption in contact with the electrolyte. A correct choice of the electrolyte is important and a stable solid electrolyte interface (SEI) layer is required.
- (iv) Safety concerns: lithium metal is highly reactive and it is hard to find the proper electrolyte to limit highly exothermic reactions.

Recent research also focuses on the electrolyte [23,50,51], which is considered to have the major responsibility for the performances of the electrodes. In addition to the standard requirements, an electrolyte for Li–air cells should also be:

- (i) stable to oxidation/reduction and toward reduced  $O_2$  species within the voltage range of the cell [52];
- (ii) negligibly volatile to avoid evaporation at the interface of the gas phase;
- (iii) capable of wetting the electrode surface; and
- (iv) a good solvent for  $O_2$  to ensure satisfactory rate capability.

The task to find a proper electrolyte showing all these features is really a challenge. It has been proven that the organic carbonate electrolytes, successfully employed in the Li-ions cells, are not stable and suitable in the Li–air case, due to their reaction with the  $O_2^-$  species that provide a nucleophilic attack to the organic carbonate. Better results were obtained with ether-based electrolytes (e.g., tetraglyme, DME, and PEO), which are less reactive toward the  $O_2^-$  species [23,53]. Interesting alternatives are the Li-ion ceramic electrolytes (LAGP) [54] and the ionic liquids (ILs) [55], but advantages and disadvantages of these compounds are still under investigation.

Concerning the Li–air cells with aqueous electrolyte (see Figure 1.3), some issues are common to those already discussed for the cells with nonaqueous electrolyte. An advantage in the use of aqueous electrolyte resides in the fact that the membrane for the cathode should be selective only for the  $CO_2$ , which can form the undesired  $Li_2CO_3$  [3]. In alkaline media the discharge product is  $LiOH$ , whose concentration rapidly increases, reaching the solution saturation and forming a precipitate. In these conditions, the Li–air cells will deliver a specific capacity barely higher than that of a Li-ion cell. To increase the capacity, two approaches seem viable: the use of a flow cell, where the electrolyte is constantly replenished [56], and an anionic exchange membrane to separate the cathode from the electrolyte, which blocks the  $Li^+$  entering the electrode, preventing the  $LiOH$  precipitation in the pores of the carbon cathode. The use of catalysts to enhance ORR and OER in Li–air batteries was also considered. In the case of aqueous electrolyte, the use of a proper catalyst (typically Pt, but also other manganese oxides and perovskites are under consideration) for the cleavage of the  $O-O$  bond to reduce  $O_2$  to  $OH^-$  is mandatory [56,57].

The use of an aqueous electrolyte also implies the need for Li anode protection. The most common protection is a ceramic conducting membrane such as LISICON;

however, this presents a nontrivial problem: it is reduced in contact with Li and Li<sub>2</sub> ceramic interphase is difficult to cycle. This problem could be solved with the introduction of a LIPON interlayer or a thin film of a nonaqueous liquid or gel electrolyte. Moreover, the membrane itself can be attacked by the alkaline electrolyte, thus increasing the overall impedance of the cell, and the LiOH precipitation in the membrane can clog its pores, too. A conducting polymer on the electrolyte side of the ceramic can overcome the problem [58]. It can be seen that all these protections lead to a very complex design of the device, thus making the expected time-to-market very long.

The other promising battery that meets tomorrow's energy storage demand is the Li–S cell. Thanks to the light weight of sulfur, this cell can deliver theoretical capacities of about 2500 Wh Kg<sup>-1</sup> and an energy density of 2199 Wh l<sup>-1</sup>, a value at least five times higher at a much lower cost of the commercial Li-ion cells [23]. A schematic representation of the cell is reported in Figure 1.3. The main discharge reaction forms Li<sub>2</sub>S, an insoluble sulfide. Another possible insoluble product is Li<sub>2</sub>S<sub>2</sub>, but a series of polysulfides richer in sulfur and typically soluble in the liquid electrolyte usually forms [10]. These polysulfides play a main role in the electrochemical performances of the cell, in particular on the rapid capacity fading of the battery. The phenomenon, known as "polysulfides shuttle," comes from the formation at the sulfur cathode of high-order polysulfides (Li<sub>2</sub>S<sub>n</sub> with  $n \geq 4$ ) that can migrate to the Li anode and react to form low-order polysulfides or even the insoluble Li<sub>2</sub>S and Li<sub>2</sub>S<sub>2</sub> compounds. The low-order polysulfides can rediffuse toward the cathode and can give oxidation to higher-order polysulfides; this migration can be repeated several times and is responsible for the capacity fading of the Li–S cell [59,60]. The solid reduction products and the sulfur itself are responsible for poor electrode rechargeability and for limited rate capability.

The cathode active material is sulfur, typically S<sub>8</sub>; unfortunately, it is not directly applicable due to its insulating character, and because, during cycling, it undergoes a solid–solid phase transformation that passes through a series of intermediate polysulfides. These polysulfides can also migrate to the anode and can be accommodated into a porous structure to give reoxidation. To increase the electronic conductivity of sulfur, it should be combined with a conducting, nonactive, and porous material (i.e., typically carbon). A high porosity is also needed to accommodate the significant volume increase (79%) when elemental sulfur passes to Li<sub>2</sub>S [10]. However, this carbon addition leads to a decrease of the capacity with respect to the theoretical one; the advantages of the Li–S cell can be maintained with at least a 70% wt of sulfur in the cathode. The simple mixing of carbon and sulfur was first used to prepare the cathode, but low capacities and poor discharge/cycling were observed, due to a nonoptimized electrical contact. In this regard, the addition of a binder such as PEO or PVdF may contribute to maintain the integrity of the electrode during cycling, by buffering the huge volume changes during the solid–solid state transformation from S to Li<sub>2</sub>S or Li<sub>2</sub>S<sub>2</sub>. [61]. More recently, other approaches and more complex cathodes configurations were proposed, such as carbon coating on sulfur particles, S/MWCNT composites, use of mesoporous carbons, and 3-D architectures based on graphene or graphene oxide sheets [59,62].

Another proposed configuration of the Li–S cell is based on the use of Li<sub>2</sub>S cathode [2,59]. This cathode presents the same but reverse electrochemical reaction with sulfur and maintains also an interesting theoretical capacity of about 1166 mAh g<sup>-1</sup>.

A significant advantage of this cathode design is that Li metal anodes can be avoided, thereby eliminating all the related safety and stability problems. Nevertheless, several problems are still present:  $\text{Li}_2\text{S}$  is highly hydroscopic and unstable in air, and possesses poor ionic and electronic conductivity. To solve the last problem, a combination with carbon is desired. Recent research is active in investigating other sulfides ( $\text{MoS}_2$ ,  $\text{FeS}_2$ , organic sulfides) as potential cathodes that can be converted into  $\text{Li}_2\text{S}$  upon deep discharge.

The anode is typically Li metal. In addition to the dendrite formation, which is not so severe as in the cases of the other Li anode batteries, other problems related to its use have been identified: reaction with the electrolyte, which forms gaseous and solid products causing capacity fading; and reaction with the soluble polysulfides, which may cause thermal runaway, low coulombic efficiency, and rough morphology of Li plating [10]. To prevent these problems, a protection layer on Li anode is mandatory. A limited number of materials can be used, due to the high reactivity of lithium. The most important methods proposed for anode protection are a physical barrier layer [63], the use of solid or gel polymer electrolytes [64], a prepassivation layer [65], and Li alloying [66]. Metallic Li-free anodes, such as those based on Si and Sn, have been also proposed, due to the ease in forming alloys with Li. Also, in this case, the same limiting factors discussed about LIBs still hold.

The electrolyte plays a relevant role in Li–S batteries, due to its close interactions with the electrodes during cycling. The cell performances can be dramatically influenced by the different solubility of polysulfides in various electrolyte solvents. It has been demonstrated that polysulfides can react with the most common electrolyte solvents, such as esters, carbonates, and phosphates. So, the most suitable solvents are the linear and cyclic ethers, such as DME, DOL and TEGDME, and their mixtures, that can dissolve polysulfides very well due to their high basicity [59,60]. Concerning the Li salts, the classical  $\text{LiPF}_6$ ,  $\text{LiBF}_4$ , and  $\text{LiBOB}$  were investigated and it was demonstrated that they can react with polysulfides and cannot be used with DOL. Both LiTFS and LiTFSI, which can be used to obtain electrolytes with good stability, unfortunately dissolve Al substrate and stainless-steel current collectors [10]. An alternative is offered by the use of additives such as  $\text{LiNO}_3$  and  $\text{P}_2\text{S}_5$  in the liquid electrolyte, which can cause the passivation of the anode surface [59,60].

An interesting application of ILs as the electrolyte is they improve cell safety due to their low vapor pressure and nonflammability. But, at the moment, they do not seem as promising in the Li–S devices, due to high viscosity that limits the shuttle of polysulfides and  $\text{Li}^+$  transport, so reducing the sulfur specific capacity at high discharge rates.

Solid-state electrolytes seem really promising in replacing the liquid ones due to their superior voltage, temperature, and mechanical stability [60]. They act as separators of the electrodes and confine the polysulfides near the cathode. Both gel and solid polymer electrolytes, such as PEO, PEGDME, and PVdF-HFP, have been investigated; the main reported problem is their low ionic conductivity at room temperature. This disadvantage can be overcome by using inorganic solid electrolytes.

Although radical redesigns seem the only way to overcome Li-ion limitations, it is worth mentioning that recent work has demonstrated that significant performance enhancements can be achieved by engineering the electrodes' microstructure.

Li-ion battery cathodes and anodes are composites consisting of both active and inactive (binder and conductive carbon) materials, and the optimization of electrodes' composition and microstructure is crucial for the fabrication of batteries with higher performances. Tailoring of the particle size polydispersity, surface area density, and roughness is of tremendous importance to maximize charge capacity and device reliability [67,68]. The complexity of the chemical and electrochemical reactions occurring in LIBs is influenced by each single component and mixture of components, and production techniques can lead to heterogeneous transport processes and concentration gradients that adversely affect battery response [69]. The combination of developments in electrode architectures with changes of electrodes' chemical composition offer excellent opportunities for commercialization of next generation Li-ion batteries and emerging alternative chemistries.

### 1.3.3 *Goals and technological roadmaps*

In the past two years, LIB technology has emerged as the faster-growing platform for stationary storage applications in the United States [8]. The large manufacturing scale of Li-ion batteries (about 30 GWh by 2015) will result in potentially lower-cost battery packs, which could also be used and integrated into systems for grid-support services. Many stationary systems have been deployed in early field trials to gain experience in siting, grid integration, and operation. Numerous small demonstration systems in the 5–25 kW size are currently underway. MW-scale short-energy-duration systems are being operated in frequency regulation applications. The expected life cycle target is 5000 cycles/year.

Concerning the automotive sector, the USABC midterm target is to reduce the pack cost from about \$1000 to \$300/kWh. The specific energy at C/3 discharge rate is expected to increase from 150 to 200 Wh kg<sup>-1</sup>. The normal recharge time is expected to reach 3 h [70]. The NEDO (Japan) roadmap points to 250 Wh kg<sup>-1</sup> for 2020 at a price of about 30,000 yen kWh<sup>-1</sup>, in fair agreement with the expected USABC's cost.

## 1.4 Future trends and developments

Lithium batteries represent a revolutionary technology in renewable energy storage, not only for PE devices but also for transportation. In the automotive field, however, some important questions are still open. In spite of the enormous advances obtained in the recent past in terms of cell performance, today the lithium-ion batteries have insufficient energy or life for use in vehicles to match the performance of internal combustion engines. In addition, such devices suffer serious safety problems, related to the thermal runaway and flammability of the electrolyte components. In particular, this topic has gained growing interest as the number of battery incidents rapidly increased. Due to the rich chemistry of lithium, great progress has been made in this technology by developing advanced materials for both electrodes and electrolyte and innovative strategies to further improve the energy density, lifetime, and safety of the cells. Enhancement in energy density of factors of 2–3, for instance, have been reached

by means of novel electrodes, like high potential systems as cathodes, namely  $\text{LiMn}_{1.5}\text{Ni}_{0.5}\text{O}_4$  or  $\text{LiMPO}_4$ . The insertion materials, however, show low Li diffusivity and the insertion reaction involves only one electron transfer for transition metal. All these aspects limit the power demands and the specific energy of the batteries. A promising alternative to the insertion materials is represented by the conversion electrodes based on multivalent cations, which may basically offer more than one electron per redox event. They involve electrochemical reduction of metal oxides, sulfides, nitrides, fluorides, and phosphides with different degrees of reversibility. The conversion electrodes show greater capacity, but suffer from a remarkable hysteresis in voltage between charge and discharge, so providing poor energy efficiency and voltages. For this reason, these kinds of materials offer huge areas of future advances, both in terms of material developments and electrode design. Significant improvements in the electrode kinetics, control of the damaging strain and reaction pathways may be further reached by switching to nanostructures, which are differently possible by means of the continuous progresses of nanotechnology.

Silicon-based or graphene-related materials seem to offer tremendous improvement in specific Li storage capacity. In addition, metals reversibly alloying with Li, including Sn,  $\text{SnO}$ , Sb, Ge, and others, basically provide excellent performance, mostly if produced with properly tailored nanoarchitectures to reduce the volume expansion caused by the Li insertion/extraction processes.

Electrolytes also provide extraordinary opportunities for innovative research to find systems that are stable in the working conditions over a broad voltage window and wide temperature range. Recently, many efforts were made to optimize the electrolyte thermal stability, particularly in case of carbonate-based liquid electrolytes. In order to reduce the thermal runaway risk, Li-doped ionic liquids, novel flame retardant additives, as well as fluorine-based solvents may be further developed. The solid polymer (SPE), polymeric ionic liquids (PIL) and polymer-in-salt electrolytes also are very promising and still up-to-date systems, which are thought to improve battery safety, due to the absence of any solvent and to a higher thermal resistance.

The pursuit of next-generation rechargeable high-energy-density sources, however, is devoting a lot of attention to Li-air and Li-S batteries. Even if considerable work is still needed to make them reliable, such technology will definitely challenge Li-ion supremacy in the near future.

Finally, sodium, magnesium, and organic-electrode batteries are other quickly emerging power topics in the development of low-cost rechargeable batteries from natural, abundant, and easy-access resources. They will become the main and innovative directions of postlithium devices with large power density to build up a low carbon society based on renewable and sustainable energy.

## 1.5 Sources of further information

In addition to the abundant scientific literature and numerous patents and books available on LBs, the scientific community is also served by other sources of primary information, which may be easily explored on online portals. Some of the most useful dissemination media are briefly suggested in the following:

- The *Office of Energy Efficiency and Renewable Energy* (EERE) aims at focusing the U.S. DOE's efforts to develop and facilitate the sustainable transportation and the energy efficiency and renewable energy technologies, including the Li batteries-based ones. A lot of information in terms of technological targets, publications, jobs, education, training, technical assistance, energy analysis, and so on may be found at the Web site <http://www.energy.gov/eere>.
- Another source of advances in LBs is also available at the Web page of *Alistore-ERI* ([www.alistore.eu](http://www.alistore.eu)). Alistore-ERI is a contractual structure composed of about 20 European countries with the common aim to develop and disseminate research strategy and programs in the renewable energy storage area, especially devoted to the Li-battery field. Several technical documents for downloading are available as well as a list of the main research groups involved in the activities on LIBs and platforms of advanced characterization techniques available in several institutes or universities.
- Sources of information also include *Knowledge Foundation* (<http://www.knowledgefoundation.com>) and *Shmuel De-Leon Energy Ltd* (<http://www.sdle.co.il>). Both of them provide, for a fee, the most recent updates about energy storage events, upcoming industry events, and conferences on several aspects of lithium batteries. Such information services also offer power databases, digital libraries, patents, consulting services, and related links.

## References

- [1] G. Girishkumar, B. McCloskey, A.C. Luntz, S. Swanson, W. Wilcke, Lithium-air battery: promise and challenges, *J. Phys. Chem. Lett.* 1 (2010) 2193–2203.
- [2] P.G. Bruce, S.A. Freunberger, L.J. Hardwick, J.-M. Tarascon, Li–O<sub>2</sub> and Li–S batteries with high energy storage, *Nat. Mater.* 11 (2012) 19–29.
- [3] D. Capsoni, M. Bini, S. Ferrari, E. Quartarone, P. Mustarelli, Recent advances in the development of Li-air batteries, *J. Power Sources* 220 (2012) 253–263.
- [4] D. Herbert, J. Ulam, US Patent US3043896 (1962).
- [5] D. Bresser, S. Passerini, B. Scrosati, Recent progress and remaining challenges in sulfur-based lithium secondary batteries—a review, *Chem. Commun.* 49 (2013) 10545–10562.
- [6] [http://ec.europa.eu/research/science-society/document\\_library/pdf\\_06/options-for-strengthening\\_en.pdf](http://ec.europa.eu/research/science-society/document_library/pdf_06/options-for-strengthening_en.pdf).
- [7] Battery Power—2010 Resource Guide, vol. 14, Issue 4.
- [8] DOE/EPRI 2013 Electricity Storage Handbook.
- [9] <http://www.lg.com/us/mobile-phones/gflex/specifications.jsp>.
- [10] S.S. Zhang, Liquid electrolyte lithium/sulfur battery: fundamental chemistry, problems, and solutions, *J. Power Sources* 231 (2013) 153–162.
- [11] S.E. Kesler, P.W. Gruber, P.A. Medina, G.A. Keoleian, M.P. Everson, T.J. Wallington, Global lithium resources: relative importance of pegmatite, brine and other deposits, *Ore Geol. Rev.* 48 (2012) 55–69.
- [12] C. Grosjan, P. Herrera Miranda, M. Perrin, P. Poggi, Assessment of world lithium resources and consequences of their geographic distribution on the expected development of the electric vehicle industry, *Renew. Sustain. Energy Rev.* 16 (2012) 1735–1744.
- [13] P.W. Gruber, P.A. Medina, G.A. Keoleian, S.E. Kesler, M.P. Everson, T.J. Wallington, Global lithium availability: a constraint for electric vehicles? *J. Ind. Ecol.* 15 (2011) 760–775.
- [14] Democracy Center Special Report, Bolivia and its lithium: can the “Gold of the 21<sup>st</sup> Century” help lift a nation out of poverty? 2010. <http://www.ifg.org/pdf/DClithiumfullreportenglish.pdf>.

- [15] Meridian International Research, “The Trouble with Lithium 2” (2008).
- [16] K. Xu, Nonaqueous liquid electrolytes for lithium-based rechargeable batteries, *Chem. Rev.* 104 (2004) 4303–4417.
- [17] C.M. Julien, A. Mauger, Review of 5-V electrodes for Li-ion batteries: status and trends, *Ionics* 19 (2013) 951–988.
- [18] K. Amine, R. Kanno, Y. Tzeng, Rechargeable lithium batteries and beyond: progress, challenges, and future directions, *MRS Bull.* 39 (2014) 395–401.
- [19] C.S. Johnson, N.C. Li, C. Lefief, J.T. Vaughey, M.M. Thackeray, Synthesis, characterization and electrochemistry of “composite” lithium battery electrodes:  $x\text{Li}_2\text{MnO}_3 \cdot (1-x)\text{LiMn}_{0.333}\text{Ni}_{0.333}\text{Co}_{0.333}\text{O}_2$  ( $0 \leq x \leq 0.7$ ), *Chem. Mater.* 20 (2008) 6095–6106.
- [20] K. Ariyoshi, Y. Maeda, T. Kawai, T. Ohzuku, Effect of primary particle size upon polarization and cycling stability of 5-V lithium insertion material of  $\text{Li}[\text{Ni}_{1/2}\text{Mn}_{3/2}]\text{O}_4$ , *J. Electrochem. Soc.* 158 (2011) A281–A284.
- [21] M.S. Wittingham, Lithium batteries and cathode materials, *Chem. Rev.* 104 (2004) 4271–4301.
- [22] B. Ellis, W.H. Kan, W.R.M. Makahnouk, L.F. Nazar, Synthesis of nanocrystals and morphology control of hydrothermally prepared  $\text{LiFePO}_4$ , *J. Mater. Chem.* 17 (2007) 3248–3254.
- [23] N.-S. Choi, Z. Chen, S.A. Freunberger, X. Ji, Y.-K. Sun, H. Amine, G. Yushin, L.F. Nazar, J. Cho, P.G. Bruce, Challenges facing lithium batteries and electrical double-layer capacitors, *Angew. Chem. Int. Ed.* 51 (2012) 9994–10024.
- [24] S. Ferrari, R. Lassarote Lavall, D. Capsoni, E. Quartarone, A. Magistris, P. Mustarelli, P. Canton, Influence of particle size and crystal orientation on the electrochemical behavior of carbon-coated  $\text{LiFePO}_4$ , *J. Phys. Chem. C* 114 (2010) 12598–12603.
- [25] H. Liu, C. Miao, Y. Meng, Y.-B. He, Q. Xu, X. Zhang, Z. Tang, Optimized synthesis of nano-sized  $\text{LiFePO}_4/\text{C}$  particles with excellent rate capability for lithium ion batteries, *Electrochim. Acta* 130 (2014) 322–328.
- [26] K. Zaghib, J. Dubé, A. Dallaire, K. Galoustov, A. Guerfi, M. Ramanathan, A. Benmayza, J. Prakash, A. Mauger, C.M. Julien, Enhanced thermal safety and high power performance of carbon-coated  $\text{LiFePO}_4$  olivine cathode for Li-ion batteries, *J. Power Sources* 219 (2012) 36–44.
- [27] A. Manthiram, Materials challenges and opportunities of lithium ion batteries, *J. Phys. Chem. Lett.* 2 (2011) 176–184.
- [28] M.S. Islam, R. Dominko, C. Masquelier, C. Sirisopanaporn, A.R. Armstrong, P.G. Bruce, Silicate cathodes for lithium batteries: alternatives to phosphates, *J. Mater. Chem.* 21 (2011) 9811–9818.
- [29] A. Nyten, A. Abouimrane, M. Armand, T. Gustafsson, J.O. Thomas, Electrochemical performance of  $\text{Li}_2\text{FeSiO}_4$  as a new Li-battery cathode material, *Electrochim. Commun.* 7 (2005) 156–160.
- [30] S. Ferrari, D. Capsoni, S. Casino, M. Destro, C. Gerbaldi, M. Bini, Electrochemistry of orthosilicate-based lithium battery cathodes: a perspective, *Phys. Chem. Chem. Phys.* 16 (2014) 10353–10366.
- [31] M. Bini, S. Ferrari, C. Ferrara, M.C. Mozzati, D. Capsoni, A.J. Pell, G. Pintacuda, P. Canton, P. Mustarelli, Polymorphism and magnetic properties of  $\text{Li}_2\text{MSiO}_4$  ( $\text{M} = \text{Fe, Mn}$ ) cathode materials, *Sci. Rep.* 3 (2013) 3452.
- [32] H. Koga, L. Crogueennec, P. Mannessiez, M. Menetrier, F. Weill, L. Burgeois, M. Duttine, E. Suard, C. Delmas,  $\text{Li}_{1.20}\text{Mn}_{0.54}\text{Co}_{0.13}\text{Ni}_{0.13}\text{O}_2$  with different particle sizes as attractive positive electrode materials for lithium-ion batteries: insights into their structure, *J. Phys. Chem. C* 116 (2012) 13497–13506.

- [33] H. Wu, Y. Cui, Designing nanostructured Si anodes for high energy lithium ion batteries, *Nano Today* 7 (2012) 414–429.
- [34] J. Cabana, L. Monconduit, D. Larcher, M.R. Palacin, Beyond intercalation-based Li-ion batteries: the state of the art and challenges of electrode materials reacting through conversion reactions, *Adv. Mater.* 22 (2010) E170–E192.
- [35] F. Kaneko, S. Wada, M. Nakayama, M. Wakihara, J. Koki, S. Kuroki, Mechanism in all solid-state lithium polymer secondary batteries using PEG-borate/aluminate ester as plasticizer for polymer electrolytes, *Adv. Funct. Mater.* 19 (2009) 918–925.
- [36] Z.H. Chen, L.Z. Zhang, R. West, K. Amine, Gel electrolyte for lithium-ion batteries, *Electrochim. Acta* 53 (2008) 3262–3266.
- [37] M. Galinski, A. Lewandowski, I. Stepnak, Ionic liquids as electrolytes, *Electrochim. Acta* 51 (2006) 5567–5580.
- [38] E. Markevich, V. Baranchugov, G. Salitra, D. Aurback, M.A. Schmidt, Behavior of graphite electrodes in solutions based on ionic liquids in *in situ* Raman studies, *J. Electrochem. Soc.* 155 (2008) A132–A137.
- [39] R. Van Noorden, The rechargeable revolution: a better battery, *Nature* 507 (2014) 26–28.
- [40] K.M. Abraham, Z. Jiang, A polymer electrolyte based rechargeable lithium/oxygen battery, *J. Electrochem. Soc.* 143 (1996) 1–5.
- [41] I. Landa-Medrano, I. Ruiz de Larramendi, N. Ortiz-Vitoriano, R. Pinedo, J.I. Ruiz de Larramendi, T. Rojo, In situ monitoring of discharge/charge processes in Li–O<sub>2</sub> batteries by electrochemical impedance spectroscopy, *J. Power Sources* 249 (2014) 110–117.
- [42] M.M. Ottakam Thotiyil, S.A. Freunberger, Z. Peng, Y. Chen, L. Ziu, P.G. Bruce, A stable cathode for the aprotic Li–O<sub>2</sub> battery, *Nat. Mater.* 12 (2013) 1050–1056.
- [43] Z. Peng, S.A. Freunberger, Y. Chen, P.G. Bruce, A reversible and higher-rate Li–O<sub>2</sub> battery, *Science* 337 (2012) 563–566.
- [44] N. Garcia-Araez, P. Novak, Critical aspects in the development of lithium-air batteries, *J. Solid State Electrochem.* 17 (2013) 1793–1807.
- [45] R. Padbury, X. Zhang, Lithium–oxygen batteries—limiting factors that affect performance, *J. Power Sources* 196 (2011) 4436–4444.
- [46] P. Andrei, J.P. Zheng, M. Hendrickson, E.J. Plichta, Some possible approaches for improving the energy density of Li-air batteries, *J. Electrochem. Soc.* 157 (2010) A1287–A1295.
- [47] K.H. Xue, T.K. Nguyen, A.A. Franco, Impact of the cathode microstructure on the discharge performance of lithium air batteries: a multiscale model, *J. Electrochem. Soc.* 161 (2014) E3028–E3035.
- [48] A.A. Franco, K.H. Xue, Carbon-based electrodes for lithium air batteries: scientific and technological challenges from a modeling perspective, *ECS J. Solid State Sci. Technol.* 2 (2013) M3084.
- [49] O. Crowther, B. Meyer, M. Morgan, M. Salomon, Primary Li-air cell development, *J. Power Sources* 196 (2011) 1498–1502.
- [50] S. Meini, N. Tsivouvaras, K. Uta Schwenke, M. Piana, H. Beyer, L. Lange, H.A. Gasteiger, Rechargeability of Li-air cathodes pre-filled with discharge products using an ether-based electrolyte solution: implications for cycle-life of Li-air cells, *Phys. Chem. Chem. Phys.* 15 (2013) 11478–11493.
- [51] H.-G. Jung, J. Hassoun, J.-B. Park, Y.-K. Sun, B. Scrosati, An improved high-performance lithium-air battery, *Nat. Chem.* 4 (2012) 579–585.
- [52] R. Black, S.H. Oh, J.H. Lee, T. Yim, B. Adams, L.F. Nazar, Screening for superoxide reactivity in Li–O<sub>2</sub> batteries: effect on Li<sub>2</sub>O<sub>2</sub>/LiOH crystallization, *J. Am. Chem. Soc.* 134 (2012) 2902–2905.

- [53] X. Guo, N. Zhao, The role of charge reactions in cyclability of lithium–oxygen batteries, *Adv. Energy Mater.* 3 (2013) 1413–1416.
- [54] B. Kumar, J. Kumar, R. Leese, J.P. Fellner, S.J. Rodrigues, K.M. Abraham, A solid-state, rechargeable, long cycle life lithium-air battery, *J. Electrochem. Soc.* 157 (2010) A50–A54.
- [55] T. Kuboki, T. Okuyama, T. Ohshaki, N. Takami, Lithium-air batteries using hydrophobic room temperature ionic liquid electrolyte, *J. Power Sources* 146 (2005) 766–769.
- [56] P. He, Y. Wang, H. Zhou, A Li-air fuel cell with recycle aqueous electrolyte for improved stability, *Electrochem. Commun.* 12 (2010) 1686–1689.
- [57] T. Zhang, N. Imanishi, Y. Shimonishi, A. Hirano, J. Xie, J. Takeda, O. Yamamoto, N. Sammes, Stability of a water-stable lithium metal anode for a lithium-air battery with acetic acid–water solutions, *J. Electrochem. Soc.* 157 (2010) A214–A218.
- [58] T. Zhang, N. Imanishi, Y. Takeda, O. Yamamoto, Aqueous lithium/air rechargeable batteries, *Chem. Lett.* 40 (2011) 668–673.
- [59] M.K. Song, E.J. Cairns, Y. Zhang, Lithium/sulfur batteries with high specific energy: old challenges and new opportunities, *Nanoscale* 5 (2013) 2186–2204.
- [60] Y.X. Yin, S. Xin, Y.G. Guo, L.G. Wan, Lithium–sulfur batteries: electrochemistry, materials, and prospects, *Angew. Chem. Int. Ed.* 52 (2013) 13186–13200.
- [61] M. Rao, X. Song, H. Liao, E.J. Cairns, Carbon nanofiber–sulfur composite cathode materials with different binders for secondary Li/S cells, *Electrochim. Acta* 65 (2012) 228–233.
- [62] A. Manthiram, Y. Fu, Y.S. Su, Challenges and prospects of lithium–sulfur batteries, *Acc. Chem. Res.* 46 (2013) 1125–1134.
- [63] J.Y. Kim, Y.G. Ryu, US Patent 20050042503 (2005).
- [64] Y. Mikhaylik, I. Kovalev, R. Schock, K. Kumaresan, J. Xu, J. Affinito, High energy rechargeable Li–S cells for EV application: status, remaining problems and solutions, *ECS Trans.* 25 (2010) 23–34.
- [65] Y.S. Nimon, M.Y. Chu, S.Y. Visco, US Patent 6632573 (2003).
- [66] M.S. Zheng, J.J. Chen, Q.F. Dong, The enhanced electrochemical performance of lithium/sulfur battery with protected lithium anode, *Adv. Mater. Res.* 476–478 (2012) 676–680.
- [67] H. Zheng, R. Yang, G. Liu, X. Song, V.S. Battaglia, Cooperation between active material, polymeric binder and conductive carbon additive in lithium ion battery cathode, *J. Phys. Chem. C* 116 (2012) 4875–4882.
- [68] D.-W. Chung, P.R. Shearing, N.P. Brandon, S.J. Harris, R.E. Garcia, Particle size polydispersity in Li-ion batteries, *J. Electrochem. Soc.* 161 (2014) A422–A430.
- [69] M. Osiak, H. Geaney, E. Armstrong, C. O'Dwyer, Structuring materials for lithium-ion batteries: advancements in nanomaterial structure, composition, and defined assembly on cell performance, *J. Mater. Chem. A* 2 (2014) 9433–9460.
- [70] 2012 DOE Vehicle Technologies Program Review.

# Materials for positive electrodes in rechargeable lithium-ion batteries

2

*F. Liu<sup>1</sup>, P.P. Mukherjee<sup>2</sup>*

<sup>1</sup>University of Texas, Arlington, TX, USA; <sup>2</sup>Texas A&M University, College Station, TX, USA

## 2.1 Introduction

Lithium-ion batteries (LiBs) first appeared in the market in the 1990s with the promise of high energy density. Since then, the demand for LiBs increased exponentially and by now already crossed \$13 billion value [1]. The battery technology can be advanced through improving materials, design, and employing better battery management practices. Among these, developing new positive electrode materials is critical to battery safety, durability, performance, charge/discharge capacities, energy density, and cost.

Extensive research has already been devoted to improvement of LiB performance through developing electrode materials [2–6], reducing particle size [7], and optimizing shape [8,9] of active material particles of the electrode, and using different additives [10–12]. In this chapter, details of LiB positive materials, their attributes, and phase transition behaviors are discussed. In addition, experimental and theoretical aspects of phase transformation phenomena will be briefly introduced, and then a summary and outlook.

## 2.2 Overview of different metal oxide cathode materials

Several criteria should be satisfied for candidate cathode or anode materials in rechargeable LiBs. Some of the most important criteria are listed below:

- Low lithium chemical potential of the cathode and high lithium chemical potential of the anode to maximize the cell voltage.
- Large amount of lithium insertion/extraction per unit weight or per unit volume to maximize cell capacity (Ah/L or Ah/kg). This depends on the coordination number of the lithium site and chemistry of the host materials.
- No significant internal strain in the host material during reversible insertion/extraction of lithium. This ensures long cyclability of the battery with no or minimal structure change.
- High electronic conductivity and high lithium-ion conductivity to facilitate fast charge/discharge (rate capability).
- Chemically and thermally stable without undergoing any reaction with the electrolyte. The redox energies of the electrodes should lie within the bandgap of the electrolyte to avoid undesired oxidative or reductive degradation of the electrolyte.
- Inexpensive, environmentally benign, and lightweight.

Intensive materials research during the past three decades has led to the identification and development of a variety of positive electrode materials. A detailed discussion of cathode materials is provided by Whittingham [13]. Transition metal oxides in different crystalline structures have become appealing cathode materials for LiBs.  $\text{LiCoO}_2$ ,  $\text{LiNiO}_2$ , and related materials such as  $\text{LiNi}_{1-x}\text{Co}_x\text{O}_2$ , have layered structures, whereas  $\text{LiMn}_2\text{O}_4$  or “spinel” materials have a three-dimensional “framework” structure, and  $\text{LiFePO}_4$  has the olivine structure.

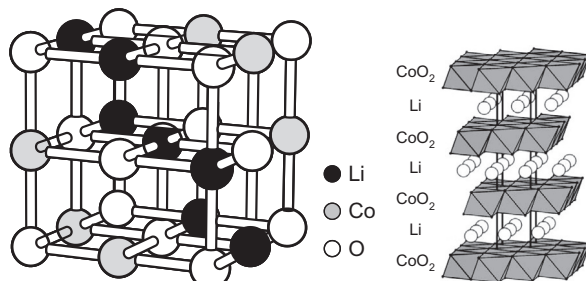
### 2.2.1 Layered oxide materials

Layered transition metal oxides such as  $\text{LiCoO}_2$  are of great importance, as they have been the most widely used positive electrode material for LiBs for nearly two decades.  $\text{LiCoO}_2$  adopts the  $\alpha\text{-NaFeO}_2$ -type crystal structure with rhombohedral symmetry (space group  $\text{R}3\bar{m}$ ). As Figure 2.1 shows, the layered  $\text{LiCoO}_2$  consists of a close-packed network of oxygen ions with Li and Co ions on alternative (111) planes of the cubic rock salt sublattice. The edges of  $\text{CoO}_6$  octahedral are shared to form  $\text{CoO}_2$  sheets and lithium ions can move in two-dimensional directions between  $\text{CoO}_2$  sheets. Decent diffusion of lithium in  $\text{LiCoO}_2$  ( $5 \times 10^{-9} \text{ cm}^2/\text{s}$ ) and high conductivity (e.g.,  $\text{Li}_x\text{CoO}_2$  with  $x=0.6$  behaves like a metal) offer high-rate cyclability. During deintercalation and reintercalation of lithium ions, oxidation and reduction reactions between  $\text{Co}^{3+}/\text{Co}^{4+}$  redox states occur with a large work function offering a high-discharge voltage up to 4.2 V (vs.  $\text{Li}^+/\text{Li}$ ).

The practical capacity of  $\text{LiCoO}_2$  was relatively low at around 130 mAh/g because only around 0.5 Li/Co can be reversibly cycled without causing cell capacity loss due to changes in the structure. Recently, the capacity of  $\text{LiCoO}_2$  has been increased to close to 180 mAh/g by modifying the surface with metal oxides like  $\text{Al}_2\text{O}_3$ ,  $\text{ZrO}_2$ ,  $\text{TiO}_2$ , or phosphate [14]. The improved capacity due to surface modification simply attributes to the blocking effect of the protecting coating, which minimizes the reactivity of  $\text{Co}^{4+}$  on charge with the electrolyte. LiB capacity fade, due to corrosion of electrode materials by HF generated from reaction of trace amount of water with lithium salt  $\text{LiPF}_6$ , is therefore somewhat alleviated.

Because SONY combined the  $\text{LiCoO}_2$  cathode with a carbon anode to make the first successful LiB, it dominates the battery market. However, high cost of Co limits the use of  $\text{LiCoO}_2$  in small cells for portable electronics, such as cell phones, PDAs, and mp3 players. In addition, a sharp change in the lattice parameters with lithium

**Figure 2.1** Crystal structure of  $\text{LiCoO}_2$  showing (left) ordered rock salt structure with Li and Co ions on alternative (111) planes and (right) layered arrangement of  $\text{Li}^+$  ions between the strongly bonded  $\text{CoO}_2$  sheets.



intercalation [15] creates internal stress and microcracking of the electrode materials [16]. Most important,  $\text{LiCoO}_2$  is thermodynamically unstable during the charging process (practically when overcharged) and decomposition proceeds according to the reaction  $\text{Li}_{0.5}\text{CoO}_2 \rightarrow 0.5 \text{ LiCoO}_2 + 1/6 \text{ Co}_3\text{O}_4 + 1/6 \text{ O}_2$  ( $x=0.5$  in  $\text{Li}_x\text{CoO}_2$ ). In addition, cobalt dissolution in the electrolyte could happen at a high potential [17]. Decomposition reactions of  $\text{LiCoO}_2$  at overcharge condition or at elevated operating temperatures are exothermic, which causes battery temperature to rise, which in turn further promotes the decomposition reactions of cathode materials with nonaqueous solvents  $\text{Li}_{0.5}\text{CoO}_2 + 0.1 \text{ C}_3\text{H}_4\text{O}_3$  (EC)  $\rightarrow 0.5 \text{ LiCoO}_2 + 0.5 \text{ CoO} + 0.3 \text{ CO}_2 + 0.2 \text{ H}_2\text{O}$  ( $x=0.5$  in  $\text{Li}_x\text{CoO}_2$ ). These reactions create more heat and the cell temperature continues to rise to a point that the battery might fail and explode. This phenomenon is called *thermal runaway* [18].

As promising alternatives, other layered oxides, such as  $\text{LiNiO}_2$ ,  $\text{LiMnO}_2$ , or mixed oxides have been attempted.  $\text{LiNiO}_2$  is not widely used because of the instability at low-lithium contents, the relatively low temperature at which self-heating ensues, and the difficulty of preparing the material consistently in chemical stoichiometry. Particularly, the material at low-lithium contents likely releases oxygen; therefore, is dangerous when in contact with organic solvents. Although  $\text{LiNiO}_2$  by itself could not be used as cathodes, solid solutions among  $\text{LiCoO}_2$ ,  $\text{LiNiO}_2$ , and other oxides have become attractive cathodes. Table 2.1 summarizes some of the layered electrode materials. It is seen that the mixed Ni-Co dioxides not only increase the specific capacity (with  $\text{LiNi}_{0.9}\text{Co}_{0.1}\text{O}_2$  being the highest) but also are more stable due to the decreased equilibrium partial pressure of oxygen. However, one drawback of the mixed oxides is low electronic conductivity, which is not uniformly high across the lithium composition range, resulting low energy storage and power capabilities, especially at high rates.

## 2.2.2 *Spinel oxide materials*

$\text{LiMn}_2\text{O}_4$  as the typical spinel material has a three-dimensional framework or tunneled structure based on  $\lambda\text{-MnO}_2$ , as shown in Figure 2.2. Lithium fills one-eighth of the tetrahedral sites within the  $\lambda\text{-MnO}_2$  structure and Mn-centered oxygen octahedral fills

**Table 2.1 Characteristics of layered positive electrode materials [19]**

Material	Specific capacity (mAh/g)	Midpoint (V) versus Li (at 0.05 °C)	Advantages and disadvantages
$\text{LiCoO}_2$	155	3.88	Commercially available, expensive
$\text{LiNi}_{0.7}\text{Co}_{0.3}\text{O}_2$	190	3.70	Intermediate cost
$\text{LiNi}_{0.8}\text{Co}_{0.2}\text{O}_2$	205	3.73	Intermediate cost
$\text{LiNi}_{0.9}\text{Co}_{0.1}\text{O}_2$	220	3.76	Highest specific capacity
$\text{LiNiO}_2$	200	3.55	Exothermic decomposition

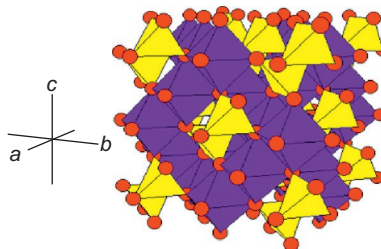


**Figure 2.2** The spinel structure of  $\text{LiMn}_2\text{O}_4$  showing Mn-centered oxygen octahedra (purple) and Li-centered oxygen tetrahedra (yellow).

one-half of the octahedral sites. Comparing to  $\text{LiCoO}_2$ ,  $\text{LiMn}_2\text{O}_4$  has about 10% less capacity, but it has somewhat better kinetics and does not have as great a tendency to evolve oxygen. It is also relatively inexpensive and environmentally benign. Though with the above advantages,  $\text{LiMn}_2\text{O}_4$  has been found to have a gradual capacity loss during cycling due to the so-called Jahn–Teller distortion of the  $\text{Mn}^{3+}$  in the octahedral sites.

One of the problems with this material is the loss of  $\text{Mn}^{2+}$  into the organic solvent due to the disproportionation reaction near the end of discharge when the potential is low (i.e.,  $2 \text{Mn}^{3+} \rightarrow \text{Mn}^{4+} + \text{Mn}^{2+}$ ). These ions travel to the negative graphite electrode and are reduced to form a layer of manganese metal that acts to block lithium ion transport. The spinel gains stability when Mn is partially replaced with other elements such as V, Cr, Fe, Co, Cu, or Ni.  $\text{LiNi}_{0.5}\text{Mn}_{1.5}\text{O}_4$  has been prepared, which provides complete reversible extraction of  $\text{Li}^+$  at ca. 4.7 V, which is more than 0.5 V above the potential for the unsubstituted spinel [20]. This compound has started a new generation of LiBs capable of operating at higher voltages.

### 2.2.3 Olivine oxide materials

$\text{LiFePO}_4$ , as a typical olivine oxide material and first reported by John Goodenough's group at the University of Texas at Austin in 1996, has undergone remarkable development recently and is nowadays being used in commercial LiBs. The GM Chevy Volt is the first gas–electric hybrid vehicle to use these battery materials. Compared to  $\text{LiCoO}_2$  and  $\text{LiMn}_2\text{O}_4$ ,  $\text{LiFePO}_4$  offers a few distinct features that make it an appealing cathode material. First, Fe is inexpensive and environmentally benign. Second, the covalently bonded  $\text{PO}_4$  groups (forming the  $\text{PO}_4$  tetrahedron as shown in Figure 2.3) together with the chemically stable  $\text{Fe}^{2+}/\text{Fe}^{3+}$  couple (within the  $\text{FeO}_6$  octahedron) offer excellent safety. During charge/discharge, lithium ions are extracted/inserted from/into  $\text{LiFePO}_4$  while the central iron ions are oxidized/reduced. Third, a discharge voltage plateau at 3.4 V with a theoretical capacity of 170 mAh/g significantly suppresses electrolyte degradation. On the other hand, the main drawbacks of the material are its low electronic conductivity and sluggish lithium diffusion. These problems have been overcome in recent years by material doping and carbon coating.

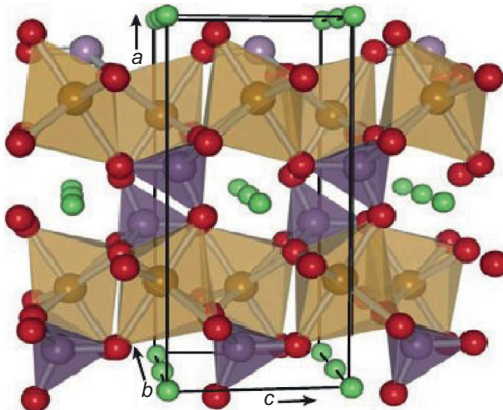


**Figure 2.3** The olivine structure of  $\text{LiFePO}_4$  showing  $\text{PO}_4$  tetrahedra and  $\text{FeO}_6$  octahedra. Lithium channels along the  $b$ -axis are also shown [21].

## 2.2.4 Recent progress

Though tremendous progress has been made over the last couple of decades, state-of-the-art LiBs still face various problems such as low energy and power density, short lifetime, and high cost. Among them, thermal instability appears as the top concern, to which anode, cathode, and electrolyte contribute jointly. Olivine-based and  $\text{LiMn}_2\text{O}_4$  have been demonstrated to improve cathode stability by depressing the peak heating rate.

One of the main challenges in the design of high-power-density and high-energy-density batteries is to ensure that the electrodes maintain their capacity over high-rate discharge–recharge cycles. Recent material development in LiBs has been focusing on the ability to achieve a high discharging/charging rate. Employment of nanomaterials in different shapes, such as nanowires, rods, spheres, fibers, tubes, and plates, has been demonstrated to enhance material transport characteristics and, therefore, discharge/charge rate. Particularly, Zhang *et al.* [22] have developed three-dimensional bicontinuous electrode nanoarchitectures consisting of a thin layer of electrolytically active material between three-dimensionally connected electrolyte and conductive scaffold phases, providing a highly conductive pathway for electrons, a short ion diffusion length in the intercalation compound, and a fast mass transport channel in the liquid electrolyte. A high discharge rate of 1114 °C was demonstrated at a capacity of 75 mAh/g.

Element doping and surface coating have also been employed to enhance transport of lithium ions and electrons in battery nanomaterials. The pioneering work [23] from the Chiang group at MIT first demonstrated a factor of  $10^8$  improvement in conductivity when doping  $\text{LiFePO}_4$  with cationic elements such as aluminium, niobium, and zirconium, though the conductivity improvement mechanism is still debatable. Coating of cathodes with either ionically or electronically conductive materials has been demonstrated to significantly improve high-rate capacity and capacity retention.  $\text{AlF}_3$  coating on  $\text{LiMn}_2\text{O}_4$  showed only 3.4% capacity loss at 55 °C after 50 cycles compared to ~18% decay without the coating [24]. Kang and Ceder [25] of MIT had created a fast ion-conducting surface phase on  $\text{LiFePO}_4$  through controlled off-stoichiometry. Their

materials would be able to discharge at  $\sim 200$  °C and still achieve a capacity more than 120 mAh/g. At this high rate, the time to fully charge a battery would be in a matter of seconds rather than hours, and this may make possible new technological applications and induce lifestyle changes. However, in their battery electrodes, an exceedingly large amount of carbon up to 65 wt.% has been used, leading to an intense debate on whether the high rates were achieved by a battery or a capacitor.

### 2.2.5 Choice of cathode materials and safety

The selection of battery materials significantly depends on open circuit voltage (OCV) of the cell. The OCV relies directly on chemical potential of the electrode materials and is described as [26]

$$V_{\text{OC}} = \frac{(\mu_A - \mu_C)}{F} \quad (2.1)$$

where  $\mu_A$  and  $\mu_C$  are the chemical potentials of the anode and cathode materials, respectively, and  $F$  is the Faraday constant. In a battery electrode, due to low conductivity of the solid phases and liquid electrolyte phase, as well as slow electrochemical reactions, the voltage  $V_{\text{dis}}$  obtained during discharge can be reduced by an amount of  $\eta_{\text{dis}}$ , which is called overpotential [26]

$$\eta_{\text{dis}} = V_{\text{OC}} - V_{\text{dis}} \quad (2.2)$$

Similarly, during charge a similar overpotential  $\eta_{\text{ch}}$  would appear and can be expressed as

$$\eta_{\text{ch}} = V_{\text{ch}} - V_{\text{OC}} \quad (2.3)$$

where  $V_{\text{ch}}$  is the potential applied when charging the cell.

The open circuit potential can be chosen according to Equation (2.1) by changing the electrode materials. But the electrode material cannot be randomly chosen as the electrolyte might decompose if the potential is beyond the stability potential window of the electrolyte. The potential window of the electrolyte system is

$$E_g = E_{\text{LUMO}} - E_{\text{HOMO}} \quad (2.4)$$

where the LUMO and HOMO are, respectively, the lowest unoccupied molecular orbital and highest occupied molecular orbital of the electrolyte, and  $E_g$  is the band gap of the electrolyte. The Fermi energy level of the anode electrode,  $E_{\text{FA}}$ , has to be lower than LUMO and the Fermi energy level of the cathode electrode,  $E_{\text{FC}}$ , has to be higher than the HOMO to prevent either oxidation or reduction of the electrolyte, which results in the following thermodynamic stability criterion:

$$eV_{\text{OC}} = E_{\text{FA}} - E_{\text{FC}} \leq E_g \quad (2.5)$$

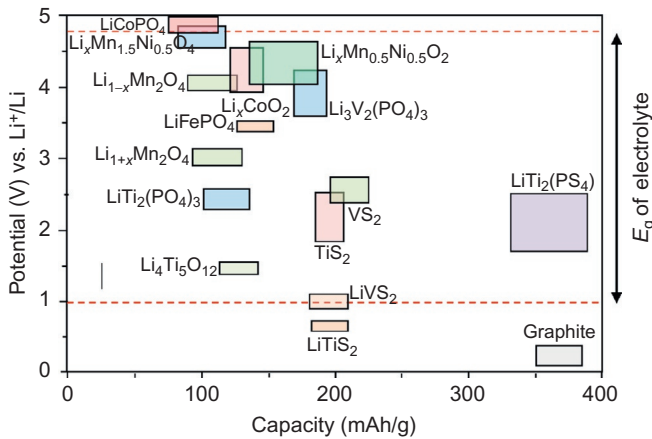


**Figure 2.4** Selection criteria for electrode materials based on the thermodynamic stability criteria of the electrolyte [27].

**Figure 2.4** lists theoretical potentials (vs.  $\text{Li}^+/\text{Li}$ ) of different electrode materials in a typical nonaqueous electrolyte system containing a mixture of organic carbonate solvents (carbonate + dimethyl carbonate). It appears that spinel  $\text{Li}-\text{Mn}-\text{Ni}$  composite oxides could yield a high cell voltage; however, as the voltage is close to LUMO of the carbonate solvents in the electrolyte, electrolyte decomposition may be difficult to avoid.

## 2.3 Lithium intercalation mechanism

### 2.3.1 Thermodynamics and kinetics

When an individual species (i.e., Li ions) is considered, it is convenient to introduce the concept of chemical potential. The chemical potential,  $\mu_i$ , of species  $i$ , also known as partial molar free energy, in a phase  $\alpha$  is defined as

$$\mu_i = \left( \frac{\partial G_\alpha}{\partial n_i} \right)_{T,P} \quad (2.6)$$

where  $G_\alpha$  is the molar Gibbs free energy of species  $i$  in phase  $\alpha$ , and  $n_i$  is the molar fraction of the species  $i$ . Equation (2.6) describes how the free energy changes with respect to the addition/subtraction of a certain species and, therefore, the chemical potential has the same dimension as the free energy. The chemical potential gradient established in a LiB (e.g., during discharge process) will drive spontaneous species (Li ions) movement in a direction of lower chemical potential (i.e., from the negative electrode to the positive one). The chemical potential difference ( $\Delta\mu_{\text{Li}}$ ) of Li ions will then

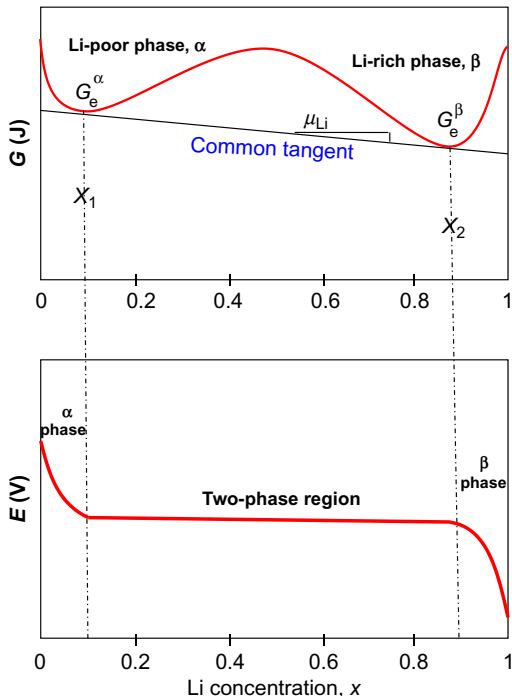
establish a potential difference between the two electrode/electrolyte interfaces according to the relation

$$E_{c \rightarrow a} = -\frac{\mu_c^{\text{Li}} - \mu_a^{\text{Li}}}{F} \quad (2.7)$$

where the subscripts “c” and “a” represent the cathode (positive) and anode (negative) electrodes, respectively.

A number of LiB materials go through phase transformation with either lithium insertion or deinsertion, respectively, during discharging and charging reactions. For the sake of simplicity, let us focus on  $\text{LiFePO}_4$  and consider the discharge process of a pure Li-deficient phase  $\alpha$  ( $\text{FePO}_4$ ) at the positive electrode, assuming that a new phase  $\beta$  ( $\text{LiFePO}_4$ ) forms at the surface as the concentration of the inserted Li ions is above  $X_1$ . The introduction of lithium causes nucleation and subsequent growth of a second phase with distinct structure and composition of  $X_2$ . This situation is presented schematically in Figure 2.5. During the initial discharge (lithium concentration is below  $X_1$ ), the battery voltage is entirely determined by the Gibbs free energy of lithium in the Li-deficient phase  $\alpha$ , assuming constant chemical potential of the negative electrode. When lithium concentration reaches beyond  $X_1$ , the battery discharge reaction starts involving two-phase transformation along the common tangent line between the two-phase minimums, that is,  $G_e^\alpha$  and  $G_e^\beta$ . The two-phase reaction is then

**Figure 2.5** Schematic illustration of free energy curves of separated two phases (top) and the corresponding equilibrium battery discharge curve (bottom).



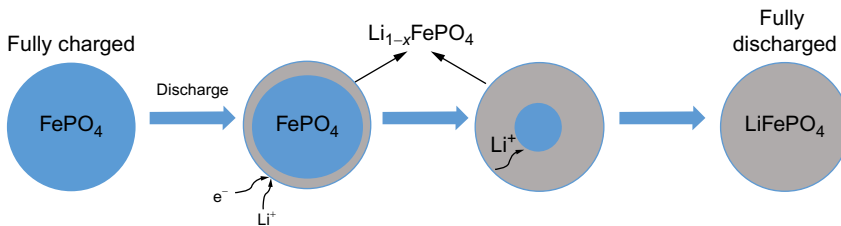


**Figure 2.6** Illustration of the shrink-core model during the discharging process with the phase change and the movement of phase boundary. Redrawn from Ref. [28].

driven by a constant chemical potential gradient, which results in a discharge curve with a constant voltage plateau according to Equation (2.7). When the overall lithium concentration reaches  $X_2$ , only  $\beta$  phase remains and the discharge voltage is governed by the chemical potential of  $\beta$  phase only.

This phase transition between  $\text{FePO}_4$  and  $\text{LiFePO}_4$  during the charge/discharge process can be simulated using a shrink-core (or core-shell) model, originally proposed by Srinivasan and Newman [28] and is shown schematically in Figure 2.6.

As current passes through the active material, the electrochemical reaction occurs on the surface of the active particle and forms a lithium-rich phase ( $\text{Li}_{1-x}\text{FePO}_4$ ), where the stoichiometry of  $\text{Li}^+$  has been denoted by  $(1 - x)$ . During the discharge process, lithiation occurs at the particle surface. Lithium ions diffuse into the core of the active material and the shell of the lithium-rich phase grows and shrinks the core of the lithium-poor phase.

The shrink-core model developed by Srinivasan and Newman [28] did not consider the mobility of the interface between the two phases. However, some studies suggested that the interface mobility is much slower than the ion diffusion in the single phase. In order to capture the interface characteristics, a “mushy-zone” approach, accounting for the sluggish Li diffusion across the two-phase boundary, has been proposed to study the kinetically induced nonequilibrium phenomenon [5]. The lithium concentration profile in Figure 2.7 shows that the moving boundary compares well with the sharp boundary obtained from the shrink-core model. In addition, the phase boundary estimated from “mushy-zone” approach is smoother than the one obtained from the shrink-core model. There is an additional region where Li concentration is between the concentration of the lithium-rich phase and the lithium-poor phase, which implies the existence of a two-phase region ( $\text{LiFePO}_4$  and  $\text{FePO}_4$ ) around the sharp boundary delineated otherwise.

The detailed mechanism of battery electrode reactions often involve a series of physical, chemical, and electrochemical steps, including not only charge transfer and transport but also phase kinetics-driven phase transformations. Basically, two different kinetic effects dominate the LiB reactions, especially at high-rate charge or discharge: (1) activation polarization, which is related to the kinetics of the heterogeneous electrochemical reactions at the interface between an electrode and an electrolyte and (2) phase transformation.

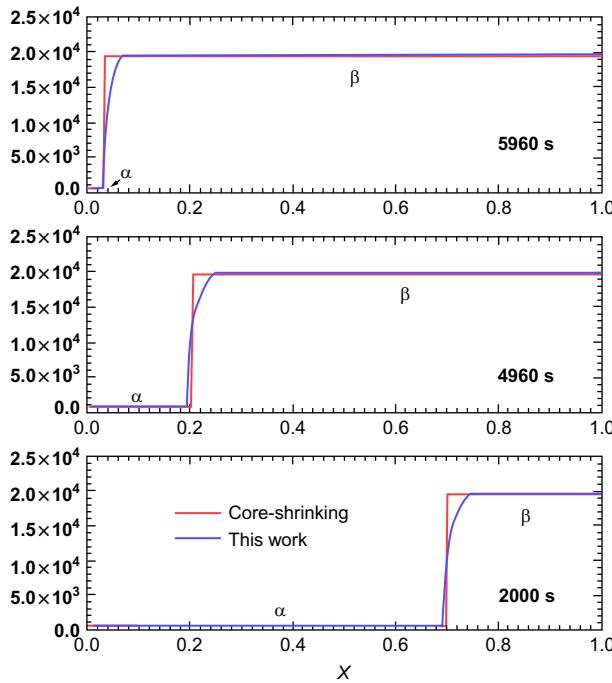


**Figure 2.7** Li concentration distribution along the normalized thickness of a 20-nm-thick active platelet at a discharge rate of 0.5 °C after different discharging time. The phases  $\alpha$  and  $\beta$  indicate the lithium-poor phase ( $\text{FePO}_4$ ) and the lithium-rich phase ( $\text{Li}_{(1-x)}\text{FePO}_4$ ), respectively [5].

Activation polarization can be best understood using the Butler–Volmer equation derived from the activation state theory as

$$i = i_o a \left\{ \exp \left[ \alpha \frac{F}{RT} \eta \right] - \exp \left[ -(1 - \alpha) \frac{F}{RT} \eta \right] \right\} \quad (2.8)$$

where  $i$  is the current flow,  $a$  is the battery electrode surface area,  $i_o$  is the exchange current,  $\eta$  is the overpotential that represents the deviation of potential from the equilibrium value, and  $\alpha$  is the transfer coefficient. The transfer coefficient is best considered as the fraction of the overall overpotential that leads to the forward reaction. Equation (2.8) indicates that both forward reaction (first term on the RHS) and reverse reaction (second term on the RHS) contribute to the net battery current. There are two influencing factors to the total battery reactions at constant temperature. The first one is the exchange current, which is directly related to the reaction rate constant, reaction activities, and battery material surface chemistry. Electrode reactions with high exchange current at room temperature are more reversible and, therefore, preferred for battery applications. The second one is the electrode surface area. Small particle size or unique particle shapes that can create more surface areas are favored as battery materials.

### 2.3.2 Phase transformation

Again, we focus here on  $\text{LiFePO}_4$  and discuss its phase transformation behavior in a LiB. During discharge, Li ion diffuses into  $\text{FePO}_4$  (heterosite) particles, which transforms into a new phase  $\text{LiFePO}_4$  (triphylite) and during charge the reverse phase transition takes place. This phase transition relies on diffusion of Li ions through the crystal structure of active materials. Diffusion of Li ions through the  $\text{LiFePO}_4$  structure is not isotropic but anisotropic along the preferred “*b*” direction, which is due to the 1D tunnel [29] shown in the structure of  $\text{LiFePO}_4$  in Figure 2.3. This anisotropic Li diffusion makes the phase transformation complicated. It is generally accepted that intercalation/deintercalation of Li into/from  $\text{LiFePO}_4$  follows the so-called domino-cascade fashion [29]. Once the delithiation starts, the change of valence state of Fe ions alters the  $\text{Fe}—\text{O}$  and  $\text{O}—\text{O}$  bond lengths in the  $\text{FeO}_6$  octahedra, which leads to structural distortions. Because  $\text{FeO}_6$  octahedron and  $\text{PO}_4$  tetrahedron shares a common  $\text{O}—\text{O}$  edge, the change in  $\text{O}—\text{O}$  bond length also affects  $\text{PO}_4$ . These changes in  $\text{FeO}_6$  and  $\text{PO}_4$  environments make it difficult to introduce a significant amount of  $\text{Fe}^{3+}$  ions in  $\text{LiFePO}_4$  and a significant amount of  $\text{Fe}^{2+}$  ions in  $\text{FePO}_4$ ; hence, a large compositional domain for solid solutions is not possible. As a result, a two-phase mixture of two end-members [ $\text{Li}_{1-\varepsilon}\text{FePO}_4$  ( $\varepsilon \sim 0$ ) and  $\text{Li}_{\varepsilon}\text{FePO}_4$  ( $\varepsilon' \sim 0$ )] exists during the charge–discharge process. When the deintercalation starts, a small polaron of  $\text{Fe}^{3+}$  forms [30] (a similar phenomenon happens for  $\text{Fe}^{2+}$  when lithiation takes place) and the change in the environment of  $\text{FeO}_6$  and  $\text{PO}_4$  push this polaron to the next  $\text{FeO}_6$  octahedron. Thus, with the lithium deintercalation along the “*a*” direction a two-phase interface moves along the “*a*” direction, as shown in Figure 2.8.

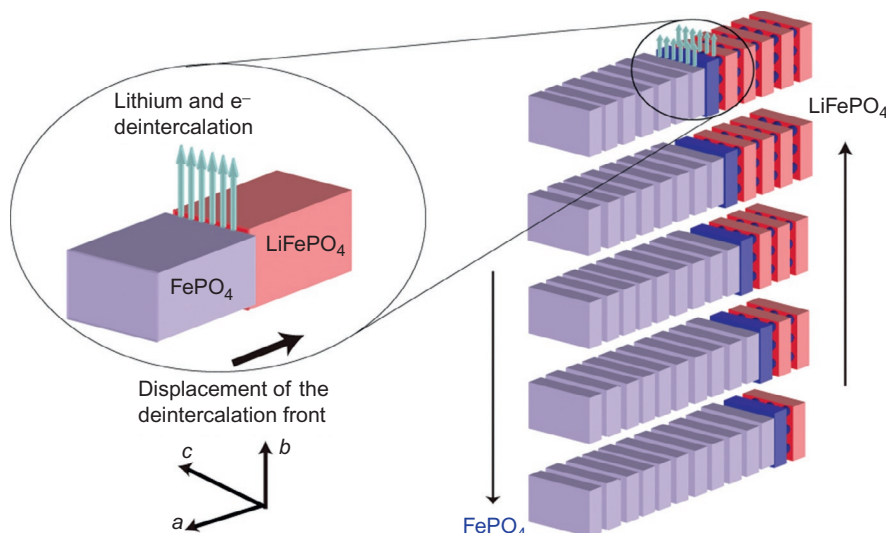


**Figure 2.8** Schematic view of the domino-cascade mechanism for the lithium deintercalation/intercalation mechanism in layered  $\text{FePO}_4$  and  $\text{LiFePO}_4$  crystallites. Adapted from Ref. [29].

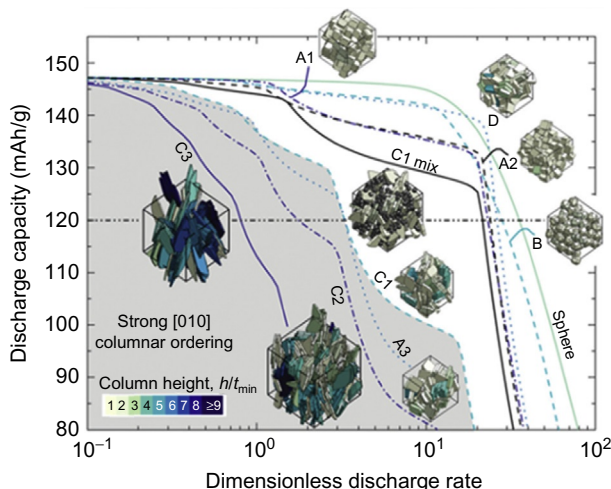
Due to the large difference in bond lengths and angles between  $\text{LiFePO}_4$  and the newly formed  $\text{FePO}_4$  block, strong distortions appear locally that causes instability to the adjacent  $[\text{FeO}_4]_n$  layers. This results in the easiness to remove lithium ions from the  $b$  tunnels adjacent to the newly formed  $\text{FePO}_4$  block instead of starting a new nucleation site to form a new  $\text{FePO}_4$  block elsewhere in the same particle. Rather, nucleation of a new  $\text{FePO}_4$  block within the same crystal particle requires higher activation energy, whereas lithium deintercalation adjacent to the already formed  $\text{FePO}_4$  block can proceed without the increase of activation energy. So, once the intercalation or deintercalation starts in any particle, it finishes very quickly for that particle. But chemical and electrochemical lithiation/delithiation can give different pictures. Chemical intercalation/deintercalation obviously has the tendency to nucleate simultaneously at different points within one crystal particle and, hence, forms the domains of two phases ( $\text{LiFePO}_4$  and  $\text{FePO}_4$ ) in one single crystal [31,32].

The importance of lithium transport along preferential crystallographic  $\langle 010 \rangle$  directions has been demonstrated for nanocrystallite  $\text{LiFePO}_4$  electrodes [33,34]. This has critical implications in  $\text{LiFePO}_4$  electrode performance. Smith *et al.* [35] has demonstrated, using a mesoscopic, granular mechanics simulation approach, that the assembly of  $\text{LiFePO}_4$  nanostructures and potential columnar stacking of  $\text{LiFePO}_4$  nanocrystallites tend to hinder lithium transport in the active material with a resultant penalty in discharge capacity and rate capability. Optimization of the dense microstructure of  $\text{LiFePO}_4$  suggests that columnar ordering of nanoplatelets with an aspect ratio of 20 could reduce ion transport rates by 50 times relative to systems without columnar ordering [35]. Figure 2.9 shows the influence of active particle morphology and aspect ratio on the columnar stacking and the resulting effect on the electrode rate capability and discharge capacity.

### 2.3.3 Experiments/diagnostics

LiB performance with advanced materials and designs has been significantly improved over the past several decades. It is important to have a set of tools to evaluate

**Figure 2.9** Influence of active particle morphology and aspect ratio on columnar stacking and performance due to lithium transport along preferential crystallographic direction representative of the  $\text{LiFePO}_4$  cathode [35].



these improvements and understand the relationship between performance and battery materials. In this section, the experimental methods of understanding LiB material intercalation kinetics and thermodynamics will be introduced.

### 2.3.3.1 Cyclic voltammetry test

Cyclic voltammetry (CV) is one of the most widely used electrochemical techniques for qualitative understanding of battery reactions. CV measurement can rapidly provide information about thermodynamics of redox processes and kinetics of heterogeneous electron-transfer reactions, as well as coupled chemical adsorption and reactions. [Figure 2.10a](#) compares CV curves of the bare and carbon-coated LiFePO<sub>4</sub>. The anodic (in positive scanning direction) and cathodic (in negative scanning direction) peaks correspond to lithium extraction and insertion into the material, respectively, according to the following reaction:



As Equation (2.9) indicates, the peaks shape and the integrated area under the peaks strongly depend on the reaction kinetics at the electrode and electrolyte interface, which involves multispecies transport and electrochemical reaction. [Figure 2.10a](#) shows that carbon coating significantly boosts peak current, which indicates that transport of lithium ions and electrons is considerably improved; thus, enhancing the electrochemical redox reaction. In addition, lithium ion diffusion in electrode materials can also be obtained from CV. Randles–Sevcik equation (Equation 2.10), describing the relationship between the peak current ( $i_p$ ) and square root of the scan rate ( $v$ ), has been used to access the chemical diffusion coefficient of the lithium ion ( $D_{\text{Li}}$ ) in LiFePO<sub>4</sub>, as shown in [Figure 2.10b](#).

$$i_p/m = 0.4463F(F/RT)^{0.5} C_{\text{Li}} v^{0.5} A D_{\text{Li}}^{0.5} \quad (2.10)$$

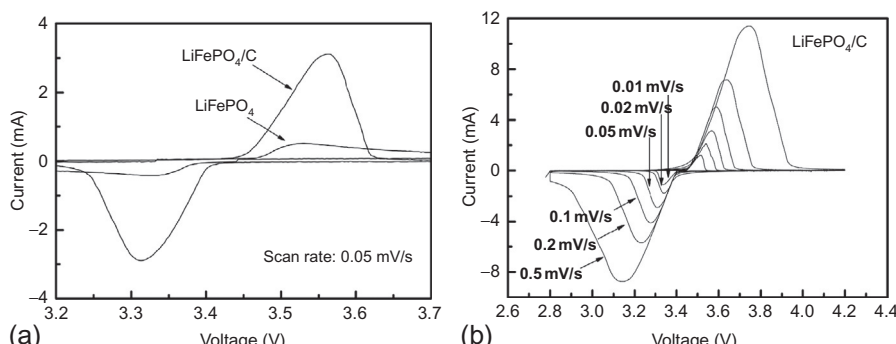


**Figure 2.10** CV profiles of (a) bare LiFePO<sub>4</sub> and carbon-coated LiFePO<sub>4</sub> at a scan rate of 0.05 mV/s and (b) carbon-coated LiFePO<sub>4</sub> at a different scan rate [36].

where  $m$  is the mass of the electrode material,  $F$  is the Faraday constant,  $C_{\text{Li}}$  is the lithium ion concentration in the material, and  $A$  is the surface area of the electrode. Figure 2.10b shows that the peak CV current increases with the scan rate. The lithium ion diffusion coefficient calculated from the slope of the linear plot between  $i_p/m$  and  $v^{0.5}$  indicated approximately 3.8 times improvement after surface carbon coating of LiFePO<sub>4</sub>. On the other hand, if the battery reactions are thermodynamically reversible, the positions of the cathodic or anodic peak potentials do not change with the potential scan rate, and the peak height is proportional to the square root of the potential scan rate,  $v^{0.5}$ , according to Equation (2.10). Figure 2.10b clearly suggests that the reactions are not completely reversible, as the anodic peak potential becomes more positive and the cathodic peak potential becomes more negative. The separation of the two peaks becomes larger with the increase of the scan rate.

### 2.3.3.2 Charge and discharge analysis

Charge and discharge cycles have been routinely employed to study battery performance. The typical curves, in which the cell voltage is plotted as a function of the state of charge shown in Figure 2.11, result from combined electrochemical oxidation/reduction reactions at the positive and negative electrodes. The voltage varies as the chemical energy is released as the cell is discharged. Likewise, it changes in the reverse direction when it is recharged. The characteristics of the curves vary widely between different electrochemical systems, as they are strictly dependent on phase-transformation-driven lithium insertion and extraction in materials.

The gap between the potential plateaus during charge and discharge in Figure 2.11, manifested by the hysteresis in cyclic behavior, is often related to mechanical strain energy; that is, dislocation generation and motion, as a consequence of volume

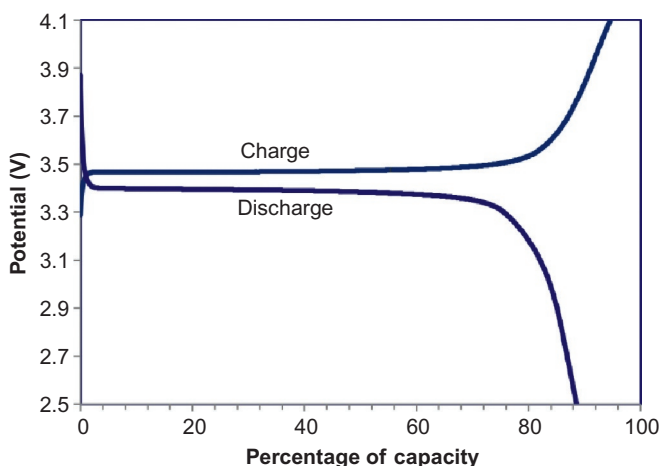


**Figure 2.11** Example of battery charge and discharge curves, showing variation of voltages as a function of the fraction of available capacity (LiFePO<sub>4</sub> vs. Li metal tested at 1 °C rate).

changes that occur due to the insertion and extraction of the lithium ions. Other factors such slow reaction kinetics and internal cell resistance also contribute to the hysteresis.

### 2.3.3.3 Galvanostatic and potentiostatic intermittent titration methods

In galvanostatic and potentiostatic intermittent titration (GITT and PITT), dynamic information about insertion–reaction electroactive components can be accessed. Using the traditional GITT method, the electrode system is subjected to a small constant current, and potential changes are measured as a function of time. Instead of a current pulse as in GITT, a small voltage step is applied to the system under the PITT method, and the resulting current is measured as a function of time. The two kinetic measurements are represented schematically in [Figure 2.12a and b](#).

In each case, stepwise measurement of the electrochemical titration curve is accompanied by an evaluation of the kinetic behavior after each step. Thus, both thermodynamic and kinetic information could be obtained as a function of electrode composition, materials, and state of charge. GITT and PITT have been widely used for *in situ* measurement of lithium ion diffusivity in particles. Assuming one-dimensional diffusion in a solid solution electrode without consideration of ohmic potential drop, double-layer charging, charge-transfer kinetics, and phase transformation, the ion diffusion coefficient can be calculated using Fick's law through the following equations [\[37,38\]](#):

$$D_{\text{GITT}} = \frac{4}{\pi} \left( \frac{IV_M}{z_A F S} \right)^2 \left[ \frac{dE(x)/dx}{dE(t)/d\sqrt{t}} \right]^2 \quad (t \ll L^2/D_{\text{GITT}}) \quad (2.11a)$$

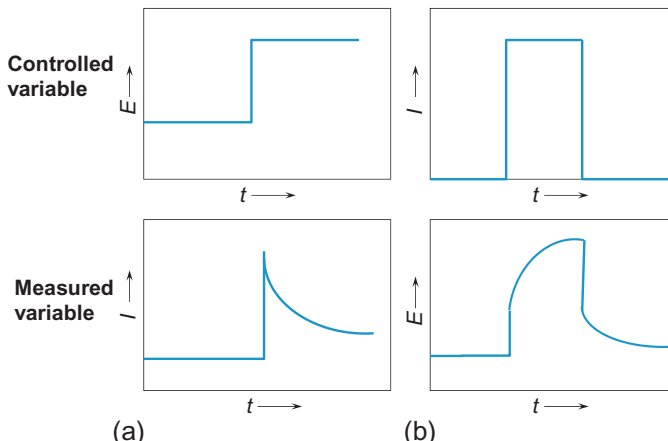


**Figure 2.12** Schematic illustration of (a) PITT and (b) GITT methods.

$$D_{\text{PITT}} = -\frac{d \ln I(t) 4L^2}{dt \pi^2} \quad (t \gg L^2/D_{\text{PITT}}) \quad (2.11b)$$

where  $L$  is the characteristic length of the electrode materials,  $F$  is the Faraday constant,  $z_A$  is the charge number of the electroactive species (for lithium ion,  $z_A = 1$ ),  $S$  is the contact area between the electrode and electrolyte,  $I$  is the applied current, and  $V_M$  is the molar volume of the electrode material.  $dE(x)/dx$  is the change of equilibrium OCV as a function of the electrode material composition after the current pulse and  $dE(t)/d\sqrt{t}$  can be calculated from a plot of the voltage versus the square root of the time during constant current pulse.

In addition, PITT can also provide thermodynamic phase transformation information, such as miscibility gap and phase diagram [39]. To minimize the material volume expansion due to nucleation or growth of a new phase, a very small voltage increment (only 5 mV) was used to charge a fully discharged battery from 2.0 V to the OCV or discharge a fully charged one from 3.8 V to the OCV until the current drops to a C/50. In this way, the capacity available at these finely resolved voltage steps with respect to the equilibrium two-phase potential could be measured. Figure 2.13 shows the PITT

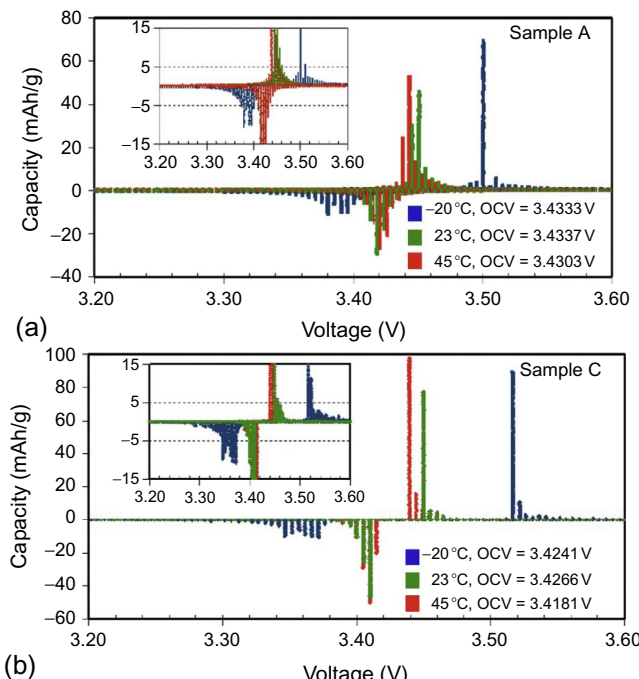


**Figure 2.13** (a) Results from PITT measurement on  $\text{Li}_{1-x}\text{FePO}_4$  composition determined from the capacity versus voltage measured potentiostatically upon charge and discharge in 5 mV steps. (b) Phase diagram for nanoscale lithium iron phosphate at three particle sizes. Particle size: Sample A (34 nm), Sample B (42 nm), and Sample C (112 nm) [39].

results and the calculated phase diagrams for  $\text{Li}_{1-x}\text{FePO}_4$  samples at three different particle sizes. The insets in Figure 2.13a show the details near the OCVs on an expanded scale. One striking feature in the PITT results (Figure 2.13a) is the peak of highest capacity, which occurs at an overpotential corresponding to the maximum amount of phase transformation.

The nonstoichiometry, that is,  $x$  in the lithium-rich  $\text{Li}_{1-x}\text{FePO}_4$  phase and  $y$  in the lithium-deficient  $\text{Li}_y\text{FePO}_4$  phase, is measured in the absence of any electrochemical driving force for the phase transformation. The capacity accumulated during charge below the OCV or during discharge above the OCV is attributed to the formation of a lithium-rich or lithium-deficient solid solution prior to the nucleation of a new phase. The calculated phase diagram for  $\text{LiFePO}_4$  at three different particle sizes from the PITT measurements clearly suggests that the two-phase field shrinks with decreasing particle size and that for each particle size, the miscibility gap shrinks with increasing temperature [39].

## Acknowledgments

The authors acknowledge the publishers for the figures reproduced in this chapter from the referenced publications of their respective journals. P.P.M. would like to thank Chien-Fan Chen and Pallab Barai for their assistance in preparing this chapter. The authors also acknowledge the financial support from their sponsors.

## References

- [1] G. Pistoia, *Lithium-Ion Batteries: Advances and Applications*, Elsevier, Oxford, 2014.
- [2] J. Akimoto, Y. Gotoh, et al., Synthesis and structure refinement of  $\text{LiCoO}_2$  single crystals, *J. Solid State Chem.* 141 (1) (1998) 298–302.
- [3] I. Belharouak, D. Vissers, et al., Thermal stability of the  $\text{Li}(\text{Ni}_{0.8}\text{Co}_{0.15}\text{Al}_{0.05})\text{O}_2$  cathode in the presence of cell components, *J. Electrochem. Soc.* 153 (11) (2006) A2030–A2035.
- [4] F. La Mantia, F. Rosciano, et al., Direct evidence of oxygen evolution from  $\text{Li}_{1+x}(\text{Ni}_{1/3}\text{Mn}_{1/3}\text{Co}_{1/3})_{1-x}\text{O}_2$  at high potentials, *J. Appl. Electrochem.* 38 (7) (2008) 893–896.
- [5] F. Liu, N.A. Siddique, et al., Nonequilibrium phase transformation and particle shape effect in  $\text{LiFePO}_4$  materials for Li-ion batteries, *Electrochem. Solid-State Lett.* 14 (10) (2011) A143–A147.
- [6] T. Thongtem, S. Thongtem, Characterization of  $\text{Li}_{1-x}\text{Ni}_{1+x}\text{O}_2$  prepared using succinic acid as a complexing agent, *Inorg. Mater.* 42 (2) (2006) 202–209.
- [7] K.T. Nam, D.-W. Kim, et al., Virus-enabled synthesis and assembly of nanowires for lithium ion battery electrodes, *Science* 312 (5775) (2006) 885–888.
- [8] B.-J. Hwang, K.-F. Hsu, et al., Template-free reverse micelle process for the synthesis of a rod-like  $\text{LiFePO}_4/\text{C}$  composite cathode material for lithium batteries, *J. Power Sources* 194 (1) (2009) 515–519.
- [9] Z. Wang, S. Su, et al., Syntheses, characterizations and electrochemical properties of spherical-like  $\text{LiFePO}_4$  by hydrothermal method, *J. Power Sources* 184 (2) (2008) 633–636.

- [10] Y.H. Chen, C.W. Wang, et al., Selection of conductive additives in Li-ion battery cathodes: a numerical study, *J. Electrochem. Soc.* 154 (10) (2007) A978–A986.
- [11] H. Joachin, T.D. Kaun, et al., Electrochemical and thermal studies of carbon-coated LiFePO<sub>4</sub> cathode, *J. Electrochem. Soc.* 156 (6) (2009) A401–A406.
- [12] J. Yang, J.J. Xu, Nonaqueous sol–gel synthesis of high-performance LiFePO<sub>4</sub>, *Electrochem. Solid-State Lett.* 7 (12) (2004) A515–A518.
- [13] M.S. Whittingham, Lithium batteries and cathode materials, *Chem. Rev.* 104 (10) (2004) 4271–4302.
- [14] H.-M. Cheng, F.-M. Wang, et al., Enhanced cycleability in lithium ion batteries: resulting from atomic layer deposition of Al<sub>2</sub>O<sub>3</sub> or TiO<sub>2</sub> on LiCoO<sub>2</sub> electrodes, *J. Phys. Chem. C* 116 (14) (2012) 7629–7637.
- [15] T. Ohzuku, A. Ueda, Solid-state redox reactions of LiCoO<sub>2</sub> (R<sub>3m</sub>) for 4 volt secondary lithium cells, *J. Electrochem. Soc.* 141 (11) (1994) 2972–2977.
- [16] J. Zhou, P.H.L. Notten, Studies on the degradation of Li-ion batteries by the use of micro-reference electrodes, *J. Power Sources* 177 (2) (2008) 553–560.
- [17] G.G. Amatucci, J.M. Tarascon, et al., Cobalt dissolution in LiCoO<sub>2</sub>-based non-aqueous rechargeable batteries, *Solid State Ionics* 83 (1–2) (1996) 167–173.
- [18] T.M. Bandhauer, S. Garimella, et al., A critical review of thermal issues in lithium-ion batteries, *J. Electrochem. Soc.* 158 (3) (2011) R1–R25.
- [19] G.M. Ehrlich, *Lithium-Ion Batteries*, *Handbook of Batteries*, third ed., McGraw Hill Books, New York, 2002 (Chapter 35).
- [20] J.C. Arreola, A. Caballero, et al., Improving the performance of lithium-ion batteries by using spinel nanoparticles, *J. Nanomater.* 2008 (2008) 1–10.
- [21] T. Maxisch, G. Ceder, Elastic properties of olivine Li<sub>x</sub>FePO<sub>4</sub> from first principles, *Phys. Rev. B* 73 (17) (2006), 174112.
- [22] H. Zhang, X. Yu, et al., Three-dimensional bicontinuous ultrafast-charge and -discharge bulk battery electrodes, *Nat. Nanotechnol.* 6 (5) (2011) 277–281.
- [23] S.-Y. Chung, J.T. Bloking, et al., Electronically conductive phospho-olivines as lithium storage electrodes, *Nat. Mater.* 1 (2) (2002) 123–128.
- [24] H. Liu, D. Tang, The effect of nanolayer AlF<sub>3</sub> coating on LiMn<sub>2</sub>O<sub>4</sub> cycle life in high temperature for lithium secondary batteries, *Russ. J. Electrochem.* 45 (7) (2009) 762–764.
- [25] B. Kang, G. Ceder, Battery materials for ultrafast charging and discharging, *Nature* 458 (7235) (2009) 190–193.
- [26] L.-X. Yuan, Z.-H. Wang, et al., Development and challenges of LiFePO<sub>4</sub> cathode material for lithium-ion batteries, *Energy Environ. Sci.* 4 (2) (2011) 269–284.
- [27] J.B. Goodenough, Y. Kim, Challenges for rechargeable Li batteries, *Chem. Mater.* 22 (3) (2009) 587–603.
- [28] V. Srinivasan, J. Newman, Discharge model for the lithium iron-phosphate electrode, *J. Electrochem. Soc.* 151 (10) (2004) A1517–A1529.
- [29] C. Delmas, M. Maccario, et al., Lithium deintercalation in LiFePO<sub>4</sub> nanoparticles via a domino-cascade model, *Nat. Mater.* 7 (8) (2008) 665–671.
- [30] T. Maxisch, F. Zhou, et al., Ab initio study of the migration of small polarons in olivine Li<sub>x</sub>FePO<sub>4</sub> and their association with lithium ions and vacancies, *Phys. Rev. B* 73 (10) (2006), 104301.
- [31] G. Chen, X. Song, et al., Electron microscopy study of the LiFePO<sub>4</sub> to FePO<sub>4</sub> phase transition, *Electrochem. Solid-State Lett.* 9 (6) (2006) A295–A298.
- [32] L. Laffont, C. Delacourt, et al., Study of the LiFePO<sub>4</sub>/FePO<sub>4</sub> two-phase system by high-resolution electron energy loss spectroscopy, *Chem. Mater.* 18 (23) (2006) 5520–5529.

- [33] K. Dokko, S. Koizumi, et al., Electrochemical reactivity of LiFePO<sub>4</sub> prepared by hydro-thermal method, *Chem. Lett.* 35 (3) (2006) 338–339.
- [34] K. Saravanan, P. Balaya, et al., Morphology controlled synthesis of LiFePO<sub>4</sub>/C nanoplates for Li-ion batteries, *Energy Environ. Sci.* 3 (4) (2010) 457–464.
- [35] K.C. Smith, P.P. Mukherjee, et al., Columnar order in jammed LiFePO<sub>4</sub> cathodes: ion transport catastrophe and its mitigation, *Phys. Chem. Chem. Phys.* 14 (19) (2012) 7040–7050.
- [36] C.K. Park, S.B. Park, et al., Li ion diffusivity and improved electrochemical performances of the carbon coated LiFePO<sub>4</sub>, *Bull. Korean Chem. Soc.* 32 (3) (2011) 836–840.
- [37] D.W. Dees, S. Kawauchi, et al., Analysis of the galvanostatic intermittent titration technique (GITT) as applied to a lithium-ion porous electrode, *J. Power Sources* 189 (1) (2009) 263–268.
- [38] W. Weppner, R.A. Huggins, Determination of the kinetic parameters of mixed-conducting electrodes and application to the system Li<sub>3</sub>Sb, *J. Electrochem. Soc.* 124 (10) (1977) 1569–1578.
- [39] N. Meethong, H.-Y.S. Huang, et al., Size-dependent lithium miscibility gap in nanoscale Li<sub>1-x</sub>FePO<sub>4</sub>, *Electrochem. Solid-State Lett.* 10 (5) (2007) A134–A138.

# Catalytic cathode nanomaterials for rechargeable lithium–air batteries: status and challenges

3

*H. Cheng, K. Scott*

School of Chemical Engineering & Advanced Materials, Newcastle University,  
Newcastle upon Tyne, UK

## 3.1 Introduction

In tackling the ever-growing challenges of security and diversity of energy supplies and environmental sustainability, the rechargeable Li–air battery appears as an attractive option for the electrification of transportation and large-scale deployment of renewable energy (e.g., solar and wind) [1–11]. This is due to the fact that the state-of-the-art batteries fall far behind the requirements; for instance, current electric vehicles driven by Li-ion batteries do not have enough storage capacity to drive electric vehicles more than 100 miles per charge. On the other hand, the Li–air battery has the potential to enhance capability to drive electric vehicles for more than 300 miles per charge, which is comparable to gasoline vehicles [6–11]. Among batteries that use lithium metal anode and oxygen (air) as cathode active materials (i.e., aprotic, aqueous, hybrid, and all solid-state electrolytes), the aprotic system has been the most attractive one because the oxygen reduction reaction (ORR) and oxygen evolution reaction (OER) could be reversible in aprotic media, giving its recharge ability [6,8–10,12]. This chapter will focus on this type of battery.

The Li–air battery is usually composed of a Li metallic anode, a solid separator, and a porous air cathode filled with organic electrolyte. External air is allowed to penetrate the pores of the cathode, diffuse through the electrolyte, and react with the Li ions according to the reactions [6,8,10,12–15].



The reactions produced high theoretical specific energies (gravimetric energy densities), 11,586 Wh kg<sup>−1</sup> based on the mass of Li alone and 3505 Wh kg<sup>−1</sup> based on the reaction (3.2) [6,8,10,12,13]. On the other hand, the cycling process involves the asymmetric ORR and OER; both are sluggish in an aprotic solution. This produces

large discharge overpotential and charge overpotential. Moreover, the instability of electrolyte and electrode under the high charging potential presents another challenge. Consequently, the current Li–air battery has low cycle life, rate capability, and low electrical energy efficiency, of the order of 60–70%. To overcome these challenges, efficient catalysts for ORR and OER at the air cathode are highly demanded, because catalyst determines the current-dependent charge/discharge potentials (i.e., the round-trip efficiency) and affects reaction direction and products [1–5,7,9,16–33]. In Li–air batteries, there are several major capacity-limiting issues, such as passivation and pore blockage by insulating discharge products, as well as O<sub>2</sub> transport limitations arising in flooded electrodes. Also, as ORR and OER occur at the surface atoms, catalyst support could play an important role because distributing catalyst atoms over a support could maximize the surface area of a catalyst and make efficient use of catalysts also occur on the substrate. Therefore, it is critical to first build an ideal host structure to constitute an effective three-phase reaction zone for Li–air batteries by using appropriate substrates [1–3,31,32].

The chapter focuses on a review of the status in development of catalysts and support materials for air cathode of rechargeable Li–air batteries, including our recent case studies. A brief review of the trends and challenges is provided.

## 3.2 Catalysts for air cathodes

One of the big challenges for the Li–air battery is its limited electrical efficiency, which is due to the overpotential or polarization losses at the cathode during discharge and charge. A high potential is needed for charging (~4.5 V) the porous carbon electrode, whereas the discharge potential is around 2.5 V; the big difference between these two values leads to a low efficiency. The improvement of this efficiency may be expected by applying effective catalysts.

### 3.2.1 Experimental aspects

A key aspect of R&D on catalysts is to understand their roles in ORR and OER. This was usually evaluated by both spectroscopic methods and electrochemical techniques. Electrochemical measurements could be classified into two types: half-cell test and battery evaluation [34,35]. The half-cell test was generally conducted in a three-electrode cell, consisting of a catalyst-coated working electrode, a counter electrode (e.g., Pt wire or mesh) and a reference electrode (e.g., Ag wire or Li foil in nonaqueous solutions and Hg/Hg<sub>2</sub>SO<sub>4</sub> or Ag/AgCl in aqueous media) (Figure 3.1a). With the aid of electrochemical measurement techniques, such as the linear sweep voltammetry and chronoamperometry, data reflected catalytic activities of a catalyst and displayed mechanism of ORR and OER could be collected [1–3,34–36]. In a battery test, galvanostatic discharge/charge curves were generated in either a Swaglok or a coin-type battery (Figure 3.1b), assembled with a Li metal anode, a Li-containing electrolyte

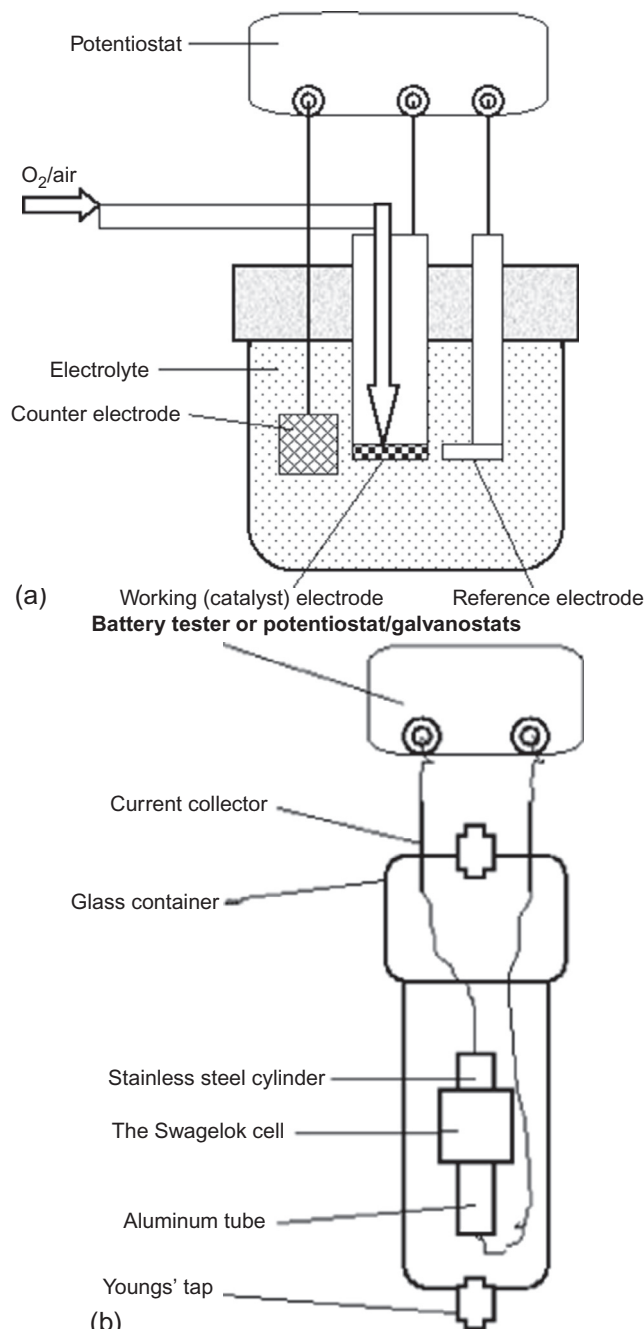


**Figure 3.1** Experimental setups devoted to the understanding of the oxygen reduction and oxygen evolution reactions on the catalysts. (a) Three-electrode half-cell. (b) Battery test system.

impregnated into a fiber (e.g., glass fiber) or a plastic (e.g., cellulose) separator and an air cathode. The air electrode was composed of a catalyst, carbon black, and a binder (e.g., Kynar or PTFE powders). The electrical connection was aided by metal mesh (e.g., Al or Ni mesh) support with pores to permit oxygen access.

Spectroscopic techniques play an essential role in understanding mechanisms of ORR and OER. For instance, cycling intermediates and products, such as Li superoxide ions and Li peroxide and Li oxides, were identified by a combination of *in situ* differential electrochemical mass spectrometry,  $^1\text{H}$  and  $^{13}\text{C}$  solid-state nuclear magnetic resonance spectroscopy, powder X-ray diffraction, a Fourier transform infrared spectroscopy, and *in situ* surface-enhanced Raman spectroscopy measurements. ORR mechanisms were proposed for the reactions on discharge and charge [8,19]. In another work, ORR and OER on nanocrystalline bifunctional  $\text{Co}_{x}\text{Mn}_{3-x}\text{O}_4$  spinel catalyst were investigated by a combination of atomic absorption spectrometry, energy-dispersive X-ray spectroscopy, Brunauer–Emmett–Teller surface analysis, scanning electron microscopy, transmission electron microscopy, X-ray diffraction (XRD), X-ray photoelectron spectroscopy, fast Fourier transform diffraction, and temperature programmed desorption/mass spectrometry measurements/analyses [36].

### 3.2.2 Metal catalysts

Owing to their effectiveness and good conductivity, metals are widely used as catalysts, especially in a form of nanomaterial, for rechargeable Li–air batteries. As is well known, ORR is sluggish in nature and traditionally requires the use of platinum-based catalysts [37]. At Newcastle, Pt and Pt alloys have been used as cathode catalysts in rechargeable Li–air batteries. As can be seen in Figure 3.2a, the shape and voltages of the discharge/charge profile for batteries with Pt and Pt alloy catalysts show some similarities, but the PtNi alloy battery delivers 40% higher initial discharge capacity than its Pt counterpart and the PtFe battery has more than a double increase, i.e., 2450 versus 1205 mAh g<sup>-1</sup> based on all cathode solids (Figure 3.2a and Table 3.1). The use of Pt alloys rather than Pt also improves cycling stability. For example, the PtFe battery retains a higher capacity than its Pt counterpart, 45% versus 21% and 28% versus 5% after 5 and 10 cycles, respectively (Figure 3.2b and Table 3.1). These data suggest a higher cycling stability of the Pt alloys over the Pt itself, although their stability is still a major concern (Figure 3.2b and Table 3.1). In addition, the Pt alloy batteries display lower efficiencies than the Pt battery (Table 3.1). The Pd catalyst also showed a similar trend as the Pt catalyst [2]. An Au catalyst was also used in Li–air batteries and, compared with a carbon cathode, it is a superior catalyst that is faster for lithium peroxide formation upon discharge, which enhanced the discharge voltage [38].

As noble metals, such as platinum, gold, and palladium, are expensive and scarce, substantial efforts have been dedicated to further improving their performance [39], and also to search for non-noble metalcatalysts [40,79]. A carbon-supported CuFe catalyst was used as the cathode in rechargeable Li–air batteries but displayed small capacity [41]. Therefore, more effort is required in this aspect.

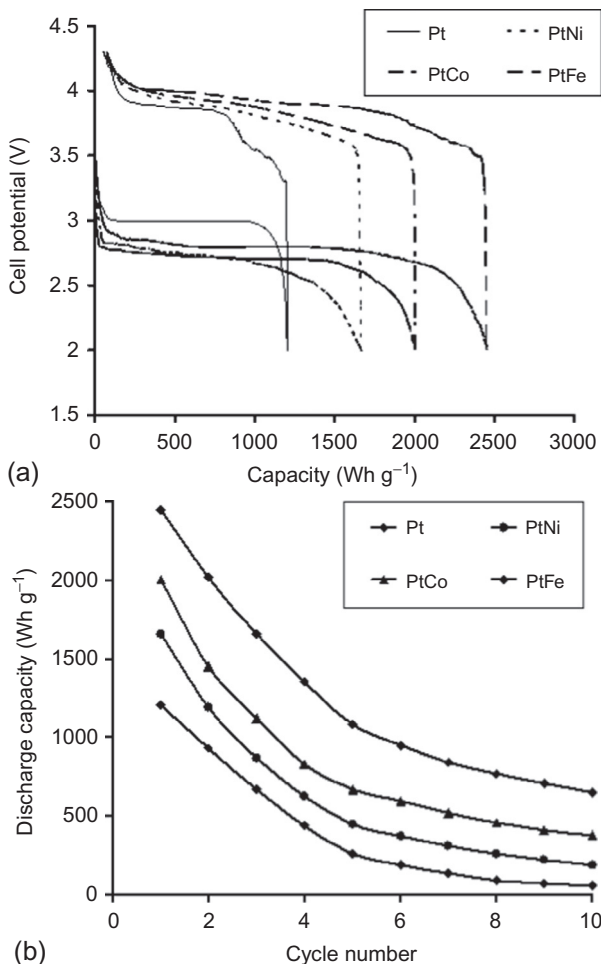


**Figure 3.2** Charge–discharge characteristics and cycle stability (between 2.0 and 4.3 V at 0.1 mA cm<sup>−2</sup> and 30 °C) of rechargeable Li–O<sub>2</sub> batteries with Pt and Pt alloy catalyst cathodes. (a) Initial charge–discharge curves. (b) Cycling performance. The capacity is based on the total catalyst mass.

### 3.2.3 Oxide catalysts

Intensive investigation on oxide catalysts has been carried out, mainly due to their low cost and higher stability than their metal counterparts.

Manganese oxides are the most studied catalysts for Li–air batteries [3,17,72]. The Newcastle group fabricated manganese oxide nanocatalysts that had particle sizes of around 50 nm, based on tunneling electron microscope measurement. They were uniformly distributed in the carbon matrix, which contributed to an improved electrical

**Table 3.1 The influence of catalyst on capacity, efficiency, and cycle ability of rechargeable Li–O<sub>2</sub>/air batteries with various catalysts<sup>a</sup>**

Catalyst	Capacity <sup>b</sup> (mAh g <sup>-1</sup> catalyst)	Efficiency <sup>c</sup> (%)	Capacity retention <sup>d</sup> (%)		
			Cycle		
			5	10	20
MnO <sub>2</sub>	1990	62	75	43	33
α-MnO <sub>2</sub> nanowire	2480	65	69	30	18
β-MnO <sub>2</sub> nanowire	3085	72	75	35	30
RuO <sub>2</sub>	1600	69	70	30	15
Pt	1205	90	21	5	
PtNi	1660	80	27	12	
PtCo	2005	80	33	20	
PtFe	2450	84	45	28	
Ag/Ni foam	1000	82	43	15	
Au/Ni foam	1760	88	52	30	
AuAg/Ni foam	2165	85	70	50	
AuNiO/Ni foam	2018	76	89	68	44
AgNiO/Ni foam	1140	72	78	58	38
AuNiOIrO <sub>2</sub> /Ni foam	2445	90	95	85	67
AgNiOIrO <sub>2</sub> /Ni foam	1475	88	89	71	54
Macrocycle 1, O <sub>2</sub>	935	95	33		
Macrocycle 2, O <sub>2</sub>	810	80	13		
Macrocycle 1, Air	600	78	27		
Macrocycle 2, Air	495	73	8		

<sup>a</sup>Discharge/charge rate: 0.1 mA cm<sup>-2</sup> unless otherwise stated.<sup>b</sup>The first cycle.<sup>c</sup>Round-trip efficiency is a ratio of total energy storage system output (discharge) divided by total energy input (charge) as measured by ratio of discharge voltage divided by charge voltage.<sup>d</sup>Capacity retention is the fraction of the full capacity available from a battery under specified conditions of discharge after it has been cycled for a number of cycles.

connection among the catalyst and current collectors. The charge/discharge tests using this material as the cathode material in a rechargeable Li–air battery showed high discharge capacities up to 4750 mAh g<sup>-1</sup>, based on carbon mass. The cycle ability of the composite electrode was superior to those of the commercial electrolytic manganese dioxide electrodes [3]. The Newcastle group also prepared rechargeable Li–air batteries with several types of manganese oxide cathodes, including α- or β-MnO<sub>2</sub> nanowires and MnO<sub>2</sub> nanoparticles. These catalysts were compared with a RuO<sub>2</sub> catalyst, as shown in Figure 3.3 and Table 3.1. The β-MnO<sub>2</sub> nanowire shows the highest efficiency. The specific initial discharge capacities for β-MnO<sub>2</sub>, α-MnO<sub>2</sub>, MnO<sub>2</sub>, and

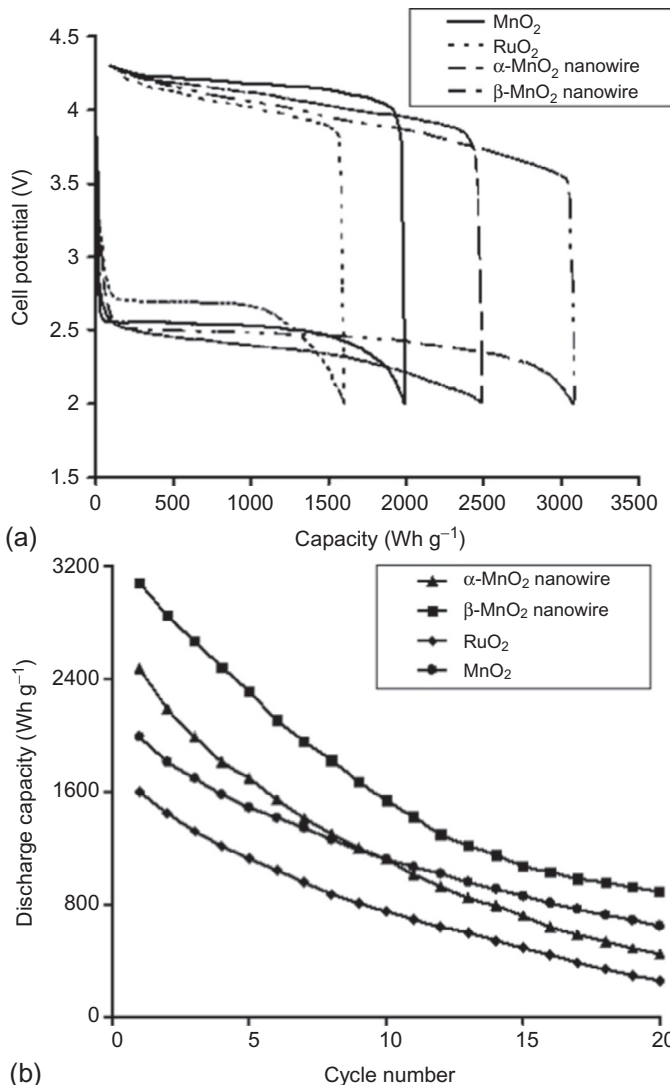


**Figure 3.3** Charge–discharge characteristics and cycle stability (between 2.0 and 4.3 V at 0.1 mA cm<sup>−2</sup> and 30 °C) of rechargeable Li–O<sub>2</sub> batteries with oxide catalyst cathodes. (a) Initial charge–discharge curves. (b) Cycling performance. The capacity is based on the total catalyst mass.

RuO<sub>2</sub>, based on the catalyst mass, were 3085, 2480, 1990, and 1600 mAh g<sup>−1</sup>, respectively (Figure 3.3a and Table 3.1). The capacities then drop steadily thereafter (Figure 3.3b). The MnO<sub>2</sub> nanoparticle exhibits the best cycling stability (i.e., 33% loss in capacity after 20 cycles), which is higher than other catalysts (Figure 3.3b and Table 3.1).

The St Andrew's group also compared several types of  $\text{MnO}_x$ , including  $\alpha\text{-MnO}_2$  nanowires,  $\beta\text{-MnO}_2$  nanowires, bulk  $\text{MnO}_2$  ( $\alpha$ ,  $\beta$ ,  $\gamma$ ,  $\lambda$ ), and commercial  $\text{Mn}_2\text{O}_3$  and  $\text{Mn}_3\text{O}_4$  and found that  $\alpha\text{-MnO}_2$  nanowires are the most effective catalysts for the rechargeable Li–air battery due to their special crystal structure and high surface area [17]. Lithium–metal oxides with a high formal  $\text{Li}_2\text{O}$  content such as  $\text{Li}_5\text{FeO}_4$  ( $5\text{Li}_2\text{O}\cdot\text{Fe}_2\text{O}_3$ ),  $\text{Li}_2\text{MnO}_3$ , and  $\text{LiFeO}_2$  composite ( $\text{Li}_2\text{O}\cdot\text{MnO}_2$ ) ( $\text{Li}_2\text{O}\cdot\text{Fe}_2\text{O}_3$ ) were used as electrocatalysts for Li–air batteries, resulting in high discharge capacities up to  $2516 \text{ mAh g}^{-1}$  (carbon) corresponding to  $931 \text{ mAh g}^{-1}$  (electrocatalyst + carbon) during the initial discharge. The reaction is reasonably reversible during the early cycles. But the battery could only be sustained for less than 10 cycles [42]. Another electrode of manganese oxide nanocatalysts (i.e.,  $\alpha\text{-MnO}_2$  nanorod) was prepared by mixing with carbon nanotubes/nanofibers and demonstrated that the charge capacity and cyclability of the battery were largely increased with the catalyst [72]. The work also found that the discharge capacity of the Li–air battery was mainly due to oxygen deficiency from the narrowing of the diffusion channel by the deposition product at the air side of the air electrode [72]. The  $\alpha\text{-MnO}_2$  nanoflake was coated on multiwalled carbon nanotubes and used (containing 60 wt.% nanoflakes) as cathode for Li–air batteries. The catalyst-enhanced kinetics of the ORR and OER, thereby effectively improving energy efficiency and reversible capacity up to  $2000 \text{ mAh g}^{-1}$ , but the stability of the battery was poor [43]. Titanium containing  $\gamma\text{-MnO}_2$  octahedral molecular sieves having hollow sphere structures was used in Li–air batteries, and the material gave high specific capacity up to  $2300 \text{ mAh g}^{-1}$  [44].

Several oxide catalysts have been studied, including  $\alpha\text{-MnO}_2$ , Fe oxides, Cu oxides, Co oxides, and mixed metal perovskite  $\text{La}_{0.8}\text{Sr}_{0.2}\text{MnO}_3$  [4,5,17]. Among them,  $\text{Fe}_2\text{O}_3$  exhibits the highest initial discharge capacity, while  $\text{Fe}_3\text{O}_4$ ,  $\text{CuO}$ , and  $\text{CoFe}_2\text{O}_4$  give the best capacity retention (6.67% per cycle), as well as the lowest charging voltage of 4 V.  $\text{Co}_3\text{O}_4$  shows the best compromise between the initial discharge capacity ( $2000 \text{ mAh g}^{-1}$ ) and the retention (6.5% per cycle). Interestingly,  $\text{MnO}_2$  exhibits a low charge potential of 3.8 V;  $\text{CoMn}_2\text{O}_4$  exhibits a good bifunctional property in ORR and OER. However, in another very recent study, a  $\text{Co}_3\text{O}_4$  catalyst only sustained several cycles with small capacity [45].

### 3.2.4 Bifunctional catalysts

The cycling process in rechargeable Li–air batteries involves the ORR and OER; the asymmetry of ORR and OER introduces different discharge and charge voltages, which lowers the battery efficiency. Hence, heterogeneous electrocatalysis has become a focal point in rechargeable Li–air battery research to reduce overpotentials in both the oxygen reduction (discharge) and oxygen evolution (charge) reactions. Past reports of traditional cathode electrocatalysis in nonaqueous Li–air batteries were mainly concentrating on ORR, but gas evolution related to electrolyte solvent decomposition was another process being catalyzed, in addition to other side reactions facilitated by the catalysts [18,19,23–25,45,46]. Therefore, an effective charging process reaction is even more important for the reversibility of Li–air batteries. This attracts a

growing interest in developing an efficient and low-cost bifunctional catalyst, which reduces both charge overpotential and discharge overpotential. Because the rates of charge and discharge depend on the catalytic activities of the ORR and OER, the use of a bifunctional catalyst could also enhance both ORR and OER and suppress side reactions, leading to higher reaction rate and selectivity [21,22,31,41,47].

A typical example is the Pt–Au system where the Au catalyst showed the high discharge activity, while the Pt catalyst exhibited extraordinarily high charging activity. The voltage gap between the ORR and OER could be reduced to less than 0.8 eV at 50 mAh g<sup>-1</sup> by using Au to enhance the ORR and Pt to lower the OER voltages, leading to a high round-trip efficiency of 77% [22]. A PtAu alloy displayed considerably lower charging voltages than manganese and cobalt oxides [21,22].

Very recently, our Newcastle group has explored a series of bifunctional catalysts based on Au or Ag, NiO, and IrO<sub>2</sub>. One special feature of using such a novel system as a catalyst in the oxygen cathode for rechargeable lithium batteries is greatly reducing charge potential; hence, high efficiencies up to 90% are achieved (Table 3.1). The batteries can deliver capacities of 2500 or 1500 mAh g<sup>-1</sup> based on total catalyst masses for the Au or Ag system, respectively, at the beginning of discharge (Figure 3.4a and b; Table 3.1). Of the catalysts studied the highest initial capacity is observed with AuNiOIrO<sub>2</sub> (2445 mAh g<sup>-1</sup>). The most striking feature of the bifunctional catalysts is their great capability to enhance cycling stability. This may be due to lower oxidation potential and less solvent decomposition. The ability of a Li–O<sub>2</sub> battery that contains bifunctional catalysts to sustain cycling is demonstrated in Figure 3.4c, in which the load curves for four different catalysts each demonstrate cycling up to 100 cycles, but only the data of 20 cycles are present here. The highest capacity retention is achieved with AuNiOIrO<sub>2</sub> (67% per cycle at 20th cycle). AuNiOIrO<sub>2</sub> gives the best compromise between initial capacity and capacity retention, as well as the highest efficiency (Figure 3.4a–c and Table 3.1). Clearly, the stabilities of the Au cathode far exceed the Ag counterpart (Figure 3.4a–c and Table 3.1).

A bifunctional catalyst (La<sub>0.5</sub>Ce<sub>0.5</sub>Fe<sub>0.5</sub>Mn<sub>0.5</sub>O<sub>3</sub>) was demonstrated to be active for both ORR and OER, leading to an average capacity of 1200 mA g<sup>-1</sup>, efficiency of 70%, and cycling stability of 100 cycles [31]. Obviously, the capacity is relatively small and charge voltages (around 3.9 V) are still too high. Another bifunctional catalyst with Sr<sub>0.95</sub>Ce<sub>0.05</sub>CoO<sub>3–δ</sub> and copper nanoparticles was found to be efficient and stable for the ORR and OER in aqueous solution [47]. But its feasibility has not yet been demonstrated in an aprotic medium.

Manganese-based nanocrystalline spinels (Co<sub>x</sub>Mn<sub>3–x</sub>O<sub>4</sub> spinels, CoMnO–P, and CoMnO–B, etc.) have long been used as alternative and low-cost electrocatalysts for ORR and OER [48,49]. A spinel nanoparticle (i.e., CoMn<sub>2</sub>O<sub>4</sub>) showed considerable catalytic activity toward the ORR/OER as a result of its high surface areas and abundant defects. It produced high capacity up to 3000 mAh g<sup>-1</sup> in rechargeable Li–air batteries [36,50]. A hollandite Ag<sub>2</sub>Mn<sub>8</sub>O<sub>16</sub> compound was synthesized as a bifunctional catalyst; although it exhibited a reduced discharge overvoltage, the discharge capacity was less than 500 mAh g<sup>-1</sup> and the cycle stability was poor [51].

The mixture of Pd and MnO<sub>2</sub> showed the high activity to oxidation and reduction of Li to form Li<sub>2</sub>O<sub>2</sub> or Li<sub>2</sub>O, respectively. The discharge plateau of the battery increased

to 2.9–2.7 V, while the charge potential decreased to 3.6 V, leading to a high specific energy efficiency up to 89% [52,53].

A pyrochlore  $\text{Pb}_2\text{Ru}_2\text{O}_{7-\delta}$  compound was also used as a bifunctional catalyst, delivering a capacity of  $1000 \text{ mAh g}^{-1}$  and a 0.5 V lower charge potential for oxygen evolution from  $\text{Li}_2\text{O}_2$  than pure carbon [54]. However, the catalyst contains toxic lead, in addition to the problems of relatively low capacity and short service life.

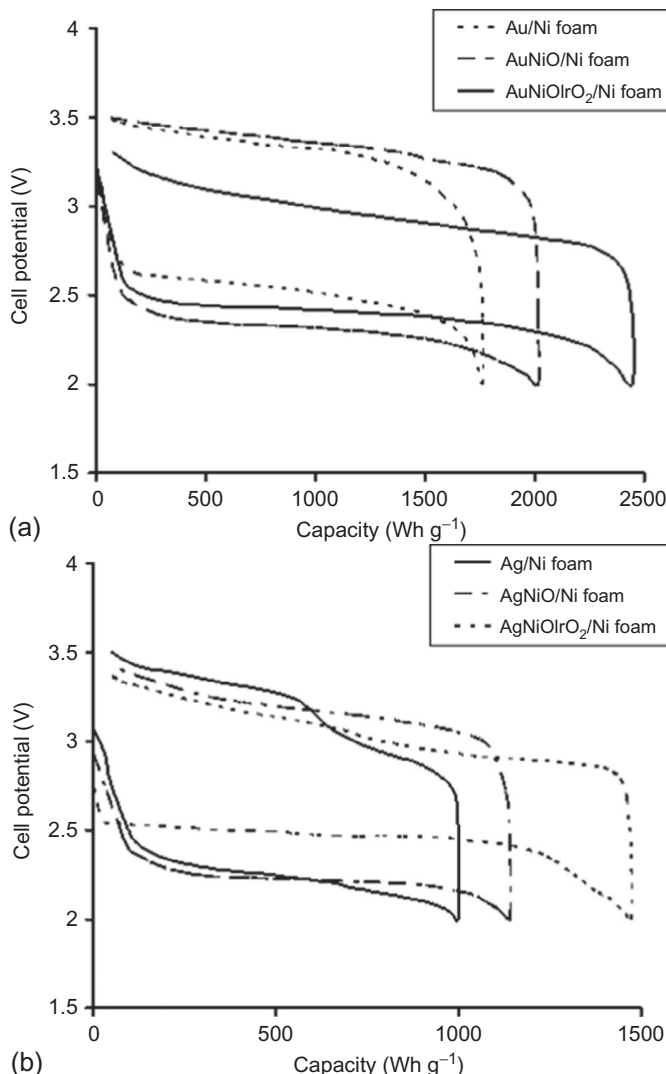


**Figure 3.4** Charge–discharge characteristics and cycle stability (between 2.0 and 3.5 V at  $0.1 \text{ mA cm}^{-2}$  and  $30^\circ\text{C}$ ) of rechargeable  $\text{Li}-\text{O}_2$  batteries with bifunctional catalyst cathodes. (a) and (b) initial charge–discharge curves.

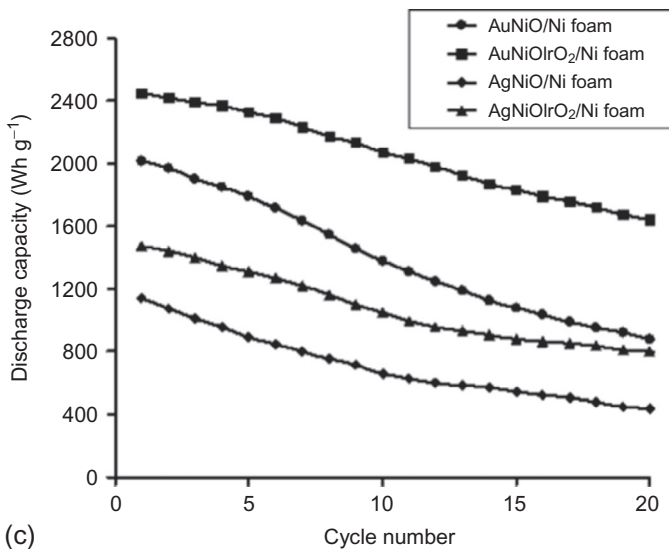


**Figure 3.4** Continued. (c) Cycling performance. The capacity is based on the total catalyst mass.

A TiN bifunctional catalyst reduced the discharge–charge voltage gap (1.05 V), increasing the battery efficiency [55]. However, the cycling life was low, raising questions about its feasibility.

### 3.2.5 Other catalysts

The earliest rechargeable Li–air battery adopted a carbon-supported cobalt phthalocyanine catalyst [12]. At Newcastle, we also explored the feasibility of this type of catalyst with an interest in its low cost. As can be seen from [Figure 3.5a and b](#) and [Table 3.1](#), their cycling stability is a major concern, although it showed reasonably high capacities, around 800 and 950 mAh g<sup>−1</sup>, when fed with air and pure oxygen, respectively. Low efficiencies (around or below 30%) are another worry for using this type of catalyst.

Some transition metal nitrides have been explored; for instance, molybdenum nitride/nitrogen-doped graphene nanosheets were synthesized and used as an air cathode in lithium–oxygen batteries. It exhibits a high discharge potential (ca. 3.1 V) and a specific capacity of 1490 mAh g<sup>−1</sup>, based on carbon + electrocatalyst. However, the stability of this catalyst is poor, less than 10 cycles [56].

Nanostructured La<sub>0.8</sub>Sr<sub>0.2</sub>MnO<sub>3</sub> was recently reported as an effective catalyst for ORR in Li–oxygen batteries; it shows higher discharge plateau and a specific capacity of up to 2000 mAh g<sup>−1</sup> but no cycle data are reported [57].

Very recently, a biologically derived electrode has been reported; it uses 3–5 wt.% of palladium and carbon nanoparticles assembled by M13 virus with earth-abundant

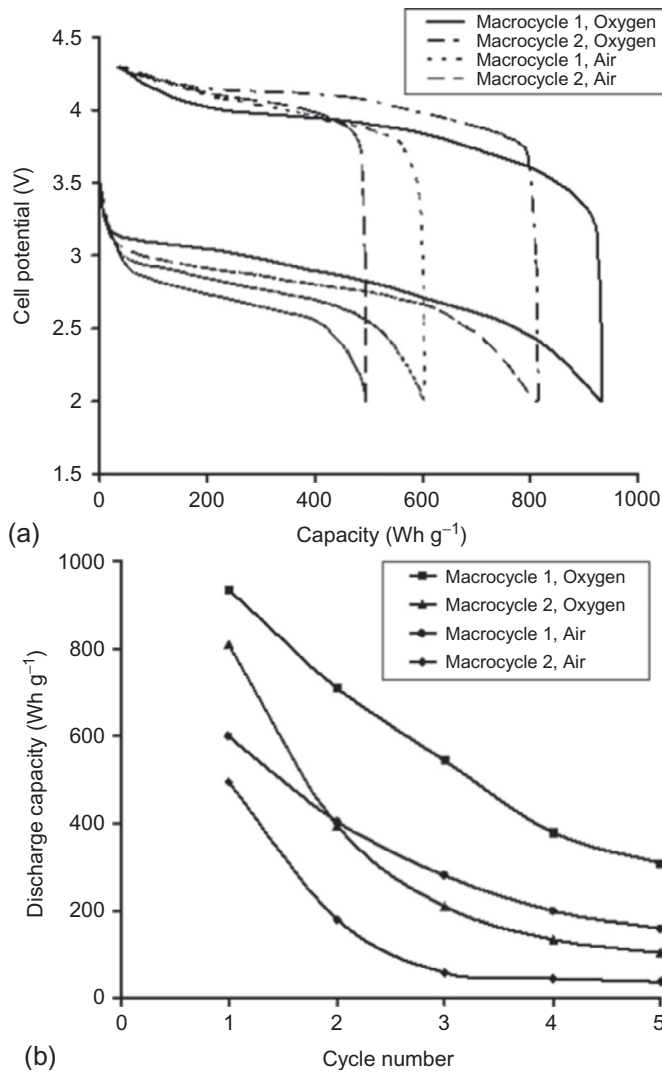


**Figure 3.5** Charge–discharge characteristics and cycle stability (between 2.0 and 4.3 V at 0.1 mA cm<sup>-2</sup> and 30 °C) of rechargeable Li–O<sub>2</sub>/air batteries with macrocycle catalyst cathodes. (a) Initial charge–discharge curves. (b) Cycling performance. The capacity is based on the total catalyst mass.

elements such as manganese oxides. The exceptionally high specific capacity is achieved, up to 13,350 mAh g<sup>-1</sup> in terms of carbon loading or 7340 mAh g<sup>-1</sup> in terms of total carbon and catalyst loading at 0.4 A g<sup>-1</sup> (in terms of carbon loading) [58]. However, the stability of the electrode is rather poor. Also, as this is an unconventional approach, its feasibility and reproducibility also require more investigation.

An attempt was made to use metal and metal oxides air cathodes without carbon [53]. The mixtures of Pd, MnO<sub>2</sub>, and poly(tetrafluoroethylene) (mole ratios of 75:15:10, 70:20:10, and 60:30:10) show the high activity to oxidation and reduction of Li to form Li<sub>2</sub>O<sub>2</sub> or Li<sub>2</sub>O, respectively. The application of Pd/MnO<sub>2</sub> without a carbon binder for the air electrode is effective to decrease the charge potential and to improve the energy efficiency from 60% to 89%. However, the discharge capacity decreased, which may be due to lower dispersion of catalyst particles in the absence of carbon support [53].

### 3.2.6 Mechanisms of ORR and OER

The performance of rechargeable Li–air batteries with nonaqueous electrolytes is limited by the oxygen evolution and oxygen reduction kinetics. Oxygen is reduced by lithium ions to form Li<sub>2</sub>O<sub>2</sub> and/or Li<sub>2</sub>O, as shown in Equations (3.1) and (3.2). The analysis of the reaction products by Raman spectroscopy and XRD has revealed Li<sub>2</sub>O<sub>2</sub> as the major discharge product, while oxygen consumption measurements during the discharge suggest a partial formation of Li<sub>2</sub>O [8,12,13,18–20,24,25]. The evidence from the above-mentioned investigation suggests that the reaction (3.1) is not direct, but divided into three steps, i.e., the irreversible reduction of oxygen to lithium superoxide:



followed by disproportionating LiO<sub>2</sub> to Li<sub>2</sub>O<sub>2</sub> and O<sub>2</sub>:



or LiO<sub>2</sub> further reduced to form Li<sub>2</sub>O<sub>2</sub>:



LiO<sub>2</sub> is also possibly formed as the ultimate reduction product of O<sub>2</sub>:



Relatively less experimental or theoretical work has yet been performed on the fundamental mechanism of the OER. In principle, the OER is essentially the decomposition of Li<sub>2</sub>O<sub>2</sub> from its surfaces; the details of the reaction path and desorption barrier will be affected by the surface structure. Based on this consideration, OER on the low-index surfaces of lithium peroxide has been studied using first-principles calculations [59]. The elementary reaction steps and the energy profile of the OER are identified on the low-index surfaces of lithium peroxide. The calculation shows that the OER processes are kinetically limited by the high-energy barrier for the evolution of oxygen molecules and that the rate of the OER processes is highly dependent on the surface orientation. The kinetics of OER are slow on the abundant surfaces but are faster on

the higher-energy surfaces. Such poor kinetics for the OER may be responsible for the low charging rate and high overpotential of the Li–air batteries. According to the calculation results in the energy profile and the reaction path of the OER for available surfaces, the OER mechanism is proposed. During charging, the OER in the Li–air battery is essentially the decomposition of  $\text{Li}_2\text{O}_2$  on the surfaces. Li-ions and electrons  $e^-$  leave the surface under the driving force of the charging potential. At the same time,  $\text{O}_2$  molecules are released from the surface. This leads to the following elementary reaction step of Li desorption and oxygen evolution:



### 3.2.7 Modeling aspects

Modeling is a powerful tool for understanding the operating principle of a battery and to improve battery performance.

At Newcastle, we have developed a micro–macro homogeneous mathematical model for a rechargeable Li–air battery using a concentrated binary electrolyte theory [60]. The model involves conservation of mass and current, species transport, and reaction kinetics in the cathode and separator to clarify the mechanism inside the cell. The dynamic behavior of the porous cathode is determined by a numerical solution of the combined continuity, transport, and kinetics equations. This model considers the time and space dependence of the battery system, including the mass transport along the depth of the cell, the local mass transfer between the lithium peroxide ( $\text{Li}_2\text{O}_2$ ) layer inside the cathode and active surface morphology changing with the  $\text{Li}_2\text{O}_2$  growth. In this model, the  $\text{Li}_2\text{O}_2$  formation inside the porous cathode is presented using a macro-homogeneous porous model, defining the electrode by its porosity, which is initially uniform but changes during discharge. For electrochemical reaction at the cathode, the Butler–Volmer equation is applied in the model using two rate coefficients related to concentrations of  $\text{Li}^+$ , oxygen, and  $\text{Li}_2\text{O}_2$ . Fick’s law was used to describe the diffusion of  $\text{Li}^+$  and  $\text{O}_2$  reactants through the  $\text{Li}_2\text{O}_2$  layer. The macroscopic theory of porous electrodes treats the solution and solid matrix phases as a superimposed continuum. In the solid matrix phase, the movement of the electron is governed by Ohm’s law, which computes the electric potential or potential of electron. The model predicts that the battery capacity and discharge potential are sensitive not only to the solubility of oxygen, which is predominantly limited by depletion of the oxygen concentration, as well as to the cathode porosity, the cathode structure, and kinetic parameters. In addition, the charging behavior is simulated by modeling the dissolution of solid  $\text{Li}_2\text{O}_2$  product. The model suggests that the charging voltage can be lowered depending on capability of the electrolyte to dissolve the  $\text{Li}_2\text{O}_2$  discharge products. As a result, a simulation of electrode behavior is obtained [60].

A micro–macro homogeneous model has also been developed at Newcastle in order to understand the deterioration of cycle performance and energy efficiency

related to nonaqueous rechargeable Li–air batteries [61]. Based on the mechanism analysis, the model pays particular attention to the impact of  $\text{Li}_2\text{CO}_3$  formation on battery cycling, which occurs by electrolyte degradation. The formation of these discharge products could limit the cyclability and passivate the porous-cathode surface. Important governing equations are obtained with the aid of the macroscopic theory of porous electrode; i.e., a material balance equation for specie transport in the Li–air electrolyte and the diffusion and migration fluxes equations for mass transfer of  $\text{Li}^+$  and all of the species transporting in the porous cathode. In the solid matrix phase, the movement of the electron is governed by Ohm's law. The charge conservation for the matrix and solution phases is proposed based on the porous electrode theory. Starting from reaction mechanisms, especially the reaction of  $\text{Li}_2\text{O}_2$  at the cathode, the  $\text{Li}_2\text{CO}_3$  formation and  $\text{CO}_2$  generation, modified versions of the Butler–Volmer equation are applied in the model to generate the electrochemical kinetic expressions for the porous cathode and for the anode reaction. The conservation equations and the boundary conditions described above were discretized using a finite element method and solved in a 1D battery system by commercial software package COMSOL multiphysics version 4.3. The COMSOL software is designed to solve a set of coupled differential and algebraic equations, and the battery simulation model is performed on a 32-bit Windows platform with 4 GB RAM, and Intel Core 2 Duo 2.93 GHz processor. The different transport equations and the electrochemical reactions were solved as time dependent until the cell voltage reached the stop condition. The solution was considered as converged solution when the difference between two results was less than  $10^{-4}$  (relative tolerance) for all variables. Finally, the model predicts the cycle performance deterioration measured in terms of retention of discharge capacity on cycling and shows a good agreement between the battery cycling simulation and porous-electrode experiment data; thus, creating a more reliable model for a rechargeable Li–air battery in nonaqueous electrolyte. Interestingly, the model indicates that the termination of the battery discharge is not from the pore blockage by the repeated depositing of discharge products as there are some available pores at the end of each discharge cycle [61].

There is a continuous interest in modeling the reactivity properties of Pt and Pt alloy catalysts, such as *ab initio* calculations. For example, the density-functional theory (DFT) is used to investigate the modification of the electronic and chemical properties of Pt(111) surfaces by subsurface 3d transition metals [62]. The Pt(111) surfaces are modeled by a  $2 \times 2$  unit cell with four layers of metal atoms periodically repeated with 4–6 equivalent layers of vacuum ( $>10 \text{ \AA}$ ) separating the slab to represent the Pt(111) surface. The four atoms in the second layer of the slab are substituted with one of the 3d transition metals between (and including) Ti and Ni. The DACAPO-2.7 code is used to calculate the electronic structure and the PW91 exchange/correlation functional is used to create ultrasoft Vanderbilt pseudopotentials. A  $4 \times 4 \times 1$  Monkhorst–Pack  $k$ -point set is used to calculate the O and H adsorption energies on Pt. The calculation displays that the Pt surface  $d$ -band is broadened and lowered in energy by interactions with the subsurface 3d metals, resulting in weaker dissociative adsorption energies of hydrogen and oxygen on these surfaces. It is found that the magnitude of the decrease in adsorption energy is largest for the early 3d transition metals

and smallest for the late 3d transition metals and, in some cases, dissociative adsorption is calculated to be endothermic. These findings are helpful in catalyst design [62].

ORR on the platinum monolayer surfaces were modeled via the spin-polarized DFT calculations [62]. This was performed in the generalized gradient approximation (GGA-PW91) using ultrasoft pseudopotentials as implemented in the DACAPO code. The platinum monolayer surfaces were modeled by a single layer of platinum placed on top of Au(111), Pd(111), Ir(111), Rh(111), and Ru(0001), at the substrate's lattice constants. Each surface was constructed from a (2 × 2) surface unit cell and modeled by a slab consisting of four layers of metal atoms. The top two layers, that is, the platinum monolayer and the first layer of the substrate metal, were relaxed. The binding energies ( $E_b = E_{\text{total}} - E_{\text{substrate}} - E_{\text{gas-phase adsorbate}}$ ) and geometries of adsorbed O, O<sub>2</sub>, and OH, as well as O<sub>2</sub> dissociation and O hydrogenation, were studied on the relaxed surfaces. Minimum-energy reaction paths were calculated using the climbing-image nudged elastic band method. The equilibrium PW91 lattice constants for bulk metals were calculated, which were in good agreement with the experimental values. The electrocatalytic activity of the ORR on a thin film of Pt deposited onto single-crystal metal substrates was established as a function of either the calculated binding energy of atomic oxygen or the calculated *d*-band center. Unfortunately, although these results provided valuable information, it was not possible to establish real systematic experimental trends [62].

In a further study, to help visualize the general trends, the kinetic current at a constant overpotential is plotted as a function of the experimentally determined *d*-band center position for the Pt-skin (and Pt-skeleton) surfaces, by generalizing from the Pt<sub>3</sub>Fe surfaces to the other Pt<sub>3</sub>M surfaces [80]. In this work, Monte Carlo (MC) simulations, containing atomic motions and exchanges of two atoms with different element types, are carried out to predict whether the equilibrium cubo-octahedral Pt<sub>75</sub>Co<sub>25</sub> nanoparticles, consisting of (111) and (100) facets bounded by low-coordination-number (edges and corners) atoms, can have a nearly pure Pt monolayer shell and Co-enriched sublayer. The MC simulations reveal that it is possible to create a thermodynamically stable Pt skin on nanoscale surfaces. As a result, a correlation is established between the experimentally determined surface electronic properties and reactivity when the average energy of the *d* states on the surface atoms is systematically changed across the periodic table. The emphasis is placed on advanced concepts that can be used to understand and predict variations in the ORR reactivity caused by the effects of alloying Pt with the 3d transition metals. Electrocatalytic trends in the ORR are established as a relation between the surface composition, specific activity (kinetic current density,  $i_k$ ), and the surface electronic structure of Pt<sub>3</sub>M (M=Ni, Co, Fe, V, Ti) alloy surfaces. In particular, the relationship between the specific activity and the *d*-band center position on the Pt-skin surfaces exhibits a volcano shape, with the maximum catalytic activity obtained for Pt<sub>3</sub>Co. The model predicts the trend is that, to create better catalysts than Pt for the ORR, the catalysts should counterbalance two opposing effects; that is, a relatively strong adsorption energy of O<sub>2</sub> and reaction intermediates (O<sub>2</sub><sup>-</sup>, O<sub>2</sub><sup>2-</sup>, H<sub>2</sub>O<sub>2</sub>, and so on) and a relatively low coverage by spectator oxygenated species and specifically adsorbed anions. Therefore, for metal surfaces that bind oxygen/oxides/anions too strongly, for example, as in the case

of Pt, the *d*-band center is too close to the Fermi level and the rate of the ORR is limited by the availability of OH<sub>ad</sub>/anion-free Pt sites. On the other hand, when the *d*-band center is too far from the Fermi level, as in the case of Pt<sub>3</sub>V and Pt<sub>3</sub>Ti, the surface is less covered by OH<sub>ad</sub> and anions, but the adsorption energy of O<sub>2</sub> and the intermediates is too low to enable a high turnover rate of the ORR. The resulting volcano, therefore, can be rationalized by the application of the Sabatier principle; that is, whereas for catalysts that bind oxygen too strongly, the rate is limited by the rate of removing surface oxides and anions, for catalysts that bind oxygen too weakly, the rate is limited by the rate of electron and proton transfer to adsorbed O<sub>2</sub>. The knowledge established by this model can be used to explain the activity pattern of the ORR on Pt<sub>3</sub>M nanocatalysts as well as to provide a fundamental basis for the improvement of existing cathode nanocatalysts [80].

The first-principles calculations on the reactivity properties of the above-mentioned bifunctional catalyst (i.e., the Co–Mn–O nanocrystalline spinels) are carried out using the Vienna *ab initio* Simulation Package and DFT [36]. The PW91 form for GGAs is used to calculate the exchange and correlation potentials. We use a plane-wave basis set and the projector augmented wave potentials. Considering the fact that electron correlation within the *d* states significantly affects the electronic structure and energetic properties of transition metal oxides, the GGA+*U* approach is used to accurately calculate the O<sub>2</sub> binding energy and to guarantee that the excess holes or electrons are properly localized, where reported *U* values and the lattice properties of the as-investigated spinel metal oxide are used. The surface energy in the given direction is also calculated with the aid of experimental data; i.e., the thicknesses of vacuum, slab, and free relaxation layer. Two different adsorption sites have been investigated for each phase for the calculation of the oxygen-binding energies. The calculated results indicate that the Co defect site possesses a little more negative oxygen-binding energy than the Mn defect site, while the cubic phase possesses much more negative oxygen-binding energy than the tetragonal phase. Based on the calculation results, a reduction–crystallization mechanism for the synthesis of Co<sub>x</sub>Mn<sub>3-x</sub>O<sub>4</sub> is proposed. Under the driving force of ion exchange, i.e., the “site preference energies” of transition-metal ions in the spinel crystal lattices, the Mn(IV) in the amorphous nanoparticulate MnO<sub>2</sub> precursor is rapidly reduced to lower-valence manganese (Mn(III) and/or Mn(II)) by a strong reducing agent, and the amorphous MnO<sub>2</sub> structure is transformed to the spinel phase. At the same time, the dissociative Co<sup>2+</sup> in the solution diffuses into the solid lattice and either occupies the manganese vacancies or partially substitutes for manganese ions in the tetrahedral or octahedral interspace [36]. Based on evidence collected from both experiment and DFT, the high catalytic activities for both ORR and OER of the Co–Mn–O nanocrystalline spinels and the related phase-dependent electrochemical characteristics are reasonably explained [36]. In summary, the cubic Co–Mn–O spinel outperforms the tetragonal phase in intrinsic ORR catalytic activity, but the tetragonal spinel surpasses the cubic phase for OER, due to the dissimilar binding energies of oxygen adsorption on cobalt and manganese defect sites. To gain further insight into the relationships between ORR activity and the phase or defects of the Co–Mn–O spinel system, a series of DFT calculations are conducted to study the oxygen adsorption

on different defect sites of two typical surfaces: cubic (113) and tetragonal (121). The calculation shows that the cobalt defect site can bind oxygen a little more strongly than the manganese defect site; whereas, on either the cobalt or manganese sites, the cubic (113) surface generates much more stable molecular oxygen adducts than the tetragonal (121) surface. Furthermore, the calculation displays that, for a given surface area, the number of available active sites on the cubic (113) surface will exceed that on the tetragonal (121) surface, suggesting that the cubic Co–Mn–O spinel outperforms the tetragonal phase in intrinsic ORR catalytic activity [36]. Similarly, regarding electrocatalytic OER, one can predict that the performance of the tetragonal spinel surpasses the cubic phase, because the OER can be viewed as a reverse process of the ORR [35,36].

### 3.2.8 Summary

The R&D of effective and low-cost catalysts for air cathode is one of the most urgent and important driving forces in the development of rechargeable Li–air batteries. The metal catalysts are still the most active systems for both ORR and OER, but they are often associated with low stability and high cost. Oxides have advantages in cost and also could provide reasonably high activities for ORR and OER, although their activities show some distances from what is required for a high-power device. The promising direction is to explore bifunctional systems, possibly combined metals with oxides, like what has been done at Newcastle and by other groups. This approach could balance activity, stability, and cost and has the potential to speed up the development of rechargeable Li–air batteries.

## 3.3 Support materials for air cathodes

Catalyst supporting materials play an important role in achieving high utilization and stabilization of nanocatalytic sites for ORR and OER in rechargeable Li–air batteries. In general, support materials have a high specific surface area. Thus, if a precursor salt of the metal can be effectively distributed over this area (say, by solution impregnation) and then decomposed, nanoscale metallic particles will result. In the case of costly materials, such as noble metals, small particles are economic necessities because they represent a larger surface-to-volume ratio and, thus, greater catalytic utilization of the metal. Maintenance of this dispersion under severe processing conditions is another function of the support, as the separation of the metal particles inhibits their agglomeration [63]. Moreover, there is strong metal–support interaction, which leads to the existence of strong bonding between catalyst particles and substrate. Thus, the substrate could influence the catalytic activities, activation energies, and selectivities [63].

An ideal supporting material should satisfy the following requirements: (1) a high specific surface area, which provides high dispersion and high utilization of nanocatalysts; (2) high conductivity; (3) high chemical and electrochemical stability under the lithium–air operating process; and (4) low reactivity with electrolytes in Li–air

batteries. Currently, the most popular support material in the Li–air system is carbon due to its high conductivity, high surface area, and low cost. In future research, efforts should be devoted to developing some novel supporting materials including oxides, carbides, nitrides, metals, and so forth, to further improve the battery performance and lifetime.

### 3.3.1 Carbon support

Carbon has attracted intensive use as a catalyst support material due to its high dispersion degree, good conductivity, and low cost.

Several carbon materials have been compared in previous studies and it is found that the surface area is not the only factor to decide the battery capacity as the discharge capacity of Li–air batteries is determined more by the volume of the pores residing in the mesopore (2–50 nm) range [3,41,64–66]. An evidence is that Super P carbon with a low surface area ( $62 \text{ m}^2 \text{ g}^{-1}$ ) exhibits a high capacity of more than  $3000 \text{ mAh (g carbon)}^{-1}$ ; however, at the same oxygen pressure, the activated carbon with the highest surface area ( $2100 \text{ m}^2 \text{ g}^{-1}$ ) shows much lower capacity than Super P. The latter has a large pore diameter of 50 nm [3]. This suggests that the main factor that influences the capacity is related to the pore size and pore volume of carbon rather than its surface area. The importance of mesopore volume in a carbon electrode is further confirmed in a rechargeable Li–air battery with a Ketjen carbon black air cathode [67,68]. The Ketjen carbon black has a total pore volume of  $7.6 \text{ cc g}^{-1}$ , most of which is contributed from mesopores (2–50 nm). A specific capacity of  $2340 \text{ mAh g}^{-1}$ , based on the carbon mass, from Ketjen carbon black-based air electrode is achieved with a high carbon loading of  $15 \text{ mg cm}^2$  in the ambient environment [67,68]. It is also realized that the formation of  $\text{Li}_2\text{O}_2$  only occurs on the triple junctions where electrolyte, carbon, and oxygen coexist; the more three-phase regions the more  $\text{Li}_2\text{O}_2$  will be produced and, therefore, the higher capacity delivered from the battery. Too small or too large pore size will not benefit the ORR process because the former will be easily blocked by  $\text{Li}_2\text{O}_2$  deposition on the pore entrance preventing further oxygen diffusion while the latter is usually flooded by the electrolyte forming two-phase instead of three-phase regions [69,70].

In order to achieve the maximum capacity and better stability, carbon nanomaterials, such as nanotubes, has attracted intensive investigation. The carbon nanotubes could provide overwhelming advantages, such as higher conductivity and better stability, compared with common carbon black [71]. As an alternative to highly porous conventional carbon, the use of single-walled carbon nanotubes as support materials for the air electrode has been reported; a capacity of  $2500 \text{ mAh g}^{-1}$  is reached at a rate of  $0.1 \text{ mA cm}^{-2}$  [67,68]. The carbon nanotubes show improved performance when they support an  $\alpha\text{-MnO}_2$  catalyst [72].

A noticeable development in the use of carbon support materials is the exploration of graphene nanomaterials. As mentioned above, in a rechargeable Li–air battery with the graphene nanosheets supported bifunctional catalyst  $\text{La}_{0.5}\text{Ce}_{0.5}\text{Fe}_{0.5}\text{Mn}_{0.5}\text{O}_3$ , a good performance is achieved. The battery is able to cycle more than 100 cycles with an average capacity of  $1200 \text{ mAh g}^{-1}$  and efficiency of 70% [31]. A graphene oxide is

tried to support  $\text{Co}_3\text{O}_4$  catalyst but can only be sustained for several cycles with small capacity [45]. Graphene porous sheets (with no catalyst) deliver an exceptionally high capacity of 15,000  $\text{mAh g}^{-1}$  in a primary lithium– $\text{O}_2$  battery. The high capacity is attributed to the unique bimodal porous structure of the electrode, which consists of microporous channels facilitating rapid oxygen diffusion while the highly connected nanoscale pores provide a high density of reactive sites for  $\text{Li}–\text{O}_2$  reactions. Also, the defects and functional groups on graphene favor the formation of isolated nanosized  $\text{Li}_2\text{O}_2$  particles and help prevent air blocking in the air electrode. The hierarchically ordered porous structure in bulk graphene enables its practical applications by promoting accessibility to most graphene sheets in this structure [32]. Graphene nanosheet is demonstrated as a better support with some catalytic properties compared to Vulcan XC-72 carbon. An initial discharge capacity of 2332  $\text{mAh g}^{-1}$  with an average charge potential of 3.97 V versus  $\text{Li}^+/\text{Li}$  are observed when the nanosheet is used as a cathode support in rechargeable Li–air batteries. Unfortunately, the stability is a concern as the battery is cycled only up to five cycles [73].

At Newcastle, carbon materials with different structures have been compared with the glass fiber, as shown in Figure 3.6. Although the carbon materials show good performance, the glass fiber is better in terms of capacity and cycling stability (Figure 3.6a and b).

In most work, carbon is used to support a catalyst. This may introduce some uncertain factors in determining the effectiveness of carbon material itself. At Newcastle, we have evaluated various carbon only air cathodes. Figure 3.7 and Table 3.2 show the influence of different carbon substrates on the performance of the  $\text{Li}–\text{O}_2$  batteries, where the capacity, efficiency, and its retention on cycling changes dramatically depending on the substrate used. The carbon nanotubes display much higher initial capacity than acetylene carbon and commercial Vulcan carbon black cathodes; 1775 versus 400 and 300  $\text{mAh g}^{-1}$ , based on the carbon mass. The Norit carbon black gives the maximum initial capacity (i.e., 1825  $\text{mAh g}^{-1}$ ) based on the carbon mass. But only the carbon nanotubes can sustain for up to 10 cycles and provide a capacity retention of 16% per cycle at the 10th cycle (Table 3.2).

Although carbon is generally considered to be a good electrode material in Li–air batteries, it may undergo corrosion/oxidation at high potentials and result in some possible side reactions in discharge/charge process in Li–air batteries [53,74]. Carbon is able to promote electrolyte decomposition, presenting problems for its use in a practical Li–air battery. Carbon is relatively stable below 3.5 V (vs.  $\text{Li}/\text{Li}^+$ ) on discharge or charge, but is unstable on charging above 3.5 V (especially in the presence of  $\text{Li}_2\text{O}_2$ ), oxidatively decomposing to form  $\text{Li}_2\text{CO}_3$  and other insoluble products, such as Li carboxylates (in DMSO and tetraglyme electrolytes). These by-products accumulate on cycling, resulting in electrode polarization, passivation, and capacity fading [74]. Moreover, the instability and ineffectiveness of carbon supporting materials also arise from other factors, such as either dropping noble-metal nanoparticles from the carbon support surface or causing their aggregation into larger particles, and changing the surface hydrophobicity, which can cause gas-transport difficulties [75–77]. As a result, seeking alternative support materials is important for the development of Li–air batteries.

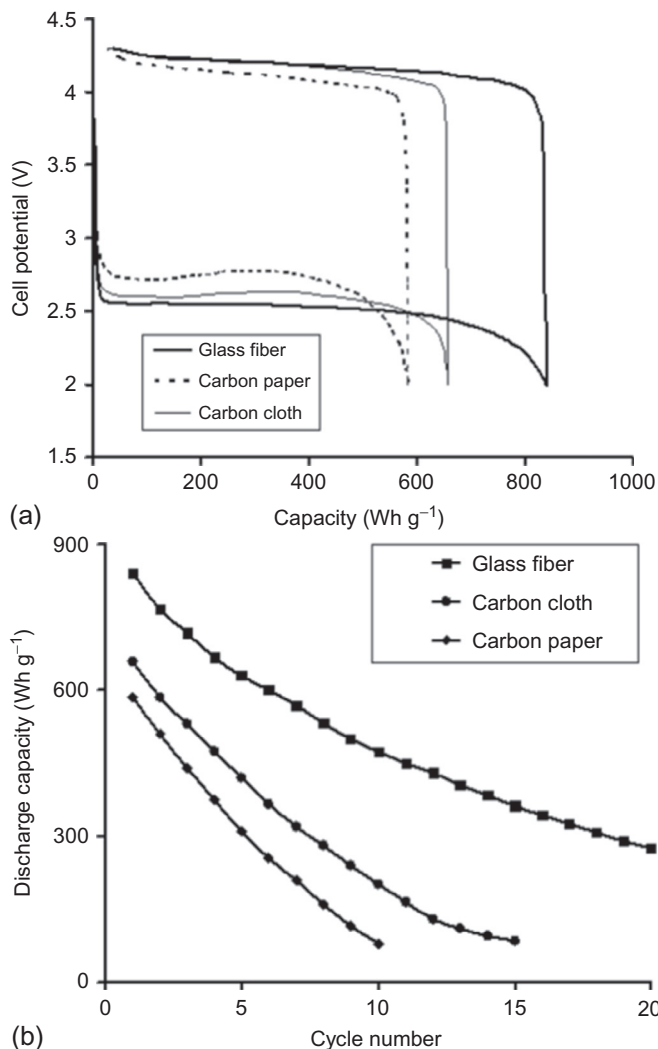


**Figure 3.6** Charge–discharge characteristics and cycle stability (between 2.0 and 4.3 V at  $0.1 \text{ mA cm}^{-2}$  and  $30^\circ\text{C}$ ) of rechargeable  $\text{Li}-\text{O}_2/\text{air}$  batteries with carbon substrate cathodes. (a) Initial charge–discharge curves. (b) Cycling performance. The capacity is based on the total solid (substrate+catalyst+binder) mass.

### 3.3.2 Other supports

Some metal oxides have attracted significant attention as catalyst supporting materials due to their improved electrochemical kinetics and effective electron transport paths; for example, growth of various nanowires ( $\text{TiO}_x$ ,  $\text{ZrO}_2$ ,  $\text{WO}_3$ ,  $\text{SnO}_2$ ,  $\text{Sn}$ ) directly on carbon paper, which forms 3D coaxial nanocable electrodes. Such a  $\text{Sn}@\text{CNT}$  3D

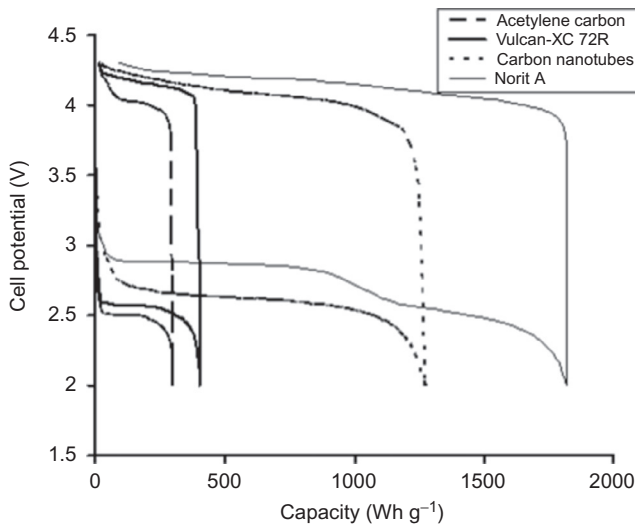


**Figure 3.7** Initial charge–discharge curves (between 2.0 and 4.3 V at  $0.1 \text{ mA cm}^{-2}$  and  $30^\circ\text{C}$ ) of rechargeable  $\text{Li}-\text{O}_2/\text{air}$  batteries with carbon substrate only cathodes. The capacity is based on the total carbon substrate mass.

**Table 3.2 The influence of catalyst on capacity, efficiency, and cycle ability of rechargeable  $\text{Li}-\text{O}_2/\text{air}$  batteries with various substrates<sup>a</sup>**

Substrate	Capacity <sup>b</sup> ( $\text{mA h g}^{-1}$ )	Efficiency <sup>c</sup> (%)	Capacity retention <sup>d</sup> (%)		
			Cycle		
			5	10	20
Norit carbon A	1825	74			
Carbon nanotubes	1775	70	64	16	
Vulcan-XC 72R carbon	404	65			
Acetylene carbon	300	63			
Ag	2300	84	25	12	
TiC	6000	75	6		
Al	265	70	32		
Ni foam	50	72			
Macrocycle 1, Air	600	78	27		
Macrocycle 2, Air	495	73	8		

Consumers were asked to score the four different components with 4 being the most important and 1 the least important.

<sup>a</sup>Discharge/charge rate:  $0.1 \text{ mA cm}^{-2}$  unless otherwise stated.

<sup>b</sup>The first cycle. The capacity is based on the total solid (substrate + catalyst + binder) mass.

<sup>c</sup>Round-trip efficiency is a ratio of total energy storage system output (discharge) divided by total energy input (charge) as measured by ratio of discharge voltage divided by charge voltage.

<sup>d</sup>Capacity retention is the fraction of the fall capacity available from a battery under specified conditions of discharge after it has been cycled for a number of cycles.

Source: Research by MORI for National Consumer Council (1994).

nanocable support has several advantages, such as enhancing effect of catalyst, higher gas permeability, improved metal–support interactions, and enhanced mass transport. This approach may considerably improve electrical contact with the external electrical circuit and the supported catalysts' utilization [78].

At Newcastle, we have explored various noncarbon supporting materials, such as titanium carbide, Ni foam, Ag powder, Al powder, and others; they have shown promising performance (Figure 3.8 and Table 3.2). Considering first Ag powder, Figure 3.8

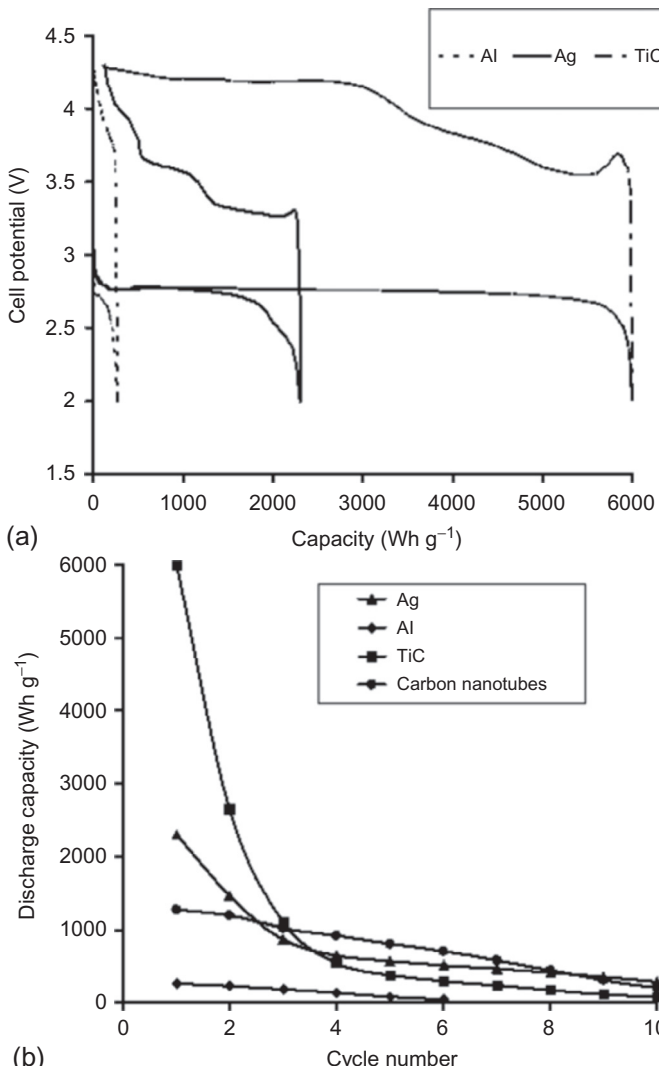


**Figure 3.8** Charge–discharge characteristics and cycle stability (between 2.0 and 4.3 V at  $0.1 \text{ mA cm}^{-2}$  and  $30^\circ \text{ C}$ ) of rechargeable  $\text{Li}-\text{O}_2/\text{air}$  batteries with different substrate cathodes. (a) Initial charge–discharge curves. (b) Cycling performance. The capacity is based on the total substrate mass.

and [Table 3.2](#) indicate that this support gives the best combination between a high first discharge capacity, around  $2300 \text{ mAh g}^{-1}$  (based on the substrate mass), low charge potential and high efficiency (84%), and capacity retention on cycling (up to 10 cycles). The TiC displays the highest initial discharge capacity ( $6000 \text{ mAh g}^{-1}$ , based on the TiC mass) but this capacity drops rapidly on cycling. Other substrates also show rapid deterioration on cycling ([Figure 3.8b](#) and [Table 3.2](#)).

### 3.3.3 Summary

Although carbon materials are widely used to support catalysts, metal and metal oxides appear as attractive replacements due to their advantages in high activity and better stability.

## 3.4 Future trends

Although many challenges need to be overcome before production of a commercially available rechargeable Li–air battery, the enormous advantages with high theoretical energy density far exceed other conventional rechargeable battery systems. More intensive research, especially in material aspects, needs to be devoted to this promising power source. As the air cathode determines the capacity, rate capability, and cycling efficiency of rechargeable Li–air batteries, its core part—catalyst—is a priority area to be paid particular attention. A major, urgent task is to search for bifunctional catalysts that are effective for both ORR ( $\text{Li}_2\text{O}_2$  formation during discharge) and OER (enhanced  $\text{Li}_2\text{O}_2$  decomposition during charge), promoting high reversible energy storage capacity. An essential research field is to understand why the rate capability of Li–air batteries is orders of magnitude lower than zinc–air batteries and fuel cells and identify the key rate and capacity-limiting factors. Although several factors are known, such as restrictions from oxygen solubility and mass transport, a further in-depth investigation is required.

One of the big challenges for the rechargeable Li–air battery is the limited electrical efficiency, which is due to the overpotential or polarization losses at the cathode during discharge and charge. For example, a high potential is needed for charging (up to 4.5 V) the porous carbon electrode, whereas the discharge potential is around 2.5 V; the big difference between these two values leads to a low efficiency. The improvement of this efficiency is achievable by applying effective catalysts that facilitate both ORR and OER, especially multiple component metal and oxide catalysts.

However, it is necessary to note the downside of the presence of a highly active catalyst; it may catalyze the electrolyte solvent decomposition, leading to the formation of insulating discharge products. These by-products cover the electrocatalytic active sites and deactivates them, significantly decreases the conductivity of the electrode, and causes pore blockage and  $\text{O}_2$  transport limitations. Therefore, we need not only effective catalysts for both ORR and OER, but also require a comprehensive

material selection and design for an air cathode, reaching a balance between its activity for Li–O<sub>2</sub> reaction, its inertness for electrolytes and Li–O<sub>2</sub> reaction intermediates/products, and its catalytic role in the formation of desired Li<sub>2</sub>O<sub>2</sub> structure and morphology to reduce pore blockage and promote O<sub>2</sub> transport.

Regarding the catalyst support, the development of novel carbon materials with a combination of suitable crystallinity, wettability, and porosity appears to be an intensive research area. It is necessary to consider the high operation potential and oxygen content in Li–air batteries and to develop noncarbon supporting materials such as various stable metal oxides with novel nanostructures (doped 3D nanomaterial, nanowire, nanorods, and nanotubes), in order to overcome corrosion challenges for the currently used carbon materials. In terms of porosity, attention should be paid to fabricate materials that have more macropore or mesopore volumes and less microporous structure, reducing diffusion limitations during cycling. The metal oxides, such as SnO<sub>2</sub>, ZrO<sub>2</sub>, WO<sub>3</sub>, and their composites, are promising candidates as cathode-supporting materials for rechargeable Li–air batteries. A potential area is the use of metal supporting materials in high surface area forms (e.g., mesh and foam); they are playing an important role in developing high-efficiency, light, and low-cost practical Li–air batteries.

More effort should be devoted to designing a novel porous air electrode via a combination approach; i.e., searching effective catalysts and optimum supporting materials together. This is able to produce a porous electrode with (1) effective catalysis site distribution for maximization of catalysts' utilization to make the Li<sub>2</sub>O<sub>2</sub> formation reversible and (2) novel support matrix with optimum porosity to facilitate high oxygen diffusivity and Li-ion transport toward the active surface of the electrode and prevent insulating particles formation. This is critical for the overall electrochemical reaction and the resulting discharge/charge capacity, rate capability, and cycling stability of the battery.

### 3.5 Sources of further information and advice

#### Books

Aifantis, K.E., Hackney, S.A., Kumar, R.V. (Eds.), High Energy Density Lithium Batteries, John Wiley & Sons, Inc., New York, 2010.

Besenhard, J.O. (Ed.), Handbook of Battery Materials, John Wiley & Sons, Inc., New York.

Brunet, Y. (Ed.), Energy Storage, John Wiley & Sons, Inc., New York, 2010.

Chandra, D., Bautista, R.G., Schlapbach, L. (Ed.), Advanced Materials for Energy Conversion II, John Wiley & Sons, Inc., New York, 2010.

Daniel, C., Besenhard, J.O. (Ed.), Handbook of Battery Materials, second ed., 2 vols., John Wiley & Sons, Inc., New York.

García-Martínez, J. (Ed.), Nanotechnology for the Energy Challenge, second ed., John Wiley & Sons, Inc., New York, 2013.

Kinoshita, K., Electrochemical Oxygen Technology, John Wiley & Sons, Inc., New York, 1992.

Lacaze, P.-C., Nanotechnologies: Concepts, Production and Applications, John Wiley & Sons, Inc., New York, 2012.

Oldham, K., Myland, J., Bond, A., *Electrochemical Science and Technology: Fundamentals and Applications*, John Wiley & Sons, Inc., New York, 2011.

Ozawa, K. (Ed.), *Lithium Ion Rechargeable Batteries: Materials, Technology, and New Applications*, John Wiley & Sons, Inc., New York, 2009.

Park, J.-K., (Ed.), *Principles and Applications of Lithium Secondary Batteries*, John Wiley & Sons, Inc., New York, 2012.

Rahn, C.D., Wang, C.-Y., *Battery Systems Engineering*, John Wiley & Sons, Inc., New York, 2013.

Scrosati, B., Hassoun, J., Abraham, K.M., van Schalkwijk, W.A. (Eds.), *Lithium Batteries—Advanced Technologies and Applications, The ECS Series of Texts and Monographs—58*, John Wiley & Sons, Inc., New York, 2013.

## ***Journals***

*Applied Catalysis A: General, Applied Catalysis B: Environmental, Applied Physics Letter, Chemical Engineering Journal, Electrocatalysis, Electrochemical and Solid State Letters, Electrochemistry Communications, Electrochimica Acta, Energies, Environmental Chemistry Letters, Fuel Cells, International Journal of Hydrogen Energy, Journal of Applied Electrochemistry, Journal of Electroanalytical Chemistry, Journal of Electrochemical Society, Journal of Hazardous Materials, Journal of Membrane Science, Journal of New Materials for Electrochemical Systems, and Journal of Power Sources.*

## ***Trade/professional bodies***

Battery and Electrical Specialists Association ([www.besabattery.com/](http://www.besabattery.com/)).

Battery Vehicle Society ([www.batteryvehiclesociety.org.uk](http://www.batteryvehiclesociety.org.uk)).

The British Battery Industry Federation ([www.bbif.co.uk/](http://www.bbif.co.uk/)).

The Electrochemical Society (ECS, [www.electrochem.org/](http://www.electrochem.org/)).

The European Association for Advanced Rechargeable Batteries ([www.rechargebatteries.org/](http://www.rechargebatteries.org/)).

The European Association for Battery, Hybrid and Fuel Cell Electric Vehicles ([www.avere.org/www/index.php](http://www.avere.org/www/index.php)).

The International Society of Electrochemistry (ISE, [www.ise-online.org/](http://www.ise-online.org/)).

The World Electric Vehicle Association ([www.wevaonline.net/](http://www.wevaonline.net/)).

## ***Research and interest groups***

Center for Innovative Fuel Cell and Battery Technologies (USA, [www.fcbt.gatech.edu/](http://www.fcbt.gatech.edu/)).

EIC Laboratories (USA, [www.eiclabs.com](http://www.eiclabs.com)).

Electrochemical Energy Laboratory (USA, [web.mit.edu/eel/](http://web.mit.edu/eel/)).

Newcastle (UK), St. Andrews (UK), Strathclyde (UK).

Newcastle (UK, [www.ncl.ac.uk/ceam/research/docs/newmfc.pdf](http://www.ncl.ac.uk/ceam/research/docs/newmfc.pdf)).

Pacific Northwest National Laboratory (USA, [www.pnnl.gov](http://www.pnnl.gov)).

St. Andrews (UK, <http://ch-www.st-andrews.ac.uk/staff/pgb/group/>).

Strathclyde (UK, [www.strath.ac.uk/chemeng/1stdegree/schoolteachersandcareersadvisors/groupdetails/profpeterhall-professor/](http://www.strath.ac.uk/chemeng/1stdegree/schoolteachersandcareersadvisors/groupdetails/profpeterhall-professor/))  
Texas Materials Institute (USA, [www.tmi.utexas.edu/](http://www.tmi.utexas.edu/)).  
The Energy Institute (USA, [www.energy.psu.edu/elc/index.html](http://www.energy.psu.edu/elc/index.html)).

## References

- [1] H. Cheng, K. Scott, Nano-structured gas diffusion electrode—a high power and stable cathode material for rechargeable Li-air batteries, *J. Power Sources* 235 (2013) 226–233.
- [2] H. Cheng, K. Scott, Selection of oxygen reduction catalysts for rechargeable lithium-air batteries—metal or oxide? *Appl. Catal. B Environ.* 108–109 (2011) 140–151.
- [3] H. Cheng, K. Scott, Carbon-supported manganese oxide nanocatalysts for rechargeable lithium-air batteries, *J. Power Sources* 195 (2010) 1370–1374.
- [4] A. Debart, J. Bao, G. Armstrong, P.G. Bruce, An  $O_2$  cathode for rechargeable lithium batteries: the effect of a catalyst, *J. Power Sources* 174 (2007) 1177–1182.
- [5] A. Debart, J. Bao, G. Armstrong, P.G. Bruce, Effect of catalyst on the performance of rechargeable lithium/air batteries, *ECS Trans.* 27 (2007) 225–232.
- [6] G. Girishkumar, B. McCloskey, A.C. Luntz, S. Swanson, W. Wilcke, Lithium–air battery: promise and challenges, *J. Phys. Chem. Lett.* 1 (2010) 2193–2203.
- [7] H.-G. Jung, J. Hassoun, J.-B. Park, Y.-K. Sun, B. Scrosati, An improved high-performance lithium-air battery, *Nat. Chem.* 4 (2012) 579–585.
- [8] T. Ogasawara, A. Debart, M. Holzapfel, P. Novak, P.G. Bruce, Rechargeable  $Li_2O_2$  electrode for lithium batteries, *J. Am. Chem. Soc.* 128 (2006) 1390–1393.
- [9] Y. Shao, F. Ding, J. Xiao, J. Zhang, W. Xu, S.K. Park, J. Zhang, Y. Wang, J. Liu, Making Li-air batteries rechargeable: material challenges, *Adv. Funct. Mater.* 23 (2013) 987–1004.
- [10] J.-M. Tarascon, M. Armand, Issues and challenges facing rechargeable lithium batteries, *Nature* 414 (2001) 359–367.
- [11] Z.G. Yang, J.L. Zhang, M.C.W. Kintner-Meyer, X.C. Lu, D.W. Choi, J.P. Lemmon, J. Liu, Electrochemical energy storage for green grid, *Chem. Rev.* 111 (2011) 3577–3613.
- [12] K.M. Abraham, Z. Jang, A polymer electrolyte-based rechargeable lithium/oxygen battery, *J. Electrochem. Soc.* 143 (1996) 1–5.
- [13] P.G. Bruce, S.A. Freunberger, L.J. Hardwick, J.M. Tarascon,  $Li-O_2$  and  $Li-S$  batteries with high energy storage, *Nat. Mater.* 11 (2012) 19–29.
- [14] J. Hassoun, F. Croce, M. Armand, B. Scrosati, Investigation of the  $O_2$  electrochemistry in a polymer electrolyte solid-state cell, *Angew. Chem. Int. Ed.* 50 (2011) 2999–3002.
- [15] J.S. Hummelshoj, J. Blomqvist, S. Datta, T. Vegge, J. Rossmeisl, K.S. Thygesen, A. Luntz, K.W. Jacobsen, J.K. Norskov, Communications: elementary oxygen electrode reactions in the aprotic Li-air battery, *J. Chem. Phys.* 132 (2010) 71101–71105.
- [16] R. Cao, J. Lee, M. Liu, J. Cho, Non-precious catalysts: recent progress in non-precious catalysts for metal-air batteries, *Adv. Energy Mater.* 2 (2012) 816–829.
- [17] A. Debart, A.J. Paterson, J. Bao, P.G. Bruce,  $\alpha$ - $MnO_2$  nanowires: a catalyst for the  $O_2$  electrode in rechargeable lithium batteries, *Angew. Chem. Int. Ed.* 47 (2008) 4521–4524.
- [18] S.A. Freunberger, Y. Chen, N.E. Drewett, L.J. Hardwick, F. Barde, P.G. Bruce, The lithium-oxygen battery with ether-based electrolytes, *Angew. Chem. Int. Ed.* 50 (2011) 8609–8613.

- [19] S.A. Freunberger, Y. Chen, Z. Peng, J.M. Griffin, L.J. Hardwick, F. Barde, P. Novak, P.G. Bruce, Reactions in the rechargeable lithium–O<sub>2</sub> battery with alkyl carbonate electrolytes, *J. Am. Chem. Soc.* 133 (2011) 8040–8047.
- [20] C.O. Laoire, S. Mukerjee, K.M. Abraham, E.J. Plichta, M.A. Hendrickson, Influence of nonaqueous solvents on the electrochemistry of oxygen in the rechargeable lithium-air battery, *J. Phys. Chem. C* 114 (2010) 9178–9186.
- [21] Y.C. Lu, H.A. Gasteiger, M.C. Parent, V. Chiloyan, Y. Shao, The influence of catalysts on discharge and charge voltages of rechargeable Li–oxygen batteries, *Electrochem. Solid-State Lett.* 13 (2010) A69–A72.
- [22] Y.C. Lu, Z.C. Xu, H.A. Gasteiger, S. Chen, K. Hamad-Schifferli, Y. Shao, Platinum–gold nanoparticles: a highly active bifunctional electrocatalyst for rechargeable lithium–air batteries, *J. Am. Chem. Soc.* 132 (2010) 12170–12171.
- [23] B.D. McCloskey, R. Scheffler, A. Speidel, G. Girishkumar, A.C. Luntz, On the mechanism of nonaqueous Li–O<sub>2</sub> electrochemistry on C and its kinetic overpotentials: some implications for Li-air batteries, *J. Phys. Chem. C* 116 (2012) 23897–23905.
- [24] B.D. McCloskey, D.S. Bethune, R.M. Shelby, G. Girishkumar, A.C. Luntz, Solvents: critical role in nonaqueous lithium-oxygen battery electrochemistry, *J. Phys. Chem. Lett.* 2 (2011) 1161–1166.
- [25] B.D. McCloskey, R. Scheffler, A. Speidel, D.S. Bethune, R.M. Shelby, A.C. Luntz, On the efficiency of electrocatalysis in nonaqueous Li–O<sub>2</sub> batteries, *J. Am. Chem. Soc.* 133 (2011) 18038–18041.
- [26] F. Mizuno, S. Nakanishi, Y. Kotani, S. Yokoishi, H. Iba, Rechargeable Li-air batteries with carbonate-based liquid electrolytes, *Electrochemistry* 78 (2010) 403–405.
- [27] T. Ottakam, M. Muhammed, S.A. Freunberger, Z. Peng, P.G. Bruce, The carbon electrode in nonaqueous Li–O<sub>2</sub> cells, *J. Am. Chem. Soc.* 135 (2013) 494–500.
- [28] Z. Peng, S.A. Freunberger, Y. Chen, P.G. Bruce, A reversible and higher rate Li–O<sub>2</sub> battery, *Science* 337 (2012) 563–566.
- [29] Z. Peng, S.A. Freunberger, L.J. Hardwick, Y. Chen, V. Giordani, F. Barde, P. Novak, D. Graham, J.-M. Tarascon, P.G. Bruce, Oxygen reactions in a non-aqueous Li<sup>+</sup> electrolyte, *Angew. Chem. Int. Ed.* 50 (2011) 6351–6355.
- [30] Y. Shao, S. Park, J. Xiao, J. Zhang, Y. Wang, J. Liu, Electrocatalysts for nonaqueous lithium-air batteries: status, challenges, and perspective, *ACS Catal.* 2 (2012) 844–857.
- [31] L. Wang, M. Ara, K. Wadumesthrige, S. Salley, K.Y. Simon Ng, Graphene nanosheet supported bifunctional catalyst for high cycle life Li-air batteries, *J. Power Sources* 234 (2013) 8–15.
- [32] J. Xiao, D. Mei, X. Li, W. Xu, D. Wang, G.L. Graff, W.D. Bennett, Z. Nie, L.V. Saraf, I.A. Aksay, J. Liu, J. Zhang, Hierarchically porous graphene as a lithium-air battery electrode, *Nano Lett.* 11 (2011) 5071–5078.
- [33] W. Xu, J. Hu, M.H. Engelhard, S.A. Towne, J.S. Hardy, J. Xiao, J. Feng, M.Y. Hu, J. Zhang, F. Ding, M.E. Gross, J. Zhang, The stability of organic solvents and carbon electrode in nonaqueous Li–O<sub>2</sub> batteries, *J. Power Sources* 215 (2012) 240–247.
- [34] A.J. Bard, L.R. Faulkner, *Electrochemical Methods: Fundamentals and Applications*, Wiley, New York, 2000.
- [35] K. Kinoshita, *Electrochemical Oxygen Technology*, Wiley, New York, 1992.
- [36] F.Y. Cheng, J.A. Shen, B. Peng, Y.D. Pan, Z.L. Tao, J. Chen, Rapid room-temperature synthesis of nanocrystalline spinels as oxygen reduction and evolution electrocatalysts, *Nat. Chem.* 3 (2011) 79–84.
- [37] B.C.H. Steele, A. Heinzel, Materials for fuel-cell technologies, *Nature* 414 (2001) 345–352.

[38] Y.C. Lu, D.G. Kwabi, K.P.C. Yao, J.R. Harding, J.G. Zhou, L. Zuin, Y. Shao, The discharge rate capability of rechargeable Li-O<sub>2</sub> batteries, *Energy Environ. Sci.* 4 (2011) 2999–3007.

[39] B. Lim, M. Jiang, P.H.C. Camargo, E.C. Cho, J. Tao, X. Lu, Y. Zhu, Y. Xia, Pd-Pt bimetallic nanodendrites with high activity for oxygen reduction, *Science* 324 (2009) 1302–1305.

[40] P. Strasser, S. Koh, T. Anniyev, J. Greeley, K. More, C. Yu, Z. Liu, S. Kaya, D. Nordlund, H. Ogasawara, M.F. Toney, A. Nilsson, Lattice-strain control of the activity in dealloyed core-shell fuel cell catalysts, *Nat. Chem.* 2 (2010) 454–460.

[41] X. Ren, S.S. Zhang, D.T. Tran, J. Read, Oxygen reduction reaction catalyst on lithium/air battery discharge performance, *J. Mater. Chem.* 21 (2011) 10118–10125.

[42] L. Trahey, C.S. Johnson, J.J.T. Vaughney, S.H. Kang, L.J. Hardwick, S.A. Freunberger, P. G. Bruce, M.M. Thackeray, Activated lithium-metal-oxides as catalytic electrodes for Li-O<sub>2</sub> cells, *Electrochem. Solid-State Lett.* 14 (2011) A64–A66.

[43] J.X. Li, N. Wang, Y. Zhao, Y.H. Ding, L.H. Guan, MnO<sub>2</sub> nanoflakes coated on multi-walled carbon nanotubes for rechargeable lithium-air batteries, *Electrochem. Commun.* 13 (2011) 698–700.

[44] L. Jin, L.P. Xu, C. Morein, C.H. Chen, M. Lai, S. Dharmarathna, A. Dobley, S.L. Suib, Titanium containing  $\gamma$ -MnO<sub>2</sub> (TM) hollow spheres: one-step synthesis and catalytic activities in Li/air batteries and oxidative chemical reactions, *Adv. Funct. Mater.* 20 (2010) 3373–3382.

[45] R. Black, J. Lee, B. Adams, C.A. Mims, L.F. Nazar, The role of catalysts and peroxide oxidation in lithium-oxygen batteries, *Angew. Chem. Int. Ed. Engl.* 52 (2013) 392–396.

[46] R. Black, S.H. Oh, J. Lee, T. Yim, B. Adams, L.F. Nazar, Screening for superoxide reactivity in Li-O<sub>2</sub> batteries: effect on Li<sub>2</sub>O<sub>2</sub>/LiOH crystallization, *J. Am. Chem. Soc.* 134 (2012) 2902–2905.

[47] W. Yang, J. Salim, S. Li, C. Sun, L. Chen, J.B. Goodenough, Y. Kim, Perovskite Sr<sub>0.95</sub>Ce<sub>0.05</sub>CoO<sub>3- $\delta$</sub>  loaded with copper nanoparticles as a bifunctional catalyst for lithium-air batteries, *J. Mater. Chem.* 22 (2012) 18902–18907.

[48] H.N. Cong, K. Abbassi, P. Chartier, Electrocatalysis of oxygen reduction on polypyrrole/mixed valence spinel oxide nanoparticles, *J. Electrochem. Soc.* 149 (2002) A525–A530.

[49] E. Rios, J.L. Gautier, G. Poillerat, P. Chartier, Mixed valency spinel oxides of transition metals and electrocatalysis: case of the Mn<sub>x</sub>Co<sub>3-x</sub>O<sub>4</sub> system, *Electrochim. Acta* 44 (1998) 1491–1497.

[50] L. Wang, X. Zhao, Y.H. Lu, M.W. Xu, D.W. Zhang, R.S. Ruoff, K.J. Stevenson, J. B. Goodenough, CoMn<sub>2</sub>O<sub>4</sub> spinel nanoparticles grown on graphene as bifunctional catalyst for lithium-air batteries, *J. Electrochem. Soc.* 158 (2011) A1379–A1382.

[51] G.Q. Zhang, M. Hendrickson, E.J. Plichta, M. Au, J.P. Zheng, Preparation, characterization and electrochemical catalytic properties of Hollandite Ag<sub>2</sub>Mn<sub>8</sub>O<sub>16</sub> for Li-air batteries, *J. Electrochem. Soc.* 159 (2012) A310–A314.

[52] A.K. Thapa, T. Ishihara, Mesoporous  $\alpha$ -MnO<sub>2</sub>/Pd catalyst air electrode for rechargeable lithium-air battery, *J. Power Sources* 196 (2011) 7016–7020.

[53] A.K. Thapa, K. Saimen, T. Ishihara, Pd/MnO<sub>2</sub> air electrode catalyst for rechargeable lithium/air battery, *Electrochem. Solid-State Lett.* 13 (2010) A165–A167.

[54] S.H. Oh, R. Black, E. Pomerantseva, J. Lee, L.F. Nazar, Synthesis of a metallic mesoporous pyrochlore as a catalyst for lithium-O<sub>2</sub> batteries, *Nat. Chem.* 4 (2012) 1004–1010.

[55] F. Li, R. Ohnishi, Y. Yamada, J. Kubota, K. Domen, A. Yamada, H. Zhou, Carbon supported TiN nanoparticles: an efficient bifunctional catalyst for non-aqueous Li-O<sub>2</sub> batteries, *Chem. Commun. (Camb.)* 49 (2013) 1175–1177.

[56] S.M. Dong, X. Chen, K.J. Zhang, L. Gu, L.X. Zhang, X.H. Zhou, L.F. Li, Z.H. Liu, P. X. Han, H.X. Xu, J.H. Yao, C.J. Zhang, X.Y. Zhang, C.Q. Shang, G.L. Cui, L. Q. Chen, Molybdenum nitride based hybrid cathode for rechargeable lithium-O<sub>2</sub> batteries, *Chem. Commun.* 47 (2011) 11291–11293.

[57] Z.H. Fu, X.J. Lin, T. Huang, A.S. Yu, Nano-sized La<sub>0.8</sub>Sr<sub>0.2</sub>MnO<sub>3</sub> as oxygen reduction catalyst in nonaqueous Li/O<sub>2</sub> batteries, *J. Solid State Electrochem.* 16 (2012) 1447–1452.

[58] D. Oh, J. Qi, Y. Lu, Y. Zhang, Y. Shao, A.M. Belcher, Biologically enhanced cathode design for improved capacity and cycle life for lithium-oxygen batteries, *Nat. Commun.* 4 (2013) 1–8.

[59] Y. Mo, S.P. Ong, G. Ceder, First-principles study of the oxygen evolution reaction of lithium peroxide in the lithium-air battery, *Phys. Rev. B* 84 (2011) 205446–205455.

[60] U. Sahapatsombut, H. Cheng, K. Scott, Modeling the micro-macro homogeneous cycling behaviour of a lithium-air battery, *J. Power Sources* 227 (2013) 243–253.

[61] U. Sahapatsombut, H. Cheng, K. Scott, Modeling of electrolyte degradation and cycling behaviour in a lithium-air battery, *J. Power Sources* 243 (2013) 409–418.

[62] J.R. Kitchin, J.K. Norskov, M.A. Barteau, J.G. Chen, Modification of the surface electronic and chemical properties of Pt(111) by subsurface 3d transition metals, *J. Chem. Phys.* 120 (2004) 10240–10247.

[63] S.J. Tauster, S.C. Fung, R.T.K. Baker, J.A. Horsley, Strong interactions in supported-metal catalysts, *Science* 211 (1981) 1121–1125.

[64] T. Kuboki, T. Okuyama, O. Ohsaki, N. Takami, Lithium-air batteries using hydrophobic room temperature ionic liquid electrolyte, *J. Power Sources* 146 (2005) 766–769.

[65] M. Mirzaeian, P.J. Hall, Characterizing capacity loss of lithium oxygen batteries by impedance spectroscopy, *J. Power Sources* 195 (2010) 6817–6824.

[66] X.H. Yang, P. He, Y.Y. Xia, Preparation of mesocellular carbon foam and its application for lithium/oxygen battery, *Electrochem. Commun.* 11 (2009) 1127–1130.

[67] G.Q. Zhang, J.P. Zheng, R. Liang, C. Zhang, B. Wang, M. Hendrickson, E.J. Plichta, Lithium-air batteries using SWNT/CNF buckypapers as air electrodes, *J. Electrochem. Soc.* 157 (2010) A953–A956.

[68] G.J. Zhang, D.Y. Wang, W. Xu, J. Xiao, R.E. Williford, Ambient operation of Li/air batteries, *J. Power Sources* 195 (2010) 4332–4337.

[69] J.S. Lee, S.T. Kim, R. Cao, N.S. Choi, M. Liu, K.T. Lee, J. Cho, Metal-air batteries with high energy density: Li-air versus Zn-air, *Adv. Energy Mater.* 1 (2011) 34–50.

[70] J.P. Zheng, R.Y. Liang, M. Hendrickson, E.J. Plichta, Theoretical energy density of Li-air batteries, *J. Electrochem. Soc.* 155 (2008) A432–A437.

[71] S.L. Candelaria, Y. Shao, W. Zhou, X. Li, J. Xiao, J.-G. Zhang, Y. Wang, J. Liu, J. Li, G. Cao, Nanostructured carbon for energy storage and conversion, *Nano Energy* 1 (2012) 195–220.

[72] G.Q. Zhang, J.P. Zheng, R. Liang, C. Zhang, B. Wang, M. Au, M. Hendrickson, E.J. Plichta,  $\alpha$ -MnO<sub>2</sub>/carbon nanotube/carbon nanofiber composite catalytic air electrodes for rechargeable lithium-air batteries, *J. Electrochem. Soc.* 158 (2011) A822–A827.

[73] B. Sun, B. Wang, D. Su, L. Xiao, H. Ahn, G. Wang, Graphene nanosheets as cathode catalysts for lithium-air batteries with an enhanced electrochemical performance, *Carbon* 50 (2012) 727–733.

[74] O. Thotiyil, M. Muhammed, S.A. Freunberger, Z. Peng, P.G. Bruce, The carbon electrode in nonaqueous Li-O<sub>2</sub> cells, *J. Am. Chem. Soc.* 135 (2013) 494–500.

[75] R. Borup, J. Meyers, B. Pivovar, Y.S. Kim, R. Mukundan, N. Garland, D. Myers, M. Wilson, F. Garzon, D. Wood, P. Zelenay, K. More, K. Stroh, T. Zawodzinski, J. Boncella, J.E. McGrath, M. Inaba, K. Miyatake, M. Hori, K. Ota, Z. Ogumi, S. Miyata, A. Nishikata, Z. Siroma, Y. Uchimoto, K. Yasuda, K.I. Kimijima,

N. Iwashita, Scientific aspects of polymer electrolyte fuel cell durability and degradation, *Chem. Rev.* 107 (2007) 3904–3951.

- [76] Y. Shao, G. Yin, Y. Gao, P. Shi, Durability study of Pt/C and Pt/CNTs catalysts under simulated PEM fuel cell conditions, *J. Electrochem. Soc.* 153 (2006) A1093–A1097.
- [77] X. Wang, W. Li, Z. Chen, M. Waje, Y. Yan, Durability investigation of carbon nanotube as catalyst support for proton exchange membrane fuel cell, *J. Power Sources* 158 (2006) 154–159.
- [78] S.H. Sun, G.X. Zhang, D.S. Geng, Y.G. Chen, M.N. Banis, R.Y. Li, M. Cai, X.L. Sun, Direct growth of single-crystal Pt nanowires on Sn@CNT nanocable: 3D electrodes for highly active electrocatalysts, *Chem. Eur. J.* 16 (2010) 829–835.
- [79] R. Bashyam, P. Zelenay, A class of non-precious metal composite catalysts for fuel cells, *Nature* 443 (2006) 63–66.
- [80] V.R. Stamenkovic, B.S. Mun, M. Arenz, K.J.J. Mayrhofer, C.A. Lucas, G. Wang, P.N. Ross, N.M. Markovic, Trends in electrocatalysis on extended and nanoscale Pt-bimetallic alloy surfaces, *Nat. Mater.* 6 (2007) 241–247.

# Electrolytes for rechargeable lithium batteries

4

M. Montanino<sup>1</sup>, S. Passerini<sup>2</sup>, G.B. Appetecchi<sup>3</sup>

<sup>1</sup>ENEA, Agency for New Technologies, Energy and Sustainable Economic Development, Portici, Italy; <sup>2</sup>Helmholtz Institute Ulm, Karlsruhe Institute of Technology, Ulm, Germany; <sup>3</sup>ENEA, Agency for New Technologies, Energy and Sustainable Economic Development, Rome, Italy

## 4.1 Introduction

Rechargeable lithium batteries are very promising candidates for next-generation power sources because of their high gravimetric and volumetric energies with respect to other cell chemistries. The lithium-ion battery technology is based on the use of electrode materials able to reversibly intercalate lithium cations, which are transferred between two host structures (positive and negative electrodes) during the charge and discharge processes. Commercial lithium-ion batteries commonly use liquid electrolytes based on suitable lithium salts and organic (volatile) solvents.

In recent years, gel polymer electrolytes have begun to progressively replace the above-mentioned electrolytes based on organic liquids as solvents. Additionally, a wide variety of alternative solvents as well as additives have been proposed, mainly aiming to improve the safety and compatibility of the electrolytes with high-voltage cathodes. In addition, completely dry, solvent-free electrolytes, both polymeric and inorganic, are worldwide under investigation worldwide because of the possibility to realize all solid-state lithium batteries, which are undoubtedly appealing from safety and engineering points of view and open new perspectives on applications. Here, a survey of the most appealing types of electrolytes proposed for modern rechargeable lithium batteries and taking a look at future trends is reported.

## 4.2 Organic liquid electrolytes

### 4.2.1 Solvents

#### 4.2.1.1 Standard organic solvents

A liquid organic compound has to satisfy the following requirements to be used as solvent in lithium battery systems [1–5]:

- High dielectric constant (to favor dissociation of the lithium salt).
- Low volatility (i.e., high boiling point).
- Low viscosity (assuring fast ion movement).
- No reactivity toward electrode materials.

The chemical structure and the physicochemical properties of the most common electrolyte solvents for lithium batteries are summarized in [Figure 4.1](#) and [Table 4.1](#), respectively. Cyclic carbonates (namely, EC, PC,  $\gamma$ -butyrolactone) are generally characterized by high dielectric constant value (which enables them to dissolve lithium salts) and low volatility, but also rather high viscosity, thus depleting their transport

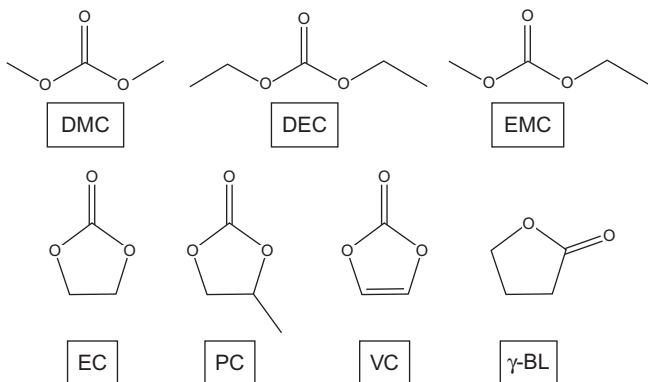


**Figure 4.1** Chemical structure of the most common electrolyte solvents for lithium battery systems.

**Table 4.1 Physicochemical properties of the most common electrolyte solvents for lithium battery systems determined at 25 °C**

Solvent	Molecular weight	Boiling point (°C)	Dielectric constant	Viscosity (cP)	Density (g cm <sup>-3</sup> )
ACN	41.05	81.6	35.95	0.341	0.777
$\gamma$ -BL	86.09	204	39.1	1.75	1.13
DEC	118.13	126	2.84	0.81	0.975
DMC	90.08	90.1	3.1	2.4	1.07
DME	90.12	84.0	7.20	0.455	0.859
DMF	73.10	158	36.71	0.796	0.944
DMSO	78.13	189.0	46.45	1.991	1.095
EC	88.06	248	89.6	1.85 (40 °C)	1.322
EMC	104.1	109	2.4	0.65	1.00
MF	60.06	31.5	8.5	0.333	0.974
NM	61.04	101.2	35.94	0.694	1.131
PC	102.1	241	64.4	2.53	1.19
THF	72.12	65.0	7.39	0.46	0.880
VC	86.05	162	127	—	1.36

properties. Therefore, linear carbonates, usually exhibiting low viscosity, are added in order to increase the fluidity of the resulting electrolyte. On the other hand, modest viscosity values are accomplished by low flash points (e.g., below 40 °C) [1–5], thus enhancing the volatility and flammability of the solvent mixture and leading to safety concerns [1–5]. Additionally, organic compounds such as EC and VC show very good film-forming ability (i.e., formation of solid electrolyte interface, SEI) onto carbonaceous anodes, thus being considered mandatory for assuring good cycling performance in lithium battery systems [1–5,7]. Note, however, that EC melts at 40 °C, and therefore, it needs to be blended with other low-viscosity solvents. Therefore, commercial lithium-ion battery electrolytes are mainly based on mixtures (binary or ternary) of EC and linear carbonates, namely, DEC, DMC, and EMC, as solvents [1–5].

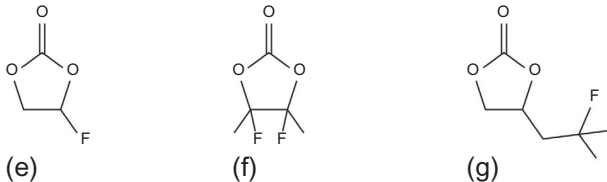
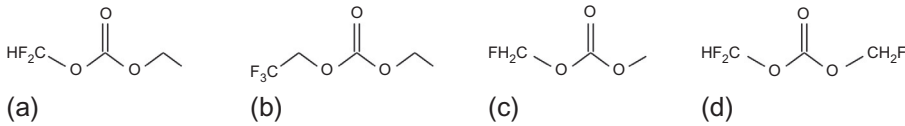
However, the presence of flammable and volatile organics represent a major safety problem [2–4,8,9], when dangerous events such as internal heat generation and thermal runaway take place, increasing the probability or the extent of cell venting, fire, and, therefore, rapid disassembly [10–13]. For instance, uncontrolled heat development, sharply increasing the temperature above 140 °C, might cause combustion of the vaporized organic electrolyte with oxygen becoming available from the decomposition of the (delithiated) positive electrode. Successively, the delivery of additional heat might, in turn, provoke catastrophic events such as explosion. In addition, it is noteworthy that the electrolyte burning causes decomposition of the lithium salt, LiPF<sub>6</sub>, and the PVdF-based electrode binder, leading to development of highly toxic, hydrofluoric acid (HF) and other fluorinated gases [9]. Finally, the oxidative decomposition of the alkyl carbonates represents one of the limiting factors for the use of high-voltage (>5 V) cathode materials.

Remarkable efforts have been devoted to develop alternative solvents with reduced flammability and enhanced oxidation stability toward high-voltage cathodes aiming to realize high-energy lithium batteries with improved safety. Among them, four families of solvents, namely fluorinated carbonates, sulfones, nitriles, and ionic liquids (ILs), were found to exhibit the most promising properties. These organic compounds were recently reviewed by Lex-Balducci *et al.* [8]. ILs are worthy to be separately cited and will discussed in [Section 4.3](#). The chemical structure and the physicochemical properties of the most interesting alternative solvents proposed for lithium battery electrolytes are summarized in [Figure 4.2](#) and [Table 4.2](#), respectively. The room temperature ionic conductivity values of lithium salt-containing electrolyte solutions based on different fluorinated carbonates, sulfones, and nitriles are reported in [Table 4.3](#), whereas [Figure 4.3](#) compares the electrochemical stability window of various sulfone-based and alkyl phosphate-based electrolytes.

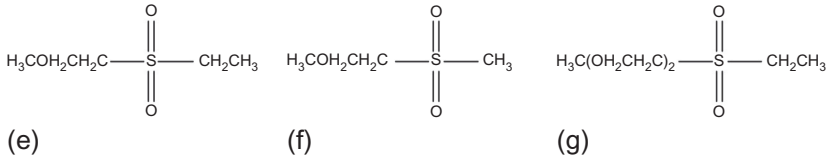
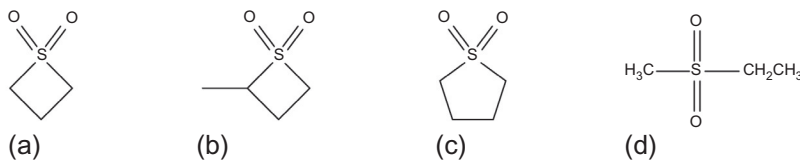
#### 4.2.1.2 Fluorinated carbonates

The investigation of fluorinated carbonates has regarded a wide range of organic compounds. Ihara *et al.* [24] found that the replacement of EC/DMC with MFA is able to enhance the thermal stability with respect to carbonaceous anodes of about 100 °C. Nanbu *et al.* [18] demonstrated that FPC-based electrolytes exhibit a wider

## Fluorinated carbonates



## Sulfones



## Dinitriles

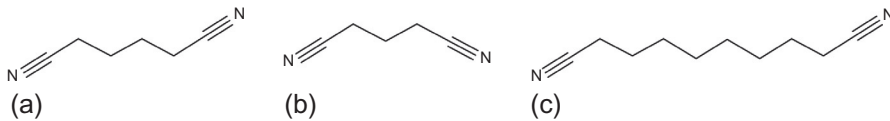


**Figure 4.2** Chemical structure of a few among the most appealing alternative solvents for lithium battery electrolytes. *Fluorinated carbonates*: (a) DFMEC; (b) TFDEC; (c) FDMC; (d) FMDFMC; (e) FEC; (f) DFDFMEC; (g) FNPEC. *Sulfones*: (a) TrMS; (b) MTrMS; (c) TMS; (d) EMS; (e) MMES; (f) EMES; (g) EMEES. *Dinitriles*: (a) ADN; (b) GLN; (c) SEN.

electrochemical stability (especially on the anodic verse) and suppress the exfoliation in carbonaceous anodes, even if in combination with a lower conductivity due to its higher viscosity (7.64 mPa s at 25 °C), with respect to analogous solutions based on PC (2.53 mPa s). The incorporation of fluorinated ethers and carbonates was proposed by Achiha *et al.* [25,26], which have observed a wider electrochemical stability window (both in oxidation and in reduction) with respect to nonfluorinated compounds.

**Table 4.2 Room temperature physicochemical properties of a few among the most appealing alternative solvents for lithium battery electrolytes**

Solvent	Molecular weight	Boiling point (°C)	Dielectric constant	Viscosity (cP)	Density (g cm <sup>-3</sup> )
MFA <sup>a</sup>	110.06	86	—	—	1.26
FPC <sup>a</sup>	120.09	65	190	7.6	—
EMS <sup>a</sup>	108.16	87	—	95	—
TFPMS <sup>a</sup>	176.17	180	—	—	—
GLN <sup>b</sup>	94.11	287	37	5.3	0.995
ADN <sup>c</sup>	108.14	295	30	5.8	0.951
SEN <sup>a</sup>	164.25	200	—	—	0.915

<sup>a</sup>From Refs. [14,15].<sup>b</sup>From Ref. [16].<sup>c</sup>From Ref. [17].**Table 4.3 Room temperature (25 °C) ionic conductivity of lithium salt electrolyte solutions based on various families of sulfones, nitriles, and alkyl phosphates**

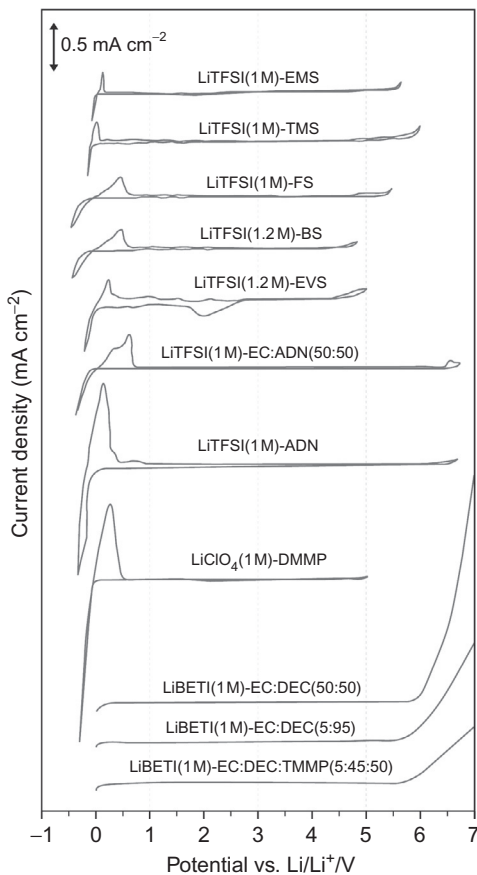
Lithium salt	Solvent	Conductivity at 25 °C (mS cm <sup>-1</sup> )
LiTFSI (1.2 M) <sup>a</sup>	EVS	3.0 <sup>a</sup>
LiTFSI (1.2 M) <sup>b</sup>	TMS	1.8 <sup>a</sup>
LiTFSI (1 M) <sup>c</sup>	AND	1.7 <sup>b</sup>
LiTFSI (1 M) <sup>d</sup>	GLN	1.7 <sup>c</sup>
LiClO <sub>4</sub> (0.8 M) <sup>e</sup>	DMMP	6.0 <sup>d</sup>
LiBOB (0.6 M) <sup>f</sup>	DMMP	4.0 <sup>e</sup>

<sup>a</sup>From Ref. [18].<sup>b</sup>From Ref. [17].<sup>c</sup>From Ref. [16].<sup>d</sup>From Ref. [19].<sup>e</sup>From Ref. [20].<sup>f</sup>From Ref. [21].

#### 4.2.1.3 Sulfones

The interest in this solvent family originated from their high anodic stability. Xu and Angell [27] have investigated electrolytes based on EMS, recording an increase of the oxidation potential up to about 5.9 V (vs. Li/Li<sup>+</sup>) on platinum working electrode. However, EMS does not show SEI-forming ability onto carbonaceous electrodes.

**Figure 4.3** Room temperature electrochemical stability window of lithium salt electrolyte solutions based on various families of sulfones and alkyl phosphates. From Refs. [17,19,22,23].



This pushed the investigation toward a wide variety of sulfones (cyclic and linear), differing in the aliphatic side chain structure as proposed by Angell and coworkers [28–30]. Among these organic compounds showing an anodic potential limit exceeding 5.5 V (vs. Li/Li<sup>+</sup>) in conjunction with relatively low melting points and transport properties, TFPMS was found to exhibit a good SEI-forming ability [28].

#### 4.2.1.4 Nitriles

Abu-Lebdeh and Davidson [16,17] and Nagahama *et al.* [31] proposed GLN, ADN, and SEN as lithium battery electrolyte solvents. Lithium salt solutions in these solvents showed electrochemical stability window about 2 V wider than that of electrolytes using standard solvents, at the same time displaying room temperature conductivities ranging from 3 to 5 mS cm<sup>-1</sup>. SEN-based electrolytes were successfully used in combination with the high-voltage Li<sub>2</sub>NiPO<sub>4</sub>F cathode material [31].

## 4.2.2 Salts

### 4.2.2.1 State of the art

Commercial lithium-ion batteries use  $\text{LiPF}_6$  [1–5] as the electrolyte salt because of the favorable properties, such as high ion conduction, wide electrochemical stability window and good SEI-forming ability of the  $\text{LiPF}_6$ -based alkyl carbonate solutions; the last property also preventing corrosion of aluminum cathodic current collectors. However,  $\text{LiPF}_6$  exhibits a few disadvantages such as poor thermal stability and easy development of HF, which is able to dissolve transition metal ions from the cathode material.

### 4.2.2.2 Alternative lithium salts

Therefore, various alternative salts [1–6] have been proposed for replacing  $\text{LiPF}_6$  such as  $\text{LiAsF}_6$ ,  $\text{LiClO}_4$ ,  $\text{LiBF}_4$ ,  $\text{LiOSO}_2\text{CF}_3$ , and imide salts ( $\text{LiN}(\text{SO}_2\text{F})_2$ ,  $\text{LiN}(\text{SO}_2\text{CF}_3)_2$ ,  $\text{LiN}(\text{SO}_2\text{C}_2\text{F}_5)_2$ ), which, however, display unwelcome issues such as toxicity ( $\text{LiAsF}_6$ ), risk of explosion ( $\text{LiClO}_4$ ), low conduction in common solvents ( $\text{LiBF}_4$ ), and modest or absent film-forming ability to protect Al current collectors ( $\text{LiOSO}_2\text{CF}_3$  and all imides). Xiao *et al.* [32] synthesized derivative salts, such as  $\text{LiPF}_4(\text{C}_2\text{O}_4)$ , which was found to show similar conductivity and higher thermal stability than  $\text{LiPF}_6$ . Xu *et al.* [33] have reviewed different salt families (reported in Figure 4.4) such as lithium fluoroalkyl phosphates [34–36], lithium chelatoborates [37–39], lithium chelatophosphates [40,41], lithium imidazolides [42], and lithium imidazolates [43].

A very interesting salt, first reported by Angell and coworkers [39–44] and recently reviewed by Lex-Balducci *et al.* [8], is lithium bis(oxalate)borate (LiBOB). The main appealing peculiarities of LiBOB are (1) high thermal stability and safety; (2) protective

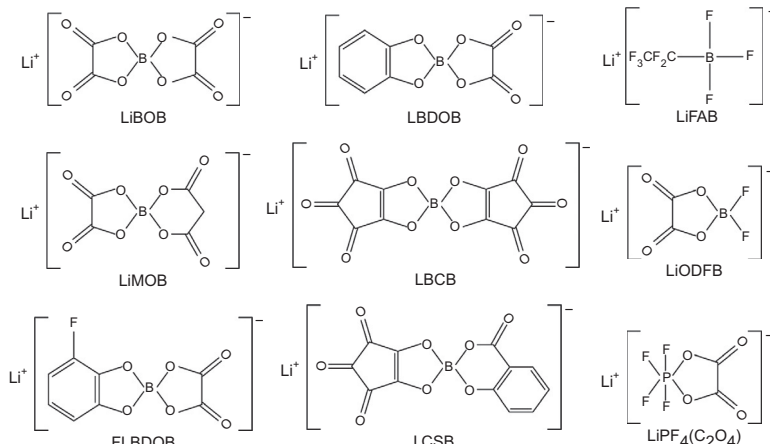


**Figure 4.4** Chemical structure of a few among the most appealing alternative salts for lithium battery electrolytes.

**Table 4.4 Physicochemical characteristics of selected LiMOB-based electrolyte solutions**

Thermal stability	273 °C	
Anodic breakdown voltage	4.3 V	
Propylene carbonate 0.1 M	Solubility (25 °C) γ-Butyrolactone 0.7 M	Dimethylsulfoxide 1.5 M

From Ref. [33].

SEI-forming ability onto aluminum current collectors and graphite anodes [44]; (3) relatively low environmental impact of its decomposition products ( $B_2O_3$  and  $CO_2$ ); and (4) capability to reduce  $Fe^{2+}$  and  $Mn^{2+}$  dissolution from  $LiFePO_4$  [45] and  $LiMn_2O_4$  [46], respectively. Conversely, LiBOB displays disadvantages such as (1) modest solubility in alkyl carbonates; (2) lower conductivity (i.e., higher viscosity) of LiBOB-based solutions with respect to  $LiPF_6$ -containing electrolytes [47]; (3) decomposition in presence of  $LiCoO_2$  and  $LiNi_xCo_yMn_{1-x-y}O_2$  [48]; and (4) cell venting phenomena due to oxalate and carboxylate impurities resulting in  $CO_2$  formation [48].

These issues have pushed the research toward a wide variety of different lithium chelatoborate salts (Figure 4.4). Among these new alternative salts is to be mentioned LiMOB, proposed by Xu *et al.* [33], whose main physicochemical characteristics are summarized in Table 4.4. Xue *et al.* have prepared and electrochemically investigated LBCB, LCSB [49,50], and LBDOB [51]. These salts were found to be thermally stable up to 250 °C and partially insoluble in standard lithium battery electrolyte solvents [39,44]. Zhang [52] have studied LiDFOB, obtained by replacing one oxalate moiety with two fluorine atoms. The LiDFOB salt was found to exhibit higher solubility in alkyl carbonate solvents, better power capability, and compatibility with electrodes (i.e., good film-forming ability onto graphite anodes due to the oxalatoborate moieties) [52,53] with respect to LiBOB. Arai *et al.* [54] have synthesized  $Li_2DFB$ , showing thermal stability up to 400 °C and redox shuttle reactions at high voltage, for example, about 4.5 V (depending on the solvent).

Derivative lithium salts from  $LiBF_4$ , reported by Zhou *et al.* [55], were prepared by substituting fluorine atoms of the  $BF_4^-$  anion with perfluoroalkyl groups, aiming to increase their low conductivity in alkyl carbonate solutions without affecting their thermal stability and moisture sensibility. The conductivity of these salts, highly soluble in standard lithium battery solvents [56], was found to decrease with increasing perfluoroalkyl chain length, whereas the anodic breakdown potential showed an opposite behavior.

#### 4.2.3 Additives

The main purpose of additive incorporation into lithium-ion battery electrolytes is enhancing the safety of these systems without, at the same time, depleting their electric performance. Generally, these compounds are flame retardants, FRs, or

high-flash-point solvents and may also be used as “single” solvents. Mainly, five different FR additive families (Figure 4.5), recently reviewed by Lex-Baldacci *et al.* [8], have been investigated: (1) alkyl phosphates; (2) alkyl phosphonates; (3) phosphazenes; (4) hydrofluoroethers; and (5) fluorinated esters. The physicochemical properties of such additives are summarized in Table 4.5.

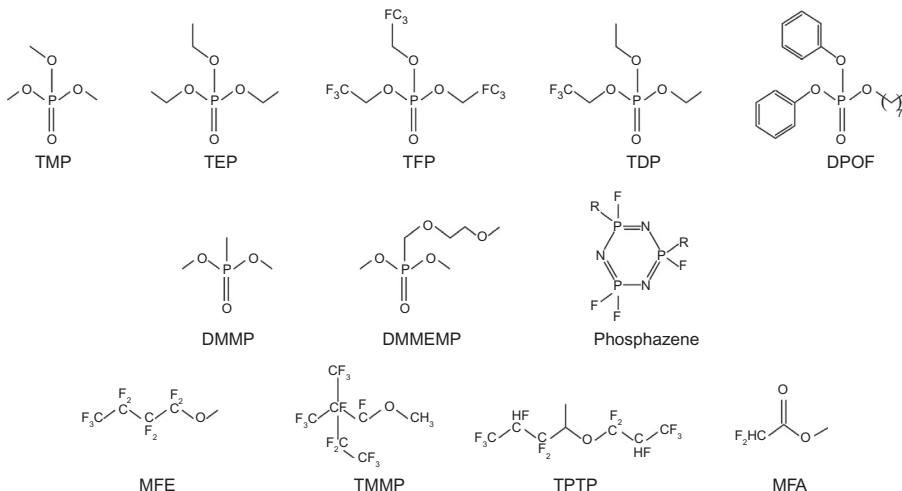


**Figure 4.5** Chemical structure of a few among the most appealing additives for lithium battery electrolytes.

**Table 4.5** Room temperature physicochemical properties of the mostly investigated additives for lithium battery electrolytes

Additive	Molecular weight (g mol <sup>-1</sup> )	Boiling point (°C)	Dielectric constant	Viscosity (cP)	Density (g cm <sup>-3</sup> )
TEP <sup>a</sup>	182.15	215	–	1.6	1.072
TMP <sup>a</sup>	140.07	180	–	2.0	1.197
TFP <sup>a</sup>	340.07	82	–	–	1.594
DMMP <sup>b</sup>	124.08	180	22.3	1.75	1.145
DMMEMP <sup>c</sup>	198.15	280	>77	4.85	–
MFE <sup>a</sup>	250.06	60	–	–	1.529
MFA <sup>a</sup>	110.06	85	–	–	1.272

<sup>a</sup>From Ref. [14].

<sup>b</sup>From Ref. [57].

<sup>c</sup>From Ref. [58].

#### 4.2.3.1 Alkyl phosphates

Xu *et al.* [59] demonstrated that TMP and TEP are able to sharply reduce the flammability of common lithium-ion battery electrolytes. However, the “no flammability” condition is achieved only when the TMP or TEP fraction overcomes 40% in volume, whereas a considerable capacity fading in full cells is observed already at contents as low as 5% in volume, due to the alkyl phosphate instability toward graphite anodes. In addition, a large alkyl phosphate content increases the electrolyte resistance. The cell performance decay can be mitigated through fluorination of the phosphate alkyl chains. Among the most common fluorinated phosphates proposed, TFP, BMP, and TDP, the former showed the best results.

Shim *et al.* [60] have investigated DPOF as additive, which leads to enhanced thermal stability and lower irreversible capacity and charge-transfer resistance but, at the same time, promoting the growth of a thick SEI layer onto the anode.

#### 4.2.3.2 Alkyl phosphonates

Alkyl phosphonates were investigated both as electrolyte additives [61,62] and solvents [58,63]. Among these compounds, DMMP and DMEMEP were found by Dalavi *et al.* [62] and Zhang *et al.* [63], respectively, not depleting the transport properties of conventional electrolytes and achieving high conductivity when used as single solvent with lithium salts because of their modest viscosity, high dielectric constant, and low melting point.

#### 4.2.3.3 Phosphazenes

These organic compounds were found to effectively suppress the flammability of conventional electrolytes [59,64,65]. In particular, fluorinated phosphazenes behave as self-extinguishing additives. However, their high viscosity affects the transport properties of the electrolyte solutions, thus decreasing the cell performance.

#### 4.2.3.4 Hydrofluoroethers

Hydrofluoroethers (HFEs) are appealing additives to produce safe lithium battery electrolytes because of their negligible flash point, low surface tension, modest viscosity, and low volatility and freezing temperature [66]. Among the HFE family, Arai [67] have investigated MFE. However, no flammable electrolyte solutions are obtained only for very large MFE contents (i.e., from 70% to 90%), thus remarkably reducing their ionic conductivity. The use of branched HFEs with higher fluorine content, for example, TMMP and TPTP, proposed by Naoi *et al.* [66] and Shim *et al.* [60], respectively, allowed to reduce the amount (50%) of additive. Conversely, these compounds show modest miscibility with cyclic alkyl carbonates (EC) and behave as poor solvents.

#### 4.2.3.5 Fluorinated esters

The most interesting among this additive family is MFA reported by Tanaka *et al.* [68]. MFA-based electrolytes were found to show superior thermal stability (400 vs. 270 °C) together with higher ion conductivity with respect to conventional lithium-ion battery electrolytes.

### 4.3 Ionic liquid electrolytes

#### 4.3.1 Ionic liquids

ILs, molten salts at room temperatures or below, are a very interesting new class of neoteric fluids because of their unique properties such as nonflammability; negligible vapor pressure; remarkable ionic conductivity; high thermal, chemical, and electrochemical stabilities; low heat capacity; ability to dissolve inorganic (including lithium salts), organic, and polymeric materials; and, in some cases, hydrophobicity [69–72]. ILs have attracted growing attention as electrolyte additives or solvents for replacing organic compounds currently used not only in lithium batteries [9] but also in a wide variety of electrochemical devices [73–79], resulting in improved safety in case of overheating/overcharging, which can lead to flaming/explosion. The safety issues of ILs were proved through flammability and volatility tests illustrated in Figure 4.6. No burning and cell volume change (due to internal pressure increase) were observed in IL materials even upon prolonged exposition to fire or extreme heating.

The possibility to widely combine a large variety of cations and anions gives the freedom to design the most suitable ILs for matching the requirements of the final electrochemical device. Viable lithium battery ILs are formed by alkylimidazolium, saturated alkyl quaternary ammonium [cyclic (pyrrolidinium, piperidinium) or

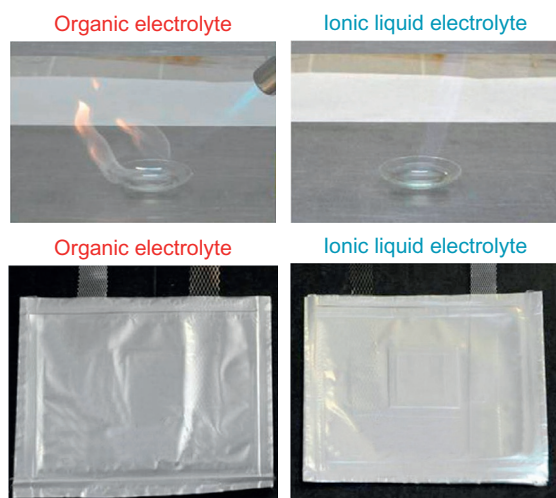


**Figure 4.6** Flammability (upper panels) and volatility (lower panels) tests performed on conventional (left panels) and ionic liquid (right panels) lithium battery electrolytes.

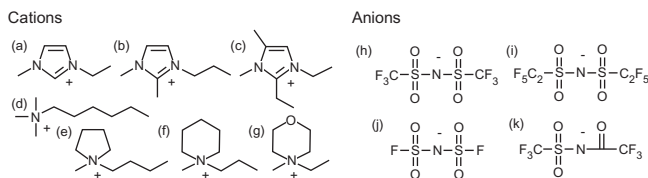


**Figure 4.7** Chemical structure of the most common IL cations and anions used as lithium battery electrolyte solvents. (a)  $\text{EMI}^+$ ; (b)  $\text{DMPI}^+$ ; (c)  $\text{DEDMI}^+$ ; (d)  $\text{TMHA}^+$ ; (e)  $\text{PYR}_{14}^+$ ; (f)  $\text{PIP}_{13}^+$ ; (g)  $\text{MORP}_{12}^+$ ; (h)  $\text{TFSI}^-$ ; (i)  $\text{BETI}^-$ ; (j)  $\text{FSI}^-$ ; (k)  $\text{TSAC}$ .

acyclic (tetraalkylammonium) cations, in combination with hydrophobic perfluoroalkylsulfonylimide anions. The chemical structure of the most common IL cations and anions as lithium battery electrolyte solvents is depicted in Figure 4.7, whereas their physicochemical properties are summarized in Table 4.6.

Most of the IL materials reported in Table 4.6 exhibit a melting point below room temperature, thus mainly ascribable to the asymmetry of the IL ions (particularly, for the  $\text{Im}_{14}^-$  anion), which hinder the IL crystallization (e.g., crystal packing of the ions), in conjunction with wide thermal stability. Also, the introduction of a hetero atom in the cation side aliphatic chain was found to considerably decrease the melting temperature as a result of enhanced flexibility of the ether group, thus interfering with the ion packing [85,86] but affecting the thermal and electrochemical stability of the IL [80,81]. Imidazolium-based ILs (having two-dimensional structure) display higher conductivity than that of aliphatic quaternary ammonium ones (three-dimensional), whereas pyrrolidinium- and piperidinium-based ILs (having an intermediate structure) exhibit a much wider cathodic stability ( $>5$  V) than noncyclic quaternary ammonium- [80] and, especially, imidazolium-based [86,87] because of the absence of acidic protons and double bonds in the cation ring.

Among the anions, the members of the perfluoroalkylsulfonylimide family were successfully proposed as IL counterions for lithium battery electrolytes [76,88–90] because of the resulting good conductivities even at subambient temperature, wide electrochemical and thermal stability, and hydrophobicity. MacFarlane *et al.* [91–94], Passerini *et al.* [95–98], and Tatsumi *et al.* [86,99] have clearly showed the feasibility of pyrrolidinium TFSI (Figure 4.7 and Table 4.6) ILs as lithium battery electrolyte components, improving the cycling performance, long-term stability, and safety of the full cells. A growing interest is actually attracted by the FSI anion because its reduced steric hindrance, leading to lower viscosity and, therefore, higher conductivity [81,100,101] in combination with much lower melting point, results in high conductivities even at subambient temperatures. On the other hand, the reactivity of the fluorine atoms directly bound to the sulfonyl groups [102,103] reduces the electrochemical and thermal stability of the FSI anion.

### 4.3.2 IL-lithium salt electrolyte mixtures

ILs were found to be able to dissolve lithium salt [71,72,90] as demonstrated by Cooper and Angell [104,105], who have focused on the “ionicity” concept

**Table 4.6 Physicochemical properties of various lithium battery ionic liquids**

Ionic liquid	m.p. (°C)	Ther. stab. (°C)		$\sigma$ (mS cm <sup>-1</sup> )		ESW (V)
		N <sub>2</sub>	Air	-10 °C	20 °C	
PYR <sub>13</sub> TFSI	11.4	—	—	<10 <sup>-5</sup>	2.7	5.84
PYR <sub>14</sub> TFSI	-6.5	392.2	381.1	6.2 × 10 <sup>-4</sup>	1.8	5.83
PYR <sub>15</sub> TFSI	13.6	—	—	<10 <sup>-5</sup>	1.3	5.91
PYR <sub>16</sub> TFSI	2.2	—	—	<10 <sup>-5</sup>	1.0	5.95
PYR <sub>17</sub> TFSI	16.7	389.3	373.4	<10 <sup>-5</sup>	0.8	5.96
PYR <sub>18</sub> TFSI	-13.7	—	—	7.4 × 10 <sup>-2</sup>	0.54	5.83
PYR <sub>1,10</sub> TFSI	9.6	—	—	<10 <sup>-5</sup>	0.33	5.63
PYR <sub>1(2O<sub>1</sub>)</sub> TFSI	<-40 °C	414.8	416.4	0.47	2.4	4.84
PYR <sub>1(2O<sub>2</sub>)</sub> TFSI	<-40 °C	—	—	0.41	2.1	4.38
PIP <sub>13</sub> TFSI	12.3	—	—	<10 <sup>-5</sup>	0.92	5.82
PIP <sub>14</sub> TFSI	-10.0	427.8	420.5	2.4 × 10 <sup>-4</sup>	0.64	5.80
PIP <sub>15</sub> TFSI	-3.5	—	—	1.5 × 10 <sup>-5</sup>	0.54	5.85
PIP <sub>16</sub> TFSI	21.7	—	—	<10 <sup>-5</sup>	2.0 × 10 <sup>-4</sup>	5.91
PIP <sub>17</sub> TFSI	6.2	423.6	408.5	<10 <sup>-5</sup>	0.26	5.89
PIP <sub>18</sub> TFSI	-12.4	—	—	8.0 × 10 <sup>-5</sup>	0.22	5.89
PIP <sub>24</sub> TFSI	7.5	—	—	<10 <sup>-5</sup>	0.53	5.00
PIP <sub>25</sub> TFSI	3.7	—	—	<10 <sup>-5</sup>	0.35	5.06
EMITFSI	-9.7	—	390	2.4 × 10 <sup>-3</sup>	4.7	3.98
PYR <sub>13</sub> BETI	6.5	—	—	<10 <sup>-5</sup>	0.53	5.52
PYR <sub>14</sub> BETI	8.9	—	—	<10 <sup>-5</sup>	0.42	5.68
EMIBETI	-1.3	—	—	<10 <sup>-5</sup>	2.0	3.72
PYR <sub>11</sub> Im <sub>14</sub>	<-40 °C	—	—	0.01	0.18	5.39
PYR <sub>13</sub> Im <sub>14</sub>	<-40 °C	—	—	0.024	0.30	4.79
PYR <sub>14</sub> Im <sub>14</sub>	<-40 °C	—	—	0.025	0.28	5.51
EMIIm <sub>14</sub>	<-40 °C	—	—	0.15	1.1	3.69
Et <sub>4</sub> NIm <sub>14</sub>	<-40 °C	—	—	4.3 × 10 <sup>-3</sup>	0.13	5.30
PYR <sub>13</sub> FSI	-13.6	240	240	0.08	5.6	5.48
PYR <sub>14</sub> FSI	-20.0	230	230	1.3	4.1	5.50
PYR <sub>1(2O<sub>2</sub>)</sub> FSI	-26.3	200	200	1.3	4.1	4.97

m.p., melting point; Ther. stab., thermal stability;  $\sigma$ , ionic conductivity; ESW, electrochemical stability window. From Refs. [80-84].

[70,106,107], and Nicotera *et al.* [108] and Borodin *et al.* [109,110], who have evidenced strong Li<sup>+</sup> cation-TFSI anion interactions in pyrrolidinium TFSI ILs. The latter explain the conductivity decrease in molten ILs after lithium salt incorporation as evidenced in Table 4.7. The Li<sup>+</sup> motion through the IL medium is due to two

**Table 4.7 Ionic conductivity values as a function of the temperature for lithium salt–ionic liquid electrolyte mixtures**

	Ionic conductivity (mS cm <sup>-1</sup> )						
	-40 °C	-30 °C	-20 °C	-10 °C	0 °C	20 °C	40 °C
<i>(a)</i> $(x)\text{LiFSI}-(1-x)\text{PYR}_{14}\text{FSI}$ electrolyte mixture							
$x=0$	$6.2 \times 10^{-4}$	$4.2 \times 10^{-3}$	$7.6 \times 10^{-2}$	1.3	2.0	4.1	7.1
$x=0.1$	$4.1 \times 10^{-3}$	$7.6 \times 10^{-2}$	0.5	0.9	1.4	3.1	5.8
$x=0.2$	$2.5 \times 10^{-2}$	$9.4 \times 10^{-2}$	0.2	0.5	0.9	2.0	4.0
$x=0.3$	$1.4 \times 10^{-2}$	$4.5 \times 10^{-2}$	0.1	0.3	0.5	1.3	2.8
<i>(b)</i> $(x)\text{LiTFSI}-(1-x)\text{PYR}_{14}\text{TFSI}$ electrolyte mixture							
$x=0$	$3.7 \times 10^{-5}$	$3.9 \times 10^{-5}$	$4.0 \times 10^{-5}$	$5.7 \times 10^{-5}$	0.7	1.8	3.7
$x=0.1$	$3.3 \times 10^{-5}$	$4.1 \times 10^{-5}$	$8.9 \times 10^{-5}$	$8.4 \times 10^{-3}$	0.33	1.1	2.5

From Refs. [81,98,101].

different contributions [110]: exchange of the anions in the lithium first coordination shell (about 70% of total) and diffusion with the lithium coordination shell. Kunze *et al.* [111] have reported that pyrrolidinium cations, including oxygen atom in the alkyl side chain, are able to coordinate  $\text{Li}^+$  ions (even if this does not result in any enhanced lithium mobility), whereas Castiglione *et al.* [112] have shown  $\text{Li}^+$  mobility enhancement with temperature, probably due to the disruption/formation of the anion coordination shell surrounding the lithium cation. Henderson and Passerini [98] have found crystalline phases in  $\text{LiTFSI}-\text{PYR}_{1A}\text{TFSI}$  ( $A=2, 3, 4$ ) electrolyte mixtures with an eutectic composition for a  $\text{Li}^+$  mole fraction equal to 0.33. Different behavior was observed by Paillard *et al.* [101] in  $\text{LiFSI}-\text{PYR}_{14}\text{FSI}$  mixtures, which showed more extended liquid range down to glass transition temperature. On the other hand, addition of lithium salts decreases the melting point of ILs (Table 4.7), resulting in appreciable conductivity values even at low temperatures [81,98,101] (e.g., about  $10^{-3}$  S cm<sup>-1</sup> are observed at -20 °C for  $\text{LiFSI}-\text{PYR}_{14}\text{FSI}$  mixtures).

IL electrolytes based on saturated, cyclic, quaternary ammonium cations (pyrrolidinium and piperidinium) were found to be more electrochemically stable with respect to those based on imidazolium and noncyclic, tetraalkylammonium cations [80,83]. Analogously, the TFSI anion exhibits the widest electrochemical stability window (ESW) among the perfluoroalkylsulfonylimide family [83]. The data summarized in Table 4.8 evidence an ESW for the  $\text{LiTFSI}-\text{PYR}_{14}\text{TFSI}$  mixture exceeding 5 V, whereas the replacement of TFSI with FSI leads to reduction in cathodic stability. Similarly, TFSI-based IL electrolytes were found to be more thermally stable than the FSI ones [81,83,100,101]. Note that long-term thermal stability has to be evaluated by isothermal experiments instead of the commonly used variable-temperature thermo-gravimetical analysis (TGA) measurements as highlighted in Table 4.9.

**Table 4.8 Cathodic and anodic potential values, detected vs. Ag/Ag<sup>+</sup> at various current densities, for different ionic liquids and ionic liquid–lithium salt electrolyte mixtures**

<i>Current density</i> ( $\mu\text{A cm}^{-2}$ )	Cathodic verse				Anodic verse			
	5	10	50	100	5	10	50	100
<i>IL samples</i>	<i>Potential vs. Ag/Ag<sup>+</sup> (V)</i>							
PYR <sub>14</sub> TFSI	−2.86	−3.13	−3.60	−3.70	0.14	1.20	2.0	2.05
(0.1)LiTFSI–(0.9)	−0.13	−1.65	−1.86	−3.55	1.06	1.25	1.98	2.07
PYR <sub>14</sub> TFSI								
PYR <sub>14</sub> FSI	−1.45	−1.72	−1.75	−3.40	0.67	0.91	1.89	1.95
(0.1)LiFSI–(0.9)	−0.01	−0.12	−0.70	−3.01	0.90	1.10	1.86	1.96
PYR <sub>14</sub> FSI								

$T = 20^\circ\text{C}$ .

From Refs. [101,113].

### 4.3.3 IL blends

A successful approach for enhancing the transport properties of IL electrolytes (especially at low temperatures) is represented by the use of mixed ILs [114–120]. The basic idea is to combine different IL species to obtain electrolytes with improved performance (Table 4.10). According to this scenario, bulky and/or asymmetric ion ILs, showing low melting point [113–116], are generally blended with light-ion ILs that exhibit high conductivity [114–117]. Appeteccchi *et al.* [114], Castiglione *et al.* [115], Montanino *et al.* [116], and Kunze *et al.* [117] have demonstrated how mixed ILs hinder the ability of the electrolyte to crystallize. For instance, LiTFSI (or LiPF<sub>6</sub>)–PYR<sub>14</sub>TFSI–PYR<sub>13</sub>FSI mixtures have shown much lower melting points ( $< -35^\circ\text{C}$ ) with respect to the single IL electrolytes, resulting in conductivity values approaching  $10^{-4}\text{ S cm}^{-1}$  at very low temperatures [118–120] ( $-30^\circ\text{C}$ ). Also, the synergistic effect due to IL blending has been observed in terms of electrochemical stability [118–120].

### 4.3.4 ILs as electrolyte additives

The transport properties of IL electrolytes, however, are generally lower with respect to those of organic solutions because of their higher viscosity. In this scenario, ILs have been proposed as nonflammable and nonvolatile additives for lithium battery electrolytes with the aim to achieve an optimal compromise between good conductivity and high safety. Guerfi *et al.* [121] and Kühnel *et al.* [122] have investigated mixed electrolytes composed of ILs (namely, EMITFSI and PYR<sub>14</sub>TFSI) and organic solvents (EC/DEC and PC, respectively). Table 4.10 summarizes the physicochemical properties of different families of IL-based electrolytes.

**Table 4.9 Weight loss detected during variable-temperature TGA scan (A) and after 2-h isothermal TGA heating (B) for different LiFSI–PYR<sub>1A</sub>FSI lithium salt–ionic liquid electrolyte mixtures**

Temperature (°C)	25	50	100	150	200	250	300	350
<i>(A) Ionic liquid electrolyte</i>								
(0.1)LiFSI–(0.9)PYR <sub>13</sub> FSI	0.00	0.27	0.37	0.72	1.85	2.92	8.16	78.50
(0.1)LiFSI–(0.9)PYR <sub>14</sub> FSI	0.00	0.30	0.39	0.97	1.83	2.42	9.55	78.18
(0.1)LiFSI – (0.9)PYR <sub>1(2O<sub>2</sub>)</sub> FSI	0.00	0.19	0.31	0.87	3.69	8.73	56.06	76.92
Temperature (°C)	100	150	200	250				
<i>(B) Ionic liquid electrolyte</i>								
(0.1)LiFSI–(0.9)PYR <sub>13</sub> FSI	3.46	–	3.87	17.26				
(0.1)LiFSI–(0.9)PYR <sub>14</sub> FSI	3.24	3.26	3.44	22.57				
(0.1)LiFSI – (0.9)PYR <sub>1(2O<sub>2</sub>)</sub> FSI	2.04	2.29	10.86	–				

From Refs. [81,101].

**Table 4.10 Physicochemical properties of various lithium salt–ionic liquid electrolytes for lithium battery systems**

Ionic liquid electrolyte	m.p. (°C)	$\eta$ (mPa s)	$\sigma$ (S cm <sup>-1</sup> )
(0.1)LiTFSI–(0.9)PYR <sub>14</sub> TFSI <sup>a</sup>	−10.6	—	$1.1 \times 10^{-3}$
(0.1)LiTFSI–(0.9)PYR <sub>(2O<sub>1</sub>)</sub> TFSI <sup>a</sup>	—	104	$1.8 \times 10^{-3}$
(0.1)LiBETI–(0.9)PYR <sub>14</sub> BETI <sup>a</sup>	—	414	$2.9 \times 10^{-4}$
(0.1)LiIM <sub>14</sub> –(0.9)PYR <sub>14</sub> IM <sub>14</sub> <sup>a</sup>	—	758	$1.6 \times 10^{-4}$
(0.1)LiFSI–(0.9)PYR <sub>13</sub> FSI <sup>a</sup>	−16.6	60	$5.5 \times 10^{-3}$
(0.1)LiFSI–(0.9)PYR <sub>14</sub> FSI <sup>a</sup>	−25.1	93	$3.2 \times 10^{-3}$
(0.2)LiFSI–(0.8)PYR <sub>14</sub> FSI <sup>a</sup>	−35.3	132	$2.1 \times 10^{-3}$
(0.3)LiFSI–(0.7)PYR <sub>14</sub> FSI <sup>a</sup>	n.d.	194	$1.3 \times 10^{-3}$
(0.1)LiFSI–(0.9)PYR <sub>1(2O<sub>2</sub>)</sub> FSI <sup>a</sup>	−24.9	—	$3.1 \times 10^{-3}$
(0.1)LiFSI–(0.9)PYR <sub>14</sub> FSI <sup>a</sup>	—	80	$3.2 \times 10^{-3}$
(0.3 M)LiTFSI–EMITFSI <sup>b</sup>	—	55	$5.1 \times 10^{-3}$
(0.3 M)LiTFSI–PYR <sub>13</sub> TFSI <sup>b</sup>	—	130	$2.0 \times 10^{-3}$
(0.3 M)LiTFSI–PIP <sub>13</sub> TFSI <sup>b</sup>	—	330	$7.3 \times 10^{-4}$
(0.3 M)LiTFSI–EMIFSI <sup>b</sup>	—	24	$1.1 \times 10^{-2}$
(0.3 M)LiTFSI–PYR <sub>13</sub> FSI <sup>b</sup>	—	51	$5.5 \times 10^{-3}$
(0.3 M)LiTFSI–PIP <sub>13</sub> FSI <sup>b</sup>	—	124	$2.5 \times 10^{-3}$
(0.7 M)LiFSI–EMIFSI <sup>b</sup>	—	25	$1.1 \times 10^{-2}$
(0.3 M)LiTFSI–PYR <sub>13</sub> FSI <sup>b</sup>	−9.0	—	$4.9 \times 10^{-3}$
(0.3 M)LiTFSI–(0.75)PYR <sub>14</sub> TFSI–(0.25)PYR <sub>13</sub> FSI <sup>b,c</sup>	−36.0	—	$1.5 \times 10^{-3}$
(0.3 M)LiTFSI–(0.42)PYR <sub>14</sub> TFSI–(0.58)PYR <sub>13</sub> FSI <sup>b,c</sup>	n.d.	—	$2.5 \times 10^{-3}$
(0.3 M)LiPF <sub>6</sub> –PYR <sub>14</sub> TFSI <sup>b</sup>	−6.0	—	$6.2 \times 10^{-3}$
(0.3 M)LiPF <sub>6</sub> –PYR <sub>13</sub> FSI <sup>b</sup>	−9.0	—	$4.6 \times 10^{-3}$
(0.3 M)LiPF <sub>6</sub> –(0.75)PYR <sub>14</sub> TFSI–(0.25)PYR <sub>13</sub> FSI <sup>b,c</sup>	n.d.	—	$1.4 \times 10^{-3}$
(0.3 M)LiPF <sub>6</sub> –(0.42)PYR <sub>14</sub> TFSI–(0.58)PYR <sub>13</sub> FSI <sup>b,c</sup>	n.d.	—	$2.6 \times 10^{-3}$
(1 M)LiPF <sub>6</sub> –EMITFSI <sup>b</sup>	Inflammable	36.3	$8.6 \times 10^{-3}$
(1 M)LiPF <sub>6</sub> –(0.9)EMITFSI–(0.1)EC/DEC/VC <sup>b,d</sup>	Inflammable	30.5	$9.8 \times 10^{-3}$
(1 M)LiPF <sub>6</sub> –(0.4)EMITFSI–(0.6)EC/DEC/VC <sup>b,d</sup>	Inflammable	14.9	$1.0 \times 10^{-2}$
(1 M)LiPF <sub>6</sub> –(0.3)EMITFSI–(0.7)EC/DEC/VC <sup>b,d</sup>	Flammable	14.1	$9.4 \times 10^{-3}$
(1 M)LiPF <sub>6</sub> –(0.1)EMITFSI–(0.9)EC/DEC/VC <sup>b,d</sup>	Flammable	12.7	$9.4 \times 10^{-3}$
(0.3 M)LiTFSI–(0.48)PYR <sub>14</sub> TFSI–(0.52)PC <sup>b,c</sup>	Inflammable	39	$2.9 \times 10^{-3}$
(0.3 M)LiTFSI–(0.19)PYR <sub>14</sub> TFSI–(0.81)PC <sup>b,c</sup>	Flammable	11	$5.3 \times 10^{-3}$
(0.3 M)LiTFSI–(0.05)PYR <sub>14</sub> TFSI–(0.95)PC <sup>b,c</sup>	Flammable	7	$3.8 \times 10^{-3}$

<sup>a</sup>Lithium salt concentration in mole fraction.<sup>b</sup>Lithium salt concentration in mol dm<sup>-3</sup>.<sup>c</sup>Ionic liquid mole fraction.<sup>d</sup>Ionic liquid and organic compound volume fraction (from Refs. [86,101,116,121–126]).

## 4.4 Polymer electrolytes

### 4.4.1 Introduction

Ionically conducting membranes, namely polymer electrolytes, can be divided into two conceptually different families.

The first one, namely gel polymer electrolytes, refers to systems (schematized in Figure 4.8) basically formed by liquid solution (composed by lithium salt, e.g.,  $\text{LiPF}_6$ ,  $\text{LiClO}_4$ , and organic solvents, e.g., EC, DMC, DEC, PC) entrapped in polymeric matrix, giving an electrolyte membrane exhibiting mechanical characteristics typical of plastic solid materials in conjunction with transport properties approaching those of liquid electrolytes [127,128]. The polymer host might not behave as a simple porous sponge. In fact, it can also interact with the liquid solution (mainly through the solvent molecules), which results being more than physically retained by the matrix itself [127,128]. This process, involving solvent–polymer interaction, is generally named *swelling*.

The second family, namely dry polymer electrolytes, is constituted by solvent-free, polymer–salt systems [129] composed of suitable lithium salt dissolved in a polymer matrix, generally linear polyethyleneoxide (PEO, monomer unit  $-\text{CH}_2\text{CH}_2\text{O}-$ ), as first demonstrated by Wright [130]. Armand suggested the use of  $\text{LiX/PEO}$  systems as lithium battery electrolytes [131,132]. The dissolution of the lithium salt within the polymer host, which behaves as the solvent to form a true solid solution, is promoted by Lewis acid–base interactions [129,130,133,134] of the  $\text{Li}^+$  cations (because of its

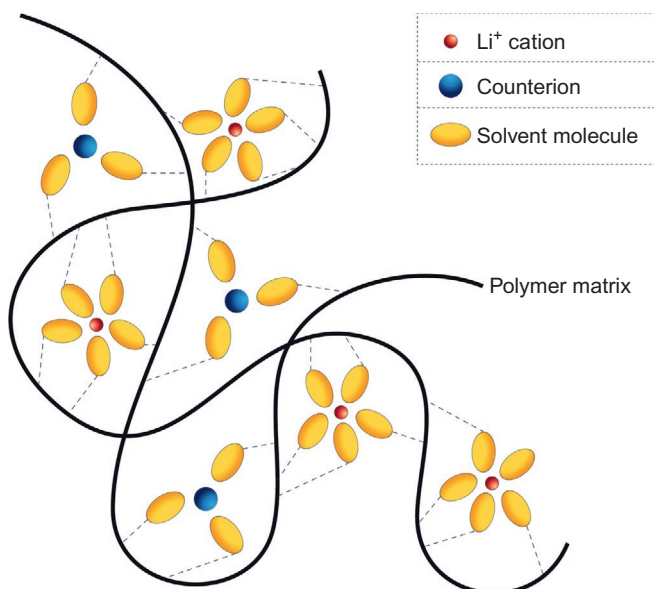


**Figure 4.8** Schematization of a gel polymer electrolyte system.

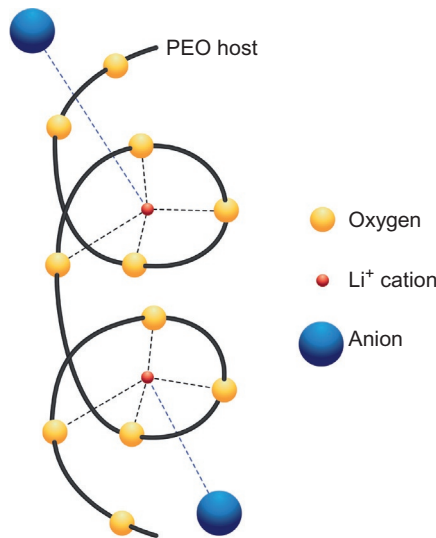


**Figure 4.9** Schematic representation of the  $\text{Li}^+$ –PEO coordination in dry polymer electrolytes.

high surface charge density) and the electron pairs of the PEO oxygens [133,134] as shown in Figure 4.9. Large-size anions ( $\text{BF}_4^-$ ,  $\text{ClO}_4^-$ ,  $\text{CF}_3\text{SO}_3^-$ ,  $\text{TFSI}^-$ ,  $\text{BETI}^-$ ) are proposed as counterions [129,133–136] because of their low  $\text{Li}^+ \cdots \text{Anion}^-$  lattice energy promoting the lithium salt dissolution within the PEO host.

#### 4.4.2 Gel polymer electrolytes

Gel electrolytes are characterized by polymer host  $\cdots$  solvent  $\cdots$  lithium salt interactions, which drive the chemical stability of these ternary systems. Strong polymer–solvent– $\text{Li}^+$  interactions, as in complexes based on PEO hosts, give stable gel electrolytes. Otherwise, when weak interactions occur among the electrolyte components, the polymeric host acts as a porous membrane (sponge-like) loaded with liquid electrolyte.

##### 4.4.2.1 Strong gel electrolytes

Strongly interacting polymers with liquid organic solutions generally form chemically stable gel electrolytes, even if their mechanical properties are generally worse with respect to weak gel electrolytes. Choi *et al.* [137], Kang *et al.* [138], Aihara *et al.* [139,140], and Appeteccchi *et al.* [141,142] have widely investigated gel polymer electrolytes based on high molecular weight PEO ( $4 \times 10^6$  a.m.u.), detecting conductivity values approaching  $10^{-3} \text{ S cm}^{-1}$  even at low temperatures ( $-10^\circ\text{C}$ ). The mechanical characteristics of the PEO membranes (having a sticky consistency) are susceptible, however, to significant improvement by the addition of nanosize silica [139–142].

PAN-based gel electrolytes, investigated by Appetecchi *et al.* [143], have shown fast transport properties ( $4 \times 10^{-3}$  S cm $^{-1}$  at room temperature) in combination with a wide electrochemical stability window (>5 V). The incorporation of fillers [144,145] was found to improve the mechanical stability and solvent retention, resulting in time-stable ionic conductivity even upon prolonged storage at 75 °C in open cells. Gel electrolytes based on PMMA were found to be much more chemically stable because of the stronger polymer–solvent interaction with respect to PAN but, at the same time, exhibiting lower transport properties [146–149]. Another approach, first proposed by Wieczorek and Stevens [150], is represented by the adoption of polymer blends, aiming to prepare gel electrolytes with improved properties with respect to those of individual polymeric materials. Particularly, blend materials characterized by three-dimensionally interpenetrated, cocontinuous microstructures are of most interest, as reported by Willemse *et al.* [151,152] and Jordhamo *et al.* [153], because of the possibility of combining polymer materials having different peculiarities. In this scenario, Passerini *et al.* [154], Momma *et al.* [155], and Nara *et al.* [156] have developed gel electrolytes based on cocontinuous, two-component polymer blends formed by polystyrene (i.e., assuring mechanical stability to the electrolyte membrane) and PEO (i.e., enabling ionic conductivity through swelling in the electrolytic solution). Room temperature conductivities approaching 10 $^{-3}$  S cm $^{-1}$  were achieved by these electrolytes.

Finally, gel electrolytes based on thermally cross-linked poly(fluorosilicone)-ethylene oxide matrices, investigated by Appetecchi *et al.* [157,158], have exhibited high ion conductivities (>10 $^{-3}$  S cm $^{-1}$  at room temperature) and liquid uptakes in combination with wide electrochemical stability (5 V) and excellent mechanical properties.

#### 4.4.2.2 Weak gel electrolytes

Among the most common polymer hosts for gel electrolytes characterized by weak polymer–solvent interactions, PVdF [159,160] is the worthiest to be mentioned. Different approaches have been followed aiming to decrease the crystallinity of the PVdF matrix: (1) use of branched PVdF–HFP or PVdF–TrFE copolymers rather than linear PVdF monomers [161–180]; (2) incorporation of nanometric fillers such as BaTiO<sub>3</sub> [161], Al<sub>2</sub>O<sub>3</sub> [160,161], SiO<sub>2</sub> [160,161,163], and TiO<sub>2</sub> [160,164] (even to stabilize the lithium interfacial properties); and (3) addition of a different polymeric component to obtain blend polymer hosts [181–183]. The above-mentioned PVdF-based gel electrolytes exhibit fast ion transport properties [184], for example, room temperature conductivities well above 10 $^{-3}$  S cm $^{-1}$ , in combination with good mechanical characteristics. Conversely, such electrolyte systems are chemically unstable due to phase separation between the polymer host and the liquid electrolyte, thus leading to liquid leakage and, therefore, depleting the gel performance.

#### 4.4.3 Dry polymer electrolytes

Solvent-free, all-solid-state, polymer electrolytes represent a breakthrough in the field of lithium battery electrolytes in terms of safety, engineering (possibility to be

manufactured into thicknesses and shapes not allowed to liquid electrolytes, mechanical and design flexibility, robustness), and new perspectives of applications for electrochemical devices [132,133,185–187]. PEO–LiX electrolytes are composed of crystalline (e.g., PEO and P(EO)<sub>6</sub>LiX) and amorphous phases [129,130,133,134] and, therefore, the ion motion occurs through two different mechanisms [188,189]: ion hopping (slow motion) from (defective) site to site, occurring in the crystalline regions, only granting low conductivity values (e.g.,  $\leq 10^{-6}$  S cm<sup>-1</sup>) [129–134]; and migration of ionic species, promoted by the micro-Brownian segmental motion of the PEO backbone, occurring in the amorphous regions and allowing much faster ion conduction ( $> 10^{-4}$  S cm<sup>-1</sup>) [129–134].

However, binary PEO electrolytes are in the full amorphous state only above the melting temperature of the polymer (65 °C) [129–134], and therefore, conductivities suitable for practical applications are achieved only above 70 °C. This issue has been pushing the research efforts toward preventing the crystallization of the polymer host to extend the domain of the amorphous phase at lower temperatures, as demonstrated by Berthier *et al.* [188]. Different approaches have been followed to reach this goal, which are summarized below.

#### 4.4.3.1 *Modifications of the polymeric host*

Marzantowicz *et al.* [190], Wieczorek [191], and Aihara *et al.* [192] proposed branched (PPO) and cross-linked polymers as replacements for linear polymers (PEO). Dendronized polymeric materials, for example, basically a subgroup of comb polymers where the graft linear chains are replaced by synthetic macromolecules with more complex architectures (dendrons) in order to obtain polymers with improved properties, as dry polymer electrolyte hosts were investigated by Chakrabarti *et al.* [193]. Rocco *et al.* [194] and Wieczorek [191] proposed polymer blend matrices. In particular, polymer materials as poly(methylmethacrylate), PMMA, or PVdF–HFP were added to the PEO host to form block or comb copolymers. However, only moderate (although significant) gains in conductivity were achieved with the exception of PEO/PMMA–LiX polymer blend electrolytes, which exhibited room temperature conductivity of  $10^{-4}$  S cm<sup>-1</sup> but were found chemically and physically unstable toward phase separation phenomena.

#### 4.4.3.2 *Use of suitable lithium salts*

Large anion lithium salts such as LiTFSI, LiBETI, and LiBOB were found to hinder the polymer chain crystallization [135,136,195], thus enhancing the amorphous phase content in the polymer electrolyte. For instance, Appeteccchi *et al.* [136,195] have detected conductivity approaching  $10^{-4}$  S cm<sup>-1</sup> already at 40 °C in PEO–LiBETI and PEO–LiBOB electrolytes. Kurian *et al.* [196] proposed “single-ion” conductor polymer hosts in which the anions are bound to the polymeric chains whereas lithium cations result the only mobile ionic species. However, no lithium salt (neither large anion containing nor single-ion) allowed matching conduction values suitable for practical applications at room temperature.

#### 4.4.3.3 Incorporation of additives

The addition of liquid plasticizers, mainly low molecular weight (400–500) polar molecules (poly(ethylene glycol dimethyl ether)) or oligomers, was proposed by Appetecchi *et al.* [197,198], resulting in ion conductivity increase of two orders of magnitude but, at the same time, depleting the intrinsic safety and mechanical characteristics of the polymer electrolyte. Large attention was devoted from the end of 90s to the addition of ceramic filler, first reported by Wieckzorek [191] who observed relevant improvement of the mechanical properties of PEO electrolytes. This is an important issue especially in case of detrimental effect on the mechanical performance due to the polymer host modification (e.g., incorporation of liquid additives) devoted to enhance the transport properties [199]. Croce *et al.* [200,201] and, successively, several research teams have proposed, in the past 15 years, the incorporation of micro- and nanosize fillers, such as  $\text{TiO}_2$  [201,202],  $\text{SiO}_2$  [203–208],  $\text{Al}_2\text{O}_3$  [209–211],  $\text{ZrO}_2$  [212–214],  $\text{CuO}$  [215], and  $\text{ZnAl}_2\text{O}_4$  [216], to improve the transport properties of PEO electrolytes. These ceramic additives were thought to reduce the crystalline phase content of the polymer host and interact with the polymeric chains and ionic species. However, other authors [217–220] have observed no practical increase either in conductivity or in interfacial properties upon filler addition when the PEO electrolytes were prepared through solvent-free routes.

The most recent and promising approach to overcome the room temperature limitation of PEO–LiX electrolytes is represented by the addition of ILs as first reported by Passerini *et al.* [95,97,221–225] and followed by several other authors [226–241]. The presence of these salts results in a double effect. First, ILs, characterized by very low lattice cation–anion energy [71,72,108,242], are fully dissociated into the polymer electrolyte without any practical interaction with the polymeric host. This reduces the PEO and PEO-salt crystalline phase content. In particular, the anions involved in the coordination of the densely charged  $\text{Li}^+$  cations prevent the formation of the crystalline  $\text{P}(\text{EO})_6\text{LiX}$  phase [95–97]. Second, the incorporation of ILs results in large anion excess with respect to  $\text{Li}^+$  cations, thus reducing the strength of the  $\text{Li}^+\cdots\text{PEO}$  interactions and, therefore, enhancing mobility of the  $\text{Li}^+$  ion through the polymer host at a temperature below the (polymer) melting point. The beneficial role of the IL incorporation into PEO–LiX complexes is shown in Table 4.11 and widely supported by the results obtained in numerous battery tests performed at room or near-room

**Table 4.11 Conductivity values as a function of the temperature for ionic liquid-free and ionic liquid-containing PEO electrolytes**

Temperature (°C)	Ionic conductivity (°C)						
	-10	0	10	20	30	40	60
Ionic liquid-free	$4.6 \times 10^{-10}$	$9.3 \times 10^{-9}$	$1.6 \times 10^{-7}$	$1.3 \times 10^{-6}$	$1.0 \times 10^{-5}$	$1.0 \times 10^{-4}$	$3.5 \times 10^{-4}$
Ionic liquid-containing	$4.1 \times 10^{-6}$	$1.3 \times 10^{-5}$	$4.5 \times 10^{-5}$	$1.1 \times 10^{-4}$	$2.6 \times 10^{-4}$	$4.5 \times 10^{-4}$	$1.0 \times 10^{-3}$

From Ref. [234].

temperature [221–225]. Conversely, at medium temperatures the IL effect is less pronounced because, when the polymer host is fully amorphous, the chain flexibility grants high conductivity to the system.

Thermally [225] and UV-cured [243] ternary polymer electrolytes were successfully proposed with the aim to increase the IL content without depleting the mechanical properties (obtaining rubber-like materials). Finally, among the polymeric hosts investigated for replacing PEO in IL-based polymer electrolytes are worthy to be mentioned PVdF (allowing room temperature conduction values approaching  $10^{-3}$  S cm $^{-1}$ ) [244] and polymeric ILs (good affinity with IL compounds) [245,246].

## 4.5 Solid inorganic electrolytes

As for dry polymer electrolytes, the development of solvent-free, solid inorganic electrolytes starts from the more and more stringent requirement to fabricate highly safe and, at the same time, high-performance lithium batteries. In addition, such electrolyte systems exhibit numerous technological issues generally not allowed to liquid cells. With respect to polymer electrolytes, the inorganic ones are more chemically and thermally robust but, also, more fragile and less flexible, leading to contact loss at the interface with electrodes. A few solid electrolytes exhibit room temperature conductivities (Table 4.12) of interest for lithium battery applications [255–259]. Fergus [184] and Henderson *et al.* [8] have recently reviewed this class of materials, which can be mainly classified into three classes (oxides, phosphates, and sulfides).

### 4.5.1 Oxides

The top players of this electrolyte family are represented by the perovskites,  $\text{La}_x\text{Li}_y\text{TiO}_3$  [247] or  $\text{La}_3\text{Li}_5\text{Ta}_2\text{O}_{12}$  (the latter also doped with Ca or Sr or Ba), which were found to match or overcome, for suitable La/Li ratios, conductivity values of  $10^{-3}$  S cm $^{-1}$  at room temperature [260,261]. The conduction mechanism is due to site vacancies resulting when the La/Li ratio is above 1. Aluminum doping [248] as well as  $\text{SiO}_2$  incorporation [262] was found to enhance the ionic conductivity, likely due to improvement of the transport properties at grain boundary interface. Conversely, the addition of sodium as well as the introduction of fluorine in the place of oxygen did not lead to any enhancement in conductivity.

Other solid oxide ion conductors have been investigated such as  $\text{Li}_3\text{BO}_{2.5}\text{N}_{0.5}$ ,  $\text{Li}_9\text{SiAlO}_8$ , silicates, and titanates [248], but their room temperature conductivity was found to be comparable or lower with respect to the perovskites.

### 4.5.2 Phosphates

The solid Li $^{+}$ -conducting phosphate electrolytes are generally characterized by the chemical formula  $\text{Li}_{1+x}\text{M}^1_y\text{M}^2_z(\text{PO}_4)_3$  where M<sup>1</sup> and M<sup>2</sup> are aluminum, germanium, titanium, and zirconium. The most interesting material class is represented by

**Table 4.12 Ionic conductivity values (25 °C) of the most common solid inorganic electrolytes for lithium batteries**

Solid inorganic electrolytes	Ionic conductivity (25 °C)(S cm <sup>-1</sup> )
<i>Oxides</i>	
$\text{Li}_{0.34}\text{La}_{0.51}\text{TiO}_{2.94}$ <sup>a</sup>	$1.0 \times 10^{-3}$
$\text{Li}_{0.34}\text{La}_{0.56}\text{TiO}_3$ (cubic, <i>ap</i> ) <sup>a</sup>	$1.53 \times 10^{-3}$
$(\text{Li}_{0.1}\text{La}_{0.5})_{0.9}\text{Sr}_{0.1}\text{TiO}_3$ <sup>a</sup>	$1.5 \times 10^{-3}$
$\text{La}_{0.55}\text{Li}_{0.36}\text{Ti}_{0.995}\text{Al}_{0.005}\text{O}_3$ <sup>a</sup>	$1.1 \times 10^{-3}$
$\text{La}_{0.51}\text{Li}_{0.36}\text{Ti}_{0.95}\text{W}_{0.05}\text{O}_3$ <sup>a</sup>	$7.3 \times 10^{-4}$
$\text{La}_{0.55}\text{Li}_{0.36}\text{Ti}_{0.95}\text{Ge}_{0.05}\text{O}_3$ <sup>a</sup>	$3.6 \times 10^{-4}$
$\text{La}_{0.55}\text{Li}_{0.36}\text{Ti}_{0.95}\text{Ru}_{0.05}\text{O}_3$ <sup>a</sup>	$5.2 \times 10^{-5}$
$\text{Li}_{3.09}\text{BO}_{2.53}\text{N}_{0.52}$ <sup>b</sup>	$2.3 \times 10^{-6}$
$\text{Li}_{2.9}\text{PO}_{3.3}\text{N}_{0.46}$ <sup>b</sup>	$2.0 \times 10^{-6}$
<i>Phosphates</i>	
$\text{Li}_{1.3}\text{Al}_{0.3}\text{Ti}_{1.7}(\text{PO}_4)_3$ <sup>c</sup>	$7 \times 10^{-4}$
$\text{Li}_{1.4}\text{Ge}_{1.6}(\text{PO}_4)_3$ <sup>c</sup>	$4 \times 10^{-4}$
$\text{Li}_{1.4}\text{Al}_{0.4}(\text{Ge}_{0.67}\text{Ti}_{0.33})_{1.6}(\text{PO}_4)_3$ <sup>c</sup>	$6.2 \times 10^{-4}$
$\text{Li}_{1.5}\text{Al}_{0.5}\text{Ge}_{1.5}(\text{PO}_4)_3$ <sup>c</sup>	$5.1 \times 10^{-3}$
$\text{Li}_3\text{N}\text{Li}_3\text{PO}_4$ <sup>d</sup>	$1.8 \times 10^{-6}$
<i>Sulfides</i>	
$54\text{Li}_2\text{S}\cdot46\text{PS}_{2.5}$ <sup>e</sup>	$3.2 \times 10^{-3}$
$80\text{Li}_2\text{S}\cdot20\text{P}_2\text{S}_5$ <sup>f</sup>	$5 \times 10^{-4}$
$\text{Li}_{3.25}\text{Ge}_{0.25}\text{P}_{0.75}\text{S}_4$ <sup>g</sup>	$2.2 \times 10^{-3}$
$\text{Li}_4\text{SiS}_4\text{--Li}_3\text{PS}_4$ <sup>g</sup>	$6.4 \times 10^{-4}$
$\text{Li}_5\text{GaS}_4\text{--Li}_4\text{GeS}_4$ <sup>h</sup>	$6.5 \times 10^{-5}$
$\text{Li}_2\text{ZnGeS}_4\text{--Li}_4\text{GeS}_4$ <sup>h</sup>	$3 \times 10^{-7}$
$\text{Li}_4\text{SiS}_4\text{--Li}_5\text{AlS}_4$ <sup>g</sup>	$2.3 \times 10^{-7}$

<sup>a</sup>From Ref. [247].

<sup>b</sup>From Ref. [248].

<sup>c</sup>From Ref. [249].

<sup>d</sup>From Ref. [250].

<sup>e</sup>From Ref. [251].

<sup>f</sup>From Ref. [252].

<sup>g</sup>From Ref. [253].

<sup>h</sup>From Ref. [254].

$\text{Li}_{1+x}\text{Al}_x\text{Ge}_{2-x}(\text{PO}_4)_3$  [184], showing the highest conductivity values (Table 4.12),  $\text{LiTi}_{0.5}\text{Zr}_{1.5}(\text{PO}_4)_3$  and  $\text{Li}_{1+x}\text{Ti}_{2-x}\text{Al}_x(\text{PO}_4)_3$  [263,264]. The last material (previously investigated in lithium-ion batteries) exhibits very good  $\text{Li}^+$  conduction; however, it was found to be unstable at the interface with both low-voltage anodes and high-voltage cathodes [263]. The partial replacement of phosphorous with silicon to obtain  $\text{Li}_{1+x+y}\text{Ti}_{2-x}\text{Al}_x\text{Si}_y(\text{PO}_4)_{3-y}$  is able to reduce this issue. Nevertheless, Iriyama *et al.* [265] and Yada *et al.* [264] have reported that the electrochemical processes occurring at the electrolyte/electrode interface can be exploited to obtain *in situ* growth of

such an active material. Another phosphate-based solid electrolyte of interest is  $\text{Li}_3\text{N}\text{Li}_3\text{PO}_4$  [250] (LIPON).

### 4.5.3 Sulfides

Among the sulfide solid electrolytes, the compounds having chemical formula  $\text{Li}_2\text{S}-\text{P}_2\text{S}_5$ , ( $\text{Li}_2\text{S}$  content ranging from 70% to 80%) show the highest  $\text{Li}^+$  ion conduction and may display crystalline or amorphous or mixed crystalline–amorphous structure. Unexpectedly, a few among the materials exhibiting crystalline phase were found to be more conductive with respect to the amorphous ones. Sulfide electrolytes have been used in lithium batteries based on different chemistry cells, including more commonly used [252,266–270] and more innovative [271–275] active materials.

From the same sulfide family derives  $\text{Li}_2\text{S}-\text{GeS}_2-\text{P}_2\text{S}_5$ , a crystalline electrolyte material showing high lithium conduction and good performance with  $\text{LiCoO}_2$  [270] and sulfide [276] cathodes, but incompatibility toward graphite anodes [270].

Finally, an interesting electrolytic material is represented by  $\text{Li}_{3.25}\text{Ge}_{0.25}\text{P}_{0.75}\text{S}_4$  (LISICON), which was used as separator in  $\text{Li}-\text{Al}/\text{Mo}_6\text{S}_8$  lithium-ion cells, exhibiting good cycling performance. These cells are considered susceptible to scaling-up.

## 4.6 Future trends

First of all, a deeper understanding of various electrolytes restricted inside the electrode pores is needed to optimize the design of proper electrolytes. In a recent manuscript, Kiyohara *et al.* [277] reported Monte Carlo simulations for electrolytes in porous electrodes, showing that their electrical properties dramatically change depending on the pore size and the dielectric constant of the medium. Ongoing from low to high dielectric constant of the medium, the behavior of the porous electrode capacitance is seen to fully reverse. In fact, while an increase of the capacitance is proposed upon pore size decrease for low dielectric constant electrolytes, for a high dielectric constant of the medium, on the contrary, the capacitance is proposed to decrease as the pore size decreases. Such pore size dependency is explained in terms of the balance among the electrostatic interactions and the volume exclusion ones in the porous electrode. However, this behavior might substantially differ for nonliquid electrolytes (gel, polymer, and solid state) as well as for those composed solely of ions (IL-based electrolytes).

Considering material development, a few main trends in lithium-ion-conducting electrolytes shall be mentioned. The first is focused on increasing the anodic stability to allow the use of higher-voltage cathodes, such as  $\text{LiNi}_x\text{Mn}_{2-x}\text{O}_2$  spinel or  $\text{LiMPO}_4$  ( $\text{M}=\text{Ni, Co, Mn}$ ), capable of granting higher cell-specific energies and powers.

The research on electrolytes capable of granting cheaper but safer, more benign, and environmentally friendly cells will also expand in view of a massive deployment of lithium batteries in EV and delocalized small stationary storage systems. Finding a replacement for the expensive, toxic, and unstable  $\text{LiPF}_6$  is certainly a target to shoot for. The main target is certainly the elimination of fluorinated anions. However,

replacing  $\text{LiPF}_6$  with the more stable and less hygroscopic  $\text{LiTFSI}$  would already grant improved benignity, lower cost, and recyclability.

The ongoing expansion of Li-ion batteries into automotive applications has resulted in intense scientific interest. The multitude of reactions occurring at the electrode/electrolyte interface together with difficulties in characterization has made calculations and simulations an important part of the research in Li-ion batteries. The knowledge concerning the basic chemistry of the Li-ion battery, especially as applied to electrolytes, including the SEI that is a key component of many Li-ion batteries, may strongly benefit from the application of atomic-level methods. An extensive approach was presented by Ferguson and Curtiss in a recent manuscript [278], where a review of atomic-level computations and simulations of Li-ion battery electrolytes (with a focus on the chemistry of the organic solvents of the electrolyte) is combined with the application of quantum chemical methods to study the reactions of organic solvent on model systems (to form an oligomeric SEI layer), and the use of data from *ab initio* calculations to screen electrolytes for improved reactivity.

Finally, the development of electrolytes allowing the use of lithium metal electrodes necessary for the development of high-energy, “next-generation” lithium batteries such as Li–S and Li–air will be addressed by more and more academic and industrial researchers. For these applications, especially Li–air, IL-based electrolytes are certainly among the best candidates.

## 4.7 Sources of further information and advice

The available literature in the field of lithium-ion-conducting electrolytes is steadily increasing due to the tremendously increasing interest of researchers around the world in electrochemical energy storage. In addition, manuscripts reporting new salts, solvents, additives, and their combinations are appearing in large numbers, which provide further insight into already reported materials.

A good overview on the development of lithium-ion electrolytes can be achieved from reading the following review articles focused on different issues:

- Ref. [33] by Xu *et al.* (organic electrolytes and lithium salts).
- Ref. [279] by Geiculescu *et al.* (fluorinated electrolytes).
- Ref. [280] by Hallinan and Balsara; Ref. [281] by Trombly *et al.*; Ref. [282] by Ratner and Shriver; Ref. [283] by MacCallum and Vincent; and Ref. [284] by Armand (polymer electrolytes).
- Ref. [285] by Passerini *et al.*; Ref. [9] by Appetecchi *et al.*; Ref. [8] by Lex-Balducci *et al.*; Ref. [286] by Park *et al.*; Ref. [287] by Armand *et al.*; and Ref. [288] by Galinski *et al.* (IL-based electrolytes).

## References

- [1] J.M. Tarascon, M. Armand, Issues and challenges facing lithium batteries, *Nature* 414 (2001) 359.
- [2] G. Pistoia, (Ed.), *Lithium Batteries: New Materials, Developments and Perspectives*, Industrial Chemistry Library, vol. 5, Elsevier, Amsterdam, 1994.

- [3] B. Scrosati, Challenge of portable power, *Nature* 373 (1995) 557.
- [4] W.A. van Schalkwijk, B. Scrosati, *Advances in Lithium-Ion Batteries*, Kluwer Academic Plenum Publisher, New York, 2002.
- [5] G.-A. Nazri, G. Pistoia, *Lithium Batteries*, Kluwer Academic/Plenum Publishers, Boston, 2004.
- [6] J.T. Dudlet, D.P. Wilkinson, G. Thomas, R. LeVae, S. Woo, H. Blom, C. Horvath, M.W. Juzkow, B. Denis, P. Juric, P. Aghakhian, J.R. Dahn, Conductivity of electrolytes for rechargeable lithium batteries, in: *Second International Meeting of Lithium Batteries (IMLB)*, 1990.
- [7] L. El Ouatani, R. Dedryvère, C. Siret, P. Biensan, D. Gonbeau, Effect of vynilene carbonate additive in li-ion batteries: comparison of  $\text{LiCoO}_2/\text{C}$ ,  $\text{LiFePO}_4/\text{C}$ , and  $\text{LiCoO}_2/\text{Li}_4\text{Ti}_5\text{O}_{12}$  systems, *J. Electrochem. Soc.* 156 (6) (2009) A468.
- [8] A. Lex-Balducci, W.A. Henderson, S. Passerini, *Lithium-ion batteries advanced materials and technologies*, in: J. Yuan, X. Liu, H. Zhang (Eds.), *Electrolytes for Lithium Batteries*, CRC Press, 2011, print ISBN 978-1-4398-4128-0, eBook ISBN 978-1-4398-4129-7 (Chapter 4).
- [9] G.B. Appetecchi, M. Montanino, S. Passerini, Ionic liquid-based electrolytes for high-energy lithium batteries, in: A.E. Visscher, N.J. Bridges, R.D. Rogers (Eds.), *Ionic Liquids: Science and Applications*, ACS Symposium Series 1117, Oxford University Press, Inc., American Chemical Society, Washington, DC, USA, 2013.
- [10] T.M. Bandhauer, S. Garimella, T.F. Fuller, A critical review on thermal issues in lithium-ion batteries, *J. Electrochem. Soc.* 158 (2011) R1.
- [11] R. Spotnitz, J. Franklin, Abuse behavior of high-power, lithium-ion cells, *J. Power Sources* 113 (2003) 81.
- [12] H. Yang, S. Amiruddin, H.J. Bang, Y.K. Sun, J. Prakash, A review of Li-ion cell chemistries and their potential use in hybrid electric vehicles, *J. Ind. Eng. Chem.* 12 (2006) 12.
- [13] D.P. Abraham, E.P. Roth, R. Kostecky, K. McCarthy, S. MacLaren, D.H. Doughty, Diagnostic examination of thermally abused high-power lithium-ion cells, *J. Power Sources* 161 (2006) 648.
- [14] <http://www.sigmaldrich.com/technical-service-home/product-catalog.html>.
- [15] [http://www.rafoeg.de/20,Dokumentenarchiv/20,Daten/dielectric\\_chart.pdf](http://www.rafoeg.de/20,Dokumentenarchiv/20,Daten/dielectric_chart.pdf).
- [16] Y. Abu-Lebdeh, I. Davidson, New electrolytes based on glutaronitrile for high energy/power Li-ion batteries, *J. Power Sources* 189 (2009) 576.
- [17] Y. Abu-Lebdeh, I. Davidson, High-voltage electrolytes based on adiponitrile for Li-ion batteries, *J. Electrochem. Soc.* 156 (2009) A60.
- [18] N. Nanbu, K. Takimoto, M. Takehara, M. Ue, Y. Sasaki, Electrochemical properties of fluoropropylene carbonate and its application to lithium-ion batteries, *Electrochem. Commun.* 10 (2008) 783.
- [19] J.K. Feng, X.J. Sun, X.P. Ai, Y.L. Cao, H.X. Yang, Dimethyl methyl phosphate: a new nonflammable electrolyte solvent for lithium-ion batteries, *J. Power Sources* 184 (2008) 570.
- [20] J.K. Feng, X.P. Ai, Y.L. Cao, H.X. Yang, Possible use of non-flammable phosphonate ethers as pure electrolyte solvent for lithium batteries, *J. Power Sources* 177 (2008) 194.
- [21] J.-y. Huang, X.-j. Liub, X.-li. Kangc, Z.-x. Yua, T.-t. Xua, W.-h. Qiu, Study on  $\gamma$ -butyrolactone for LiBOB-based electrolytes, *J. Power Sources* 189 (2009) 458.
- [22] A. Abouimrane, I. Belharouak, K. Amine, Sulfone-based electrolytes for high-voltage Li-ion batteries, *Electrochem. Commun.* 11 (2009) 1073.
- [23] K. Naoi, E. Iwama, N. Ogihara, Y. Nakamura, H. Segawa, Y. Inob, Nonflammable hydrofluoroether for lithium-ion batteries: enhanced rate capability, cyclability, and low-temperature performance, *J. Electrochem. Soc.* 156 (2009) A272.

- [24] M. Ihara, B.T. Hang, K. Sato, M. Egashira, S. Okada, J. Yamaki, Properties of carbon anodes and thermal stability in LiPF<sub>6</sub>/methyl difluoroacetate electrolyte, *J. Electrochem. Soc.* 150 (2003) A1476.
- [25] T. Achiha, T. Nakajima, Y. Ohzawa, M. Koh, A. Yamauchi, M. Kagawa, H. Aoyama, Thermal stability and electrochemical properties of fluorine compounds as nonflammable solvents for lithium-ion batteries, *J. Electrochem. Soc.* 157 (2010) A707.
- [26] T. Achiha, T. Nakajima, Y. Ohzawa, M. Koh, A. Yamauchi, M. Kagawa, H. Aoyama, Fluorinated electrolytes based on lithium salts of strong Bronsted acids, *J. Electrochem. Soc.* 156 (2009) A483.
- [27] K. Xu, C.A. Angell, High anodic stability of a new electrolyte solvent: unsymmetric noncyclic aliphatic sulfone, *J. Electrochem. Soc.* 145 (1998) L70.
- [28] K. Xu, C.A. Angell, Sulfone-based electrolytes for lithium-ion batteries, *J. Electrochem. Soc.* 149 (2002) A920.
- [29] X.G. Sun, C.A. Angell, New sulfone electrolytes: part II. Cyclo alkyl group containing sulfones, *Solid State Ionics* 175 (2004) 257.
- [30] X.G. Sun, C.A. Angell, New sulfone electrolytes for rechargeable lithium batteries: part I. Oligoether-containing sulfones, *Electrochem. Commun.* 7 (2005) 261.
- [31] M. Nagahama, N. Hasegawa, S. Okada, High voltage performances of Li<sub>2</sub>NiPO<sub>4</sub>F cathode with dinitrile-based electrolytes, *J. Electrochem. Soc.* 157 (2010) A748.
- [32] A. Xiao, L. Yang, B. Lucht, Thermal reactions of LiPF<sub>6</sub> with added LiBOB: electrolyte stabilization and generation of LiF<sub>4</sub>OP, *Electrochem. Solid-State Lett.* 10 (2007) A241.
- [33] W. Xu, A.J. Shusterman, R. Marzke, C.A. Angell, LiMOB, an unsymmetrical nonaromatic orthoborate salt for nonaqueous solution electrochemical applications, *J. Electrochem. Soc.* 151 (2004) A632.
- [34] M. Schmidt, U. Heider, A. Kuehner, R. Oesten, M. Jungnitz, N. Ignat'ev, P. Sartori, Lithium fluoroalkylphosphates: a new class of conducting salts for electrolytes for high energy lithium-ion batteries, *J. Power Sources* 97–98 (2001) 557.
- [35] J.S. Gnanaraj, M.D. Levi, Y. Gofer, D. Aurbach, M. Schmidt, LiPF<sub>3</sub>(CF<sub>2</sub>CF<sub>3</sub>)<sub>3</sub>: a salt for rechargeable lithium ion batteries, *J. Electrochem. Soc.* 150 (2003) A445.
- [36] J.S. Gnanaraj, E. Zinigrad, L. Asraf, M. Sprecher, H.E. Gottlieb, W. Geissler, M. Schmidt, D. Aurbach, On the use of LiPF<sub>3</sub>(CF<sub>2</sub>CF<sub>3</sub>)<sub>3</sub> (LiFAP) solutions for Li-ion batteries. Electrochemical and thermal studies, *Electrochem. Commun.* 5 (2003) 946.
- [37] J. Barthel, R. Buestrich, E. Carl, H.J. Gores, A new class of electrochemically and thermally stable lithium salts for lithium battery electrolytes: III. Synthesis and properties of some lithium organoborates, *J. Electrochem. Soc.* 143 (1996) 3572.
- [38] J. Barthel, A. Schmid, H.J. Gores, A new class of electrochemically and thermally stable lithium salts for lithium battery electrolytes. V. Synthesis and properties of lithium bis [2,3-pyridinediolato(2-)O,O']borate, *J. Electrochem. Soc.* 147 (2000) 21.
- [39] W. Xu, C.A. Angell, Weakly coordinating anions and the exceptional conductivity of their nonaqueous solutions, *Electrochem. Solid-State Lett.* 4 (2001) E1.
- [40] M. Handa, M. Suzuki, J. Suzuki, H. Kanematsu, Y. Sasaki, A new lithium salt with a chelate complex of phosphorus for lithium battery electrolytes, *Electrochem. Solid-State Lett.* 2 (1999) 60.
- [41] M. Eberwein, A. Schmid, M. Schmidt, M. Zabel, T. Burgemeister, J. Barthel, W. Kunz, H.J. Gores, Synthesis and electrochemical properties of some lithium chelatophosphates, *J. Electrochem. Soc.* 150 (2003) A994.
- [42] T.J. Barbarich, P.F. Driscoll, A lithium salt of a Lewis acid-base complex of imidazolide for lithium-ion batteries, *Electrochem. Solid-State Lett.* 6 (2003) A113.

- [43] T.J. Barbarich, P.F. Driscoll, S. Izquierdo, L.N. Zakharov, C.D. Incarvito, A.-L. Rheingold, New family of lithium salts for highly conductive nonaqueous electrolytes, *Inorg. Chem.* 43 (2004) 7764.
- [44] K. Xu, S. Zhang, T.R. Jow, W. Xu, C.A. Angell, LiBOB as salt for lithium-ion batteries: a possible solution for high temperature operation, *Electrochem. Solid-State Lett.* 5 (2002) A26.
- [45] S.S. Zhang, K. Xu, T.R. Jow, An improved electrolyte for the LiFePO<sub>4</sub> cathode working in a wide temperature range, *J. Power Sources* 159 (2006) 702.
- [46] K. Amine, J. Liu, S. Kang, I. Belharouak, Y. Hyung, D. Vissers, G. Henriksen, Improved lithium manganese oxide spinel-graphite Li-ion cells for high-power applications, *J. Power Sources* 129 (2004) 14.
- [47] K. Xu, Tailoring electrolyte composition for LiBOB, *J. Electrochem. Soc.* 155 (2008) A733.
- [48] K. Xu, B. Devaney, K. Nechev, Y. Lam, T.R. Jow, Evaluating LiBOB/lactone electrolytes in large-format lithium-ion cells based on nickelate and iron phosphate, *J. Electrochem. Soc.* 155 (2008) A959.
- [49] Z.M. Xue, K.N. Wu, B. Liu, C.H. Chen, New lithium salts with croconato-complexes of boron for lithium battery electrolytes, *J. Power Sources* 171 (2007) 944.
- [50] Z.M. Xue, C.Q. Ji, W. Zhou, C.H. Chen, A new lithium salt with 3-fluoro-1,2-benzene-diolato and oxalato complexes of boron for lithium battery electrolytes, *J. Power Sources* 195 (2010) 3689.
- [51] Z.M. Xue, J.F. Zhao, J. Ding, C.H. Chen, LBDOB, a new lithium salt with benzenediolato and oxalato complexes of boron for lithium battery electrolytes, *J. Power Sources* 195 (2010) 853.
- [52] S.S. Zhang, An unique lithium salt for the improved electrolyte of Li-ion battery, *Electrochim. Commun.* 8 (2006) 1423.
- [53] S.S. Zhang, Electrochemical study of the formation of a solid electrolyte interface on graphite in a LiBC<sub>2</sub>O<sub>4</sub>F<sub>2</sub>-based electrolyte, *J. Power Sources* 163 (2007) 713.
- [54] J. Arai, A. Matsuo, T. Fujisaki, K. Ozawa, A novel high temperature stable lithium salt (Li<sub>2</sub>B<sub>12</sub>F<sub>12</sub>) for lithium ion batteries, *J. Power Sources* 193 (2009) 851.
- [55] Z.B. Zhou, M. Takeda, M. Ue, Novel electrolyte salts based on perfluoroalkyltrifluoroborate anions: 1. Synthesis and characterization, *J. Fluor. Chem.* 123 (2003) 127.
- [56] M. Ue, T. Fujii, Z.B. Zhou, M. Takeda, S. Kinoshita, Electrochemical properties of Li[C<sub>n</sub>F<sub>2n+1</sub>BF<sub>3</sub>] as electrolyte salts for lithium-ion cells, *Solid State Ionics* 177 (2006) 323.
- [57] H.F. Xiang, Q.Y. Jin, C.H. Chen, X.W. Ge, S. Guo, J.H. Sun, Dimethyl methylphosphonate-based nonflammable electrolyte and high safety lithium-ion batteries, *J. Power Sources* 174 (2007) 335.
- [58] L. Wu, Z.P. Song, L.S. Liu, X.F. Guo, L.B. Kong, H. Zhan, Y.H. Zhou, Z.Y. Li, A new phosphate-based nonflammable electrolyte solvent for Li-ion batteries, *J. Power Sources* 188 (2009) 570.
- [59] K. Xu, S.S. Zhang, J.L. Allen, T.R. Jow, Nonflammable electrolytes for Li-ion batteries based on a fluorinated phosphate, *J. Electrochem. Soc.* 149 (8) (2002) A1079.
- [60] E.G. Shim, T.H. Nam, J.G. Kim, H.S. Kim, S.I. Moon, Effect of the concentration of diphenyloctyl phosphate as a flame-retarding additive on the electrochemical performance of lithium-ion batteries, *Electrochim. Acta* 54 (2009) 2276.
- [61] J.K. Feng, X.J. Sun, X.P. Ai, Y.L. Cao, H.X. Yang, Dimethyl methyl phosphate: a new nonflammable electrolyte solvent for lithium-ion batteries, *J. Power Sources* 184 (2008) 570.

- [62] S. Dalavi, M.Q. Xu, B. Ravdel, L. Zhou, B.L. Lucht, Nonflammable electrolytes for lithium-ion batteries containing dimethyl methylphosphonate, *J. Electrochem. Soc.* 157 (2010) A1113.
- [63] S.S. Zhang, K. Xu, T.R. Jow, Tris(2,2,2-trifluoroethyl) phosphite as a co-solvent for non-flammable electrolytes in Li-ion batteries, *J. Power Sources* 113 (2003) 166.
- [64] T. Tsujikawa, K. Yabuta, T. Matsushita, T. Matsushima, K. Hayashi, M. Arakawa, Characteristics of lithium-ion battery with non-flammable electrolyte, *J. Power Sources* 189 (2009) 429.
- [65] J. Arai, A novel non-flammable electrolyte containing methyl nonafluorobutyl ether for lithium secondary batteries, *J. Appl. Electrochem.* 32 (2002) 1071.
- [66] K. Naoi, E. Iwama, Y. Honda, F. Shimodate, Discharge behavior and rate performances of lithium-ion batteries in nonflammable hydrofluoroethers (II), *J. Electrochem. Soc.* 157 (2010) A190.
- [67] J. Arai, Nonflammable methyl nonafluorobutyl ether for electrolytes used in lithium secondary batteries, *J. Electrochem. Soc.* 150 (2003) A219.
- [68] T. Tanaka, T. Doi, S. Okada, J.I. Yamaki, Effects of salts in methyl difluoroacetate-based electrolytes on their thermal stability in lithium-ion batteries, *Fuel Cells* 9 (2009) 269.
- [69] Z.-B. Zhou, H. Matsumoto, K. Tatsumi, Low-melting, low-viscous, hydrophobic ionic liquids: aliphatic quaternary ammonium salts with perfluoroalkyltrifluoroborates, *Chem. Eur. J.* 11 (2005) 752.
- [70] W. Xu, E. Cooper, A.A. Angell, Ionic liquids: ion mobilities, glass temperatures, and fragilities, *J. Phys. Chem. B* 107 (2003) 6170.
- [71] J.R.D. Rogers, K.R. Seddon, *Ionic Liquids: Industrial Application to Green Chemistry*, ACS Symposium Series, 818 American Chemical Society, Washington, 2002.
- [72] H. Ohno (Ed.), *Electrochemical Aspects of Ionic Liquids*, John Wiley & Sons Inc., Hoboken, NJ, 2005.
- [73] A.I. Bhatt, I. Maycbe, V.A. Volkovich, M.E. Hetherington, B. Lewin, R.C. Thied, N. J. Ertok, Group 15 quaternary alkyl bistriflimides: ionic liquids with potential application in electropositive metal deposition and as supporting electrolytes, *J. Chem. Soc. Dalton Trans.* (2002) 4532.
- [74] S. Panozzo, M. Armand, O. Stephan, Light-emitting electrochemical cells using a molten delocalized salt, *Appl. Phys. Lett.* 80 (2002) 679.
- [75] P. Wang, S.M. Zakeeruddin, I. Exnar, M. Gratzel, High efficiency dye-sensitized nanocrystalline solar cells based on ionic liquid polymer gel electrolyte, *Chem. Commun. (Camb.)* (2002) 2972.
- [76] J. Fuller, A.C. Breda, R.T. Carlin, Ionic liquid–polymer gel electrolytes from hydrophilic and hydrophobic ionic liquids, *J. Electroanal. Chem.* 459 (1998) 29.
- [77] H. Nakagawa, S. Izuchi, K. Kunawa, T. Nukuda, Y. Aihara, Liquid and polymer gel electrolytes for lithium batteries composed of room-temperature molten salt doped by lithium salt, *J. Electrochem. Soc.* 150 (2003) A695.
- [78] A. Noda, M.A.B.H. Susan, K. Kudo, S. Mitsushima, K. Hayamizu, M. Watanabe, Brønsted acid–base ionic liquids as proton-conducting nonaqueous electrolytes, *J. Phys. Chem. B* 107 (2003) 4024.
- [79] A. Balducci, W.A. Henderson, M. Mastragostino, S. Passerini, P. Simon, F. Soavi, Cycling stability of a hybrid activated carbon//poly(3-methylthiophene) supercapacitor with *N*-butyl-*N*-methylpyrrolidinium bis(trifluoromethanesulfonyl)imide ionic liquid as electrolyte, *Electrochim. Acta* 50 (2005) 2233.
- [80] G.B. Appeticchi, M. Montanino, M. Carewska, M. Moreno, F. Alessandrini, S. Passerini, Chemical–physical properties of bis (perfluoroalkylsulfonyl) imide-based ionic liquids, *Electrochim. Acta* 58 (2011) 1300.

[81] G.B. Appetecchi, M. Montanino, M. Carewska, F. Alessandrini, S. Passerini, LiFSI-PYR<sub>1</sub>-AFSI binary electrolyte mixtures for lithium batteries, *ECS Trans.* 25 (36) (2010) 49.

[82] G.B. Appetecchi, M. Montanino, D. Zane, M. Carewska, F. Alessandrini, S. Passerini, Effect of the alkyl group on the synthesis and the electrochemical properties of *N*-alkyl-*N*-methyl-pyrrolidinium bis(trifluoromethanesulfonyl)imide ionic liquids, *Electrochim. Acta* 54 (2009) 1325.

[83] M. Montanino, M. Carewska, F. Alessandrini, S. Passerini, G.B. Appetecchi, The role of the cation aliphatic side chain length in piperidinium bis(trifluoromethanesulfonyl)imide ionic liquids, *Electrochim. Acta* 57 (2011) 153.

[84] S. Zhang, N. Sun, X. He, X. Lu, X. Zhang, Physical properties of ionic liquids: database and evaluation, *J. Phys. Chem. C* 35 (2006) 4.

[85] J.C. Dearden, The QSAR prediction of melting point, a property of environmental relevance, *Sci. Total Environ.* 109 (1991) 59.

[86] Z.-B. Zhou, H. Matsumoto, K. Tatsumi, Cyclic quaternary ammonium ionic liquids with perfluoroalkyltrifluoroborates: synthesis, characterization, and properties, *Chem. Eur. J.* 12 (2006) 2196.

[87] V.R. Koch, C. Nanjundiah, G.B. Appetecchi, B. Scrosati, The interfacial stability of Li with two new solvent-free ionic liquids: 1,2-dimethyl-3-propylimidazolium imide and methide, *J. Electrochem. Soc.* 142 (1995) L116.

[88] R.T. Carlin, J. Fuller, U.S. Patent 5,552,238 issued on Sept. 3, 1996.

[89] R.T. Carlin, J. Fuller, R.T. Carlin, S. Deki, M. Matsunaga, D.S. Newman, J.R. Selman, G.R. Stafford (Eds.), *Molten Salts, 96–97*, The Electrochemical Society, Pennington, NJ, 1996, p. 62.

[90] P. Bonhote, A.P. Dias, N. Papageorgiou, K. Kalyanasundaram, M. Grätzel, Hydrophobic, highly conductive ambient-temperature molten salts, *Inorg. Chem.* 35 (1996) 1168.

[91] J. Sun, M. Forsyth, D.R. MacFarlane, Room-temperature molten salts based on the quaternary ammonium ion, *J. Phys. Chem. B* 102 (4) (1998) 8858.

[92] D.R. MacFarlane, J. Huang, M. Forsyth, Lithium-doped plastic crystal electrolytes exhibiting fast ion conduction for secondary batteries, *Nature* 402 (1999) 792.

[93] D.R. MacFarlane, P. Meakin, J. Sun, N. Amini, M. Forsyth, Pyrrolidinium imides: a new family of molten salts and conductive plastic crystal phases, *J. Phys. Chem. B* 103 (1999) 4164.

[94] P.C. Howlett, D.R. MacFarlane, A.F. Hollenkamp, High lithium metal cycling efficiency in a room-temperature ionic liquid, *Electrochim. Solid-State Lett.* 7 (2004) A97.

[95] J.-H. Shin, W.A. Henderson, S. Passerini, Ionic liquids to the rescue? Overcoming the ionic conductivity limitations of polymer electrolytes, *Electrochim. Commun.* 5 (2003) 1016.

[96] J.-H. Shin, W.A. Henderson, S. Passerini, An elegant fix for polymer electrolytes, *Electrochim. Solid-State Lett.* 8 (2005) A125.

[97] J.-H. Shin, W.A. Henderson, S. Passerini, PEO-based polymer electrolytes with ionic liquids and their use in lithium metal–polymer electrolyte batteries, *J. Electrochem. Soc.* 152 (2005) A978.

[98] W.A. Henderson, S. Passerini, Phase behavior of ionic liquid–LiX mixtures: pyrrolidinium cations and TFSI<sup>–</sup> anions, *Chem. Mater.* 16 (15) (2004) 2881.

[99] H. Matsumoto, H. Sakaebe, K. Tatsumi, Preparation of room temperature ionic liquids based on aliphatic onium cations and asymmetric amide anions and their electrochemical properties as a lithium battery electrolyte, *J. Power Sources* 45 (2005) 146.

[100] Q. Zhou, W.A. Henderson, G.B. Appetecchi, M. Montanino, S. Passerini, Physical and electrochemical properties of *N*-Alkyl-*N*-methylpyrrolidinium bis(fluorosulfonyl)imide ionic liquids: PY<sub>13</sub>FSI and PY<sub>14</sub>FSI, *J. Phys. Chem. B* 112 (2008) 13580.

- [101] E. Paillard, Q. Zhou, W.A. Henderson, G.B. Appeteccchi, M. Montanino, S. Passerini, Electrochemical and physicochemical properties of PY<sub>14</sub>FSI-based electrolytes with LiFSI, *J. Electrochem. Soc.* 156 (2009) A891.
- [102] L. Conte, G. Gambaretto, G. Caporiccio, F. Alessandrini, S. Passerini, Perfluoroalkane-sulfonylimides and their lithium salts: synthesis and characterisation of intermediates and target compounds, *J. Fluorine Chem.* 125 (2004) 243.
- [103] F. Toulgoat, B.R. Langlois, M. Medebielle, J.-Y. Sanchez, An efficient preparation of new sulfonyl fluorides and lithium sulfonates, *J. Org. Chem.* 72 (2007) 9046.
- [104] E.I. Cooper, C.A. Angell, Versatile organic iodide melts and glasses with high mole fractions of LiI: glass transition temperatures and electrical conductivities, *Solid State Ionics* 9–10 (1983) 617.
- [105] E.I. Cooper, C.A. Angell, Ambient temperature plastic crystal fast ion conductors (PLIC-FICS), *Solid State Ionics* 18–19 (1986) 570.
- [106] C. Liu, C.A. Angell, Phase equilibria, high conductivity ambient temperature liquids, and glasses in the pseudo-halide systems AlC<sub>13</sub>-MSCN (M=Li, Na, K), *Solid State Ionics* 86–88 (1996) 467.
- [107] W. Xu, L.M. Wang, R.A. Nieman, C.A. Angell, Ionic liquids of chelated orthoborates as model ionic glassformers, *J. Phys. Chem. B* 107 (2003) 11749.
- [108] I. Nicotera, C. Oliviero, W.A. Henderson, G.B. Appeteccchi, S. Passerini, NMR investigation of ionic liquid-LiX mixtures: pyrrolidinium cations and TFSI anions, *J. Phys. Chem. B* 109 (2005) 22184.
- [109] O. Borodin, G.D. Smith, Structure and dynamics of *N*-methyl-*N*-propylpyrrolidinium bis (trifluoromethanesulfonyl)imide ionic liquid from molecular dynamics simulations, *J. Phys. Chem. B* 110 (23) (2006) 11481.
- [110] O. Borodin, G.D. Smith, W.A. Henderson, Li<sup>+</sup> cation environment, transport, and mechanical properties of the LiTFSI doped *N*-methyl-*N*-alkylpyrrolidinium<sup>+</sup> TFSI<sup>-</sup> ionic liquids, *J. Phys. Chem. B* 110 (2006) 16879.
- [111] M. Kunze, E. Paillard, S.S. Jeong, G.B. Appeteccchi, M. Schönhoff, M. Winter, S. Passerini, Inhibition of self-aggregation in ionic liquid electrolytes for high-energy electrochemical devices, *J. Phys. Chem. C* 115 (2011) 19431.
- [112] F. Castiglione, E. Ragg, A. Mele, G.B. Appeteccchi, M. Montanino, S. Passerini, Molecular environment and enhanced diffusivity of Li<sup>+</sup> ions in lithium-salt-doped ionic liquid electrolytes, *J. Phys. Chem. Lett.* 2 (2011) 153.
- [113] M. Montanino, F. Alessandrini, S. Passerini, G.B. Appeteccchi, Water-based synthesis of hydrophobic ionic liquids for high-energy electrochemical devices, *Electrochim. Acta* 96 (2013) 124.
- [114] G.B. Appeteccchi, M. Montanino, M. Carewska, F. Alessandrini, S. Passerini, Ionic liquid binary mixtures for low temperature applications, *Adv. Sci. Technol.* 72 (2010) 315.
- [115] F. Castiglione, G. Raos, G.B. Appeteccchi, M. Montanino, S. Passerini, M. Moreno, A. Famulari, A. Mele, Blending ionic liquids: how physico-chemical properties change, *J. Phys. Chem. Chem. Phys.* 12 (2010) 1784.
- [116] M. Montanino, M. Moreno, F. Alessandrini, G.B. Appeteccchi, S. Passerini, Q. Zhou, W. A. Henderson, Physical and electrochemical properties of binary ionic liquid mixtures: (1-x)PYR<sub>14</sub>TFSI-(x)PYR<sub>14</sub>IM<sub>14</sub>, *Electrochim. Acta* 60 (2012) 163.
- [117] M. Kunze, S.S. Jeong, G.B. Appeteccchi, M. Schönhoff, M. Winter, S. Passerini, Mixtures of ionic liquids for low temperature electrolytes, *Electrochim. Acta* 82 (2012) 69.
- [118] G.B. Appeteccchi, M. Montanino, A. Balducci, S.F. Lux, M. Winter, S. Passerini, Lithium insertion in graphite from ternary ionic liquid-lithium salt electrolytes: I. Electrochemical characterization of the electrolytes, *J. Power Sources* 192 (2009) 599.

[119] S.F. Lux, M. Schmuck, G.B. Appetecchi, S. Passerini, M. Winter, A. Balducci, Lithium insertion in graphite from ternary ionic liquid–lithium salt electrolytes: II. Evaluation of specific capacity and cycling efficiency and stability at room temperature, *J. Power Sources* 192 (2009) 606.

[120] S. Lux, M. Schmuck, B. Rupp, W. Kern, G.B. Appetecchi, S. Passerini, M. Winter, A. Balducci, Mixtures of ionic liquids in combination with graphite electrodes: the role of electrolyte additives and Li-salt, *ECS Trans.* 16 (2009) 45.

[121] A. Guerfi, M. Dontigny, Y. Kobayashi, A. Vlijh, K. Zaghib, Investigation on some electrochemical aspects of lithium-ion ionic liquid/gel polymer battery systems, *J. Solid State Electrochem.* 13 (2009) 1003.

[122] R.-S. Kuhnel, N. Böckenfeld, S. Passerini, M. Winter, A. Balducci, Mixtures of ionic liquid and organic carbonate as electrolyte with improved safety and performance for rechargeable lithium batteries, *Electrochim. Acta* 56 (2011) 4092.

[123] M. Egashira, S. Okada, J.-I. Yamaki, D.A. Dri, F. Bonadies, B. Scrosati, The preparation of quaternary ammonium-based ionic liquid containing a cyano group and its properties in a lithium battery electrolyte, *J. Power Sources* 138 (2004) 240.

[124] H. Matsumoto, H. Sakaebi, K. Tatsumi, M. Kikuta, E. Ishiko, M. Kono, Fast cycling of Li/LiCoO<sub>2</sub> cell with low-viscosity ionic liquids based on bis(fluorosulfonyl)imide [FSI]<sup>−</sup>, *J. Power Sources* 160 (2006) 1313.

[125] Report of the basic energy sciences workshop on electrical energy storage “Basic Research Needs for Electrochemical Energy Storage”, April 2–4, 2007, Office of Basic Energy Sciences, Department of Energy, July 2007.

[126] A. Lewandosky, M. Bieguin, M. Galinski, Kinetics of Li<sup>+</sup> reduction in 1-methyl-3-propylpiperidinium bis(trifluoromethylsulfonyl) imide room temperature ionic liquid, *Electrochim. Acta* 63 (2012) 204.

[127] P. Arora, Z. Zhang, Battery separators, *Chem. Rev.* 104 (10) (2004) 4419.

[128] A.M. Stephan, Review on gel polymer electrolytes for lithium batteries, *Eur. Polym. J.* 42 (1) (2006) 21.

[129] D.E. Fenton, J.M. Parker, P.V. Wright, Complexes of alkali metal ions with poly(ethylene oxide), *Polymers* 14 (1973) 589.

[130] P.V. Wright, Electrical conductivity in ionic complexes of poly(ethylene oxide), *Br. Polym. J.* 7 (1975) 319.

[131] M. Armand, J.M. Chabagno, M. Duclot, Second International Meeting on Solid Electrolytes, St Andrews, Scotland, 20–22 Sept., 1978.

[132] M. Armand, J.M. Chabagno, M. Duclot, Polyethers as solid electrolytes, in: P. Vashitshta, J.N. Mundy, G.K. Shenoy (Eds.), *Fast Ion Transport in Solids, Electrodes and Electrolytes*, North Holland Publishers, Amsterdam, 1979.

[133] F.M. Gray, *Polymer Electrolytes*, Royal Society of Chemistry Monographs, Cambridge, 1997.

[134] P.V. Wright, Developments in polymer electrolytes for lithium batteries, *MRS Bulletin*, August 2002, p. 597.

[135] M.C. Borghini, M. Mastragostino, S. Passerini, B. Scrosati, Electrochemical properties of polyethylene oxide–Li[(CF<sub>3</sub>SO<sub>2</sub>)<sub>2</sub>N]–γ-LiAlO<sub>2</sub> composite polymer electrolytes, *J. Electrochem. Soc.* 142 (1995) 2118.

[136] G.B. Appetecchi, W. Henderson, P. Villano, M. Berrettoni, S. Passerini, PEO-LiN (SO<sub>2</sub>CF<sub>2</sub>CF<sub>3</sub>)<sub>2</sub> polymer electrolytes: I. XRD, DSC, and ionic conductivity characterization, *J. Electrochem. Soc.* 148 (2001) 1171.

[137] B.K. Choi, K.H. Shin, Y.W. Kim, Lithium ion conduction in PEO–salt electrolytes gelled with PAN, *Solid State Ionics* 113–115 (1998) 123.

- [138] Y. Kang, H.J. Kim, E. Kim, B. Oh, J.H. Cho, Photocured PEO-based solid polymer electrolyte and its application to lithium–polymer batteries, *J. Power Sources* 92 (1–2) (2001) 255.
- [139] Y. Aihara, G.B. Appetecchi, B. Scrosati, A new concept for the formation of homogeneous, poly(ethylene oxide)-based, gel-type polymer electrolyte, *J. Electrochem. Soc.* 149 (2002) A849.
- [140] Y. Aihara, G.B. Appetecchi, B. Scrosati, K. Hayamizu, Investigation of the ionic conduction mechanism of composite poly(ethyleneoxide) PEO-based polymer gel electrolytes including nano-size  $\text{SiO}_2$ , *J. Phys. Chem. C* 4 (2002) 3443.
- [141] G.B. Appetecchi, Y. Aihara, B. Scrosati, Investigation of swelling phenomena in poly(ethylene oxide)-based polymer electrolytes: III. Preliminary battery tests, *J. Electrochem. Soc.* 150 (2003) A301.
- [142] G.B. Appetecchi, Y. Aihara, B. Scrosati, Investigation of swelling phenomena in PEO-based polymer electrolytes: II. Chemical and electrochemical characterization, *Solid State Ionics* 170 (2004) 63.
- [143] F. Croce, F. Gerace, G. Dautzenberg, S. Passerini, G.B. Appetecchi, B. Scrosati, Synthesis and characterization of highly conducting gel electrolytes, *Electrochim. Acta* 39 (1994) 2187.
- [144] G.B. Appetecchi, F. Croce, P. Romagnoli, B. Scrosati, U. Heider, R. Oesten, High-performance gel-type lithium electrolyte membranes, *Electrochim. Commun.* 1 (1999) 83.
- [145] G.B. Appetecchi, P. Romagnoli, B. Scrosati, Composite gel membranes: a new class of improved polymer electrolytes for lithium batteries, *Electrochim. Commun.* 3 (2001) 281.
- [146] G.B. Appetecchi, F. Croce, B. Scrosati, Kinetics and stability of the lithium electrode in poly(methylmethacrylate)-based gel electrolytes, *Electrochim. Acta* 40 (1995) 991.
- [147] E. Cazzanelli, G. Mariotto, F. Croce, G.B. Appetecchi, B. Scrosati, Study of ion–molecule interaction in poly(methylmethacrylate) based gel electrolytes by raman spectroscopy, *Electrochim. Acta* 40 (1995) 2379.
- [148] E. Cazzanelli, G. Mariotto, G.B. Appetecchi, F. Croce, Raman study of ion–molecules interaction in poly(methylmethacrylate)-based gel electrolytes, *Ionics* 2 (1996) 81.
- [149] G.B. Appetecchi, F. Croce, B. Scrosati, High-performance electrolyte membranes for plastic lithium batteries, *J. Power Sources* 66 (1997) 77.
- [150] W. Wieczorek, J. Stevens, Impedance spectroscopy and phase structure of polyether–poly(methyl methacrylate)– $\text{LiCF}_3\text{SO}_3$  blend-based electrolytes, *J. Phys. Chem. B* 101 (1997) 1529.
- [151] R.C. Willemse, A. Posthuma de Boer, J. van Dam, A.D. Gotsis, Co-continuous morphologies in polymer blends: the influence of the interfacial tension, *Polymer* 40 (1999) 827.
- [152] R.C. Willemse, A. Posthuma de Boer, J. van Dam, A.D. Gotsis, Co-continuous morphologies in polymer blends: a new model, *Polymer* 39 (1998) 5879.
- [153] G.M. Jordhamo, J.A. Manson, L.H. Sperling, Phase continuity and inversion in polymer blends and simultaneous interpenetrating networks, *Polym. Eng. Sci.* 26 (1986) 517.
- [154] T. Momma, H. Ito, H. Nara, H. Mukaiho, S. Passerini, T. Osaka, Characteristics of interpenetrated polymer network system made of polyethyleneoxide– $\text{LiBF}_4$  complex and polystyrene as the electrolyte for lithium secondary battery, *Electrochemistry* 71 (2003) 1182.
- [155] S. Passerini, F. Alessandrini, T. Momma, H. Ohta, H. Ito, T. Osaka, Co-continuous polymer blend based lithium-ion conducting gel-polymer electrolytes, *Electrochim. Solid State Lett.* 4 (2001) A124.

[156] H. Nara, T. Momma, T. Osaka, Feasibility of an interpenetrated polymer network system made of diblock copolymer composed of polyethylene oxide and polystyrene as the gel electrolyte for lithium secondary batteries, *Electrochemistry* 76 (2008) 276.

[157] G.B. Appetecchi, F. Alessandrini, S. Passerini, G. Caporiccio, B. Boutevin, F. Guida-Pietra Santa, Novel polymeric systems for lithium-ion batteries gel electrolytes: I. Cross-linked polyfluorosilicone, *Electrochim. Acta* 50 (2004) 149.

[158] G.B. Appetecchi, F. Alessandrini, S. Passerini, G. Caporiccio, B. Boutevin, F. Guida-Pietra Santa, Novel polymeric systems for lithium ion batteries gel electrolytes: II. Hybrid cross-linked poly(fluorosilicone-ethyleneoxide), *Electrochim. Acta* 50 (2005) 4396.

[159] Y.J. Wang, D. Kim, Crystallinity, morphology, mechanical properties and conductivity study of in situ formed PVdF/LiClO<sub>4</sub>/TiO<sub>2</sub> nanocomposite polymer electrolytes, *Electrochim. Acta* 52 (2007) 3181.

[160] V. Gentili, S. Panero, P. Reale, B. Scrosati, Composite gel-type polymer electrolytes for advanced, rechargeable lithium batteries, *J. Power Sources* 170 (2007) 185.

[161] P. Raghavan, X.H. Zhao, J.K. Kim, J. Manuel, G.S. Chauhan, J.H. Ahn, C. Nah, Ionic conductivity and electrochemical properties of nanocomposite polymer electrolytes based on electrospun poly(vinylidene fluoride-co-hexafluoropropylene) with nano-sized ceramic fillers, *Electrochim. Acta* 54 (2008) 228.

[162] Z.H. Li, H.P. Zhang, P. Zhang, Y.P. Wu, X.D. Zhou, Macroporous nanocomposite polymer electrolyte for lithium-ion batteries, *J. Power Sources* 184 (2008) 562.

[163] J.K. Kim, G. Cheruvally, X. Li, J.H. Ahn, K.W. Kim, H.J. Ahn, Preparation and electrochemical characterization of electrospun, microporous membrane-based composite polymer electrolytes for lithium batteries, *J. Power Sources* 178 (2008) 815.

[164] R.Y. Miao, B.W. Liu, Z.Z. Zhu, Y. Liu, J.L. Li, X.D. Wang, Q.F. Li, PVDF-HFP-based porous polymer electrolyte membranes for lithium-ion batteries, *J. Power Sources* 184 (2008) 420.

[165] Z. Ren, K.N. Sun, Y.Y. Liu, X.L. Zhou, N.Q. Zhang, X.D. Zhu, Polymer electrolytes based on poly(vinylidene fluoride-co-hexafluoropropylene) with crosslinked poly(ethylene glycol) for lithium batteries, *Solid State Ionics* 180 (2009) 693.

[166] Y.H. Ding, W. Di, Y. Jiang, F. Xu, Z.L. Long, F.M. Ren, P. Zhang, The morphological evolution, mechanical properties and ionic conductivities of electrospinning P(VDF-HFP) membranes at various temperatures, *Ionics* 15 (2009) 731.

[167] Z.Y. Cui, Y.Y. Xu, L.P. Zhu, J.Y. Wang, B.K. Zhu, Investigation on PVDF-HFP micro-porous membranes prepared by TIPS process and their application as polymer electrolytes for lithium ion batteries, *Ionics* 15 (2009) 469.

[168] Z. Jiang, B. Carroll, K.M. Abraham, Studies of some poly(vinylidene fluoride) electrolytes, *Electrochim. Acta* 42 (17) (1997) 2667.

[169] J. Li, Exchange coupling in P(VDF-TrFE) copolymer based all-organic composites with giant electrostriction, *Phys. Rev. Lett.* 90 (21) (2003) 217601.

[170] G.B. Appetecchi, F. Croce, A. De Paolis, B. Scrosati, A poly(vinylidene fluoride)-based gel electrolyte membrane for lithium batteries, *J. Electroanal. Chem.* 463 (1999) 248.

[171] D. Djian, F. Alloin, S. Martinet, H. Lignier, Macroporous poly(vinylidene fluoride) membrane as a separator for lithium-ion batteries with high charge rate capacity, *J. Power Sources* 187 (2) (2009) 575.

[172] C.M. Costa, L.C. Rodrigues, V. Sencadas, M.M. Silva, J.G. Rocha, S. Lanceros-Méndez, Effect of degree of porosity on the properties of poly(vinylidene fluoride-trifluoroethylene) for Li-ion battery separators, *J. Membr. Sci.* 407–408 (2012) 193.

[173] J. Saunier, F. Alloin, J.Y. Sanchez, L. Maniguet, Plasticized microporous poly(vinylidene fluoride) separators for lithium-ion batteries. III. Gel properties and irreversible

modifications of poly(vinylidene fluoride) membranes under swelling in liquid electrolytes, *J. Polym. Sci., Part B: Polym. Phys.* 42 (12) (2004) 2308.

[174] J. Saunier, F. Alloin, J.Y. Sanchez, B. Barrière, Plasticized microporous poly(vinylidene fluoride) separators for lithium-ion batteries. I. Swelling behavior of dense membranes with respect to a liquid electrolyte—characterization of the swelling equilibrium, *J. Polym. Sci., Part B: Polym. Phys.* 42 (3) (2004) 532.

[175] T. Nakajima, H. Groult, *Fluorinated Materials for Energy Conversion*, Elsevier Science, Amsterdam, 2005.

[176] C.M. Costa, M.M. Silva, S. Lanceros-Méndez, Battery separators based on vinylidene fluoride (VDF) polymers and copolymers for lithium ion battery applications, *RSC Adv.* (2013).

[177] C.M. Costa, V. Sencadas, J.G. Rocha, M.M. Silva, S. Lanceros-Méndez, Evaluation of the main processing parameters influencing the performance of poly(vinylidene fluoride-trifluoroethylene) lithium-ion battery separators, *J. Solid State Electrochem.* 17 (3) (2013) 861.

[178] C.M. Costa, L.C. Rodrigues, V. Sencadas, M.M. Silva, S. Lanceros-Méndez, Effect of the microstructure and lithium-ion content in poly[(vinylidene fluoride)-co-trifluoroethylene]/lithium perchlorate trihydrate composite membranes for battery applications, *Solid State Ionics* 217 (2012) 19.

[179] C.M. Costa, J. Nunes-Pereira, L.C. Rodrigues, M.M. Silva, J.L.G. Ribelles, S. Lanceros-Méndez, Novel poly(vinylidene fluoride-trifluoroethylene)/poly(ethylene oxide) blends for battery separators in lithium-ion applications, *Electrochim. Acta* 88 (2013) 473.

[180] C.M. Costa, J.L. Gomez Ribelles, S. Lanceros-Méndez, G.B. Appetecchi, B. Scrosati, Poly(vinylidene fluoride)-based, co-polymer separator electrolyte membranes for lithium-ion battery systems, *J. Power Sources* 245 (2014) 779.

[181] Z. Ren, Y.Y. Liu, K.N. Sun, X.L. Zhou, N.Q. Zhang, A microporous gel electrolyte based on poly(vinylidene fluoride-co-hexafluoropropylene)/fully cyanoethylated cellulose derivative blend for lithium-ion battery, *Electrochim. Acta* 54 (2009) 1888.

[182] P. Raghavan, X. Zhao, C. Shin, D.H. Baek, J.W. Choi, J. Manuel, M.Y. Heo, J.H. Ahn, C. Nah, Preparation and electrochemical characterization of polymer electrolytes based on electrospun poly(vinylidene fluoride-co-hexafluoropropylene)/polyacrylonitrile blend/composite membranes for lithium batteries, *J. Power Sources* 195 (2010) 6088.

[183] A.I. Gopalan, P. Santhosh, K.M. Manesh, J.H. Nho, S.H. Kim, C.G. Hwang, K.P. Lee, Development of electrospun PVdF-PAN membrane-based polymer electrolytes for lithium batteries, *J. Membr. Sci.* 325 (2008) 683.

[184] J.W. Fergus, Ceramic and polymeric solid electrolytes for lithium-ion batteries, *J. Power Sources* 195 (2010) 4554.

[185] P. Lightfoot, M.A. Metha, P.G. Bruce, Crystal structure of the polymer electrolyte poly (ethylene oxide)<sub>3</sub>:LiCF<sub>3</sub>SO<sub>3</sub>, *Science* 262 (1993) 883.

[186] C.A. Vincent, B. Scrosati, *Modern Batteries, An Introduction to Electrochemical Power Sources*, second ed., Arnold, London, 1993.

[187] F.M. Gray, M. Armand, T. Osaka, M. Datta (Eds.), *Energy Storage System for Electronics*, Gordon and Breach Science Publications, Amsterdam, 2000.

[188] C. Berthier, W. Gorecki, M. Minier, M.B. Armand, J.M. Chabagno, P. Rigaud, Microscopic investigation of ionic conductivity in alkali metal salts-poly(ethylene oxide) adducts, *Solid State Ionics* 11 (1983) 91.

[189] M. Minier, C. Berthier, W. Gorecki, Thermal analysis and NMR study of a poly(ethylene oxide) complex electrolyte:PEO(LiCF<sub>3</sub>SO<sub>3</sub>)<sub>x</sub>, *J. de Physique* 45 (1984) 739.

[190] M. Marzantowicz, J.R. Dygas, F. Krok, A. Tomaszewska, Z. Florjanczyk, E. Zygaplo-Monikowska, G. Lapienis, Star-branched poly(ethylene oxide)  $\text{LiN}(\text{CF}_3\text{SO}_2)_2$ : a promising polymer electrolyte, *J. Power Sources* 194 (2009) 51.

[191] W. Wieczorek, Composite PolyEther-Based Electrolytes, Oficina Wydawnicza Politechniki Warszawskej, Warsaw, 1995.

[192] Y. Aihara, S. Arai, K. Hayamizu, Ionic conductivity, DSC and self diffusion coefficients of lithium, anion, polymer, and solvent of polymer gel electrolytes: the structure of the gels and the diffusion mechanism of the ions, *Electrochim. Acta* 45 (2000) 1321.

[193] A. Chakrabarti, A. Juilfs, R. Filler, B.K. Mandal, Novel PEO-based dendronized polymers for lithium-ion batteries, *Solid State Ionics* 181 (2010) 982.

[194] A.M. Rocco, A.D. Carias, R.P. Pereira, Polymer electrolytes based on a ternary miscible blend of poly(ethylene oxide), poly(bisphenol A-*co*-epichlorohydrin) and poly(vinyl ethyl ether), *Polymer* 51 (2010) 5151.

[195] G.B. Appetecchi, D. Zane, B. Scrosati, PEO-based electrolyte membranes based on  $\text{LiBC}_4\text{O}_8$  salt, *J. Electrochem. Soc.* 151 (2004) A1369.

[196] M. Kurian, M.E. Galvin, P.E. Trapa, D.R. Sadoway, A.M. Mayes, Single-ion conducting polymer silicate nanocomposite electrolytes for lithium battery applications, *Electrochim. Acta* 50 (2005) 2125.

[197] G.B. Appetecchi, G. Dautzenberg, B. Scrosati, A new class of advanced polymer electrolytes and their relevance in plastic-like, rechargeable lithium batteries, *J. Electrochem. Soc.* 143 (1996) 6.

[198] G.B. Appetecchi, G. Dautzenberg, B. Scrosati, Highly conductive gel electrolyte membranes, *Proceedings of International Workshop on Advanced Batteries*, 1995, p. 72.

[199] J.F. Snyder, R.H. Carter, E.D. Wetzel, Electrochemical and mechanical behavior in mechanically robust solid polymer electrolytes for use in multifunctional structural batteries, *Chem. Mater.* 19 (2007) 3793.

[200] F. Capuano, F. Croce, B. Scrosati, Composite polymer electrolytes, *J. Electrochem. Soc.* 138 (1991) 1918.

[201] F. Croce, G.B. Appetecchi, L. Persi, B. Scrosati, Nanocomposite polymer electrolytes for lithium batteries, *Nature* 394 (1998) 456.

[202] C.W. Lin, C.L. Hung, M. Venkateswarlu, B.J. Hwang, Influence of  $\text{TiO}_2$  nano-particles on the transport properties of composite polymer electrolyte for lithium-ion batteries, *J. Power Sources* 146 (2005) 397.

[203] S. Liu, N. Imanishi, T. Zhang, A. Hirano, Y. Takeda, O. Yamamoto, J. Yang, Effect of nano-silica filler in polymer electrolyte on Li dendrite formation in Li/poly(ethylene oxide)- $\text{Li}(\text{CF}_3\text{SO}_2)_2\text{N}/\text{Li}$ , *J. Power Sources* 195 (2010) 6847.

[204] C. Shen, J.M. Wang, Z. Tang, H.J. Wang, H.Q. Lian, J.Q. Zhang, C.N. Cao, Physico-chemical properties of poly(ethylene oxide)-based composite polymer electrolytes with a silane-modified mesoporous silica SBA-15, *Electrochim. Acta* 54 (2009) 3490.

[205] Y.W. Chen-Yang, Y.L. Wang, Y.T. Chen, Y.K. Li, H.C. Chen, H.Y. Chiu, Influence of silica aerogel on the properties of polyethylene oxide-based nanocomposite polymer electrolytes for lithium battery, *J. Power Sources* 182 (2008) 340.

[206] C. Capiglia, P. Mustarelli, E. Quararone, C. Tomasi, A. Magistris, Effects of nanoscale  $\text{SiO}_2$  on the thermal and transport properties of solvent-free, poly(ethylene oxide) (PEO)-based polymer electrolytes, *Solid State Ionics* 118 (1999) 73.

[207] H.J. Walls, J. Zhou, J.A. Yerian, P.S. Fedkiw, S.S. Khan, M.K. Stowe, G.L. Baker, Fumed silica-based composite polymer electrolytes: synthesis, rheology, and electrochemistry, *J. Power Sources* 89 (2000) 156.

[208] Y. Liu, J.Y. Lee, L. Hong, Functionalized  $\text{SiO}_2$  in poly(ethylene oxide)-based polymer electrolytes, *J. Power Sources* 109 (2002) 507.

[209] T.K.J. Koster, L. van Wullen, Cation–anion coordination, ion mobility and the effect of  $\text{Al}_2\text{O}_3$  addition in PEO based polymer electrolytes, *Solid State Ionics* 181 (2010) 489.

[210] H.M.J.C. Pitawala, M.A.K.L. Dissanayake, V.A. Seneviratne, B.E. Mellander, I. Albinson, Effect of plasticizers (EC or PC) on the ionic conductivity and thermal properties of the  $(\text{PEO})_9\text{LiTf}: \text{Al}_2\text{O}_3$  nanocomposite polymer electrolyte system, *J. Solid State Electrochem.* 12 (2008) 783.

[211] P.A.R.D. Jayathilaka, M.A.K.L. Dissanayake, I. Albinsson, B.-E. Mellander, Effect of nano-porous  $\text{Al}_2\text{O}_3$  on thermal, dielectric and transport properties of the  $(\text{PEO})_9\text{LiTFSI}$  polymer electrolyte system, *Electrochim. Acta* 47 (2002) 3257.

[212] F. Croce, S. Sacchetti, B. Scrosati, Advanced, lithium batteries based on high-performance composite polymer electrolytes, *J. Power Sources* 162 (2006) 685.

[213] F. Croce, S. Sacchetti, B. Scrosati, Advanced, high-performance composite polymer electrolytes for lithium batteries, *J. Power Sources* 161 (2006) 560.

[214] G. Derrien, J. Hassoun, S. Sacchetti, S. Panero, Nanocomposite PEO-based polymer electrolyte using a highly porous, super acid zirconia filler, *Solid State Ionics* 180 (2009) 1267.

[215] M.R. Johan, L.B. Fen, Combined effect of  $\text{CuO}$  nanofiller and DBP plasticizer on ionic conductivity enhancement in the solid polymer electrolyte  $\text{PEO}-\text{LiCF}_3\text{SO}_3$ , *Ionics* 16 (2010) 335.

[216] L.S. Wang, W.S. Yang, J. Wang, D.G. Evans, New nanocomposite polymer electrolyte comprising nanosized  $\text{ZnAl}_2\text{O}_4$  with a mesopore network and  $\text{PEO}-\text{LiClO}_4$ , *Solid State Ionics* 180 (2009) 392.

[217] G.B. Appetecchi, F. Croce, J. Hassoun, B. Scrosati, M. Salomon, F. Cassel, Hot-pressed, dry, composite, PEO-based electrolyte membranes: I. Ionic conductivity characterization, *J. Power Sources* 114 (2003) 105.

[218] G.B. Appetecchi, F. Alessandrini, M. Carewska, T. Caruso, P.P. Prosini, S. Scaccia, S. Passerini, Investigation on lithium–polymer electrolyte batteries, *J. Power Sources* 97 (2001) 790.

[219] G.B. Appetecchi, S. Scaccia, S. Passerini, Investigation on the stability of the lithium–polymer electrolyte interface, *J. Electrochem. Soc.* 147 (2000) 4448.

[220] J.H. Shin, S. Passerini,  $\text{PEO}-\text{LiN}(\text{SO}_2\text{CF}_2\text{CF}_3)_2$  polymer electrolytes: V. Effect of fillers on ionic transport properties, *J. Electrochem. Soc.* 151 (2004) A238.

[221] J.H. Shin, W.A. Henderson, G.B. Appetecchi, F. Alessandrini, S. Passerini, Recent developments in the ENEA lithium metal battery project, *Electrochim. Acta* 50 (2005) 3859.

[222] J.-H. Shin, W.A. Henderson, S. Scaccia, P.P. Prosini, S. Passerini, Solid-state  $\text{Li}/\text{LiFePO}_4$  polymer electrolyte batteries incorporating an ionic liquid cycled at 40 °C, *J. Power Sources* 156 (2006) 560.

[223] J.-H. Shin, W.A. Henderson, C. Tizzani, S. Passerini, S.-S. Jeong, K.-W. Kim, Characterization of solvent-free polymer electrolytes consisting of ternary  $\text{PEO}-\text{LiTFSI}-\text{PYR}_{14}\text{TFSI}$ , *J. Electrochem. Soc.* 153 (9) (2006) A1649.

[224] G.-T. Kim, G.B. Appetecchi, F. Alessandrini, S. Passerini, Solvent-free,  $\text{PYR}_{14}\text{TFSI}$  ionic liquid-based ternary polymer electrolyte systems: I. Electrochemical characterization, *J. Power Sources* 171 (2007) 861.

[225] G.-T. Kim, G.B. Appetecchi, M. Carewska, M. Joost, A. Balducci, M. Winter, S. Passerini, UV cross-linked, lithium-conducting ternary polymer electrolytes containing ionic liquids, *J. Power Sources* 195 (2010) 6130.

[226] Y.P. Wang, X.H. Gao, J.C. Chen, Z.W. Li, C.L. Li, S.C. Zhang, Imidazolium-organic solvent–alkali metal salt mixtures as nonflammable electrolytes incorporated into PVDF–PEG polymer electrolyte, *J. Appl. Polym. Sci.* 113 (2009) 2492.

[227] C. Sirisopanaporn, A. Fericola, B. Scrosati, New, ionic liquid-based membranes for lithium battery application, *J. Power Sources* 186 (2009) 490.

[228] A. Lewandowski, A. Swiderska-Mocek, Ionic liquids as electrolytes for Li-ion batteries—an overview of electrochemical studies, *J. Power Sources* 194 (2009) 601.

[229] S. Kim, S.J. Park, Preparation and electrochemical properties of composite polymer electrolytes containing 1-ethyl-3-methylimidazolium tetrafluoroborate salts, *Electrochim. Acta* 54 (2009) 3775.

[230] S. Ahmad, Polymer electrolytes; characteristics and peculiarities, *Ionics* 15 (3) (2009) 309.

[231] J.H. Shin, E.J. Cairns, *N*-Methyl-(*n*-butyl)pyrrolidinium bis(trifluoromethanesulfonyl) imide-LiTFSI–poly(ethylene glycol) dimethyl ether mixture as a Li/S cell electrolyte, *J. Power Sources* 177 (2008) 537.

[232] D.M. Tigelaar, M.A.B. Meador, W.R. Bennett, Composite electrolytes for lithium batteries: ionic liquids in APTES cross-linked polymers, *Macromolecules* 40 (2007) 4159.

[233] T.E. Sutto, Hydrophobic and hydrophilic interactions of ionic liquids and polymers in solid polymer gel electrolytes, *J. Electrochem. Soc.* 154 (2007) P101.

[234] H. Cheng, C.B. Zhu, B. Huang, M. Lu, Y. Yang, Synthesis and electrochemical characterization of PEO-based polymer electrolytes with room temperature ionic liquids, *Electrochim. Acta* 52 (2007) 5789.

[235] Y. Zhao, R.Y. Tao, T. Fujinami, Enhancement of ionic conductivity of PEO–LiTFSI electrolyte upon incorporation of plasticizing lithium borate, *Electrochim. Acta* 51 (2006) 6451.

[236] R. Kawano, H. Tokuda, T. Katakabe, H. Nakamoto, H. Kokubo, S. Imabayashi, M. Watanabe, Specific charge transport in ionic liquids and ion gels and the importance in material science, *Kobunshi Ronbunshu* 63 (2006) 31.

[237] O. Borodin, G.D. Smith, O. Geiculescu, S.E. Creager, B. Hallac, D. DesMarteau, Li<sup>+</sup> transport in lithium sulfonylimide-oligo(ethylene oxide) ionic liquids and oligo(ethylene oxide) doped with LiTFSI, *J. Phys. Chem. B* 110 (2006) 24266.

[238] S. Seki, A.B.H. Susan, T. Kaneko, H. Tokuda, A. Noda, M. Watanabe, Distinct difference in ionic transport behavior in polymer electrolytes depending on matrix polymers and incorporated salts, *J. Phys. Chem. B* 109 (2005) 3886.

[239] C. Gerbaldi, J.R. Nair, S. Ahmad, G. Meligrana, R. Bongiovanni, S. Bodoardo, N. Penazzi, UV-cured polymer electrolytes encompassing hydrophobic room temperature ionic liquid for lithium batteries, *J. Power Sources* 195 (2010) 1706.

[240] F. Gayet, L. Viau, F. Leroux, S. Monge, J.J. Robin, A. Vioux, Polymer nanocomposite ionogels, high-performance electrolyte membranes, *J. Mater. Chem.* 20 (2010) 9456.

[241] E. Abitelli, S. Ferrari, E. Quartarone, P. Mustarelli, A. Magistris, M. Fagnoni, A. Albini, C. Gerbaldi, Polyethylene oxide electrolyte membranes with pyrrolidinium-based ionic liquids, *Electrochim. Acta* 55 (2010) 5478.

[242] M. Castriota, T. Caruso, R.G. Agostino, E. Cazzanelli, W.A. Henderson, S. Passerini, Raman investigation of the ionic liquid *N*-methyl-*N*-propylpyrrolidinium bis(trifluoromethanesulfonyl)imide and its mixture with LiN(SO<sub>2</sub>CF<sub>3</sub>)<sub>2</sub>, *J. Phys. Chem. A* 109 (2005) 92.

[243] J. Rymarczyk, M. Carewska, G.B. Appetecchi, D. Zane, F. Alessandrini, S. Passerini, A novel ternary polymer electrolyte for LMP batteries based on thermal cross-linked poly(urethane acrylate) in presence of a lithium salt and an ionic liquid, *Eur. Polym. J.* 44 (2008) 2153.

[244] C. Tizzani, G.B. Appeticchi, M. Carewska, G.-T. Kim, S. Passerini, Investigation of the electrochemical properties of polymer-LiX-ionic liquid ternary systems, *Aust. J. Chem.* 60 (2007) 47.

[245] A.L. Pont, R. Marcilla, I. De Meatza, H. Grande, D. Mecerreyes, Pyrrolidinium-based polymeric ionic liquids as mechanically and electrochemically stable polymer electrolytes, *J. Power Sources* 188 (2009) 558.

[246] G.B. Appeticchi, G.-T. Kim, M. Montanino, M. Carewska, R. Marcilla, D. Mecerreyes, I. De Meatza, Pyrrolidinium-based polymeric ionic liquids as mechanically and electrochemically stable polymer electrolytes, *J. Power Sources* 195 (2010) 3668.

[247] S. Stramare, V. Thangadurai, W. Weppner, Lithium lanthanum titanates: a review, *Chem. Mater.* 15 (2003) 3974.

[248] J.M. Kim, G.B. Park, K.C. Lee, H.Y. Park, S.C. Nam, S.W. Song, Li–B–O–N electrolytes for all-solid-state thin film batteries, *J. Power Sources* 189 (2009) 211.

[249] J.S. Thokchom, N. Gupta, B. Kumar, Superionic conductivity in a lithium aluminum germanium phosphate glass-ceramic, *J. Electrochem. Soc.* 155 (12) (2008) A915.

[250] Y. Hamon, A. Douard, F. Sabary, C. Marcel, P. Vinatier, B. Pecquenard, A. Levasseur, Influence of sputtering conditions on ionic conductivity of LiPON thin films, *Solid State Ionics* 177 (2006) 257.

[251] T. Minami, A. Hayashi, M. Tatsumisago, Recent progress of glass and glass-ceramics as solid electrolytes for lithium secondary batteries, *Solid State Ionics* 177 (2006) 2715.

[252] A. Sakuda, H. Kitaura, A. Hayashi, K. Tadanaga, M. Tatsumisago, Improvement of high-rate performance of all-solid-state lithium secondary batteries using LiCoO<sub>2</sub> coated with Li<sub>2</sub>O–SiO<sub>2</sub> glasses, *Electrochem. Solid-State Lett.* 11 (2008) A1.

[253] R. Kanno, M. Murayama, Lithium ionic conductor thio-LISICON: the Li<sub>2</sub>-S-GeS<sub>2</sub>-P<sub>2</sub>S<sub>5</sub> system, *J. Electrochem. Soc.* 148 (7) (2001) A742.

[254] R. Kanno, T. Hata, Y. Kawamoto, M. Irie, Synthesis of a new lithium ionic conductor, thio-LISICON–lithium germanium sulfide system, *Solid State Ionics* 130 (2000) 97.

[255] N.A. Anurova, V.A. Blatov, G.D. Ilyushin, O.A. Blatova, A.K. Ivanov-Schitz, L. N. Dem'yanets, Migration maps of Li<sup>+</sup> cations in oxygen-containing compounds, *Solid State Ionics* 179 (2008) 2248.

[256] V. Thangadurai, W. Weppner, Recent progress in solid oxide and lithium ion conducting electrolytes research, *Ionics* 12 (2006) 81.

[257] J. Schwenzel, V. Thangadurai, W. Weppner, Investigation of thin film all-solid-state lithium ion battery materials, *Ionics* 9 (2003) 348.

[258] V. Thangadurai, W. Weppner, Solid state lithium ion conductors: design considerations by thermodynamic approach, *Ionics* 8 (2002) 281.

[259] Y. Inda, T. Katoh, M. Baba, Development of all-solid lithium-ion battery using Li-ion conducting glass-ceramics, *J. Power Sources* 174 (2007) 741.

[260] J. Ibarra, A. Varez, C. Leon, J. Santamaria, L.M. Torres-Martinez, J. Sanz, Influence of composition on the structure and conductivity of the fast ionic conductors La<sub>2/3-x</sub>Li<sub>3x</sub>TiO<sub>3</sub> (0.03 ≤ x ≤ 0.167), *Solid State Ionics* 134 (2000) 219.

[261] Y. Inaguma, M. Itoh, Influences of carrier concentration and site percolation on lithium ion conductivity in perovskite-type oxides, *Solid State Ionics* 86–8 (1996) 257.

[262] A. Mei, X.L. Wang, Y.C. Feng, S.J. Zhao, G.J. Li, H.X. Geng, Y.H. Lin, C.W. Nan, Enhanced ionic transport in lithium lanthanum titanium oxide solid state electrolyte by introducing silica, *Solid State Ionics* 179 (2008) 2255.

[263] J. Xie, N. Imanishi, T. Zhang, A. Hirano, Y. Takeda, O. Yamamoto, Li-ion transport in all-solid-state lithium batteries with LiCoO<sub>2</sub> using NASICON-type glass ceramic electrolytes, *J. Power Sources* 189 (2009) 365.

[264] C. Yada, Y. Iriyama, T. Abe, K. Kikuchi, Z. Ogumi, A novel all-solid-state thin-film-type lithium-ion battery with *in situ* prepared positive and negative electrode materials, *Electrochem. Commun.* 11 (2009) 413.

[265] Y. Iriyama, K. Nishimoto, C. Yada, T. Abe, Z. Ogumi, K. Kikuchi, Charge-transfer reaction at the lithium phosphorus oxynitride glass electrolyte/lithium manganese oxide thin-film interface and its stability on cycling batteries, fuel cells, and energy conversion, *J. Electrochem. Soc.* 153 (2006) A821.

[266] A. Sakuda, H. Kitaura, A. Hayashi, K. Tadanaga, M. Tatsumisago, Modification of interface between  $\text{LiCoO}_2$  electrode and  $\text{Li}_2\text{S}-\text{P}_2\text{S}_5$  solid electrolyte using  $\text{Li}_2\text{O}-\text{SiO}_2$  glassy layers batteries and energy storage, *J. Electrochem. Soc.* 156 (2009) A27.

[267] A. Sakuda, H. Kitaura, A. Hayashi, K. Tadanaga, M. Tatsumisago, All-solid-state lithium secondary batteries with oxide-coated  $\text{LiCoO}_2$  electrode and  $\text{Li}_2\text{S}-\text{P}_2\text{S}_5$  electrolyte, *J. Power Sources* 189 (2009) 527.

[268] H. Kitaura, A. Hayashi, K. Tadanaga, M. Tatsumisago, High-rate performance of all-solid-state lithium secondary batteries using  $\text{Li}_4\text{Ti}_5\text{O}_{12}$  electrode, *J. Power Sources* 189 (2009) 145.

[269] H. Kitaura, A. Hayashi, K. Tadanaga, M. Tatsumisago, A novel all-solid-state thin-film-type lithium-ion battery with *in situ* prepared positive and negative electrode materials, *J. Electrochem. Soc.* 156 (2009) A114.

[270] K. Takada, T. Inada, A. Kajiyama, H. Sasaki, S. Kondo, M. Watanabe, M. Murayama, R. Kanno, Solid-state lithium battery with graphite anode, *Solid State Ionics* 158 (2003) 269.

[271] Y. Nishio, H. Kitaura, A. Hayashi, M. Tatsumisago, All-solid-state lithium secondary batteries using nanocomposites of  $\text{NiS}$  electrode/ $\text{Li}_2\text{S}-\text{P}_2\text{S}_5$  electrolyte prepared via mechanochemical reaction, *J. Power Sources* 189 (2009) 629.

[272] A. Hayashi, Y. Nishio, H. Kitaura, M. Tatsumisago, Novel technique to form electrode–electrolyte nanointerface in all-solid-state rechargeable lithium batteries, *Electrochem. Commun.* 10 (2008) 1860.

[273] A. Hayashi, R. Ohtsubo, M. Tatsumisago, Electrochemical performance of all-solid-state lithium batteries with mechanochemically activated  $\text{Li}_2\text{S}-\text{Cu}$  composite electrodes, *Solid State Ionics* 179 (2008) 1702.

[274] M. Nagao, H. Kitaura, A. Hayashi, M. Tatsumisago, Characterization of all-solid-state lithium secondary batteries using  $\text{Cu}_x\text{Mo}_6\text{S}_{8-y}$  electrode and  $\text{Li}_2\text{S}-\text{P}_2\text{S}_5$  solid electrolyte, *J. Power Sources* 189 (2009) 672.

[275] A. Hayashi, A. Inoue, M. Tatsumisago, Electrochemical performance of  $\text{NiP}_2$  negative electrodes in all-solid-state lithium secondary batteries, *J. Power Sources* 189 (2009) 669.

[276] T. Inada, T. Kobayashi, N. Sonoyama, A. Yamada, S. Kondo, M. Nagao, R. Kanno, All solid-state sheet battery using lithium inorganic solid electrolyte, thio-LISICON, *J. Power Sources* 194 (2009) 1085.

[277] K. Kiyohara, T. Sugino, K. Asaka, *J. Chem. Phys.* 132 (2010) 144705.

[278] G. Ferguson, L.A. Curtiss, *Applications of Molecular Modeling to Challenges in Clean Energy*, ACS Symposium Series, vol. 1133, 2013, pp. 217–233 (Chapter 12). <http://dx.doi.org/10.1021/bk-2013-1133.ch012>; ISBN 13: 9780841228207; eISBN: 9780841228214; Publication Date (Web), June 3.

[279] O.E. Geiculescu, Y. Xie, R. Rajagopal, S.E. Creager, D.D. DesMarteau, Fluorinated materials for energy conversion, in: G. Nakajima (Ed.), *Fluorinated Electrolytes Based on Lithium Salts of Strong Bronsted Acids*, first ed., Elsevier Science, 2005 (Chapter 10). Print Book ISBN: 9780080444727; eBook ISBN: 9780080531786; Released on 20 May.

[280] D.T. Hallinan Jr., N.P. Balsara, Polymer electrolytes, *Annu. Rev. Mater. Res.* 43 (2013) 503.

[281] D.M. Trombly, V. Pryamitsyn, V. Ganesan, Surface energy and self-assembly of block copolymers on grafted surfaces, *Phys. Rev. Lett.* 107 (2011) 148304.

[282] M.A. Ratner, D.F. Shriver, Ion transport in solvent-free polymers, *Chem. Rev.* 88 (1988) 109.

[283] J.R. MacCallum, C.A. Vincent, *Polymer Electrolyte Reviews* 1, Elsevier Applied Science, London, 1987. ISBN 1851660712, 9781851660711.

[284] M. Armand, Polymer electrolytes, *Annu. Rev. Mater. Sci.* 16 (1986) 245.

[285] S. Passerini, M. Montanino, G.B. Appetecchi, Lithium polymer batteries based on ion liquids, in: Vikas Mittal (Ed.), *Polymers for Energy Storage and Conversion*, John Wiley and Scriverner Publishing, USA, 2013.

[286] M.J. Park, I. Choi, J. Hong, O. Kim, Polymer electrolytes integrated with ionic liquids for future electrochemical devices, *J. Appl. Polym. Sci.* 129 (2013) 2363.

[287] M. Armand, F. Endres, D.R. MacFarlane, H. Ohno, B. Scrosati, Ionic-liquid materials for the electrochemical challenges of the future, *Nat. Mater.* 8 (8) (2009) 621.

[288] M. Galiński, A. Lewandowski, I. Stepienak, Ionic liquids as electrolytes, *Electrochim. Acta* 51 (26) (2006) 5567.

## Appendix: list of acronyms

### Chemicals

#### Standard solvents

Acetonitrile	ACN
$\gamma$ -Butyrolactone	$\gamma$ -BL
Diethyl carbonate	DEC
Dimethyl carbonate	DMC
Dimethyl ether	DME
Dimethyl formamide	DMF
Dimethylsulfoxide	DMSO
Ethylene carbonate	EC
Ethyl methyl carbonate	EMC
Methylformate	MF
Nitromethane	NM
Propylene carbonate	PC
Tetrahydrofuran	THF
Vinylene carbonate	VC

#### Fluorinated carbonates

1,2-Difluoro-1,2-dimethyl ethylene carbonate	DFDMEC
Difluoromethyl ethyl carbonate	DFMEC
Fluorodimethyl carbonate	FDMC
Fluoroethylene carbonate	FEC
Fluoromethyl (difluoromethyl) carbonate	FMDFMC
Fluoroneopentyl ethylene carbonate	FNPEC

Fluoropropylene carbonate	FPC
2,2,2-Trifluorodiethyl carbonate	TFDEC
<i>Sulfones</i>	
Butylsulfone	BS
Ethyl (methyl-ethoxy-ethoxy) sulfone	EMEES
Ethyl (methyl-ethoxy) sulfone	EMES
Ethyl methyl sulfone	EMS
Ethyl vinyl sulfone	EVS
1-Fluoro-2-(methyl sulfonyl) benzene	FS
Methyl (methyl ethoxy) sulfone	MMES
1-Methyl (trimethylene) sulfone	MTrMS
Trifluoropropyl methyl sulfone	TFPMS
Tetramethylene	TMS
Trimethylene sulfone	TrMS
<i>Nitriles</i>	
Adiponitrile	ADN
Glutaronitrile	GLN
Sebaconitrile	SEN
<i>Lithium salt</i>	
Lithium 3-fluoro-1,2-benzenediolato (2-)O,O' (oxalate) borate	FLBDOB
Lithium bis(croconato) borate	LBCB
Lithium [1,2-benzenediolato(2-)O,O'-oxalate] borate	LBDOB
Lithium [croconato salicylato(2-)] borate	LCSB
Lithium dodecafluorododecaborate	Li <sub>2</sub> DFB
Lithium difluorooxalateborate	LiDFOB
Lithium fluoroalkylborate	LiFAB
Lithium (malonate oxalate) borate	LiMOB
Lithium oxalyldifluoroborate	LiODFB
<i>Alkyl phosphates</i>	
Bis(2,2,2-trifluoroethyl)methyl phosphate	BMP
Diphenyloctyl phosphate	DPOF
(2,2,2-Trifluoro)diethyl phosphate	TDP
Triethyl phosphate	TEP
Tri(2,2,2-trifluoroethyl) phosphate	TFP
Trimethyl phosphate	TMP
<i>Alkyl phosphonates</i>	
Dimethyl(2-methoxyethoxy)methyl phosphonate	DMMEMP
Dimethyl methyl phosphonate	DMMP
<i>Hydrofluoroethers</i>	
Methyl nonafluorobutyl ether	MFE
2-Trifluoromethyl-3-methoxyperfluoropentane	TMMP
2-(Trifluoro-2-fluoro-3-difluoropropoxy)-3-difluoro-4-fluoro-5-trifluoropentane	TPTP

*Fluorinated esters*

Methyl difluoroacetate	MFA
------------------------	-----

*Ionic liquid cations*

1,2-Diethyl-3,4(5)-dimethylimidazolium	DEDMI
1,2-Dimethyl-3-propylimidazolium	DMPI
1-Ethyl-3-methyl imidazolium	EMI
Tetraethyl ammonium	Et <sub>4</sub> N
<i>N</i> -Ethyl- <i>N</i> -methyl morpholinium	MORP <sub>12</sub>
<i>N</i> -Methyl- <i>N</i> -propyl piperidinium	PIP <sub>13</sub>
<i>N</i> -Butyl- <i>N</i> -methyl piperidinium	PIP <sub>14</sub>
<i>N</i> -Methyl- <i>N</i> -pentyl piperidinium	PIP <sub>15</sub>
<i>N</i> -Hexyl- <i>N</i> -methyl piperidinium	PIP <sub>16</sub>
<i>N</i> -Ethyl- <i>N</i> -methyl piperidinium	PIP <sub>17</sub>
<i>N</i> -Methyl- <i>N</i> -octyl piperidinium	PIP <sub>18</sub>
<i>N</i> -Butyl- <i>N</i> -ethyl piperidinium	PIP <sub>24</sub>
<i>N</i> -Methyl- <i>N</i> -pentyl piperidinium	PIP <sub>25</sub>
<i>N,N</i> -Dimethyl pyrrolidinium	PYR <sub>11</sub>
<i>N</i> -Methyl- <i>N</i> -propyl pyrrolidinium	PYR <sub>13</sub>
<i>N</i> -Butyl- <i>N</i> -methyl pyrrolidinium	PYR <sub>14</sub>
<i>N</i> -Methyl- <i>N</i> -pentyl pyrrolidinium	PYR <sub>15</sub>
<i>N</i> -Hexyl- <i>N</i> -methyl pyrrolidinium	PYR <sub>16</sub>
<i>N</i> -Ethyl- <i>N</i> -methyl pyrrolidinium	PYR <sub>17</sub>
<i>N</i> -Methyl- <i>N</i> -octyl pyrrolidinium	PYR <sub>18</sub>
<i>N</i> -Decyl- <i>N</i> -methyl pyrrolidinium	PYR <sub>1,10</sub>
<i>N</i> -Ethoxymethyl- <i>N</i> -methyl pyrrolidinium	PYR <sub>1(2O<sub>1</sub>)</sub>
<i>N</i> -Ethoxyethyl- <i>N</i> -methyl pyrrolidinium	PYR <sub>1(2O<sub>2</sub>)</sub>
Trimethylhexylammonium	TMHA

*Ionic liquid anions*

Bis(pentafluoroethanesulfonyl)imide	BETI
Trifluoromethanesulfonate	CF <sub>3</sub> SO <sub>3</sub>
Bis(fluorosulfonyl)imide	FSI
(Nonafluorobutanesulfonyl)(trifluoromethanesulfonyl)imide	Im <sub>14</sub>
Bis(trifluoromethanesulfonyl)imide	TFSI
(Trifluoromethanesulfonyl)(trifluoromethane)acetamide	TSAC

*Polymers*

Poly(acrylonitrile)	PAN
Poly(ethylene glycol dimethyl ether)	PEGDME
Poly(ethylene oxide)	PEO
Poly(methyl methacrylate)	PMMA
Poly(propylene oxide)	PPO
Poly(vinylidene difluoride)	PVdF
Poly(vinylidene difluoride)-hexa fluoropropylene	PVdF-HFP

# Materials and technologies for rechargeable lithium–sulfur batteries

5

*N. Azimi<sup>1</sup>, Z. Xue<sup>1</sup>, S.S. Zhang<sup>2</sup>, Z. Zhang<sup>1</sup>*

<sup>1</sup>Argonne National Laboratory, Argonne, IL, USA; <sup>2</sup>U.S. Army Research Laboratory, Adelphi, MD, USA

## 5.1 Introduction

In recent years, there has been renewed interest in developing advanced batteries toward application for hybrid, plug-in hybrid, and electric vehicles. Most of this interest has focused on lithium-ion (Li-ion) batteries based on a lithium transitional metal oxide as the cathode and a carbon material as the anode. Due to the limited theoretical capacities of  $\text{Li}^+$  ion intercalation materials, the Li-ion battery cannot offer a suitably long driving range for pure electric vehicles (PEVs). To compete with gasoline-based vehicles, new batteries with higher energy density and lower cost are required for the development of next-generation electric vehicles [1–3]. In theory, this can be met by the conversion cathode materials, which show more than triple energy density of the  $\text{Li}^+$ -ion intercalation cathode materials.

Lithium–sulfur (Li–S) batteries are a very appropriate candidate, and recently have received considerable interest due to their high theoretical energy density of about 2600 W h/kg [4–9]. The operation of the Li–S battery is based on multiple redox reactions between the metallic lithium and elemental sulfur, which can be described by an overall reaction (Equation (5.1)):



The sulfur cathode is typically composed of elemental sulfur, a conducting agent, and a binder, which are coated on an aluminum current collector. The cathode is separated from the Li anode by a separator soaked with an organic electrolyte. Despite the high theoretical energy density, the Li–S battery is faced by many technological barriers such as rapid capacity fading and low coulombic efficiency, which are mainly due to the loss of sulfur active material during repeated charging and discharging, caused by the dissolution of lithium polysulfides (PS, having a general formula of  $\text{Li}_2\text{S}_n$ ) in the organic electrolyte and the resulting side reactions with the electrolyte solvents and the lithium anode [4–9].

## 5.2 Fundamental chemistry of lithium–sulfur (Li–S) battery

### 5.2.1 Properties of sulfur

Sulfur is the seventeenth richest element in the Earth's crust. In nature, the most common form is cyclic octasulfur ( $S_8$ ), followed by the cyclic  $S_{12}$  allotrope. Sulfur has a melting point of 112.8 °C (rhombic) or 119.0 °C (monoclinic), a boiling point of 444.6 °C, a gravity density of 2.07 g/cm<sup>3</sup> (rhombic) or 1.957 g/cm<sup>3</sup> (monoclinic) at 20 °C, and sublimes easily. It is a pale yellow, brittle, odorless solid, which is insoluble in water but highly soluble in carbon disulfide. In the molten state, sulfur exhibits a unique viscosity-temperature correlation. With an increase in temperature, the viscosity of sulfur gradually decreases, followed by a significant increase between 160 and 190 °C due to the ring-opening polymerization of the  $S_8$ , and decreases again at higher temperatures due to the depolymerization of PS chains. This behavior has been widely used to impregnate elemental sulfur into the porous materials such as carbon to synthesize sulfur–carbon composite materials [9].

### 5.2.2 Voltage characteristic of Li–S battery

Figure 5.1 shows a typical discharge and charge profile for the first cycle of a Li–S cell. The discharge process can be divided into four stages [9–11].

**Stage 1:** Elemental sulfur is reduced to form  $Li_2S_8$ , which is highly soluble in organic electrolyte and, therefore, dissolves into the liquid electrolyte.

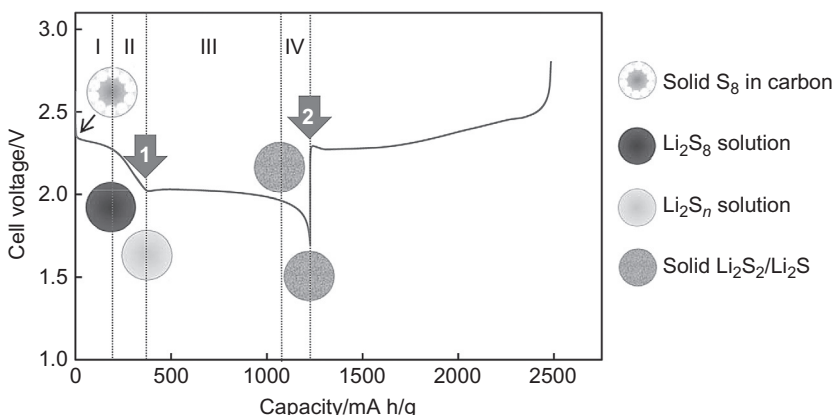


**Figure 5.1** A typical discharge and charge voltage profile of the first cycle of a Li–S cell. Reproduced from Ref. [9]. Copyright Elsevier. Reproduced with permission.

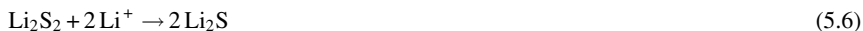
**Stage 2:** The dissolved  $\text{Li}_2\text{S}_8$  is reduced to different order PS with a  $4 \leq n \leq 8$  in  $\text{Li}_2\text{S}_n$ , which are still soluble in the electrolyte. During this stage, the cell’s voltage linearly decreases and the solution’s viscosity gradually increases.



**Stage 3:** The soluble PS are reduced to the insoluble lithium disulfide ( $\text{Li}_2\text{S}_2$ ) or lithium sulfide ( $\text{Li}_2\text{S}$ ), which accumulates on the carbon surface in the cathode, forming an insulating passivation layer. This stage corresponds to the second voltage plateau and contributes to the major capacity of the Li–S cell.



**Stage 4:** The final discharging step relates to a solid–solid reduction from the insoluble  $\text{Li}_2\text{S}_2$  to insoluble  $\text{Li}_2\text{S}$ . This stage is reflected by a steep voltage decline in the discharging profile [12].

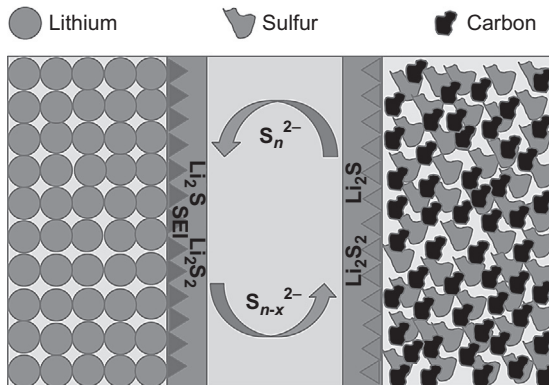


The voltage profile in charging is more complicated than that in discharging due to the redox shuttle of dissolved PS and the poor nucleation of elemental sulfur. Typically, the charging voltage shows a sharp rise at the very beginning and two shallow plateaus, ended by a sharp increase, as shown in Figure 5.1. The initial sharp rise is due to the polarization of the  $\text{Li}_2\text{S}$  passivation layer on the cathode surface and the following shallow dip is due to the depolarization by the electrochemical oxidation of insoluble  $\text{Li}_2\text{S}$  to soluble PS. Two major voltage plateaus are attributed to the oxidation of short- to long-chain PS and of long-chain PS to elemental sulfur, respectively. The last sharp increase in the voltage may not appear when the redox shuttle of PS is severe or the nucleation of elemental sulfur is difficult.

### 5.2.3 Redox shuttle phenomena

The dissolution of PS is proven to facilitate the electrochemical reaction of insulating sulfur species. However, this can cause severe redox shuttle between the sulfur cathode and the Li anode, which results in low coulombic efficiency for charging and fast self-discharge for storage. As mentioned above, in the charging step, long-chain PS are formed, which are highly soluble in the organic electrolyte. The PS can diffuse to the Li anode surface, and are either electrochemically reduced on the anode or chemically react with metallic lithium to regenerate short-chain PS. The formed short-chain PS diffuse back to the sulfur cathode surface and get oxidized to long-chain PS again (Figure 5.2). These parasitic reactions cause severe problems such as reducing charging coulombic efficiency, corroding the Li anode, and polarizing the Li anode once the insoluble  $\text{Li}_2\text{S}$  and  $\text{Li}_2\text{S}_2$  are formed and deposited on the Li surface [9].

**Figure 5.2** Schematic diagram of the redox shuttle of PS in Li–S battery.



## 5.3 Problems and challenges

### 5.3.1 Sulfur cathode

There are several problems in relation to the sulfur cathode in the Li–S batteries. Because sulfur is an electrical insulator, high amounts of conductive carbon are needed to promise reasonable utilization of the sulfur active material. However, sulfur content of at least 70% is required to achieve the high energy density of the Li–S battery.

In addition, the insoluble discharge products ( $\text{Li}_2\text{S}_2$  and  $\text{Li}_2\text{S}$ ) accumulate on the cathode after the battery is fully discharged. Because they are insulating, this can result in the formation of a passivation layer on the electrode and reduce the utilization of sulfur active material. When the Li–S battery is discharged at high current rates, elemental sulfur may be directly reduced into insoluble  $\text{Li}_2\text{S}$ . These  $\text{Li}_2\text{S}$  deposit on the carbon surface and prevent the contact of unreacted sulfur with the reaction sites (carbon), which significantly reduces the utilization of sulfur active material and leads to low capacity.

Another challenge is the significant volumetric change of about 79% in the conversion process between elemental sulfur and lithium sulfide occurring during cycling of the Li–S battery. Due to the repeated dissolution and precipitation of the sulfur active material, the structure of the cathode may be degraded, leading to fast capacity fading. By trapping sulfur into porous carbon, the pores of carbon matrix can provide extra buffer for the expansion and contraction of sulfur, which can benefit the cycling stability.

The next problem is the formation of voids in the early stage of discharge due to the dissolution of the long-chain PS into the organic electrolyte. Conventional binders, such as poly(vinylidene fluoride) (PVDF), which is widely used in the state-of-art Li-ion batteries, swell in the organic electrolyte and cannot retain the porous structure of the cathode, leading to capacity fading of the Li–S batteries [13–15].

### 5.3.2 *Lithium anode*

The main problems with the Li anode in the Li–S battery are the corrosion, low coulombic efficiency, and rough morphology of the Li plating, which are related to the parasitic reactions with dissolved PS. The lithium reacts with both PS and organic electrolyte solvents. These reactions consume Li metal and form an unwanted passivation layer, which as a result leads to the capacity fading of Li–S cells. In addition, the reaction between the dissolved PS and the Li anode has been recognized as the most important factor in initializing thermal runaway of the Li–S battery at high temperatures [16–18].

### 5.3.3 *Electrolyte*

The requirements for the electrolytes used in the Li–S battery include high ionic conductivity, moderate PS solubility, low viscosity, wide electrochemical window, good chemical stability against Li, and reliable safety. However, none of a single organic solvent can satisfy all those requirements. A practical solution is to optimize the electrolyte formula by a solvent mixture and an additive. As for the salt, the chemical compatibility with PS is the highest priority. Conventional salts used in Li-ion batteries such as LiPF<sub>6</sub>, LiBOB, and LiBF<sub>4</sub> cannot be used in the Li–S batteries due to side reactions with PS. LiN(SO<sub>2</sub>CF<sub>3</sub>)<sub>2</sub> and LiSO<sub>3</sub>CF<sub>3</sub> are among the best salts for the Li–S battery because they are chemically stable with PS and capable of forming a stable protective film on the Li surface [3,19].

### 5.3.4 *Self-discharge*

Due to the dissolution of elemental sulfur and high-chain PS in liquid electrolyte as well as resulting reactions with the Li anode, Li–S batteries suffer from severe self-discharge, which is affected by the electrolyte composition and the storage temperature. There have been only a few studies on the self-discharge behavior of Li–S batteries. Ryu *et al.* reported that stainless steel is not appropriate for the current collector of the Li–S cells. By analyzing the current collector after storage, they concluded that the self-discharge of the Li–S battery is related to the corrosion of the stainless current collector and the reaction of the dissolved elemental sulfur with the Li anode, of which the latter results in the formation of PS such as Li<sub>2</sub>S<sub>n</sub> on the Li surface [20].

## 5.4 Current advances in the Li–S battery

### 5.4.1 *Sulfur active materials*

To overcome the challenges stated above, many efforts have been dedicated to improving the performance of the Li–S battery by enhancing the cathode properties. The development of the sulfur cathode materials can be divided into several

categories: sulfur–carbon composite, sulfur–graphene composite, and sulfur–polymer composite.

#### 5.4.1.1 *Sulfur–carbon composite*

During the past decades, various kinds of sulfur–carbon (S–C) composites have been developed with the aim to reduce the PS diffusion out of the cathode and to increase the conductivity of the electrode. Early work in this area was performed by Shim *et al.* [21], who reported that more than 10% carbon black is necessary to meet the cathode conductivity. The capacity fading was influenced by the carbon content of the electrode. An increase in the carbon content of the cathode generally resulted in higher initial capacity but faster capacity fading. Another example is the composite based on a highly porous carbon (HPC) material with good conductivity and high-specific surface area ( $1500\text{ m}^2/\text{g}$ ). After using HPC as the conductive matrix and adsorbent agent for PS, the Li–S cell presented a capacity of 770 mA h/g at 110 cycles [22].

A novel concept on the S–C composite is the nanostructured polymer-modified (polyethylene glycol) mesoporous carbon sulfur composites (CMK-3/S nanocomposite) as reported by Ji *et al.* [23]. In this composite, the close contact between carbon frameworks and sulfur increases the utilization of sulfur active material, and the nanopores accommodate volume changes of the sulfur species during cycling. Furthermore, the polymer coating on the surface of the composite prevents the PS from diffusing out of the composite particles. This approach proves to be very effective for improving the performance of the Li–S battery with low sulfur-loading cathode. However, this strategy is still not satisfactory for those with high sulfur-loading cathode.

It has been reported [8] that the pore size considerably affects the voltage profile and cycling performance of the Li–S cell. For example, the S–C composites based on a mesoporous or macroporous carbon show the normal two voltage plateaus, whereas those based on the microporous carbon exhibit only one voltage plateau. It is believed that the  $S_8$ -ring structure of elemental sulfur is changed in the microporous carbon due to the strong chemoabsorption.

Carbon nanotubes offer a great opportunity for the design of S–C composites, in which the carbon nanotubes not only trap PS but also serve as a reservoir for the redox reaction of PS. An example is given by Ji *et al.*, who encapsulated sulfur within the porous carbon nanofibers (CNFs) [24]. Using this material as the cathode, both the capacity retention and rate capability of the Li–S battery are improved. SEM observation shows that the uniform distribution of sulfur remains even after 30 cycles because the sulfur species are trapped within the carbon nanotubes.

Zheng *et al.* [25] reported about a novel conductive sulfur-containing nanocomposite cathode material, which was prepared by heating a mixture of sublimed sulfur and multiwalled carbon nanotubes (MWNTs) in certain conditions. The Li–S cell containing this type of cathode shows considerable improvement in the capacity retention and prevents redox shuttle behavior, which is attributed to the fact that the MWNTs not only strongly adsorb the sulfur and resulting PS within the nanotubes but also are an excellent electronic conductor. A similar result was demonstrated by Ahn *et al.* [26], who synthesized a homogeneous sulfur–MWCNTs composite and found that the

resulting Li–S cell exhibited outstanding performance with an initial-specific capacity of 1355 mA h/g and much improved cell life as compared with the same cells without MWCNTs. The SEM images reveal that the sulfur particles are well wrapped by the highly conductive MWCNTs, which contributes to the greatly improved cycling performance of the Li–S battery.

#### 5.4.1.2 *Sulfur–graphene composite*

Graphene is a two-dimensional crystalline allotrope of carbon; it consists of planar sheets of carbon atoms and has high electrical conductivity. Due to the superior electrical conductivity, high-specific surface area of over 2600 m<sup>2</sup>/g, and excellent chemical tolerance, graphene has attracted considerable attention in the research of electrochemical energy storage [27]. A functionalized graphene–sulfur nanocomposite (FGSS) with sandwich-like architecture has been investigated as the cathode material for the Li–S batteries, which led to a Li–S cell with 84% of capacity retention after 100 cycles [28]. Wang *et al.* further wrapped the sulfur–graphene composite with poly(ethylene glycol) (PEG), finding that the graphene and PEO play synergistic roles in trapping PS and accommodating the volume expansion of sulfur species. This composite led to a Li–S cell having a specific capacity of up to 600 mA h/g over more than 100 cycles [29].

In addition, Li *et al.* [30] obtained excellent cycling performance by coating a reduced graphene oxide (RGO) onto the S–C nanocomposite. The Li–S cell with this cathode material showed a specific capacity of 667 mA h/g and a coulombic efficiency of 96% at 0.95 °C even after 200 cycles. This excellent performance is partially attributed to the strong adsorption of PS on the RGO coating layer in addition to the highly conductive carbon framework that efficiently prevents the diffusion of PS out of the cathode structure. Overall, the sulfur–graphene composite functions in a very similar manner to the S–C composites. The only difference is that the graphene can be chemically functionalized to strengthen the adsorption for PS.

#### 5.4.1.3 *Sulfur–polymer composite*

The electrical insulation of elemental sulfur and its reduction products is one of the major challenges that must be overcome to assure the high energy and power densities of the Li–S battery. Conducting carbon in the S–C composite and the sulfur cathode only makes electrical connection between sulfur species/particles. In order to further enhance the electrical conductivity of sulfur active materials, more intimate connection between the sulfur active material and the supporting conductive network can be established by attaching sulfur active species onto conductive polymer backbones or encapsulating sulfur active species within conductive polymer shells.

##### Sulfurized polyacrylonitrile

Polyacrylonitrile (PAN) is an excellent precursor for the conductive polymer of sulfur–polymer composites. An *in situ* dehydrogenation, cyclization, and sulfurization process has been employed to produce the so-called sulfurized polyacrylonitrile

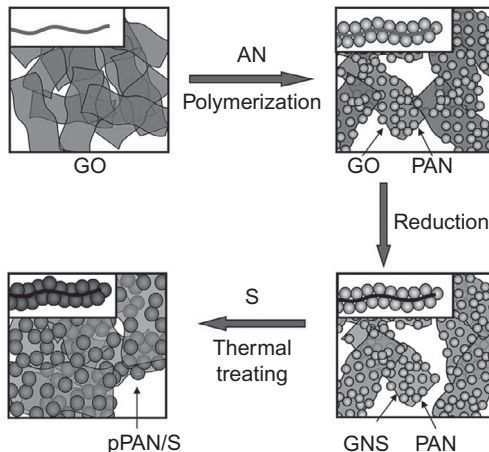
(SPAN). The SPAN materials have comparable specific capacities with today's state-of-the-art S-C composite, and are compatible with the Li-ion battery electrolytes based on  $\text{LiPF}_6$  salt and carbonate-based solvents [31,32]. The rate capability of SPANs can be further improved by the incorporation of MWCNTs, in which the MWCNTs enhance the structural stability and electronic conductivity of SPANs [33,34]. In the same line of work, a pyrolyzed PAN–sulfur–graphene nanosheet (pPAN-S-GNS) composite was prepared by impregnating sulfur into a PAN–GNS composite synthesized by *in situ* polymerization of acrylonitrile and chemical reduction of graphene oxide (Figure 5.3) [35]. With 4 wt.% GNS added, the composite showed a specific capacity of 800 mA h/g at relatively high C-rates (up to 6 °C) and a 99.9% of coulombic efficiency. The excellent performance is attributed to the three-dimensional GNS networks that enhance electronic conductivity and facilitate distribution of the active material in the composite.

### Polypyrrole

Polypyrrole (PPy) is a well-known conductive polymer that has been studied to make the conductive sulfur–polypyrrole (S–PPy) composite. The S–PPy composite is typically synthesized via deposition of sulfur on preformed PPy nanowires [36], nanoparticles [37,38], or tubular microfibers [39]. With PPy acting as a sufficiently conductive matrix and facilitating the dispersion of sulfur within the network, the capacity retention remained moderate. Alternatively, the S–PPy composite can be synthesized via *in situ* polymerization of pyrrole monomer in the sulfur suspension, which generally leads to a core–shell structured composite [40–42]. The core–shell structured S–PPy composite shows higher cycling performance as compared with their PPy-supported counterparts, suggesting better electrical contact and more effective confinement of the soluble PS in the core–shell structured composite.

**Figure 5.3** Schematic diagram of the *in situ* polymerization and synthesis of the pPAN-S/GNS composite, in which the insets are cross-sectional views of the samples.

Reproduced from Ref. [35]. Copyright RSC Publishing. Reproduced with permission.



## Polyaniline

Chemical oxidation polymerization of aniline monomer in the presence of sulfur/MWCNT [43] or S–C composite [44] was used to synthesize polyaniline (PANI)-coated sulfur cathodes. The PANi coating enhances the electronic conductivity of the polymer-coated sulfur composites and, as a result, the capacity retention, coulombic efficiency, and rate capability are significantly improved as compared to the unmodified S–C and S–MWCNT composites. It is also noteworthy that the PANi coating effectively prevents the PS shuttle reaction by providing a secondary barrier between the sulfur active material and the electrolyte. Similar to other sulfur-conductive polymer composites, PANi in the composite provides a conductive media on which elemental sulfur is anchored [45–47]. In particular, PANi nanotubes behave as a flexible, three-dimensional network to accommodate the volume changes of sulfur active species during charging and discharging. The polar functional groups on the PANi backbone are believed to be favorable for retaining the soluble PS intermediates within the polymer matrix through electrostatic interactions, providing “molecular-level encapsulation” of sulfur [45].

## Polythiophene

As one of the important conductive polymers, polythiophene (PTh) was also studied to develop the sulfur–polymer composites. Core–shell structured S–PTh composites were prepared by chemical oxidation polymerization of thiophene [48,49] or 3,4-ethylene dioxythiophene (EDOT) [50] in the presence of sulfur. With sulfur encapsulated within PTh, the S–PTh composite forms a porous and conductive network, which greatly improves the utilization and cycling performance of sulfur [48]. The poly(3,4-ethylene dioxythiophene) (PEDOT) coating around the sulfur nanoparticles restricts the diffusion of PS into the electrolyte; this effectively reduces the redox shuttle effect and, therefore, self-discharge of the cell. Another example is a ternary composite consisting of CMK-3 mesoporous S–C composite as the core and poly(3,4-ethylenedioxythiophene)–poly(styrene sulfonate) (PEDOT:PSS) as the secondary confinement for sulfur [51]. This architecture was demonstrated to be capable of effectively trapping PS and, thereby, minimizing the loss of active material. At a C/5 current rate (1C=1673 mA/g), the discharge capacity remained over 600 mA h/g after 150 cycles with a notable coulombic efficiency of 97%.

It is evident that the conductive polymer coating on the surface of sulfur active cathode material, either being bare elemental sulfur or S–C composite, is beneficial in several ways to the successful development of composite sulfur cathodes. The proven benefits include increasing the electronic conductivity, facilitating sulfur distribution, alleviating PS dissolution, and the loss of sulfur active material during charge/discharge cycling.

### 5.4.2 Binder

In the first stage of discharge, elemental sulfur is first reduced to highly soluble  $\text{Li}_2\text{S}_8$ , which inevitably diffuses out of the cathode into the liquid electrolyte, leaving voids in the cathode. In the third stage of discharge, the short-chain PS diffuse back to the

cathode from the solution and are reduced to insoluble  $\text{Li}_2\text{S}_2$  and  $\text{Li}_2\text{S}$  on the carbon surface. These processes result in significant volume changes. The polymer binder that ensures the physical integrity of the cathode thus is needed to be capable of retaining the highly porous structure during the cycling process. Conventional binders such as PVDF fail to retain the structural integrity because they are swollen or gelled by the electrolyte solvents. On the other hand, due to the high reactivity of PS, polymers that contain functional groups susceptible to nucleophilic attack may not be appropriate for the binder of sulfur cathode.

Polymers such as Nafion [52], blend of polyvinyl pyrrolidone (PVP) and polyethyleneimine (PEI) [53], and cross-linked vinyl ethers [54] are shown to lead to good cycling performance of the Li–S battery. In several accounts, PEO was studied as the binder [55,56] and found to function similarly to the PEO coating on the sulfur cathode and polyethylene glycol dimethyl ether (PEGDME) solvent in the electrolyte, which trap PS and suppress the passivation of the cathode surface [56].

A class of water-based binders show promise in Li–S battery systems. Wang *et al.* [57] added chemically oxidized  $\beta$ -cyclodextrin ( $\beta$ -CD) into water-soluble carbonyl- $\beta$ -cyclodextrin (C- $\beta$ -CD), and used C- $\beta$ -CD as the binder for a SPAN-based cathode. As shown in Figure 5.4, compared with the PVDF and polytetrafluoroethylene (PTFE) binders, C- $\beta$ -CD was shown to assist the distribution of sulfur active material and improve the mechanical stability of the electrode upon cycling, leading to the improved cycling performance. Other water-soluble or water-dispersible binders include Na-alginate [58], polyacrylic acid (PAA) [59], poly(acrylamide-*co*-diallyldimethylammonium chloride) (AMAC) [60], styrene-butadiene rubber (SBR)-carboxymethyl cellulose (CMC) [61,62], and PTFE/CMC [63]. Demonstrated by AMAC binder [60], the water-based binders feature low swellability in the organic liquid electrolytes. As a result, during cycling these binders are able to retain the highly porous structure of the sulfur cathode, which leads to better capacity retention. Another well-studied water-soluble binder is gelatin-based natural polymer [64–69]. This binder is shown to be superior to the conventional PEO in terms of cycling performance and charge–discharge behavior in the Li–S battery. The functionalities in the gelatin polymer backbone were found to be helpful in dispersing the sulfur active material, improving adhesion as well as maintaining the structural stability of the electrode.

Polymer binder in the Li–S battery is more than an “adhesive” to ensure the mechanical integrity of the sulfur cathode. Given the many variations in the architecture and composition of the sulfur cathode and electrolyte, the physical and chemical stability of the polymer binders in the Li–S environment must be taken into account. An ideal binder for the Li–S battery should be able to not only endure the structural changes of the electrode, but also facilitate ion transport in the charge–discharge processes.

### 5.4.3 Electrolyte

Due to the high solubility of PS in the organic electrolytes and the high reactivity of PS with the electrolyte components, common electrolytes used in Li-ion batteries are not suitable for the Li–S battery. For example, Barchasz *et al.* [70] reported that carbonate

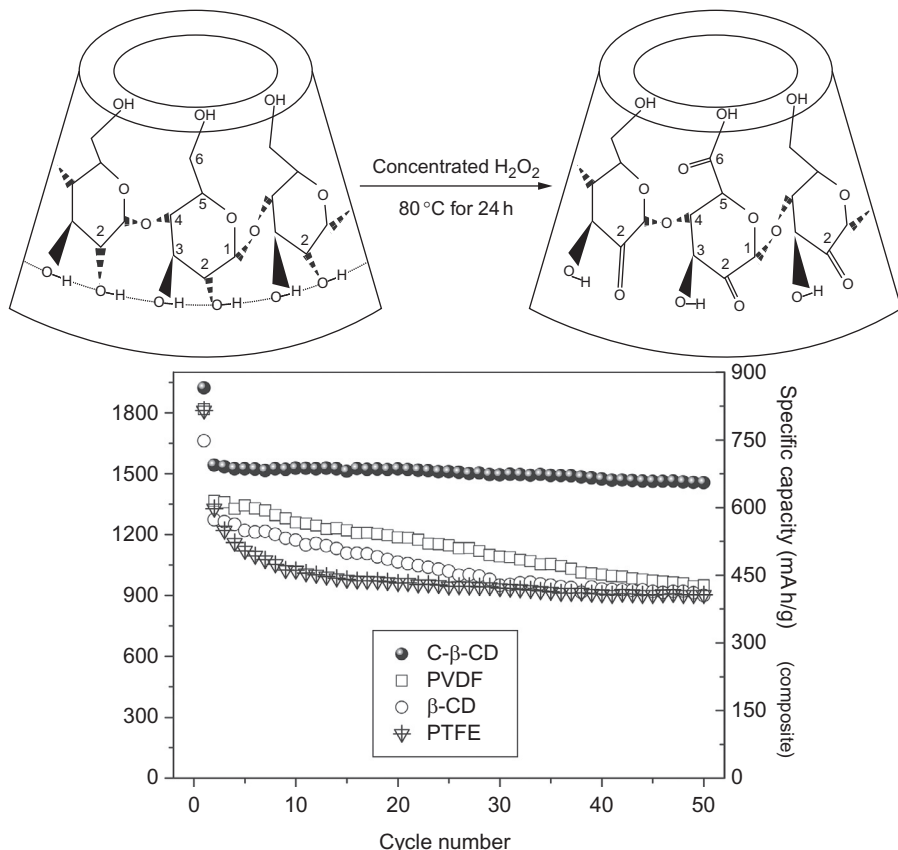


**Figure 5.4** Schematic reaction of  $\beta$ -CD with  $\text{H}_2\text{O}_2$  (top); cycle performance of cathodes with  $\beta$ -CD, C- $\beta$ -CD, PVDF, and PTFE binders at  $0.2\text{ }^\circ\text{C}$  (bottom).

Reproduced from Ref. [57]. Copyright WILEY-VCH Verlag GmbH & Co. KGaA. Reproduced with permission.

solvents severely react with PS, and therefore cannot be used in the electrolyte of the Li–S batteries. It is also reported [71] that in discharge, PS may precipitate out of the electrolyte in the forms of elemental sulfur and  $\text{Li}_2\text{S}_2$  or  $\text{Li}_2\text{S}$  due to the disproportionation, which not only clogs the pores of the separator but also makes these sulfur species electrochemically inactive. This results in the loss of sulfur active materials and the capacity fading of the Li–S battery. In view of the battery performance, an ideal electrolyte for the Li–S battery should be able to solvate and stabilize PS, and be capable of forming solid electrolyte interphase (SEI) on the Li surface to protect the Li anode from reaction with PS. Recent efforts on the Li–S battery electrolytes are summarized below.

#### 5.4.3.1 Solvent

Because carbonate solvents are chemically incompatible with the Li–S chemistry and the voltages for the charging of Li–S batteries are not more than 3 V, the linear and cyclic ethers seem to be the best choice for the solvent of Li–S battery electrolytes. Therefore, most of the studies have been focused on the ether solvents, including 1,2-dimethoxyethane (DME), 1,3-dioxolane (DOL), tetra(ethylene glycol)dimethyl ether (TEGDME), and their mixture. It is unlikely for a single solvent to satisfy all requirements for the Li–S battery electrolytes. A practical solution is to use a mixture of solvents and additives. Among common ethers, DME has good ability to dissolve elemental sulfur and PS, and to stabilize PS, whereas DOL is superior for forming the stable SEI to protect metallic Li from corrosion [72]. Therefore, the combination of DME and DOL has become the most popular solvent system for the Li–S battery electrolytes, and the electrolytes based on their mixture have been often employed as the baseline for the evaluation of new electrolytes.

As reported by Barchasz *et al.* [70], ether solvents offer interesting features, and it is possible to improve the electrochemical performance by combining different ether solvents. This is because ether chain length affects the solvation ability. Solvents DME, diethylene glycol dibutyl ether (DEGDBE), and DOL can dissolve PS to some extent, which induces the redox shuttle and leads to low coulombic efficiency. Because the electrolytes with these solvents often lead to fast active material precipitation and positive electrode passivation, PEGDME has been used to mitigate these problems. The incorporation of PEGDME is shown to alleviate the buildup of the electrode passivation layer and increase the length (capacity) of the second discharge voltage plateau. By using PEGDME as the cosolvent, a discharge capacity of about 1100 mA h/g was reached for the first discharge of a Li–S cell, and remained at 550 mA h/g after 10 cycles.

In this regard, Wang *et al.* [73] observed that sulfur has appropriate solubilities and undergoes a three-step reduction in the PEGDME-based electrolyte in comparison with the DOL/DME electrolyte in which sulfur shows a typical two-step reduction process. These results indicate that the discharge mechanism of the Li–S battery is quite complicated and involves many intermediate compounds. Shim *et al.* [21] studied PEGDME 250 and 500 solvents and found that these solvents reduced the redox shuttle of PS and, accordingly, increased the coulombic efficiency of the Li–S battery. In particular, the Li–S cell containing the PEGDME 500 electrolyte showed the best cycling behavior, yielding a specific capacity of more than 100 mA h/g after 600 cycles. This is attributed to the higher viscosity and better ability in stabilizing PS of these solvents. The viscosity generally influences the penetration of the liquid electrolyte into the sulfur cathode and the diffusion of the dissolved PS. Meanwhile, the electrolyte affects the disproportionation of PS and, further, the utilization of sulfur active material and the capacity retention of the Li–S battery.

Regarding the effect of solvent composition on the performance of the Li–S cell, Kim *et al.* [74] reported that the specific capacity and capacity retention are dependent on the nature of the solvents as well as the composition of mixed solvents. Because DOL solvent forms better SEI with the Li anode, the specific capacity of the Li–S

battery for a DOL solvent system is shown to increase with the content of DOL within a limited content range.

Ryu *et al.* [75] investigated the effect of temperature on the discharge behavior of the Li–S cell with TEGDME-based electrolytes. The specific capacity of the Li–S cell fell greatly as the temperature decreased to  $-10\text{ }^{\circ}\text{C}$  due to a dramatic increase in the viscosity of electrolyte, especially in the presence of PS. In addition, TEGDME freezes at  $-27\text{ }^{\circ}\text{C}$ , which also limits the operation temperature range of the TEGDME-based electrolytes. In order to reduce the electrolyte viscosity and enable the Li–S battery operating at low temperature, the TEGDME is often combined with solvents having low viscosity and low melting point, such as DME and DOL.

A major improvement was made by Azimi *et al.* [76], who developed an electrolyte based on an organofluorine solvent. It is shown that the organofluorine solvent effectively prevents the redox shuttle, leading to great improvement in the performance of the Li–S battery. More importantly, the organofluorine solvent participates in the formation of an SEI on the cathode surface, as confirmed by the electrochemical studies. The resulting SEI physically suppresses the diffusion of PS out of the cathode, and therefore improves the capacity retention and coulombic efficiency of the Li–S cell. The organofluorine electrolyte is also shown to prevent the self-discharge of the Li–S batteries, which is attributed to the SEI formed with the fluorinated solvent on both surfaces of the sulfur cathode and Li anode. It is believed that the SEI on the sulfur cathode suppresses the diffusion of long-chain PS out of the cathode and the one on the Li anode prevents parasitic reactions between the dissolved PS and the metallic Li.

In the cycling of the Li–S battery, PS undergoes a series of reduction and oxidation reactions, and the chemical equilibriums in the electrolyte solution vary with the PS concentration [77]. As the PS concentration is determined by the amount of liquid electrolyte in the battery, there is an optimized electrolyte/sulfur (E/S) ratio for the cyclability of the Li–S cell system. The E/S ratio affects the cell’s performance through the viscosity of PS solution and the chemical stability of PS in the solution. It is shown that high PS concentration favors suppressing the disproportionation of PS but increases the viscosity of the solution, which oppositely affects the cycling performance of the Li–S battery; that is, the reduced disproportionation increases the utilization of sulfur active material, whereas the increased viscosity reduces the ionic conductivity of the electrolyte. Interaction of these two opposite effects leads to an optimized E/S ratio for each of the Li–S cell systems. From Li–S coin cells, Zhang obtained an optimized E/S ratio of 10 mL/g for a 0.25 M LiSO<sub>3</sub>CF<sub>3</sub>–0.25 M LiNO<sub>3</sub> DME:DOL (1:1 wt.) electrolyte. By using the optimized E/S ratio (10 mL/g), the Li–S cell with a cathode containing 77% sulfur and 2 mg/cm<sup>2</sup> sulfur-loading is shown to retain a specific capacity of 780 mA h/g after 100 cycles at 0.5 mA/cm<sup>2</sup> between 1.7 and 2.8 V.

Similar results were demonstrated by Choi *et al.* [78], who reported that a large amount of electrolyte (i.e., high E/S ratio) led to higher initial capacity but faster capacity fading. They explained that a high amount of electrolyte increased the utilization of sulfur active material through the dissolution of PS and, meanwhile, resulted in more loss of sulfur active material in the form of insoluble Li<sub>2</sub>S and Li<sub>2</sub>S<sub>2</sub> through the disproportionation of PS. They also showed that the Li–S cell had good capacity

retention when a small amount of electrolyte was used as long as the battery components (sulfur cathode, separator, and Li anode) could be properly wetted by the liquid electrolyte.

The effect of electrolyte composition on the cell performance for a TEGDME/DOL binary solvent system was investigated by Barchasz *et al.* [79]. It was shown that the best TEGDME/DOL ratio was around 15/85 by volume, which formed a high conductive electrolyte with good solvation ability for the PS and lithium bis(trifluoromethanesulfonyl) imide (LiTFSI). The presence of DOL was shown to improve the ionic conductivity and discharge capacity by reducing the electrolyte viscosity. However, high amount of DOL negatively affected the performance of the Li–S battery as the conductivity was severely decreased. This result suggests that the viscosity may not be the only factor to determine the ionic conductivity of the electrolyte. The dielectric constant and the donor number of the solvents seem not to be sufficient to explain the ionic conductivity and lithium salt's dissociation. A more reasonable explanation could be that the high amount of DOL promotes the disproportionation of PS, which produces neither soluble nor conductive elemental sulfur,  $\text{Li}_2\text{S}$  and  $\text{Li}_2\text{S}_2$ . Due to the precipitation, these sulfur species (disproportionation products) become electrochemically inactive and, meanwhile, clog the pores of the separator, resulting in low sulfur utilization and high polarization.

Lithium salt is shown to affect the electrochemical performance of the Li/S cells. In comparison with  $\text{LiCF}_3\text{SO}_3$ , LiTFSI provides higher ionic conductivity [79]. The concentration of lithium salts affects the ionic conductivity of the electrolyte through the salt dissociation, charge carrier number, and ionic mobility, which generally results in a maximum conductivity in a certain salt concentration region. A more recent work by Suo *et al.* [80] showed that when the salt concentration in a LiTFSI-TEGDME electrolyte is increased until reversed to a “solvent-in-salt” system, the  $\text{Li}^+$  ion transfer number is dramatically increased to 0.73, and the redox shuttle of PS is greatly reduced. Using such an electrolyte, the Li–S cell was able to retain over 800 mA h/g at 0.2 °C for 100 cycles with nearly 100% coulombic efficiency. The similar approach was pursued by Dokko *et al.* [81] who first made a glyme–Li salt molten complex and then mixed it with a nonflammable hydrofluoroether solvent (1,1,2,2-tetrafluoroethyl 2,2,3,3-tetrafluoropropyl ether (HFE)) to form a  $[\text{Li}(\text{glyme})_1][\text{TFSA}]/\text{HFE}$  electrolyte, which resulted in improved performances, including higher coulombic efficiency, better cycle stability, and higher rate capability.

#### 5.4.3.2 Ionic liquid

An ionic liquid typically consists of weakly Lewis acidic cations and weakly Lewis basic anions, and features nonflammability and involatility. Special significance of the ionic liquids in the Li–S battery is their weakly Lewis acidic cations, which are capable of stabilizing PS anions. Based on the “hard and soft (Lewis) acids and bases” (HSAB) theory, the cation of ionic liquid is a soft acid, and PS anion is a soft base, their combination leads to a stable compound (salt). In addition to stabilizing the PS anion, the ionic liquid also affects the mobility of PS anion (an redox shuttle issue) through the interaction between the ionic liquid cation and PS anion. The ionic liquids

have been used in Li–S batteries in two forms: (1) employing as an “ionic” solvent to dissolve a lithium salt, and (2) adding as an additive into the conventional liquid electrolyte.

Yuan *et al.* [82] reported a binary salt electrolyte based on a *N*-methyl-*N*-butyl-piperidinium bis(trifluoromethanesulfonyl) imide room temperature ionic liquid (PP14-RTIL) and a LiTFSI lithium salt. Cyclic voltammetry (CV) results showed that the RTIL electrolyte has a wide potential window of 5.2–0.15 V (vs. Li) and is chemically stable with metallic lithium and sulfur active materials. The Li–S cells using the ionic liquid electrolyte showed an initial capacity of 1055 mA h/g and retained a reversible capacity of 750 mA h/g after a few cycles.

In order to reduce the viscosity and increase the ionic conductivity of the ionic liquid electrolyte, Wang *et al.* [83] added a small amount of DME as the cosolvent into a *N*-methyl-*N*-propylpiperidinium bis(trifluoromethanesulfonyl)imide-LiTFSI (PP13-TFSI) ionic liquid electrolyte. It was observed that the PP13-TFSI/DME electrolyte afforded outstanding capacity retention and high coulombic efficiency for the Li–S cell. In a similar approach, Park *et al.* [84] made an ionic liquid electrolyte by mixing a *N,N*-diethyl-*N*-methyl-*N*-(2-methoxyethyl)ammonium bis(trifluoromethanesulfonyl)amide (DEME-TFSI) with a LiTFSI salt, and compared it with a 0.98 M LiTFSI/TEGDME liquid electrolyte. Results indicated that the ionic liquid electrolyte cell outperformed the liquid electrolyte cell. The performance improvement by the ionic liquid electrolyte is attributed to the fact that the ionic liquid suppresses the redox shuttle of PS, which results in a higher coulombic efficiency for the Li–S cell.

#### 5.4.3.3 Polymer electrolyte

Leakage and flammability are the intrinsic problems for all liquid electrolytes, and the severe redox shuttle of PS originates from the high solubility and fast diffusion of PS in the liquid electrolyte. For these reasons, polymer electrolytes have been proposed to overcome the problems of liquid electrolytes. Based on the composition and ionic conduction mechanism, the polymer electrolytes can be classified as the solvent-free solid polymer electrolyte (SPE) and gel polymer electrolyte (GPE).

#### Solid polymer electrolyte

Polyethylene oxide (PEO) is the most intensively studied polymer for solvent-free SPE, in which the Li<sup>+</sup> ions are solvated by the ether oxygen atoms in PEO chains and conducted through the segmental motion of the PEO chains [85]. The ionic conduction in such SPEs mainly occurs in the amorphous phase; therefore, an elevated temperature (>60 °C) is needed to retain sufficient conductivity. In this effort, Cairns [86] and Kim [87] independently studied PEO-based electrolytes for the Li–S cells, and showed that the Li–S cells had an high initial capacity of 1600 mA h/g, followed by fast fading in further cycling. This unsatisfactory performance can be attributed to the low ionic conductivity of the SPE and the insulating nature of elemental sulfur and its reduction products. Unlike in the liquid electrolytes, in the SPE the sulfur reduction products are unable to diffuse off the carbon surface; instead, they accumulate on the

carbon surface as an insulating passivation layer to block the outer sulfur from electrical contact with the carbon. As a result, the SPE Li–S battery suffers low utilization of sulfur active material and fast capacity fading. Shin *et al.* [88] found that ball-milling could effectively reduce the crystallinity of PEO and, therefore, improved the ionic conductivity of SPE. This led to a significant improvement in the specific capacity and capacity retention of the Li–S battery.

### Gel polymer electrolyte

In order to overcome the low ionic conductivity of solvent-free SPEs, PEO-miscible electrolyte solvent has been used as the plasticizer to promote the segmental motion of PEO chains. When the amount of the liquid plasticizer reaches a level where the ionic conduction is dominated by the liquid-in-polymer instead of the segmental motion of polymer chains, the SPE becomes a GPE. The GPE combines the advantages of the polymer electrolyte (high viscoelasticity) and liquid electrolyte (high ionic conductivity), and is of great significance in the Li–S batteries. The earliest practice for this concept was to plasticize the PEO-based SPE with a TEGDME solvent [89]; however, later the fluorinated polymer-based GPEs, such as those based on PVDF [90] and poly(vinylidenefluoride)-hexafluoropropylene (PVDF–HFP) copolymer [91], have been more intensively studied due to the easiness of *in situ* formation of these GPEs by activating a porous polymer membrane with a liquid electrolyte. The GPEs typically have an ionic conductivity ranging from  $10^{-4}$  to  $10^{-3}$  S/cm at room temperature, depending on the type and amount of liquid electrolyte. Interestingly, ionic liquid is found to be miscible with PVDF–HFP polymer and has been successfully prepared into a GPE, showing good thermal property and stability toward oxidation [92]. The Li–S cell with this GPE exhibited capacities comparable to the liquid electrolyte-based cells and had high coulombic efficiencies of over 95%, indicating that the GPE effectively suppresses the redox shuttle of PS.

### Composite polymer electrolyte

PEO-based composite electrolyte with inorganic fillers, such as  $\text{Al}_2\text{O}_3$  [87],  $\gamma\text{-LiAlO}_2$  [93], and  $\text{SiO}_2$  [94], have been developed for Li–S batteries. In this practice, Scrosati [95] used a nano- $\text{ZrO}_2$ -PEO- $\text{LiCF}_3\text{SO}_3$  membrane as the separator and  $\text{Li}_2\text{S}$  as the sulfur active material to assemble an all solid-state Li–S cell, in which the  $\text{Li}_2\text{S}$  is in the discharged state and can be coupled with the carbon or silicon anode material to build a metallic lithium-free Li-ion battery. The cell assembled this way delivered a specific capacity of 900 mA h/g at 90 °C and decreased to less than 400 mA h/g at 70 °C, clearly indicating the effect of ionic conductivity of the solid-state electrolyte. On the other hand, the cell had over 99% coulombic efficiency even at high temperatures, which validates the effectiveness of this solid-state electrolyte in preventing PS shuttling redox. Other composite gel polymer electrolytes (CGPEs) are based on a fluorinated polymer and an inorganic filler, such as the one consisting of a PVDF–HFP and a nanosized silicate [96] or mesoporous silica [97]. The CGPEs are typically made by first preparing a porous composite membrane and then gelling it with a liquid electrolyte. The incorporated inorganic filler is found to be capable of adsorbing PS,

being favorable for increasing coulombic efficiency and capacity retention over prolonged cycles. The CGPE can also be prepared with high filler content in favor of high conductivity and wettability. A composite membrane containing at least 50%  $\text{SiO}_2$  in high-molecular weight PEO has been made in the form of an electrode-supporting electrode-membrane assembly (EMA) [98], a freestanding membrane [98], or a coating on a conventional separator [99]. The high-filler content enables high uptake of liquid electrolyte or ionic liquid without dimensional shrinkage. However, the high amount of  $\text{SiO}_2$  adsorbs PS and makes these PS electrochemically inactive by trapping PS in the membrane, resulting in lower specific capacity.

### Ceramic solid-state electrolyte

Ceramic solid-state electrolyte is the most effective approach to avoid the PS dissolution and resulting redox shuttle. In this approach, nearly all efforts have been centered on the  $\text{Li}_2\text{S}-\text{P}_2\text{S}_5$  (LPS) family of solid electrolyte glasses, mainly because of their chemical compatibility with the sulfur cathode and metallic Li. Liang *et al.* assembled an all-solid-state Li–S cell by using a  $\text{Li}_3\text{PS}_4$  (namely a form of the  $3\text{Li}_2\text{S}-\text{P}_2\text{S}_5$  glass) as the solid electrolyte and a  $\text{Li}_3\text{PS}_{4+n}$  ( $n = 2 \sim 8$ ) as the cathode [100]. In their cells, nanostructured electrolyte and cathode materials allowed for intimate contact to reduce the particle boundary resistance and similar chemistry of the electrolyte and cathode materials allowed a favorable electrolyte–electrode interface to form. As a result, the all solid-state Li–S cell showed a capacity of 1200 mA h/g after 300 cycles at 60 °C. Thio-LISICON ( $\text{Li}_{3.25}\text{Ge}_{0.25}\text{P}_{0.75}\text{S}_4$ ), a version of the Ge-doped LPS glasses, has an ionic conductivity of  $2.2 \times 10^{-3}$  S/cm at 25 °C [101,102] and is demonstrated to be suitable for the solid-state electrolyte used in the Li–S battery. Hayashi *et al.* systematically studied the  $\text{Li}_2\text{S}-\text{P}_2\text{S}_5$  glass electrolytes by coupling it with sulfur/copper [103,104] or sulfur/carbon [105] composite cathodes. In particular, an all solid-state cell with sulfur/carbon composite cathode and  $\text{Li}_2\text{S}-\text{P}_2\text{S}_5$  electrolyte could be cycled in a wide temperature range from –20 to 80 °C. The cell performance remained above 800 mA h/g at ambient temperature for 200 cycles with coulombic efficiency of about 100%. By ball-milling to reduce the crystallinity and particle size of the electrode and electrolyte materials, an all solid-state  $\text{Li}_2\text{S}/\text{carbon}$  cell was shown to have a specific capacity of 700 mA h/g when cycled between 3.6 and 0.6 V at 25 °C [106].

#### 5.4.3.4 Electrolyte additives

With the aim to eliminate or reduce the above-mentioned obstacles of Li–S batteries, many electrolyte additives have been studied for improving the Li/S battery electrolytes. The functions of these additives include (1) protecting the Li anode, (2) enhancing the solubility and stability of PS, and (3) reducing the viscosity of the liquid electrolyte.

The most important finding is [107] that  $\text{LiNO}_3$  can remarkably inhibit the redox shuttle of PS. Using  $\text{LiNO}_3$  additive, Liang *et al.* showed that the Li–S cell had a high coulombic efficiency of 95% and discharge capacity of *ca.* 527 mA h/g after 50 cycles. It is believed that on a Li anode, the  $\text{LiNO}_3$  endorses the formation of a

passivation film composed of  $\text{Li}_x\text{NO}_y$  and  $\text{Li}_x\text{SO}_y$ , which prevents the electrochemical reduction of PS at the anode and the chemical reduction of PS by metallic Li. Because stripping of Li in the following discharging destroys the already-formed passivation film, new passivation film must be re-formed in the next charging. Thus,  $\text{LiNO}_3$  will be slowly consumed with the repeated cycling of the Li–S battery [108]. Beside the above, Zhang observed that  $\text{LiNO}_3$  might be reduced on the cathode at below 1.6 V, which adversely affected the cycling performance of the Li–S batteries [109], and concluded that the  $\text{LiNO}_3$  additive is helpful for the Li–S battery only when the irreversible reduction on the sulfur cathode is avoided. This can be done easily by raising the discharge cutoff voltage of the Li–S batteries above 1.7 V.

Lithium bis(oxalato) borate (LiBOB) has been studied as the electrolyte additive in a concentration range of 1–10 wt.% by Xiong *et al.* [12]. The Li–S batteries containing the LiBOB additive demonstrate improvement in both the discharge capacity and cycle performance, with a maximum discharge capacity of 1191 mA h/g when a 4 wt.% LiBOB was added. Based on the EIS and SEM analysis, this improvement is due to the formation of a passivating surface film on the Li anode, which reduces the parasitic reaction between PS and the Li anode.

In another study by Lin *et al.* [110],  $\text{P}_2\text{S}_5$  was shown to enhance the dissolution of PS and protect the Li anode. In the electrolyte,  $\text{P}_2\text{S}_5$  combines insoluble  $\text{Li}_2\text{S}$  and  $\text{Li}_2\text{S}_2$  to form soluble LPS complexes, which suppresses the precipitation of sulfur species out of the electrolyte. On the Li anode,  $\text{P}_2\text{S}_5$  combines with predeposited  $\text{Li}_2\text{S}$  to form a highly conductive  $\text{Li}_3\text{PS}_4$  passivation layer, which protects the Li anode from reactions with PS and, meanwhile, reduces the cell's polarization. As a result, both the specific capacity and capacity retention of the Li–S cell are significantly improved, which leads to a specific capacity of 800 mA h/g after 40 cycles.

#### 5.4.4 New concepts

In recent years, many new concepts have been proposed to improve the performance of Li–S batteries that include novel materials and innovative cell designs and are introduced below.

##### 5.4.4.1 Binder-free cathode

Zu *et al.* [111] introduced a binder-free, interwoven S–C cathode, in which a binder-free CNF paper was used as the current collector, and elemental sulfur was directly impregnated into the pores of CNFs. This cathode has the advantages of low manufacturing cost and high sulfur-loading in comparison to the conventional sulfur cathodes. The outstanding improvement of this cathode is because (1) the 3D interwoven structure of the CNF paper allows sulfur reactions within a confined environment and (2) CNFs offer a long and continuous electron conduction pathway. SEM and XRD analyses reveal that crystalline  $\text{Li}_2\text{S}$  species are found within the large inter-spaces of the 3D electrode after the first discharge, which avoids the formation of a dense passivation layer on the surface of the cathode. A Li–S battery with such a cathode exhibited an initial capacity of 1094 mA h/g after 80 cycles at a C/5 rate and

coulombic efficiencies of more than 98% with a sulfur loading of  $1.7 \text{ mg/cm}^2$ . After increasing the sulfur loading to  $5.1 \text{ mg/cm}^2$ , a stable reversible capacity of  $900 \text{ mA h/g}$  was obtained, making this battery configuration very promising for practical applications.

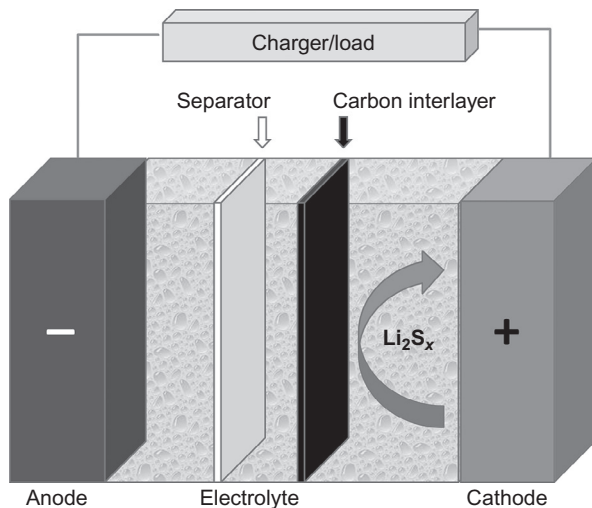
In another study, Hassoun *et al.* [112] assembled a new type of Li–S cell by starting with a carbon–lithium sulfide (C–Li<sub>2</sub>S) composite cathode. Cycling tests demonstrate that this cell has a good performance, high reversibility, and coulombic efficiency. It is verified by *in situ* XRD that the Li<sub>2</sub>S formed after each discharging step can be converted into sulfur in the following charge and reconverted back to Li<sub>2</sub>S again in the next discharge process. The Li<sub>2</sub>S–C cathode is further coupled with a tin–carbon composite by using a GPE composed of PEO, LiCF<sub>3</sub>SO<sub>3</sub>, and nano-ZrO<sub>2</sub> filler. The resulting tin/sulfur Li-ion cell showed a capacity of over  $500 \text{ mA h/g}$  at a current rate of C/20. Therefore, the Li<sub>2</sub>S–C composite offers an opportunity for the development of novel rechargeable Li-ion sulfur batteries, in which the highly reactive and unsafe lithium metal anode is replaced by a reliable tin–carbon composite.

Following the same principle, Fu *et al.* [113] reported a novel cathode configuration that was composed of pristine Li<sub>2</sub>S powder sandwiched between two layers of self-weaving, binder-free carbon nanotube (CNT) papers. Specific capacities of 680 and  $502 \text{ mA h/g}$  were obtained after 100 cycles at C/10 and 1C rates, respectively. The excellent performances of these cells are attributed to (1) efficient electron conduction within the sandwiched electrode, (2) fast ion transport through the nanospace within the carbon nanotube electrode, and (3) trapping of dissolved PS within the sandwiched electrode. In order to investigate the phase change of Li<sub>2</sub>S within the sandwiched cathode, *ex situ* XRD was performed. It was observed that in the initial stage, sharp peaks corresponding to the (111), (220), and (311) planes of Li<sub>2</sub>S were present, and these peaks almost disappeared after the first charge. The following discharge resulted in the reappearance of the peaks of crystalline Li<sub>2</sub>S. These observations confirm that the conversion between the crystalline Li<sub>2</sub>S particles and the amorphous PS or elemental sulfur reversibly takes place during the cycling of such Li–S cells.

#### 5.4.4.2 Carbon paper interlayer

As shown in Figure 5.5, Su and Manthiram [114] designed a new cell configuration by placing a bifunctional microporous carbon paper between the cathode and separator, which resulted in significant improvement in the capacity retention of the cell. This interlayer improves the cycling performances of the Li–S cells on the one hand by absorbing the PS diffused out of the cathode and on the other hand by providing additional reaction sites to accommodate the formed Li<sub>2</sub>S<sub>2</sub> or Li<sub>2</sub>S. It is shown that the pore size of carbon in the carbon interlayer strongly affects the effectiveness of improvement. For example, the improvement by a mesoporous carbon paper (micropores  $\sim 1.5 \text{ nm}$ ; mesopores  $\sim 6 \text{ nm}$ ) is not as effective as that by the microporous carbon paper under the same conditions. In a similar work, Zu *et al.* [15] employed a treated carbon paper, prepared by an alcohol-alkaline/thermal treatment of a commercial Toray carbon paper, as the interlayer, and showed that the Li–S cells had an

**Figure 5.5** Schematic configuration of a Li–S cell with a carbon interlayer inserted between the sulfur cathode and the separator. Reproduced from Ref. [114]. Copyright Nature Publishing Group. Reproduced with permission.



initial capacity of 1651 mA h/g at 1.5–2.8 V at a rate of C/5. This excellent capacity is attributed to the fact that the treatment introduced hydroxyl functional groups and microcracks into the carbon surfaces, which enhances the PS’s chemoadsorption and the carbon paper’s surface areas. The insertion of the carbon interlayer generally reduces the interfacial resistance of the sulfur cathode and delocalizes the PS in the electrolyte. The interlayer configuration offers a possible approach for making the Li–S batteries more viable for practical applications.

#### 5.4.4.3 Alternative anode

Use of lithium metal is one of the main causes for the safety issues of the Li–S batteries. Therefore, much effort has been devoted to the development of lithium metal-free anodes. For example, Yang *et al.* [115] proposed a Li<sub>2</sub>S-mesoporous carbon composite as the starting cathode and silicon nanowires as the anode. Thus, the Li–S cell is assembled in the discharged state, and Li<sub>2</sub>S is the only source for Li<sup>+</sup> ions. By overcoming the poor electrical conductivity and volume expansion of the sulfur cathode and silicon anode, the resulting Li–S Li-ion battery is shown to have four times the theoretical capacity of the current Li-ion battery technology. Following the above concept, Hassoun *et al.* [116] assembled a lithium metal-free silicon–sulfur cell using a high-rate S–C composite cathode, a prelithiated Si–C nanocomposite anode, and a glycol-based electrolyte. Results showed that such a cell could deliver a specific capacity of about 500 mA h/g, which declined to 300 mA h/g after 100 cycles. Based on the same cell chemistry, Liu *et al.* [117] used elemental sulfur as the cathode material and prelithiated silicon nanowires as the anode material. They stated that by a 20 min prelithiation process, the amount of lithium equivalent to a capacity of ~2000 mA h/g Si could be lithiated into the SiNWs, and that the amount of prelithiation can be controlled by changing the prelithiation time. Using this anode

material, the Li-free Li–S cell can maintain  $\sim$ 80% of its initial capacity after 10 cycles; however, the capacity fades with a constant slope throughout cycling.

#### 5.4.4.4 Catholyte

Based on the fact that long-chain PS are highly soluble in the organic electrolytes, Zhang *et al.* [118] used a 0.25 m  $\text{Li}_2\text{S}_9$  solution as the catholyte and a porous carbon electrode as the current collector to build a “liquid” Li–S cell. In order to protect the Li anode from corrosion and increase the cell’s coulombic efficiency,  $\text{LiNO}_3$  is used as a cosalt in the  $\text{Li}_2\text{S}_9$  catholyte. Results indicate that Li/Li<sub>2</sub>S<sub>9</sub> “liquid” cells are superior to the conventional Li/S cells in specific capacity and capacity retention. The capacity of such cells is affected by two factors: (1) the porosity of the carbon electrode, and (2) the PS concentration in catholyte and the amount of catholyte in the cell; namely, the former determines how much  $\text{Li}_2\text{S}$  can be accommodated by the porous carbon electrode, and the latter determines how much sulfur active materials can be contained in the battery.

In order to avoid the difficulty of filling highly viscous PS catholyte in the battery assembly and increase the PS concentration of catholyte, Zhang and Tran [119] further suggested that the “liquid” Li–S cell could be built by using a HPC cloth and a porous sulfur paper. This innovative technique led to a Li/S cell having an initial capacity of 778 mA h/g, equal to an area-specific capacity of 10.1 mA h/cm<sup>2</sup>. The other significance of this work is to reveal that the initial mixing state of the sulfur and carbon is not important for the performance of the Li–S batteries as elemental sulfur will eventually be converted to highly soluble  $\text{Li}_2\text{S}_8$  and dissolve into the electrolyte in the first discharge.

Fu *et al.* [120] demonstrated a similar approach by using a PS catholyte and a self-weaving and freestanding MWCNT paper as the carbon electrode. Due to the high porosity and high conductivity of the MWCNT paper, the catholyte-based Li/S cell showed high-specific capacity of 1411 mA h/g after 50 cycles at C/10 rate and much improved rate capability, as indicated by the very similar capacity at C/10, C/5, and C/2.

Beside the sealed cell design, the PS catholyte also has been proposed to build an opened semiflow battery [121]. In this design, the PS catholyte solution is stored in a separate tank, and is pumped into the cell as needed; however, the anode still uses metallic Li and is sealed in the cell. To maintain the PS cathode solution flowability, the PS species are controlled to cycle only in the solution range (i.e.,  $n \geq 4$  in  $\text{Li}_2\text{S}_n$ ). A proof-of-concept cell has shown a constant capacity of 200 mA h/g over 2000 cycles. This excellent cyclability is attributed to the fact that the operation of PS catholyte is only limited within the solution region without the formation of solid-state  $\text{Li}_2\text{S}_2$  and  $\text{Li}_2\text{S}$ .

Alternatively, the low-concentration PS catholyte can be used as the normal electrolyte to provide extra capacity for the conventional Li–S battery. To demonstrate this, Chen *et al.* [122] used a PS-containing electrolyte to activate the conventional Li–S cell with a C–S composite as the cathode active material. The amount and concentration of PS was shown to affect the capacity as well as sulfur utilization. An optimal concentration of PS was found to be 2 M based on sulfur, which maximized the utilization of sulfur active materials as compared with the PS catholyte of higher

concentration. A specific capacity of 1250 mA h/g was obtained after 40 cycles under optimized conditions.

## 5.5 Conclusions and outlook

The Li–S batteries are promising because of the high energy density, low cost, and natural abundance of sulfur material. However, these advantages can be achieved only when the Li–S battery uses elemental sulfur as the cathode active material and the sulfur approaches the theoretical capacity with low process cost. In recent years, great improvement in the cycling performances of Li–S batteries has been made; however, all these achievements are obtained in exchange for the energy density and process cost. Nanostructured sulfur composites based on various types of carbon materials and conducting polymers have driven the specific capacity of sulfur to a level approaching the theoretical value with acceptable cycling efficiency and cycle number. However, syntheses of these composites are very costly and, furthermore, the cathodes using these composites contain low sulfur content (<60%) and low sulfur-loading (<2 mg/cm<sup>2</sup>), which dramatically reduces the energy density of Li–S batteries. On the other hand, Li–S batteries are fundamentally a liquid electrochemical system, in which elemental sulfur must dissolve into the liquid electrolyte in the form of long-chain PS and serve as the liquid catholyte. Dissolution of PS in the liquid electrolyte on the one hand facilitates the electrochemical reactions of insulating sulfur species, and on the other hand causes severe redox shuttle and parasitic reactions with the Li anode. Therefore, future improvement should be made to balance the various positive and negative effects of the PS dissolution, which can be recommended as follows:

1. *Sulfur cathode*: To meet the requirements of low cost and high energy density, elemental sulfur should be preferentially considered as the cathode active material, and the cathode should contain at least 70% sulfur and have a sulfur-loading of not lower than 2 mg/cm<sup>2</sup>. Furthermore, the cathode structure should be tolerant enough to stand the large volume expansion and contraction incurred by the discharging and charging of sulfur active material.
2. *Anode material*: When metallic Li is used as the anode material, it is essential to develop an effective and cost-acceptable approach for the protection of the Li anode from reactions with the dissolved PS and from the growth of Li dendrites. To completely solve the problem of Li dendrites, developing an alternative anode material free of Li metal is essential for the safety of Li–S batteries. In this case, a facile and cost-acceptable lithiation technique should be explored either for the anode or for the sulfur cathode.
3. *Electrolyte*: Electrolyte is the key to determining the operation temperature range of Li–S batteries, and affecting the dissolution and chemical stability of PS. The PS in the electrolyte will spontaneously disproportionate into low soluble or insoluble short-chain PS and elemental sulfur, which could precipitate out of the liquid electrolyte and clog the pores of the separator. Therefore, in view of the sulfur utilization and reaction kinetics, a liquid electrolyte that can well dissolve and stabilize the PS is highly demanded; however, this promotes the redox shuttle of PS. Electrolyte also affects the coulombic efficiency of the Li anode and the formation of a passivation layer on the Li surface.

**4. Battery design:** The electrochemical process in Li–S batteries is much more complicated than all other rechargeable batteries. The battery design plays a crucial role in affecting the cycling performance of Li–S batteries. As suggested by the fundamental chemistry of the Li–S battery, the dissolution of PS in the liquid electrolyte is essential to enable the electrochemical reactions to insulate sulfur species; however, it meanwhile causes severe redox shuttle and Li corrosion. All sulfur composites, such as S–C composites and S–polymer composites, are designed to confine the dissolved PS within the composites. In this case, the electrolyte absorbed in the pores between the composite (and the conducting carbon) particles cannot be utilized to dissolve PS; a design that can confine the dissolved PS within the whole cathode, other than within the composite particles, must increase the loading and utilization of sulfur in Li–S batteries.

Although the current status of Li–S batteries is still faraway from the requirements for practical applications, it is possible that in near future, major advances in materials and battery designs drive Li–S batteries toward practical applications.

## References

- [1] B. Scrosati, J. Garche, Lithium batteries: status, prospects and future, *J. Power Sources* 195 (9) (2010) 2419–2430, <http://dx.doi.org/10.1016/j.jpowsour.2009.11.048>.
- [2] B. Scrosati, J. Hassoun, Y.-K. Sun, Lithium-ion batteries, A look into the future, *Energy Environ. Sci.* 4 (9) (2011) 3287–3295, <http://dx.doi.org/10.1039/c1ee01388b>.
- [3] M.S. Whittingham, Electrical energy storage and intercalation chemistry, *Science* 192 (4244) (1976) 1126–1127, <http://dx.doi.org/10.1126/science.192.4244.1126>.
- [4] P.G. Bruce, L.J. Hardwick, K.M. Abraham, Lithium–air and lithium–sulfur batteries, *MRS Bull.* 36 (07) (2011) 506–512, <http://dx.doi.org/10.1557/mrs.2011.157>.
- [5] J. Nelson, S. Misra, Y. Yang, A. Jackson, Y. Liu, H. Wang, H. Dai, J.C. Andrews, Y. Cui, M.F. Toney, In operando X-ray diffraction and transmission X-ray microscopy of lithium sulfur batteries, *J. Am. Chem. Soc.* 134 (14) (2012) 6337–6343, <http://dx.doi.org/10.1021/ja2121926>.
- [6] W. Weng, V.G. Pol, K. Amine, Ultrasound assisted design of sulfur/carbon cathodes with partially fluorinated ether electrolytes for highly efficient Li/S batteries, *Adv. Mater.* 25 (11) (2013) 1608–1615, <http://dx.doi.org/10.1002/adma.201204051>.
- [7] Y. Yang, G. Zheng, S. Misra, J. Nelson, M.F. Toney, Y. Cui, High-capacity micrometer-sized Li<sub>2</sub>S particles as cathode materials for advanced rechargeable lithium-ion batteries, *J. Am. Chem. Soc.* 134 (37) (2012) 15387–15394, <http://dx.doi.org/10.1021/ja3052206>.
- [8] B. Zhang, X. Qin, G.R. Li, X.P. Gao, Enhancement of long stability of sulfur cathode by encapsulating sulfur into micropores of carbon spheres, *Energy Environ. Sci.* 3 (10) (2010) 1531–1537, <http://dx.doi.org/10.1039/c002639e>.
- [9] S.S. Zhang, Liquid electrolyte lithium/sulfur battery: fundamental chemistry, problems, and solutions, *J. Power Sources* 231 (2013) 153–162, <http://dx.doi.org/10.1016/j.jpowsour.2012.12.102>.
- [10] C. Barchasz, F. Molton, C. Duboc, J.-C. Leprêtre, S. Patoux, F. Alloin, Lithium/sulfur cell discharge mechanism: an original approach for intermediate species identification, *Anal. Chem.* 84 (9) (2012) 3973–3980, <http://dx.doi.org/10.1021/ac2032244>.
- [11] N.A. Cañas, S. Wolf, N. Wagner, K.A. Friedrich, In-situ X-ray diffraction studies of lithium–sulfur batteries, *J. Power Sources* 226 (2013) 313–319, <http://dx.doi.org/10.1016/j.jpowsour.2012.10.092>.

- [12] S. Xiong, X. Kai, X. Hong, Y. Diao, Effect of LiBOB as additive on electrochemical properties of lithium–sulfur batteries, *Ionics* 18 (3) (2012) 249–254, <http://dx.doi.org/10.1007/s11581-011-0628-1>.
- [13] S. Jeong, D. Bresser, D. Buchholz, M. Winter, S. Passerini, Carbon coated lithium sulfide particles for lithium battery cathodes, *J. Power Sources* 235 (2013) 220–225, <http://dx.doi.org/10.1016/j.jpowsour.2013.01.084>.
- [14] X. Ji, L.F. Nazar, Advances in Li–S batteries, *J. Mater. Chem.* 20 (44) (2010) 9821–9826, <http://dx.doi.org/10.1039/b925751a>.
- [15] C. Zu, Y.-S. Su, Y. Fu, A. Manthiram, Improved lithium–sulfur cells with a treated carbon paper interlayer, *Phys. Chem. Chem. Phys.* 15 (7) (2013) 2291–2297, <http://dx.doi.org/10.1039/c2cp43394j>.
- [16] K.-i Chung, W.-S. Kim, Y.-K. Choi, Lithium phosphorous oxynitride as a passive layer for anodes in lithium secondary batteries, *J. Electroanal. Chem.* 566 (2) (2004) 263–267, <http://dx.doi.org/10.1016/j.jelechem.2003.11.035>.
- [17] Y.M. Lee, N.-S. Choi, J.H. Park, J.-K. Park, Electrochemical performance of lithium/sulfur batteries with protected Li anodes, *J. Power Sources* 119–121 (2003) 964–972, [http://dx.doi.org/10.1016/S0378-7753\(03\)00300-8](http://dx.doi.org/10.1016/S0378-7753(03)00300-8).
- [18] Y.V. Mikhaylik, I. Kovalev, R. Schock, K. Kumaresan, J. Xu, J. Affinito, High energy rechargeable Li–S cells for EV application: status, remaining problems and solutions, *ECS Trans.* 25 (35) (2010) 23–34, <http://dx.doi.org/10.1149/1.3414001>.
- [19] Y. Aihara, T. Bando, H. Nakagawa, H. Yoshida, K. Hayamizu, E. Akiba, W.S. Price, Ion transport properties of six lithium salts dissolved in  $\gamma$ -butyrolactone studied by self-diffusion and ionic conductivity measurements, *J. Electrochem. Soc.* 151 (1) (2004) A119–A122, <http://dx.doi.org/10.1149/1.1630592>.
- [20] H.S. Ryu, H.J. Ahn, K.W. Kim, J.H. Ahn, J.Y. Lee, E.J. Cairns, Self-discharge of lithium–sulfur cells using stainless-steel current-collectors, *J. Power Sources* 140 (2) (2005) 365–369, <http://dx.doi.org/10.1016/j.jpowsour.2004.08.039>.
- [21] J. Shim, K.A. Striebel, E.J. Cairns, The lithium/sulfur rechargeable cell: effects of electrode composition and solvent on cell performance, *J. Electrochem. Soc.* 149 (10) (2002) A1321–A1325, <http://dx.doi.org/10.1149/1.1503076>.
- [22] C. Lai, X.P. Gao, B. Zhang, T.Y. Yan, Z. Zhou, Synthesis and electrochemical performance of sulfur/highly porous carbon composites, *J. Phys. Chem. C* 113 (11) (2009) 4712–4716, <http://dx.doi.org/10.1021/jp809473e>.
- [23] X. Ji, K.T. Lee, L.F. Nazar, A highly ordered nanostructured carbon-sulphur cathode for lithium–sulfur batteries, *Nat. Mater.* 8 (6) (2009) 500–506, <http://dx.doi.org/10.1038/nmat2460>.
- [24] L. Ji, M. Rao, S. Aloni, L. Wang, E.J. Cairns, Y. Zhang, Porous carbon nanofiber-sulfur composite electrodes for lithium/sulfur cells, *Energy Environ. Sci.* 4 (12) (2011) 5053–5059, <http://dx.doi.org/10.1039/c1ee02256c>.
- [25] W. Zheng, Y.W. Liu, X.G. Hu, C.F. Zhang, Novel nanosized adsorbing sulfur composite cathode materials for the advanced secondary lithium batteries, *Electrochim. Acta* 51 (7) (2006) 1330–1335, <http://dx.doi.org/10.1016/j.electacta.2005.06.021>.
- [26] W. Ahn, K.-B. Kim, K.-N. Jung, K.-H. Shin, C.-S. Jin, Synthesis and electrochemical properties of a sulfur-multi walled carbon nanotubes composite as a cathode material for lithium sulfur batteries, *J. Power Sources* 202 (2012) 394–399, <http://dx.doi.org/10.1016/j.jpowsour.2011.11.074>.
- [27] J.-Z. Wang, L. Lu, M. Choucair, J.A. Stride, X. Xu, H.-K. Liu, Sulfur-graphene composite for rechargeable lithium batteries, *J. Power Sources* 196 (16) (2011) 7030–7034, <http://dx.doi.org/10.1016/j.jpowsour.2010.09.106>.

- [28] Y. Cao, X. Li, I.A. Aksay, J. Lemmon, Z. Nie, Z. Yang, J. Liu, Sandwich-type functionalized graphene sheet-sulfur nanocomposite for rechargeable lithium batteries, *Phys. Chem. Chem. Phys.* 13 (17) (2011) 7660–7665, <http://dx.doi.org/10.1039/c0cp02477e>.
- [29] H. Wang, Y. Yang, Y. Liang, J.T. Robinson, Y. Li, A. Jackson, Y. Cui, H. Dai, Graphene-wrapped sulfur particles as a rechargeable lithium–sulfur battery cathode material with high capacity and cycling stability, *Nano Lett.* 11 (7) (2011) 2644–2647, <http://dx.doi.org/10.1021/nl200658a>.
- [30] N. Li, M. Zheng, H. Lu, Z. Hu, C. Shen, X. Chang, G. Ji, J. Cao, Y. Shi, High-rate lithium–sulfur batteries promoted by reduced graphene oxide coating, *Chem. Commun.* 48 (34) (2012) 4106–4108, <http://dx.doi.org/10.1039/c2cc17912a>.
- [31] J. Wang, J. Yang, C. Wan, K. Du, J. Xie, N. Xu, Sulfur composite cathode materials for rechargeable lithium batteries, *Adv. Funct. Mater.* 13 (6) (2003) 487–492, <http://dx.doi.org/10.1002/adfm.200304284>.
- [32] J. Wang, J. Yang, J. Xie, N. Xu, A novel conductive polymer–sulfur composite cathode material for rechargeable lithium batteries, *Adv. Mater.* 14 (13–14) (2002) 963–965, [http://dx.doi.org/10.1002/1521-4095\(20020705\)14:13/14<963::aid-adma963>3.0.co;2-p](http://dx.doi.org/10.1002/1521-4095(20020705)14:13/14<963::aid-adma963>3.0.co;2-p).
- [33] W. Wei, J. Wang, L. Zhou, J. Yang, B. Schumann, Y. NuLi, CNT enhanced sulfur composite cathode material for high rate lithium battery, *Electrochem. Commun.* 13 (5) (2011) 399–402, <http://dx.doi.org/10.1016/j.elecom.2011.02.001>.
- [34] L. Yin, J. Wang, J. Yang, Y. Nuli, A novel pyrolyzed polyacrylonitrile-sulfur@MWCNT composite cathode material for high-rate rechargeable lithium/sulfur batteries, *J. Mater. Chem.* 21 (19) (2011) 6807–6810, <http://dx.doi.org/10.1039/c1jm00047k>.
- [35] L. Yin, J. Wang, F. Lin, J. Yang, Y. Nuli, Polyacrylonitrile/graphene composite as a precursor to a sulfur-based cathode material for high-rate rechargeable Li–S batteries, *Energy Environ. Sci.* 5 (5) (2012) 6966–6972, <http://dx.doi.org/10.1039/c2ee03495f>.
- [36] M. Sun, S. Zhang, T. Jiang, L. Zhang, J. Yu, Nano-wire networks of sulfur–polypyrrole composite cathode materials for rechargeable lithium batteries, *Electrochem. Commun.* 10 (12) (2008) 1819–1822, <http://dx.doi.org/10.1016/j.elecom.2008.09.012>.
- [37] Y. Fu, A. Manthiram, Enhanced cyclability of lithium–sulfur batteries by a polymer acid-doped polypyrrole mixed ionic–electronic conductor, *Chem. Mater.* 24 (15) (2012) 3081–3087, <http://dx.doi.org/10.1021/cm301661y>.
- [38] Y. Fu, Y.-S. Su, A. Manthiram, Sulfur-polypyrrole composite cathodes for lithium–sulfur batteries, *J. Electrochem. Soc.* 159 (9) (2012) A1420–A1424, <http://dx.doi.org/10.1149/2.027209jes>.
- [39] X. Liang, Y. Liu, Z. Wen, L. Huang, X. Wang, H. Zhang, A nano-structured and highly ordered polypyrrole-sulfur cathode for lithium–sulfur batteries, *J. Power Sources* 196 (16) (2011) 6951–6955, <http://dx.doi.org/10.1016/j.jpowsour.2010.11.132>.
- [40] Y. Fu, A. Manthiram, Core-shell structured sulfur-polypyrrole composite cathodes for lithium–sulfur batteries, *RSC Adv.* 2 (14) (2012) 5927–5929, <http://dx.doi.org/10.1039/c2ra20393f>.
- [41] Y. Fu, A. Manthiram, Orthorhombic bipyramidal sulfur coated with polypyrrole nano-layers as a cathode material for lithium–sulfur batteries, *J. Phys. Chem. C* 116 (16) (2012) 8910–8915, <http://dx.doi.org/10.1021/jp300950m>.
- [42] J. Wang, J. Chen, K. Konstantinov, L. Zhao, S.H. Ng, G.X. Wang, Z.P. Guo, H.K. Liu, Sulfur-polypyrrole composite positive electrode materials for rechargeable lithium batteries, *Electrochim. Acta* 51 (22) (2006) 4634–4638, <http://dx.doi.org/10.1016/j.electacta.2005.12.046>.

- [43] F. Wu, J. Chen, L. Li, T. Zhao, R. Chen, Improvement of rate and cycle performance by rapid polyaniline coating of a MWCNT/sulfur cathode, *J. Phys. Chem. C* 115 (49) (2011) 24411–24417, <http://dx.doi.org/10.1021/jp207893d>.
- [44] G.-C. Li, G.-R. Li, S.-H. Ye, X.-P. Gao, A polyaniline-coated sulfur/carbon composite with an enhanced high-rate capability as a cathode material for lithium/sulfur batteries, *Adv. Energy Mater.* 2 (10) (2012) 1238–1245, <http://dx.doi.org/10.1002/aenm.201200017>.
- [45] L. Xiao, Y. Cao, J. Xiao, B. Schwenzer, M.H. Engelhard, L.V. Saraf, Z. Nie, G. J. Exarhos, J. Liu, A soft approach to encapsulate sulfur: polyaniline nanotubes for lithium–sulfur batteries with long cycle life, *Adv. Mater.* 24 (9) (2012) 1176–1181, <http://dx.doi.org/10.1002/adma.201103392>.
- [46] S.-c. Zhang, L. Zhang, W.-k. Wang, W.-j. Xue, A novel cathode material based on polyaniline used for lithium/sulfur secondary battery, *Synth. Met.* 160 (17–18) (2010) 2041–2044, <http://dx.doi.org/10.1016/j.synthmet.2010.07.029>.
- [47] X. Zhao, J.-K. Kim, H.-J. Ahn, K.-K. Cho, J.-H. Ahn, A ternary sulfur/polyaniline/carbon composite as cathode material for lithium sulfur batteries, *Electrochim. Acta* 109 (2013) 145–152, <http://dx.doi.org/10.1016/j.electacta.2013.07.067>.
- [48] F. Wu, J. Chen, R. Chen, S. Wu, L. Li, S. Chen, T. Zhao, Sulfur/polythiophene with a core/shell structure: synthesis and electrochemical properties of the cathode for rechargeable lithium batteries, *J. Phys. Chem. C* 115 (13) (2011) 6057–6063, <http://dx.doi.org/10.1021/jp1114724>.
- [49] F. Wu, S. Wu, R. Chen, J. Chen, S. Chen, Sulfur–polythiophene composite cathode materials for rechargeable lithium batteries, *Electrochem. Solid-State Lett.* 13 (4) (2010) A29–A31, <http://dx.doi.org/10.1149/1.3290668>.
- [50] H. Chen, W. Dong, J. Ge, C. Wang, X. Wu, W. Lu, L. Chen, Ultrafine sulfur nanoparticles in conducting polymer shell as cathode materials for high performance lithium/sulfur batteries, *Sci. Rep.* 3 (2013), Article 1910, <http://dx.doi.org/10.1038/srep01910>.
- [51] Y. Yang, G. Yu, J.J. Cha, H. Wu, M. Vosgueritchian, Y. Yao, Z. Bao, Y. Cui, Improving the performance of lithium–sulfur batteries by conductive polymer coating, *ACS Nano* 5 (11) (2011) 9187–9193, <http://dx.doi.org/10.1021/nn203436j>.
- [52] H. Schneider, A. Garsuch, A. Panchenko, O. Gronwald, N. Janssen, P. Novák, Influence of different electrode compositions and binder materials on the performance of lithium–sulfur batteries, *J. Power Sources* 205 (2012) 420–425, <http://dx.doi.org/10.1016/j.jpowsour.2011.12.061>.
- [53] Y. Jung, S. Kim, New approaches to improve cycle life characteristics of lithium–sulfur cells, *Electrochem. Commun.* 9 (2) (2007) 249–254, <http://dx.doi.org/10.1016/j.elecom.2006.09.013>.
- [54] B.A. Trofimov, L.V. Morozova, M.V. Markova, A.I. Mikhaleva, G.F. Myachina, I.V. Tatarinova, T.A. Skotheim, Vinyl ethers with polysulfide and hydroxyl functions and polymers therefrom as binders for lithium–sulfur batteries, *J. Appl. Polym. Sci.* 101 (6) (2006) 4051–4055, <http://dx.doi.org/10.1002/app.23222>.
- [55] S.-E. Cheon, J.-H. Cho, K.-S. Ko, C.-W. Kwon, D.-R. Chang, H.-T. Kim, S.-W. Kim, Structural factors of sulfur cathodes with poly(ethylene oxide) binder for performance of rechargeable lithium sulfur batteries, *J. Electrochem. Soc.* 149 (11) (2002) A1437–A1441, <http://dx.doi.org/10.1149/1.1511187>.
- [56] M.J. Lacey, F. Jeschull, K. Edstrom, D. Brandell, Why PEO as a binder or polymer coating increases capacity in the Li–S system, *Chem. Commun.* 49 (76) (2013) 8531–8533, <http://dx.doi.org/10.1039/c3cc44772c>.

- [57] J. Wang, Z. Yao, C.W. Monroe, J. Yang, Y. Nuli, Carbonyl- $\beta$ -cyclodextrin as a novel binder for sulfur composite cathodes in rechargeable lithium batteries, *Adv. Funct. Mater.* 23 (9) (2013) 1194–1201, <http://dx.doi.org/10.1002/adfm.201201847>.
- [58] W. Bao, Z. Zhang, Y. Gan, X. Wang, J. Lia, Enhanced cyclability of sulfur cathodes in lithium–sulfur batteries with Na-alginate as a binder, *J. Energy Chem.* 22 (5) (2013) 790–794, [http://dx.doi.org/10.1016/S2095-4956\(13\)60105-9](http://dx.doi.org/10.1016/S2095-4956(13)60105-9).
- [59] Z. Zhang, W. Bao, H. Lu, M. Jia, K. Xie, Y. Lai, J. Li, Water-soluble polyacrylic acid as a binder for sulfur cathode in lithium–sulfur battery, *ECS Electrochem. Lett.* 1 (2) (2012) A34–A37, <http://dx.doi.org/10.1149/2.009202eel>.
- [60] S.S. Zhang, Binder based on polyelectrolyte for high capacity density lithium/sulfur battery, *J. Electrochem. Soc.* 159 (8) (2012) A1226–A1229, <http://dx.doi.org/10.1149/2.039208jes>.
- [61] M. He, L.-X. Yuan, W.-X. Zhang, X.-L. Hu, Y.-H. Huang, Enhanced cyclability for sulfur cathode achieved by a water-soluble binder, *J. Phys. Chem. C* 115 (31) (2011) 15703–15709, <http://dx.doi.org/10.1021/jp2043416>.
- [62] M. Rao, X. Song, H. Liao, E.J. Cairns, Carbon nanofiber–sulfur composite cathode materials with different binders for secondary Li/S cells, *Electrochim. Acta* 65 (2012) 228–233, <http://dx.doi.org/10.1016/j.electacta.2012.01.051>.
- [63] N.-I. Kim, C.-B. Lee, J.-M. Seo, W.-J. Lee, Y.-B. Roh, Correlation between positive-electrode morphology and sulfur utilization in lithium–sulfur battery, *J. Power Sources* 132 (1–2) (2004) 209–212, <http://dx.doi.org/10.1016/j.jpowsour.2003.12.028>.
- [64] Y. Huang, J. Sun, W. Wang, Y. Wang, Z. Yu, H. Zhang, A. Wang, K. Yuan, Discharge process of the sulfur cathode with a gelatin binder, *J. Electrochem. Soc.* 155 (10) (2008) A764–A767, <http://dx.doi.org/10.1149/1.2967191>.
- [65] J. Sun, Y. Huang, W. Wang, Z. Yu, A. Wang, K. Yuan, Application of gelatin as a binder for the sulfur cathode in lithium–sulfur batteries, *Electrochim. Acta* 53 (24) (2008) 7084–7088, <http://dx.doi.org/10.1016/j.electacta.2008.05.022>.
- [66] J. Sun, Y. Huang, W. Wang, Z. Yu, A. Wang, K. Yuan, Preparation and electrochemical characterization of the porous sulfur cathode using a gelatin binder, *Electrochim. Commun.* 10 (6) (2008) 930–933, <http://dx.doi.org/10.1016/j.elecom.2008.04.016>.
- [67] Q. Wang, W. Wang, Y. Huang, F. Wang, H. Zhang, Z. Yu, A. Wang, K. Yuan, Improve rate capability of the sulfur cathode using a gelatin binder, *J. Electrochem. Soc.* 158 (6) (2011) A775–A779, <http://dx.doi.org/10.1149/1.3583375>.
- [68] Y. Wang, Y. Huang, W. Wang, C. Huang, Z. Yu, H. Zhang, J. Sun, A. Wang, K. Yuan, Structural change of the porous sulfur cathode using gelatin as a binder during discharge and charge, *Electrochim. Acta* 54 (16) (2009) 4062–4066, <http://dx.doi.org/10.1016/j.electacta.2009.02.039>.
- [69] W. Zhang, Y. Huang, W. Wang, C. Huang, Y. Wang, Z. Yu, H. Zhang, Influence of pH of gelatin solution on cycle performance of the sulfur cathode, *J. Electrochem. Soc.* 157 (4) (2010) A443–A446, <http://dx.doi.org/10.1149/1.3299323>.
- [70] C. Barchasz, J.-C. Leprêtre, S. Patoux, F. Alloin, Electrochemical properties of ether-based electrolytes for lithium/sulfur rechargeable batteries, *Electrochim. Acta* 89 (2013) 737–743, <http://dx.doi.org/10.1016/j.electacta.2012.11.001>.
- [71] S.S. Zhang, New insight into liquid electrolyte of rechargeable lithium/sulfur battery, *Electrochim. Acta* 97 (2013) 226–230, <http://dx.doi.org/10.1016/j.electacta.2013.02.122>.
- [72] D. Aurbach, E. Pollak, R. Elazari, G. Salitra, C.S. Kelley, J. Affinito, On the surface chemical aspects of very high energy density, rechargeable Li–sulfur batteries, *J. Electrochem. Soc.* 156 (8) (2009) A694–A702, <http://dx.doi.org/10.1149/1.3148721>.

[73] Y.-X. Wang, S.-L. Chou, H.-K. Liu, S.-X. Dou, The electrochemical properties of high-capacity sulfur/reduced graphene oxide with different electrolyte systems, *J. Power Sources* 244 (2013) 240–245, <http://dx.doi.org/10.1016/j.jpowsour.2012.11.152>.

[74] S. Kim, Y. Jung, H.S. Lim, The effect of solvent component on the discharge performance of lithium–sulfur cell containing various organic electrolytes, *Electrochim. Acta* 50 (2–3) (2004) 889–892, <http://dx.doi.org/10.1016/j.electacta.2004.01.093>.

[75] H.-S. Ryu, H.-J. Ahn, K.-W. Kim, J.-H. Ahn, K.-K. Cho, T.-H. Nam, J.-U. Kim, G.-B. Cho, Discharge behavior of lithium/sulfur cell with TEGDME based electrolyte at low temperature, *J. Power Sources* 163 (1) (2006) 201–206, <http://dx.doi.org/10.1016/j.jpowsour.2005.12.061>.

[76] N. Azimi, W. Weng, C. Takoudis, Z. Zhang, Improved performance of lithium–sulfur battery with fluorinated electrolyte, *Electrochim. Commun.* 37 (2013) 96–99, <http://dx.doi.org/10.1016/j.elecom.2013.10.020>.

[77] S. Zhang, Improved cyclability of liquid electrolyte lithium/sulfur batteries by optimizing electrolyte/sulfur ratio, *Energies* 5 (12) (2012) 5190–5197, <http://dx.doi.org/10.3390/en5125190>.

[78] J.-W. Choi, J.-K. Kim, G. Cheruvally, J.-H. Ahn, H.-J. Ahn, K.-W. Kim, Rechargeable lithium/sulfur battery with suitable mixed liquid electrolytes, *Electrochim. Acta* 52 (5) (2007) 2075–2082, <http://dx.doi.org/10.1016/j.electacta.2006.08.016>.

[79] C. Barchasz, J.-C. Leprêtre, S. Patoux, F. Alloin, Revisiting TEGDME/DIOX binary electrolytes for lithium/sulfur batteries: importance of solvation ability and additives, *J. Electrochem. Soc.* 160 (3) (2013) A430–A436, <http://dx.doi.org/10.1149/2.022303jes>.

[80] L. Suo, Y.-S. Hu, H. Li, M. Armand, L. Chen, A new class of solvent-in-salt electrolyte for high-energy rechargeable metallic lithium batteries, *Nature Commun.* 4 (2013) 1481, <http://dx.doi.org/10.1038/ncomms2513>.

[81] K. Dokko, N. Tachikawa, K. Yamauchi, M. Tsuchiya, A. Yamazaki, E. Takashima, J.-W. Park, K. Ueno, S. Seki, N. Serizawa, M. Watanabe, Solvate ionic liquid electrolyte for Li–S batteries, *J. Electrochem. Soc.* 160 (8) (2013) A1304–A1310, <http://dx.doi.org/10.1149/2.111308jes>.

[82] L.X. Yuan, J.K. Feng, X.P. Ai, Y.L. Cao, S.L. Chen, H.X. Yang, Improved dischargeability and reversibility of sulfur cathode in a novel ionic liquid electrolyte, *Electrochim. Commun.* 8 (4) (2006) 610–614, <http://dx.doi.org/10.1016/j.elecom.2006.02.007>.

[83] L. Wang, H.R. Byon, N-Methyl-N-propylpiperidinium bis(trifluoromethanesulfonyl) imide-based organic electrolyte for high performance lithium–sulfur batteries, *J. Power Sources* 236 (2013) 207–214, <http://dx.doi.org/10.1016/j.jpowsour.2013.02.068>.

[84] J.-W. Park, K. Yamauchi, E. Takashima, N. Tachikawa, K. Ueno, K. Dokko, M. Watanabe, Solvent effect of room temperature ionic liquids on electrochemical reactions in lithium–sulfur batteries, *J. Phys. Chem. C* 117 (9) (2013) 4431–4440, <http://dx.doi.org/10.1021/jp400153m>.

[85] F. Croce, G.B. Appetecchi, L. Persi, B. Scrosati, Nanocomposite polymer electrolytes for lithium batteries, *Nature* 394 (6692) (1998) 456–458, <http://dx.doi.org/10.1038/28818>.

[86] D. Marmorstein, T.H. Yu, K.A. Striebel, F.R. McLarnon, J. Hou, E.J. Cairns, Electrochemical performance of lithium/sulfur cells with three different polymer electrolytes, *J. Power Sources* 89 (2) (2000) 219–226, [http://dx.doi.org/10.1016/S0378-7753\(00\)00432-8](http://dx.doi.org/10.1016/S0378-7753(00)00432-8).

[87] S.S. Jeong, Y.T. Lim, Y.J. Choi, G.B. Cho, K.W. Kim, H.J. Ahn, K.K. Cho, Electrochemical properties of lithium sulfur cells using PEO polymer electrolytes prepared under three different mixing conditions, *J. Power Sources* 174 (2) (2007) 745–750, <http://dx.doi.org/10.1016/j.jpowsour.2007.06.108>.

[88] J.H. Shin, Y.T. Lim, K.W. Kim, H.J. Ahn, J.H. Ahn, Effect of ball milling on structural and electrochemical properties of (PEO)<sub>n</sub>LiX (LiX=LiCF<sub>3</sub>SO<sub>3</sub> and LiBF<sub>4</sub>) polymer electrolytes, *J. Power Sources* 107 (1) (2002) 103–109, [http://dx.doi.org/10.1016/S0378-7753\(01\)00990-9](http://dx.doi.org/10.1016/S0378-7753(01)00990-9).

[89] B.H. Jeon, J.H. Yeon, K.M. Kim, I.J. Chung, Preparation and electrochemical properties of lithium–sulfur polymer batteries, *J. Power Sources* 109 (1) (2002) 89–97, [http://dx.doi.org/10.1016/S0378-7753\(02\)00050-2](http://dx.doi.org/10.1016/S0378-7753(02)00050-2).

[90] H.-S. Ryu, H.-J. Ahn, K.-W. Kim, J.-H. Ahn, J.-Y. Lee, Discharge process of Li/PVdF/S cells at room temperature, *J. Power Sources* 153 (2) (2006) 360–364, <http://dx.doi.org/10.1016/j.jpowsour.2005.05.037>.

[91] J.H. Shin, S.S. Jung, K.W. Kim, H.J. Ahn, J.H. Ahn, Preparation and characterization of plasticized polymer electrolytes based on the PVdF-HFP copolymer for lithium/sulfur battery, *J. Mater. Sci. Mater. Electron.* 13 (12) (2002) 727–733, <http://dx.doi.org/10.1023/a:1021521207247>.

[92] J. Jin, Z. Wen, X. Liang, Y. Cui, X. Wu, Gel polymer electrolyte with ionic liquid for high performance lithium sulfur battery, *Solid State Ion.* 225 (2012) 604–607, <http://dx.doi.org/10.1016/j.ssi.2012.03.012>.

[93] X. Zhu, Z. Wen, Z. Gu, Z. Lin, Electrochemical characterization and performance improvement of lithium/sulfur polymer batteries, *J. Power Sources* 139 (1–2) (2005) 269–273, <http://dx.doi.org/10.1016/j.jpowsour.2004.07.002>.

[94] X. Liang, Z. Wen, Y. Liu, H. Zhang, L. Huang, J. Jin, Highly dispersed sulfur in ordered mesoporous carbon sphere as a composite cathode for rechargeable polymer Li/S battery, *J. Power Sources* 196 (7) (2011) 3655–3658, <http://dx.doi.org/10.1016/j.jpowsour.2010.12.052>.

[95] J. Hassoun, B. Scrosati, Moving to a solid-state configuration: a valid approach to making lithium–sulfur batteries viable for practical applications, *Adv. Mater.* 22 (45) (2010) 5198–5201, <http://dx.doi.org/10.1002/adma.201002584>.

[96] K. Jeddi, Y. Zhao, Y. Zhang, A. Konarov, P. Chen, Fabrication and characterization of an effective polymer nanocomposite electrolyte membrane for high performance lithium/sulfur batteries, *J. Electrochem. Soc.* 160 (8) (2013) A1052–A1060, <http://dx.doi.org/10.1149/2.010308jes>.

[97] K. Jeddi, K. Sarikhani, N.T. Qazvini, P. Chen, Stabilizing lithium/sulfur batteries by a composite polymer electrolyte containing mesoporous silica particles, *J. Power Sources* 245 (2014) 656–662, <http://dx.doi.org/10.1016/j.jpowsour.2013.06.147>.

[98] S.S. Zhang, A concept for making poly(ethylene oxide) based composite gel polymer electrolyte lithium/sulfur battery, *J. Electrochem. Soc.* 160 (9) (2013) A1421–A1424, <http://dx.doi.org/10.1149/2.058309jes>.

[99] S.S. Zhang, D.T. Tran, How a gel polymer electrolyte affects performance of lithium/sulfur batteries, *Electrochim. Acta* 114 (2013) 296–302, <http://dx.doi.org/10.1016/j.electacta.2013.10.069>.

[100] Z. Lin, Z. Liu, W. Fu, N.J. Dudney, C. Liang, Lithium polysulfidophosphates: a family of lithium-conducting sulfur-rich compounds for lithium–sulfur batteries, *Angew. Chem. Int. Ed.* 52 (29) (2013) 7460–7463, <http://dx.doi.org/10.1002/anie.201300680>.

[101] R. Kanno, M. Murayama, Lithium ionic conductor thio-LISICON: the Li<sub>2</sub>S–GeS<sub>2</sub>–P<sub>2</sub>S<sub>5</sub> system, *J. Electrochem. Soc.* 148 (7) (2001) A742–A746, <http://dx.doi.org/10.1149/1.1379028>.

[102] T. Kobayashi, Y. Imade, D. Shishihara, K. Homma, M. Nagao, R. Watanabe, T. Yokoi, A. Yamada, R. Kanno, T. Tatsumi, All solid-state battery with sulfur electrode and thio-LISICON electrolyte, *J. Power Sources* 182 (2) (2008) 621–625, <http://dx.doi.org/10.1016/j.jpowsour.2008.03.030>.

- [103] A. Hayashi, T. Ohtomo, F. Mizuno, K. Tadanaga, M. Tatsumisago, All-solid-state Li/S batteries with highly conductive glass–ceramic electrolytes, *Electrochim. Commun.* 5 (8) (2003) 701–705, [http://dx.doi.org/10.1016/S1388-2481\(03\)00167-X](http://dx.doi.org/10.1016/S1388-2481(03)00167-X).
- [104] A. Hayashi, T. Ohtomo, F. Mizuno, K. Tadanaga, M. Tatsumisago, Rechargeable lithium batteries, using sulfur-based cathode materials and  $\text{Li}_2\text{S}-\text{P}_2\text{S}_5$  glass-ceramic electrolytes, *Electrochim. Acta* 50 (2–3) (2004) 893–897, <http://dx.doi.org/10.1016/j.electacta.2004.02.061>.
- [105] M. Nagao, A. Hayashi, M. Tatsumisago, Sulfur–carbon composite electrode for all-solid-state Li/S battery with  $\text{Li}_2\text{S}-\text{P}_2\text{S}_5$  solid electrolyte, *Electrochim. Acta* 56 (17) (2011) 6055–6059, <http://dx.doi.org/10.1016/j.electacta.2011.04.084>.
- [106] M. Nagao, A. Hayashi, M. Tatsumisago, High-capacity  $\text{Li}_2\text{S}$ -nanocarbon composite electrode for all-solid-state rechargeable lithium batteries, *J. Mater. Chem.* 22 (19) (2012) 10015–10020, <http://dx.doi.org/10.1039/c2jm16802b>.
- [107] Y.V. Mikhaylik, *Electrolytes for lithium sulfur cells* (2008), U.S. Patent, 7,354,680.
- [108] X. Liang, Z. Wen, Y. Liu, M. Wu, J. Jin, H. Zhang, X. Wu, Improved cycling performances of lithium sulfur batteries with  $\text{LiNO}_3$ -modified electrolyte, *J. Power Sources* 196 (22) (2011) 9839–9843, <http://dx.doi.org/10.1016/j.jpowsour.2011.08.027>.
- [109] S.S. Zhang, Role of  $\text{LiNO}_3$  in rechargeable lithium/sulfur battery, *Electrochim. Acta* 70 (2012) 344–348, <http://dx.doi.org/10.1016/j.electacta.2012.03.081>.
- [110] Z. Lin, Z. Liu, W. Fu, N.J. Dudney, C. Liang, Phosphorous pentasulfide as a novel additive for high-performance lithium–sulfur batteries, *Adv. Funct. Mater.* 23 (8) (2013) 1064–1069, <http://dx.doi.org/10.1002/adfm.201200696>.
- [111] C. Zu, Y. Fu, A. Manthiram, Highly reversible Li/dissolved polysulfide batteries with binder-free carbon nanofiber electrodes, *J. Mater. Chem. A* 1 (35) (2013) 10362–10367, <http://dx.doi.org/10.1039/c3ta11958k>.
- [112] J. Hassoun, Y.-K. Sun, B. Scrosati, Rechargeable lithium sulfide electrode for a polymer tin/sulfur lithium-ion battery, *J. Power Sources* 196 (1) (2011) 343–348, <http://dx.doi.org/10.1016/j.jpowsour.2010.06.093>.
- [113] Y. Fu, Y.-S. Su, A. Manthiram,  $\text{Li}_2\text{S}$ -carbon sandwiched electrodes with superior performance for lithium–sulfur batteries, *Adv. Energy Mater.* 4 (1) (2014), <http://dx.doi.org/10.1002/aenm.201300655>.
- [114] Y.-S. Su, A. Manthiram, Lithium–sulphur batteries with a microporous carbon paper as a bifunctional interlayer, *Nature Commun.* 3 (2012) 1166, <http://dx.doi.org/10.1038/ncomms2163>.
- [115] Y. Yang, M.T. McDowell, A. Jackson, J.J. Cha, S.S. Hong, Y. Cui, New nanostructured  $\text{Li}_2\text{S}/\text{silicon}$  rechargeable battery with high specific energy, *Nano Lett.* 10 (4) (2010) 1486–1491, <http://dx.doi.org/10.1021/nl100504q>.
- [116] J. Hassoun, J. Kim, D.-J. Lee, H.-G. Jung, S.-M. Lee, Y.-K. Sun, B. Scrosati, A contribution to the progress of high energy batteries: a metal-free, lithium-ion, silicon–sulfur battery, *J. Power Sources* 202 (2012) 308–313, <http://dx.doi.org/10.1016/j.jpowsour.2011.11.060>.
- [117] N. Liu, L. Hu, M.T. McDowell, A. Jackson, Y. Cui, Prelithiated silicon nanowires as an anode for lithium ion batteries, *ACS Nano* 5 (8) (2011) 6487–6493, <http://dx.doi.org/10.1021/nn2017167>.
- [118] S.S. Zhang, J.A. Read, A new direction for the performance improvement of rechargeable lithium/sulfur batteries, *J. Power Sources* 200 (2012) 77–82, <http://dx.doi.org/10.1016/j.jpowsour.2011.10.076>.
- [119] S.S. Zhang, D.T. Tran, A proof-of-concept lithium/sulfur liquid battery with exceptionally high capacity density, *J. Power Sources* 211 (2012) 169–172, <http://dx.doi.org/10.1016/j.jpowsour.2012.04.006>.

- [120] Y. Fu, Y.-S. Su, A. Manthiram, Highly reversible lithium/dissolved polysulfide batteries with carbon nanotube electrodes, *Angew. Chem. Int. Ed.* 52 (27) (2013) 6930–6935, <http://dx.doi.org/10.1002/anie.201301250>.
- [121] Y. Yang, G. Zheng, Y. Cui, A membrane-free lithium/polysulfide semi-liquid battery for large-scale energy storage, *Energy Environ. Sci.* 6 (5) (2013) 1552–1558, <http://dx.doi.org/10.1039/c3ee00072a>.
- [122] S. Chen, F. Dai, M.L. Gordin, D. Wang, Exceptional electrochemical performance of rechargeable Li–S batteries with a polysulfide-containing electrolyte, *RSC Adv.* 3 (11) (2013) 3540–3543, <http://dx.doi.org/10.1039/c3ra23070h>.

# Electrochemistry of rechargeable lithium–air batteries

6

J. Hou<sup>1</sup>, X. Jie<sup>2</sup>, J. Graetz<sup>3</sup>, M.W. Ellis<sup>1</sup>, R.B. Moore<sup>1</sup>, K. Uosaki<sup>2,4</sup>

<sup>1</sup>Institute for Critical Technology and Applied Science (ICTAS), Virginia Tech, Blacksburg, VA, USA; <sup>2</sup>Global Research Center for Environment and Energy based on Nanomaterials

Science (GREEN), National Institute for Materials Science (NIMS), Tsukuba, Japan;

<sup>3</sup>HRL Laboratories, LLC, Malibu, CA, USA; <sup>4</sup>International Center for Materials

Nanoarchitectonics (WPI-MANA), National Institute for Materials Science (NIMS);

Tsukuba, Japan

## 6.1 Introduction

According to the *World Energy Outlook 2012* released by the International Energy Agency (IEA), global energy demand will grow by more than one-third over the period to 2035. Although the global energy map is being redrawn by the resurgence in oil and gas production in the United States, the energy trend that fossil fuels will remain dominant and that renewable energy will continue to increase in the global energy mix, will be not change. As an important segment of the renewable energy sector, the development and application of energy conversion and storage devices is a hot issue for research institutes and companies worldwide. Rechargeable batteries are commonly used energy conversion and storage devices. The development of rechargeable batteries started from the previous lead acid battery, with a specific energy density of only 40 Wh/kg, to the nickel metal hydride battery, with a specific energy density of over 80 Wh/kg, to today's most popular battery, the lithium-ion battery, with a specific energy density that can reach over 250 Wh/kg. The comparisons of the volumetric and gravimetric energy densities for various types of rechargeable batteries are summarized in Table 6.1.

The lithium–ion battery is and will continue to be an important portable electronic device. However, present rechargeable Li-ion batteries do not meet such commercial requirements as long driving range, safe and fast charging, and low cost [1]. Considering Li-ion battery limitations, especially the fact that they cannot store and deliver larger energy per unit mass or volume, which is a catastrophic limitation for the applications of electric vehicles and the electricity grid, alternative energy storage technologies need to be investigated. The Li–air battery is one of these alternatives.

Unlike Li-ion batteries, a reaction of ideally reversible O<sub>2</sub> reduction and combination with Li<sup>+</sup> occurs on the cathode of Li–air batteries, and thus a porous cathode (positive electrode) usually providing an electron pathway, ion (Li<sup>+</sup>) pathway, and gas (O<sub>2</sub>) pathway is introduced in the Li–air battery rather than an intercalation material in the Li-ion battery [2]. The graphite anode (negative electrode) in the Li-ion battery is replaced by Li metal or other prelithiated materials with low electrode potential, which can work as a substitute but may decrease the specific energy. Based on the

**Table 6.1 Specific energy density for various types of rechargeable batteries**

Type	Energy density	
	(Wh kg <sup>-1</sup> )	(Wh L <sup>-1</sup> )
Lead-acid	30–40	60–75
Nickel–metal hydride	30–80	140–300
Li-ion	150–250	250–360
Li-ion polymer	130–200	300
Li iron phosphate	80–120	170

used electrolyte, the Li–air battery can be generally classified into aqueous and non-aqueous systems, though there are other architectures like solid-state and mixed aqueous–nonaqueous systems [3]. For the aqueous Li–air battery, oxygen is reduced at reaction sites in the cathode and combined with H<sub>2</sub>O and Li<sup>+</sup> from electrolyte, and LiOH·H<sub>2</sub>O is formed [4]. For the nonaqueous one, there is no water involvement and lithium oxides like Li<sub>2</sub>O<sub>2</sub> and Li<sub>2</sub>O are formed. The theoretical specific energy can be calculated based on the overall cell reaction, and the values for the aqueous and nonaqueous Li–air batteries are listed in Figure 6.1 together with the schematic representation of the cell structures. Even given the oxygen involvement, the specific energies for the nonaqueous system (3505 Wh kg<sup>-1</sup>), which is comparable to that of a regenerative fuel cell (3663 Wh kg<sup>-1</sup>), and the aqueous system (2044 Wh kg<sup>-1</sup>) are

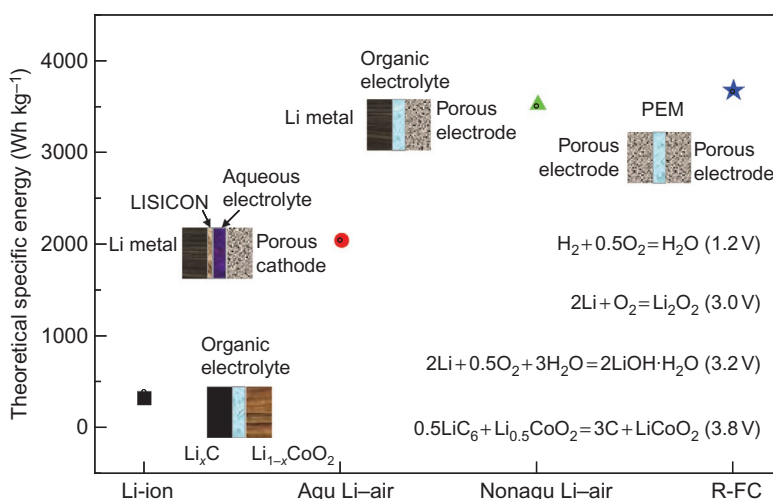


**Figure 6.1** Theoretical specific energy for Li-ion and Li–air batteries together with regenerative fuel cell.

much higher than that of the Li-ion battery (387 Wh kg<sup>−1</sup>). The theoretical specific energy can provide a benchmark comparison for the active material itself, while the practical specific energy should be considered, which is usually about 20–45% of the theoretical one depending on the cell design [5]. If fully developed, the nonaqueous Li–air battery may meet the criteria for the transport and stationary applications.

On the other hand, the Li–air battery still has some challenges. Currently, the performance of the Li–air battery still has plenty of room for improvement, due to the slow reversibility and kinetics of the electrode deposition/dissolution of the lithium oxides or lithium peroxides species. So, the understanding of the mechanism of the reactions is the key for practical application of the Li–air battery.

In this chapter, we introduce the fundamental electrochemical analysis of reactions in the nonaqueous Li–air battery. Starting from the investigation of oxygen reduction and evolution reactions (ORR/OER) in a nonaqueous system without and with the Li<sup>+</sup> cation and related effects of electrolyte solutions and the electrode materials, the object of this chapter is to introduce some results in fundamental electrochemistry and apply it to the study of Li–air battery application. Moreover, the different electrochemical reaction interface referring to the material, structure, conductivity, and distribution during charging and discharging processes are also discussed in this chapter.

## 6.2 Fundamental electrochemical analysis of the lithium–air (Li–air) battery

Understanding the reaction mechanism and kinetics of the ORR/OER in the nonaqueous solvents is essential and critical for the practical application of the Li–air battery. However, some critical issues in the electrochemical deposition/dissolution of Li–O<sub>2</sub> species corresponding to the discharging/charging process are still unclear, such as the elementary reactions, the rate-determination step, as well as the kinetics parameters. Currently, some studies are being carried out on the effects of the solvents, electrolytes, and electrode materials on the kinetics and reversibility of these reactions [6–8], yet a stable reaction system should be established first. In this section, we summarize the previous work on the electrochemical fundamental in nonaqueous solutions to get insight into the main influences during Li–air battery operation.

### 6.2.1 Oxygen reduction reaction

The study of the ORR in a nonaqueous system can be traced back a few decades [9]. However, knowledge of oxygen electrochemistry in nonaqueous solutions is rather limited compared to that in aqueous solutions. The cations of the electrolyte salts substituted for the proton in the aqueous solution will greatly affect the oxygen reduction process owing to its polarity [10]. Moreover, the electrochemical reaction interface is completely different from that of the aqueous system according to the organic

solvents and electrode materials. We will discuss the electrochemical fundamental along with the effects of electrode materials and electrolyte solutions in detail.

### 6.2.1.1 ORR in electrolyte solution without $\text{Li}^+$ cation

Electrochemistry in nonaqueous solutions containing large cations such as tetrabutylammonium ( $\text{TBA}^+$ ) and tetraethylammonium ( $\text{TEA}^+$ ) cations has been studied extensively [6,11]. As shown in Figure 6.2a, the symmetrical CVs in 0.1 M tetrabutylammonium hexafluorophosphate ( $\text{TBAPF}_6$ )/acetonitrile (AN) solution on the glassy carbon (GC)

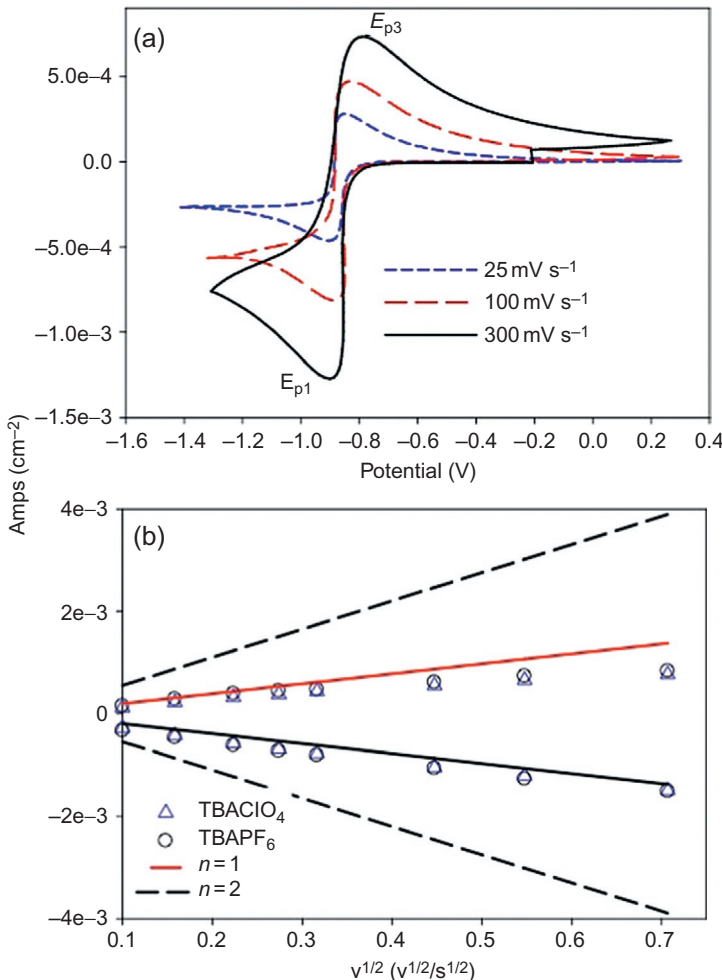


**Figure 6.2** (a) Cyclic voltammograms for ORR in 0.1 M  $\text{TBAPF}_6$ /AN on the GC electrode at sweep rate of  $0.3 \text{ V s}^{-1}$  (solid),  $0.1 \text{ V s}^{-1}$  (long dash), and  $0.025 \text{ V s}^{-1}$  (short dash) and (b) Randles–Sevcik plot of peak current versus square root of the sweep rate [11].

electrode indicate that the first reduction step of ORR is a quasi-reversible reaction to generate superoxide ( $O_2^-$ ) as shown below:



The Randles–Sevcik plots, which are dependent of the peak current on the root of sweep rate [presented in Figure 6.2b] are linear and pass through the origin as per theory, indicating a fast and diffusion-controlled electrochemical process of ORR. The influence of the electrode materials (e.g., glassy carbon, Au, Pt, and Ru) on the formal potential of CVs is limited, revealing that ORR has nothing to do with the electrode materials and surface [12]. Yeager suggested that ORR to superoxide proceeds through a one-electron transfer of the outer sphere type to an oxygen molecule in the outer Helmholtz plane [13]. On the other hand, recently a few papers reported the observation of a monolayer of oxygen adsorb onto the Au microelectrode surface with a rate constant  $k \approx 480 \text{ s}^{-1}$  in the transient potential step chronoamperometric studies [14]. Furthermore, the effect of solvents, for example, *N,N*-dimethylformamide (DMF), dimethylsulphoxide (DMSO), and acetonitrile (AN) on the CVs is more obvious than that of electrode materials [12]. The differences of the peak current and potential separation can be attributed to the solubility and diffusion coefficient of oxygen and ion–dipole interaction, respectively. It should be emphasized that peroxide ( $O_2^{2-}$ ), which is formed after further reduction of superoxide, is quite unstable in this case. Three possible reasons can be attributed to the complication of the successive reduction process: (1) the dismutation process of superoxide itself ( $2O_2^- \rightarrow O_2 + O_2^{2-}$ ), (2) the reaction of peroxide anion with the solvent, and (3) the effect of moisture impurity. A recent paper published in *Science* mentioned a method to facilitate the reversible reduction of oxygen to peroxide using molecular recognition, which can be introduced to a Li–air battery to prevent overreduction of discharge product [15].

Actually, the supply of oxygen on a gas-diffusion electrode, such as the Li–air battery cathode, and that on the disk electrode usually used in electrochemical fundamental study is not in the same order of magnitude. A hanging meniscus configuration of electrode, which has no sidewall for sealing and contacts with the electrolyte solution, is employed to investigate the effect of three-phase, gas/solution/electrode, boundary (TPB) on the kinetics of ORR [a schematic representation of both configurations are shown in Figure 6.3a].

As shown in Figure 6.3b, the asymmetrical CVs and enhanced ORR currents in three different nonaqueous solvents indicate that ORR current at TPB contributed dominantly to the observed current [16]. Here, it should be pointed out that the kinetics of ORR obtained from current electrochemical fundamental studies may not reflect the real situation within the application. As a model electrode, the hanging meniscus configuration of electrode shows the promise for the mechanism investigation of the Li–air battery as closer to the practical situation.

### 6.2.1.2 ORR in electrolyte solution with $Li^+$ cation

The ORR is significantly changed when the large cations are substituted for the  $Li^+$  cation. A similar asymmetrical CV result, as shown in Figure 6.4, can be obtained from different experiments even in different reaction systems [6].

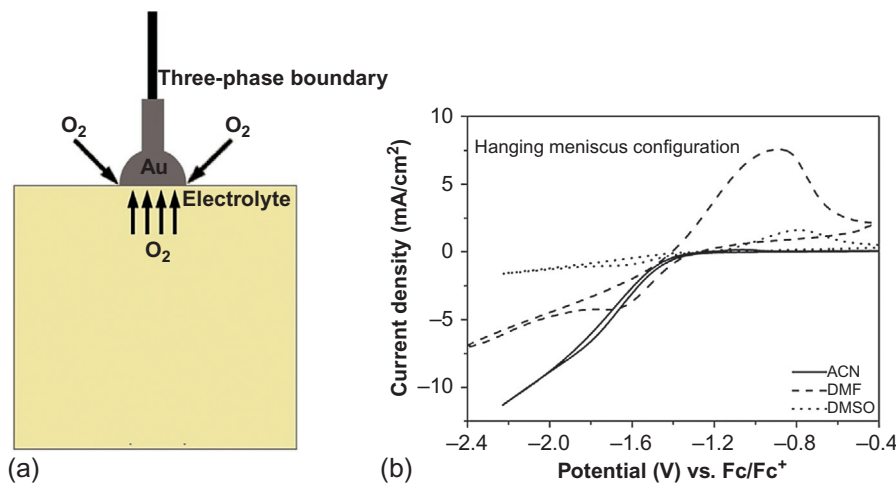


**Figure 6.3** (a) Schematic representation of the working area of a working electrode with the hanging meniscus configuration. (b) A Au disk electrode ( $\varphi=2.8$  mm) without sealing in the meniscus configuration in oxygen-saturated AN (solid line), DMF (broken line), and DMSO (dotted line) containing 0.1 M TBAPF<sub>6</sub>. Sweep rate: 100 mV s<sup>-1</sup> [16].

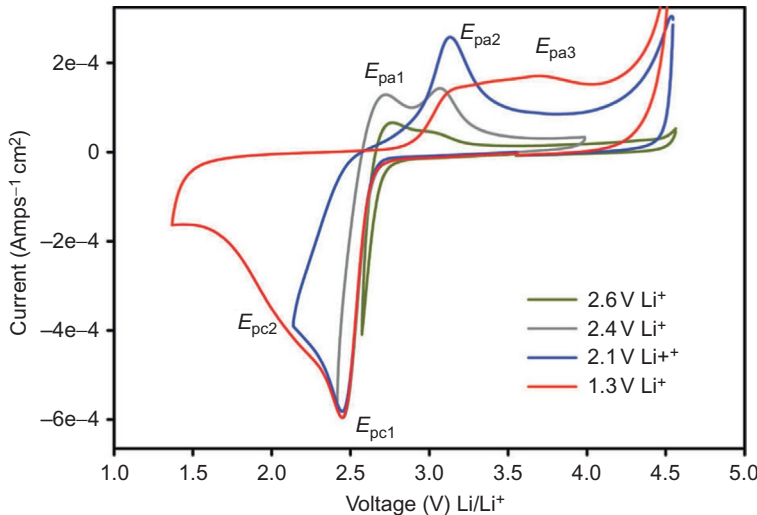
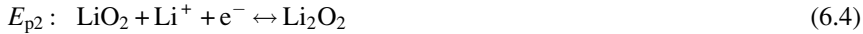


**Figure 6.4** Cyclic voltammograms for the ORR in 0.1 M LiPF<sub>6</sub>/DMSO within various electrochemical windows [6].

Abraham and his coworker suggested that the redox peak in Figure 6.4 could be related to the reaction pathway as follows [14]:





In the meantime, Pearson's hard and soft acids and bases (HSAB) theory was introduced to explain the ORR mechanism. According to HSAB, superoxide and  $\text{TBA}^+$  cations are soft species owing to their relative large radius and low charge density on the surface, whereas  $\text{Li}^+$  cation and peroxide are hard. Thus, superoxide coordinated with  $\text{TBA}^+$  cation and can be efficiently stabilized in the electrolyte solution without  $\text{Li}^+$  cation [1]. Conversely, due to the low affinity between  $\text{Li}^+$  cation and superoxide, superoxide generated as the product of the first reduction step of ORR was probably either disproportionate (Equation (6.3)) or further reduced (Equation (6.4)) to form another hard base, peroxide. Superoxide, peroxide, and oxide were generated as relative stable intermediates in a stepwise fashion during the oxygen reduction process. However, *in situ* surface-enhanced Raman spectroscopy (SERS) results exhibited only observation of  $\text{Li}_2\text{O}_2$  product and  $\text{LiO}_2$  intermediate under the condition of discharge, as shown in Figure 6.5a [17].

Bruce and his coworker proposed that the reaction pathway during the battery discharge process is as shown in the following [17]:

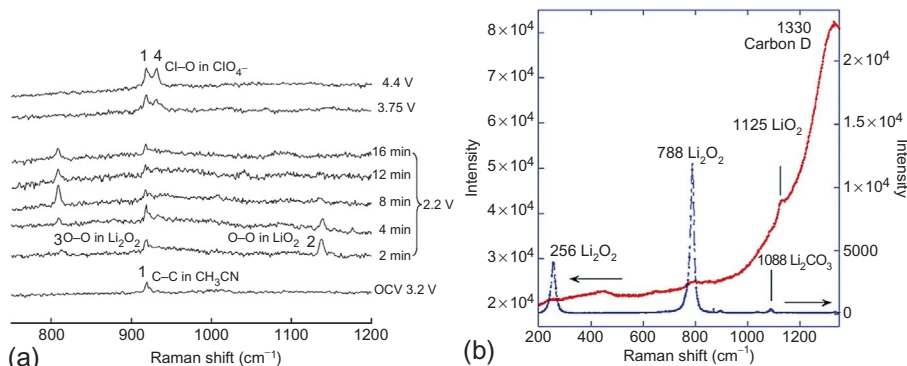


**Figure 6.5** (a) *In situ* SERS of ORR and reoxidation on a Au electrode in  $\text{O}_2$ -saturated 0.1 M  $\text{LiClO}_4/\text{AN}$  [17]. (b) Raman spectrum of the discharged cathode surface showing graphite D band, weak  $\text{Li}_2\text{O}_2$  and  $\text{LiO}_2$  bands (red trace). Commercial  $\text{Li}_2\text{O}_2$  (blue trace) is also shown for comparison [101].

They believed that a one-electron EC process rather than a two-electron transfer process played a major role during the discharge process of the Li-air battery.

Referring to the mechanism of ORR involving  $\text{Li}^+$  cation, we must pay attention to the reaction condition. It seems that the two reaction pathways described above are completely different from each other. However, they are very similar when we view their fundamentals. Actually, discharging can be considered as a slow sweeping process corresponding to the CV with sweep rate less than  $0.01 \text{ mV s}^{-1}$  [18]. Meanwhile, the potential plateau of the discharge process is usually around  $2.7\text{--}2.5 \text{ V}$  with respect to the potential of  $\text{Li}/\text{Li}^+$  [19]. In other words, the discharge process is equivalent to a slow potential sweeping in a small region. This can be used to explain why we can detect different reaction products for ORR within different reaction systems as mentioned above. During the discharge process, all of the superoxide was completely consumed by  $\text{Li}^+$  cation, and this can be regarded as the main reason for the observation of  $\text{LiO}_2$  rather than superoxide as the intermediate product. Afterwards, the disproportionation are considered to make a major contribution to the transformation of  $\text{LiO}_2$  to  $\text{Li}_2\text{O}_2$ , as the discharge potential is not negative enough to directly reduce the  $\text{LiO}_2$  to  $\text{Li}_2\text{O}_2$  (Equation (6.4)) [17], and also the discharge time is long enough to decompose all of the intermediate.

Regardless of the two different reaction pathways mentioned above,  $\text{Li}_2\text{O}_2$  has been detected to be the main discharge product in the proper reaction system without any side reactions [20,21]. As a vital intermediate in both schematic diagrams,  $\text{LiO}_2$ -like surface species has identified on the surface of discharge product for the first time by using Raman and magnetic measurements [as shown in Figure 6.5b] [14]. Besides that, the DFT calculation also gives the rational explanation, that is, the  $(\text{LiO}_2)_2$  dimer is thermodynamically more stable than  $\text{Li}_2\text{O}_2 + \text{O}_2$  (Equation (6.3)), thus the disproportionate of  $(\text{LiO}_2)_2$  will not occur at very low  $\text{LiO}_2$  concentration unless the  $\text{LiO}_2$  molecules can aggregate [22].

So far, the investigation of ORR in the electrolyte with  $\text{Li}^+$  cation only provided some limited information about the reaction pathway and the probable intermediate product. The most critical issues are the confirmation of elementary reaction and rate-determination step, as well as the determination of the kinetic parameters, such as reaction order and reaction rate constant. All of these fundamentals are important to the development of the effective electrode materials and electrolyte solution.

#### 6.2.1.3 Effect of the cathode materials

Currently, many studies have reported the effect of cathode materials on discharge performance, such as noble metal (Pt) and metal oxide ( $\text{Fe}_2\text{O}_3$ ,  $\text{NiO}$ ,  $\text{Fe}_3\text{O}_4$ ,  $\text{Co}_3\text{O}_4$ ,  $\text{CuO}$ , and  $\text{CoFe}_2\text{O}_4$ ) [23], especially manganese oxides ( $\alpha\text{-MnO}_2$  in bulk and nanowire form,  $\beta\text{-MnO}_2$  in bulk and nanowire form,  $\gamma\text{-MnO}_2$ ,  $\lambda\text{-MnO}_2$ ,  $\text{Mn}_2\text{O}_3$ , and  $\text{Mn}_3\text{O}_4$ ), and so on [24]. They believe that the proper cathode material, as an electrocatalyst, can decrease the overpotential for the reduction reaction and enhance the discharge performance. On the other hand, several groups declared that the discharge potential is independent of the cathode material, and even carbon itself

can provide high enough activity for the reduction [21]. Moreover, those so-called cathodic catalysts are only efficient for facilitating the decomposition of electrolyte solution, not for the oxygen reduction process. These two contradictory viewpoints have triggered argument; that is, whether an electrocatalyst is necessary for the ORR in the Li–air battery.

Actually, the oxygen reduced to superoxide ( $O_2 + e^- \rightarrow O_2^-$ ) in the electrolyte solution with TBA<sup>+</sup>-like cations is usually considered as a catalytically insensitive reaction, as mentioned above. And this first electron transfer process is supposed to be the only electrochemical reaction during the discharge process as well [17]. It seems rational that the electrocatalyst is unnecessary for the cathode. However, we also need to pay attention the generation of lithium oxides species rather than the superoxide deposited on the electrode surface. This deposition process, which probably includes the adsorption of Li<sup>+</sup> cation, nucleation, and growth of lithium oxides species, should be strongly affected by the cathode material. Markovic *et al.* reported the comparison of three types of single-crystal electrodes (i.e., Au (111), Au (110), and Au (100)). According to the CVs (see Figure 6.6), it is proposed that ORR in non-aqueous solution with Li<sup>+</sup> cation is an electrode structure-sensitive process. Besides that, Au (100) provides the highest ORR activity of all the others [25].

Xu and Shelton compared the intrinsic reactivity of Au (111) and Pt (111) for ORR with Li<sup>+</sup> cation, and periodic DFT calculations results revealed that Au (111) is more effective for ORR with Li<sup>+</sup> cation than Pt (111) because Pt (111) stabilizes Li<sup>+</sup> species much less than it stabilizes oxygen [26]. Actually, there is another possibility: that the thickness of Li–O<sub>2</sub> species at the time of “sudden death” of the Li–air battery might be affected a lot by the electrode material itself. In other words, the effect of electrode material on the discharge capacity is much more serious than that on the intrinsic reactivity of ORR. Very recently, TiC was chosen as a cathode catalyst with the DMSO-based electrolyte, and the cell can achieve >99.5% purity of Li<sub>2</sub>O<sub>2</sub> formation on each discharge and its complete oxidation on charge, with >98% capacity retention after

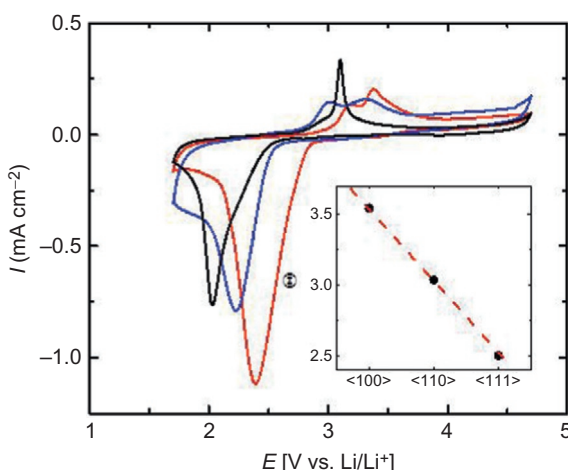


**Figure 6.6** Cyclic voltammograms for the ORR in 0.1 M LiPF<sub>6</sub>/DME at three types of single-crystal electrodes: Au (111) (black), Au (110) (blue), and Au (100) (red) [25].

100 cycles [27]. A detailed experiment to figure out the role of electrode material on cell capacity is still needed.

So far, the evaluation of catalytic activity for ORR in the Li–air battery is usually conducted in the single cell. However, the electrode performance does not directly indicate the intrinsic activity of a catalyst due to the electrode structure effect, especially the surface passivation, pore blockage, and the use of high mass ratio of carbon materials in the Li–air battery. It is very important to find a proper model electrode to quantify these cathode materials appropriately. As mentioned, the hanging meniscus configuration of a working electrode is a very good candidate to simulate the oxygen reduction process during cell operation as it has the same obvious three-phase boundary (TPB) effect as in the Li–air battery.

#### 6.2.1.4 *Effect of the electrolyte solution*

Unlike in the aqueous solution, the organic solvents and electrolytes in the nonaqueous solution, as the reaction media and the ionic conductor, have a great effect on the ORR with respect to the  $\text{Li}^+$  cation in the following aspects [28]: (1) a stable potential window; (2) the solubility of oxygen and  $\text{Li}^+$ ; (3) solvation effect relate to the transfer of  $\text{Li}^+$  cation; (4) reaction with the intermediate; and (5) volume loss when exposed to oxygen flow.

In fact, the organic solvents easily interact strongly with the electrode surface. It has been proved by low-temperature ultrahigh vacuum (UHV) scanning tunneling microscopy (STM) measurements that dimethylsulfoxide (DMSO) could be adsorbed on the reconstructed Au (111) and Au (100) single-crystal surfaces [29]. The observation of order at the DMSO/Au (111) interface is consistent with the understanding that the interactions between Au and DMSO are stronger and more dependent on the atomic structure of the Au surfaces than those between Au and water [30]. In other words, it is probable that the different organic solvents could substantially reorganize on the electrode surface, and this reorganization has consequences for the structure of the electrochemical double layer. On the other hand, Abraham and his coworkers discussed the interaction between  $\text{Li}^+$  cation and solvent in the electrolyte solution [6]. The results of ORR in four different solvents containing  $\text{Li}^+$  cation, i.e., DMF, DMSO, AN, and tetraethylene glycol dimethyl ether (TEGDME), demonstrated the different oxygen reduction product can be ascribed to stability of  $\text{Li}^+ \text{-(solvent)}_n$  complexes with respect to the donor number of organic solvents. Besides, as we know, the electrolyte solution would be decomposed during the operation of the Li–air battery. The decomposition of electrolyte solution also seriously affects the ORR with  $\text{Li}^+$  cation and will be discussed in detail below.

#### 6.2.2 *Oxygen evolution reaction in nonaqueous solution*

The study of the oxygen evolution reaction (OER) in a nonaqueous system is more complicated than that of ORR, due to the ambiguity in the influence of different discharge product structures and chemistries associated with catalysts in Li–air batteries on the charging overpotential. As illustrated in Figure 6.7, the common charge curve indicated

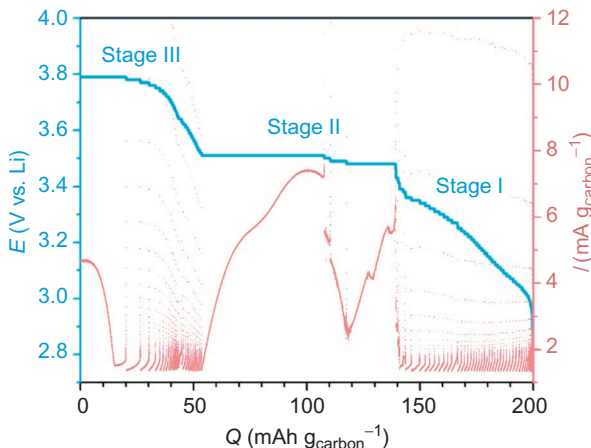


**Figure 6.7** Potential steps (blue) and corresponding current response (red) during potentiostatic intermittent titration technique (PITT) measurements (10 mV steps, 1.3 mA  $\text{gc}^{-1}$  current cutoff or 50 h durations) on charging of an electrode that was discharged to 200 mA  $\text{gc}^{-1}$  at 100 mA  $\text{gc}^{-1}$  in  $\text{O}_2$ -saturated 1.0 M  $\text{LiClO}_4$  in TEGDME [31].

two OER stages: the first OER stage occurs at low overpotential (<400 mV) and the second stage takes place at high overpotential (400–1200 mV) [31].

The studies of SERS and differential electrochemical mass spectroscopy (DEMS) suggested that these two potential regions are corresponding to the oxidation of  $\text{LiO}_2$  and  $\text{Li}_2\text{O}_2$ , respectively [17]. Accounting for the disproportionation of  $\text{LiO}_2$  to  $\text{Li}_2\text{O}_2$  by the end of long-time battery operation, the proposed reaction pathway during the battery charge process is shown in the following:



The potentiostatic intermittent titration technique (PITT) and galvanostatic intermittent titration technique (GITT), which are quasi-equilibrium techniques to probe the kinetics of electrochemical reaction, were applied to investigate the kinetics of the charging process [14]. The results revealed that the first OER stage with a slopping voltage profile is relatively insensitive to charge rates and catalysts, and it could be ascribed to the delithiation of sub-nm layer of  $\text{Li}_2\text{O}_2$  to form  $\text{LiO}_2$ -like species on the surface via a solid-solution route (see the equations below):



The overall  $2\text{e}^-/\text{O}_2$  OER process is the same as Equation (6.8). However, the second OER stage with a voltage plateau is sensitive to discharge/charge rates and catalysts, and it can be attributed to the oxidation of bulk  $\text{Li}_2\text{O}_2$  particles. Although the proposed mechanisms mentioned above might not be true, they gave us the inspiration to

understand the fundamental; that is, the charge process of the Li–air battery is strongly potential dependent.

### 6.2.2.1 Effect of the cathode materials

Generally speaking, the Li–air battery presents a modest overpotential of around 0.3 V for the discharge process, but a much higher overpotential of more than 1.0 V for the charge process [32]. Thus, developing an effective catalyst to reduce the overpotential of OER in nonaqueous solution is one of the critical issues for the Li–air battery. Similarly, the efficacy of the catalyst on charge is disputed as much as that on discharge currently. McCloskey *et al.* reported that no enhanced OER kinetics were detected in the presence of catalysts as the so-called catalyst only contributed to the electrolyte solvent decomposition rather than the OER [21]. Conversely, a number of studies demonstrated that the overpotential of OER was decreased due to the application of catalysts as the Li–air batteries were operated at a high capacity from 1000 to 5000 mA g<sup>-1</sup> [33,34]. As mentioned in the last section, Lu and Shao-Horn suggested that the catalyst on charge plays a crucially important role for the oxidation of bulk Li<sub>2</sub>O<sub>2</sub> at relatively high overpotential (e.g., >1000 mV) [31]. Currently, catalysts on the charge process are concentrated on carbon-supported noble metals, as the primarily used catalysts in fuel cells; for example, the Au, Pt, and Ru nanoparticles supported on Vulcan carbon [35]. The investigation of nonprecious metals containing metal oxide, as promising candidates to be an effective and low-cost Li–air battery catalyst, could be a future trend [27,36].

### 6.2.2.2 Effect of the electrolyte solution

There are several papers addressing the impact of electrolyte solution on the charge process of the Li–air battery, such as increasing the solubility of Li<sub>2</sub>O<sub>2</sub> so as to oxidize all of the depositions primarily in the solution at the electrode surface [14]. Here, we want to introduce the concept of the redox mediator, which can be regarded as an additive in the electrolyte solution to improve the OER performance. The mediator is a highly soluble shuttle that can be easily oxidized at the electrode and then, in turn, oxidizes the discharge product as Li<sub>2</sub>O<sub>2</sub> through a direct chemical reaction. The role of the redox mediator can be explained by an electrochemical–chemical (EC) catalytic reaction (the scheme is presented in Figure 6.8).

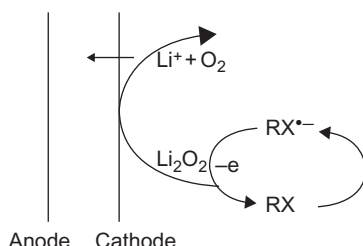


**Figure 6.8** How a shuttle oxides the Li–O<sub>2</sub> species on the electrode surface.

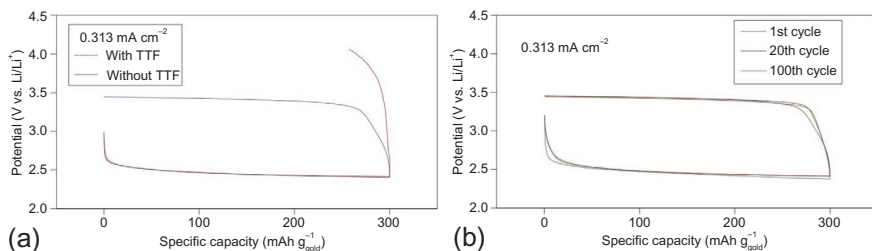


**Figure 6.9** (a) First-cycle load curves (constant-current discharge/charge) with and without the redox mediator. (b) Cycling stability of Li–O<sub>2</sub> cathodes that employ a redox mediator [37].

The redox shuffle requires that the reversible potential be more positive than the redox potential of Li<sub>2</sub>O<sub>2</sub>, and it should be stable in the potential range during the cell operation. Bruce's group reported a redox-active molecule tetrathiafulvalene (TTF) as the electron–hole transfer agent, and its oxidized form (TTF<sup>+</sup>) is capable of oxidizing Li<sub>2</sub>O<sub>2</sub> in a short time and effectively reducing the polarization on charging [37]. Moreover, the cell containing the redox mediator of TTF can be cycled 100 times at a rate that is impossible in the absence of TTF (see Figure 6.9).

There is no doubt that the redox mediator can catalyze the sluggish OER at the air electrode. However, if a metallic Li-anode is used, some parts of the unreduced mediator could diffuse through the electrolyte solution and be reduced at the Li-anode, which would bring about disastrous effects on the cell performance and cycling stability [38].

### 6.2.3 Decomposition of the electrolyte solution

Given the high oxidability of superoxide, LiO<sub>2</sub>, and even Li<sub>2</sub>O<sub>2</sub> as well as the potential range on the air electrode, the solvent may not be chemically and electrochemically stable. It was proved that carbonate-based solvents, such as propylene carbonate (PC), ethylene carbonate (EC), and dimethyl carbonate (DMC), are not suitable for the Li–air battery as the decomposition of carbonates form LiCO<sub>3</sub> and Li alkyl carbonates, which decomposed to CO<sub>2</sub> upon cell charging.

By using a combination of mass spectrometry (MS), X-ray diffraction (XRD), Fourier transform infrared spectroscopy (FTIR), and SERS, the products formed during discharge in PC solvent were lithium propyl dicarbonate, C<sub>3</sub>H<sub>6</sub>(OCO<sub>2</sub>Li)<sub>2</sub>, Li<sub>2</sub>CO<sub>3</sub>, HCO<sub>2</sub>Li, CH<sub>3</sub>CO<sub>2</sub>Li, CO<sub>2</sub>, and H<sub>2</sub>O. In the electrolyte of EC/DMC with LiPF<sub>6</sub> as the salt, thick coatings of reaction products were found on both carbon and MnO<sub>2</sub>-coated carbon cathodes (see Figure 6.10), and the products were mainly composed of Li, F, C, O, and P [39]. Pure dimethoxymethane (DME) can lead to Li<sub>2</sub>O<sub>2</sub> formation but its decomposition may happen at high potential during charge [40]. Dimethylformamide (DMF)-based electrolyte has also been confirmed as not suitable for the Li–air battery due to its instability at the cathode side [41]. DFT calculations confirmed nucleophilic substitution with superoxide is a common mechanism of nonaqueous solvents decomposition, and chemical functionalities, including *N*-alkyl substituted

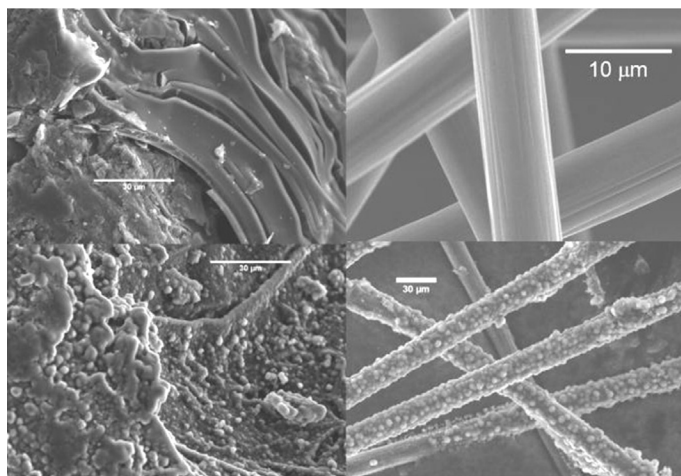


**Figure 6.10** SEM images of graphite foam (top left), the carbon veil (top right), discharge products on graphite foam (lower left), and discharge products on the carbon veil (lower right) [39].

amides, lactams, nitriles, and ethers, were found stable against nucleophilic substitution [42]. Experimental and DFT computational studies of an electrolyte based on a tri(ethylene glycol)-substituted trimethylsilane (1NM3) provide evidence that ether-based solvents are more stable toward oxygen reduction discharge species [43]. Although the ethers are more stable than the organic carbonates, their decomposition in Li–air batteries has also been found [14]. Currently, we do not have a perfect electrolyte solution with a high Li–air battery performance and without decomposition during the cyclic cell operation. Mixed solvent-based electrolytes might be a promising choice of the electrolyte for Li–air batteries, as for Li-ion batteries.

## 6.3 Application of model electrode

### 6.3.1 Overview of anode

Anodes in the Li–air battery usually employ Li metal, which has the lowest electrode potential and is very chemically reactive. These chemical and electrochemical properties make most electrolytes unstable on a Li metal surface. Fortunately, a passive film or solid electrolyte interface/interphase (SEI) will form on a Li metal surface due to the decomposition of and reaction with the electrolyte. This film will keep fresh lithium away from the electrolyte, stop the further reaction, and stabilize the interface, though it introduces additional ohmic loss and mass transport resistance to the anode. Unfortunately, this SEI on a Li metal surface is not stable during the charge–discharge cycling, as shown in Figure 6.11 [44]. Lithium dissolution when discharging and lithium deposition when charging may shift the interface or change the anode thickness. The preformed SEI may not endure the dramatically large change of the electrode

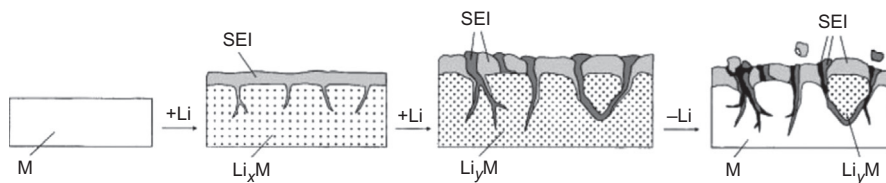


**Figure 6.11** Illustration of SEI formation and evolution on the surfaces of Li or Li alloy metal [44].

volume and fracture. New SEI may form on the newly formed interface and cause uneven distribution of the current density, making more severe dendrite growth. Like Zn, Li favors dendrite growth. On charging, Li dendrites may grow out from the anode and possibly penetrate into the separator leading to lithium loss and even worse internal short circuit. There may exist two research directions addressing this issue: chemical and mechanical. The anode processes on charging–discharging can be considered as electroplating and electropolishing of Li metal. Techniques and knowledge in electroplating and electropolishing such as current distribution, leveling agent, surface morphology, and roughness can be applied to the study of the anode cycling. SEI consideration should also be incorporated into such study. Another way is to choose a solid Li-conducting membrane, especially a ceramic one, and wrap or press it on the anode so that the dendrites’ growth is mechanically prohibited [45]. But, such a membrane should have a high Li-ion conductivity at room temperature, chemical and electrochemical stability, and high mechanical strength, which so far remains challenging. Also, it must be noted that not every electrolyte will form a stable SEI, which not only stops further reaction of Li metal with electrolyte but also prevents O<sub>2</sub> diffused from the air electrode from reacting with the anode.

### 6.3.2 Cathode

Because the use of electrolytic manganese dioxide (EMD) was demonstrated in a rechargeable Li–O<sub>2</sub> battery [46], the exploration of the role of catalyst regarding ORR and oxygen evolution reaction (OER related to the charge process) in nonaqueous systems becomes more and more common. Examples include screening of materials including metal (Pt), perovskite (La<sub>0.8</sub>Sr<sub>0.2</sub>MnO<sub>3</sub>), and metal oxides (Fe<sub>2</sub>O<sub>3</sub>, NiO, Fe<sub>3</sub>O<sub>4</sub>, Co<sub>3</sub>O<sub>4</sub>, CuO, and CoFe<sub>2</sub>O<sub>4</sub>) [23]; exploration of various manganese oxides ( $\alpha$ -MnO<sub>2</sub> in bulk and nanowire form,  $\beta$ -MnO<sub>2</sub> in bulk and nanowire form,  $\gamma$ -MnO<sub>2</sub>,  $\lambda$ -MnO<sub>2</sub>, Mn<sub>2</sub>O<sub>3</sub>, and Mn<sub>3</sub>O<sub>4</sub>) [47]; synthesis of carbon-supported manganese oxides (MnO<sub>x</sub>/C) and its application in air electrodes [48]; influence of C, Au/C, and Pt/C catalysts on the charge and discharge voltages [49]; PtAu nanoparticles supported on carbon (PtAu/C) as a bifunctional (ORR and OER) electrocatalyst [50]; H<sub>2</sub>O<sub>2</sub> decomposition reaction as a selecting tool for choosing catalysts [51]; and comparison of metals and metal oxides [52] and heat-treated metal phthalocyanine complex as the catalyst [53]. As discussed before, ORR in the nonaqueous Li–air cathode is not a catalytically sensitive reaction because the carbon possesses catalytic activity.

Furthermore, the electrode performance in electrochemical devices like PEM fuel cells does not directly indicate the intrinsic activity of a catalyst because of the electrode structure effect, especially the surface passivation, pore blockage, and the use of a high mass ratio of carbon materials in the Li–air battery. To more accurately determine the catalyst activity, testing the materials on a thin film electrode rather than in a single cell may be more appropriate. We also need to point out three things. First, even when the thin-film electrode is used to quantify the catalyst activity, complication may arise from the unstable solvents. For example, the ORR activity trend ranks in the descending order of  $\text{Au} > \text{GC} > \text{Pt}$  in  $\text{PC} + \text{DME}$  [54] while the trend follows the sequence of  $\text{Pt} > \text{Au} > \text{GC}$  in DME [55]. Second, the normalized current or activity based on the true surface area of catalyst or catalyst mass may be not as critical as in the PEM fuel cells, especially when nonnovel catalysts are used in the Li–air battery. The focus should be on the large surface area, particularly the electrochemical effective surface area, but this does not mean smaller particle size implies better ORR activity. Once the product film covers a catalyst particle, it would not work as the reaction site any more. The morphology of the catalyst, like nanorods, nanowires, dendrites, and random clusters [56] or hollow spheres [57], may impact the ORR activity. Third, novel metals should be finally avoided in the Li–air battery [58] to prevent walking the same road as PEM fuel cells in terms of cost issues.

Designing novel 3D electrode structures is another high-impact research area. As shown in Figure 6.12a,  $\text{MnO}_2$  nanoflakes were uniformly coated on multiwalled carbon nanotubes (MWNTs) by immersing MWNTs into an aqueous  $\text{KMnO}_4$  solution. Directly using the  $\text{MnO}_2/\text{MWNT}$  composites (containing 40 wt.% MWNTs) as Li–air battery electrodes enhances the kinetics of the oxygen reduction [59]. In Figure 6.12b, hollow carbon fibers with diameters on the order of 30 nm were grown on a porous alumina substrate and were used as the oxygen electrode in  $\text{Li} - \text{O}_2$  batteries. These all carbon–fiber (binder-free) electrodes were found to yield high discharge capacity up to  $7200 \text{ mAh g}^{-1}$  carbon even at  $63 \text{ mAg}^{-1}$  carbon and high gravimetric energy up to  $2500 \text{ Wh kg}^{-1}$  [34]. As shown in Figure 6.13, a novel freestanding-type electrode

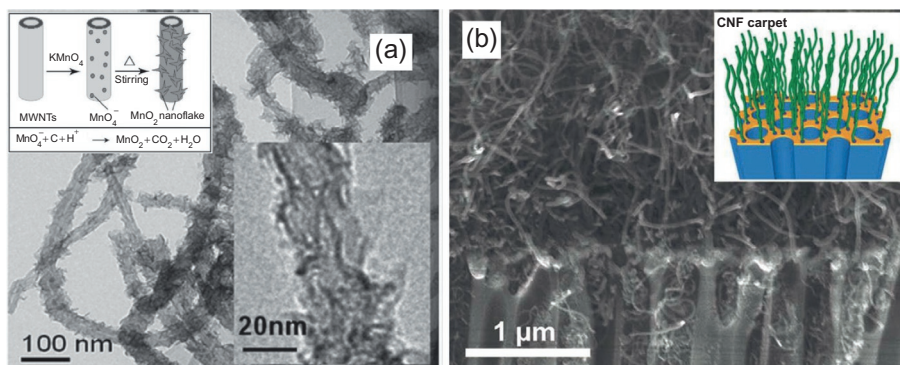


**Figure 6.12** (a) TEM image of the  $\text{MnO}_2/\text{MWNT}$  nanocomposites [59] and (b) SEM image of carbon nanofibers carpet based on the porous anodized aluminum oxide temperate [34].

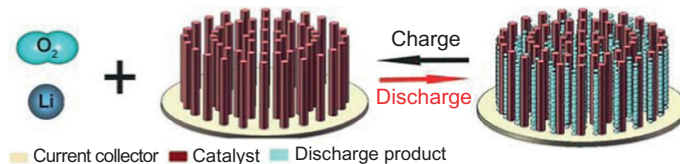


**Figure 6.13** The schematic diagram of the freestanding catalyst-based electrode during cycling in the Li–O<sub>2</sub> battery [60].

composed of only Co<sub>3</sub>O<sub>4</sub> catalyst and Ni foam current collector was designed and constructed [60]. The new air electrode was found to yield noticeably higher specific capacity and improved cycle efficiency over the conventional carbon-supported electrode with almost the highest discharge voltage (2.95 V), the lowest charge voltage (3.44 V), the highest specific capacity (4000 mAh g<sup>-1</sup> cathode), and the minimum capacity fading. Another example is the construction of 3D hierarchically bimodal porous air electrodes with functionalized graphene sheets (FGSs) (see Figure 6.14) [61], which are hot research materials in electrochemical energy conversion and storage [62]. A very high discharge capacity (15,000 mAh g<sup>-1</sup> carbon) was obtained, which results from facilitated oxygen transport and unique lithium oxide growth. SEM images (a and b) in Figure 6.14 show that the graphene-based air electrode contains numerous large tunnels that facilitate continuous oxygen flow into the air electrode while other small “pores” provide ideal triphase regions for the oxygen reduction. DFT calculations show that Li<sub>2</sub>O<sub>2</sub> prefers to nucleate and grow near functionalized lattice defect sites on graphene. Also, SEM and TEM images (c–e in Figure 6.14, indicated by white arrows), show that the deposited Li<sub>2</sub>O<sub>2</sub> forms the isolated nanosized “islands” on FGS, avoiding surface passivation and pore clogging and ensuring smooth oxygen transport during the discharge process. Another very interesting electrode structure is based on MnO<sub>2</sub>-decorated electrospun hollow core-porous shell carbon fibers, which was developed at Virginia Tech. Co-electrospinning of

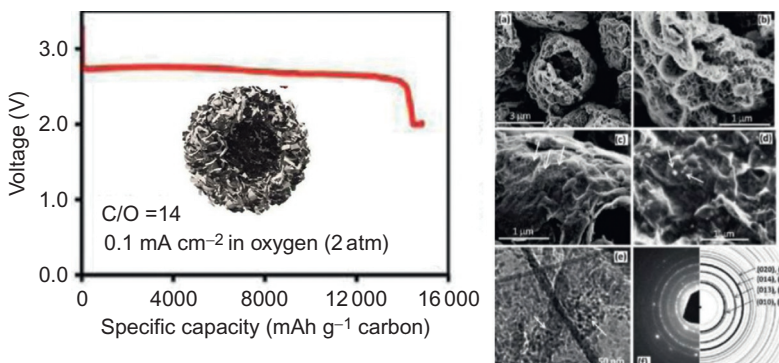


**Figure 6.14** The discharge curve of a Li–O<sub>2</sub> cell using functionalized graphene sheets and morphologies of the graphene-based air electrode [61].

PAN (polyacrylonitrile) with PMMA (poly(methylmethacrylate)) followed by subsequent heat treatment has given rise to carbon fibers with controlled morphologies. During thermal treatment of the precursor fibers, PAN is converted into carbon while PMMA is burned away to leave voids of tailored dimensions based on the morphology of the electrospun precursor fibers. The use of solutions of  $\text{KMnO}_4$  to oxidize the surface of the hollow core microfibers following thermal treatment gives the porous shell with manganese oxide decorated on the surface (Figure 6.15).

### 6.3.3 The importance of three-phase boundary

With respect to the air electrode, what happens during discharge of Li–air batteries is electrochemically and physically very similar to that during cold start of PEM fuel cells at subzero temperatures. What is known in the field of subzero PEM fuel cells will help in understanding fundamentals and challenges in Li–air batteries [63]. For the air electrode in a PEM fuel cell, the microstructure of the catalyst layer can be depicted as catalyst-loaded carbon particles flooded with the electrolyte form agglomerates covered with a thin film of electrolyte. The reactant gas first passes the channels among the agglomerates, diffuses through the ionomer thin film and, thereafter, in the agglomerates, and then reaches the reaction sites. During cold start, the generated water due to the ORR will freeze once the heat produced is not enough to warm the membrane electrode assembly (MEA) above the freezing temperature. The freezing of the generated water covers the catalyst sites, reduces the TPBs, and blocks the reactant gas accessing the reaction sites [64,65]. The increased polarization will usually lead to a cold start failure, as shown in Figure 6.16a. For most state-of-the-art air electrodes in the Li–air battery, the microstructure is basically the same as that in the PEM fuel cell but it is usually flooded by liquid electrolyte. During discharge, an electrochemical combination of oxygen and lithium ion is expected to form  $\text{Li}_2\text{O}_2$  and/or  $\text{Li}_2\text{O}$  solids, which are generally thought to be insulators and hard to be dissolved in the solvents. Like water freezing, the precipitation of lithium oxides will passivate reaction sites, block pores, and increase mass transport resistance, which limits

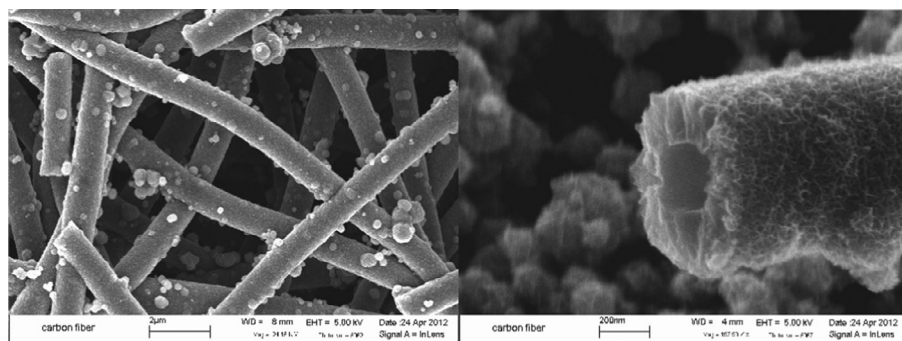


**Figure 6.15**  $\text{MnO}_2$  decorated electrospun hollow core-porous shell carbon fibers.

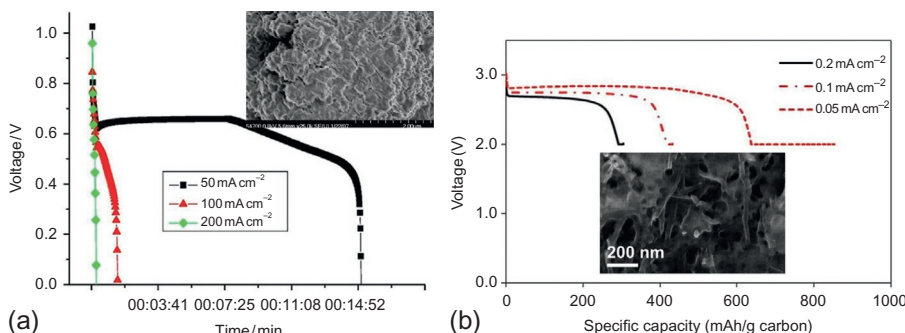


**Figure 6.16** (a) Cold start failure of PEM fuel cell due to water freezing: start curve [102] and SEM image of catalyst layer [103]; (b) discharge behavior of Li–air battery with lithium oxides precipitation: discharge curve [70] and SEM image of air electrode [34].

the discharge capacity and rate capability, as shown in Figure 6.16b. For cycle performance, the volume change due to phase transition, like water/ice transition in the subzero PEM fuel cells, may damage the electrode structure in the Li–air battery.

### 6.3.4 Surface passivation and pore block

Where are lithium oxides located? It depends on where the ORR reaction occurs and, accordingly, can be ascribed to triple-phase boundaries (TPBs) ( $O_2$ , electrolyte, and catalyst) or double-phase boundaries (DPBs) (electrolyte and catalyst), the latter of which is reasonable due to the fact that oxygen dissolves in the nonaqueous electrolyte. A combination of TPBs and DPBs is the most likely case in the present air electrode, as indicated and confirmed by the correlation of discharge capacity with oxygen transport properties of organic electrolytes [66], wetting property and affinity to carbon pores of the solvents [67], effect of oxygen pressures on the electrochemical profile [68], 20% pore volume occupation by discharge product [69], formation of extra pores in Ketjen black (KB) electrode [70], increased oxygen solubility in the blended solvents [71], and increased oxygen concentration by using perfluorinated compounds as oxygen carriers [72]. Furthermore, TPBs are essential and critical to the discharge capacity regarding  $O_2$  mass transport [14]. It thus can be expected that lithium oxides may deposit on and passivate the carbon surface [see Figure 6.17a] and may be stored in the pores within the carbon agglomerates and among agglomerates (see Figure 6.17b, where four agglomerates form the two types of pores).

For the former case, it is important to understand the lithium oxides precipitation, as a simplified flat electrode model can be used rather than the porous electrode one. Understanding surface passivation helps elucidate the relationship between film growth and the capacity limitation. Surface passivation was indicated by the RDE data in that increasing the rotating rate actually decreased the disc current [11]. Later, morphology of the discharge product film and discharge curves on flat GC were conducted, and simulation results based on continuum-scale cell model indicated that

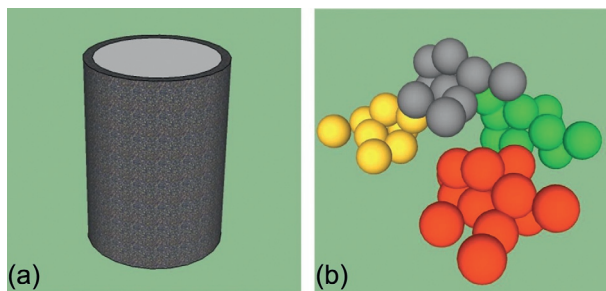


**Figure 6.17** Schematic show for the location of lithium oxides formation: (a) surface passivation and (b) pore blockage and clogging.

discharge product film with a thickness of tens of nanometers was highly electronically resistive and was the main contribution for the capacity limitation in the Li-air battery [73]. A galvanostatic discharge at  $0.6 \mu\text{A cm}^{-2}$  generates a product film with a thickness of 40–70 nm [see Figure 6.18a]. Surprisingly, the discharge capacity shows rate dependence even on a flat electrode, as shown in Figure 6.18b. Two questions arise here: Why does discharge at higher current density give smaller capacity? If passivation happens at a critical thickness of product film, why does this critical thickness depend on the discharge rate? Almost the same authors later designed a clever and rigorous experiment using the ferrocene/ferrocenium redox couple to probe charge transport through films of  $\text{Li}_2\text{O}_2$  on a GC electrode. By combining the electrochemical results and metal–insulator–metal (MIM) model they concluded that the

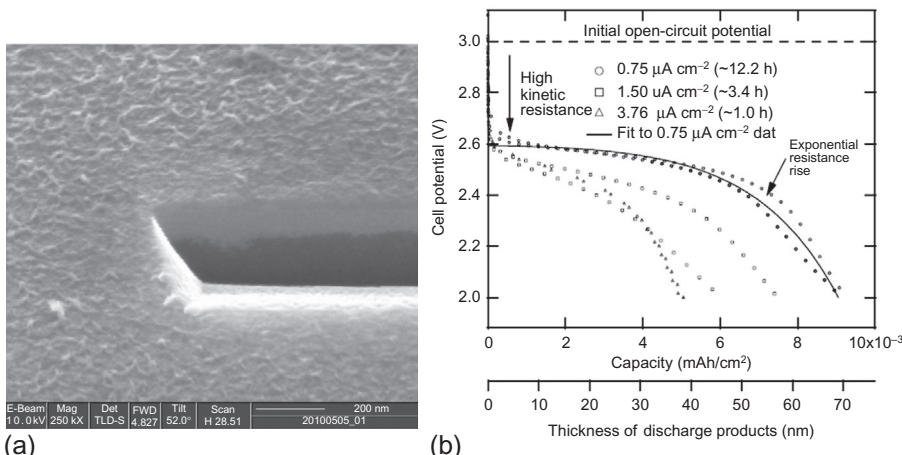


**Figure 6.18** (a) SEM image of the discharge film (40–70 nm thickness) produced by the end of a  $0.6 \mu\text{A cm}^{-2}$  discharge on a flat glassy carbon electrode and (b) discharge curves of flat-electrode cells at three current densities [73].

charge transport within the product film ( $\text{Li}_2\text{O}_2$ ) determined the discharge capacity or “sudden death” [74]. The critical thickness is determined by the tunneling of holes within the passivation film and calculated at about 5–10 nm. To answer the questions mentioned above and explain the discrepancy in critical thickness, two fundamental things need to be clarified: (1) the mechanism of  $\text{Li}_2\text{O}_2$  film growth and (2) the destination of  $\text{LiO}_2$  intermediate. The  $\text{Li}_2\text{O}_2$  growth may follow a discrete spiral growth mechanism rather than layer-by-layer growth, and this is plausible as the crystal nucleation prefers the kink and step sites on the surface. Discrete spiral growth at its initial state may also favor the charge transport along the  $\text{Li}_2\text{O}_2$  surface, which has been approved metallic [75,76] not through the bulk  $\text{Li}_2\text{O}_2$ . If so, the critical thickness of 5–10 nm may be underestimated and it can explain the thick discharge film that was observed [see Figure 6.18a]. But, it may need further investigations coupling electrochemical tests with SEM or atomic force microscopy (AFM). The  $\text{LiO}_2$  intermediate may detach from the reaction sites as indicated in RDE tests [54,77], and its movement and solvation within the double layer might be governed by the overpotential. This can explain the dependence of discharge capacity on discharge rate, but still needs further study to confirm validity. The solvated  $\text{LiO}_2$  may disproportionate to  $\text{Li}_2\text{O}_2$  on the preformed  $\text{Li}_2\text{O}_2$  surfaces, which means discharge coulombs would not be directly correlated to the surface coverage. If intermediates can detach from the reaction sites even in the stationary condition, as it is believed, this will account for the pore clogging. Otherwise, it is hard to image there would be extra lithium oxides blocking the pores either within or between agglomerates because the passivation film with 5–10 nm thickness will stop the ORR. At the same time, we need to be aware that the blocked pores must be electrolyte-wetted considering TPBs or DPBs and the movement of  $\text{LiO}_2$  intermediate.

As with the pore clogging and blockage, the effects of pore size, pore size distribution, pore volume, and surface area should be emphasized along with the pores wetted or not wetted by the electrolyte. The single point Brunauer–Emmett–Teller (BET) surface area for Black Pearls 2000 (BP2000), Shawinigan Black acetylene black (SAB), and Super P were reported as 1475, 75, and  $62\text{ m}^2\text{ g}^{-1}$ , respectively, and the specific capacity for these three carbon black powders did not follow the sequence of BET surface area [78]. These results suggested that wetting of the carbon black is an important factor in determining discharge capacity, and the BET surface area cannot be used to predict the trend in discharge capacity. In the same study, by comparing discharge capacity for the PVDF and PTFE electrodes, which had identical pore volume (73%), discharge capacity was found to be correlated with the available specific pore volume (mL per gram of carbon black). Later, discharge capacity was actually found to be related to the mesopore volume of the carbon material [79], but the evidence is not strong as the carbon material with large mesopore volume also showed large total pore volume in that study. By deliberately controlling the porosity of carbon aerogels, that is, preparing carbons with similar pore sizes and pore size distributions but different pore volumes and preparing carbons with similar pore volumes but different pore diameters, mesopores were firmly proved to be important to improve the discharge capacity, and large pore volume and wide pore size exhibited high discharge capacity [80]. This is possibly due to (1) better accessibility of electrolyte to the

carbon surface; (2) better diffusion of oxygen to the carbon–electrolyte interface; and (3) larger storage volume for discharge. The critical role of mesopore volume in determining discharge capacity was also confirmed by comparing different carbon-based electrodes; that is, BP2000, Calgon, Denka, Ketjen black (KB), milled KB, and home-made mesopore carbon (JMC) [70]. However, we need to point out that only porosity of carbon powder itself and not that of the air electrode has been related to the discharge capacity, so care must be taken in considering these results because the porosity of air electrode may differ from that of carbon powder. As shown in Figure 6.19a, carbon particles may form agglomerates during electrode preparation, especially in the presence of binders. There are at least two factors affecting the porosity of the air electrode: (1) porosity from carbon powder itself and (2) stacking state. Taking Figure 6.19a as an example, most likely there are micropores and/or mesopores on the carbon surface, mesopores within agglomerates, and mesopores or even macropores among agglomerates. If any binder is used in the electrode preparation, the porosity will change. It was reported that PVDF binder blocked the majority of the pores with a diameter below 30 nm, causing a decrease in discharge capacity [81]. Bimodal pore distribution of the air electrode in PEM fuel cells has been widely accepted and experimentally proved [82]. Because the synthesized mesocellular carbon foam (MCF-C) has bimodal pore distribution, it is hard to say the same situation exists for other carbon powder-based electrode. In the same article, MCF-C showed a higher discharge capacity; about 40% increased capacity compared to several commercial carbon blacks. The enhanced performance was ascribed to the large pore volume and ultralarge mesoporous structure, which allowed more lithium oxides to be deposited during the discharge process. One needs to notice that after discharge the characteristic peaks in the pore distribution curve disappear. But, this still does not confirm that lithium oxides fill in the pores or clog the open area of the pores. A lithium oxides accommodation model was built by considering the electrochemical discharge and porosimetry [83], as shown in Figure 6.19b. It was thought that micropores

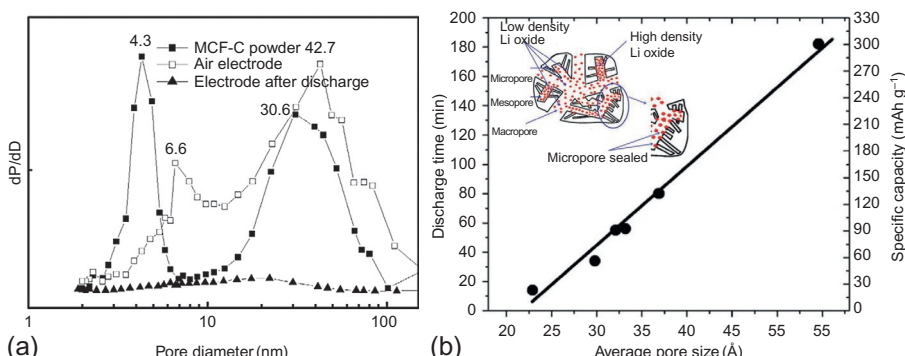


**Figure 6.19** (a) Pore size distribution curves of carbon powder, electrode before and after discharge at  $0.1 \text{ mA cm}^{-2}$  [104] and (b) discharge time and specific capacity as a function of average pore diameter and inset shows lithium oxides accommodation in pores [105].

and some of mesopores would be blocked by Li oxides at the beginning of discharge, and Li oxides mainly reside inside the large mesopores. The density of the oxides increases as the reduction proceeds, until the density is high enough to completely block mass transfer. For this model, two things need clarification, as noted above: mechanism of  $\text{Li}_2\text{O}_2$  film growth and movement of  $\text{LiO}_2$  intermediates, because very thin passivation film would stop the reaction, which contradicts such a model. We have to say the failure mechanism in the Li–air battery is actually not similar to that of alkaline fuel cells (as the authors claimed in that study), due to the chemical reaction of the alkaline electrolyte and  $\text{CO}_2$  in the air for alkaline fuel cells and the electrochemical reaction requiring TPBs or DPBs in the Li–air battery.

### 6.3.5 Product distribution

How do the lithium oxides distribute on the surface and within the electrode? The distribution may need to be considered in two scales: (1) carbon particle or fiber surface and (2) interface or reaction zone within the whole electrode. For the former, if the catalysts are decorated on the carbon surface how do they influence the product morphology? Because the carbon itself is electroactive to the ORR, what is the role of the catalyst? The latter is highly related to the lithium oxide distribution across the electrode and may be correlated with the oxygen profile along the depth of the electrode and is highly associated with the rate capacity, especially when the electrode is thick. Another important factor is the electrolyte distribution as the electrochemical interface, either TPBs or DPBs, which at least requires liquid–solid interface, is essential for the ORR.

#### 6.3.5.1 Distribution on carbon surface

As mentioned before, carbon materials themselves are electroactive toward the ORR in nonaqueous Li–air batteries. All-carbon materials without heterogeneous catalyst have been demonstrated as the active materials for the air electrodes; that is, a free-standing carbon nanotube/nanofiber mixed bulky paper [84], nitrogen doped KB and Calgon activated (CA) carbon [85], nitrogen doped carbon nanotubes [86], nanostructured diamond-like carbon thin film [87], and graphene nanosheets [88]. Although experimental results show enhanced discharge capacity before and after nitrogen doping [85,86] or by comparing graphene with Vulcan XC72 [88], mechanistic understanding of the action of carbon in the Li–air cathode and details of molecular-level surface chemistry interacting with lithium oxides are not fully explored. DFT calculations have been performed to examine the ORR on several model carbon structures including g(0001) basal plane (including graphene), the (8,0) single-wall nanotube (SWNT) to represent curvature, the armchair-type edge (henceforth referred to as armchair edge) of a graphene nanoribbon (GNR) to represent the edge of graphite, and a di-vacancy in graphene to represent point vacancies (see [Figure 6.20](#)) [89]. The basal plane and the curved surface of the SWNT do not well stabilize the key intermediate and limits the complete  $\text{O}_2$  reduction. The armchair edge and di-vacancy are highly reactive and can form oxidized carbon structures ( $\text{CO}_x$ ) that will serve as the active

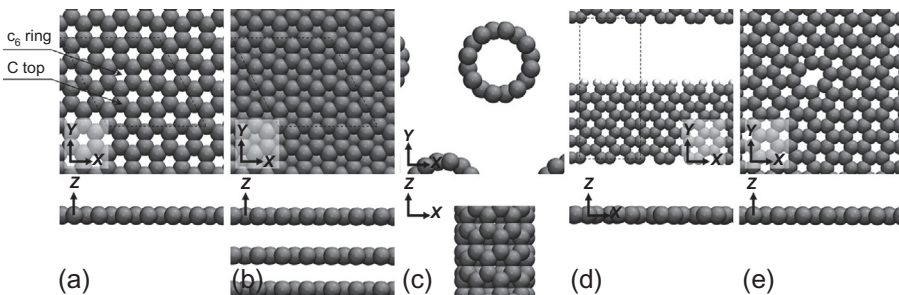


**Figure 6.20** Structural models in top (upper panels) and side (lower panels) views for: (a) graphene; (b) 3-layer g(0001); (c) (8,0) SWNT; (d) GNR with armchair edge; and (e) graphene with a di-vacancy [89].

sites for catalyzing  $O_2$  reduction. Furthermore,  $LiO_2$  can be chelated and stabilized by neighboring oxygen ligands. From the experimental evidence in Figure 6.21, the deposited  $Li_2O_2$  would form isolated nanosized “islands” on the FGS defect sites. Also from Figure 6.21 [34], it is evident that the nuclei formation and particle growth of lithium oxides prefer some sites on the carbon fibers where the defects and functionalities are probably rich. Referring back to the heterogeneous metal- or oxide-loaded carbon, such metal or oxide particles to some extent can be considered to increase the defects or functionalities on the carbon surface, which will definitely influence the distribution and morphology of the discharge product. For example, without the catalyst, the air electrode was covered by a film-like discharge product, while with the  $MnO_2$  catalyst, some granulated-type voids within the discharge product were observed that would allow oxygen diffusion [90]. One needs to be aware that the decoration of heterogeneous catalysts would consume the defects and functionalities originally presented on the carbon surface, and the preference of lithium oxides on the heterogeneous catalysts and carbon is different.

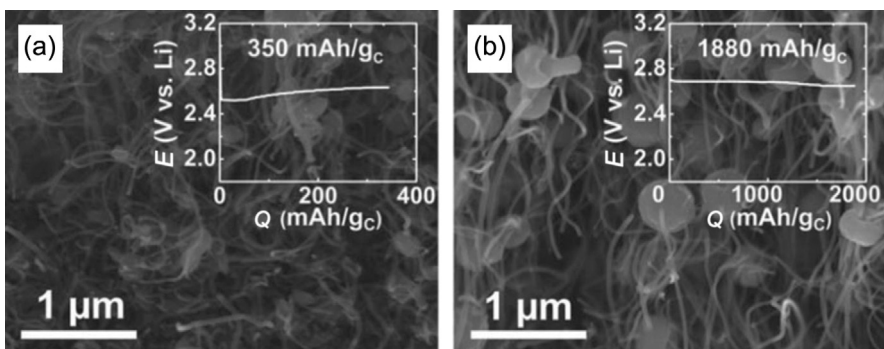


**Figure 6.21** Evolution of discharge product morphology and insets show the corresponding discharge voltage profile [34] (a) discharge at low current density and (b) discharge at high current density.

### 6.3.5.2 Electrolyte distribution

Electrolyte distribution within the air electrode directly affects the electrochemical interface and probably impacts  $O_2$  mass transport. Figure 6.22a shows discharge curves of three  $Li-O_2$  cells with different electrolyte-filling statuses. With insufficient electrolyte, more discharge products were observed by SEM deposition on the separator side, while for the excess electrolyte case a denser deposition in the air side was found. When the amount of the electrolyte is appropriate the discharge products can be evenly deposited throughout the air electrode, resulting in high specific capacity [91]. This was explained by the authors using fast  $O_2$  mass transport within nonelectrolyte-occupied pores and slow transport in the liquid electrolyte. It is believed that the cell with insufficient electrolyte might show lower discharge capacity than the one with excess electrolyte once the electrochemical interface is too small. Figure 6.22a gives an example of the effects of the electrolyte amount and distribution on the cell performance and, thus, the product of lithium oxides. To precisely depict the relation of electrolyte distribution to product formation within the air electrode or give an ideal electrolyte distribution, a schematic map presenting partly and fully wetted electrode structure is demonstrated in Figure 6.22b [92]. If the electrolyte can evenly distribute along the inner wall of the pore, the oxygen can diffuse easily through the pores in the cathode and then penetrate the thin layer of the electrolyte. The advantages of the fully wetted electrode structure are obvious: large electrochemical interface or effective surface area, facilitated gas mass transport, and possible avoidance of pore clogging

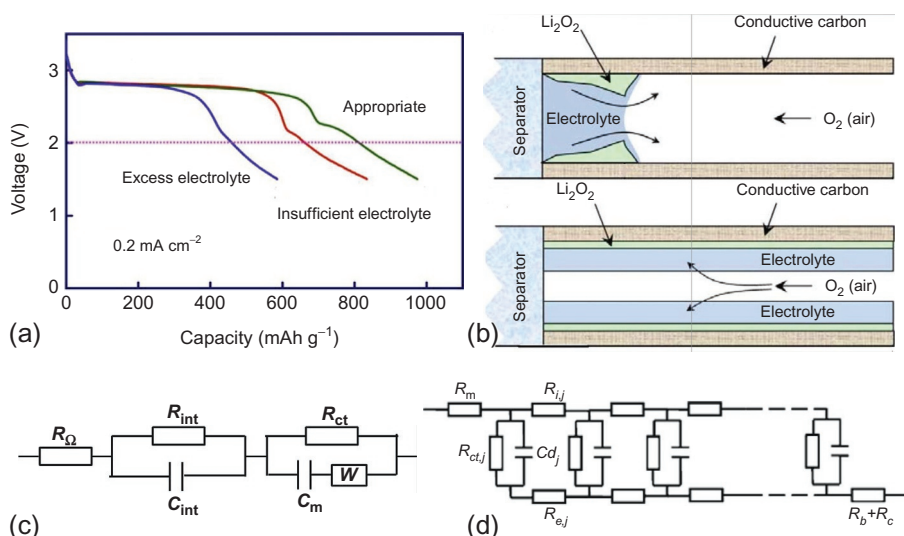


**Figure 6.22** (a) Discharge curves of three  $Li-O_2$  cells with different electrolyte-filling status, which were recorded at  $0.2 \text{ mA cm}^{-2}$  [91]; (b) partly (above) and fully (below) wetted electrode structure [92]; (c) equivalent circuit used for the analysis of the lithium oxides precipitated air electrode [93]; and (d) the finite transmission-line equivalent circuit including the double layer and the charge transfer resistance [94].

by products. One question now remains: How do you quickly and effectively measure or quantitatively determine the electrolyte distribution? Volatile liquid within 3D electrodes makes general imaging techniques unsuitable but, fortunately, the liquid electrolyte and carbon solids form an electrochemical interface, which is important for the ORR. The electrochemical impedance spectroscopy (EIS) technique proves to be a good diagnostic tool that is able to separate the responses of the charge transfer and mass transport processes occurring simultaneously on the electrode. The capacitance of the double layer is a direct index of the area of the interface which is covered by electrolyte. Although the mass transport resistance can be deconvoluted from the EIS results, it cannot be used to measure the thickness of the electrolyte film covering on the interface because the mass transport resistance for the partially and fully wetted electrodes [see [Figure 6.22b](#)] may be the same. EIS was demonstrated as a powerful technique for studying the capacity loss due to the interfacial changes occurring at the air cathode of a lithium–oxygen battery [93]. The equivalent circuit used in that study is shown in [Figure 6.22c](#). The first semicircle consisting of parallel connection of interfacial resistance ( $R_{\text{int}}$ ) and interfacial capacitance ( $C_{\text{int}}$ ) can be assigned to the electrochemical process on the oxide surface films as the charge is stored capacitively across the oxide barrier film on the electrode. The parallel connection of charge transfer resistance ( $R_{\text{ct}}$ ) and capacitance ( $C_{\text{m}}$ ), which contains the double layer capacitance from the carbon–electrolyte interface and pseudocapacitance from  $\text{MnO}_2$  catalysts, induces the second semicircle. Warburg impedance may include the effects of the limited diffusion of Li ions and  $\text{O}_2$  mass transport. Therefore, EIS can be used to determine the electrolyte distribution and even the product. When the impedance response exhibits a Warburg-like straight line at about  $45^\circ$  in the high-frequency region, this region is dominated by the charging process of the double layer coupled with the ionic transport in the CL, and it can be depicted by the finite transmission-line equivalent circuit [see [Figure 6.22d](#)] [94]. The ionic resistance or its profile can be another measure of the electrolyte distribution, which may need further investigation and confirmation in the Li–air electrode.

### 6.3.5.3 Distribution across electrode

Reaction zone or, more accurately, utilization efficiency of the active sites within the electrode, usually associated with oxygen mass transport, ionic resistance loss, and kinetics of electrochemical reaction, may be another important factor leading to “sudden death” during the discharge process in the Li–air battery. Generally, for a nonporous active layer in PEM fuel cells [95], diffusion is the rate-limiting step with respect to ionic resistance drop and best performance is obtained for catalyst particles located close to the gas diffusion layer side; for a porous active layer, ionic ohmic drop becomes the rate-limiting step and performance is improved when the catalyst particles are located close to the proton exchange membrane side; for porous electrode, at high current density, the reaction zone should shift to the region close to membrane or the utilization efficiency should be higher in the region close to the membrane rather than close to the gas diffusion layer side. Referring to the Li–air battery, as the electrolyte distribution is previously discussed, excess electrolyte makes the air electrode

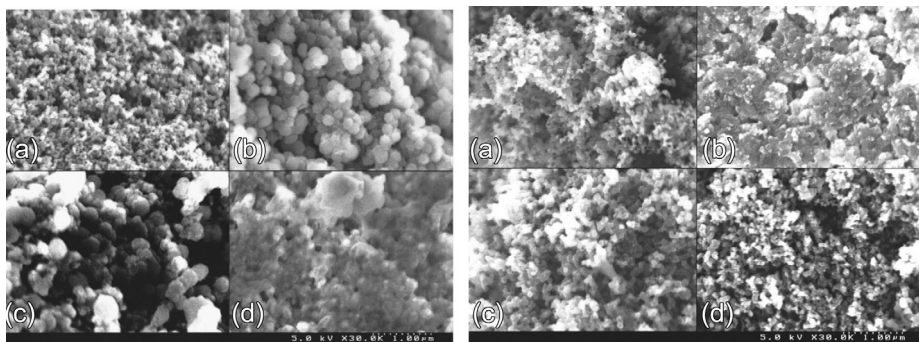


**Figure 6.23** SEM micrographs of PTFE/Super P air cathodes (left: air side of electrode; right: center of electrode): (a) undischarged and discharged at (b)  $0.05 \text{ mA cm}^{-2}$ ; (c)  $0.2 \text{ mA cm}^{-2}$ , and (d)  $1.0 \text{ mA cm}^{-2}$  [78].

more like a nonporous electrode and introduces  $\text{O}_2$  mass transport limitation, and insufficient electrolyte results in the limitation of Li ions migration. These are consistent with the SEM results [91] and similar to the situation in a PEM fuel cell. A little more detail about the effect of electrochemical reaction kinetics or current density or specifically rate capability in Li–air electrode on the reaction zone will be given. Figure 6.23 shows SEM images on the air side of an electrode (left) and in the center of an electrode (right) when the electrodes are discharged at three rates [78]. After discharge at  $0.05 \text{ mA cm}^{-2}$ , the electrode surface contains spheres of lithium oxides with diameters of 150–200 nm. After discharge at  $0.2 \text{ mA cm}^{-2}$ , the spheres on the surface appear to be larger at 300 nm and at  $1.0 \text{ mA cm}^{-2}$  the deposit appears to be more of a film. The deposit in the center of the electrode is not visible at  $1.0 \text{ mA cm}^{-2}$  and fills the pores at  $0.05 \text{ mA cm}^{-2}$ . This phenomenon is also confirmed by a recent report [96], which indicated that when discharging at a low rate the utilization efficiency is uniform through the electrode and the products distribute evenly within the air electrode, and when discharging at a high rate the reaction zone shifts to the region close to the air side, and the products block oxygen access to the electrode. This may be why Li–air batteries usually show smaller discharge capacity at a higher discharge rate and only at a very small discharge rate is there a straightforward relationship of discharge capacity and electrode porosity. Interestingly, by using a thin electrode (20  $\mu\text{m}$ ) it was found that the reduction in the discharge capacity at high rates is not a result of the depletion of  $\text{O}_2$  in the electrolyte-filled pores across the electrode thickness based on the transport properties of 0.1 M  $\text{LiClO}_4$  DME [97]. The reduction in the discharge voltage and capacity with increasing rates was attributed to the resistance associated with solid-state Li-ion diffusion in the lithium peroxide. We need to be careful with the profile of  $\text{O}_2$  concentration within the electrode. Although there is a certain amount of  $\text{O}_2$  in a particular position of the electrode, which can be calculated by considering the consumption of electrochemical reaction, this does not mean that  $\text{O}_2$  can access the reaction sites once there is a solid product film blocking the gas pathway. This is very similar to the case of water freezing in a PEM fuel cell

even if the catalyst layer is thin ( $<20\text{ }\mu\text{m}$ ) [98]. Therefore, we can only say the depletion of  $\text{O}_2$  will definitely cause the “sudden death,” but nondepletion of  $\text{O}_2$  in the electrode does not guarantee a electrochemical reaction, especially if surface passivation and pore clogging by the products exist. Numerical modeling may be a very useful tool in this field to explore the fundamentals behind this [99]. Recently, a report on three-dimensional spatial distribution of lithium products in electrochemically discharged Li–air cathodes proved that neutron tomographic imaging will be a very powerful technique for clarifying lithium oxides distribution [100].

## 6.4 Future trends

In this chapter, we summarized the fundamental studies for nonaqueous Li–air batteries with respect to the reaction mechanism of cathode and anode, the effects of electrode materials, electrolyte solutions, as well as the application of model electrode for the battery characterization. Currently, regarding the fundamental electrochemistry in nonaqueous Li–air batteries, the understanding of the detail mechanisms of ORR/OER in the presence of  $\text{Li}^+$  cation still requires further systematic investigation. So far, only the final product of ORR without side reactions, which is lithium peroxide, has been confirmed by experimental results. The kinetics of the discharge process is considered to be much faster than that of the charge process, although the efficacy of cathode catalyst is still unclear. At this time, it’s urgent to find a relatively stable reaction system consisting of a stable electrolyte solution without decomposition during cycling and a high-efficiency electrode material especially for OER. Furthermore, an accurate assessment system is necessary to get insight about the Li–air battery. The working electrode with a hanging meniscus configuration is strongly recommended due to its obvious TPB effect.

Surface passivation and pore clogging are responsible for the sudden death of the battery. Regarding the challenges on anode and especially on cathode, the design of materials and electrode structure may be still hot research areas. At the same time, the physics of product film growth and chemistry of  $\text{LiO}_2$  intermediates also need further study. The location of lithium oxides is determined both by TPBs and DPBs. The distribution of lithium oxides has been discussed in two scales: that is, on the carbon particles or fiber surface and within the whole electrode. The roles of defects, functionalities, and nanocatalysts on the carbon surface may need systematic investigation. Electrolyte distribution in the electrode and utilization efficiency of active sites contributes to the product profile within the electrode. In these studies, EIS has shown to be a very useful technique, and numerical modeling and image technology would be helpful.

## References

- [1] J.B. Goodenough, Y. Kim, Challenges for rechargeable Li batteries, *Chem. Mater.* 22 (3) (2009) 587–603.

- [2] P.G. Bruce, et al., Li–O<sub>2</sub> and Li–S batteries with high energy storage, *Nat. Mater.* 11 (1) (2011) 19–29.
- [3] G. Girishkumar, B. McCloskey, A.C. Luntz, S. Swanson, W. Wilcke, Lithium–air battery: promise and challenges, *J. Phys. Chem. Lett.* 1 (2010) 2193–2203.
- [4] J.P. Zheng, et al., Theoretical energy density of Li–air batteries, *J. Electrochem. Soc.* 155 (6) (2008) A432.
- [5] P.G. Bruce, L.J. Hardwick, K.M. Abraham, Lithium–air and lithium–sulfur batteries, *MRS Bull.* 36 (07) (2011) 506–512.
- [6] C.O. Laoire, et al., Influence of nonaqueous solvents on the electrochemistry of oxygen in the rechargeable lithium–air battery, *J. Phys. Chem. C* 114 (19) (2010) 9178–9186.
- [7] W. Xu, et al., Effects of nonaqueous electrolytes on the performance of lithium/air batteries, *J. Electrochem. Soc.* 157 (2) (2010) A219–A224.
- [8] A. Kraysberg, Y. Ein-Eli, The impact of nano-scaled materials on advanced metal–air battery systems, *Nano Energy* 2 (4) (2013) 468–480.
- [9] E. Yeager, Electrocatalysts for O<sub>2</sub> reduction, *Electrochim. Acta* 29 (11) (1984) 1527–1537.
- [10] D.T. Sawyer, et al., Effects of media and electrode materials on the electrochemical reduction of dioxygen, *Anal. Chem.* 54 (11) (1982) 1720–1724.
- [11] C.O. Laoire, et al., Elucidating the mechanism of oxygen reduction for lithium–air battery applications, *J. Phys. Chem. C* 113 (46) (2009) 20127–20134.
- [12] D. Vasudevan, H. Wendt, Electroreduction of oxygen in aprotic media, *J. Electroanal. Chem.* 392 (1–2) (1995) 69–74.
- [13] E. Yeager, Dioxygen electrocatalysis: mechanisms in relation to catalyst structure, *J. Mol. Catal.* 38 (1–2) (1986) 5–25.
- [14] K.M. Abraham, Z. Jiang, A polymer electrolyte-based rechargeable lithium/oxygen battery, *J. Electrochem. Soc.* 143 (1) (1996) 1–5.
- [15] N. Lopez, et al., Reversible reduction of oxygen to peroxide facilitated by molecular recognition, *Science* 335 (6067) (2012) 450–453.
- [16] X. Jie, K. Uosaki, Electrochemical reduction of oxygen in organic solvents with and without Li<sup>+</sup> cation—effect of oxygen supply, *ECS Meeting Abstracts MA2013-02* (6) (2013) 409.
- [17] Z. Peng, et al., Oxygen reactions in a non-aqueous Li<sup>+</sup> electrolyte, *Angew. Chem. Int. Ed. Engl.* 50 (28) (2011) 6351–6355.
- [18] J. Hassoun, et al., Investigation of the O<sub>2</sub> electrochemistry in a polymer electrolyte solid-state cell, *Angew. Chem. Int. Ed.* 50 (13) (2011) 2999–3002.
- [19] Z. Peng, et al., A reversible and higher-rate Li–O<sub>2</sub> battery, *Science* 337 (6094) (2012) 563–566.
- [20] M.M. Ottakam Thotiyil, et al., The carbon electrode in nonaqueous Li–O<sub>2</sub> cells, *J. Am. Chem. Soc.* 135 (1) (2012) 494–500.
- [21] B.D. McCloskey, et al., On the efficacy of electrocatalysis in nonaqueous Li–O<sub>2</sub> batteries, *J. Am. Chem. Soc.* 133 (45) (2011) 18038–18041.
- [22] V.S. Bryantsev, M. Blanco, F. Faglioni, Stability of lithium superoxide LiO<sub>2</sub> in the gas phase: computational study of dimerization and disproportionation reactions, *J. Phys. Chem. A* 114 (31) (2010) 8165–8169.
- [23] A. Débart, et al., An O<sub>2</sub> cathode for rechargeable lithium batteries: the effect of a catalyst, *J. Power Sources* 174 (2) (2007) 1177–1182.
- [24] A. Débart, et al., Alpha-MnO<sub>2</sub> nanowires: a catalyst for the O<sub>2</sub> electrode in rechargeable lithium batteries, *Angew. Chem. Int. Ed. Engl.* 47 (24) (2008) 4521–4524.
- [25] N.M. Markovic, Li–O<sub>2</sub> Electrochemistry in Organic Solvents, *JCESR*(2013), <https://app.box.com/s/mtb9esw4fhdaswv232o9>.

- [26] Y. Xu, W.A. Shelton, O<sub>2</sub> reduction by lithium on Au(111) and Pt(111), *J. Chem. Phys.* 133 (2) (2010) 024703.
- [27] M.M. Ottakam Thotiyil, et al., A stable cathode for the aprotic Li–O<sub>2</sub> battery, *Nat. Mater.* 12 (11) (2013) 1050–1056.
- [28] K. Xu, Nonaqueous liquid electrolytes for lithium-based rechargeable batteries, *Chem. Rev.* 104 (10) (2004) 4303–4418.
- [29] N. Ikemiya, A.A. Gewirth, Structure sensitive adsorption of DMSO on Au surfaces, *J. Phys. Chem. B* 104 (5) (2000) 873–877.
- [30] S.K. Si, A.A. Gewirth, Solvent organization above metal surfaces: ordering of DMSO on Au, *J. Phys. Chem. B* 104 (46) (2000) 10775–10782.
- [31] Y.-C. Lu, Y. Shao-Horn, Probing the reaction kinetics of the charge reactions of nonaqueous Li–O<sub>2</sub> batteries, *J. Phys. Chem. Lett.* 4 (1) (2012) 93–99.
- [32] S.H. Oh, L.F. Nazar, Oxide catalysts for rechargeable high-capacity Li–O<sub>2</sub> batteries, *Adv. Energy Mater.* 2 (7) (2012) 903–910.
- [33] J.-H. Lee, et al., The role of vacancies and defects in Na<sub>0.44</sub>MnO<sub>2</sub> nanowire catalysts for lithium–oxygen batteries, *Energy Environ. Sci.* 5 (11) (2012) 9558–9565.
- [34] R.R. Mitchell, et al., All-carbon-nanofiber electrodes for high-energy rechargeable Li–O<sub>2</sub> batteries, *Energy Environ. Sci.* 4 (8) (2011) 2952.
- [35] J.R. Harding, et al., Evidence of catalyzed oxidation of Li<sub>2</sub>O<sub>2</sub> for rechargeable Li–air battery applications, *Phys. Chem. Chem. Phys.* 14 (30) (2012) 10540–10546.
- [36] S.H. Oh, et al., Synthesis of a metallic mesoporous pyrochlore as a catalyst for lithium–O<sub>2</sub> batteries, *Nat. Chem.* 4 (12) (2012) 1004–1010.
- [37] Y. Chen, et al., Charging a Li–O<sub>2</sub> battery using a redox mediator, *Nat. Chem.* 5 (6) (2013) 489–494.
- [38] Y. Wang, Y. Xia, Li–O<sub>2</sub> batteries: an agent for change, *Nat. Chem.* 5 (6) (2013) 445–447.
- [39] G.M. Veith, et al., Spectroscopic characterization of solid discharge products in Li–air cells with aprotic carbonate electrolytes, *J. Phys. Chem. C* 115 (29) (2011) 14325–14333.
- [40] B.D. McCloskey, et al., Solvents’ critical role in nonaqueous lithium–oxygen battery electrochemistry, *J. Phys. Chem. C* 2 (10) (2011) 1161–1166.
- [41] Y. Chen, et al., Li–O<sub>2</sub> battery with a dimethylformamide electrolyte, *J. Am. Chem. Soc.* 134 (18) (2012) 7952–7957.
- [42] V.S. Bryantsev, et al., Predicting solvent stability in aprotic electrolyte Li–air batteries: nucleophilic substitution by the superoxide anion radical (O<sub>2</sub><sup>–</sup>), *J. Phys. Chem. A* 115 (44) (2011) 12399–12409.
- [43] Z. Zhang, et al., Increased stability toward oxygen reduction products for lithium–air batteries with oligoether-functionalized silane electrolytes, *J. Phys. Chem. C* 115 (51) (2011) 25535–25542.
- [44] M. Winter, et al., Studies on the anode/electrolyte interface in lithium ion batteries, *Monatsh. Chem.* 132 (4) (2001) 473–486.
- [45] N. Imanishi, et al., Lithium anode for lithium–air secondary batteries, *J. Power Sources* 185 (2) (2008) 1392–1397.
- [46] T. Ogasawara, et al., Rechargeable Li<sub>2</sub>O<sub>2</sub> electrode for lithium batteries, *J. Am. Chem. Soc.* 128 (4) (2006) 1390–1393.
- [47] A. Débart, et al.,  $\alpha$ -MnO<sub>2</sub> nanowires: a catalyst for the O<sub>2</sub> electrode in rechargeable lithium batteries, *Angew. Chem. Int. Ed.* 47 (24) (2008) 4521–4524.
- [48] H. Cheng, K. Scott, Carbon-supported manganese oxide nanocatalysts for rechargeable lithium–air batteries, *J. Power Sources* 195 (5) (2010) 1370–1374.
- [49] Y.-C. Lu, et al., The influence of catalysts on discharge and charge voltages of rechargeable Li–oxygen batteries, *Electrochim. Solid-State Lett.* 13 (6) (2010) A69–A72.

- [50] Y.-C. Lu, et al., Platinum–gold nanoparticles: a highly active bifunctional electrocatalyst for rechargeable lithium–air batteries, *J. Am. Chem. Soc.* 132 (35) (2010) 12170–12171.
- [51] V. Giordani, et al.,  $\text{H}_2\text{O}_2$  decomposition reaction as selecting tool for catalysts in  $\text{Li}-\text{O}_2$  cells, *Electrochem. Solid-State Lett.* 13 (12) (2010) A180–A183.
- [52] H. Cheng, K. Scott, Selection of oxygen reduction catalysts for rechargeable lithium–air batteries—metal or oxide? *Appl. Catal. Environ.* 108–109 (2011) 140–151.
- [53] S.S. Zhang, X. Ren, J. Read, Heat-treated metal phthalocyanine complex as an oxygen reduction catalyst for non-aqueous electrolyte Li/air batteries, *Electrochim. Acta* 56 (12) (2011) 4544–4548.
- [54] Y.-C. Lu, et al., Electrocatalytic activity studies of select metal surfaces and implications in Li–air batteries, *J. Electrochem. Soc.* 157 (9) (2010) A1016–A1025.
- [55] Y.-C. Lu, H.A. Gasteiger, Y. Shao-Horn, Catalytic activity trends of oxygen reduction reaction for nonaqueous Li–air batteries, *J. Am. Chem. Soc.* 133 (47) (2011) 19048–19051.
- [56] E.M. Benbow, et al., Oxygen reduction properties of bifunctional  $\alpha$ -manganese oxide electrocatalysts in aqueous and organic electrolytes, *J. Phys. Chem. C* 115 (44) (2011) 22009–22017.
- [57] L. Jin, et al., Titanium containing  $\gamma$ - $\text{MnO}_2$  (TM) hollow spheres: one-step synthesis and catalytic activities in Li/air batteries and oxidative chemical reactions, *Adv. Funct. Mater.* 20 (19) (2010) 3373–3382.
- [58] L. Wang, et al.,  $\text{CoMn}_2\text{O}_4$  spinel nanoparticles grown on graphene as bifunctional catalyst for lithium–air batteries, *J. Electrochem. Soc.* 158 (12) (2011) A1379–A1382.
- [59] J. Li, et al.,  $\text{MnO}_2$  nanoflakes coated on multi-walled carbon nanotubes for rechargeable lithium–air batteries, *Electrochim. Commun.* 13 (7) (2011) 698–700.
- [60] Y. Cui, Z. Wen, Y. Liu, A free-standing-type design for cathodes of rechargeable  $\text{Li}-\text{O}_2$  batteries, *Energy Environ. Sci.* 4 (11) (2011) 4727.
- [61] J. Xiao, et al., Hierarchically porous graphene as a lithium–air battery electrode, *Nano Lett.* 11 (11) (2011) 5071–5078.
- [62] J. Hou, et al., Graphene-based electrochemical energy conversion and storage: fuel cells, supercapacitors and lithium ion batteries, *Phys. Chem. Chem. Phys.* 13 (34) (2011) 15384–15402.
- [63] J. Hou, et al., Lithium oxides precipitation in nonaqueous Li–air batteries, *Phys. Chem. Chem. Phys.* 14 (39) (2012) 13487–13501.
- [64] J. Hou, et al., Electrochemical impedance investigation of proton exchange membrane fuel cells experienced subzero temperature, *J. Power Sources* 171 (2) (2007) 610–616.
- [65] J. Hou, et al., Investigation of resided water effects on PEM fuel cell after cold start, *Int. J. Hydrogen Energy* 32 (17) (2007) 4503–4509.
- [66] J. Read, et al., Oxygen transport properties of organic electrolytes and performance of lithium/oxygen battery, *J. Electrochem. Soc.* 150 (10) (2003) A1351–A1356.
- [67] W. Xu, et al., Optimization of nonaqueous electrolytes for primary lithium/air batteries operated in ambient environment, *J. Electrochem. Soc.* 156 (10) (2009) A773–A779.
- [68] X.-h. Yang, Y.-y. Xia, The effect of oxygen pressures on the electrochemical profile of lithium/oxygen battery, *J. Solid State Electrochem.* 14 (1) (2010) 109–114.
- [69] J.-G. Zhang, et al., Ambient operation of Li/air batteries, *J. Power Sources* 195 (13) (2010) 4332–4337.
- [70] J. Xiao, et al., Optimization of air electrode for Li/air batteries, *J. Electrochem. Soc.* 157 (4) (2010) A487.
- [71] S.S. Zhang, K. Xu, J. Read, A non-aqueous electrolyte for the operation of Li/air battery in ambient environment, *J. Power Sources* 196 (8) (2011) 3906–3910.

- [72] Y. Wang, et al., High rate oxygen reduction in non-aqueous electrolytes with the addition of perfluorinated additives, *Energy Environ. Sci.* 4 (9) (2011) 3697–3702.
- [73] P. Albertus, et al., Identifying capacity limitations in the Li/oxygen battery using experiments and modeling, *J. Electrochem. Soc.* 158 (3) (2011) A343–A351.
- [74] V. Viswanathan, et al., Electrical conductivity in  $\text{Li}_2\text{O}_2$  and its role in determining capacity limitations in non-aqueous Li– $\text{O}_2$  batteries, *J. Chem. Phys.* 135 (21) (2011) 214704.
- [75] J. Chen, et al., The role of transition metal interfaces on the electronic transport in lithium–air batteries, *Catal. Today* 165 (1) (2011) 2–9.
- [76] M.D. Radin, et al., Lithium peroxide surfaces are metallic, while lithium oxide surfaces are not, *J. Am. Chem. Soc.* 134 (2) (2012) 1093–1103.
- [77] Y.-C. Lu, H.A. Gasteiger, Y. Shao-Horn, Method development to evaluate the oxygen reduction activity of high-surface-area catalysts for Li–air batteries, *Electrochem. Solid-State Lett.* 14 (5) (2011) A70–A74.
- [78] J. Read, Characterization of the lithium/oxygen organic electrolyte battery, *J. Electrochem. Soc.* 149 (9) (2002) A1190–A1195.
- [79] T. Kuboki, et al., Lithium–air batteries using hydrophobic room temperature ionic liquid electrolyte, *J. Power Sources* 146 (1–2) (2005) 766–769.
- [80] M. Mirzaeian, P.J. Hall, Preparation of controlled porosity carbon aerogels for energy storage in rechargeable lithium oxygen batteries, *Electrochim. Acta* 54 (28) (2009) 7444–7451.
- [81] S.R. Younesi, et al., Influence of the cathode porosity on the discharge performance of the lithium–oxygen battery, *J. Power Sources* 196 (22) (2011) 9835–9838.
- [82] T. Soboleva, et al., On the micro-, meso-, and macroporous structures of polymer electrolyte membrane fuel cell catalyst layers, *ACS Appl. Mater. Interfaces* 2 (2) (2010) 375–384.
- [83] R.E. Williford, J.-G. Zhang, Air electrode design for sustained high power operation of Li/air batteries, *J. Power Sources* 194 (2) (2009) 1164–1170.
- [84] G.Q. Zhang, et al., Lithium–air batteries using SWNT/CNF buckypapers as air electrodes, *J. Electrochem. Soc.* 157 (8) (2010) A953–A956.
- [85] P. Kichambare, et al., Electrochemical performance of highly mesoporous nitrogen doped carbon cathode in lithium–oxygen batteries, *J. Power Sources* 196 (6) (2011) 3310–3316.
- [86] Y. Li, et al., Nitrogen-doped carbon nanotubes as cathode for lithium–air batteries, *Electrochem. Commun.* 13 (7) (2011) 668–672.
- [87] Y. Yang, et al., Nanostructured diamond like carbon thin film electrodes for lithium air batteries, *J. Electrochem. Soc.* 158 (10) (2011) B1211–B1216.
- [88] B. Sun, et al., Graphene nanosheets as cathode catalysts for lithium–air batteries with an enhanced electrochemical performance, *Carbon* 50 (2) (2012) 727–733.
- [89] Y. Xu, W.A. Shelton, Oxygen reduction by lithium on model carbon and oxidized carbon structures, *J. Electrochem. Soc.* 158 (10) (2011) A1177–A1184.
- [90] G.Q. Zhang, et al.,  $\alpha\text{-MnO}_2$ /carbon nanotube/carbon nanofiber composite catalytic air electrodes for rechargeable lithium–air batteries, *J. Electrochem. Soc.* 158 (7) (2011) A822–A827.
- [91] S.S. Zhang, D. Foster, J. Read, Discharge characteristic of a non-aqueous electrolyte Li/ $\text{O}_2$  battery, *J. Power Sources* 195 (4) (2010) 1235–1240.
- [92] P. Andrei, et al., Some possible approaches for improving the energy density of Li–air batteries, *J. Electrochem. Soc.* 157 (12) (2010) A1287–A1295.
- [93] M. Mirzaeian, P.J. Hall, Characterizing capacity loss of lithium oxygen batteries by impedance spectroscopy, *J. Power Sources* 195 (19) (2010) 6817–6824.

- [94] J. Hou, et al., Ionic resistance of the catalyst layer after the PEM fuel cell suffered freeze, *J. Power Sources* 176 (1) (2008) 118–121.
- [95] O. Antoine, et al., Catalyst gradient for cathode active layer of proton exchange membrane fuel cell, *Electrochim. Acta* 45 (27) (2000) 4493–4500.
- [96] X. Ren, et al., Oxygen reduction reaction catalyst on lithium/air battery discharge performance, *J. Mater. Chem.* 21 (27) (2011) 10118–10125.
- [97] Y.-C. Lu, et al., The discharge rate capability of rechargeable Li–O<sub>2</sub> batteries, *Energy Environ. Sci.* 4 (8) (2011) 2999–3007.
- [98] J. Hou, et al., Reversible performance loss induced by sequential failed cold start of PEM fuel cells, *Int. J. Hydrogen Energy* 36 (19) (2011) 12444–12451.
- [99] A.A. Franco, K.-H. Xue, Carbon-based electrodes for lithium air batteries: scientific and technological challenges from a modeling perspective, *ECS J. Solid State Sci. Technol.* 2 (10) (2013) M3084–M3100.
- [100] J. Nanda, et al., Anomalous discharge product distribution in lithium–air cathodes, *J. Phys. Chem. C* 116 (15) (2012) 8401–8408.
- [101] J. Yang, et al., Evidence for lithium superoxide-like species in the discharge product of a Li–O<sub>2</sub> battery, *Phys. Chem. Chem. Phys.* 15 (11) (2013) 3764–3771.
- [102] Z. Miao, et al., Characteristics of proton exchange membrane fuel cells cold start with silica in cathode catalyst layers, *Int. J. Hydrogen Energy* 35 (11) (2010) 5552–5557.
- [103] J. Li, S. Lee, J. Roberts, Ice formation and distribution in the catalyst layer during freeze-start process—CRYO-SEM investigation, *Electrochim. Acta* 53 (16) (2008) 5391–5396.
- [104] X.-h Yang, P. He, Y.-y. Xia, Preparation of mesocellular carbon foam and its application for lithium/oxygen battery, *Electrochem. Commun.* 11 (6) (2009) 1127–1130.
- [105] C. Tran, X.-Q. Yang, D. Qu, Investigation of the gas-diffusion-electrode used as lithium/air cathode in non-aqueous electrolyte and the importance of carbon material porosity, *J. Power Sources* 195 (7) (2010) 2057–2063.

# Electrochemical characterization of rechargeable lithium batteries

7

C. Villevieille

Paul Scherrer Institute, Villigen PSI, Switzerland

## 7.1 Introduction

Since the commercialization of lithium-ion batteries by Sony in 1991 [1], researchers have aimed at increasing the specific energy of both negative and positive electrode materials by replacing graphite and  $\text{LiCoO}_2$ , respectively [2]. Both materials are based on insertion processes, which means that there are lithium-ion sites that can alternatively be empty or occupied. At the negative electrode, research is currently focused on conversion materials, such as tin [3], antimony [4], phosphorus [5], and silicon [6], which exhibit outstanding specific charges compared with graphite. Although their specific charges are highly attractive, these materials participate in alloying reaction that lead to increases in volume of at least 200% during cycling (resulting in mechanical strain) [7].

New lithium-based batteries (also called post-lithium batteries) have been developed for a decade.  $\text{Li-S}$  [8] and  $\text{Li-O}_2$  [9] batteries are subject to intensive investigation. Like lithium-ion batteries, these two systems consist of two different electrodes and an electrolyte. Lithium metal is used as the negative electrode material in both batteries. In  $\text{Li-S}$  batteries, we find sulfur at the positive electrode, which exhibits a high specific charge close to 1650 mAh/g but suffers from highly electrically and ionically insulating reaction products and the so-called polysulfide shuttle [10]. For the  $\text{Li-O}_2$  system, the positive electrode is mainly composed of carbon capable of trapping the oxygen. The main challenge of such a system is to protect the lithium from the oxygen and the moisture in the system [11].

These novel electroactive materials exhibit new reaction mechanisms during electrochemical cycling, the investigation and understanding of which requires new tools for the characterization of surface and/or bulk properties [12,13]. There are two different approaches to understanding the reaction mechanism of electroactive materials during cycling, namely using *ex situ* samples or specially developed, reliable cells to study the reaction mechanism *in situ/operando*. In this chapter, different techniques that can be used to elucidate the reaction mechanisms of lithium-based batteries will be discussed.

## 7.2 Advantages and disadvantages of *ex situ* and *in situ/operando* techniques

Understanding the reaction mechanisms of battery materials is never an easy task. Numerous challenges need to be addressed. Therefore, different techniques have been developed over the last decade in order to follow and elucidate these reaction mechanisms. In the literature, a specific terminology is used by the researchers. In fact, we can find three main expressions: (1) *ex situ*, (2) *in situ*, and (3) *operando*. *Ex situ* measurement involves the cycling of a standard electrochemical cell and stopping it at the desired potential, followed by extraction of the powder from the electrochemical cell in order to analyze it with the desired technique. During *in situ* measurement, the materials are cycled in dedicated cells. Subsequently, the cells are stopped to measure directly the electrode inside the cell at OCV. Finally, *operando* measurements involve investigating the cells via a chosen technique and performing the measurement while the cell is cycling. The latter two methods provide the most useful information that is directly related to changes within the cell.

For the *ex situ* samples, there are several problems to take into account: (1) When a cell is stopped at the desired potential, the system is in a metastable state, which leads to a phenomenon called “relaxation” of the materials, which means that by the time the characterizations are performed, the metastable phase may have changed and does not adequately reflect what occurs during cycling. (2) The amount of sample needed to study a full reaction mechanism is quite large and the reproducibility of each sample may not be guaranteed, which makes it difficult to acquire reliable results. (3) The samples usually become air and moisture sensitive during cycling versus lithium, leading to the possibility of spontaneous redox reactions before or while performing the subsequent characterizations. For all these reasons, *in situ* measurements are preferred and serve to avoid air and moisture exposure as well as relaxation of the cycled materials. However, the development of reliable cells for *in situ* investigation is a real challenge due to the necessary compromise between having good electrochemistry during cycling and the constraints due to the apparatuses in which the cells are placed for further characterization [14]. In the end, both experiments (*ex situ* and *in situ*) are needed to fully understand the reaction mechanisms. In this chapter, we will mainly describe *in situ* characterizations of lithium-based batteries. Different categories, such as bulk analysis, surface analysis, and optical analysis will be presented.

## 7.3 Common *in situ* cell designs

Many designs for *in situ* cells are reported in the literature. In this chapter, we will present the main two designs described in the literature, followed by further *in situ* cells meeting various constraints. The two cells presented here can be used in several characterization techniques such as X-ray diffraction (XRD), Mössbauer spectroscopy, X-ray absorption spectroscopy, and so forth. The first cell described here is a cell that can be adapted to many techniques thanks to the flexibility of its design.

Commonly called a “coffee bag cell” or pouch cell (because it is built in aluminum bags used in coffee packaging), this design is a reliable electrochemical cell for operando experiments and is adaptable to synchrotron beamlines as well as in-house devices with reflection and/or transmission geometry [15]. The “coffee bag” electrochemical cells consist of several flat parts assembled to a maximum thickness of 1 mm. The primary goal is to minimize the presence of the different elements, such as the current collector, the lithium metal, and the separator and to maximize the amount of electroactive elements in the beam. Figure 7.1 presents a schematic drawing of a conventional “coffee bag” cell [17]. Due to the high reactivity of lithium toward air and moisture, “coffee bag” cells must be air and moisture tight, which presents a challenge for this type of cell, especially when special windows have to be used. For this reason, the cells are built and sealed in an aluminum bag (approximately 100  $\mu\text{m}$  thick), in which the foil is usually composed of four layers, from the inside to the outside: (1) polyethylene (PE), (2) aluminum, (3) PE, and (4) oriented polyamide (OPA). The PE layer is essential to ensure thermosealability of the bag. An approximately 25- $\mu\text{m}$  thick aluminum layer is a necessary barrier to  $\text{O}_2$  and  $\text{H}_2\text{O}$ . The only problem of the aluminum foil is that it introduces an additional contribution in some patterns such as a neutron, XRD, and so on. To overcome this problem, many groups decided to punch a hole in the “coffee bags” in order to create a window capable of letting through the beam and avoiding side peaks (Figure 7.1). The window is usually composed of Kapton foil, which helps to prevent air exposure but does not completely solve the moisture issue.

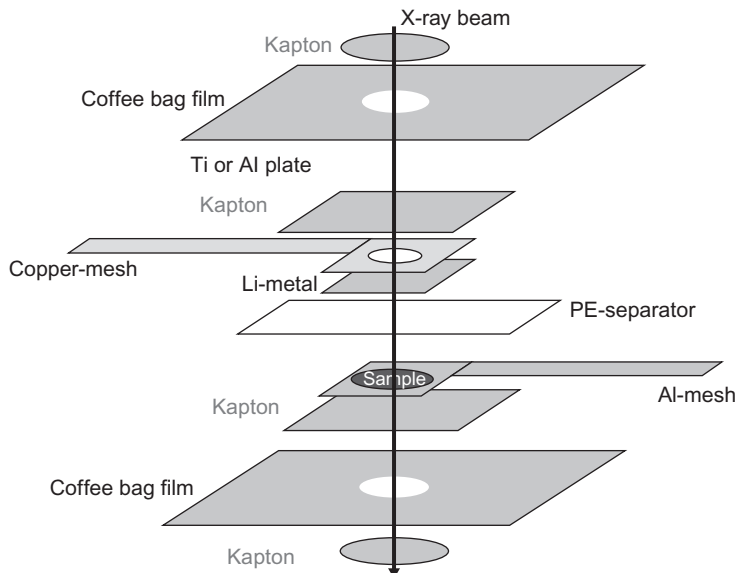


**Figure 7.1** Schematic of a standard coffee bag cell.

Reproduced from Ref. [16] with permission from the Royal Society of Chemistry.

Due to these problems of moisture, air exposure, and/or contributions of the cell housing to the measurements (signal-to-noise ratio, set of new peaks in XRD, etc.), some groups decided to improve this cell and/or develop a completely new design.

The design of the coffee bag cell described above has recently been improved by Villevieille *et al.* [16], who introduced a hard spring to increase the pressure and, thus, designed a reliable cell for *in situ*/operando electrochemical measurements. The new cell is shown in Figure 7.2. Thanks to this new, more flexible coffee bag design, the Kapton window can be replaced by a harder material, such as aluminum or even titanium. In this approach, a spring can be applied to the window and ensures high contact pressure. According to the authors, the cell can be adapted to different beamlines, as well as in-house devices, due to the flexibility of this design.

Other groups developed cells based on a Swagelok design commonly used in the battery community. In this configuration, the cell is completely air and moisture tight, but the pressure problem still remains. This cell design (Figure 7.3) was first described in a paper by Morcrette *et al.* [18]. Their goal was to test the cell in *in situ* XRD studies (in-house and *in situ* synchrotron). The cell is a half-Swagelok design, in which a beryllium window is used on the active element side of the electrode. Thanks to this design, the cell can be taken apart, cleaned, and reassembled without displacing the Be window and, therefore, changing the cell alignment.

Further development of *in situ*/operando characterization techniques led to the modification of this cell by Leriche *et al.* [19] to fulfill the criteria of other beamlines and to be capable of being used in transmission mode (Figure 7.4). The cell is now composed of two beryllium windows, one to let the incident beam through and another to pass the reflected beam. The main advantages of this cell are that (1) it is easy to

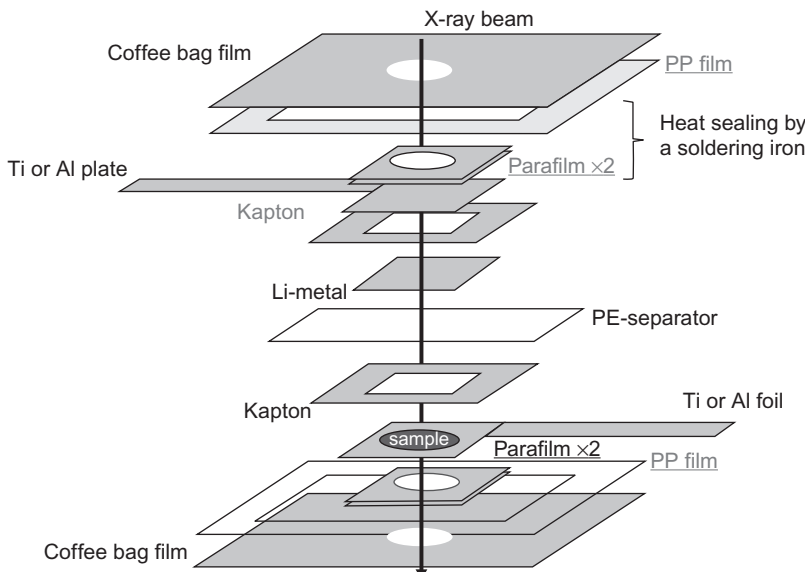


**Figure 7.2** Modified coffee bag cell design.

Reproduced from Ref. [16] with permission from the Royal Society of Chemistry.

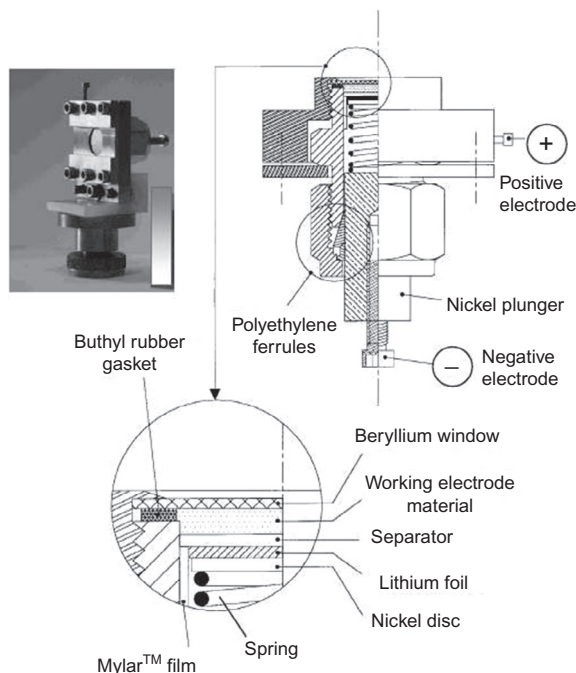


**Figure 7.3** Cross-section of the Swagelok *in situ* X-ray cell. Expanded view: zoom of the electrochemically active cell part.

Reprinted from Ref. [18] with permission from Elsevier.

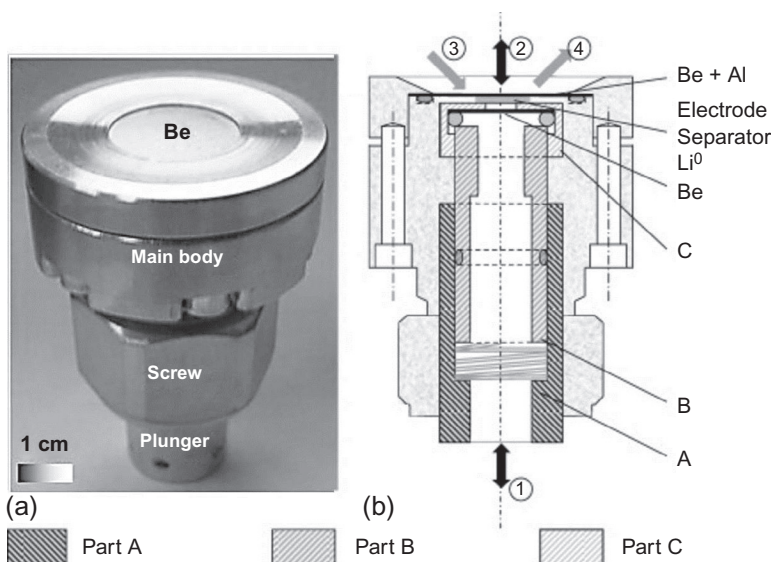


**Figure 7.4** Electrochemical cell for operando measurements. (a) Photo and (b) detailed view of the cell with incident and transmitted beam paths in transmission geometry.

Reprinted with permission from Ref. [19]. Copyright 2014, The Electrochemical Society.

assemble by the user in a standard Ar-filled glove box; (2) it is easy to clean; (3) it is highly hermetic, stable, and reusable; and (4) it is easy to connect to a potentiostat. But although the cell presents numerous advantages, there are three crucial issues that need to be addressed: (1) Beryllium is brittle and easily broken when pressure is applied (the spring inside the Swagelok cell cannot be compressed significantly without breaking the window). (2) Beryllium is a highly toxic material that requires extreme care when oxidation occurs and the material turns into BeO. (3) Beryllium alloys with lithium at high potential, which implies that the windows must be protected.

The cells described in this section are common designs for bulk analysis. In the following section, we will discuss different techniques that can be used to understand the reaction mechanism from a bulk point of view.

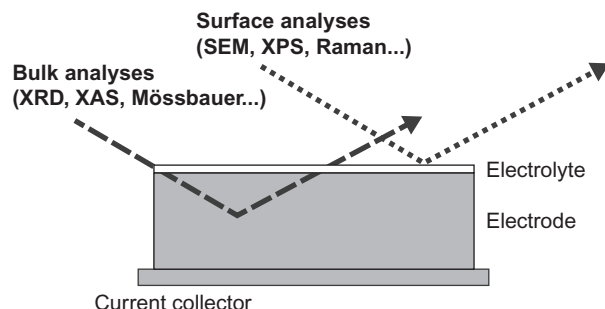
## 7.4 Bulk characterizations

In a battery, there are different reaction mechanisms that can occur at the bulk or at the interface, as one can see in [Figure 7.5](#). This section is dedicated to the main characterizations used for the study of bulk reaction mechanisms involving mainly interactions with matter, such as XRD (in-house and at large facilities), neutron diffraction, Mössbauer spectroscopy, X-ray absorption spectroscopy, and so forth.

### 7.4.1 X-ray diffraction and neutron diffraction

Neutron diffraction and XRD are extensively used to study the bulk structural changes occurring in electroactive materials during the cycling process. X-rays and neutrons are known to have different interactions with matter. On the one hand, X-rays interact with the electron cloud of an atom and are scattered depending on the weight of the elements. Neutrons on the other hand are scattered by the nuclei and, hence, show no relationship with the number of electrons in the atom. Thus, both complementary techniques are needed to study the reaction mechanisms. Neutron diffraction is especially important because most reaction mechanisms involve light elements such as lithium and carbon, which are hardly scattered by X-rays but show a relative good scattering

**Figure 7.5** Schematic of bulk and interface characterizations of a test cell.



factor for neutrons. Nevertheless, this imposes significant constraints on the electrochemical cell. Due to the different interactions with matter, the amount of active material needed is different, which, in turn, means that different cell designs have to be used for the two methods. For X-rays, it is not necessary to have a large amount of materials due to the strong interaction with matter, but for neutron diffraction, the interaction with matter is extremely weak, which necessitates the use of a large amount of material to reduce the time required to collect diffraction patterns. Due to this important difference between neutron diffraction and XRD, the same cell cannot be used for both techniques and two different designs are needed to fulfill the different requirements. As an example, in [Figure 7.6](#), we can follow the phase evolution occurring during the cycling of  $\text{LiCoO}_2$  versus lithium recorded at the ID11 beamline at ESRF (Grenoble, France) using the modified Swagelok cell described in [Figure 7.4](#) [20]. In the example described by the authors [18], six phases were identified and refined (lattice parameter, space group, cobalt and oxygen, elemental position, and reliability factor), using the Rietveld method. From the analysis it was concluded that lithium extraction leads to a single phase (named  $R_1$ ). Subsequently, a two-phase region (named  $R_1 + R_2$ ) was observed, which, upon continued delithiation, leads to a single phase ( $R_2$ ), which crystallizes in the same space group  $R\bar{3}m$ , but differs in its c lattice parameter [21]. Upon further delithiation, the authors noticed a transition from  $R_2$  to  $M_1$ , which crystallizes in a monoclinic structure. At 4.2 V vs.  $\text{Li}^+/\text{Li}$ , another phase transformation occurs and the  $M_1$  phase is transformed into a phase isotype of  $R_2$  (denoted  $R'_2$  in [Figure 7.6](#)). After this transformation, a two-phase process occurs, whose space group (monoclinic  $C2/m$  or rhombohedral  $R\bar{2}m$ ) is difficult to determine despite the fact that high resolution XRD experiments were performed. Finally, full extraction of lithium leads to a  $\text{CoO}_2$  phase denoted T1 (rhombohedral  $P\bar{3}m1$ ) with ABABAB ordering, as opposed to  $\text{LiCoO}_2$ , which exhibits ABCABC ordering.

It is clear from this work that *in situ* X-ray techniques are the method of choice to understand and determine the phase evolution during cycling. In the literature, many other X-ray studies are reported for positive and negative electrode. As far as conversion reaction mechanisms are concerned, it was clearly shown that Sb is converted into  $\text{Li}_3\text{Sb}$  [22] (fcc), Sn into  $\text{Li}_7\text{Sn}_2$  [23], P into  $\text{Li}_3\text{P}$  [24], and Si into  $\text{Li}_{4.4}\text{Si}$  [25] (similar to the intermetallics  $\text{NiP}_2$  [26,27],  $\text{NiSb}_2$  [28],  $\text{FeSn}_2$  [29,30],  $\text{FeSb}_2$  [31], etc., reported in the literature). At the positive electrode, the analyses are a bit more complicated. Numerous studies of cathode materials, such as  $\text{LiNiO}_2$  [32],  $\text{Li}_{1+x}(\text{Ni}_{0.33}\text{Mn}_{0.33}\text{Co}_{0.33})_{1-x}\text{O}_2$  [33–36], NCA [37], and others, are reported but most of them are layered–layered structures including lithium, which, being a light element, is difficult to track via XRD. Also, in the case of  $\text{LiCoO}_2$ , we pointed out that this technique has some limitations, especially as some phases are difficult to determine because of their low amounts of lithium and oxygen. Hence, it is of paramount importance to couple XRD with other characterization techniques, such as neutron diffraction, which can then estimate and refine the amount of light elements.

The challenge while using neutron diffraction is to have a sufficient amount of material in the beam to have a time resolution of less than 30 min. Above this limit, the phases may evolve and subsequently relax unnoticed, which will not give any clue

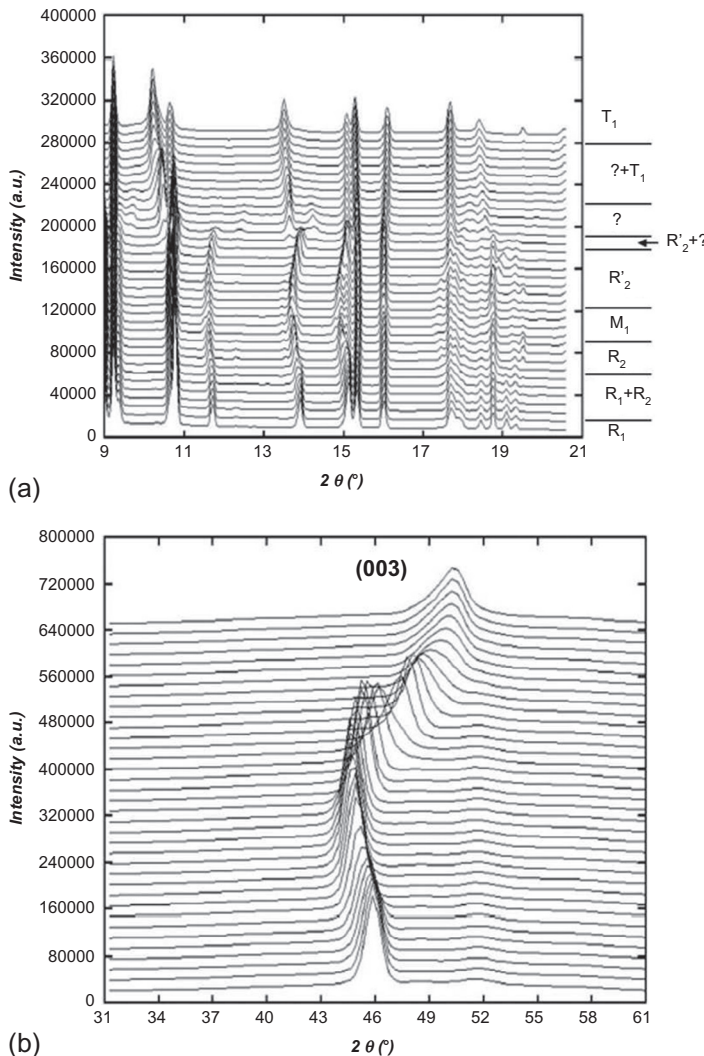


**Figure 7.6** *In situ* synchrotron X-ray diffraction patterns of a  $\text{LiCoO}_2/\text{Li}$  cell collected during cell charging. For reasons of conciseness, only a narrow  $2\theta$  domain centered at the position of the (110) reflection for  $\text{LiCoO}_2$  is shown (a). The evolution of the (003) reflection is shown as well (b).

Reprinted from Ref. [18] with permission from Elsevier.

to the metastable phase described in the literature. There are different geometries such as rectangular, full cell in the beam (including peaks of the cell housing, lithium, and separator), and circular. To the best of our knowledge, the most suitable design is a cylindrical cell where we can minimize the different path lengths traveled by the diffracted beam through the electrode mass and cell (Figure 7.7). However, even

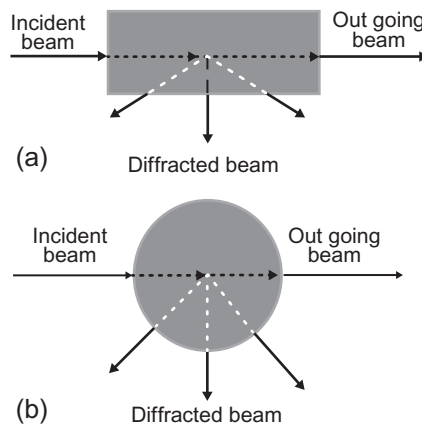


**Figure 7.7** Top schematic view of the Al container holding the electrode mass of the *in situ* neutron diffraction cell of (a) rectangular design and (b) circular design.

this design leads to attenuation of the diffracted beam and may rule out Rietveld refinement.

In Novak's group, a lot of research has been undertaken to develop a suitable cell for neutron diffraction studies [38–40], in which only the active material and the electrode container (mainly aluminum or titanium) are in the beam. The first attempt was made at the HRPT (SINQ, PSI, Villigen PSI, Switzerland), where the cell was of rectangular design but where only the active material and the container were in the beam. This first attempt showed that it was possible to cycle a cell with a large amount of material (approximately 3 g of electroactive material,  $\text{Li}_4\text{Ti}_5\text{O}_{12}$  in this study) and to determine the lithium content upon lithiation as well as the phase transition. Nevertheless, the following limitations were noted: (1) the long path length attenuates the beam (due to the rectangular design); (2) the substantial electroactive mass increases the polarization during cycling; and (3) the weakness of the source used for this experiment leads to acquisition times of 8 h (significant relaxation of the electroactive powder during this time, which leads to structural change while recording the pattern) [40].

Having identified these drawbacks, another strategy was proposed by Godbole *et al.* [38]; i.e., to work at the D20 beamline at ILL (Grenoble, France), whose source is 25 times stronger than the SINQ source. This results in a pattern in 20–25 min instead of 8 h and decreases the required amount of active material from 3 g to 300 mg. The new cell is presented in Figure 7.8. This cell was used for the study of electroactive materials (Figure 7.9) such as graphite and  $\text{LiFePO}_4$ . Graphite intercalation followed by *in situ* neutron diffraction is presented in Figure 7.10. As one can see in this cell, the container for the electroactive material can be changed depending on the working potential of the active material. Titanium was used in most of the study because titanium is stable at 0–5 V vs.  $\text{Li}^+/\text{Li}$  (even if some problems have been reported after a certain number of cycles in the 5 V region) and the scattering from

**Figure 7.8** Cross-section of the new circular *in situ* NPD cell: (a) Al/Ti container for the electrode material (only partially in the neutron beam); (b) Ti plunger for Li counter electrode; (c) spring; (d) Ti current collector; (e) Al cell body part; (f) PEEK cell; and (g) polymeric attachment for D20 beamline.

Reproduced from Ref. [38] with permission from the Royal Society of Chemistry.

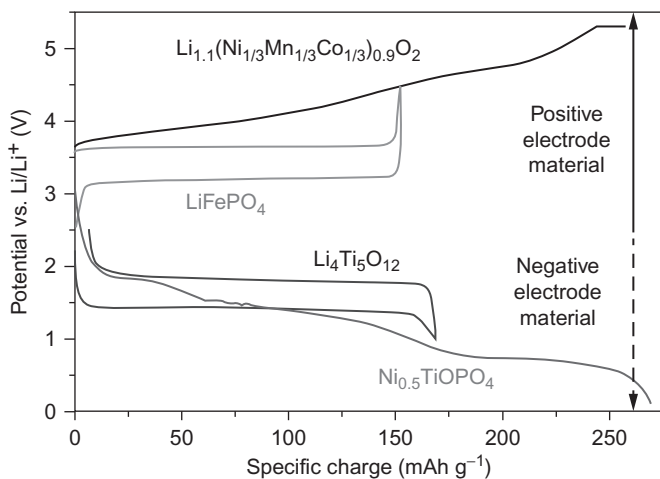
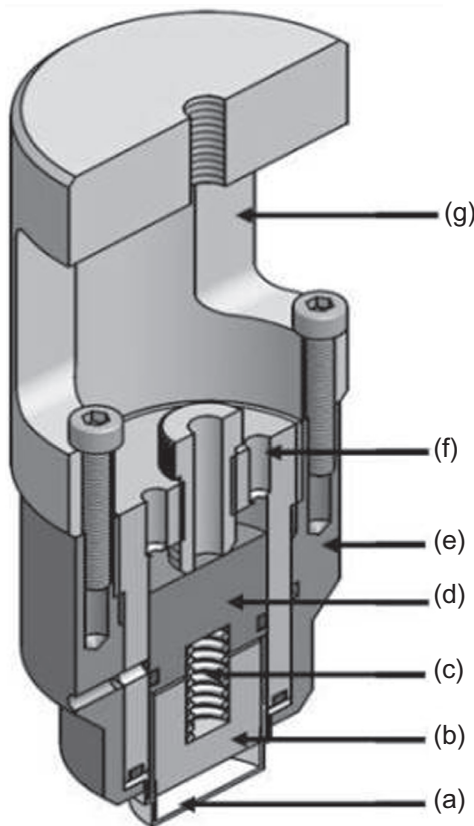


**Figure 7.9** Electrochemical cycling of various electroactive materials in the circular *in situ* neutron diffraction cell versus a Li counterelectrode in EC/DMC 1 M LiPF<sub>6</sub>.  
Reproduced from Ref. [38] with permission from the Royal Society of Chemistry.

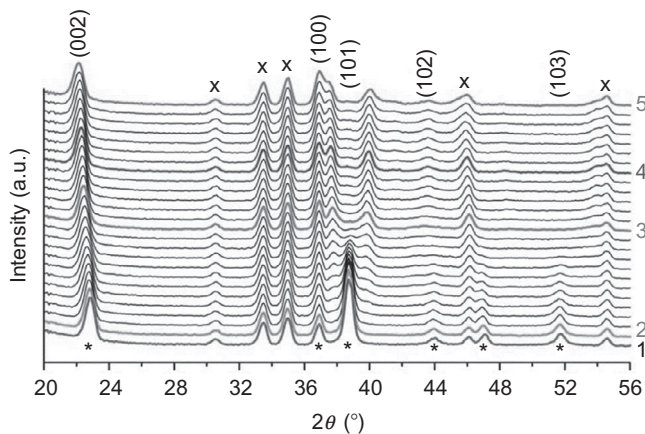


**Figure 7.10** *In situ* NPD patterns ( $\lambda=1.36$  Å) recorded during first lithiation of graphite between 0.23 and 0.11 V vs.  $\text{Li}^+/\text{Li}$ . (\*) and (x) mark peaks from graphite and titanium, respectively.

Reproduced from Ref. [38] with permission from the Royal Society of Chemistry.

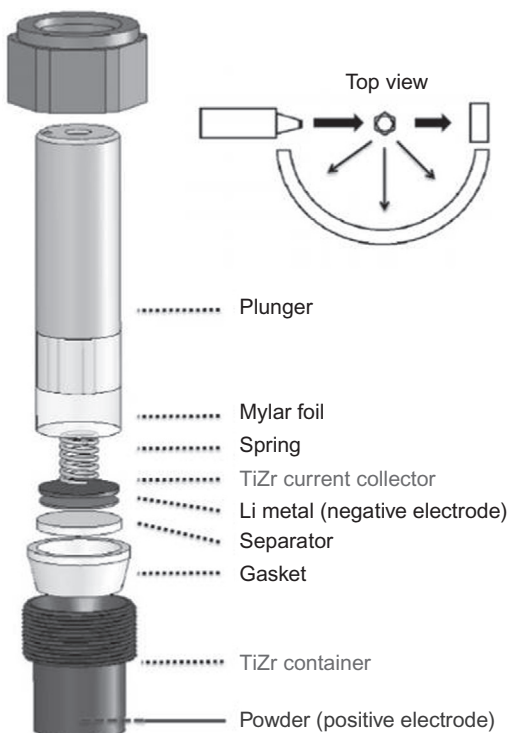
titanium is weak in neutron diffraction, so only small peaks will be visible in the pattern. Another advantage of this cell is the fact that the pressure inside is similar to the pressure we find in commercial batteries. Even if the cell is cycled with a large amount of material (approximately 300 mg), the polarization is still reasonable and the only problem occurs in 5 V materials (such as high-energy NMC [41,42]), where the total potential (including polarization) is above 5 V and, thus, electrolyte decomposition is too fast to perform a reliable experiment.

One example of an *in situ* neutron diffraction experiment in this cell is presented in Figure 7.10. The aim of this study performed by Hess *et al.* was to investigate the structural evolution of graphite between stage 4 and stage 2/2 L at high temperature. Several peaks visible in the pattern and symbolized by a star are ascribable to the titanium container used for the measurements. Fortunately, the main peaks from graphite do not overlap those of titanium. In the *in situ* neutron diffraction patterns, the main peak indexed as (002) shifts to lower angles, which indicates an increase in the *c* unit cell parameter.

Nowadays, many other groups are also developing *in situ* neutron diffraction cells based on this design where only the active materials and the powder container are in the beam. Some groups continue to use full cells with negative and positive electrodes, separator and cell container in the beam, and explore specific regions to understand the reaction mechanism of the cycled electrodes.

In 2013, two other neutron cells were presented in the literature. The first one, developed by Bianchini *et al.* [43], allows Rietveld refinement of *in situ/operando* measurements. The cell is shown in Figure 7.11. The main advantage of this cell is the powder container (named “null matrix material” by the authors), which is the only element in the beam. It is transparent to the neutron beam, inert toward lithium, and cannot be oxidized or reduced.

**Figure 7.11** Schematic of the electrochemical cell designed for *in situ* or operando neutron diffraction. Reprinted with permission from Ref. [43]. Copyright 2014, The Electrochemical Society.



Roberts *et al.* [44,45] also worked on a new cell prototype for *in situ* neutron measurements (Figure 7.12). This design is similar to a commercial battery with a cylindrical part including the three components of the battery: the anode, the cathode, and the separator. Although having all components in the beam increases the number of peaks in the diffraction pattern, the large amount of material with reliable electrochemistry due to the “roll-type” configuration reduces the acquisition time of the pattern.

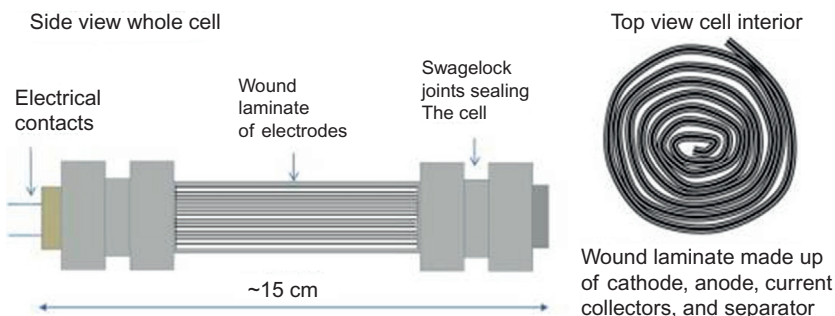


**Figure 7.12** Images of the battery cell for *in situ* neutron diffraction measurements. Reprinted from Ref. [44] with permission from Elsevier.

These two cells were used to study the reaction mechanisms of LiFePO<sub>4</sub> *in situ* operando, show the reliability of the cells from an electrochemical point of view, and explore the possibility to perform Rietveld refinement.

Although XRD, whether combined with neutron diffraction or not, is the most commonly used technique to study the evolution of structural changes of electrode materials, it is significantly less suitable when the materials are amorphous and/or nanostructured, which is often the case when cycling Li-ion batteries. Thus, other sets of characterizations such as atomic scale investigations are in great demand. The following sections will describe other characterization techniques capable of probing the bulk of the materials.

#### 7.4.2 Mössbauer spectroscopy

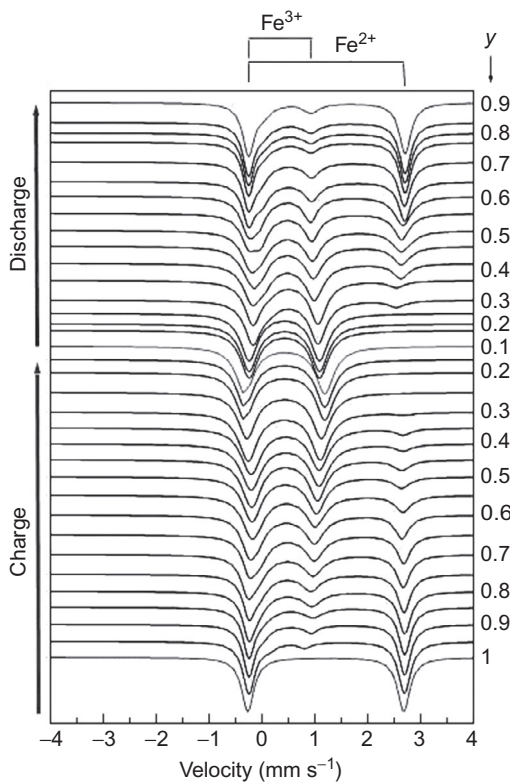
A number of new electrode materials (such as LiFePO<sub>4</sub> as positive electrode material and Sn as negative electrode material) contain iron or tin atoms, which means that Mössbauer spectroscopy can be used to study their reaction mechanisms [46,47]. For this technique, different types of cells have been used in the past and the first measurement was performed by Geronov *et al.* [48] for the investigation of an iron electrode in an alkaline solution. In 2010, Dunlap *et al.* [49,50] developed a new *in situ* cell for <sup>57</sup>Fe and <sup>119</sup>Sn Mössbauer spectroscopy of FeSn<sub>2</sub>. A cylindrical cell was used by Wattiaux *et al.* [51] and an aluminum-laminated PE bag by Ariyoshi and Ohzuku [52]. Some researchers such as Tarascon [53,54] and Jumas [55–62] have performed Mössbauer experiments using coffee bag technology for tin-based anodes [17,63–65]. According to the authors, this type of cell can easily be mounted in a Mössbauer setup. Once again, without sufficient pressure inside the cell, the results are not reliable and the successful elucidation of the reaction mechanisms is compromised. Thus, the cell described in Figure 7.4 developed for *in situ* XRD and XAS was adapted to the settings of the Mössbauer source [19]. As already discussed, the problem of this cell is the lack of pressure, which is able to maintain the electrical contact between particles only when the cycled materials exhibit hardly any volume change during cycling (mainly topotactic reactions). For electrodes with large volume changes, the cell has its limitations and suffers from reliability problems.

Another type of cell, based on a low-cost Swagelok-design with excellent, gas-tight sealing, has been developed by Lippens *et al.* [66]. The cell was made using commercial plastic Swagelok tubes made of perfluoroalkoxy polymer and stainless steel tubes capped by  $\gamma$ -transparent PMMA windows. The results obtained with this type of cell are described in Figure 7.13.

LiFePO<sub>4</sub> is a well-known material for <sup>57</sup>Fe Mössbauer spectroscopy. Substitution of some of the Fe by Mn helps to increase the potential from 3.4 V vs. Li<sup>+</sup>/Li to 4.1 V vs. Li<sup>+</sup>/Li. The reaction mechanism is summarized in Figure 7.13. As we can see, the galvanostatic profile is formed by two plateaus due to the Fe<sup>3+</sup>/Fe<sup>2+</sup> and Mn<sup>3+</sup>/Mn<sup>2+</sup> redox reactions, identified clearly by *in situ* Mössbauer spectroscopy [67,68].

**Figure 7.13**  $^{57}\text{Fe}$  Mössbauer spectra of  $\text{Li}_y\text{Fe}_{0.75}\text{Mn}_{0.25}\text{PO}_4$  (with  $0.1 < y < 1$ ) in a modified XRD–XAS cell for operando measurements during the first cycle at  $C/40$  and at room temperature.

With kind permission from Springer Science and Business Media [66].



#### 7.4.3 X-ray absorption spectroscopy

X-ray absorption spectroscopy is another bulk characterization method that gives valuable clues about the local electronic and atomic structure of the scanned element. We used  $\text{LiFePO}_4$  electrode materials as an example [69–71]. The measurement was performed at a synchrotron source using the half-Swagelok cell described in Figure 7.4.

Leriche *et al.* [19] performed an *in situ* XAS measurement at the Fe K edge to follow the reaction mechanism of the  $\text{LiFePO}_4$  electrode during charge/discharge. The spectra were collected in transmission mode and are plotted in Figure 7.14.

As one can see, and as described by the authors, during lithium extraction, the K Fe edge position is shifting to higher energies as a result of the oxidation of  $\text{Fe}^{2+}$  to  $\text{Fe}^{3+}$ . Due to the biphasic nature of the reaction mechanism of  $\text{LiFePO}_4$ , the spectra can be deconvoluted by a linear combination of  $\text{LiFePO}_4$  and  $\text{FePO}_4$ .

Recently, Cuisinier *et al.* [72] have conducted a similar study on Li–S batteries. The challenge of this kind of study was that part of the elemental sulfur dissolved in the electrolyte during cycling and generated polysulfides. For this purpose, a new *in situ* cell was developed and is presented in Figure 7.15. The authors [72] decided to adapt the design of a type 2325 coin cell and used a transparent window to allow X-ray beam penetration (aluminized Kapton window).

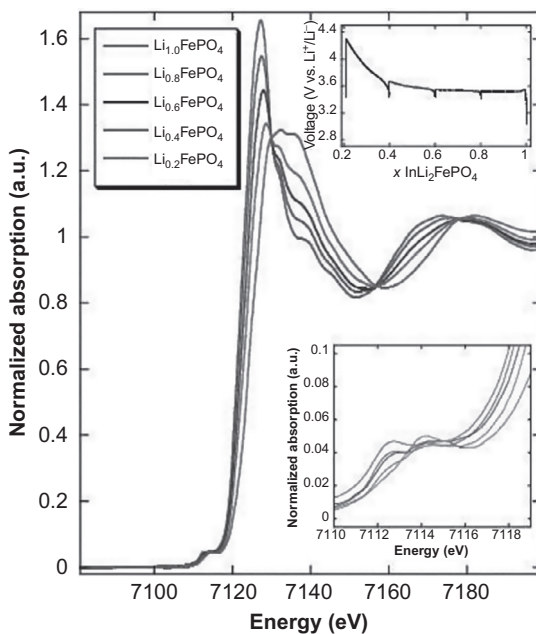


**Figure 7.14** Normalized absorption at the iron K edge recorded at the equilibrium for various states of charging of the LiFePO<sub>4</sub>/FePO<sub>4</sub> system. The top inset is the corresponding charging curve and the bottom inset is an expanded view of the pre-edge part. Reprinted with permission from Ref. [19]. Copyright 2014, The Electrochemical Society.

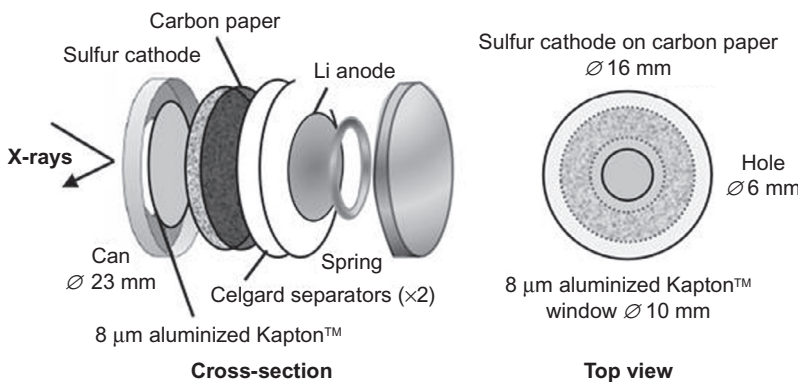


**Figure 7.15** Schematic of the operando cell of Cuisinier *et al.*

Reprinted with permission from Ref. [72]. Copyright 2014, American Chemical Society.

Figure 7.16 shows the charge and discharge profile of a Li–S battery. Upon charge, the authors observed that the consumption of Li<sub>2</sub>S is accompanied by the formation of short chains such as S<sub>6</sub><sup>2-</sup> and S<sub>4</sub><sup>2-</sup>. It is interesting to note that the species S<sub>6</sub><sup>2-</sup> is detected at an early stage and increases during the cycling at the expense of the S<sub>4</sub><sup>2-</sup>, which appears as a metastable phase that allows the oxidation of Li<sub>2</sub>S into

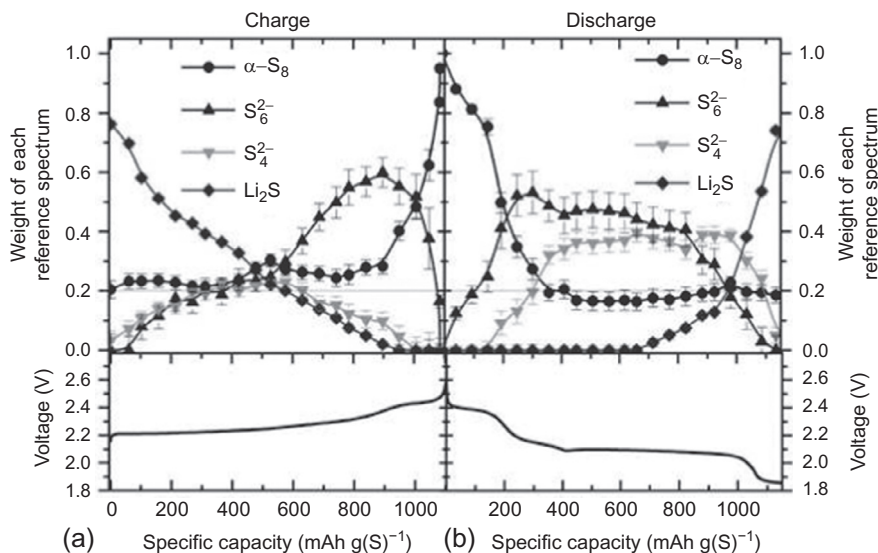


**Figure 7.16** Evolution of the sulfur K-edge XANES upon electrochemical cycling based on linear combination analysis shown upon (a) charge and (b) discharge at a rate of C/10. Reprinted with permission from Ref. [72]. Copyright 2014, American Chemical Society.

the more stable phase  $\text{Li}_2\text{S}_6$ . With a rise in voltage, the authors noticed the disappearance of intermediate species such as  $\text{Li}_2\text{S}$  and  $\text{S}_4^{2-}$ , which signals final oxidation of  $\text{S}_6^{2-}$  to  $\alpha\text{-S}_8$ . The same study was also performed during discharge. The first plateau is often ascribable to the reduction of  $\text{S}_8$ , but it was shown in the literature that there is a disproportionation of the elemental sulfur into  $\text{S}_6^{2-}$  species. Following lithiation, the contribution of the polysulfides (including  $\text{S}_4^{2-}$ ) increases at the expense of the elemental sulfur. At 2.1 V vs.  $\text{Li}^+/\text{Li}$ , the consumption of elemental sulfur ends and, at the same time, the concentration of the polysulfides reaches a maximum. Surprisingly, the  $\text{Li}_2\text{S}$  is not detected before the end of the second plateau. The final stage of lithiation leads to an increase in  $\text{Li}_2\text{S}$ , which, in turn, causes a conversion of all polysulfides into  $\text{Li}_2\text{S}$  followed by a voltage drop.

#### 7.4.4 X-ray tomography microscopy

X-ray tomography microscopy is a new bulk technique used to visualize and quantify the morphology of electrodes. As described by Ebner *et al.* [73], monochromatic X-rays are directed onto the sample under investigation, which is rotated through 180° (Figure 7.17a). Three-dimensional microstructure representations are then calculated numerically from the recorded projection images by a tomographic reconstruction algorithm [74]. The cell used for this experiment is presented in Figure 7.17b and is

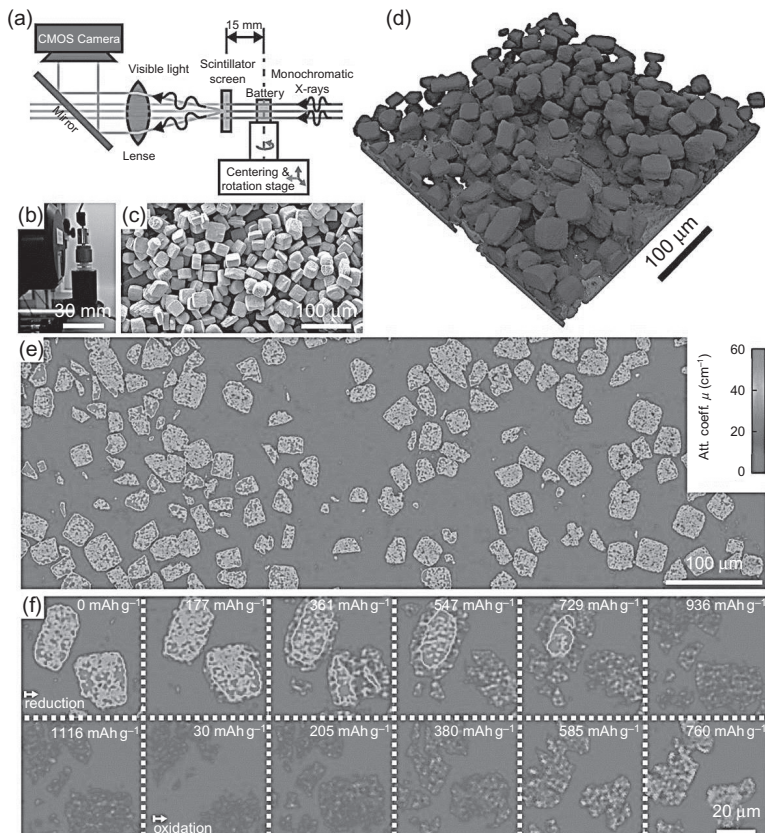


**Figure 7.17** (a) Sketch and (b) photograph of the X-ray tomography setup. (c) Scanning electron micrograph of the  $\text{SnO}$  particles. (d) 3D visualization of X-ray tomograms recorded during battery operation. (e) Unprocessed cross-sectional tomogram showing individual  $\text{SnO}$  particles in the electrode with high resolution and good contrast against a low-attenuation carbon black, binder, and electrolyte phase. Att. coeff, attenuation coefficient. (f) A series of cross-sections through two particles.

based on a Swagelok design made of PP with a diameter of 1 mm. The study was performed on a  $\text{SnO}$  negative electrode to follow the impact of high-volume changes in cubic particles (Figure 7.17c). Thanks to a tomographic reconstruction linked to the attenuation coefficient (Figure 7.17e), two major trends are observed during cycling, that is, the conversion reaction leading to  $\text{Li}_2\text{O}$  followed by the alloying of the Sn particles to  $\text{Li}_{3.5}\text{Sn}$  (Figure 7.17f) [23,75,76]. At the same time, the authors [73] noticed that cracks appeared during cycling due to the high-volume change undergone during lithiation.

### 7.4.5 Nuclear magnetic resonance

Nuclear magnetic resonance (NMR) is another useful tool to probe the structural changes that occur in electrode materials during cycling [77–80]. For years, the studies were mainly performed using *ex situ* samples, but as already described in the first section, those measurements do not provide any information about short-lived metastable phases. Thus, the need to develop suitable cells for *in situ* NMR, which can complement *in situ* X-ray powder diffraction measurements or *in situ* X-ray absorption experiments, has motivated studies in this area. Nowadays, *in situ* NMR is implemented by many groups despite the main challenge of isolating the resonances of a  ${}^7\text{Li}$  in the active material from other components, such as electrolyte, lithium ions in the solid electrolyte interphase (SEI), or even the lithium metal used as counterelectrode. To date, most of the *in situ* studies are performed in a half-cell setup, using lithium metal as the counter electrode, which is convenient due to the fact that the lithium metal is shifted to approximately 250 ppm (called the Knight shift) [17,81,82]. Because graphite is the most commonly used negative electrode for lithium-ion batteries, we decided to discuss the  ${}^7\text{Li}$  *in situ* NMR study of a graphite electrode. The measurement was performed with a coffee bag cell and investigated by two different groups in Orléans and Amiens (Letellier, Chevallier, Morcrette, Tarascon, and coworkers) [80,83,84]. The coffee bag cell was placed directly into a conventional static NMR probe (Figure 7.18). The main goal of this study was to determine the structural changes in graphitic and amorphous carbon electrodes.

The results are presented in Figure 7.19. As described by the authors [80,83], different processes, associated with the different stages of graphite formed until the fully lithiated stage was reached, were observed. Due to the metallic nature of  $\text{LiC}_x$ , the  ${}^7\text{Li}$  resonances are affected by the already described Knight shift. Accordingly, the peaks shift to higher frequency with each stage:  ${}^7\text{Li}$  NMR resonances appear at 2, 6.8, 12.2, 45, and 42.6 ppm for stages 4' ( $\text{LiC}_{36}$ ), 3' ( $\text{LiC}_{27}$ ), 2' ( $\text{LiC}_{18}$ ), 2 ( $\text{LiC}_{12}$ ), and 1 ( $\text{LiC}_6$ ), respectively.

By contrast, in the  ${}^7\text{Li}$  *in situ* NMR spectra of disordered carbons, distinct crystalline  $\text{LiC}_x$  peaks are no longer visible. Instead, only a quasi-metallic (Knight shifted)  $\text{Li}_x\text{C}_6$  peak appears, which shifts gradually to higher frequency (to 104 ppm) as more lithium is inserted into the carbon. Upon lithium extraction, the peak shifts back to 0 ppm.

Recently, Poli *et al.* [81] designed a new *in situ* cell dedicated to NMR measurements of Li-ion batteries. The setup and the design of the cell are presented in Figure 7.20. The cell represents a Swagelok-based design with a cylindrical housing made of PP. The upper part is composed of a screw-like cap for tight sealing. The cell is 2 cm in length and 1 cm in outer diameter and is readily placed inside a 10 mm solenoid of a NMR probe (Figure 7.20b).

The cell was used to study the reaction mechanisms of  $\text{Cu}_3\text{P}$  electrode material by probing the  ${}^{31}\text{P}$  NMR as shown in Figure 7.21. As described by the authors [81], the initial  ${}^{31}\text{P}$  spectrum displays a typical asymmetrical signal of  $\text{Cu}_3\text{P}$  and a multiple signal of  $\text{LiPF}_6$ . The electrochemical reaction of  $\text{Cu}_3\text{P}$  with lithium is indicated by the changes in the  ${}^{31}\text{P}$  spectra. The significant shift of the  ${}^{31}\text{P}$  signal indicates the formation of  $\text{Li}_3\text{P}$  at

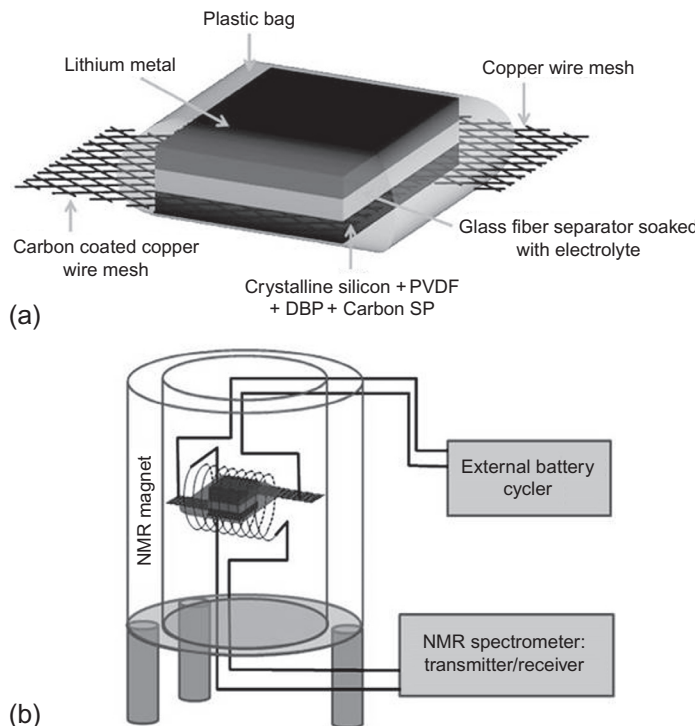


**Figure 7.18** *In situ* NMR setup using coffee bag cell. (a) Schematic of a coffee bag cell. (b) Setup of the coffee bag cell in the NMR magnet.

Reprinted with permission from Ref. [82]. Copyright 2014, American Chemical Society.

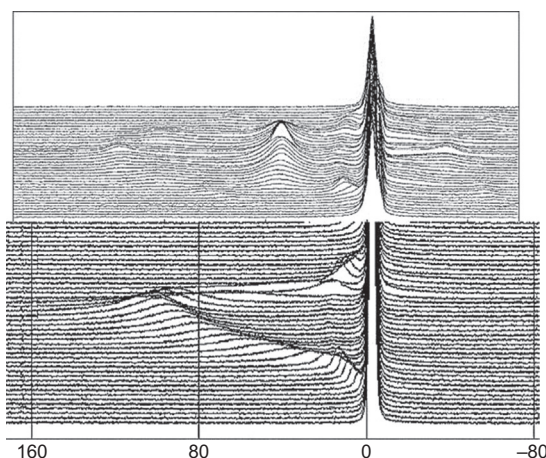


**Figure 7.19**  ${}^7\text{Li}$  *In situ* NMR of (top) graphitic carbon and (bottom) disordered carbon for the first cycle.

Reprinted from Ref. [80] with permission from Elsevier.

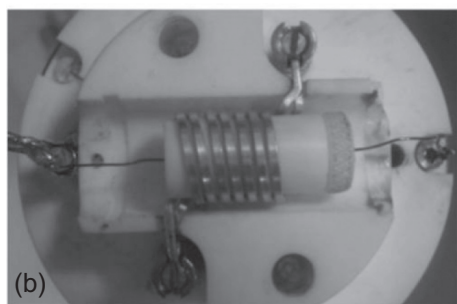
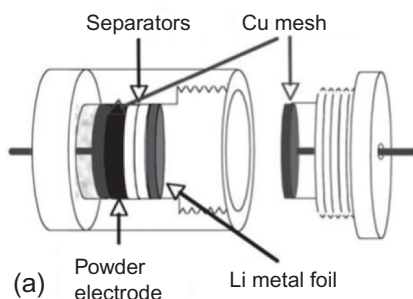


**Figure 7.20** (a) Schematic drawing of the cylindrical cell design for *in situ* NMR experiments. (b) Top view of the NMR probe with the cylindrical cell inside a 10 mm solenoid.

Reprinted from Ref. [81] with permission from Elsevier.

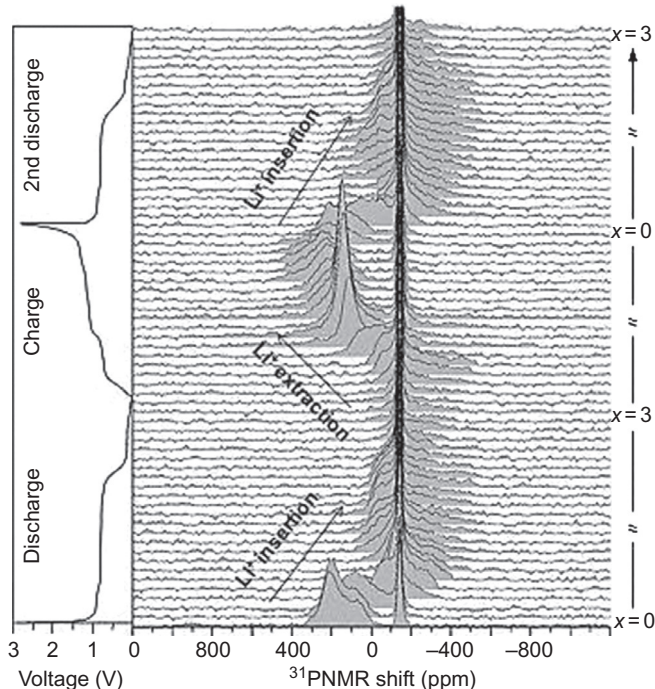


**Figure 7.21** Stack plot of selected *in situ*  $^{31}\text{P}$  NMR spectra recorded during the first and second half-cycle of a  $\text{Cu}_3\text{P}$  electrode. The vertical axis represents the molar fraction ( $x$ ) of Li ions. Reprinted from Ref. [81] with permission from Elsevier.

the end of full lithiation. Based on this observation, it was shown that a  $\text{Li}_3\text{P}$  disorder phase is created during cycling, which was not detectable by XRD. Another interesting point is that a shift occurs at the initial stage of the discharge, suggesting that a small amount of lithium can be inserted into  $\text{Cu}_3\text{P}$ , as indicated by theoretical calculation. As expected, upon charge, the opposite reaction occurred, leading to the regeneration of  $\text{Cu}_3\text{P}$ .

Nowadays, NMR studies are commonly used for the study of reaction mechanisms of Li-based batteries. *In situ/operando* NMR characterizations are well suited to understanding and to detecting the metastable phases upon cycling.  $\text{Li}-\text{O}_2$  batteries are also subject to intensive investigation, especially aimed at following the  $^{14}\text{C}$  NMR signal to understand the reactions of the carbon electrode [85,86].

#### 7.4.6 Acoustic emission

Acoustic emission (AE) is a useful nondestructive technique to study the elastic waves generated by the cracks that occur in the particles during their reaction with lithium [87,88]. This cheap technique (compared with XRD or XAS), which involves “listening” to the formation of cracks in the particles while they are cycled versus lithium, is based on ultrasound measurements. The setup is easy to handle and can be adapted to all types of cell designs. Two sensors are placed on both sides of a battery (positive and negative electrodes), they are then connected to a preamplifier. Finally, the signal is analyzed and processed via a computer, as illustrated in Figure 7.22.

Villevieille *et al.* [89] demonstrated for  $\text{NiSb}_2$  materials that the particles that undergo a direct conversion reaction with a significant release of energy are linked to a significant change in the electric waves, as illustrated in Figure 7.23. As one

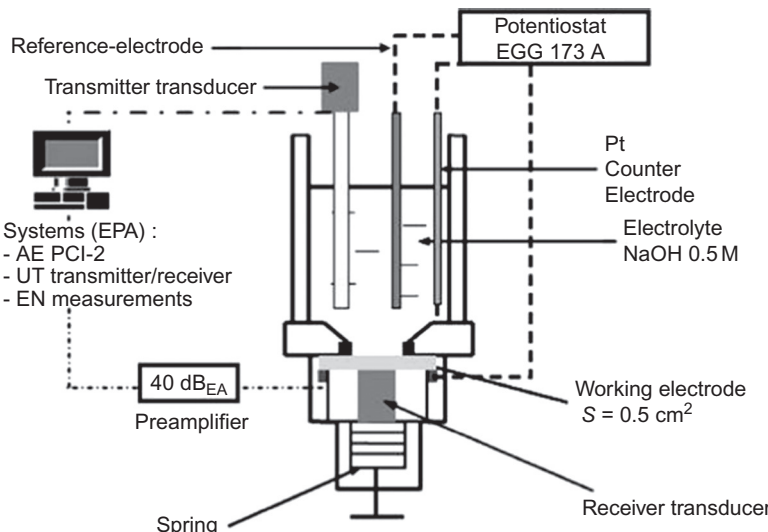


**Figure 7.22** Acoustic emission setup.

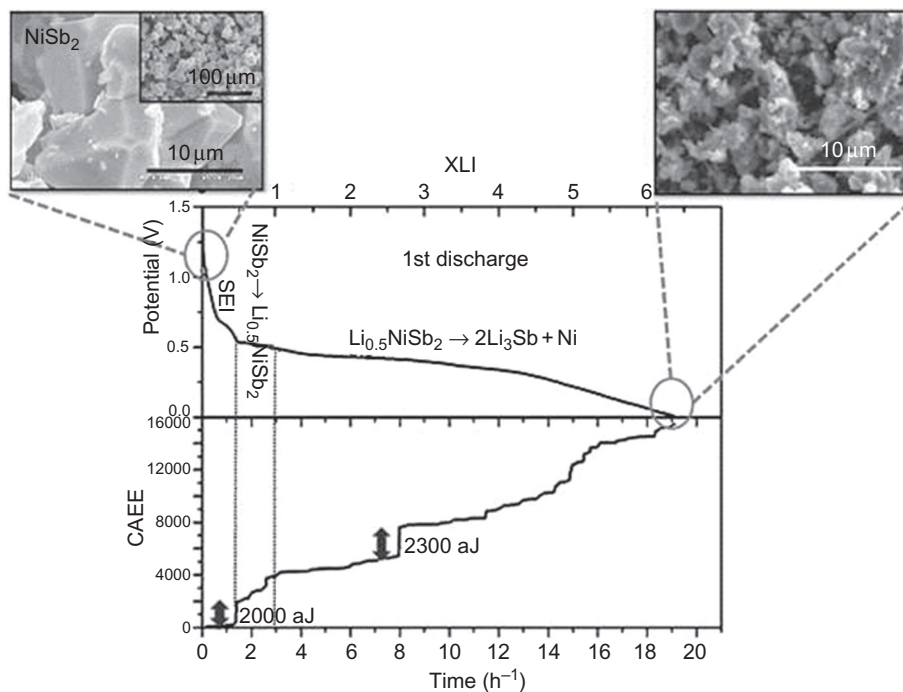


**Figure 7.23** CAEE and voltage profiles of the first discharge of  $\text{NiSb}_2/\text{Li}$  cell vs. time (h), cycled at a rate of  $C/10$  between 1.5 and 0 V vs.  $\text{Li}^+/\text{Li}$ . Left inset: SEM image of the starting  $\text{NiSb}_2$  powder. Right inset:  $\text{NiSb}_2$ -based electrode after full discharge.

Reprinted from Ref. [89] with permission from Elsevier.

can see, there is an increase in the AE energy (denoted CAEE hereafter) at about  $t = 1.5$  h. According to the authors, this first jump in energy is associated with the formation of organic layers on the carbon grains, most probably SEI formation. Other small increases between  $t = 1.5$  and 8 h are assigned to lithium insertion into the materials. Then, at  $t = 8$  h, the signal increases significantly, which was interpreted as a biphasic conversion process ( $\text{Li}_{0.5}\text{NiSb}_2 \rightarrow 2\text{Li}_3\text{Sb}$  and  $\text{Ni}$  nanoparticles).

Other studies in the literature report similar findings, especially for conversion materials such as Si [87]. The materials undergo a conversion followed by a large volume change of the electrode, which is ascribable to a significant increase in the AE energy.

Section 7.4 has provided an overview of the principal *in situ* characterizations used to study the reaction mechanism of lithium-based batteries. Nevertheless, the reaction mechanisms of a battery are composed of many interfaces, and the study of the bulk property itself cannot resolve the full reaction mechanism. A careful analysis of the surface has to be performed in order to investigate the electrode/electrolyte interface. Section 7.5 is dedicated to the surface characterizations used in lithium-based batteries.

## 7.5 Surface characterizations

This section is dedicated to the study of the surface properties of electrodes during cycling. The constraints on surface characterizations are different from the ones on the bulk. New cells adapted to different surface investigation techniques have been designed. Most of the *in situ* surface techniques (such as SEM, XPS, and TEM) require a high-vacuum environment. When using these techniques, it is then better to work with electrolytes based on ionic liquids, as they are not as volatile as organic-based electrolytes.

### 7.5.1 Scanning electron microscopy

The first *in situ* cell prototypes for SEM analysis were developed during the previous decade [90–92]. A first attempt to design a suitable *in situ* cell design was not successful because that cell had to be disassembled and the electrolyte removed before measurement [93,94]. As already mentioned in the Section 7.4, *ex situ* samples are air- and moisture-sensitive and, thus, can be easily contaminated or damaged. Extra care must be taken to protect them from oxygen, nitrogen, or water contamination [95].

Further improvements were achieved in the development of a reliable *in situ* SEM setup. For example, Baudry and Armand [90] used a polymeric electrolyte. However, this type of electrolyte had to be heated to let lithium react within a reasonable time because of its low ionic conductivity. In the same group, Orsini *et al.* [91] decided to use a standard organic electrolyte, LP30. To avoid evaporation of the electrolyte under high-vacuum conditions, the battery was cooled down to  $-20\text{ }^{\circ}\text{C}$  and then transferred to the SEM chamber. Unfortunately, the authors were not able to cycle the cell. To avoid fast evaporation of the electrolyte, ionic liquids were selected instead as electrolyte. The setup described by Chen *et al.* [96] is shown in Figure 7.24. Several steps are needed to build this type of cell. A part of the cell can be assembled inside the glove box (Figure 7.24a) while the top part of the cell containing the electrode to be

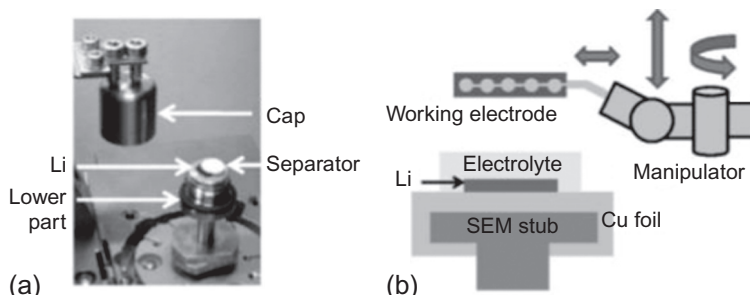


**Figure 7.24** (a) Homebuilt transfer system (opened) containing the lower part of the cell. The container can be opened by removing the cap inside the SEM chamber under high vacuum. (b) Inside the SEM, the electrode under investigation is placed on top of the separator. Reprinted from Ref. [96] with permission from Elsevier.

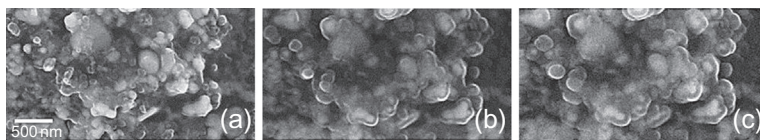


**Figure 7.25** A portion of the  $\text{SnO}_2$  electrode (a) before lithium insertion, (b) after the first lithium insertion, and (c) after the second lithium insertion. The micrographs were taken with the same magnification.

Reprinted from Ref. [96] with permission from Elsevier.

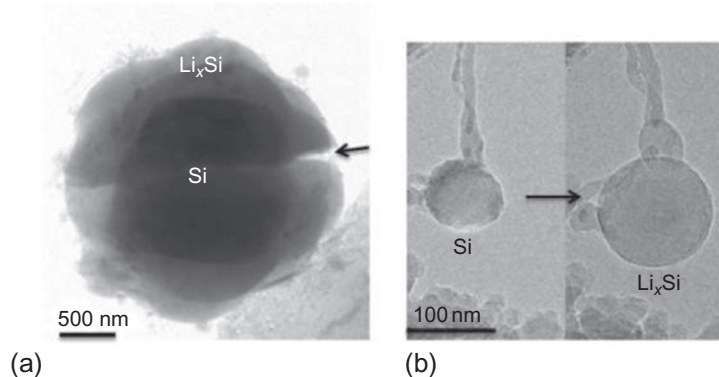
measured is placed directly inside the SEM chamber (Figure 7.24a). The cell is then closed on top of the antechamber of the SEM microscope using a micromanipulator, which also ensures electrical contact with the working electrode (Figure 7.24b).

The experiment was performed on a  $\text{SnO}_2$  electrode. The micrographs are shown in Figure 7.25. The analysis was performed on an area of the electrode containing small particles with dimensions below 100 nm. During the reaction of the first equivalent of lithium with  $\text{SnO}_2$ , the volume change increased above 150% and the smallest particles showed volume expansions of more than one order of magnitude (Figure 7.25b) [23,97]. The particle size continued to increase slightly during the following cycle as can be observed in Figure 7.25c.

Chen *et al.* [96] analyzed different materials. They observed a dependence of the reaction mechanism on the particle size. Small particles exhibit a drastic volume change, whereas larger particles do not. SEM is a good technique to study the changes in morphology at the surface of electrodes. However, its resolution is limited and cannot provide information at the nanoscale. Transmission electron microscopy (TEM) is a powerful tool capable of imaging with a significantly higher resolution than standard microscopes.

### 7.5.2 Transmission electron microscopy

Nowadays, a lot of researchers work on the synthesis of nanomaterials as electrode materials for lithium-based batteries [98]. These nanoparticles show very promising performances, particularly for batteries based on conversion/alloying reactions for which the volume changes can be above 200% during lithiation [97]. Nevertheless, few tools are able to detect and analyze the products resulting from reactions between the nanoparticles and lithium. The challenge of such a technique is to design and build a setup suitable for a battery working under high vacuum [99–101]. Many setups are described in the literature but differ significantly from the standard setup for a Li-ion battery. First of all, the cell geometry requires that only one end of a nanowire or nanotube electrode can be in contact with the electrolyte [99]. The second crucial problem, as already mentioned for the *in situ* SEM, is the use of special electrolytes that do not evaporate under high vacuum. Currently, ionic liquids or polymer electrolytes are the best candidates [100]. Finally, the high energy of the beam itself ( $\sim 80\text{--}300$  keV) can impact the electrochemical properties of the materials [102].



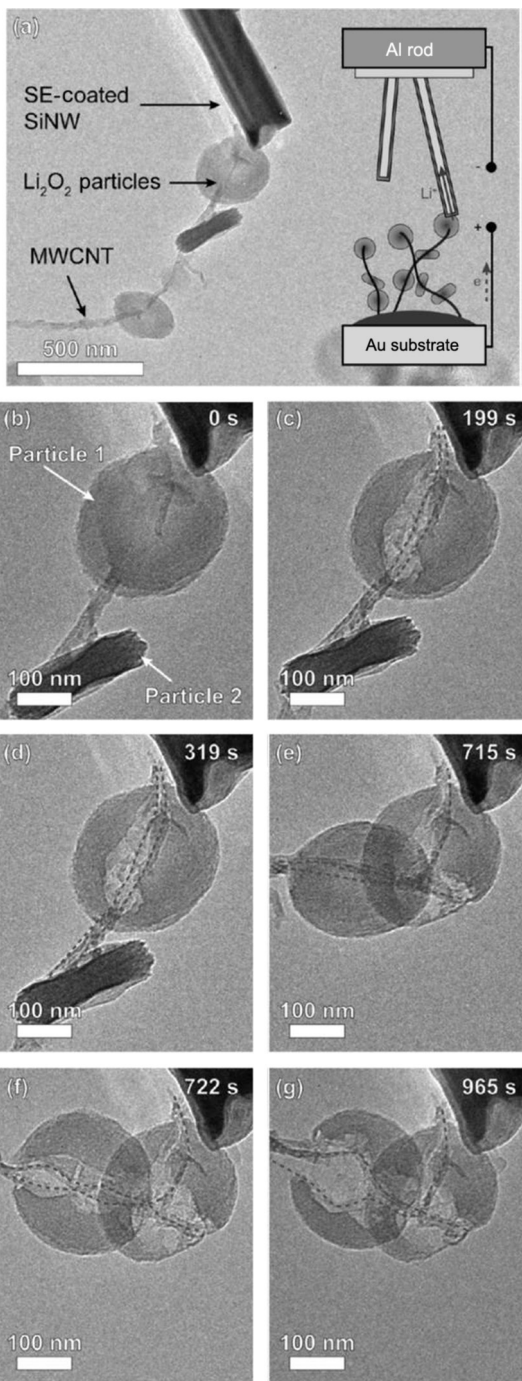
**Figure 7.26** Surface crack in Si nanoparticles during lithiation. (a) *In situ* experimental micrograph of the nucleation of a crack at the surface of the Li<sub>x</sub>Si shell and its propagation inward during lithiation of a large Si nanoparticle of a diameter of 1800 nm. (b) Lithiation of a small Si nanoparticle without any cracks. The diameter increased from 80 to 130 nm. Reprinted from Ref. [103] with permission from John Wiley and Sons.

Figure 7.26 shows the results of an *in situ* TEM study performed on a nano Si negative electrode. Silicon particles suffer from a volume change above 200% while cycling vs. lithium. In the case of “big” nanoparticles, ~150 nm, cracks always nucleated at the surface and propagated through the entire particle (Figure 7.26a) upon lithiation [104]. Smaller-sized particles (Figure 7.26b) exhibited a significant volume change upon lithiation. This *in situ* result clearly demonstrates the ability of nanoparticles to support higher mechanical stress [105]. This kind of study allows a deeper understanding of the conversion/alloying reaction mechanism.

We showed here that *in situ* TEM is an advanced tool to investigate the reaction mechanisms of standard lithium-ion batteries at the nanoscale. Zhong *et al.* [106] used a similar TEM setup to study Li–O<sub>2</sub> batteries. Such batteries, also based on Li metal, are the subject of intensive research. Insets (a) and (b) in Figure 7.27 clearly illustrate the way Li<sub>2</sub>O<sub>2</sub> particles are connected to the Si electrode. Following the reaction mechanism under the TEM beam revealed that the oxidation of the Li<sub>2</sub>O<sub>2</sub> particles to Li<sup>+</sup> and oxygen lead to a stripe of weak contrast in the middle of the particles. As suggested by the authors, the oxidation occurs at the carbon (MWCNT)/Li<sub>2</sub>O<sub>2</sub> interface but not particularly at the solid electrolyte/Li<sub>2</sub>O<sub>2</sub> interface. In the present case, it was demonstrated that the Li<sub>2</sub>O<sub>2</sub> oxidation is electron-transport-limited and not lithium-ion-transport-limited. As a result, the electrical contact between the carbon (MWCNT) and Li<sub>2</sub>O<sub>2</sub> also weakens upon Li<sub>2</sub>O<sub>2</sub> oxidation. Upon further lithiation, the carbon (MWCNT) was bent, thus putting particle 1 in contact with particle 2. Hence, the oxidation reaction started again (Figure 7.27e). This *in situ* study demonstrated that the oxidation of a second particle starts only if it is in direct contact with a particle that is already oxidized. This helps to form a pathway for the lithium. This study demonstrates that the rate capability of Li–O<sub>2</sub> batteries is governed by electronic transport and not by lithium transport.

**Figure 7.27** Oxidation of  $\text{Li}_2\text{O}_2$  particles. (a) Schematic illustration of the *in situ* TEM of a microbattery (TEM image of a SE-coated Si NW contacting a single  $\text{Li}_2\text{O}_2$  particle). (b) Higher-magnification TEM image of the particles showing a MWCNT bundle contacting two physically separated  $\text{Li}_2\text{O}_2$  particles labeled as Particle 1 and Particle 2, respectively. (c–g) Oxidation of Particles 1 and 2 during application of a 10 V potential to the MWCNT/ $\text{Li}_2\text{O}_2$  positive electrode against the Si NW negative electrode.

Reprinted with permission from Ref. [106]. Copyright 2014, American Chemical Society.



SEM and TEM analyses provide useful information, mainly on the shape of the particles. However, no precise information on the chemical composition of the surface layer can be obtained. XPS and Raman/FTIR are more suitable techniques to analyze the chemical composition of the surface layer. These techniques are described in the following sections.

### 7.5.3 X-ray photoelectron spectroscopy

Upon operation, side reactions between the electrolyte and the active material significantly impact the performance of the battery. Thorough investigation of this interface is thus required. A main technique that gives chemical information on surface (interface) layers is XPS, whose analysis depth is a few nanometers. Nevertheless, the high vacuum needed to run the experiment and the cell configuration required to study the interface do not yet allow *in situ* or *operando* studies. This is the reason why mainly *ex situ* studies on Li-based batteries are reported in the literature. But, once again, analyzing *ex situ* samples raises some questions. One can wonder about the contamination resulting from air and moisture exposure or about the evolution of the surface layer taking place upon disassembly of the cell. Electrodes are usually washed before measurement in order to remove the remaining electrolyte. Washing can affect the nature and composition of the surface of the electrodes to some extent [107].

Two examples are discussed here to demonstrate how powerful XPS analysis is and how the electrolyte and the cycling can influence the thin-layer polymer at the surface of particles. Malmgren *et al.* [108] used XPS to study the effects of air exposure and washing of lithiated graphite electrodes on the SEI [109–112]. Their XPS spectra are reported in Figures 7.28 and 7.29. After air exposure, the decrease in the graphite component (at 282 eV) of the lithiated graphite electrode indicates an increase in the layer thickness covering the graphite electrode. When the electrodes are washed and exposed to air, the amount of oxygenated species at the graphite/electrolyte interface increases as much as for the unwashed sample that has been exposed to air. But according to the authors, the way the samples were treated influences the interface layer. For the unwashed samples exposed to air, the C 1 s and O 1 s spectra showed more pronounced components ascribed to carbonate and ether environments. However, for the washed samples exposed to air, a new component assigned to LiOH is observed in the O 1 s spectrum. This study shows that air exposure influences the composition of the SEI. It also shows that the washing processes commonly used in the battery field lead to the formation of new components and affect the sensitive SEI.

Silicon particles are known to suffer large volume changes during lithiation. Philippe *et al.* [113] studied the impact of the salt used in the electrolyte on the electrode/electrolyte properties of a Si electrode by XPS [114–116]. Figure 7.30 presents a summary of their results together with a comparison of the different possible mechanisms occurring at the surface of Si nanoparticles upon cycling with LiPF<sub>6</sub> or LiFSI salts. The authors [113,116] were able to demonstrate that lithium reacts with the SiO<sub>2</sub> layer to form first Li<sub>2</sub>O and Li<sub>4</sub>SiO<sub>4</sub> and then, upon further lithiation, Li<sub>x</sub>Si alloys. After

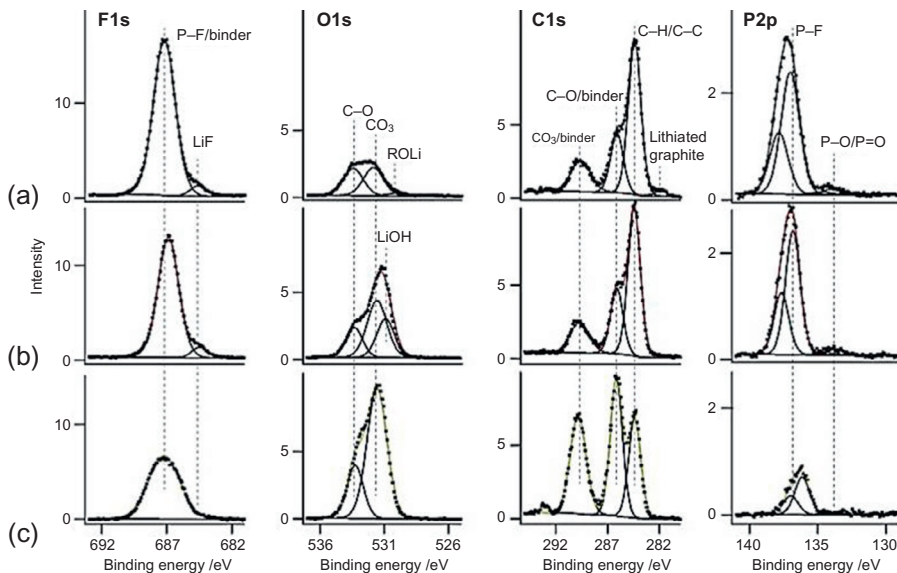


**Figure 7.28** XPS spectra of unwashed lithiated graphite (a) unexposed, (b) exposed after vacuum treatment, and (c) exposed before insertion into the vacuum.

Reprinted from Ref. [108] with permission from Elsevier.

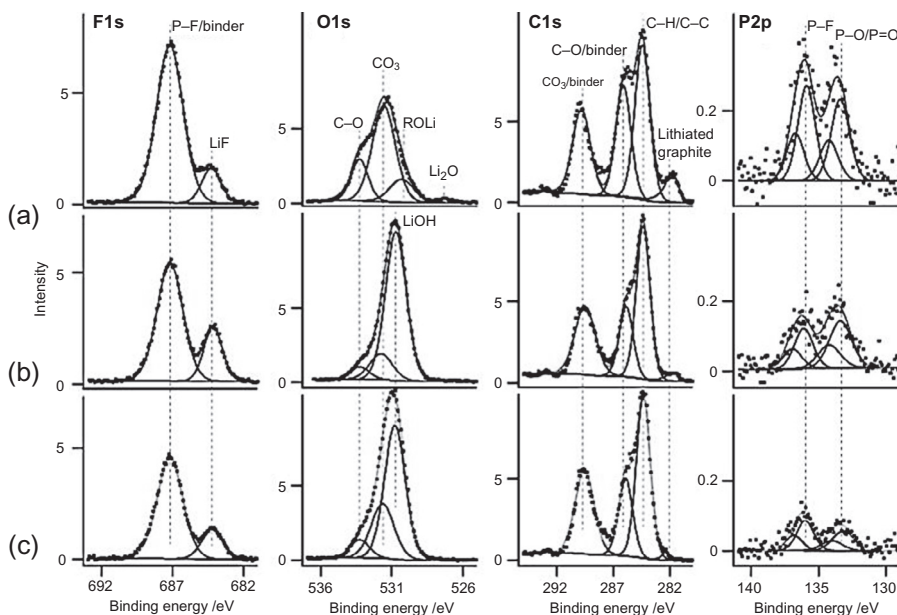


**Figure 7.29** XPS spectra of washed lithiated graphite electrodes (a) unexposed, (b) exposed after vacuum treatment, and (c) exposed before insertion into the vacuum.

Reprinted from Ref. [108] with permission from Elsevier.

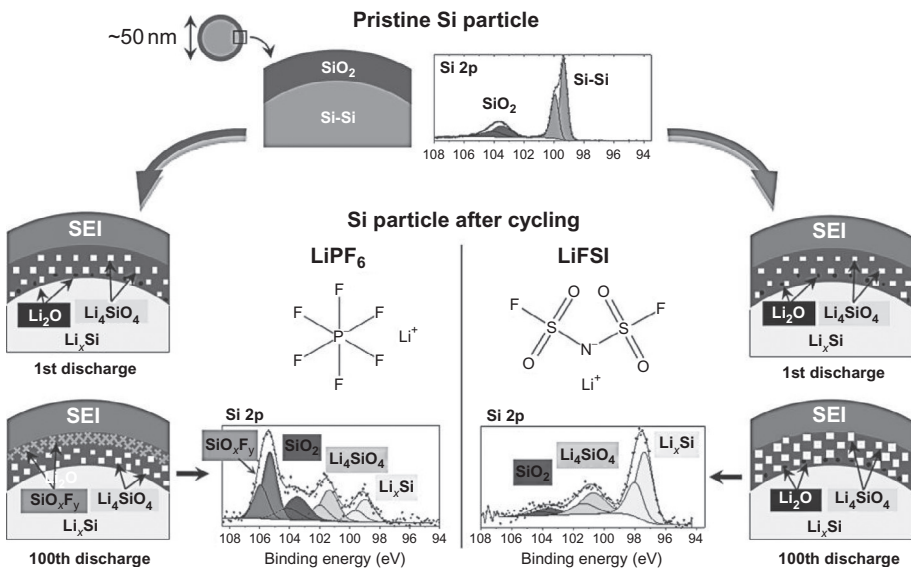


**Figure 7.30** Schematic comparison of the reaction mechanisms occurring at the surface of a silicon nanoparticle upon cycling of a Li/Si cell using either  $\text{LiPF}_6$  or  $\text{LiFSI}$  salts. XPS is an appropriate technique to investigate the chemical composition of surface layers.

Reprinted with permission from Ref. [113]. Copyright 2014, American Chemical Society.

long-term cycling, significant differences between the two salts were clearly visible. It is well known that HF can develop within electrolytes containing  $\text{LiPF}_6$  [117]. As a result,  $\text{Li}_2\text{O}$  species disappear from the surface of the Si particles and  $\text{SiO}_x\text{F}_y$  species form. Thus, the presence of  $\text{LiFSI}$  salt prevents the formation of HF and as a consequence no  $\text{SiO}_x\text{F}_y$  is detected. It is obvious that the different surface chemistries lead to different interaction, not only with the electroactive materials but also with the other components of the electrode (binder, conductive carbon, current collector). According to the authors, these differences explain the better electrochemical behavior observed for Li–Si batteries containing  $\text{LiFSI}$  salt compared with  $\text{LiPF}_6$  salt.

Nevertheless, and as explained before, *in situ* characterizations with XPS are not possible at the moment due to the constraints on the electrolyte and the cell design. Other techniques such as Raman and FTIR spectroscopy can be used to track the formation and evolution of the SEI layer on the surface of the particles. They are presented in the following section.

#### 7.5.4 Raman and Fourier transform infrared spectroscopy

FTIR and Raman spectroscopy are relevant techniques to study the electrode/electrolyte interface. Nevertheless, as already highlighted for the other techniques, the development of a suitable spectroelectrochemical setup combining optimized measurement condition and good electrochemistry is a real challenge. One of the key problems is the selection of a suitable material for the window. The material should be transparent to

Raman/FTIR and strong enough to sustain the pressure inside the cell required to measure good electrochemistry data. Another difficulty often cited in the literature is the strong absorption of IR radiation by the electrolyte. Decreasing the distance between the windows of the cell and the electrode will reduce the amount of electrolyte in the beam. This will increase the IR signal. Bewick *et al.* [118,119] were the first people to design a cell in which the distance between the electrode and the measurement window can be minimized thanks to a special screw. Nevertheless, even if the distance between the window and the electrode is short enough, reflectance issues need to be solved. In fact, FTIR and Raman spectroscopy are based on reflectance measurements [120,121]. Thus, polished electrodes, instead of porous electrodes, are more suitable. In the literature, metals such as nickel, copper [122,123], or noble metals [124] or even glassy carbon [121] have been studied because of their flat and highly reflective surfaces. In this section, we will discuss studies performed on the surface of carbonaceous electrodes of lithium-ion batteries. Numerous studies in the literature are devoted to the understanding of the SEI properties [125–127]. The SEI formed during the first lithium reaction with graphite has been extensively investigated in the previous decades using *ex situ* [128] and *in situ* [122] infrared spectroscopy.  $\text{Li}_2\text{CO}_3$ , lithium alkyl carbonate, lithium alkyl oxide, and other species resulting from decomposition (e.g., LiF) of the  $\text{LiPF}_6$ -based electrolyte were identified as the different components of the SEI [112]. Additives were added to the electrolyte to improve its properties. Zhang *et al.* [129] reported that addition of VC and ES to the electrolyte improves the properties of the SEI. Aurbach *et al.* [130] studied the impact of VC additive using FTIR. They showed that VC polymerizes on the graphite surface, thus creating poly-alkyl-lithium-carbonate species and suppressing the reduction of the salt and the solvents. Thus, the SEI formation mechanism remains uncertain and further studies are needed to understand the processes occurring at the electrolyte/electrode interface. The challenge, in this case, is the development of a cell able to study directly the surface of the electrode and to suppress the signal from the electrolyte. In summary, Raman and FTIR spectroscopies are very useful complementary techniques to gain information on the electrolyte/electrode interface. Pérez-Villar *et al.* [131] used a novel custom-made spectroelectrochemical cell to study the properties of the SEI of a model electrode (glassy carbon) and the impact of additives using combined *in situ* FTIR/Raman. The cell is presented in Figure 7.31. The authors used two different approaches for the *in situ* FTIR measurements, both based on external reflectance spectroscopy. As described in Figure 7.31, the cell contained a  $\text{CaF}_2$  window, which is transparent to light and stable against the electrolyte.

The results obtained with the combined FTIR/Raman setup using the spectroelectrochemical cell are presented in Figure 7.32. The two techniques differ in the signal-to-noise ratio, which is weaker in the case of the combined FTIR/Raman compared to the *in situ* FTIR spectrometer. This is related to the larger area from which the IR radiation is collected in standard FTIR spectroscopy. In any case, both techniques allow the detection of the typical positive and negative bands. The authors [131] concluded that ion migration through the thin electrolyte layer of the cell is the main reason for the continuous increase in the absolute intensities of the SNIFTIRS bands when moving toward more negative potentials.

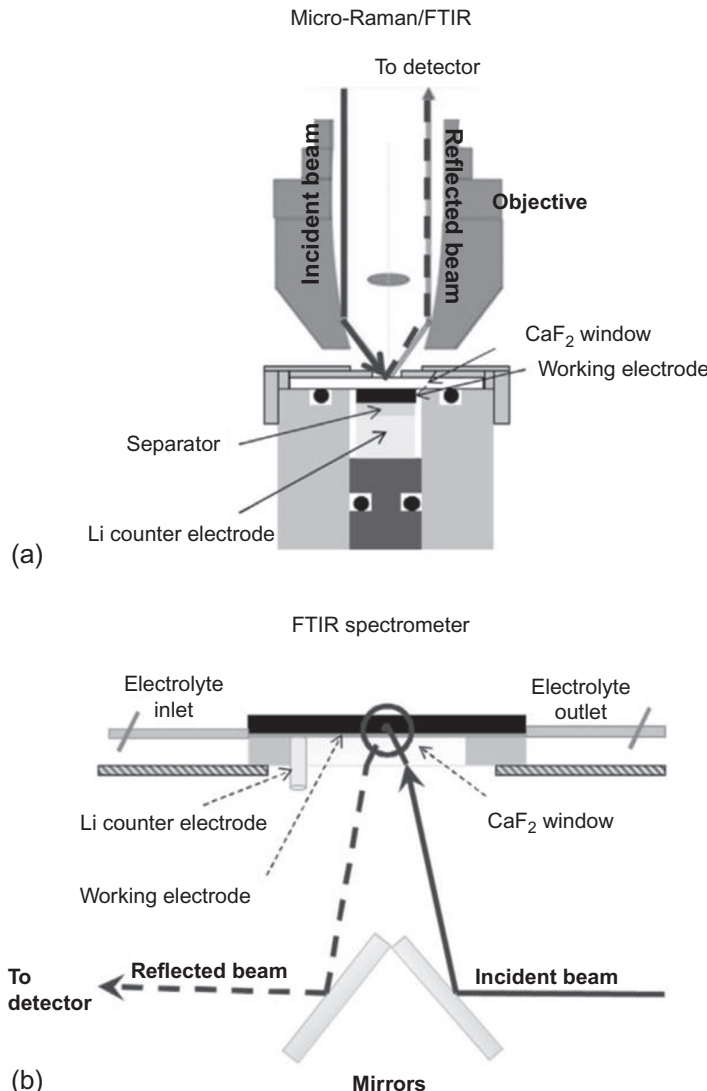


**Figure 7.31** Schematic of the IR paths and the spectroelectrochemical cells used in (a) combined Raman/FTIR microscopy and (b) conventional FTIR spectroscopy. Reprinted from Ref. [131] with permission from Elsevier.

Thus, Pérez-Villar *et al.* [131] demonstrated the reliability of the combined techniques to study the electrode interface of Li-ion batteries.

We saw in the previous sections that during cycling, a surface layer is formed at the surface of the particles but also that the different components of the electrode (binder, conductive agent) and the electrolyte can be decomposed and degraded and, thus, generate gas upon cycling. Mass spectrometry is of primary interest to study gas

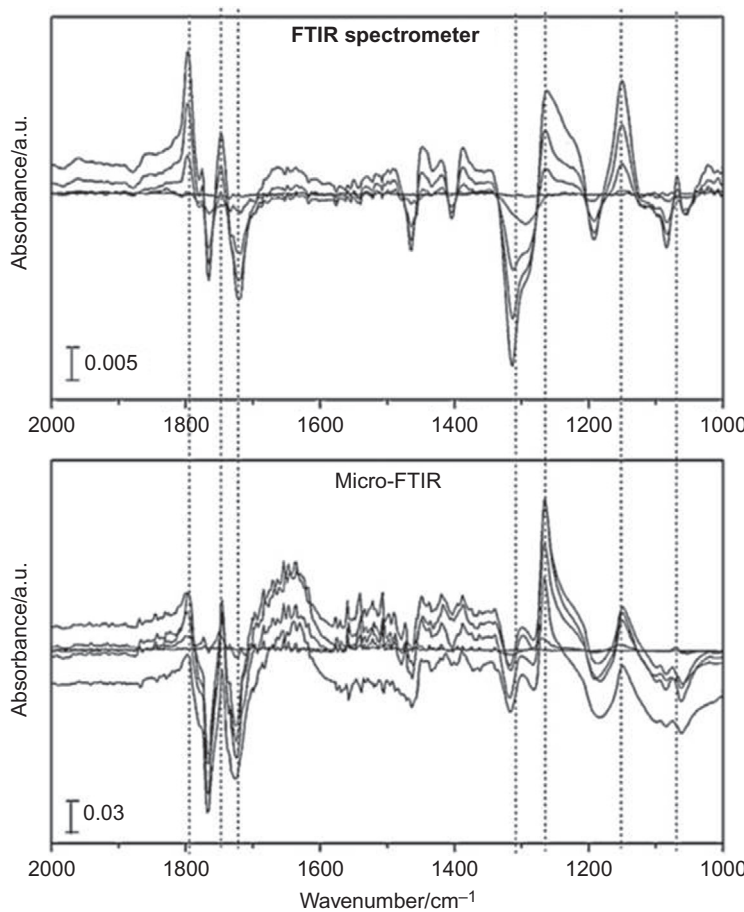


**Figure 7.32** Comparison of the *in situ* SNIFTIRS spectra, recorded from the GC electrodes with the spectrometer and the microscope in 1 M LiClO<sub>4</sub> EC/DMC 1:1 with no additive recorded during potential steps from OCP to 0.2 V.

Reprinted from Ref. [131] with permission from Elsevier.

evolution. The use of such a combination (battery/mass spectrometer) is described in the next section.

### 7.5.5 Differential electrochemical mass spectrometry

During cycling, reactions between the different cell components (active material, Li metal, electrolyte) can generate gaseous or volatile electrochemical reactants as intermediates reaction and/or products. Differential electrochemical mass spectrometry (DEMS) is an analytical *in situ* technique combining an electrochemical cell and a mass spectrometer [132–135]. A special electrochemical cell was designed for that measurement (Figure 7.33). The most important requirement of such a cell is that

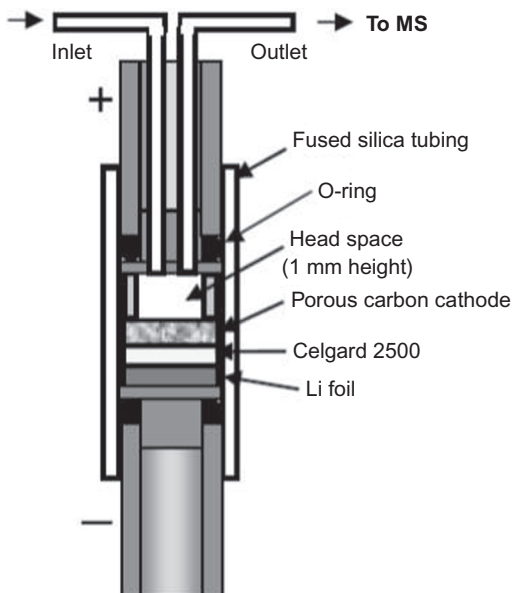


**Figure 7.33** Schematic of a DEMS electrochemical cell. The stainless steel cathode and anode rod tips are sealed with ethylene propylene O-rings against a fused silica cell wall. Reprinted with permission from Ref. [136]. Copyright 2014, American Chemical Society.

the evolved gases must be transferred from the electrolyte phase to the vacuum in a short period of time. One way to reduce that time is to have the electrode very close to the membrane of the spectrometer. The presence of an additional convection system can also help the transport of the gaseous species to the mass spectrometer.

Nowadays, DEMS is mainly used to study the interfacial reaction mechanisms taking place at positive and negative electrodes of conventional lithium-ion batteries and to follow the reaction mechanism involved when a Li-air battery is connected directly to an O<sub>2</sub> tank by analyzing the gases generated upon cycling. La Mantia *et al.* [137] followed the reaction mechanism and the oxygen release occurring in 5 V positive electrode materials called high-voltage NMC (Li<sub>1+x</sub>(Ni<sub>1/3</sub>Mn<sub>1/3</sub>Co<sub>1/3</sub>)O<sub>2-x</sub>). The evolution of CO<sub>2</sub> and O<sub>2</sub> during cyclic voltammetry measurements is reported in Figure 7.34. The authors [137] observed that, for overlithiated NMC samples, the generation of O<sub>2</sub> starts at a more positive potential than that of CO<sub>2</sub>. O<sub>2</sub> release is only visible during the first delithiation and forms in the Li<sub>2</sub>MnO<sub>3</sub> domains during activation of Mn. According to the authors, the CO<sub>2</sub> evolution is mainly due to the high potential and oxidative condition, which favor decomposition of the electrolyte.

Similar studies using a DEMS setup were performed on Li–O<sub>2</sub> batteries [138,139]. Figure 7.35 presents the measurement of gas evolution and current as a function of the cell voltage for a discharged DME-based cell. As described by McCloskey *et al.* [136], the DME-based cell discharged under O<sub>2</sub> exhibits different gas evolution. Three gases were investigated; namely, O<sub>2</sub>, CO<sub>2</sub>, and H<sub>2</sub>. According to the authors, no H<sub>2</sub> and no CO<sub>2</sub> could be detected before reaching a potential of 4.5 V vs. Li<sup>+</sup>/Li. H<sub>2</sub> results from electrolyte decomposition. CO<sub>2</sub> also results from electrolyte decomposition but in addition from the oxidation of the DME by Li<sub>2</sub>O<sub>2</sub> at high potential. O<sub>2</sub> evolves in

**Figure 7.34** Comparative plot of the normalized and background-corrected mass signal intensities for the stoichiometric  $x=0$  and overlithiated  $x=0.1$  NMC oxides in 1 M LiPF<sub>6</sub> in EC: DMC (1:1 by weight). Reprinted with permission from Ref. [137]. Copyright 2014, The Electrochemical Society.

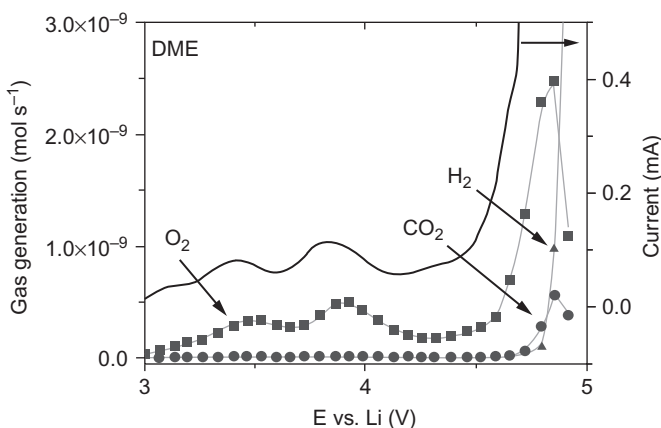
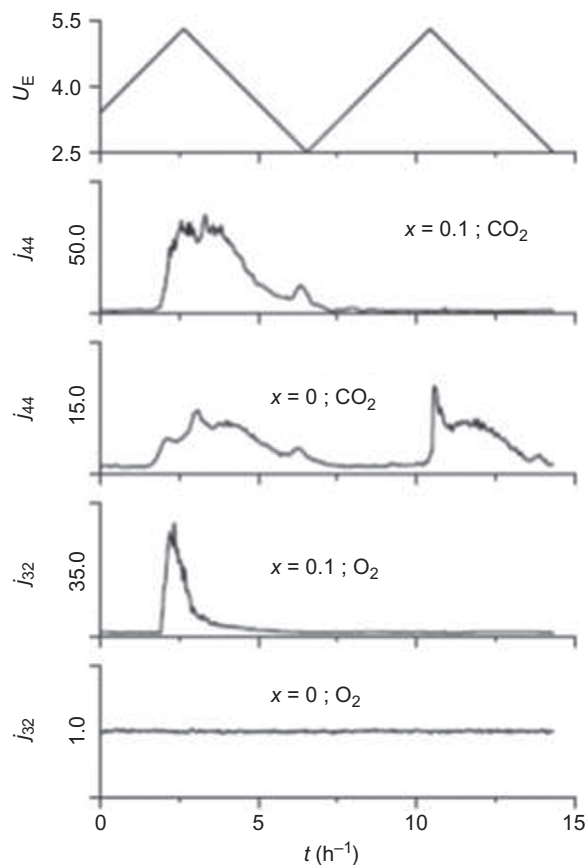


**Figure 7.35** Gas evolution and current versus cell voltage during a 0.075 m Vs<sup>-1</sup> linear oxidative potential scan of a discharged DME-based Li-air cell. Reprinted with permission from Ref. [136]. Copyright 2014, American Chemical Society.

a different manner between 3 and 5 V. At high potential,  $O_2$  is generated by electrolyte decomposition.

We showed in the two previous sections that a combination of surface and bulk characterizations is crucial to understand the reaction mechanism taking place in lithium-based batteries. Nevertheless, some techniques cannot be classified into bulk and/or surface categories, but are of interest when it comes to understanding the reaction mechanisms and to following gas evolution or inhomogeneous reactions. Most of them involve visual observation and are summarized in the next section.

## 7.6 Optical characterizations

Some techniques, such as neutron imaging and colorimetry, are useful to study a full pack of batteries (many stacks) and verify the absence of issues, such as inhomogeneous reactions resulting from overcharge and/or overdischarge, which could lead to unsafe operating conditions. For certain types of lithium-based batteries, like the Li–S battery, optical characterizations, particularly UV/Vis spectroscopy (Figure 7.36) are among the few methods able to analyze reaction mechanisms involving the formation of aqueous species.

### 7.6.1 Neutron imaging

As already described in previous sections, the volume changes occurring during cycling of a conversion material electrode can lead to fracture and safety issue in a lithium-based battery. Many techniques have been developed to quantify or visualize this expansion. Nowadays, neutron imaging is used to visualize and follow the volume changes occurring during charge/discharge and especially to visualize the evolution and repartition of lithium and hydrogen (light elements) upon electrolyte decomposition.

As described by Siegel *et al.* [140], Figure 7.37, a coffee bag cell is mounted and fixed in front of the detector so that the neutron beam can go through the cell along the  $z$ -axis. The results are then displayed in a two-dimensional projection.

The 2D images may be blurred as they are a projection obtained through multiple layers. To avoid that problem, the cell is first imaged using X-ray tomography to

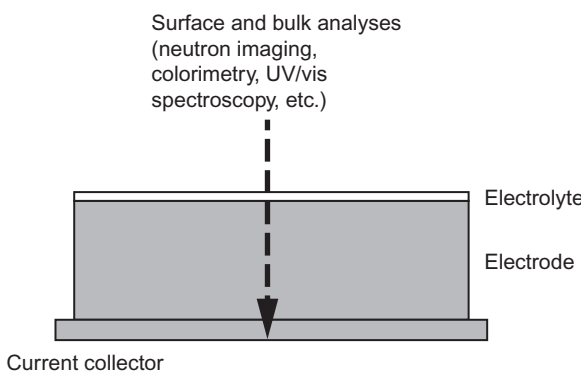
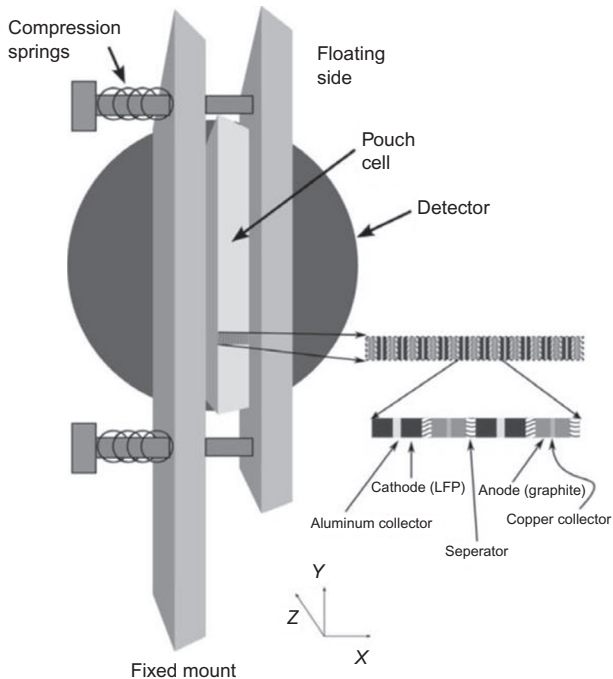


**Figure 7.36** Schematic of a battery investigated via optical characterization.

**Figure 7.37** The coffee bag cell is positioned in front of the neutron-sensitive detector so that the beam axis ( $z$ -direction) is parallel to the separator. The inset shows a cross-section of the layered battery structure. Reprinted with permission from Ref. [140]. Copyright 2014, The Electrochemical Society.



ensure the flatness of the layers. As explained by Siegel *et al.* [140], the copper current collectors of the negative electrode correspond to the very bright regions in Figure 7.38 (left). In their setup, the coffee bag cell is maintained by a Teflon piece clearly visible in gray on the right side of the battery [141]. The expansion of the battery layers are presented in Figure 7.38 (right). The authors observed a nonuniform expansion of the different layers according to their position. The expansion is more pronounced at the center of the cell than on the edge close to the Teflon cell support.

The main advantages of neutron imaging techniques are that the full system can be checked for expansion and not only a single area like in dilatometry, and the neutron imaging technique is also able to distinguish a displacement of the cell from a volume change or even gas release that can generate a shift of the layer. Other techniques such as tomography or dilatometry are not able to do so. Nevertheless, although neutron imaging is a useful technique, it is difficult to distinguish the inhomogeneous reactions taking place in the battery. Colorimetry measurement can be of great help for that type of investigation.

## 7.6.2 Colorimetry

The determination of homogeneous reactions in lithium-based batteries is crucial for postmortem analysis and safety-related issues. This quantification can be conducted at different scales. TEM allows the investigation of the homogeneity only at the

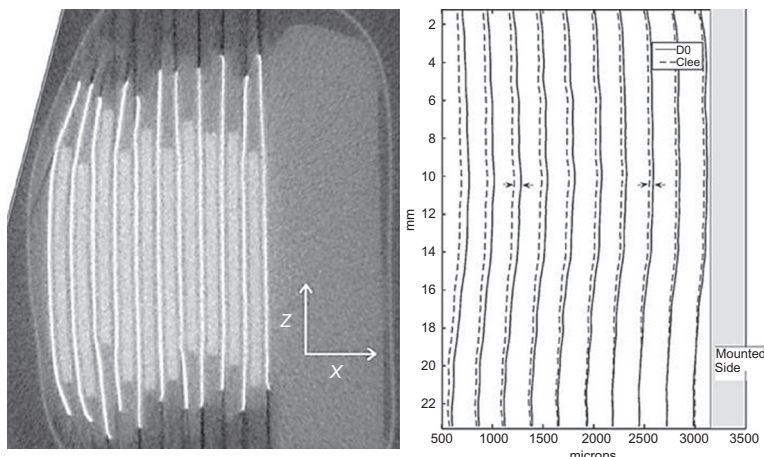


**Figure 7.38** (Left) A horizontal cross-section of the battery ( $x$ - $z$  plane) obtained by X-ray tomography is used to check the flatness of the battery layers. (Right) Fitted locations of the 10 peaks corresponding to the aluminum layers at the beginning and end of the experiment, before and after charging the battery.

Reprinted with permission from Ref. [140]. Copyright 2014, The Electrochemical Society.

nanoscale [142]. The lithium content can also be determined by Raman spectroscopy or even neutron diffraction [143]. However, these two latter techniques give only an average composition of the lithium. They are also difficult to handle and expensive to perform. Only a postmortem analysis on different areas can determine the homogeneity inside the electrodes. Maire *et al.* [144] developed a fast and simple quantification technique to assess visually the homogeneity of a reaction. The setup described in Figure 7.39 is used for this colorimetry measurement. The cell is composed of a glass window covered by an antireflective layer that permits the color changes to be followed via *in situ* electrochemistry and to take pictures during cycling.

To validate the concept, the authors [144] cycled a graphite electrode during a discharge/charge cycle and quantified the lithium content. The images were fitted using a calibration method (see Figure 7.40a). Thanks to this method, the authors were able to establish a contour plot as shown in Figure 7.40b. It is well known that an inhomogeneous reaction can lead to an accelerated decline in cell performance due to local overcharge or overdischarge [145]. They showed that, at the end of the lithiation process, the anode material (i.e., the graphite electrode) is in an intermediate state between stage I and stage II.

This technique is useful only if the material itself changes color during cycling (limitation). It cannot properly distinguish the change in color of the electrolyte and, in any case, it cannot perform a chemical analysis of the products. UV/Vis spectroscopy is used especially for this purpose in the case of Li–S batteries.

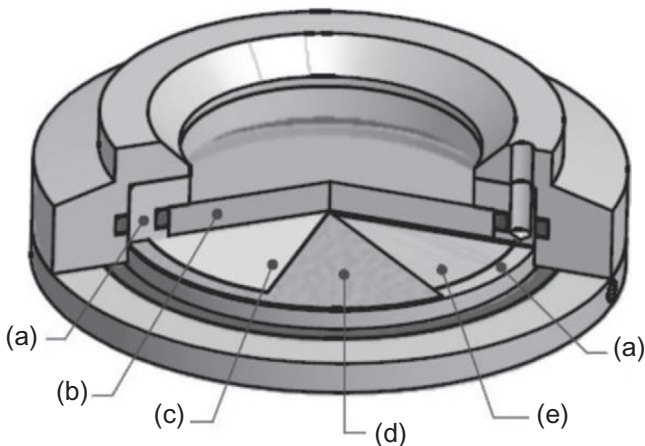


**Figure 7.39** Drawing of the electrochemical cell with glass windows: (a) titanium current collectors; (b) glass window; (c) graphite (or other) electrode on stainless steel mesh; (d) separator; and (e) lithium counterelectrode.

Reprinted with permission from Ref. [144]. Copyright 2014, The Electrochemical Society.

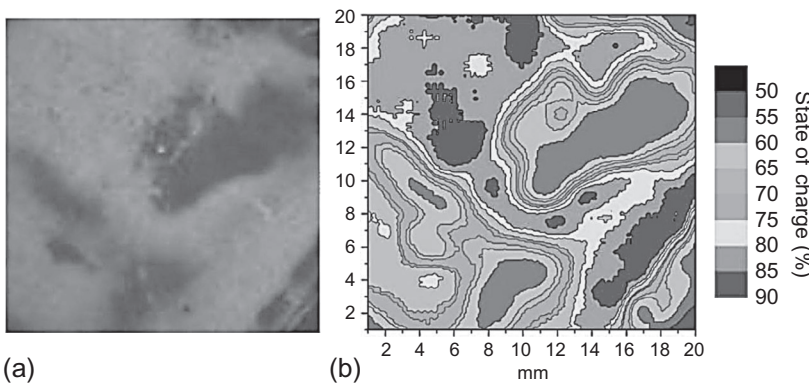


**Figure 7.40** (a) An aged graphite anode translated into (b) a contour map of lithium distribution.

Reprinted with permission from Ref. [144]. Copyright 2014, The Electrochemical Society.

### 7.6.3 UV/Visible spectroscopy

In some batteries, a change in the color of the electrolyte can occur during cycling or some reaction products can be visible to the naked eye because of their particular color. This is the case for Li-S batteries, for example [146]. During the cycling of a Li-S battery, part of the sulfur is dissolved into the electrolyte and generates polysulfides [147–149]. Those polysulfides can be a long or a short chain and their color depends on the number of sulfur atoms (from  $\text{Li}_2\text{S}_8$  to  $\text{Li}_2\text{S}_2$ ). Following the change in

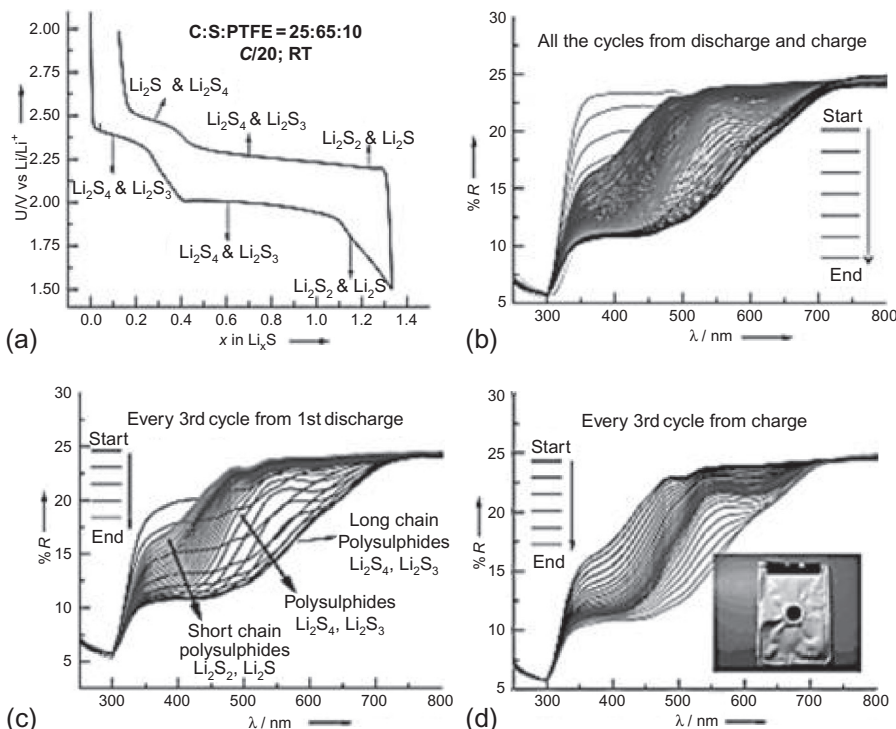


**Figure 7.41** (a) First discharge and charge of the Li–S battery and (b) the corresponding V/Vis spectra measured in the operando mode. Selected spectra during (c) the first discharge and (d) the first charge.

Reprinted from Ref. [152] with permission from John Wiley and Sons.

color of the electrolyte (polysulfides) can lead to a better understanding of the Li–S reaction mechanisms [150,151].

Patel *et al.* [152] followed the reaction mechanism of a Li–S battery using UV/Vis spectroscopy. For their setup they used a modified coffee bag cell by replacing the transparent Kapton window with a glass window. Their cell was placed in the beam of a UV/Vis spectrometer and the measurements were performed in reflection mode. Their results are summarized in Figure 7.41, where, in (a), the typical reaction mechanism of a Li–S battery is described. During the first discharge, presented in Figure 7.41c, the authors observed a significant evolution of long-chain polysulfides in the electrolyte. Further lithiation led to a reduction of the concentration of polysulfides and to the appearance of short chains. They conducted the same experiment during charge, and observed the reverse process. The UV/Vis spectra moved from short-chain to long-chain polysulfides (Figure 41d).

All the techniques described in this optical section provide information at the macroscale but no information at the atomic scale. *In situ* AFM can be used to describe the atomic scale of lithium-based batteries.

### 7.6.4 AFM

*In situ* AFM applied to lithium-ion batteries was introduced by Hirasawa *et al.* in 1997 [153]. They obtained the first images of topographic insertion of lithium into a graphite sheet. AFM images provide valuable information about the electrode morphology during cycling. However, compared with other *in situ* techniques, such as XRD or *in situ* FTIR, *in situ* AFM studies are rarely mentioned in the literature. AFM gives high-resolution topographic images; nevertheless, one of the drawbacks of the AFM techniques is the need of a relatively flat surface for scanning. The setup of the AFM cells is presented in Figure 7.42. In the literature we can find two types of cells, a three-electrode and a two-electrode configuration [155,156]. In the case of the three-electrode cell for *in situ* AFM, the working electrode is placed in a confined area with electrolyte using an O-ring and a spring-loaded pin and clip mechanism. Furthermore, this cell contains a shallow reservoir, so the electrolyte will

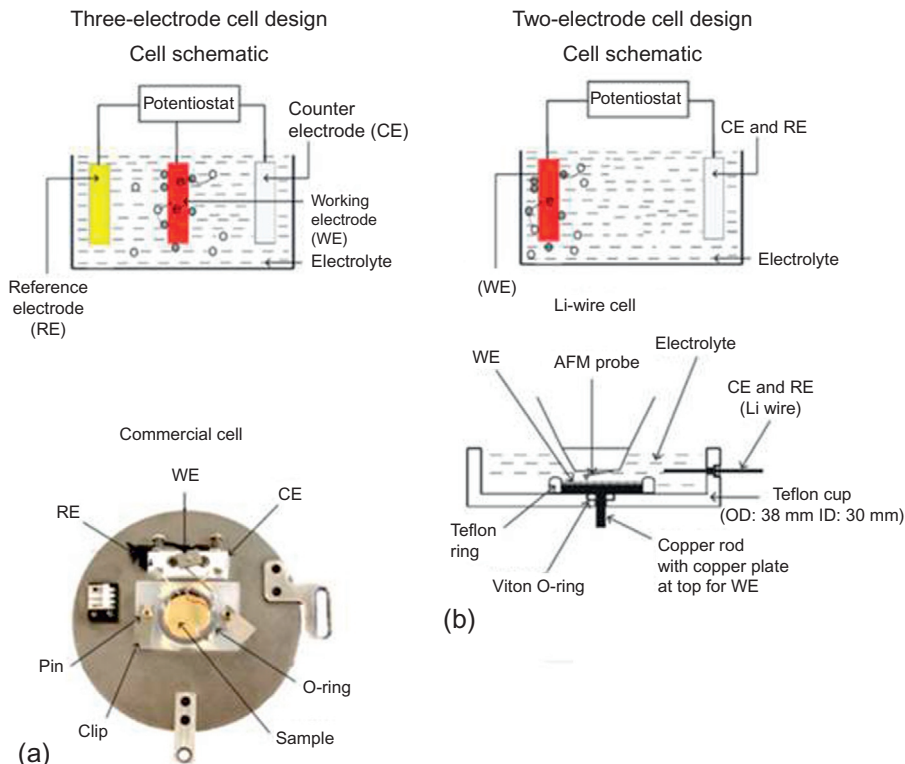


**Figure 7.42** AFM electrochemical cell designs proposed for *in situ* electrochemical experiments. (a) Three-electrode with cell schematic (top) and commercial cell (bottom), and (b) two-electrode cell design with cell schematic (top), Li-wire cell (middle), and coin cell (bottom).

Reprinted from Ref. [154] with permission from Elsevier.

evaporate in a shorter time than the duration of the experiment, which can last several hours. Despite its ingenious design, the cell is difficult to handle and, thus, a two-electrode setup configuration was selected, as shown in Figure 7.42b. The cell looks like the three-electrode setup where a Li-wire is used both as the counterelectrode and the reference electrode. A full description of the cell is given by Ramdon *et al.* [154].

Figure 7.43 summarizes the results obtained with the cell described in Figure 7.42b. This figure shows the height and deflection images as well as the area of the cathode analyzed. The study shows the images of the OCV starting point, the charge and the

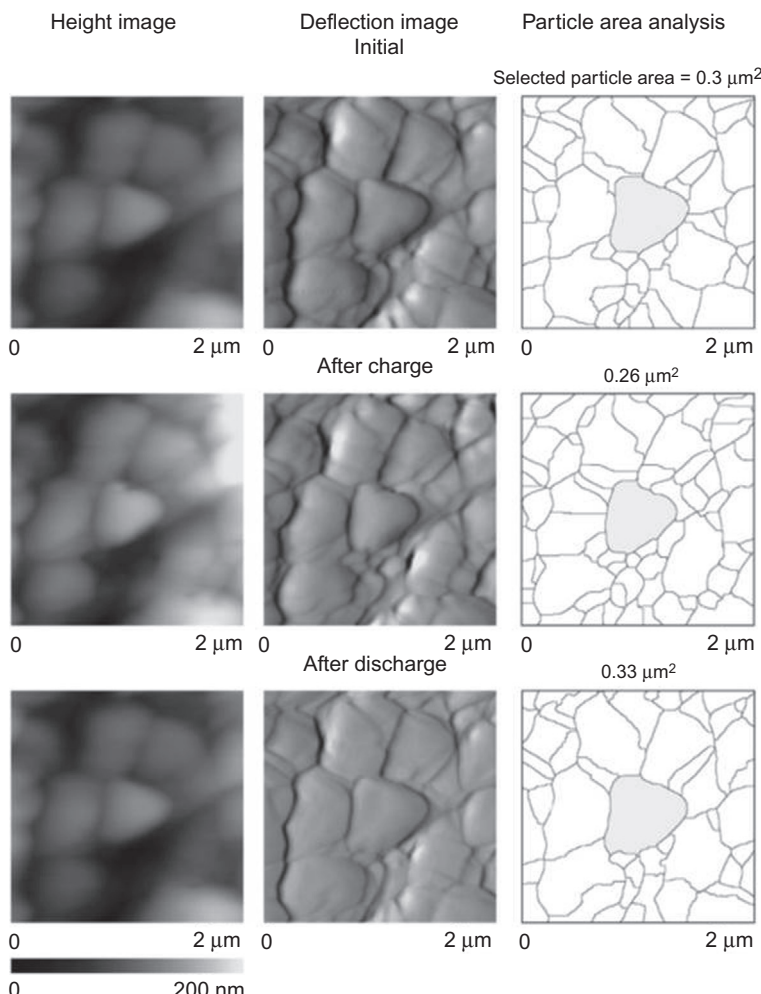


**Figure 7.43** *In situ* AFM height and deflection images as well as particle area analysis of a LiFePO<sub>4</sub> positive electrode showing a change in particle size between charged and discharged state.

Reprinted from Ref. [154] with permission from Elsevier.

discharge of LiFePO<sub>4</sub> cathode. The authors [154] observed a significant change in the shape of the particles: the particles became more rounded after charge. This phenomenon is reversible: the particles go back to a shape rather similar to that observed for the pristine electrode. Calculation performed for that particular area indicates that the particles seem to be larger after discharging than after charging. This trend agrees with a model proposed by Srinivasan and Newman, which described shrinking core behavior [157].

As we saw in this section, most optical characterizations are based on visual observation such as a change in color or in particle size. These techniques, although they are not often used by the community working in the batteries field, can provide precious information about safety-related issues, especially overdischarge/overcharge.

## 7.7 Conclusion

In this chapter, we have presented an overview of the different techniques that can be used to elucidate the reaction mechanisms in lithium-based batteries. We pointed out that the main challenge while developing an *in situ* cell is to ensure good electrochemistry while taking into account the constraints imposed by the technique such as beam-line absorption (XRD), the amount of active material needed for good absorption (neutron diffraction), the amount of electrolyte (infrared spectroscopy), and so on. It was shown that different techniques have to be coupled to elucidate the full reaction mechanisms. In particular, the relationship between surface and bulk properties has to be understood for further development of suitable materials for lithium-ion batteries and postlithium-ion batteries (Li–S and Li–O<sub>2</sub>).

## Acknowledgments

The author is very grateful to Mr. Patrick Lanz and Dr. Aurélie Guéguen for their precious assistance in improving this manuscript. Furthermore, I am also grateful to Professor Petr Novák, Dr. Sigitá Urbonaite, Ms. Joanna Conder, and the entire Electrochemistry Laboratory of PSI, especially the Electrochemical Energy Storage Section and my group Battery Materials for their support and help to write and improve this chapter of the book.

## References

- [1] K. Ozawa, Lithium-ion rechargeable batteries with LiCoO<sub>2</sub> and carbon electrodes: the LiCoO<sub>2</sub>/C system, *Solid State Ion.* 69 (3–4) (1994) 212–221.
- [2] J.M. Tarascon, M. Armand, Issues and challenges facing rechargeable lithium batteries, *Nature* 414 (6861) (2001) 359–367.
- [3] J.O. Besenhard, J. Yang, M. Winter, Will advanced lithium-alloy anodes have a chance in lithium-ion batteries? *J. Power Sources* 68 (1) (1997) 87–90.

- [4] J.-M. Tarascon, et al., New concepts for the search of better electrode materials for rechargeable lithium batteries, *C. R. Chim.* 8 (1) (2005) 9–15.
- [5] R.A. Huggins, Lithium alloy negative electrodes, *J. Power Sources* 81–82 (1999) 13–19.
- [6] K. Kushida, K. Kuriyama, T. Nozaki, Hundred-micron-sized all-solid-state Li secondary battery arrays embedded in a Si substrate, *Appl. Phys. Lett.* 81 (26) (2002) 5066–5068.
- [7] M. Armand, J.M. Tarascon, Building better batteries, *Nature* 451 (7179) (2008) 652–657.
- [8] Z. Liu, W. Fu, C. Liang, Lithium sulfur batteries, in: C. Daniel, J.O. Besenhard (Eds.), second ed., *Handbook of Battery Materials*, vol. 1, Wiley-VCH Verlag GmbH & Co. KGaA, Hoboken, NJ, 2011, pp. 811–840.
- [9] T. Zhang, N. Imanishi, Lithium–air batteries, in: T. Osaka, Z. Ogumi (Eds.), *Nanoscale Technology for Advanced Lithium Batteries*, Springer, New York, 2014, pp. 227–241.
- [10] B. Jin, J.-U. Kim, H.-B. Gu, Electrochemical properties of lithium–sulfur batteries, *J. Power Sources* 117 (1–2) (2003) 148–152.
- [11] P.G. Bruce, L.J. Hardwick, K.M. Abraham, Lithium–air and lithium–sulfur batteries, *MRS Bull.* 36 (07) (2011) 506–512.
- [12] P. Novák, et al., Advanced in situ methods for the characterization of practical electrodes in lithium-ion batteries, *J. Power Sources* 90 (1) (2000) 52–58.
- [13] S.F. Amalraj, D. Aurbach, The use of in situ techniques in R&D of Li and Mg rechargeable batteries, *J. Solid State Electrochem.* 15 (5) (2011) 877–890.
- [14] J. Vetter, et al., Application of in situ techniques for investigations in lithium-ion battery materials, *ECS Trans.* 3 (27) (2007) 29–43.
- [15] T. Gustafsson, et al., The polymer battery as an environment for in situ X-ray diffraction studies of solid-state electrochemical processes, *Electrochim. Acta* 37 (9) (1992) 1639–1643.
- [16] C. Villevieille, T. Sasaki, P. Novak, Novel electrochemical cell designed for operando techniques and impedance studies, *RSC Adv.* 4 (13) (2014) 6782–6789.
- [17] J.M. Tarascon, et al., Performance of Bellcore’s plastic rechargeable Li-ion batteries, *Solid State Ion.* 86–88 (Part 1(0)) (1996) 49–54.
- [18] M. Morcrette, et al., In situ X-ray diffraction techniques as a powerful tool to study battery electrode materials, *Electrochim. Acta* 47 (19) (2002) 3137–3149.
- [19] J.B. Leriche, et al., An electrochemical cell for operando study of lithium batteries using synchrotron radiation, *J. Electrochem. Soc.* 157 (5) (2010) A606–A610.
- [20] A.H. Thompson, Electrochemical potential spectroscopy: a new electrochemical measurement, *J. Electrochem. Soc.* 126 (4) (1979) 608–616.
- [21] S. Levasseur, et al., Evidence for structural defects in non-stoichiometric HT-LiCoO<sub>2</sub>: electrochemical, electronic properties and <sup>7</sup>Li NMR studies, *Solid State Ion.* 128 (1–4) (2000) 11–24.
- [22] K.C. Hewitt, L.Y. Beaulieu, J.R. Dahn, Electrochemistry of InSb as a Li insertion host: problems and prospects, *J. Electrochem. Soc.* 148 (5) (2001) A402–A410.
- [23] I.A. Courtney, J.R. Dahn, Electrochemical and in situ X-ray diffraction studies of the reaction of lithium with tin oxide composites, *J. Electrochem. Soc.* 144 (6) (1997) 2045–2052.
- [24] O. Crosnier, L.F. Nazar, Facile reversible displacement reaction of Cu<sub>3</sub>P with lithium at low potential, *Electrochem. Solid-State Lett.* 7 (7) (2004) A187–A189.
- [25] J. Li, J.R. Dahn, An in situ X-ray diffraction study of the reaction of Li with crystalline Si, *J. Electrochem. Soc.* 154 (3) (2007) A156–A161.
- [26] F. Gillot, et al., Electrochemical reactivity and design of NiP<sub>2</sub> negative electrodes for secondary Li-ion batteries, *Chem. Mater.* 17 (25) (2005) 6327–6337.
- [27] A. Hayashi, A. Inoue, M. Tatsumisago, Electrochemical performance of NiP<sub>2</sub> negative electrodes in all-solid-state lithium secondary batteries, *J. Power Sources* 189 (1) (2009) 669–671.

- [28] C. Villevieille, et al., NiSb<sub>2</sub> as negative electrode for Li-ion batteries: an original conversion reaction, *J. Power Sources* 172 (1) (2007) 388–394.
- [29] C.Q. Zhang, et al., Preparation and electrochemical performances of nanoscale FeSn<sub>2</sub> as anode material for lithium ion batteries, *J. Alloys Compd.* 457 (1–2) (2008) 81–85.
- [30] M. Chamas, et al., Quantitative analysis of the initial restructuring step of nanostructured FeSn<sub>2</sub>-based anodes for Li-ion batteries, *Chem. Mater.* 25 (12) (2013) 2410–2420.
- [31] C. Villevieille, et al., A new ternary Li<sub>4</sub>FeSb<sub>2</sub> structure formed upon discharge of the FeSb<sub>2</sub>/Li cell, *J. Power Sources* 189 (1) (2009) 324–330.
- [32] T. Ohzuku, A. Ueda, M. Nagayama, Electrochemistry and structural chemistry of LiNiO<sub>2</sub> ( $R\bar{3}m$ ) for 4 volt secondary lithium cells, *J. Electrochem. Soc.* 140 (7) (1993) 1862–1870.
- [33] D. Mohanty, et al., Structural transformation of a lithium-rich Li<sub>1.2</sub>Co<sub>0.1</sub>Mn<sub>0.55</sub>Ni<sub>0.15</sub>O<sub>2</sub> cathode during high voltage cycling resolved by in situ X-ray diffraction, *J. Power Sources* 229 (2013) 239–248.
- [34] V.A. Godbole, J.-F. Colin, P. Novák, Study of overcharge behavior of Li<sub>1+x</sub>(Ni<sub>1/3</sub>Mn<sub>1/3</sub>Co<sub>1/3</sub>)<sub>1-x</sub>O<sub>2</sub> using in situ and ex situ X-ray synchrotron diffraction, *J. Electrochem. Soc.* 158 (9) (2011) A1005–A1010.
- [35] D. Mohanty, et al., Investigating phase transformation in the Li<sub>1.2</sub>Co<sub>0.1</sub>Mn<sub>0.55</sub>Ni<sub>0.15</sub>O<sub>2</sub> lithium-ion battery cathode during high-voltage hold (4.5 V) via magnetic, X-ray diffraction and electron microscopy studies, *J. Mater. Chem. A* 1 (20) (2013) 6249–6261.
- [36] M.M. Thackeray, et al., Li<sub>2</sub>MnO<sub>3</sub>-stabilized LiMO<sub>2</sub> (M=Mn, Ni, Co) electrodes for lithium-ion batteries, *J. Mater. Chem.* 17 (30) (2007) 3112–3125.
- [37] T. Sasaki, et al., Morphological and structural changes of Mg-substituted Li(Ni, Co, Al)O<sub>2</sub> during overcharge reaction, *J. Electrochem. Soc.* 158 (11) (2011) A1214–A1219.
- [38] V.A. Godbole, et al., Circular in situ neutron powder diffraction cell for study of reaction mechanism in electrode materials for Li-ion batteries, *RSC Adv.* 3 (3) (2013) 757–763.
- [39] J.-F. Colin, V. Godbole, P. Novák, In situ neutron diffraction study of Li insertion in Li<sub>4</sub>Ti<sub>5</sub>O<sub>12</sub>, *Electrochim. Commun.* 12 (6) (2010) 804–807.
- [40] F. Rosciano, et al., A novel electrochemical cell for in situ neutron diffraction studies of electrode materials for lithium-ion batteries, *J. Appl. Crystallogr.* 41 (2008) 690–694.
- [41] O. Dolotko, et al., Understanding structural changes in NMC Li-ion cells by in situ neutron diffraction, *J. Power Sources* 255 (2014) 197–203.
- [42] S.C. Yin, et al., X-ray/neutron diffraction and electrochemical studies of lithium de/re-intercalation in Li<sub>1-x</sub>Co<sub>1/3</sub>Ni<sub>1/3</sub>Mn<sub>1/3</sub>O<sub>2</sub> ( $x=0\rightarrow 1$ ), *Chem. Mater.* 18 (7) (2006) 1901–1910.
- [43] M. Bianchini, et al., A new null matrix electrochemical cell for Rietveld refinements of in-situ or operando neutron powder diffraction data, *J. Electrochem. Soc.* 160 (11) (2013) A2176–A2183.
- [44] M. Roberts, et al., Design of a new lithium ion battery test cell for in-situ neutron diffraction measurements, *J. Power Sources* 226 (2013) 249–255.
- [45] J.J. Biendicho, et al., New in-situ neutron diffraction cell for electrode materials, *J. Power Sources* 248 (2014) 900–904.
- [46] S. Naille, et al., <sup>119</sup>Sn Mössbauer parameters as predictive tool for future Sn-based negative electrode materials, *J. Power Sources* 189 (1) (2009) 814–817.
- [47] L. Aldon, et al., Mössbauer spectrometry as a powerful tool to study lithium reactivity mechanisms for battery electrode materials, *Hyperfine Interact.* 156–157 (1–4) (2004) 497–503.
- [48] Y. Geronov, T. Tomov, S. Georgiev, Mössbauer spectroscopy investigation of the iron electrode during cycling in alkaline solution, *J. Appl. Electrochem.* 5 (4) (1975) 351–358.

[49] R.A. Dunlap, O. Mao, J.R. Dahn, Application of *in situ* Mössbauer effect methods for the study of electrochemical reactions in lithium-ion battery electrode materials, *Phys. Rev. B* 59 (5) (1999) 3494–3500.

[50] O. Mao, et al., In situ Mössbauer effect studies of the electrochemical reaction of lithium with mechanically alloyed  $\text{Sn}_2\text{Fe}$ , *J. Electrochem. Soc.* 145 (12) (1998) 4195–4202.

[51] A. Wattiaux, L. Fournès, C. Delmas, Two decades of Mössbauer dedicated to batteries, *Mössbauer Eff. Ref. Data. J.* 33 (2010) 37.

[52] K. Ariyoshi, T. Ohzuku, In situ  $^{57}\text{Fe}$  Mössbauer investigation of Li insertion electrodes for advanced batteries, *Mössbauer Eff. Ref. Data. J.* 33 (2010) 43.

[53] M. Sathiya, et al., Reversible anionic redox chemistry in high-capacity layered-oxide electrodes, *Nat. Mater.* 12 (9) (2013) 827–835.

[54] D. Larcher, et al., Combined XRD, EXAFS, and Mössbauer studies of the reduction by lithium of  $\alpha\text{-Fe}_2\text{O}_3$  with various particle sizes, *J. Electrochem. Soc.* 150 (12) (2003) A1643–A1650.

[55] K. Adouby, et al., X-ray diffraction,  $^{119}\text{Sn}$  Mössbauer and thermal study of  $\text{SnSe}-\text{Bi}_2\text{Se}_3$  system, *J. Alloys Compd.* 453 (1–2) (2008) 161–166.

[56] L. Aldon, et al., Lithium insertion mechanism in Sb-based electrode materials from  $^{121}\text{Sb}$  Mössbauer spectrometry, *J. Power Sources* 119–121 (2003) 585–590.

[57] L. Aldon, J.C. Jumas, Lithium-induced conversion reaction in wüstite  $\text{Fe}_{1-x}\text{O}$  studied by  $^{57}\text{Fe}$  Mössbauer spectroscopy, *Solid State Sci.* 14 (3) (2012) 354–361.

[58] L. Aldon, et al., Redox behaviour of iron during delithiation in  $\text{Li}_x\text{Co}_{1-y}\text{Fe}_y\text{O}_2$  solid solution: an *in situ*  $^{57}\text{Fe}$  Mössbauer study, *J. Power Sources* 146 (1–2) (2005) 259–263.

[59] L. Aldon, et al., Determination of the Lamb-Mössbauer factors of  $\text{LiFePO}_4$  and  $\text{FePO}_4$  for electrochemical *in situ* and *operando* measurements in Li-ion batteries, *J. Solid State Chem.* 183 (1) (2010) 218–222.

[60] L. Baggetto, et al., Reaction mechanism of tin nitride (de)lithiation reaction studied by means of  $^{119}\text{Sn}$  Mössbauer spectroscopy, *Electrochim. Acta* 55 (22) (2010) 6617–6631.

[61] J. Chouvin, et al.,  $^{119}\text{Sn}$  Mössbauer study of  $\text{Li}_x\text{Sn}$  alloys prepared electrochemically, *Chem. Phys. Lett.* 308 (5–6) (1999) 413–420.

[62] F. Robert, et al., Mössbauer spectra as a “fingerprint” in tin-lithium compounds: applications to Li-ion batteries, *J. Solid State Chem.* 180 (1) (2007) 339–348.

[63] C.M. Ionica-Bousquet, et al., *In situ*  $^{119}\text{Sn}$  Mössbauer effect study of  $\text{Li}-\text{CoSn}_2$  electrochemical system, *Chem. Mater.* 18 (26) (2006) 6442–6447.

[64] L. Aldon, et al., *In situ*  $^{119}\text{Sn}$  Mössbauer spectroscopy used to study lithium insertion in c- $\text{Mg}_2\text{Sn}$ , *Hyperfine Interact.* 167 (1–3) (2006) 729–732.

[65] A. Aboulaich, et al., *In situ*  $^{119}\text{Sn}$  Mössbauer spectroscopy study of Sn-based electrode materials, *Hyperfine Interact.* 167 (1–3) (2006) 733–738.

[66] P.-E. Lippens, et al., How Mössbauer spectroscopy can improve Li-ion batteries, *Hyperfine Interact.* 206 (1–3) (2012) 35–46.

[67] A. Perea, et al., Study of C-coated  $\text{LiFe}_{0.33}\text{Mn}_{0.67}\text{PO}_4$  as positive electrode material for Li-ion batteries, *J. Solid State Chem.* 192 (2012) 201–209.

[68] A. Perea, et al., Operando  $^{57}\text{Fe}$  Mössbauer and XRD investigation of  $\text{Li}_x\text{Mn}_y\text{Fe}_{1-y}\text{PO}_4/\text{C}$  composites ( $y=0; 0.25$ ), *RSC Adv.* 2 (5) (2012) 2080–2086.

[69] Y. Orikasa, et al., Phase transition analysis between  $\text{LiFePO}_4$  and  $\text{FePO}_4$  by *in-situ* time-resolved X-ray absorption and X-ray diffraction, *J. Electrochem. Soc.* 160 (5) (2013) A3061–A3065.

[70] C.T. Love, et al., Review of  $\text{LiFePO}_4$  phase transition mechanisms and new observations from X-ray absorption spectroscopy, *J. Electrochem. Soc.* 160 (5) (2013) A3153–A3161.

- [71] O. Haas, et al., Synchrotron X-ray absorption study of LiFePO<sub>4</sub> electrodes, *J. Electrochem. Soc.* 152 (1) (2005) A191–A196.
- [72] M. Cuisinier, et al., Sulfur speciation in Li–S batteries determined by operando X-ray absorption spectroscopy, *J. Phys. Chem. Lett.* 4 (19) (2013) 3227–3232.
- [73] M. Ebner, et al., Visualization and quantification of electrochemical and mechanical degradation in Li ion batteries, *Science* 342 (6159) (2013) 716–720.
- [74] F. Marone, M. Stampanoni, Regridding reconstruction algorithm for real-time tomographic imaging, *J. Synchrotron Radiat.* 19 (Pt 6) (2012) 1029–1037.
- [75] I.A. Courtney, J.R. Dahn, Key factors controlling the reversibility of the reaction of lithium with SnO<sub>2</sub> and Sn<sub>2</sub>BPO<sub>6</sub> glass, *J. Electrochem. Soc.* 144 (9) (1997) 2943–2948.
- [76] I.A. Courtney, W.R. McKinnon, J.R. Dahn, On the aggregation of tin in SnO composite glasses caused by the reversible reaction with lithium, *J. Electrochem. Soc.* 146 (1) (1999) 59–68.
- [77] F. Blanc, M. Leskes, C.P. Grey, In situ solid-state NMR spectroscopy of electrochemical cells: batteries, supercapacitors, and fuel cells, *Acc. Chem. Res.* 46 (9) (2013) 1952–1963.
- [78] N.M. Trease, et al., In situ NMR of lithium ion batteries: bulk susceptibility effects and practical considerations, *Solid State Nucl. Magn. Reson.* 42 (2012) 62–70.
- [79] R. Bhattacharyya, et al., In situ NMR observation of the formation of metallic lithium microstructures in lithium batteries, *Nat. Mater.* 9 (6) (2010) 504–510.
- [80] M. Letellier, F. Chevallier, F. Béguin, In situ <sup>7</sup>Li NMR during lithium electrochemical insertion into graphite and a carbon/carbon composite, *J. Phys. Chem. Solids* 67 (5–6) (2006) 1228–1232.
- [81] F. Poli, et al., New cell design for in-situ NMR studies of lithium-ion batteries, *Electrochem. Commun.* 13 (12) (2011) 1293–1295.
- [82] B. Key, et al., Real-time NMR investigations of structural changes in silicon electrodes for lithium-ion batteries, *J. Am. Chem. Soc.* 131 (26) (2009) 9239–9249.
- [83] M. Letellier, F. Chevallier, M. Morcrette, In situ <sup>7</sup>Li nuclear magnetic resonance observation of the electrochemical intercalation of lithium in graphite; 1st cycle, *Carbon* 45 (5) (2007) 1025–1034.
- [84] M. Letellier, et al., The first in situ <sup>7</sup>Li nuclear magnetic resonance study of lithium insertion in hard-carbon anode materials for Li-ion batteries, *J. Chem. Phys.* 118 (13) (2003) 6038–6045.
- [85] M. Leskes, et al., Direct detection of discharge products in lithium–oxygen batteries by solid-state NMR spectroscopy, *Angew. Chem.* 124 (34) (2012) 8688–8691.
- [86] M. Leskes, et al., Monitoring the electrochemical processes in the lithium–air battery by solid state NMR spectroscopy, *J. Phys. Chem. C* 117 (51) (2013) 26929–26939.
- [87] K. Rhodes, et al., Understanding the degradation of silicon electrodes for lithium-ion batteries using acoustic emission, *J. Electrochem. Soc.* 157 (12) (2010) A1354–A1360.
- [88] T. Ohzuku, H. Tomura, K. Sawai, Monitoring of particle fracture by acoustic emission during charge and discharge of Li/MnO<sub>2</sub> cells, *J. Electrochem. Soc.* 144 (10) (1997) 3496–3500.
- [89] C. Villevieille, M. Boinet, L. Monconduit, Direct evidence of morphological changes in conversion type electrodes in Li-ion battery by acoustic emission, *Electrochem. Commun.* 12 (10) (2010) 1336–1339.
- [90] P. Baudry, M. Armand, In situ observation by SEM of positive composite electrodes during discharge of polymer lithium batteries, *Solid State Ion.* 28–30 (1988) 1567–1571.
- [91] F. Orsini, et al., In situ scanning electron microscopy (SEM) observation of interfaces within plastic lithium batteries, *J. Power Sources* 76 (1998) 19–29.

- [92] P.R. Raimann, et al., Monitoring dynamics of electrode reactions in Li-ion batteries by *in situ* ESEM, *Ionics* 12 (2006) 253–255.
- [93] D. Aurbach, Y. Gofer, J. Langzam, The correlation between surface chemistry, surface morphology, and cycling efficiency of lithium electrodes in a few polar aprotic systems, *J. Electrochem. Soc.* 136 (11) (1989) 3198–3205.
- [94] T. Osaka, et al., Surface characterization of electrodeposited lithium anode with enhanced cycleability obtained by CO<sub>2</sub> addition, *J. Electrochem. Soc.* 144 (5) (1997) 1709–1713.
- [95] N.P.W. Langenhuizen, The effect of mass transport on Li deposition and dissolution, *J. Electrochem. Soc.* 145 (9) (1998) 3094–3099.
- [96] D. Chen, et al., *In situ* scanning electron microscopy on lithium-ion battery electrodes using an ionic liquid, *J. Power Sources* 196 (15) (2011) 6382–6387.
- [97] J. Yang, M. Winter, J.O. Besenhard, Small particle size multiphase Li-alloy anodes for lithium-ion batteries, *Solid State Ion.* 90 (1–4) (1996) 281–287.
- [98] U. Kasavajjula, C. Wang, A.J. Appleby, Nano- and bulk-silicon-based insertion anodes for lithium-ion secondary cells, *J. Power Sources* 163 (2) (2007) 1003–1039.
- [99] J.Y. Huang, et al., *In situ* observation of the electrochemical lithiation of a single SnO<sub>2</sub> nanowire electrode, *Science* 330 (6010) (2010) 1515–1520.
- [100] X.H. Liu, J.Y. Huang, *In situ* TEM electrochemistry of anode materials in lithium ion batteries, *Energy Environ. Sci.* 4 (10) (2011) 3844–3860.
- [101] N. de Jonge, F.M. Ross, Electron microscopy of specimens in liquid, *Nat. Nanotechnol.* 6 (11) (2011) 695–704.
- [102] Y.-M. Chiang, Building a better battery, *Science* 330 (6010) (2010) 1485–1486.
- [103] X.H. Liu, et al., *In situ* TEM experiments of electrochemical lithiation and delithiation of individual nanostructures, *Adv. Energy Mater.* 2 (7) (2012) 722–741.
- [104] S. Huang, T. Zhu, Atomistic mechanisms of lithium insertion in amorphous silicon, *J. Power Sources* 196 (7) (2011) 3664–3668.
- [105] X.H. Liu, et al., Size-dependent fracture of silicon nanoparticles during lithiation, *ACS Nano* 6 (2) (2012) 1522–1531.
- [106] L. Zhong, et al., *In situ* transmission electron microscopy observations of electrochemical oxidation of Li<sub>2</sub>O<sub>2</sub>, *Nano Lett.* 13 (5) (2013) 2209–2214.
- [107] K.W. Schroder, et al., Examining solid electrolyte interphase formation on crystalline silicon electrodes: influence of electrochemical preparation and ambient exposure conditions, *J. Phys. Chem. C* 116 (37) (2012) 19737–19747.
- [108] S. Malmgren, et al., Consequences of air exposure on the lithiated graphite SEI, *Electrochim. Acta* 105 (2013) 83–91.
- [109] E. Peled, The electrochemical behavior of alkali and alkaline earth metals in nonaqueous battery systems—the solid electrolyte interphase model, *J. Electrochem. Soc.* 126 (12) (1979) 2047–2051.
- [110] R. Fong, U. von Sacken, J.R. Dahn, Studies of lithium intercalation into carbons using nonaqueous electrochemical cells, *J. Electrochem. Soc.* 137 (7) (1990) 2009–2013.
- [111] S. Malmgren, et al., Comparing anode and cathode electrode/electrolyte interface composition and morphology using soft and hard X-ray photoelectron spectroscopy, *Electrochim. Acta* 97 (2013) 23–32.
- [112] P. Verma, P. Maire, P. Novák, A review of the features and analyses of the solid electrolyte interphase in Li-ion batteries, *Electrochim. Acta* 55 (22) (2010) 6332–6341.
- [113] B. Philippe, et al., Improved performances of nanosilicon electrodes using the salt LiFSI: a photoelectron spectroscopy study, *J. Am. Chem. Soc.* 135 (26) (2013) 9829–9842.

- [114] N.S. Hochgatterer, et al., Silicon/graphite composite electrodes for high-capacity anodes: influence of binder chemistry on cycling stability, *Electrochim. Solid-State Lett.* 11 (5) (2008) A76–A80.
- [115] D. Munao, et al., Role of the binder on the failure mechanism of Si nano-composite electrodes for Li-ion batteries, *J. Power Sources* 196 (16) (2011) 6695–6702.
- [116] B. Philippe, et al., Role of the LiPF<sub>6</sub> salt for the long-term stability of silicon electrodes in Li-ion batteries—a photoelectron spectroscopy study, *Chem. Mater.* 25 (3) (2013) 394–404.
- [117] D. Aurbach, et al., A comparative study of synthetic graphite and Li electrodes in electrolyte solutions based on ethylene carbonate-dimethyl carbonate mixtures, *J. Electrochim. Soc.* 143 (12) (1996) 3809–3820.
- [118] A. Bewick, K. Kunimatsu, B. Stanley Pons, Infra red spectroscopy of the electrode-electrolyte interphase, *Electrochim. Acta* 25 (4) (1980) 465–468.
- [119] A. Bewick, K. Kunimatsu, Infra red spectroscopy of the electrode–electrolyte interphase, *Surf. Sci.* 101 (1–3) (1980) 131–138.
- [120] B. Pettinger, J. Lipkowski, M. Hoon-Khosla, Simulation of SNIFTIRS experiments, *J. Electroanal. Chem.* 500 (1–2) (2001) 471–478.
- [121] R. Imhof, P. Novák, In situ investigation of the electrochemical reduction of carbonate electrolyte solutions at graphite electrodes, *J. Electrochim. Soc.* 145 (4) (1998) 1081–1087.
- [122] F. Joho, P. Novák, SNIFTIRS investigation of the oxidative decomposition of organic-carbonate-based electrolytes for lithium-ion cells, *Electrochim. Acta* 45 (21) (2000) 3589–3599.
- [123] Y. Ikezawa, H. Nishi, In situ FTIR study of the Cu electrode/ethylene carbonate +dimethyl carbonate solution interface, *Electrochim. Acta* 53 (10) (2008) 3663–3669.
- [124] D. Aurbach, O. Chusid, The study of surface films formed on lithium and noble metal electrodes in polar aprotic systems by the use of in situ Fourier transform infrared spectroscopy, *J. Electrochim. Soc.* 140 (1) (1993) L1–L4.
- [125] D. Aurbach, et al., A short review of failure mechanisms of lithium metal and lithiated graphite anodes in liquid electrolyte solutions, *Solid State Ion.* 148 (3–4) (2002) 405–416.
- [126] G.V. Zhuang, et al., Lithium ethylene dicarbonate identified as the primary product of chemical and electrochemical reduction of EC in 1.2 M LiPF<sub>6</sub>/EC:EMC electrolyte, *J. Phys. Chem. B* 109 (37) (2005) 17567–17573.
- [127] M.-S. Zheng, et al., Formation and influence factors of solid electrolyte interphase film on the negative electrode surface in lithium-ion batteries, *J. Electrochim. Soc.* 152 (11) (2005) A2207–A2210.
- [128] D. Aurbach, et al., The correlation between the surface chemistry and the performance of Li–carbon intercalation anodes for rechargeable ‘rocking-chair’ type batteries, *J. Electrochim. Soc.* 141 (3) (1994) 603–611.
- [129] S.S. Zhang, A review on electrolyte additives for lithium-ion batteries, *J. Power Sources* 162 (2 SPEC. ISS) (2006) 1379–1394.
- [130] D. Aurbach, et al., On the use of vinylene carbonate (VC) as an additive to electrolyte solutions for Li-ion batteries, *Electrochim. Acta* 47 (9) (2002) 1423–1439.
- [131] S. Pérez-Villar, et al., Characterization of a model solid electrolyte interphase/carbon interface by combined in situ Raman/Fourier transform infrared microscopy, *Electrochim. Acta* 106 (2013) 506–515.

- [132] Z. Peng, et al., A reversible and higher-rate Li–O<sub>2</sub> battery, *Science* 337 (6094) (2012) 563–566.
- [133] P. Novák, et al., Advanced in situ characterization methods applied to carbonaceous materials, *J. Power Sources* 146 (1–2) (2005) 15–20.
- [134] G. Eggert, J. Heitbaum, Electrochemical reactions of propylenecarbonate and electrolytes solved therein—a dems study, *Electrochim. Acta* 31 (11) (1986) 1443–1448.
- [135] H. Baltruschat, Differential electrochemical mass spectrometry, *J. Am. Soc. Mass Spectrom.* 15 (12) (2004) 1693–1706.
- [136] B.D. McCloskey, et al., Solvents’ critical role in nonaqueous lithium–oxygen battery electrochemistry, *J. Phys. Chem. Lett.* 2 (10) (2011) 1161–1166.
- [137] F. La Mantia, et al., Quantification of oxygen loss from  $\text{Li}_{1+x}(\text{Ni}_{1/3}\text{Mn}_{1/3}\text{Co}_{1/3})_{1-x}\text{O}_2$  at high potentials by differential electrochemical mass spectrometry, *J. Electrochem. Soc.* 156 (11) (2009) A823–A827.
- [138] W. Xu, et al., Investigation on the charging process of Li<sub>2</sub>O<sub>2</sub>-based air electrodes in Li–O<sub>2</sub> batteries with organic carbonate electrolytes, *J. Power Sources* 196 (8) (2011) 3894–3899.
- [139] Y. Chen, et al., Li–O<sub>2</sub> battery with a dimethylformamide electrolyte, *J. Am. Chem. Soc.* 134 (18) (2012) 7952–7957.
- [140] J.B. Siegel, et al., Expansion of lithium ion pouch cell batteries: observations from neutron imaging, *J. Electrochem. Soc.* 160 (8) (2013) A1031–A1038.
- [141] J.B. Siegel, et al., Neutron imaging of lithium concentration in LFP pouch cell battery, *J. Electrochem. Soc.* 158 (5) (2011) A523–A529.
- [142] X.Y. Song, K. Kinoshita, T.D. Tran, Microstructural characterization of lithiated graphite, *J. Electrochem. Soc.* 143 (6) (1996) L120–L123.
- [143] D.E. Irish, Z. Deng, M. Odziedkowski, Raman spectroscopic and electrochemical studies of lithium battery components, *J. Power Sources* 54 (1) (1995) 28–33.
- [144] P. Maire, et al., Colorimetric determination of lithium-ion mobility in graphite composite electrodes, *J. Electroanal. Chem.* 644 (2) (2010) 127–131.
- [145] T.F. Fuller, M. Doyle, J. Newman, Relaxation phenomena in lithium-ion-insertion cells, *J. Electrochem. Soc.* 141 (4) (1994) 982–990.
- [146] S. Evers, L.F. Nazar, New approaches for high energy density lithium–sulfur battery cathodes, *Acc. Chem. Res.* 46 (5) (2012) 1135–1143.
- [147] R. Demir-Cakan, et al., Cathode composites for Li–S batteries via the use of oxygenated porous architectures, *J. Am. Chem. Soc.* 133 (40) (2011) 16154–16160.
- [148] C. Barchasz, et al., Lithium/sulfur cell discharge mechanism: an original approach for intermediate species identification, *Anal. Chem.* 84 (9) (2012) 3973–3980.
- [149] Y. Diao, et al., Analysis of polysulfide dissolved in electrolyte in discharge–charge process of Li–S battery, *J. Electrochem. Soc.* 159 (4) (2012) A421–A425.
- [150] R. Dominko, et al., Analytical detection of soluble polysulphides in a modified Swagelok cell, *Electrochem. Commun.* 13 (2) (2011) 117–120.
- [151] S.-I. Tobishima, H. Yamamoto, M. Matsuda, Study on the reduction species of sulfur by alkali metals in nonaqueous solvents, *Electrochim. Acta* 42 (6) (1997) 1019–1029.
- [152] M.U.M. Patel, et al., Li–S battery analyzed by UV/Vis in operando mode, *ChemSusChem.* 6 (7) (2013) 1177–1181.
- [153] K.A. Hirasawa, et al., In situ electrochemical atomic force microscope study on graphite electrodes, *J. Electrochem. Soc.* 144 (4) (1997) L81–L84.
- [154] S. Ramdon, B. Bhushan, S.C. Nagpure, In situ electrochemical studies of lithium-ion battery cathodes using atomic force microscopy, *J. Power Sources* 249 (2014) 373–384.

- [155] R. Vidu, F.T. Quinlan, P. Stroeve, Use of *in situ* electrochemical atomic force microscopy (EC-AFM) to monitor cathode surface reaction in organic electrolyte, *Ind. Eng. Chem. Res.* 41 (25) (2002) 6546–6554.
- [156] J. Park, et al., *In situ* atomic force microscopy studies on lithium (de)intercalation-induced morphology changes in  $\text{Li}_x\text{CoO}_2$  micro-machined thin film electrodes, *J. Power Sources* 222 (2013) 417–425.
- [157] V. Srinivasan, J. Newman, Discharge model for the lithium iron-phosphate electrode, *J. Electrochem. Soc.* 151 (10) (2004) A1517–A1529.

# Atomistic modeling of the behavior of materials in rechargeable lithium-ion and lithium–air batteries

8

*P. Kaghazchi*  
Freie Universität Berlin, Berlin, Germany

## 8.1 Introduction

Recent trends in miniaturization of electronics devices and the development of electric cars necessitate the use of highly efficient energy storages. Li-based batteries are promising candidates for these purposes as they can provide a high storage capacity, long lifetime, and flexible design. Although Li-ion batteries (LiBs) are currently used for portable electronics devices (e.g., mobile phones and laptop computers), there is still need for further research and development to improve the performance of LiBs to make them suitable for the use in electric vehicles. The other types of Li-based batteries, namely Li–S and Li–air batteries, are also still in the development stage.

There have been many studies aimed at finding appropriate cathode materials in LiBs. The most attractive materials for this purpose have been found to be  $\text{Li}_x\text{FePO}_4$  [1,2],  $\text{Li}_x\text{CoO}_2$  [3,4],  $\text{Li}_x\text{MnO}_2$  [5], and  $\text{Li}_x\text{FeSiO}_4$  [6]. However, less attention has been paid to the development of new anode materials with high capacities. For a long time, only graphite with a low capacity of 372 mAh g<sup>−1</sup> has been used in LiBs. The demand for higher capacities has recently motivated searches for alternative anode materials. Recent studies show that silicon (Si) and tin (Sn) are very promising anode materials owing to their large theoretical capacities of  $\sim$ 4200 mAh g<sup>−1</sup> [7] and  $\sim$ 990 mAh g<sup>−1</sup> [8], respectively.

Extensive experimental investigations show that the charge/discharge processes in LiBs with Si or Sn anodes cause the alloying/dealloying of these materials with Li, leading to large volume changes and instability of the anodes. The poor performance of Si and Sn anodes can, however, be improved by using nanostructures such as nanoparticles and nanowires [9,10]. To improve the performance of LiBs, we need a deep understanding of structures, stabilities, and processes in nanostructured Si or Sn. Theoretical studies can help us to understand these issues at the atomic scale and thereby improve the performance of future LiBs. In fact, theoretical investigations are not only useful in interpreting observed phenomena but they also have considerable predictive power.

This chapter gives an overview of the concepts behind density functional theory (DFT) (Section 8.2), which is the commonly used theoretical approach in energy

research, and its application to study electrode materials in Li-based batteries such as Si anodes (Section 8.3) and their interfaces with electrolytes (Section 8.4) as well as Sn anodes (Section 8.5) and also Li–air batteries (Section 8.6).

## 8.2 Method

The performance of a Li-based battery is mainly determined by the electronic and atomic structure as well as energetics of cathode, anode, and electrolytes and their interfaces. These properties can be calculated by using DFT, which can in principle solve exactly the (many-body) Schrödinger equation. In the following, we briefly summarize the essential concepts behind this theory.

### 8.2.1 The many-body problem

For a stationary nonrelativistic system consisting of a set of nuclei and electrons the (many-body) Schrödinger equation is written as

$$H\Psi(\mathbf{r}_i\sigma_i, \mathbf{R}_I) = E\Psi(\mathbf{r}_i\sigma_i, \mathbf{R}_I) \quad (8.1)$$

where  $H$ ,  $\Psi(\mathbf{r}_i\sigma_i, \mathbf{R}_I)$ , and  $E$  are the Hamilton operator, many-body wave function, and total energy of the system, respectively.  $\Psi(\mathbf{r}_i\sigma_i, \mathbf{R}_I)$  is a function of spin ( $\sigma_i$ ) and spatial ( $\mathbf{r}_i$ ) coordinates of electron  $i$  as well as spatial coordinate ( $\mathbf{R}_I$ ) of nucleus. The many-body Hamiltonian (in atomic units) is written as

$$H = -\sum_{I=1}^{N_n} \frac{1}{2M_I} \nabla_I^2 - \sum_{i=1}^{N_e} \frac{1}{2} \nabla_i^2 + \sum_{I=1}^{N_n} \sum_{J>I}^{N_n} \frac{Z_I Z_J}{|\mathbf{R}_I - \mathbf{R}_J|} + \sum_{i=1}^{N_e} \sum_{j>i}^{N_e} \frac{1}{|\mathbf{r}_i - \mathbf{r}_j|} - \sum_{i=1}^{N_e} \sum_{I=1}^{N_n} \frac{Z_I}{|\mathbf{r}_i - \mathbf{R}_I|} \quad (8.2)$$

where  $M_I$  and  $Z_I$  are the mass and atomic number of nucleus  $I$ , while  $N_n$  and  $N_e$  are the total numbers of nuclei and electrons of the system, respectively.

Except for simple systems consisting of one electron and one nucleus (e.g., H atom,  $\text{He}^+$  ion), solving the many-body Schrödinger equation (Equations (8.1) and (8.2)) is nontrivial. This is because a system consisting of electrons and nuclei is a coupled system in which these particles interact with each other and themselves. A first step to approximate this problem is using the Born–Oppenheimer approximation.

### 8.2.2 Born–Oppenheimer (BO) approximation

The nuclei of atoms are often much more massive than electrons. This means that electrons can instantaneously follow the motion of the nuclei. Based on this fact, Born and Oppenheimer [11] proposed that the electronic and ionic degrees of freedom can be decoupled. Within the Born–Oppenheimer (BO) approximation, on the timescale of

the motion of the electrons, the ions appear almost stationary and, therefore, the total wave function can be decoupled as

$$\Psi(\mathbf{r}_i\sigma_i, \mathbf{R}_I) = \psi_e(\mathbf{r}_i\sigma_i, \{\mathbf{R}_I\})\psi_n(\mathbf{R}_I) \quad (8.3)$$

where  $\psi_e(\mathbf{r}_i\sigma_i, \{\mathbf{R}_I\})$  is the electronic wave function, which (as before) depends on the spatial and spin coordinate of electrons as well as the nuclear spatial coordinate that now appears as a parameter. In Equation (8.3),  $\psi_n(\mathbf{R}_I)$  is the nuclei wave function. The many-body Schrödinger equation can now be separated into electronic and nuclear equations

$$\begin{aligned} & \left( -\sum_{i=1}^{N_e} \frac{1}{2} \nabla_i^2 + \sum_{i=1}^{N_e} \sum_{j>i}^{N_e} \frac{1}{|\mathbf{r}_i - \mathbf{r}_j|} - \sum_{i=1}^{N_e} \sum_{I=1}^{N_n} \frac{Z_I}{|\mathbf{r}_i - \mathbf{R}_I|} \right) \psi_e(\mathbf{r}_i\sigma_i, \{\mathbf{R}_I\}) \\ & = E_e \psi_e(\mathbf{r}_i\sigma_i, \{\mathbf{R}_I\}) \end{aligned} \quad (8.4)$$

and

$$\left( -\sum_{I=1}^{N_n} \frac{1}{2M_I} \nabla_I^2 + \sum_{I=1}^{N_n} \sum_{J>i}^{N_n} \frac{Z_I Z_J}{|\mathbf{R}_I - \mathbf{R}_J|} + E_e(\mathbf{R}_I) \right) \psi_n(\mathbf{R}_I) = E_{\text{tot}} \psi_n(\mathbf{R}_I) \quad (8.5)$$

If nonadiabatic effects arising from the coupling between the nuclear and electronic wave functions are small in the considered system, the BO approximation will introduce only a negligible error to the calculated quantities.

### 8.2.3 Density functional theory

Even after considering the BO approximation, the main challenge is still solving the electronic part (Equation (8.4)), which can only be solved exactly for one-electron systems such as H or  $\text{He}^+$ . Two common types of methods that are used for solving Equation (8.4) are wave function-based and density-based approaches [12]. The well-known DFT, which is commonly used to study Li-based batteries, is a density-based approach. Since the results of this chapter are based on DFT, we will discuss this method in more detail after a short summary of wave function-based methods.

A popular wave function-based method is Hartree–Fock (HF), in which the total wave function is approximated by a single Slater determinant of a set of orthonormal single-particle orbitals. The total energy and the wave function of the system are determined by minimizing the expectation value of the Hamiltonian with respect to the wave function (i.e., the variational principle). An important consequence of this approach is that the exchange interaction, which is the result of imposing Pauli's exclusion principle on the electrons of like spin, is exactly calculated. The main problem of HF theory is, however, that it cannot describe the correlation energy, which is the result of the instantaneous correlation of electronic motions. The most widely used wave function-based approaches that can calculate total energy of a system with a high

accuracy by taking into account the correlation energy are configuration interaction (CI) [13], coupled cluster (CC) [14], or perturbation theory (such as MP2 and MP4) [15]. Although in principle these methods are highly accurate, in practice they are computationally very expensive. Therefore, only small systems consisting of a few atoms can be investigated by these approaches.

Density-based methods in which the electron density is used as the basic variable are alternative approaches to tackle the many-body problem. In particular, DFT is the most widely approach used for this purpose. Hohenberg and Kohn (HK) proposed the DFT approach in 1964 [16]. One year later, Kohn and Sham (KS) [17] showed how to use this method in practical applications.

The HK theorem states that the external potential (i.e., the potential of the ions or nuclei) can be uniquely (to within a constant) determined from the electron density. The total electronic energy  $E$  can thus be written as a functional of the electron density  $\rho$

$$E_e[\rho] = \underbrace{T[\rho] + E_{ee}[\rho]}_{F_{HK}} + \int \rho(\mathbf{r}) V_{\text{ext}}(\mathbf{r}) d\mathbf{r} \quad (8.6)$$

where  $T[\rho]$  and  $E_{ee}[\rho]$  are the kinetic energy and electron–electron interaction energy functionals, respectively. The sum of  $T[\rho]$  and  $E_{ee}[\rho]$  functionals, namely  $F_{HK}$ , is the universal HK functional, which is independent of the nature of the considered system.

The second HK theorem states that the ground-state density ( $\rho_0(\mathbf{r})$ ) and energy ( $E_e^0$ ) can be obtained by applying the variational principle

$$E_e^0 = E_e[\rho_0(\mathbf{r})] \leq E_e[\rho(\mathbf{r})] \quad (8.7)$$

with the following condition

$$\rho(\mathbf{r}) \geq 0 \text{ and } \int \rho(\mathbf{r}) d\mathbf{r} - N_e = 0 \quad (8.8)$$

Based on these two theorems, many ground-state properties can be in principle calculated exactly if we had the universal functional  $F_{HK}[\rho]$ . However, this complicated functional is not known. The main problem to find  $F_{HK}$  is the complexity of nonclassical electron–electron interactions.

One year later, Kohn together with Sham [17] showed how to approximate  $F_{HK}[\rho]$ . To do this, they split the exact kinetic energy functional  $T[\rho]$  into

- The kinetic energy of a system of noninteracting electrons

$$T_S = -\frac{1}{2} \sum_{i=1}^{N_e} \langle \phi_i | \nabla^2 | \phi_i \rangle \quad (8.9)$$

where  $\phi_i$  is a set of one-electron wave functions (known as KS orbitals).

- The neglected interactions in the noninteracting system  $T - T_S$ .

Then, the nonclassical part of  $E_{ee}$  together with the  $T - T_S$  energy is defined as the exchange–correlation energy

$$E_{xc}[\rho] = (T[\rho] - T_S[\rho]) + (E_{ee}[\rho] - J_{ee}[\rho]) \quad (8.10)$$

where  $J_{ee}[\rho]$  is the classical Coulomb repulsion. The energy functional (Equation (8.6)) can now be written as

$$E[\rho] = T_S[\rho] + J_{ee}[\rho] + E_{xc}[\rho] + \int \rho(\mathbf{r}) V_{\text{ext}}(\mathbf{r}) d\mathbf{r} \quad (8.11)$$

Finally, by applying the variational principle the KS equations are obtained

$$\left[ -\frac{1}{2} \nabla^2 + V_{\text{eff}}(\mathbf{r}) \right] \phi_i = \epsilon_i \phi_i \quad (8.12)$$

$$V_{\text{eff}}(\mathbf{r}) = V_{\text{ext}}(\mathbf{r}) + \int \frac{\rho(\mathbf{r}')}{|\mathbf{r} - \mathbf{r}'|} d\mathbf{r}' + V_{\text{xc}}(\mathbf{r}) \quad (8.13)$$

$$\rho(\mathbf{r}) = \sum_{i=1}^{\text{occ}} |\phi_i(\mathbf{r})|^2 \quad (8.14)$$

where the exchange–correlation potential is

$$V_{\text{xc}}(\mathbf{r}) = \frac{\delta E_{\text{xc}}[\rho(\mathbf{r})]}{\delta \rho(\mathbf{r})} \quad (8.15)$$

The single particle wave functions, KS orbitals, in Equation (8.12) can be determined if we have  $V_{\text{eff}}$ , which depends on  $\rho(\mathbf{r})$  (Equation (8.13)), which itself is obtained by the KS orbitals (Equation (8.14)). To solve this problem we therefore use an iterative process that is called the self-consistent field (scf) approach: we start with a guessed  $\rho(\mathbf{r})$  (Equation 8.14) and determine  $V_{\text{eff}}$  using Equation (8.14) and then obtain a new  $\rho(\mathbf{r})$  from Equations (8.12) and (8.14). This procedure is then repeated until  $\rho(\mathbf{r})$  is converged.

We could exactly calculate the total energy and density using the DFT method, if we had the exact exchange–correlation energy functional  $E_{\text{xc}}[\rho]$ . This functional is, however, very complicated and it has not been identified so far (and perhaps it cannot be identified at all). Fortunately, as will be shown in the next sections, even a simple approximation for this term gives reasonable results.

A simple approximation for the exchange–correlation term is the local density approximation (LDA). Within the LDA approximation, the exchange–correlation energy per particle at a point  $r$  is assumed to be equal to the exchange–correlation energy per particle of a uniform electron gas that has the same density at the point  $r$ . In spite of its simplicity, this functional can give reasonable lattice constants and bond lengths for materials. However, LDA often fails to predict energetics.

The generalized gradient approximation (GGA) provides a better description to calculate energetics in most cases. Within the GGA, the gradient of the density,  $\nabla\rho(\mathbf{r})$ , is also considered in addition to the density

$$E_{xc}^{\text{GGA}}[\rho] = \int \rho(\mathbf{r}) \epsilon_{xc}(\rho(\mathbf{r}), \nabla\rho(\mathbf{r})) d\mathbf{r} \quad (8.16)$$

where  $\epsilon_{xc}(\rho(\mathbf{r}), \nabla\rho(\mathbf{r}))$  is the exchange–correlation energy per particle of the homogeneous electron gas at a given point  $\mathbf{r}$ . Perdew, Burke, and Ernzerhof (PBE) [18] have developed a form of GGA that is widely used for energy research and, therefore, it has also been used to obtain the results of this chapter.

Within the PBE approximation, the correlation energy is

$$E_c^{\text{GGA}}[\rho] = \int \rho [\epsilon_c^{\text{unif}}[\rho] + H(\rho, t)] d\mathbf{r} \quad (8.17)$$

where  $H(\rho, t)$  is

$$H(\rho, t) = \gamma \ln \left[ 1 + \frac{\beta t^2}{\gamma} \left( \frac{1 + At^2}{1 + At^2 + A^2 t^4} \right) \right] \quad (8.18)$$

with

$$\gamma \simeq 0.031091; \quad \beta \simeq 0.066725; \quad A = \frac{\beta}{\gamma} \frac{1}{e^{-\epsilon_c^{\text{unif}}/\gamma} - 1}; \quad t = \frac{|\nabla\rho|}{2 \left( \sqrt{\frac{4(3\pi^2\rho)^{1/3}}{a^0\pi}} \right) \rho} \quad (8.19)$$

Here,  $t$  is a dimensionless density gradient.

The exchange energy is determined by

$$E_x^{\text{GGA}}[\rho] = \int \rho \epsilon_x^{\text{unif}}(\rho) F_x(s) d\mathbf{r} \quad (8.20)$$

where  $\epsilon_x^{\text{unif}}(\rho)$  is the exchange energy per particle of a homogeneous electron gas at point  $\mathbf{r}$  (the Dirac expression)

$$\epsilon_x(\rho(\mathbf{r})) = -\frac{3}{4} \left( \frac{3}{\pi} \right)^{1/3} \rho(\mathbf{r})^{1/3} \quad (8.21)$$

and  $F_x$  is an enhancement factor

$$F_x(s) = 1 + \kappa - \frac{\kappa}{1 + \frac{\mu s^2}{\kappa}}, \quad s = \frac{|\nabla\rho|}{2(3\pi^2\rho)^{1/3}\rho}, \quad \kappa = 0.804, \quad \mu \simeq 0.21951 \quad (8.22)$$

where  $s$  is also a dimensionless density gradient.

The results of the next sections were obtained by performing DFT calculations [19] with the GGA-PBE functional [18] to approximate the exchange–correlation energies.

## 8.3 Si anodes

Silicon is a promising anode material for LiBs because it has the highest known specific charge capacity of  $4200 \text{ mAh g}^{-1}$  [20]. Its capacity is  $\sim 10$  times larger than that of the widely used graphite in the present LiBs [21], but it shows a huge irreversible capacity loss [20]. This problem is due to large volume ( $\sim 300\%$ ) and structural changes during lithium insertion/extraction, leading to a mechanical breakdown [22,23]. The poor performance of bulk and micrometer-sized Si anodes can, however, be improved by using nanostructured Si such as nanoparticles and nanowires [9,10,24]. This is because of a better accommodation of Li in Si nanostructures where the lithiation/delithiation-induced mechanical strain can be effectively alleviated [25].

For large-scale applications (e.g., electric vehicles) a high rate of Li diffusion within the electrode is necessary. An advantage of using nanostructured Si anodes is that the length of Li diffusion is short in these cases. However, in these nanomaterials the rate of Li incorporation may be limited at electrode/electrolyte interfaces. In this chapter, the process of Li diffusion in bulk Si and surfaces will be discussed.

### 8.3.1 Bulk Si

Bulk Si has a diamond structure at room temperature and pressure (Figure 8.1). The calculated lattice constant, bulk modulus, and cohesive energy for bulk Si is listed in Table 8.1. Although both LDA (calculated by Hortamani *et al.* [26]) and our PBE calculations give satisfactory results for the lattice constant and bulk modulus, the cohesive energy within the PBE functional is in better agreement with the experimental

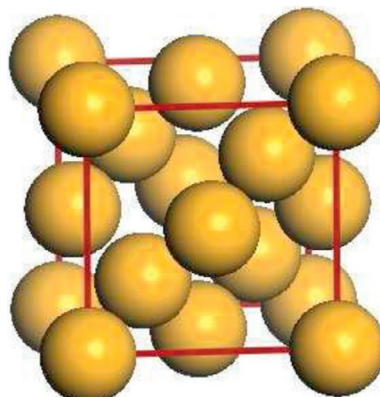


**Figure 8.1** Structure of bulk Si.

**Table 8.1 Calculated lattice constant ( $a$ ), bulk modulus ( $B$ ), and cohesive energy ( $E_{coh}$ ) for bulk Si**

	(AE) LDA [26]	(PP) PBE [26]	(AE) PW91 [27]	(PP) PBE (this work)	Exp [28]
$a$ (Å)	5.41	5.47	5.45	5.47	5.43
$B$ (GPa)	94.9	87.8	91	86.8	98.8
$E_{coh}$ (eV)	5.26	4.59	4.64	4.63	4.63

Previous all electron (AE) and pseudopotential (PP) calculations as well as experimental values are given for a comparison.

P. Kaghazchi, J. Phys.: Condens. Matter, 25 (2013) 095008.

value. Therefore, it is more reasonable to use the GGA-PBE functional to study lithiation/delithiation in Si.

Afterward, we calculated the energy barrier for the difference of Li in bulk Si with a Li/Si ratio of 1/64. The PBE value of diffusion barrier is 0.5 eV, which is close to the reported experimental values of 0.57–0.79 eV [29].

### 8.3.2 Si surfaces

Transmission electron microscopy images demonstrated that Si nanoparticles are bound mainly by the {111} and {100} facets [30]. The structures of clean (111) and (100) surfaces have been investigated extensively by using low-energy electron diffraction, scanning tunneling microscopy, and DFT. However, much less attention has been paid to the adsorption and incorporation of Li atoms into these surfaces. Recently, Jung and Han [31] investigated the incorporation of a single Li atom into Si(111) and Si(100) surfaces. However, they have not studied the Li-coverage dependence of the lithiation/delithiation process at Si surfaces.

To study these issues, we investigated the following structures:

1. *Si(111)*: Unreconstructed (1 × 1) (Figure 8.2a) and reconstructed (2 × 1) (Figure 8.2b). In the reconstructed structure, a buckled  $\pi$ -bonded chain of Si atoms is formed on the surface. Two different bucklings (tilts) of the chains are possible: positive or negative tilt, known as positive- or negative-tilt modified Pandey chains ( $\pm$ MP chains) [32]. In the present work, we considered  $\pi$ -bonded chains with negative buckling (−MP) in which atom 3 moves inward and bonds to atom 7, while atom 2 moves outward and breaks its bond with atom 7. This leads to the formation of a buckled zigzag chain by atoms 1 and 2 on the surface. A dangling bond is created at atom 2 and the dangling bond of atom 3 is removed [33]. According to the experimental studies, the reconstructed (2 × 1) structure is more stable than the unreconstructed (1 × 1) structure [32].
2. *Si(100)*: Unreconstructed (1 × 1) (Figure 8.3a) and reconstructed  $c(4 \times 2)$  (Figure 8.3b). According to the experimental studies, the latter structure is more stable [34].

In agreement with previous DFT studies and also experimental measurements, we found the reconstructed structures to be more stable than the unreconstructed ones.

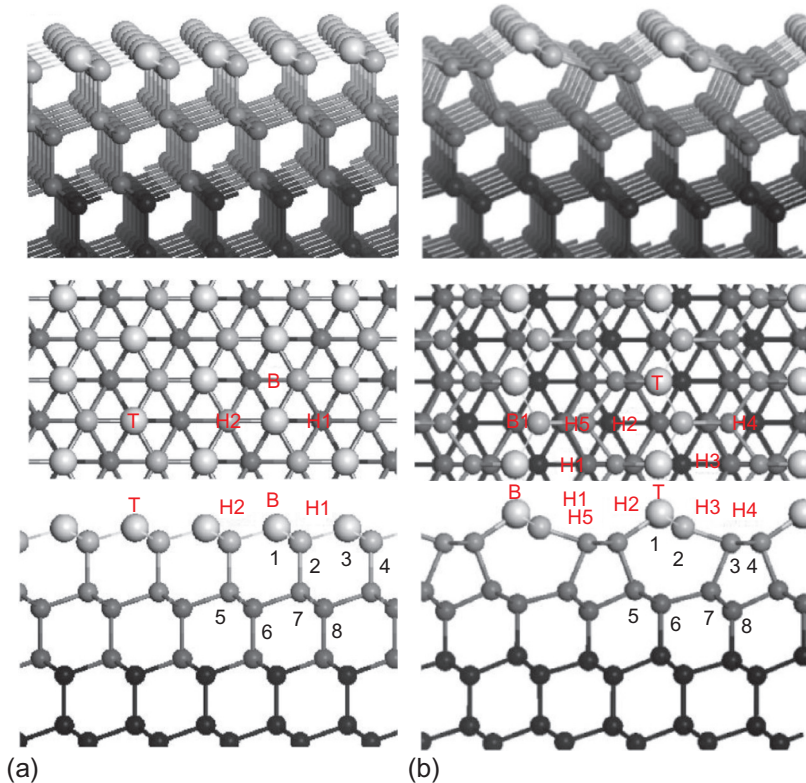


**Figure 8.2** Three-dimensional, top, and side views of (a) unreconstructed Si(111)-(1×1) and (b) reconstructed Si(111)-(2×1) showing different binding sites (hollow sites: H, bridge sites: B, top sites: T) that have been studied on these surfaces. Deeper atomic layers are represented by darker shading. The Si atoms in the topmost layers are numbered and represented by larger spheres to allow for comparison of unreconstructed and reconstructed surface structures.

P. Kaghazchi, J. Phys.: Condens. Matter, 25 (2013) 095008.

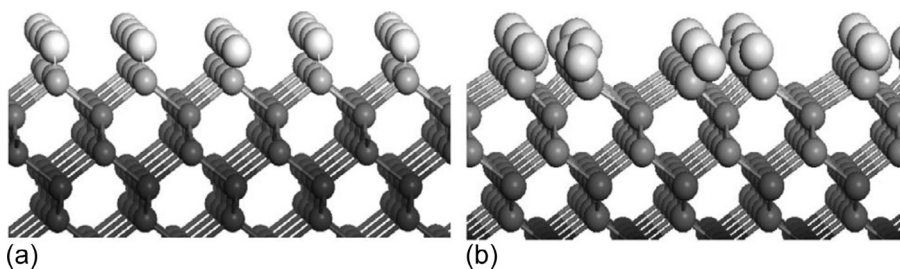


**Figure 8.3** Three-dimensional views of (a) unreconstructed Si(100)-(1×1) and (b) reconstructed Si(100)-(2×1) surfaces. Deeper atomic layers are represented by darker shading.

Kaghazchi [35].

The stability of the Si surfaces can, however, dramatically change in the presence of Li. Therefore, we also studied the Li incorporation into unreconstructed and reconstructed Si(111) and (100) surfaces by examining (i) on-surface adsorption, (ii) subsurface absorption, and (iii) combination of on-surface adsorption and subsurface absorption. Different coverages ( $\Theta$ ) of Li were considered:  $\Theta$  is the number of Li atoms per  $(1 \times 1)$  unit cell of the unreconstructed surface (in GML).

**Li/Si(111).** For  $\Theta = 0.25$  GML, the most stable sites for the adsorption of Li are the B and H1 sites on unreconstructed and reconstructed Si(111) surfaces (Figure 8.2), respectively. The calculated binding energy (BE) at the H1 site ( $-2.91$  eV) is much weaker (by  $\sim 0.57$  eV) than that at the B site. However, the total energy of the Li/Si structures is similar. The weaker BE of Li on the reconstructed surface is, therefore, due to the more stability of this surface before the adsorption of Li as discussed before.

For  $\Theta \geq 0.5$  GML, we examined different structures with Li atoms at (i) on-surface, (ii) subsurface, and (iii) mixed surface/subsurface sites and found that the structures with only on-surface adsorption on the unreconstructed surfaces offer the strongest binding energies. The BE as a function of  $\Theta$  is illustrated in Figure 8.4. It is seen that the BE of Li remains almost unchanged on Si(111)– $(1 \times 1)$  for  $\Theta \leq 1$  GML, while it decreases strongly for  $\Theta > 1$  GML, showing strong Li–Li interactions at higher coverages. Figure 8.5 illustrates the energy barrier ( $\Delta E$ ) and atomic structures for Li insertion into the clean unreconstructed surface. The energy barrier for the diffusion of Li from on-surface into subsurface sites is  $\Delta E = 0.98$  eV. At transition state (TS), Li passes through a hexagonal-like site.

The energy barriers for the penetration of a single Li atom as well as simultaneous penetration of two or three Li atoms for the 1 GML-Li/Si(111)– $(1 \times 1)$  surface are illustrated in Figure 8.6. It was found that a simultaneous penetration of two or more Li atoms is very unfavorable.

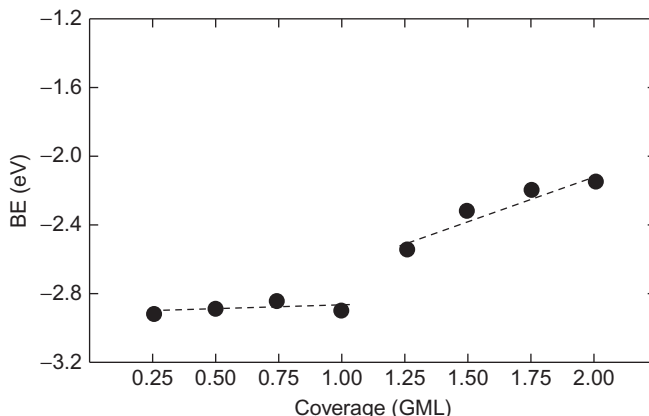


**Figure 8.4** Binding energy of Li as a function of coverage for on-surface adsorption at the Si(111) surface.

P. Kaghazchi, J. Phys.: Condens. Matter, 25 (2013) 095008.

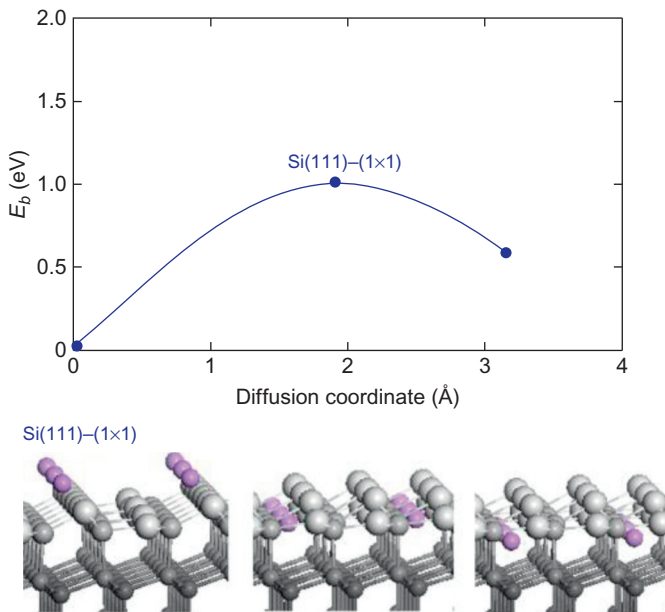


**Figure 8.5** Energy profiles and structures for diffusion of a single Li atom into the subsurface for  $\Theta=0.25$  GML on Si(111)-(1x1).

P. Kaghazchi, J. Phys.: Condens. Matter, 25 (2013) 095008.

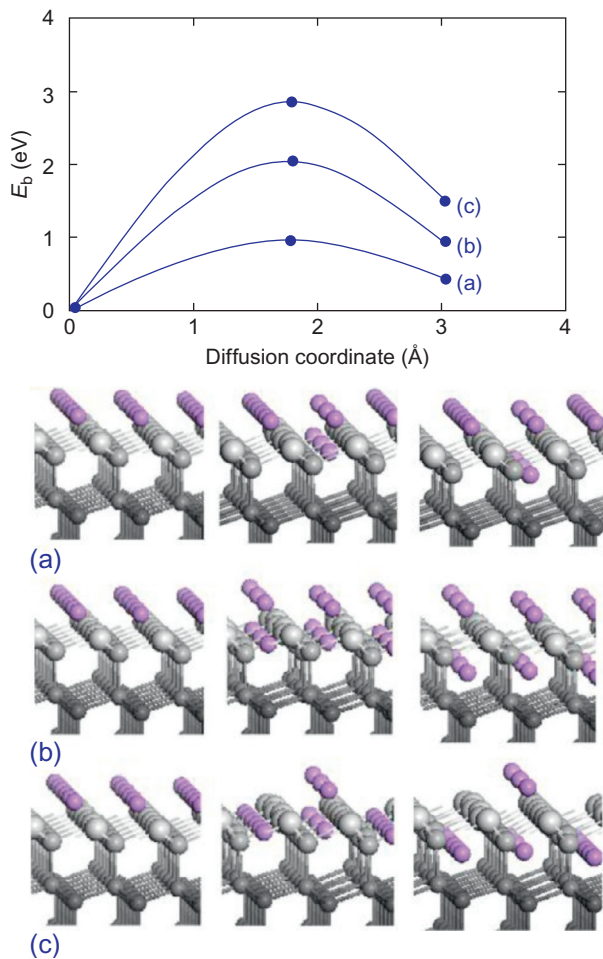
A comparison between Figures 8.5 and 8.6 shows that the presence of Li adatoms in the neighborhood of penetration sites does not affect the energy barrier of a diffused single Li ( $\Delta E_{\text{clean}}=0.98$  eV,  $\Delta E_{\text{Li-covered}}=0.92$  eV). This is because there is a negligible interaction between Li atoms on the surface, which can also be concluded from a very similar BE of Li for  $\Theta=0.25$ –1.0 GML (Figure 8.4).

Figures 8.5 and 8.6 also indicate that the barrier for the extraction of Li from the subsurface is not affected by Li–Li interactions. In both clean and Li-covered surfaces, the extraction barriers are  $\sim 0.45$  eV lower than the insertion barriers. This conclusion may show that the discharge process in nanostructured Si anodes is faster than the charge process.

**Si(100).** Similar to the case of Si(111), we have examined the adsorption of Li at different binding sites on the unreconstructed and  $c(4\times 2)$  reconstructed surfaces (see Figure 8.3) and determined the most favorable on-surface and subsurface structures. In the presence of Li, the reconstructed surfaces are still more favorable than the unreconstructed ones. Therefore, we only considered the former surfaces to study the process of Li penetration.

The diffusion barrier (1.23 eV) is very high for the clean (100) surface. This finding is in agreement with a previous DFT calculation by Jung and Han [31]. For  $\Theta\geq 0.5$  GML, the following mechanisms were considered: (i) insertion of Li via the on-surface sites that are not occupied by Li atoms (in this case, the diffused Li

**Figure 8.6** Energy profiles and structures for diffusion of (a) one, (b) two, and (c) three Li atoms from on-surface into subsurface sites for 1 GML of Li on Si(111). P. Kaghazchi, J. Phys.: Condens. Matter, 25 (2013) 095008.



atoms interact with the nearest-neighbor lithium adatoms ( $\text{Li}_3$ ) and (ii) insertion of Li through the adsorbed Li atoms. In this case, an adsorbing Li atom ( $\text{Li}_1$ ) interacts strongly with preadsorbed atoms ( $\text{Li}_2$ ) and pushes them to penetrate and occupy the subsurface sites (*pushing* mechanism). The energy barrier for the mechanism (i) was calculated to be 0.57 eV lower than that for the Li diffusion in the clean Si (100) surface. The lower penetration barrier in the former case is due to the fact that in the corresponding structure the diffusion Li<sub>1</sub> atom is energetically less favorable at the adsorption site because of the  $\text{Li}_1$ – $\text{Li}_3$  repulsive interactions. Moreover, the entrance area for the Li penetration is larger for 0.5 ML than for the clean surface, which can be also another reason for the lower penetration barrier of the mechanism (i). The adsorption and transition states are energetically less favorable in the (*pushing*) mechanism (ii) than in mechanism (i). The former mechanism is therefore energetically less favorable (by 0.17 eV) than mechanism (i) (Figure 8.7).

At 1 ML, two different pathways for the *pushing* mechanism were considered: (i)  $\text{Li}_2$  diffuses along the  $-z$  direction and then it deviates in the  $-y$  direction toward the TS and (ii)  $\text{Li}_2$  moves along the  $xz$  plane and then deviates in the  $-y$  direction toward the TS (Table 8.2).

The second pathway was found to be 0.15 eV more favorable than the first pathway. The reason is that the  $\text{Li}_1$ – $\text{Li}_2$  repulsions are smaller in mechanism (ii) compared

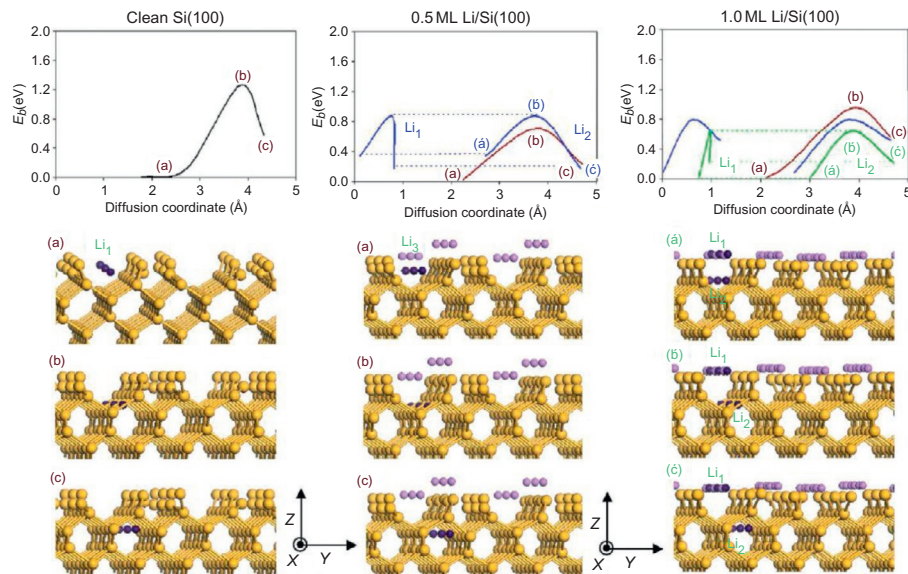


**Figure 8.7** Energy profiles for the incorporation of Li atoms into clean and Li-covered Si(100). The energy of Li-covered surfaces is referenced to that of the clean surface. Snapshots of the most favorable structures along the pathways are presented in the bottom of each case (a–c).

P. Kaghazchi, Appl. Phys. Lett. 102, 093901 (2013).

**Table 8.2 Energy barriers (in eV) of Li insertion into Si(100) and Si(111) for different mechanisms and Li coverages**

Mechanism	Si(100)			Si(111)	
	Clean	0.5 ML	1 ML	Clean	1 ML
i	1.26	0.69	0.93	0.99	0.97
ii (path 1)	–	0.86	0.70	–	–
ii (path 2)	–	–	0.63	–	–

to mechanism (i). This is because  $\text{Li}_2$  atoms deviate in the  $-x$  direction and thereby can enlarge their separations from  $\text{Li}_1$  atoms. The *pushing* mechanism is not possible for Li penetration into the Si(111) surface as there is no deep trough on this surface [35].

## 8.4 Initial stage of solid electrolyte interphase (SEI) formation on Si surfaces

The SEI layer is an electronically passivating layer that is formed from the reduced species of electrolyte on the surface of electrodes. It is formed during the first cycles of charging/discharging [36–38]. The structure of SEI layers depends on the type of solvent and salt that are used in LiBs [39,40]. In a LiB with an ethylene carbonate (EC) solvent and a  $\text{LiPF}_6$  salt, the SEI layer, which usually forms on the surface of an anode, mainly consists of inorganic  $\text{Li}_2\text{CO}_3$ ,  $\text{Li}_2\text{O}$ , and  $\text{LiF}$ , as well as organic compounds such as  $(\text{CH}_2\text{OCO}_2\text{Li})_2$  (see Ref. [41] and references therein).

The formation of the SEI layer leads to an irreversible capacity loss. Moreover, it decreases the rate of Li diffusion and, thereby, the rate of charge and discharge. However, its formation is necessary for the protection of the electrolyte from further decomposition on the surface of electrodes. A detailed study of the process of SEI formation is crucial to control the performance of LiBs.

*Ab initio*-based theoretical modeling is a useful tool to investigate the formation of a SEI layer. In this section, we summarize our recent study for the process of EC decomposition, which can lead to the formation of a SEI layer on Si anodes [42]. Using DFT calculations, we studied adsorption of EC on Li-covered Si(111) and (100) surfaces discussed in the previous section and found a strong structure sensitivity in decomposition of EC.

The structure of an EC molecule is presented in Figure 8.8. To study interaction between EC and Li-covered Si surfaces we focused on the most stable structures of Li/Si surfaces (with a coverage of  $\Theta = 0.25$  GML) that were determined in Section 8.3:

- Unreconstructed Si(111)–(1 × 1) with a (2 × 2) unit cell and a single Li adatom.
- Reconstructed Si(100)–c(4 × 2) with a (1 × 1) unit cell and a single Li adatom.

To determine the most favorable EC/Li/Si structures we examined a variety of possible adsorption sites and orientations for the adsorption of EC on the Li/Si surfaces. The possible binding sites were labeled with A to E (Figure 8.8). The orientation of molecule was labeled by a superscript ( $\uparrow$ ,  $\downarrow$ , and  $\rightarrow$ ), which indicates the orientation of molecule's **v** axis to the surface normal and a subscript ( $\alpha = \sin \varphi$ ), in which  $\varphi$  denotes the angle between the molecule's **u** axis and the normal vector of the surface unit cell.

The calculated binding energies for the adsorption of EC at different sites with different orientations are illustrated in Figure 8.9. Adsorption of the EC molecule at the most favorable sites on these surfaces is an exothermic process. The BE of EC on Li/Si (111) is 0.42 eV stronger than that on Li/Si(100).

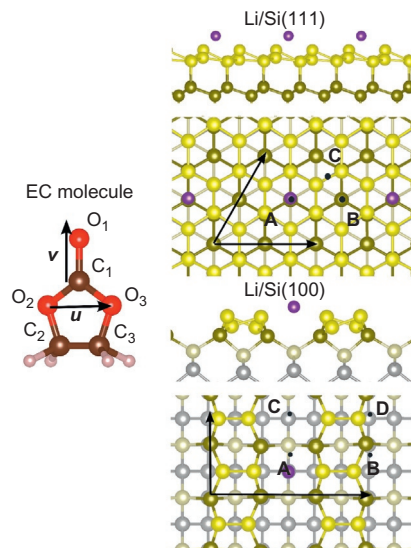


**Figure 8.8** Atomic structure of an ethylene carbonate (EC) molecule (left), and the most stable structures of Li/Si(111) and Li/Si(100) surfaces.

J. Rohrer, P. Kaghazchi, *ChemPhysChem* 15 (2014) 3950.

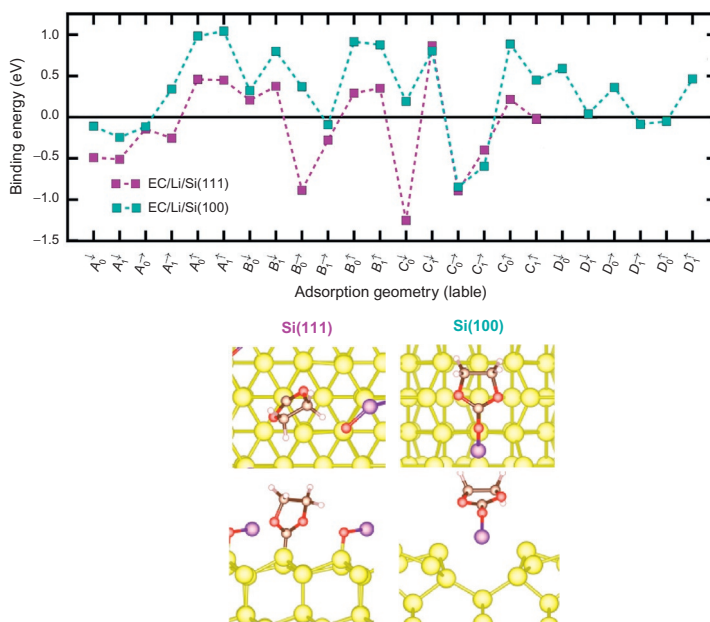


**Figure 8.9** Binding energies of relaxed EC/Li/Si( $hkl$ ) configurations and atomic structure of the most favorable configuration on each surface.

J. Rohrer, P. Kaghazchi, *ChemPhysChem* 15 (2014) 3950.

The EC molecule remains intact on the Si(100) surface. On this surface, the Si—Li bond length increases by  $+0.18 \text{ \AA}$ , showing that the Si—Li bond strength becomes weaker due to the formation of a bond between  $O_1$  and the Li adatom. However, the EC molecule decomposes into  $C_3H_4O_2$  and  $O_1$  on the Si(111) surface. The decomposition is the result of a geometry relaxation. The detached  $O_1$  atom binds to the Si surface atom and the Li adatom. The rest of the molecule, namely  $C_3H_4O_2$ , binds to the Si(111) surface via its  $C_1$  atom. Over the Si(111) surface, besides the adsorption of the  $O_1$  atom to the Li adatom, the  $C_1$  atom of the EC molecule binds to the topmost Si surface atom whose dangling bond is not saturated. However, over the Si(100) surface, the EC molecule does not bind directly to the neighboring Si atoms whose dangling bonds are partially saturated by the surface reconstruction. In this case, only the  $O_1$  atom of the EC molecule binds to the Li adatom. Therefore, it is concluded that EC molecules dissociate on Si surfaces if their  $C_1$  atoms have the possibility to bind to the neighboring Si atoms whose dangling bonds are not saturated by Li adatom (Table 8.3).

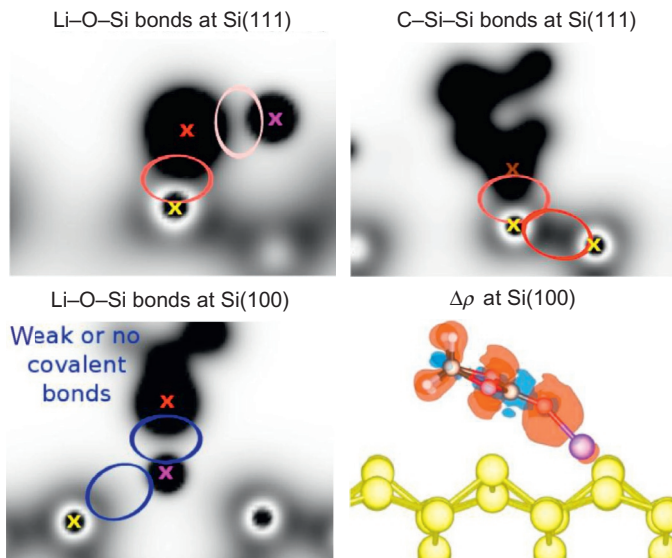
The Bader charge values [43] for the EC molecule and the Li adatom over the Si surfaces are listed in Table 8.4. We found a negligible deficit or excess of charge on EC and Li over the Si(100) surface. However, electrons are transferred from the Si(111) surface to the resulting  $C_3H_4O_2$  and  $O_1$  fragments. In this case, although the charge on the Li adatom does not change, there is a total electron transfer of  $\sim 2.4|e|$  from the surface to  $C_3H_4O_2 + O_1$ . The reduction of  $1.43|e|$  in the electronic charge of the  $C_1$  atom (in  $C_3H_4O_2$ ) shows a strong binding between the  $C_1$  atom and the Si(111) surface atoms with dangling bonds. The existence of  $\sim 2e$  charge on  $O_1$  over the Si(111) surface can trigger the formation of SEI layer components such as  $Li_2O$  or  $Li_4SiO_4$ .

Figure 8.10 illustrates the cross sections of the charge densities for the EC/Li/Si(111) and EC/Li/Si(100) surfaces where the dark color denotes high electron density, while white color denotes low electron density. The charge density difference between EC/Li/Si(100) and its fragments (i.e., Li/Si(100) and EC) is also shown in this figure

**Table 8.3 Excess (positive) and deficit (negative) of electronic charges in unit of  $|e|$  based on Bader's analysis**

Si(111)					
Li	$O_1$	$C_1$	$C_3H_4O_2$	$Si_1$	$Si_2$
-0.006	+1.858	-1.424	+0.539	-1.639	+0.690
Si(100)					
Li			EC		
0.013			-0.026		

$Si_1$  and  $Si_2$  are the Si atoms that bind to  $O_1$  and  $C_1$ , respectively.  
J. Rohrer, P. Kaghazchi, ChemPhysChem 15 (2014) 3950.



**Figure 8.10** Electronic charge densities in the most favorable EC/Li/Si(*hkl*) structures. Dark and white colors correspond to high and low densities, respectively. Positions of O, Li, and Si atomic cores are marked with red, purple, and yellow crosses.

J. Rohrer, P. Kaghazchi, *ChemPhysChem* 15 (2014) 3950.

by  $\Delta\rho$ . Red (accumulation) and blue colors (depletion) present isosurfaces of  $\Delta\rho = \pm 1.6 \times 10^{-3} \text{ e}/\text{\AA}^3$ , corresponding to 5% of the maximum change.

For the Si(100) surface, we found from the charge-density plots that the covalency is very weak in the Li—O<sub>1</sub> and Li—Si bonds. However, the electron density difference  $\Delta\rho$  plot indicates a large redistribution of charges on the EC molecule. In this case, although there is a negative charge in the region between O<sub>1</sub> and Li, this charge accumulation is located inside the Bader volume around O<sub>1</sub>. Therefore, a covalent O<sub>1</sub>—Li bond cannot be concluded. This can also be confirmed by the charge-density plots showing no charge-density between O<sub>1</sub> and Li. The Bader charge analysis also showed no excess or deficit of charges on EC, Li, and Si atoms (Table 8.4). Thus, the bonding between the Li adatom and the EC molecule has mainly a polar nature. However, for the Si(111) surface, the Li—O<sub>1</sub> and Si—C<sub>1</sub> bonds have covalent natures. There is also a covalent bond between the C<sub>3</sub>H<sub>4</sub>O<sub>2</sub> molecule and the surface Si atoms.

Figure 8.11 shows the dissociation pathway for the EC decomposition on the Li/Si(111) surface. The energy barrier as well as the atomic structures of the initial (separated) state (IS), adsorbed state (AS), TS, and final (dissociated) state (FS) were determined using the drag method with the nudged elastic band method [44,45] and the climbing-image NEB method [46]. The reaction coordinate is the additive traveling distance of the O<sub>1</sub> atom.

We found that there is no barrier for the adsorption of EC on Li/Si(111). The dissociation barrier is  $\sim 0.22$  eV, which can be easily overcome because the process of adsorption releases a large local heat of  $\sim 1.5$  eV in the semiconductor Si. The

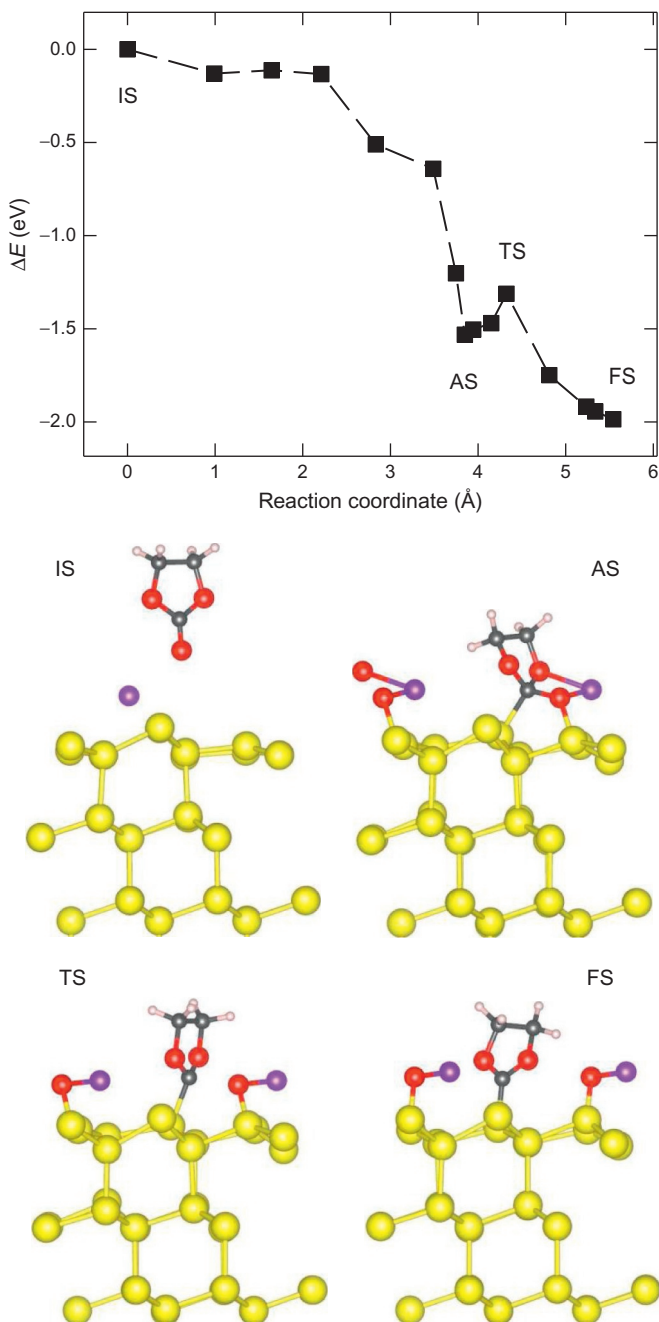


**Figure 8.11** The calculated energies and structures along the pathway of EC dissociation. J. Rohrer, P. Kaghazchi, *ChemPhysChem* 15 (2014) 3950.

adsorption well is very narrow, which can explain why the dissociation can be found even by a geometry relaxation.

It is known that without the existence of extra electrons, EC molecules do not dissociate on the surface of an electrode. Therefore, previous studies have found that the reduction of EC occurs during the charge process when extra electron is available on the electrode. The present work shows that the dissociation process occurs due to the fact that this reaction is catalyzed over the semiconductor Si surface with unsaturated dangling bonds. We found that without the Si surface, the dissociated EC molecule (FS) is about 3 eV less stable than the adsorbed EC molecule (AS), but in the presence of the Si surface the reaction is exothermic with an energy gain of  $\sim 0.5$  eV.

The mechanism of EC decomposition on the Si surface is, however, different from that on graphite. At the EC/graphite interface, the transfer of electron charge to the EC molecule causes the ring opening of this molecule [47].

The results of the previous and present sections help to better understand the process of lithiation of fresh Si anodes and the EC/Si interface in LiBs.

## 8.5 Sn anodes

Sn is a very attractive anode material for future LiBs. This is because of its high theoretical capacity. Similar to the case of Si, the main reason why Sn has not been used so far in LiBs is a dramatic decrease in its capacity in the first charge/discharge cycles [20], which is due to large volume changes of  $\sim 200\%$  during lithium insertion/extraction [48]. One way to solve this problem is using Sn nanoparticles [49] and nanosheets [21]. In these cases, the electrode/electrolyte interface plays a key role in the process of lithiation and delithiation. We have only recently studied, for the first time, the process of Li incorporation into Sn [50,51]. In the following we summarize these results.

### 8.5.1 Bulk Sn

In the bulk form, under atmospheric pressure, Sn posses a diamond structure ( $\alpha$ -phase) similar to Si for  $T < 13.2$  °C, while it has a tetragonal structure ( $\beta$ -phase) at higher temperatures [52]. Figure 8.12 presents the structure of bulk  $\beta$ - and  $\alpha$ -Sn. Similar to the case of Si, PBE gives more reasonable energy values compared to LDA. Therefore, we used the PBE functional to study Sn.

To study diffusion of Li, we modeled bulk  $\beta$ - and  $\alpha$ -Sn using  $(3 \times 3 \times 4)$  and  $(4 \times 2 \times 2)$  simulation supercells, respectively. The most stable binding sites were determined by exploring different interstitial sites for Li adsorption. The preferred binding sites were determined to be sixfold coordinated and fourfold coordinated sites in the  $\beta$ -Sn and  $\alpha$ -Sn, respectively. The BE of Li (see Table 8.4) is 0.23 eV stronger in bulk  $\alpha$ -Sn than in bulk  $\beta$ -Sn. This is related to a smaller unit-cell volume per atom in the latter phase ( $V_{\alpha\text{-Sn}} = 36.59 \text{ \AA}^{-3}/\text{atom}$ ,  $V_{\beta\text{-Sn}} = 28.59 \text{ \AA}^{-3}/\text{atom}$ ). As a result, a smaller energy cost is required to accommodate Li in the interstitial region of the less-packed  $\alpha$ -phase. The resulting deformation energy ( $\Delta E$ ) was calculated to be  $\Delta E_{\beta} = 0.55$  eV vs.  $\Delta E_{\alpha} = 0.06$  eV.

**Figure 8.12** Structures of  $\beta$ - and  $\alpha$ -Sn bulk as well as the corresponding low-index surfaces.

P. Kaghazchi, J. Phys.: Condens. Matter, 25 (2013) 382204.

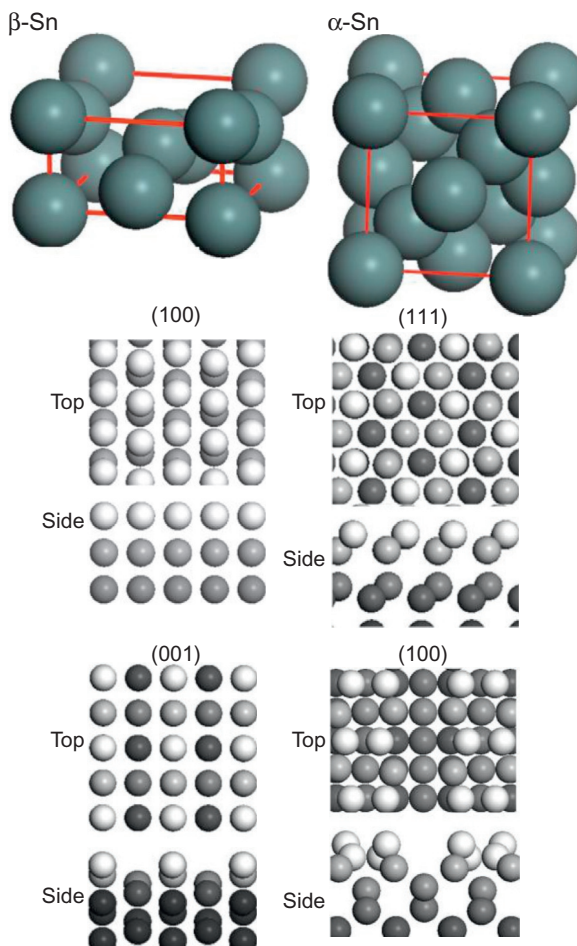


**Table 8.4** Binding energies (in eV) of Li on Sn surfaces and in bulk Sn (referenced to a Li atom)

	$\beta$ -Phase		$\alpha$ -Phase	
	(100)	(001)	(111)	(100)
On	2.16	2.55	2.30	2.20
Sub	2.08	2.52	2.48	2.27
Bulk	1.85		2.08	

Afterwards, we examined possible diffusion paths between the determined favorable adsorption sites as presented in Figure 8.13. In the case of  $\beta$ -phase, the diffusion barrier along the most favorable pathway (I), which is between sheets of Sn atoms, is only 0.04 eV (see Table 8.5). The diffusion pathway in  $\alpha$ -phase is similar to that in Si. The calculated energy barrier of 0.15 eV is also small. The lower barrier for Li diffusion in  $\beta$ -phase is related to the deformation energies at IS and TS: For the  $\beta$ -phase the deformation energy does not change during diffusion but for the  $\alpha$ -phase it increases by 0.09 eV at the TS ( $\Delta E_{IS}^{\beta} - \Delta E_{TS}^{\beta} = 0.55$  eV,  $\Delta E_{IS}^{\alpha} = 0.06$  eV,  $-\Delta E_{TS}^{\alpha} = 0.15$  eV).

A comparison between bulk Sn and Si shows that diffusion of Li within Sn bulk is kinetically more favorable than that within Si, in which the energy barrier is 0.58 eV [31]. This may be related to a smaller unit-cell volume per atom in Si ( $V_{\alpha-Si} = 20.46 \text{ \AA}^{-3}/\text{atom}$ ) compared to Sn ( $V_{\alpha-Sn} = 36.59 \text{ \AA}^{-3}/\text{atom}$ ,  $V_{\beta-Sn} = 28.59 \text{ \AA}^{-3}/\text{atom}$ ).

### 8.5.2 Sn surfaces

Afterward, we studied Li adsorption on the following Sn surfaces (see Figure 8.12):

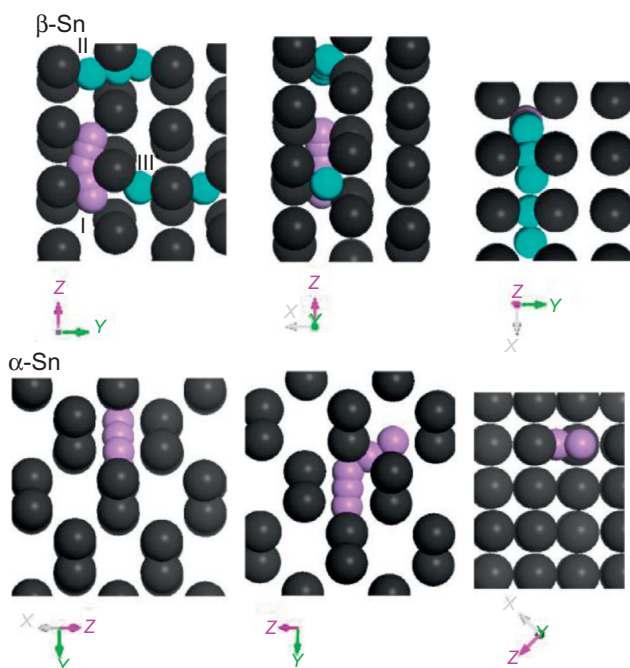


**Figure 8.13** Different pathways for Li diffusion within  $\beta$ -Sn and  $\alpha$ -Sn bulk.  
P. Kaghazchi, J. Phys.: Condens. Matter, 25 (2013) 382204.

**Table 8.5 Energy barriers (in eV) for insertion (extraction) of Li into (from)  $\alpha$ - and  $\beta$ -Sn bulk and surfaces (see Figures 8.13 and 8.14)**

	$\beta$ -Phase		$\alpha$ -Phase	
	(100)	(001)	(111)	(100)
Insertion	0.63	0.66	No	0.07
Extraction	0.55	0.63	0.18	0.14
Bulk	0.04			0.15

P. Kaghazchi, J. Phys.: Condens. Matter, 25 (2013) 382204

1. Unreconstructed  $\beta$ -Sn(100)-(1  $\times$  1)
2. Unreconstructed  $\beta$ -Sn(001)-(1  $\times$  1)
3. Unreconstructed  $\alpha$ -Sn(111)-(1  $\times$  1)
4. Reconstructed  $\alpha$ -Sn(100)-c(4  $\times$  2)

The calculated binding energies for the adsorption of Li at the most stable sites on Sn surfaces are listed in [Table 8.4](#). It was found that (similar to the case of Si) the adsorption of Li is energetically more favorable at surface and subsurface sites than in the bulk. The strongest BE is for  $\beta$ -Sn(001) ( $E_b = 2.55$  eV). This result demonstrates that when the charge process starts, Li covers first  $\beta$ -Sn(001) surfaces and then  $\beta$ -Sn(100) surfaces. The difference in binding energies of Li on  $\alpha$ -Sn surfaces is small and, therefore, Li can cover both surfaces at the same time.

Li adsorption causes restructuring of  $\beta$ -Sn surfaces ([Figure 8.14](#)). The displacements of Sn atoms at the  $\beta$ -Sn(001) surface is much larger. The  $\alpha$ -Sn surfaces are structurally more stable than  $\beta$ -Sn surfaces in the presence of Li.

For all Sn surfaces, the binding energies of Li at their subsurface sites are weaker than those at their surfaces ([Table 8.4](#)). The binding energies at subsurface sites are, however, still stronger than those in bulk Sn. Although the  $\alpha$ -Sn surface atoms remain almost at their bulk-truncated positions, the  $\beta$ -Sn surface atoms displace considerably in the presence of Li at their subsurface sites. This finding is similar to what we found for Li adsorption on the surface. This finding is in line with a recent experimental investigation, showing that upon the process of lithiation the structure of crystalline  $\alpha$ -Sn is stable, while the structure of crystalline  $\beta$ -Sn is unstable and becomes amorphous-like [[53](#)].

Finally, we studied the process of Li insertion (extraction) into (from) Sn surfaces and found that the energy barriers for diffusion of Li are much higher on  $\beta$ -Sn surfaces than on  $\alpha$ -Sn ones ([Table 8.5](#)). This is because the deformation energies (required to accommodate Li atoms) are larger at TSs than those at ISs on  $\beta$ -Sn surfaces ( $\Delta E_{IS}^{001} = 0.11$  eV,  $\Delta E_{TS}^{001} = 0.68$  eV,  $\Delta E_{IS}^{100} = 0.07$  eV,  $\Delta E_{TS}^{100} = 0.62$  eV), while the deformation energies at TSs are similar to those at ISs on  $\alpha$ -Sn surfaces ( $\Delta E_{IS}^{100} = 0.39$  eV,  $\Delta E_{TS}^{100} = 0.32$  eV,  $\Delta E_{IS}^{111} = 0.46$  eV,  $\Delta E_{TS}^{111} = 0.44$  eV).

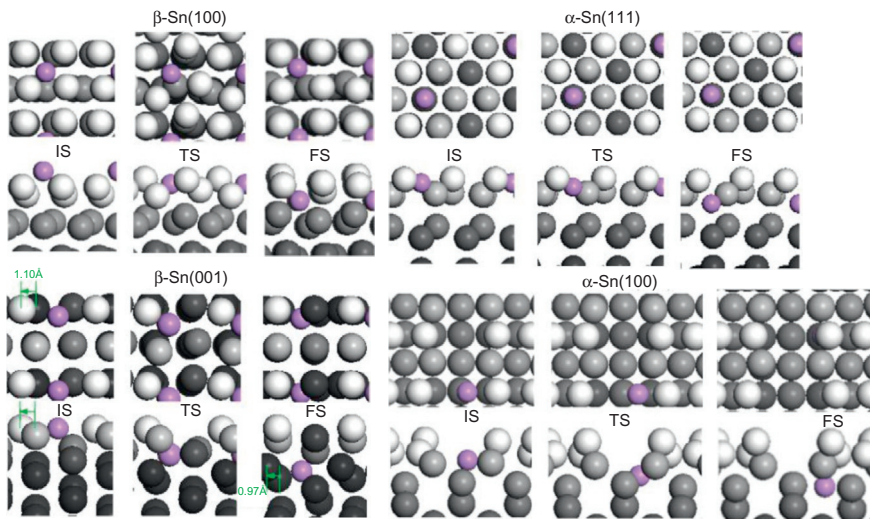


**Figure 8.14** Side and top views of the most favorable IS, TS, and FS structures for penetration of a single Li atom into the subsurface sites in  $\beta$ -Sn and  $\alpha$ -Sn surfaces.

P. Kaghazchi, J. Phys.: Condens. Matter, 25 (2013) 382204.

Because the binding energies of Li at subsurface and surface sites are only slightly different ( $<0.18$  eV), the rate of Li insertion is expected to be similar to that of Li extraction.

A comparison between the bulk and surface calculations indicate that the rate determining step for Li insertion and extraction in Sn anodes is diffusion between surface and subsurface sites. As the diffusion barriers at surfaces are lower in  $\alpha$ -phase compared to  $\beta$ -phase, Li insertion and extraction should be kinetically more favorable in nanoparticles (consisting of low-index surfaces) of the former phase. Bulk  $\beta$ -Sn is more stable than bulk  $\alpha$ -Sn at room temperature (and most likely under operation temperature of LiB). However, nanoparticles of the later phase may be stabilized in the presence of Li and electrolyte. This study is in progress in our group.

## 8.6 Role of defective graphene in lithium–air (Li–air) battery cathodes

Li–air batteries are among the most promising candidates for electric vehicles because they can store a large amount of energy density. A main problem preventing the use of these batteries is a dramatic decrease in their capacity, which arises from the blocking of the oxygen pathway due to the excessive growth of the reaction products (e.g.,  $\text{Li}_2\text{O}_2$ ) [54]. Besides many experimental studies, several *ab initio* calculations have studied this issue. For example, by using DFT calculations Xiao *et al.* [54] have found



**Figure 8.15** Structures of  $\text{Li}_2\text{O}_2$ -covered pristine graphene (left) and single-vacancy graphene (right). The calculated binding energies (BE) are also given for each structure.

that  $\text{Li}_2\text{O}_2$  monomers bind stronger to the 5–8–5 defect sites and functional groups (e.g., COOH) than to the carbon atoms of graphene. This means that  $\text{Li}_2\text{O}_2$  molecules are trapped at defective sites. Their calculations for the aggregation of  $(\text{Li}_2\text{O}_2)_n$  clusters also show that this process is unfavorable at defective sites. Finally, they showed by experimental measurements that the capacity of a LiB can increase considerably in this way.

In this section, we show that  $\text{Li}_2\text{O}_2$  molecules adsorb much stronger to single-vacant sites than to 5–8–5 defect sites or COOH molecules. Figure 8.15 shows the most stable structures for  $\text{Li}_2\text{O}_2$ /graphene with and without single-vacancy graphene. In agreement with the previous theoretical study [54], we found that there is a very weak interaction between  $\text{Li}_2\text{O}_2$  and pristine graphene. The calculated BE of 0.26 eV for  $\text{Li}_2\text{O}_2$  on perfect graphene shows that these molecules may detach from the graphene surface. However, the BE of the  $\text{Li}_2\text{O}_2$  molecule at the single-vacant site is 3.64 eV, which is much stronger than that at 5–8–5 defect sites (0.7 eV) or to COOH molecules (0.9 eV) calculated by Xiao *et al.* [54]. Because of a strong bond between O and Li atoms in the  $\text{Li}_2\text{O}_2$  molecule the O atom that binds to the vacant site does not detach from the  $\text{Li}_2\text{O}_2$  molecule (see Figure 8.15). This finding shows that single-vacant sites can trap the discharge products much more strongly than divacant sites or functional groups. Further study of aggregation of  $\text{Li}_2\text{O}_2$  clusters is necessary to elucidate the role of single-vacant sites in the performance of Li–air batteries.

## 8.7 Conclusions and outlook

Using DFT to study mechanisms of Li diffusion in Si and Sn anode materials as well as the structure of Si/electrolyte and  $\text{Li}_2\text{O}_2$ /graphene interfaces, in this chapter, we demonstrated that *ab initio* calculations can be used to simulate properties and processes in Li-based batteries.

The DFT calculations for Li incorporation in Si showed that the penetration of Li at Si surfaces (and nanoparticles) is a complicated process that depends strongly on the atomic structure of the surface and can also depend on the Li concentration. The lowest penetration barrier is found for Si(100) at a high coverage of Li. The mechanism of the Li penetration in this case is a *pushing* mechanism in which diffusing Li atoms push each other to penetrate to the Si anode. This mechanism is only possible for a fully Li-covered surface with a deep atomic trough. As the repulsive Li–Li interactions are very small for  $\Theta \leq 1$  GML (see Figure 8.4), Li atoms will first cover the

surface of Si nanostructures and then they start to penetrate. A more realistic model to study Li penetration in Si nanostructures is a model that also takes into account the interaction between Li/Si and electrolyte.

As a first step toward a realistic modeling of the Si-electrode/electrolyte interface, we investigated the structure of the interface between Li/Si surfaces and EC (a commercially used solvent material). The *ab initio* DFT calculations for the EC/Si interface showed that the structure of the interface depends strongly on the atomic structure of the Si surface. Although EC molecules (solvent) remain intact on Si(100), they dissociate to  $C_3H_4O_2$  molecules and O atoms on Si(111). The resulting  $C_3H_4O_2$  molecules bind via their unsaturated C atoms to the Si(111) surface atoms and the dissociated O atoms bind to neighboring Si surface atoms and also preadsorbed Li adatoms. This work shows that EC molecules dissociate on Li/Si(111) surface even before applying an external potential. This process can be viewed as the first step in the process of SEI formation. During the charge process, transfer of electrons to EC molecules may dissociate more and more EC molecules on Si(111) and even on Si(100). However, as we showed, a tendency for the faster nucleation of a SEI layer over Si{111} facets is larger than over Si{100} facets. Because the formation of SEI affects the rate of Li diffusion, the structure sensitivity in the decomposition of EC (and thereby SEI formation) may be a reason for the experimentally observed anisotropic lithiation of Si nanowires [55]. The next logical steps toward the modeling of Si/electrolyte interfaces are considering the real concentration of EC and also effects of Li salt (e.g., LiPF<sub>6</sub>) molecules. With this information, one can perform a realistic simulation of initial stages of SEI formation and also Li penetration to Si nanostructures.

Our DFT results for the diffusion of Li in Sn bulk and surfaces showed a strong structure sensitivity in the energy barriers. While the rate determining step of this process is bulk diffusion in  $\alpha$ -Sn, it is surface penetration in  $\beta$ -Sn. Insertion of Li through  $\alpha$ -Sn surfaces is much more favorable than  $\beta$ -Sn surfaces. Our calculations suggest that Li intercalation into  $\alpha$ -Sn nanoparticles is much more favorable than  $\beta$ -Sn ones. The next step toward a more realistic modeling of lithiation of Sn nanostructures is determining the structure of Sn/electrolyte interfaces and a study of the incorporation of Li at the interfaces.

The DFT calculations for the adsorption of Li<sub>2</sub>O<sub>2</sub> on graphene demonstrated that single-vacancy-defective graphene can strongly trap Li<sub>2</sub>O<sub>2</sub> molecules. The binding energy at this defective site is much stronger than that at divacancy 5–8–5 sites. This finding shows that graphene with a high density of vacant sites can improve the capacity of Li–air batteries, which is in agreement with previous experimental and theoretical results. The next logical step in this research is modeling aggregation of Li<sub>2</sub>O<sub>2</sub> on defective graphene in the presence of electrolyte.

## Acknowledgments

The author gratefully acknowledges support from the “Bundesministerium für Bildung und Forschung” (BMBF).

## References

- [1] F. Zhou, T. Maxisch, G. Ceder, *Phys. Rev. Lett.* 97 (2006) 155704–155710.
- [2] J. Yang, J.S. Tse, *J. Phys. Chem. A* 115 (2011) 13045.
- [3] D. Kramer, G. Ceder, *Chem. Mater.* 21 (2009) 3799.
- [4] A. Van der Ven, G. Ceder, *J. Power Sources* 97 (2001) 529.
- [5] J. Reed, G. Ceder, A. Van der Ven, *Electrochem. Solid-State Lett.* 4 (2001) A78.
- [6] F. Zhou, M. Cococcioni, K. Kang, G. Ceder, *Electrochem. Commun.* 6 (2004) 1144.
- [7] C.K. Chan, H. Peng, G. Liu, K. McIlwrath, X.F. Zhang, R.A. Huggins, Y. Cui, *Nat. Nanotechnol.* 3 (2008) 31.
- [8] J.W. Wang, X.H. Liu, S.X. Mao, J.Y. Huang, *Nano Lett.* 12 (11) (2012) 5897.
- [9] H. Li, X. Huang, L. Chen, Z. Wu, Y. Liang, *Electrochem. Solid-State Lett.* 2 (1999) 547.
- [10] H. Ma, F. Cheng, J. Chen, J. Zhao, C. Li, Z. Tao, J. Liang, *Adv. Mater.* 19 (2007) 4067.
- [11] M. Born, J.R. Oppenheimer, *Ann. Phys.* 84 (1927) 457.
- [12] A. Groß, *Theoretical Surface Science*, Springer-Verlag, Berlin, 2003.
- [13] A. Szabo, N. Ostlund, *Modern Quantum Chemistry*, Dover, New York, 1989.
- [14] R.J. Bartlett, *J. Chem. Phys.* 93 (1989) 1697.
- [15] C. Müller, M.S. Plesset, *Phys. Rev.* 46 (1934) 618.
- [16] P. Hohenberg, W. Kohn, *Phys. Rev. B* 136 (1964) 846.
- [17] W. Kohn, L. Sham, *Phys. Rev. A* 140 (1965) 1133.
- [18] J.P. Perdew, K. Burke, M. Ernzerhof, *Phys. Rev. Lett.* 88 (1996) 3865.
- [19] The DFT calculations for sections III, V, and VI were performed using the SeqQuest code [C. Verdozzi, P.A. Schultz, R.Q. Wu, A.H. Edwards, N. Kioossis, *Phys. Rev. B* 66 (2002) 125408] with localized basis sets represented by linear combinations of contracted Gaussian functions and norm-conserving pseudopotentials. The DFT calculations for section IV have been performed using the projector-augmented planewave code *vasp* [G. Kresse, J. Furthmüller, *Phys. Rev. B*, 54 (1996) 11169; *Comput. Mater. Sci.*, 6 (1996) 15; G. Kresse, D. Joubert, *Phys. Rev. B*, 59 (1999) 1758.]
- [20] U. Kasavajjula, C. Wang, A.J. Appleby, *J. Power Sources* 163 (2007) 1003.
- [21] Q. Zhang, W. Zhang, W. Wan, Y. Cui, E. Wang, *Nano Lett.* 10 (2010) 3243.
- [22] S. Huang, T. Zhu, *J. Power Sources* 196 (2011) 3664.
- [23] L.Y. Beaulieu, T.D. Hatchard, A. Bonakdarpour, M.D. Fleischauer, J.R. Dahn, *J. Electrochem. Soc.* 150 (2003) 1457.
- [24] C.K. Chan, H. Peng, G. Liu, K. McIlwrath, X.F. Zhang, R.A. Huggins, Y. Cui, *Nat. Nanotechnol.* 3 (2008) 31.
- [25] C.-M. Park, J.-H. Kim, H. Kimc, H.-J. Sohn, *Chem. Soc. Rev.* 39 (2010) 3115.
- [26] M. Horamani, Ph.D. thesis, Freie University Berlin, 2006.
- [27] N. Moll, M. Bockstedte, M. Fuchs, E. Pehlke, M. Scheffler, *Phys. Rev. B* 52 (1995) 2550.
- [28] C. Kittel, *Introduction to Solid State Physics*, Wiley, New York, 1996.
- [29] L.T. Canham, *Properties of Silicon*, Electronic Materials Information Service (EMIS) Datareviews Series, vol. 4, INSPEC, London, 2012, p. 455.
- [30] D.J. Eaglesham, A.E. White, L.C. Feldman, N. Moriya, D.C. Jacobson, *Phys. Rev. Lett.* 70 (1993) 1643.
- [31] S.C. Jung, Y.K. Han, *Phys. Chem. Chem. Phys.* 13 (2011) 21282.
- [32] G. Bussetti, B. Bonanni, S. Cirilli, A. Violante, M. Russo, C. Goletti, P. Chiaradia, O. Pulci, M. Palummo, R.D. Sole, P. Gargiani, M.G. Betti, C. Mariani, R.M. Feenstra, G. Meyer, K.H. Rieder, *Phys. Rev. Lett.* 106 (2011) 067601.
- [33] G. Xu, B. Deng, Z. Yu, S.Y. Tong, M.A. Van Hove, F. Jona, I. Zasada, *Phys. Rev. B* 70 (2004) 045307.

- [34] D. Badt, H. Wengelnik, H. Neddermeyer, *J. Vac. Sci. Technol. B* 12 (1994) 2015.
- [35] P. Kaghazchi, *Appl. Phys. Lett.* 102 (2013) 093901.
- [36] K. Xu, *Chem. Rev.* 104 (2004) 4303.
- [37] D. Aurbach, Y. Ein-Eli, O. Chusid, Y. Carmeli, M. Babai, H. Yamin, *J. Electrochem. Soc.* 141 (1994) 603.
- [38] P. Arora, R.E. White, M. Doyle, *J. Electrochem. Soc.* 145 (1998) 3647.
- [39] D. Aurbach, B. Markovsky, A. Shechter, Y. Ein-Eli, H.A. Cohen, *J. Electrochem. Soc.* 143 (1996) 3809.
- [40] D. Aurbach, M.D. Levi, E. Levi, A. Schechter, *J. Phys. Chem. B* 101 (12) (1997) 2195.
- [41] P. Verma, P. Maire, P. Nov'ak, *Electrochim. Acta* 55 (2010) 6332.
- [42] J. Rohrer, P. Kaghazchi, *ChemPhysChem* 15 (2014) 3950.
- [43] R. Bader, *Atoms in Molecules: A Quantum Theory*, Oxford University Press, New York, 1990.
- [44] G. Henkelman, H. Jónsson, *J. Chem. Phys.* 113 (2000) 9978.
- [45] H. Jónsson, G. Mills, K.W. Jacobsen, Nudged elastic band method for finding minimum energy paths of transitions, in: B.J. Berne, G. Ciccotti, D.F. Coker (Eds), *Classical and Quantum Dynamics in Condensed Phase Simulations*, World Scientific, 1998, p. 385.
- [46] G. Henkelman, B.P. Uberuaga, H. Jónsson, *J. Chem. Phys.* 113 (2000) 9901.
- [47] K. Leung, J.L. Budzien, *Phys. Chem. Chem. Phys.* 12 (2010) 6583.
- [48] B. Liu, Z. Ping Guo, G. Du, Y. Nuli, M. Faiz Hassan, D. Jia, *J. Power Sources* 195 (2010) 5382.
- [49] H. Kim, B. Han, J. Choo, J. Cho, *Angew. Chem. Int. Ed.* 47 (2008) 10151.
- [50] P. Kaghazchi, *J. Phys. Condens. Matter* 25 (382204) (2013).
- [51] P. Kaghazchi, *J. Chem. Phys.* 138 (2013) 054706.
- [52] A. Busch, R. Kern, *Solid State Phys.* 11 (1961) 1.
- [53] H.S. Im, Y.J. Cho, Y.R. Lim, C.S. Jung, D.M. Jang, J. Park, F. Shojaei, H.S. Kang, *ACS Nano* 7 (12) (2013) 11103.
- [54] J. Xiao, D. Mei, X. Li, W. Xu, D. Wang, G.L. Graff, W.D. Bennett, Z. Nie, L.V. Saraf, I. Aksay, J. Liu, J.-G. Zhang, *Nano Lett.* 11 (2011) 5071.
- [55] X.H. Liu, J.W. Wang, S. Huang, F. Fan, X. Huang, Y. Liu, S. Krylyuk, J. Yoo, S.A. Dayeh, A.V. Davydov, S.X. Mao, S.T. Picraux, S. Zhang, J. Li, T. Zhu, J.Y. Huang, *Nat. Nanotechnol.* 7 (2012) 749.

# Aging and degradation of lithium-ion batteries

9

N. Omar<sup>1</sup>, Y. Firouz<sup>1</sup>, H. Gualous<sup>2</sup>, J. Salminen<sup>3</sup>, T. Kallio<sup>4</sup>, J.M. Timmermans<sup>1</sup>, Th. Coosemans<sup>1</sup>, P. Van den Bossche<sup>1</sup>, J. Van Mierlo<sup>1</sup>

<sup>1</sup>Vrije Universiteit Brussel, Brussels, Belgium; <sup>2</sup>Université de Caen Basse Normandie, Cherbourg-Octeville, France; <sup>3</sup>VTT Technical Research Centre of Finland, Espoo, Finland;

<sup>4</sup>Aalto University, Espoo, Finland

## 9.1 Introduction

Since the beginning of the automobile era, the internal combustion engine (ICE) has been used for vehicular propulsion. In addition, motor vehicles powered by the ICE are significant contributors to air pollutants and greenhouse gasses linked to global climate change [1,2]. As the global economy begins to strain under the pressure of rising petroleum prices and environmental concerns, research has spurred the development of various types of clean energy transportation systems such as hybrid electric vehicles, battery electric vehicles, and plug-in hybrid electric vehicles [3,4]. When establishing energy storage technologies one has to consider critical aspects such as the output power during acceleration, the efficient use of the regenerative energy and the life cycle; no current battery technology can meet these often-concurrent objectives [4–7]. In the last decade, lithium-ion battery technology has acquired considerably high attention due to the beneficial performances in terms of energy, power, and life cycle compared to lead-acid and nickel metal-hydride batteries [8,9].

The term *lithium-ion* encompasses a number of chemistries based on the materials used in the anode and cathode.

It is generally well known that the lifetime of a battery is the key issue in the assessment of the most appropriate battery technology in environmental friendly vehicles [10,11]. In Ref. [12], an extended life cycle analysis has been performed for graphite anode/lithium iron phosphate cathode (C/LFP) batteries. The analysis concluded that C/LFP has a generally long life cycle. In addition to this work, Omar [13] performed a number of life cycle tests on different lithium-ion battery brands and chemistries. They observed that the cycle life of LFP and lithium titanate oxide anode/graphite cathode batteries (LTO/C) are longer than lithium nickel manganese cobalt oxide (C/NMC) or lithium nickel cobalt aluminum oxide (C/NCA) batteries.

Following these studies, Wang *et al.* [14] developed a similar life cycle model for C/LFP batteries. The model has been developed based on statistical experimental results, whereby the proposed battery has been cycled at different operating conditions for ambient temperature, current rates, and depth of discharge. The model gives good results in the investigated operating range.

However, from these studies, we can conclude that these works were limited to cycle life and the impact of calendar life was not considered.

Eddahech *et al.* [15] performed a calendar life evaluation for a C/NMC (12 Ah) battery at different operating conditions (30, 45, and 60 °C; 30% state of charge (SoC), 65% SoC, and 100% SoC). They concluded that the lifetime of the battery decreases the more the working temperature and SoC increases. In addition, they observed that the main contributors to aging are the increase of the internal resistance and capacity degradation. In Ref. [16], it is documented that the degradation is due to the loss of the active and mainly cyclable lithium ions. Furthermore, the growths of the solid electrolyte interface (SEI) and decline of the electrolyte conductivity are the major fading mechanisms [17]. These results have been also confirmed by Zhang and White [18] through experimental data and numerically with a single particle model. From their analysis, they concluded that the battery fading mechanisms changes nonlinearly as a function of the working temperature.

However, Kassem *et al.* [19] carried out a similar analysis on C/LFP batteries and they concluded that the capacity fade at higher working temperatures is attributed to the side reactions that take place at anode level due to the decomposition of the solvent, which leads to the growth of the SEI. However, the side reactions at the cathode level are less prominent than at the anode level.

From all these studies, we can conclude that the behavior of lithium-ion batteries, in particular for C/LFP batteries during calendar life at different storage conditions, is not well identified because the investigation works are only performed at high operating temperatures and, thus, an extended analysis in a wide operating window is still unknown. Therefore, there is a need for having a comprehensive analysis whereby the experimental data should be combined with numerical tools and postmortem analysis for having a clear overview of battery behavior.

## 9.2 Methodology

In order to have a clear view of battery behavior during calendar life, in the framework of this study, the methodology as presented by Figure 9.1 has been proposed.

As we can observe, the investigated batteries (C/LFP 7 Ah, pouch) have been investigated at working temperatures (60, 40, 25, 10, 0, and –10 °C) and different SoC levels (100%, 75%, 50%, and 25%).

The batteries have been stored at these conditions during 44 weeks (with inspection at 75% SoC, which was at 32 weeks). Every 4 weeks, the battery performances were checked by standard procedures at 25 °C based on both a capacity test and a hybrid pulse power characterization (HPPC) test for evaluation of the change in the internal resistance.

The capacity test was done at  $1 I_t^1$  charging (constant current constant voltage<sup>2</sup>) and then followed by the discharge step at  $1 I_t$  until the minimum voltage (2 V) was reached. The rest time between the charge and discharge steps was 30 min.

<sup>1</sup> The current  $I_t$  represents the discharge current in amperes during 1 h discharge and  $C$  is the measured capacity of a cell as specified in the standard IEC 61434 [20,21].

<sup>2</sup> Constant current constant voltage: the batteries have been charged at  $1 I_t$  until 3.65 V and then the voltage has been kept constant at 3.65 V until the current has been decreased to 0.7 A.

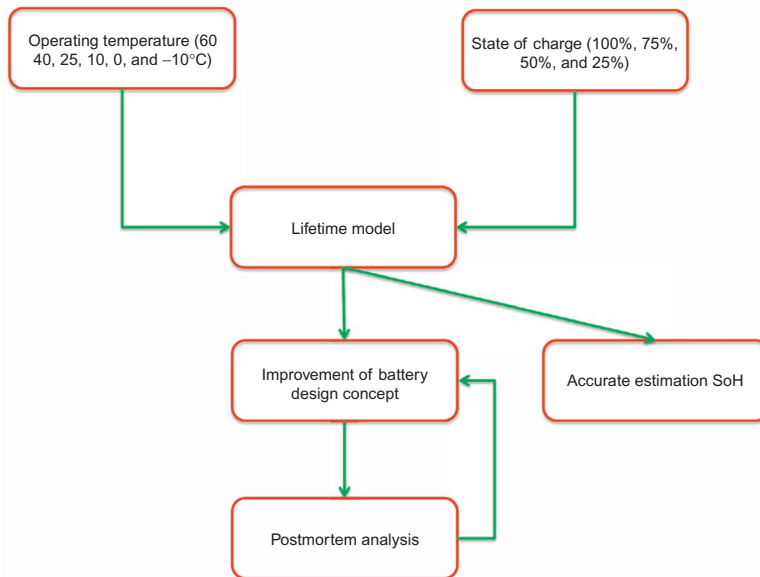


**Figure 9.1** Used methodology.

Regarding the HPPC protocol, the test was carried out at different current rates ( $0.33 I_t$ ,  $1 I_t$ ,  $2 I_t$ ,  $3 I_t$ ,  $5 I_t$ ,  $7 I_t$ ) from 100% SoC to 0% SoC with steps of 5% SoC. The charge and discharge HPPC pulses were 10 s.

In this study, the evolution of the capacity degradation and the internal resistance were investigated and analyzed.

Once the batteries reach their end of life (80% of the measured rated capacity), batteries will undergo postmortem analysis for better understanding of the physical aging phenomena inside the batteries.

## 9.3 Results

### 9.3.1 Capacity degradation

Figures 9.2–9.5 show the results of the capacity evolution as a function of the storage time at different SoC levels and storage temperatures.

As we generally can observe, the battery capacity decreases faster the higher the SoC of the battery. As an example, the capacity degradation at 40 °C storage temperature is 20% after 25 weeks, 20% after 28 weeks, and 19% after 44 weeks at 100% SoC, 50% SoC, and 25% SoC, respectively. This evolution also can be found at the other storage temperatures (60, 25, 10, 0, and -10 °C). However, the impact of the storage temperature is more significant than the SoC level. When we compare

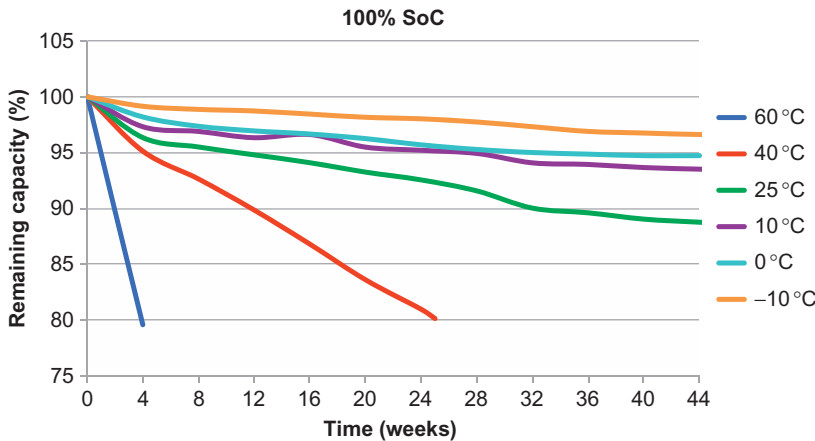


**Figure 9.2** Evolution of capacity degradation versus storage time at 100% SoC.

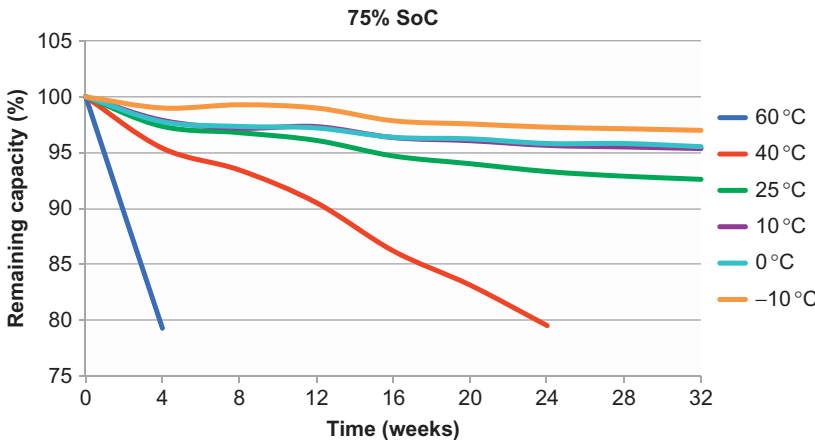


**Figure 9.3** Evolution of capacity degradation versus storage time at 75% SoC.

the mutual results, one can recognize for example at 50% SoC, the capacity degradation is 20% after 5 weeks, 20% after 28 weeks, 8% after 44 weeks, 1% after 44 weeks, and 0% after 44 weeks at storage temperatures 60, 40, 25, 10, 0, and  $-10^{\circ}\text{C}$ , respectively. Therefore, in general we can conclude that the impact of the storage temperature is more harmful than the SoC level, as shown in Figure 9.4.

From this point of view, it is clear that from the control strategy of the battery system and the vehicle that the battery needs to be kept at the desired storage temperature and SoC level when it will not be used for a long period.

The above-indicated results also have been confirmed by many researchers [22–24]. In Refs. [22–26], it is reported that the capacity degradation at higher temperatures is mainly attributed to the formation of the SEI growth as a function of time.

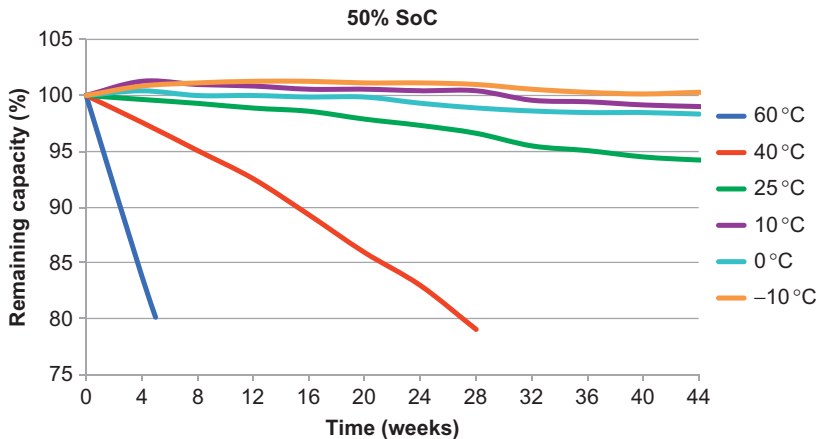


**Figure 9.4** Evolution of capacity degradation versus storage time at 50% SoC.

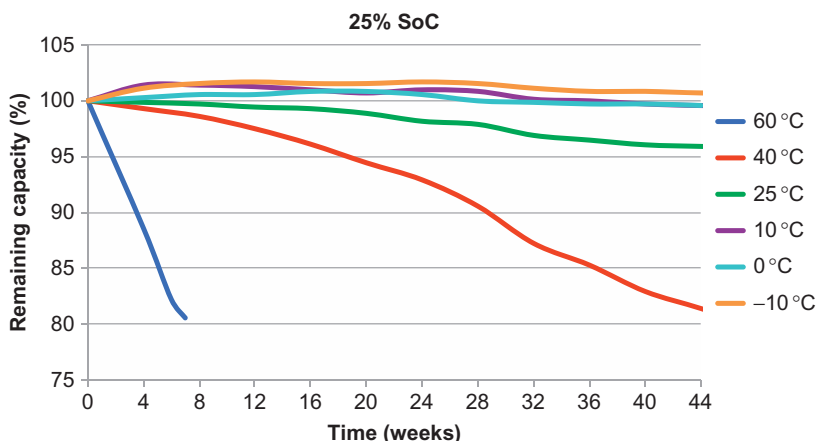


**Figure 9.5** Evolution of capacity degradation versus storage time at 25% SoC.

It was also concluded that the resistance of the battery increases and that the growth of SEI leads to a square root time dependency. Researchers at Aachen University [25] concluded that capacity fades at higher SoC levels, which implies huge overpotential at the electrode/electrolyte interface, and that calendar life can be modeled using  $t^{0.75}$  dependency [25].

The presented results in Figures 9.2 through 9.5 indicate that capacity degradation for the investigated battery type in this study shows an exponential relationship as a function of the storage time expressed by Equation (9.1):

$$\text{Capacity degradation}(t) = ae^{(bt_{\text{stor}})} + c^{(dt_{\text{stor}})} \quad (9.1)$$

### 9.3.2 Evolution of battery behavior based on impedance spectroscopy

In Section 9.3.1, the evolution of battery behavior based on capacity tests has been investigated. The experimental results show that the storage temperature has a significant impact on battery capacity degradation. However, the results could not reveal if the obtained results are due to specific physical changes in the battery. Therefore, in this section, the battery characteristics have been investigated based on electrochemical impedance spectroscopy (EIS) to examine this issue. For this purpose, the measurements have been conducted on an EIS potentiostat of Bio-Logic HCP-1500. The battery cells have been characterized every 4 weeks at 25 °C at the proposed SoC conditions as mentioned earlier in Section 9.2. The measurements have been carried out from 10 kHz to 50 mHz.

Generally, the EIS response can be considered as inductive at high frequencies and capacitance at low frequency. The first one represents more the metal connectors while the second one stands for the charge transfer phenomena.

Figures 9.6–9.10 show the Nyquist plot, whereby the imaginary part of the impedance is expressed as a function of the real part. From these results, one can indicate that the ohmic resistance of the cell (interfacial impedance) increases at higher storage temperatures during the calendar life of the battery. The ohmic resistance based on the Nyquist plot represents the intersection of the impedance with the  $x$ -axis. However, the variation on this parameter decreases the more the storage temperature goes down. The observation obtained is completely in line with the results in Section 9.3.1. Furthermore, the Nyquist plots show that the imaginary part of the impedance is

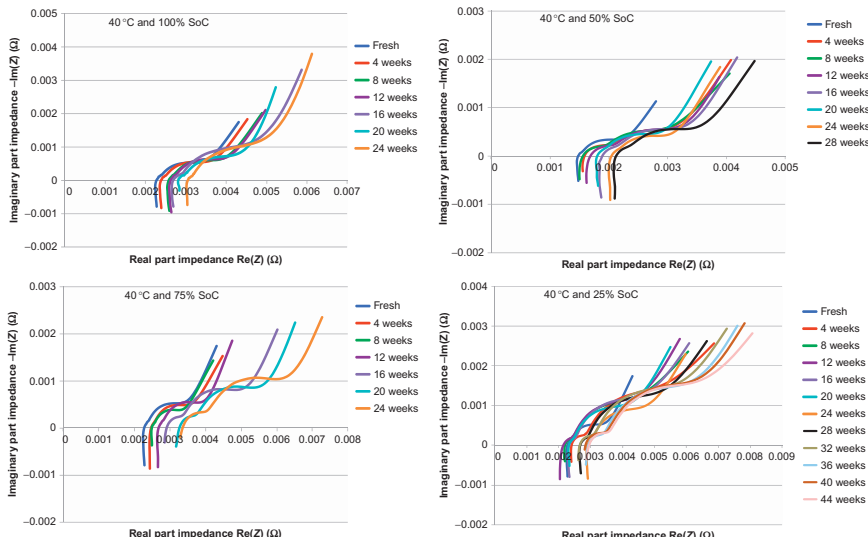


**Figure 9.6** Evolution of battery behavior at 40 °C calendar life based on impedance spectroscopy.

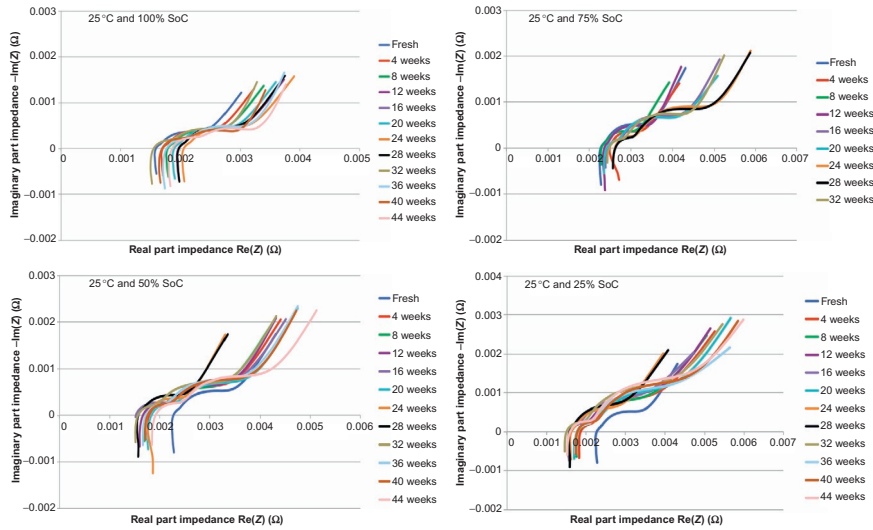


**Figure 9.7** Evolution of battery behavior at 25 °C calendar life based on impedance spectroscopy.

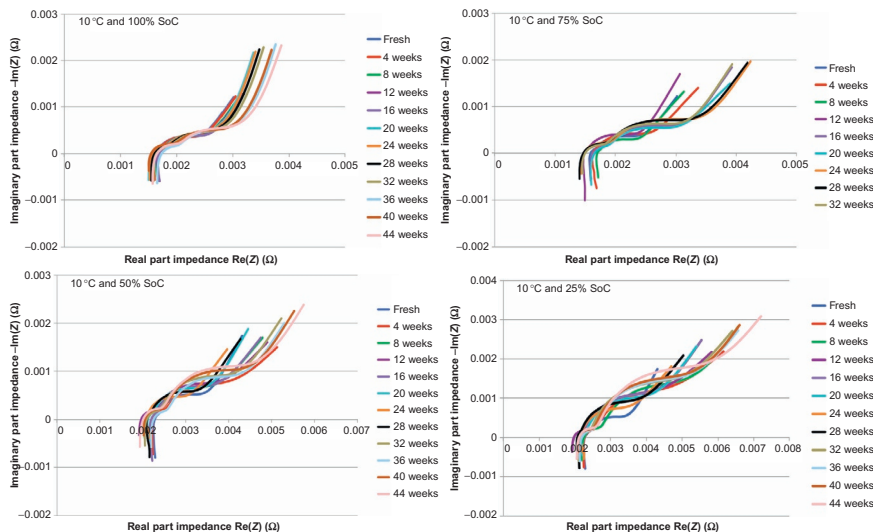


**Figure 9.8** Evolution of battery behavior at 10 °C calendar life based on impedance spectroscopy.

changing during calendar life. This indicates that the capacitance of the battery decreases based on the following relationship:

$$\text{Im}(Z) = \frac{1}{2\pi fC(f)} \quad (9.2)$$

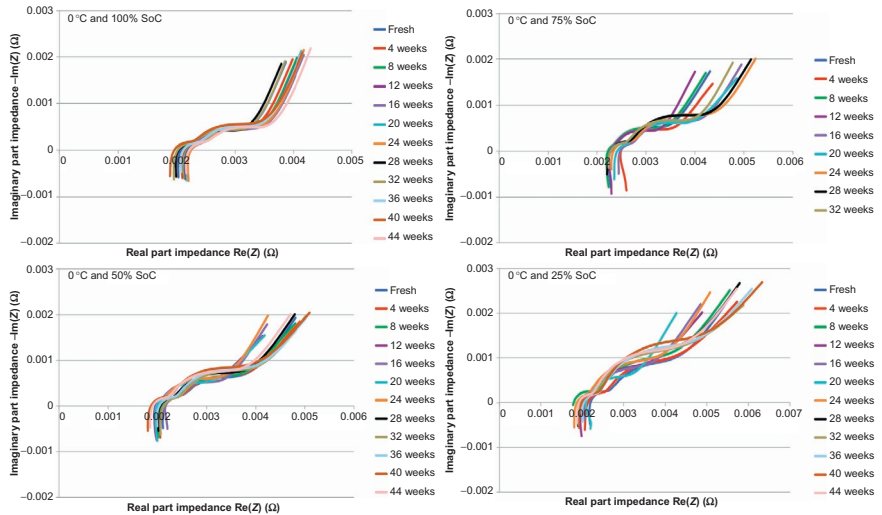


**Figure 9.9** Evolution of battery behavior at 0 °C calendar life based on impedance spectroscopy.

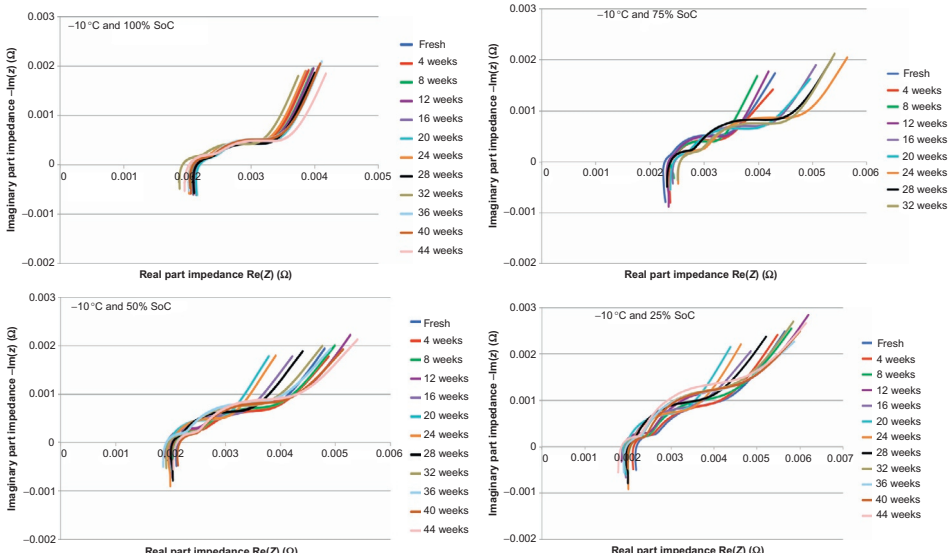


**Figure 9.10** Evolution of battery behavior at -10 °C calendar life based on impedance spectroscopy.

where  $f$  represents the frequency,  $C$  is the capacitance, and  $\text{Im}(Z)$  the imaginary part of the impedance.

In Refs. [27,28], it is documented that the capacitance characteristic is related to the surface phenomena that occur mostly on the negative electrode. If the charge transfer

resistance increases, which represents the semicircle in the Nyquist plot, this implies that the access time of the lithium-ion to the surface is longer. This observation confirms that the SEI layer growths, which contribute to internal resistance, increase and capacity degradation as a consequence. This result has been confirmed by [18] for graphite/lithium cobalt oxide pouch cells. They observed that storing the battery at high temperatures implies that some electroactive surface area becomes inaccessible due to side reactions and isolation of particles from the electrode surface. In addition, these results have been confirmed as well at half-cell level by Ref. [29].

Furthermore, from this analysis it is notable that the variation in the plots becomes smaller the more the storage temperature decreases. This results in the conclusion that the formation of the SEI layer at lower temperature grows less fast. From this point of view, the SEI consumes more lithium-ion and electrolyte decomposition accelerates at higher temperatures, which results to lower conductivity as well. These results have been confirmed by Ref. [30].

Here, it should be noted that according to the Nyquist plot the ohmic resistance (interfacial impedance) changes during the calendar life, storage temperature, and SoC. At lower SoC levels, the semicircle becomes wider and, thus, the charge transfer resistance increases. This means that the battery characteristics from the modeling point of view changes. This leads to the conclusion that development of an appropriate battery model, which is able to predict the battery behavior at different operating conditions, is complicated.

### 9.3.3 Changes of battery models parameters

In this section, the earlier-performed analysis has been extended, whereby the battery behavior has been analyzed based on the evolution of the model parameters. Therefore, the FreedomCar battery model has been used as shown in Figure 9.11. The FreedomCar battery model consists of the open circuit voltage, ohmic resistance  $R_o$ , polarization resistance  $R_p$ , and polarization capacitance  $C$ .

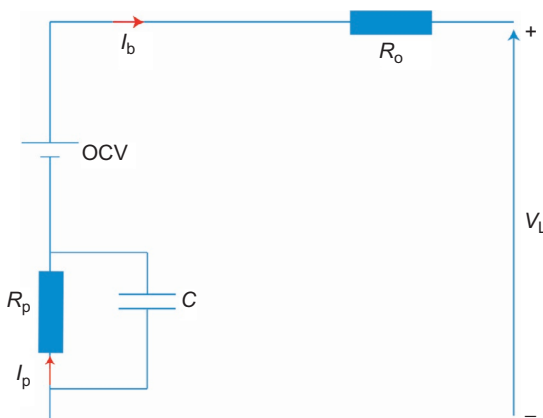


**Figure 9.11** First order FreedomCar battery model [12].

Prior to starting with estimation of battery model parameters, the batteries have been characterized based on the HPPC using 10 s pulses as illustrated in [Figure 9.12](#) [13]. In order to evaluate the model parameters as to function of current rate and SoC, the test has been repeated at the current rates and SoC values as specified in [Section 9.2](#). However, in this study the results of the model parameters at 50% SoC and current level 5  $I_t$  are proposed.

The first results of the HPPC test are shown in [Figures 9.13–9.16](#). In these figures, the total resistance during the 10 s pulse is summarized. From the obtained results one

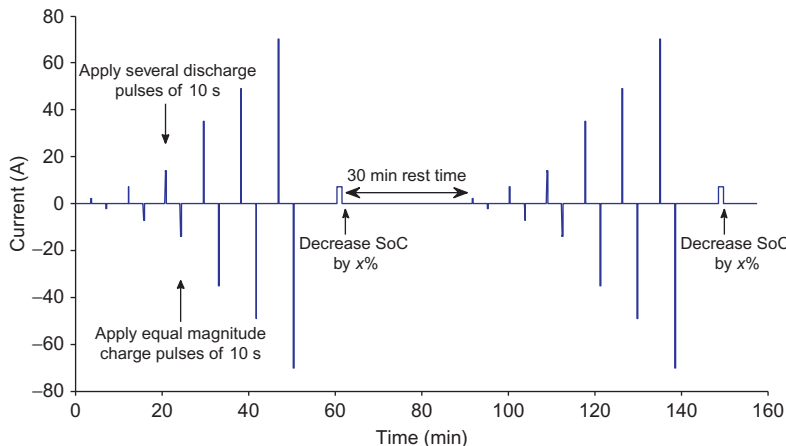


**Figure 9.12** Hybrid pulse power characterization test.

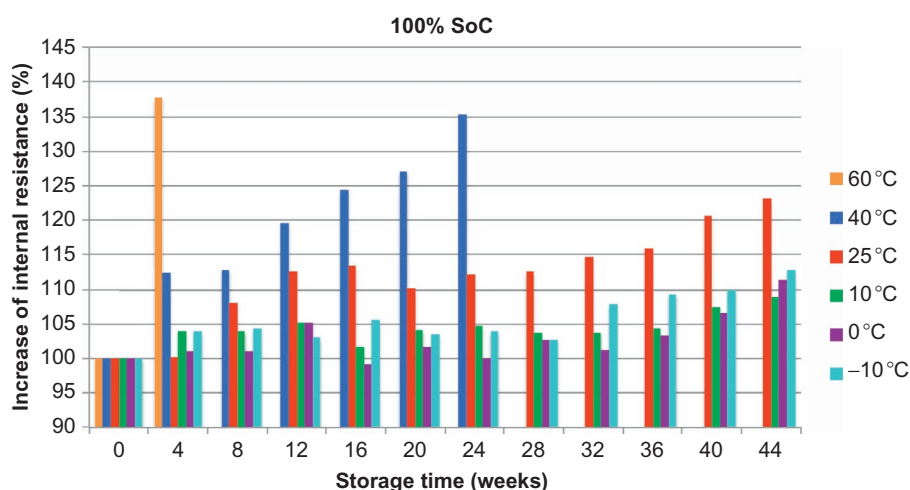


**Figure 9.13** Evolution of internal resistance versus time at 100% SoC.

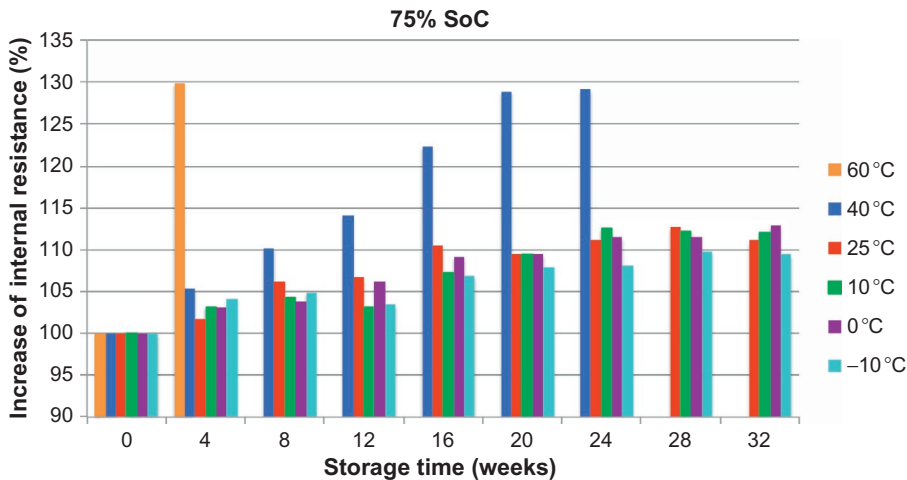


Figure 9.14 Evolution of internal resistance versus time at 75% SoC.

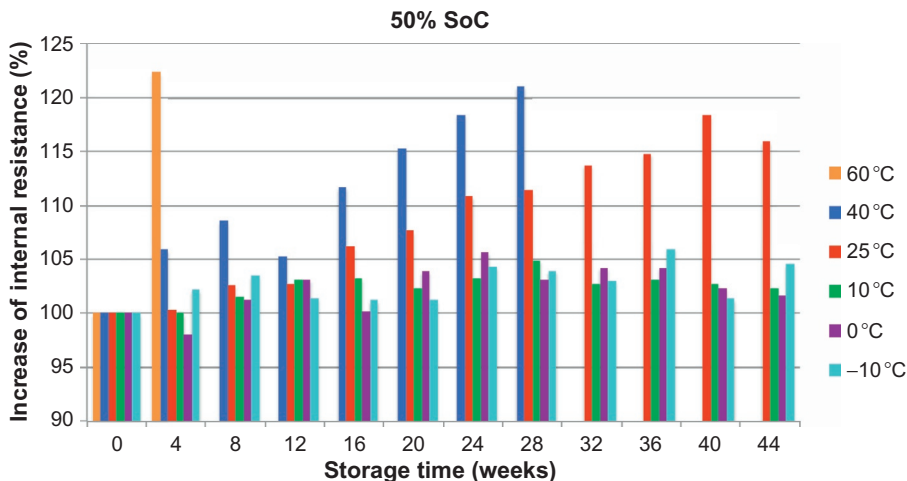
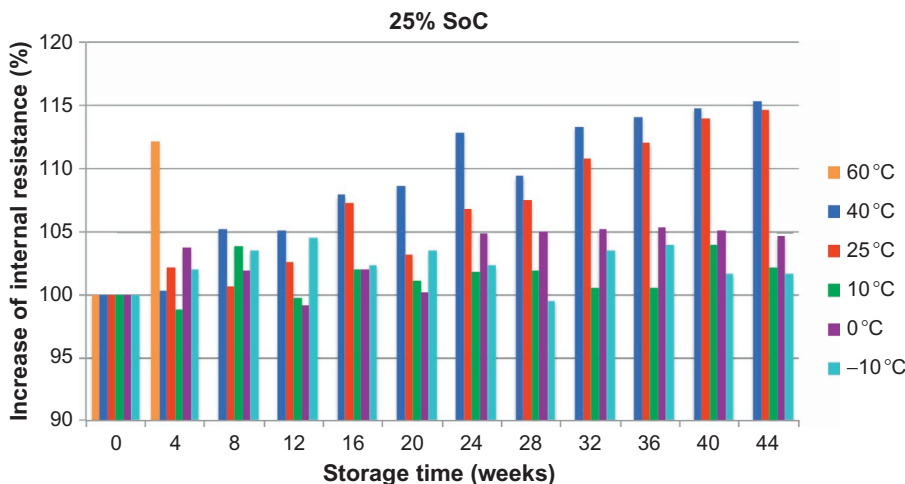


Figure 9.15 Evolution of internal resistance versus time at 50% SoC.

can notice that the internal resistance of the battery is changing remarkably. The increase of the resistance is particularly notable at higher storage temperatures and SoC levels. The increase of the resistance at 100% SoC and 40 °C is 135% after 24 weeks compared to 123% at 25 °C after 44 weeks. Here it should be noted that the battery at 25 °C does not reach its end of life. Furthermore, the increase of the resistance becomes smaller the more the storage temperature decreases. These results are in line with the performed capacity test and EIS measurements. In addition, these results have been confirmed by many studies [19–33].



**Figure 9.16** Evolution of internal resistance versus time at 25% SoC.

Kassem *et al.* [19] concluded that the decrease of the capacity is more prominent at higher storage temperatures. They conducted similar analyses at SoC levels (30%, 65%, and 100%) and storage temperatures (30, 45, and 60 °C). All examined batteries showed significant capacity fade at temperatures exceeding 30 °C. Lithium-ion loss has been identified as the source of capacity fade. This fade has been attributed to the side reactions that occur at the anode level, where electrolyte decomposition occurs and the SEI layer grows. A bigger SEI layer results in higher internal resistance, as we also observed based on our results.

However, Zhang and White [18] concluded that the lithium-ion loss is not the only source for capacity fading and increase of internal resistance. They observed that there is also a dramatic decrease of the active material. Such decrease has been related to loss of contacts between the particles during the storage test. This observation also has been confirmed by Ref. [29] at the half-cell level. These measurements were based on lithium cobalt oxide (C/LiCoO<sub>2</sub>)-based batteries, which are more sensitive to higher operating temperatures versus C/LiFePO<sub>4</sub>.

Dupré *et al.* [31] performed an extended analysis on C/LiFePO<sub>4</sub> batteries based on the MAS-NMR technique (magic angle spinning–nuclear magnetic resonance spectroscopy) to investigate the formation of species on the surface of the electrode. They came to the conclusion that the increase of the storage temperature (e.g., 55 °C in their case and for the investigated C/LiFePO<sub>4</sub> battery at  $\pm 3.2$  V) accelerates the formation of organic species in the surface of the electrode. However, after 1 month of investigation no passivation state was observed. The organic species results from bad particle contacts and inhomogeneous aging on the surface of the electrode. In addition, this process is also associated with unequal potential distribution and an unstable electrochemical process as a consequence.

Following this study, Wohlfahrt-Mehrens *et al.* [32] concluded that capacity fade and increase of internal resistance at higher temperatures is mostly attributed to structural changes and side reactions with the electrolyte, which leads to the formation of salt and  $H_2O$  impurities in the electrolyte. However, the results cannot be generalized, as the research has been done based on the lithium manganese oxide battery ( $C/LiMn_2O_4$ ). Also, the composition of the electrolyte itself has a huge effect on the degradation mechanisms. Different organic electrolyte mixtures are used for different electrode materials specifically to optimize performance and longevity.

Käbitz *et al.* [33] performed a similar study on  $C/LiNi_{1/3}Mn_{1/3}Co_{1/3}O_2$  batteries and they found that storing the batteries at 50% SoC and at storage temperature 60 °C results to exponential capacity fade and internal resistance increase. They observed as well that the increase of the resistance at 60 °C is 150% higher than at 25 °C after 400 days of calendar life. By comparing their results with ours, one can observe that the increase of the internal resistance is smaller. This difference is related to the different type of batteries that have been investigated. In addition, in our case, operating conditions of the battery cathode lie in the stable working window of the electrolyte. However, for the proposed batteries in the study of Käbitz *et al.* the charge voltage is 4.2 V, which is close to the upper limit of stability potential of the electrolyte. Then, at higher storage temperatures, dissolution of Mn into electrolyte occurs resulting in higher capacity fade and internal resistance increase.

Another remarkable observation is the fact that the increase of the internal resistance is a function of the SoC level. In Figures 9.13 through 9.16 the resistance increase at 25 °C, for example, after 44 weeks, is 23% at 100% SoC, 15% at 50% SoC, and 14% at 25% SoC. Here, it can be observed that the impact of SoC is less determinative than the storage temperature. However, when high SoC and high storage temperatures are combined as can be seen in Figure 9.13, the increase of the internal resistance can be high and the evolution of the resistance can be highly nonlinear. From this point of view, the development of an accurate calendar life model in a wide operating range becomes difficult. These results also have been confirmed and observed by Refs. [16,32,33].

From this point of view, in order to guarantee long lifetime of the battery, the battery should be kept in the most optimal conditions, where capacity fade and increase of internal resistance are small. This leads further to the conclusion that the prediction of the state of health of the battery based on the obtained results is not evident. An appropriate method to estimate this issue is to include both studied parameters (capacity fade and internal resistance) into account as proposed in Ref. [12].

In order to have a complete view of the changing parameters inside the battery during the calendar life, the model parameters as proposed in Figure 9.11 at 25 °C and at 100% and 50% SoC levels have been investigated and compared.

In Figures 9.17 and 9.18, the evolution of the ohmic and polarization resistances and time constant are demonstrated during the calendar life. In the proposed figures it is remarkable that the change of the time constant is almost negligible. However, the increase of the ohmic and polarization resistances is higher. The increase is 109% and 135% for polarization and ohmic resistances, respectively, at 100% SoC. At 50% SoC, the increase is 114% and 119% for polarization and ohmic resistances, respectively.

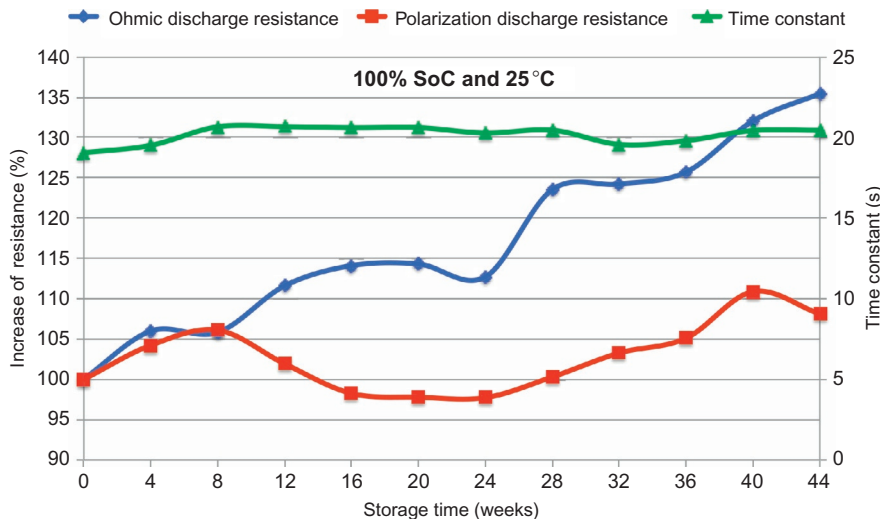


Figure 9.17 Battery model parameters change at storage temperature 25 °C and 100% SoC.

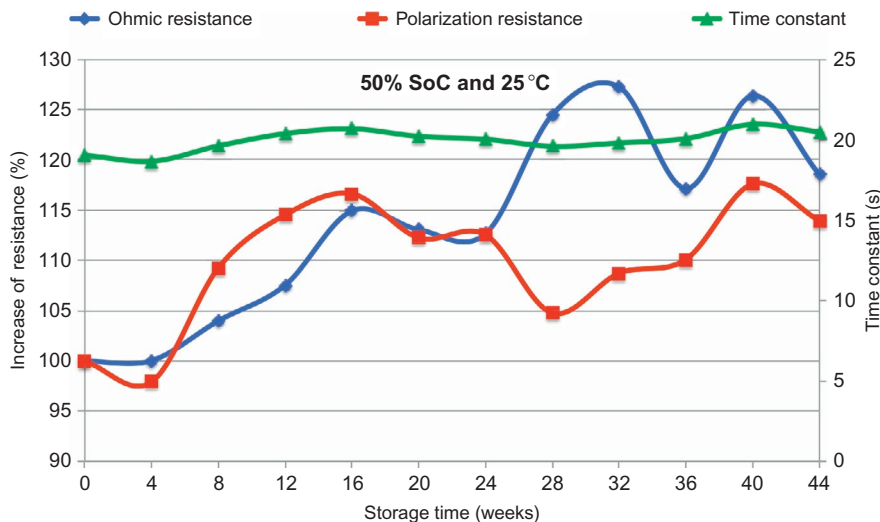


Figure 9.18 Battery model parameters change at storage temperature 25 °C and 50% SoC.

From these results, we can conclude that the increase of ohmic resistance is higher than the polarization resistance. This leads to the conclusion that the increase of the resistance confirms the degradation of the active material inside the battery. Then, from the electrical modeling point of view, the time constant can be assumed as constant. However, the polarization and ohmic resistances evolutions should be included

in the model. Regarding the state of health prediction, the ohmic resistance and the capacity degradation can be assumed as the most critical parameters. In order to have a clear understanding of the evolution of these performance parameters, there is a need for a postmortem.

## 9.4 Conclusions

In this study, the calendar life characteristics of a 7 Ah lithium iron phosphate pouch cell have been investigated at various temperatures (60, 40, 25, 10, 0, and  $-10^{\circ}\text{C}$ ) and SoC levels (100%, 75%, 50%, and 25%).

The experimental results indicate the capacity degradation is more determinative at higher temperatures. Higher states of charge levels accelerate the capacity fade.

Furthermore, the experimental results showed that higher temperatures accelerate the increase of the total internal resistance. These results can be attributed to the occurrence of parasitic reactions, whereby the loss of active material and lithium-ion are the main sources. In addition, the decomposition of the electrolyte and the evolution of the SEI layer are also major contributors to the increase of the internal resistance.

## References

- [1] J. Van Mierlo, G. Maggetto, E. Van De Burgwal, R. Gense, Driving style and traffic measures influences vehicle emissions and fuel consumption, *Proc. Inst. Mech. Eng. D: J. Automob. Eng.* 218 (1) (2003) 43–50.
- [2] J. Van Mierlo, G. Maggetto, et al., Comparison of the environmental damage caused by vehicles with different alternative fuels and drive trains in a Brussels context, *Proc. Inst. Mech. Eng. D: J. Automob. Eng.* 217 (7) (2003) 583–593.
- [3] J. Axsen, A. Burke, K. Kurani, Batteries for Plugin Hybrid Electric Vehicles (PHEVs): Goals and State of the Technology, UC Davis, internal report, Davis, CA, 2008.
- [4] N. Omar, B. Verbrugge, P. Van den Bossche, J. Van Mierlo, Power and life enhancement of battery-electrical double layer capacitor for hybrid electric and charge-depleting plug-in vehicle applications, *Electrochim. Acta* 55 (2010) 7524–7531.
- [5] P. Van den Bossche, F. Vergels, J. Van Mierlo, J. Matheys, W. Van Autenboer, SUBAT: an assessment of sustainable battery technology, *J. Power Sources* 162 (2) (2006) 913–919.
- [6] J. Axsen, K.S. Kurani, A. Burke, Are batteries ready for plug-in hybrid buyers? *J. Transp. Policy* 17 (2010) 173–180.
- [7] N. Omar, M. Daowd, B. Verbrugge, G. Mulder, P. Van den Bossche, J. Van Mierlo, M. Dhaens, S. Pauwels, F. Leemans, Assessment of performance characteristics of lithium-ion batteries for PHEV vehicles applications based on a newly test methodology, in: The 25th World Battery, Hybrid and Fuel Cell Electric Vehicle Symposium, November 5–9, 2010, Shenzhen, China, 2010.
- [8] N. Omar, B. Verbrugge, G. Mulder, P. Van den Bossche, J. Van Mierlo, M. Daowd, M. Dhaens, S. Pauwels, Evaluation of performance characteristics of various lithium-ion batteries for use, in: VPPC 2010, Lille, ISBN 978-1-4244-8220-7, 2010.

- [9] N. Omar, M. Daowd, G. Mulder, J.M. Timmermans, P. Van den Bossche, J. Van Mierlo, S. Pauwels, Assessment of performance of lithium iron phosphate oxide, nickel manganese cobalt oxide and nickel cobalt aluminum oxide based cells for using in plug-in battery electric vehicle applications, in: VPPC 2011, September 6–9, 2011, Chicago, 2011.
- [10] G.H. Kim, J. Gonder, J. Lustbader, A. Pesaran, Thermal management of batteries in advanced vehicles using phase-change materials, *World Electr. Veh. J.* 2 (2008) 46–59.
- [11] D.H. Doughty, P.C. Butler, R.G. Jungts, E.P. Roth, Lithium battery thermal models, *J. Power Sources* 110 (2002) 357–363.
- [12] N. Omar, M. Abdel Monem, Y. Firouz, J. Salminen, J. Smekens, O. Hegazy, H. Gualous, G. Mulder, P. Van den Bossche, Th. Coosemans, J. Van Mierlo, Lithium iron phosphate based battery—assessment of the aging parameters and development of cycle life model, *J. Appl. Energy* 113 (2014) 1575–1585.
- [13] N. Omar, Assessment of rechargeable energy storage systems in plug-in hybrid electric vehicles, Ph.D. dissertation, Vrije Universiteit Brussel, Brussels, Belgium, 2012.
- [14] J. Wang, P. Liu, J. Hicks-Garner, E. Sherman, S. Soukiazian, M. Verbrugge, H. Tataria, J. Musser, P. Finamore, Cycle-life model for graphite-LiFePO<sub>4</sub> cells, *J. Power Sources* 196 (2011) 3942–3948.
- [15] E. Eddhaech, O. Briat, E. Woirgard, J.M. Vinassa, Remaining useful life prediction of lithium batteries in calendar ageing for automotive applications, *Microelectron. Reliab.* 52 (2012) 2438–2442.
- [16] R.B. Wright, C.G. Motloch, J.R. Belt, J.P. Christophersen, C.D. Ho, R.A. Richardson, I. Bloom, S.A. Jones, V.S. Battaglia, G.L. Henriksen, T. Unkelhaeuser, D. Ingersoll, H. L. Case, S.A. Rogers, R.A. Sutula, Calendar- and cycle-life studies of advanced technology development program generation 1 lithium-ion batteries, *J. Power Sources* 110 (2002) 445–470.
- [17] A. Eddhaech, O. Briat, R. Chaari, N. Bertrand, H. Henry, J.M. Vinassa, Lithium-ion cell modeling from impedance spectroscopy for EV applications, in: IEEE Energy Conversion Congress and Exposition Conference, Phoenix, AZ, 2011.
- [18] Q. Zhang, R.E. White, Calendar life study of Li-ion pouch cells. Part 2: simulations, *J. Power Sources* 179 (2008) 785–792.
- [19] K. Kassem, J. Bernard, R. Revel, S. Pélissier, F. Duclaud, C. Delacourt, Calendar aging of a graphite/LiFePO<sub>4</sub> cell, *J. Power Sources* 208 (2012) 296–305.
- [20] G. Mulder, N. Omar, S. Pauwels, F. Leemans, B. Verbrugge, W. De Nijs, P. Van den Bossche, D. Six, J. Van Mierlo, Enhanced test methods to characterise automotive battery cells, *J. Power Sources* 196 (2011) 10079–10087.
- [21] N. Omar, M. Daowd, O. Hegazy, G. Mulder, J.M. Timmermans, Th. Coosemans, P. Van den Bossche, J. Van Mierlo, Standardization work for BEV and HEV applications: critical appraisal of recent traction battery documents, *Energies* 5 (2012) 138–156.
- [22] M. Broussely, S. Herreyre, P. Biensan, P. Kasztejna, K. Nechev, R. Staniewicz, Aging mechanism in Li ion cells and calendar life predictions, *J. Power Sources* 97–98 (2001) (2011) 13–21.
- [23] H.J. Phoehn, P. Ramadass, R.E. White, Solvent diffusion model for aging of lithium-ion battery cells, *J. Electrochem. Soc.* 151 (2004) A456–A462.
- [24] W. Bögel, J.P. Büchel, H. Katz, Real-life EV battery cycling in the test bench, *J. Power Sources* 72 (1998) 37–42.
- [25] P. Liu, J. Wang, J. Hicks-Garner, E. Sherman, S. Soukiazian, M. Verbrugge, H. Tataria, J. Musser, P. Finamore, Aging mechanisms of LiFePO<sub>4</sub> batteries deduced by electrochemical and structural analyses, *J. Electrochem. Soc.* 157 (2010) A499e–A507e.

- [26] J. Schmalstieg, S. Käbitz, M. Ecker, D. Uwe Sauer, A holistic aging model for  $\text{Li}(\text{NiMnCo})\text{O}_2$  based 18650 lithium-ion batteries, *J. Power Sources* 257 (2014) 325–334.
- [27] N. Omar, H. Gualous, M. Al Sakka, J. Van Mierlo, P. Van den Bossche, Electric and thermal characterization of advanced hybrid Li-ion capacitor rechargeable energy storage system, in: Proceedings 4th International Conference on Power Engineering, Energy and Electrical Drives, Istanbul, Turkey, 2013.
- [28] F. Rafik, H. Gualous, R. Gallay, A. Causaz, A. Berthon, Frequency, thermal and voltage supercapacitor characterization and modeling, *J. Power Sources* 165 (2007) 928–934.
- [29] Q. Zhang, R.E. White, Calendar life study of Li-ion pouch cells, *J. Power Sources* 173 (2007) 990–997.
- [30] R.G. Jungst, G. Nagasubramanian, H.L. Case, B.Y. Liaw, A. Urbina, T.L. Paez, D.H. Doughty, Accelerated calendar and pulse life analysis of lithium-ion cells, *J. Power Sources* 119–121 (2003) 870–873.
- [31] N. Dupré, J.F. Martin, J. Degryse, C. Fernandez, P. Soudan, D. Guyomard, Aging of the  $\text{LiFePO}_4$  positive electrode interface in electrolyte, *J. Power Sources* 195 (2010) 7415–7425.
- [32] M. Wohlfahrt-Mehrens, C. Vogler, J. Garche, Aging mechanisms of lithium cathode materials, *J. Power Sources* 127 (2004) 58–64.
- [33] S. Käbitz, J. Bernhard Gerschler, M. Ecker, Y. Yurdagel, B. Emmermacher, D. André, T. Mitsch, D. Uwe Sauer, Cycle and calendar life study of a graphite| $\text{LiNi}_{1/3}\text{Mn}_{1/3}\text{Co}_{1/3}\text{O}_2$  Li-ion high energy system. Part A: full cell characterization, *J. Power Sources* 239 (2013) 572–583.

# System-level management of rechargeable lithium-ion batteries

10

*A.G. Stefanopoulou, Y. Kim*  
University of Michigan, Ann Arbor, MI, USA

## 10.1 Introduction

Reducing dependence on imported oil and minimizing vehicular emissions are strong motivations to develop a fuel-efficient, clean, and sustainable transportation system. Vehicle electrification, one of the promising technologies for improved fuel economy, tailpipe emissions, and sustainability, has been extensively studied over the past decade. To realize vehicle electrification, various topologies for hybrid electrified vehicles have been explored, but they all rely on energy storage such as lithium-ion (Li-ion) batteries.

Indeed, Li-ion batteries have become one of the most critical components in vehicle electrification for their high specific power and energy density. The performance and longevity of these batteries rely on constraining their operation so that voltage and temperature are regulated within prescribed intervals. Enforcement of constraints is achieved by the battery management system (BMS).

The BMS, however, is responsible for more than enforcing constraints. Real-time estimation and prediction of the battery states and their proximity to the limits is an essential BMS task. For example, estimating the battery state of charge (SOC) and energy left is equivalent to the ubiquitous fuel gauge of a conventional vehicle. To ease range anxiety, modern plug-in and all-electric vehicles have complex estimation algorithms that translate the remaining battery energy to miles based on recognizing driving and terrain patterns. Broadcasting information to the driver and to other vehicle management systems ensures safe, efficient, and enjoyable driving.

Additionally, estimating the battery power capability is of vital importance in protecting Li-ion batteries from overheating as well as over-charge/discharge. The ability to estimate power capability is also important in formulating power management strategies that account for battery performance limitations while minimizing fuel consumption and emissions.

This chapter reviews the basic system-level management strategies to optimize Li-ion battery performance and durability, including monitoring and control aspects. This chapter is organized as follows. Section 10.2 presents the estimation of battery states. SOC, state of power (SOP), and state of health (SOH) indication methods are

also discussed. The need and general practice on cell balancing are reviewed in [Section 10.3](#). Thermal management systems for Li-ion batteries are described in [Section 10.4](#). Specifically, thermal systems based on media are given along with an example for battery packs in a hybrid electric vehicle. Finally, [Section 10.5](#) presents the concluding remarks.

## 10.2 Battery state estimation

Battery states in the context of this chapter are different from states of a dynamic system but refer to information describing (1) how much energy is stored in a battery; (2) how high power can be drawn from or provided to a battery; and (3) how much a battery ages compared to its initial condition. These states are critical to efficiently and robustly utilize Li-ion batteries in various applications such as automotive, robotics, mobile phones, and laptops. The following sections present the definition of each battery state and the various estimation methods.

### 10.2.1 SOC estimation

Battery SOC describes the remaining energy of a battery as an equivalent fuel gage for a battery. As battery behavior is affected by several factors such as operating temperature, current direction, and history, battery SOC becomes a function of these factors. Battery SOC is defined as the ratio of available capacity,  $C_b$ , to the nominal capacity,  $C_b^o$ :

$$\text{SOC}(t) = \frac{C_b(t, T)}{C_b^o(T)} \quad (10.1)$$

Many studies have been conducted to accurately estimate battery SOC [[1–15](#)]. These methods can be divided into three categories such as coulomb counting, voltage inversion, and model-based estimation method.

#### 10.2.1.1 Coulomb counting

To determine available capacity, coulomb counting relies on the integration of the current drawn from and supplied to a battery over time,  $\tau \in [t_0, t]$ , as given by

$$\text{SOC}(t) = \text{SOC}(t_0) - \int_{t_0}^t \frac{\eta(\tau)I(\tau)}{C_b^o} d\tau \quad (10.2)$$

where  $I$  is the current and  $\eta$  is the efficiency during charge and discharge operations [[4](#)]. Coulomb counting is advantageous in terms of a simple structure and its ease of implementation. However, some problems make it difficult to accurately estimate battery SOC by coulomb counting. Because battery capacity and efficiency are significantly influenced by operating temperature and current direction, these factors

should be considered to correct for battery SOC. Sensor accuracy is also important because accumulated errors can lead to a drift in the estimated battery SOC. Furthermore, one of the main problems in coulomb counting is that it is necessary to calibrate the initial battery SOC. In several applications, the initialization involves rest and the initial SOC is estimated based on the voltage inversion method described next.

### 10.2.1.2 Voltage inversion

Battery SOC can be estimated by using voltage measurement, which is referred to as voltage inversion method as this method utilizes the one-to-one relationship between voltage and battery SOC as follows:

$$V = f(\text{SOC}, I) \quad (10.3)$$

$$\text{SOC} = f^{-1}(V, I) \quad (10.4)$$

The relationship can be implemented or programmed using a lookup table, piecewise linear function, or mathematical function [5]. Two approaches are categorized as voltage inversion. The first approach is determining the available capacity during battery discharge operations, which has been widely used for mobile phone applications [5]. As seen from Figure 10.1, voltage at different rates of constant discharge current can be used to easily determine battery SOC. However, the battery operation needs to be

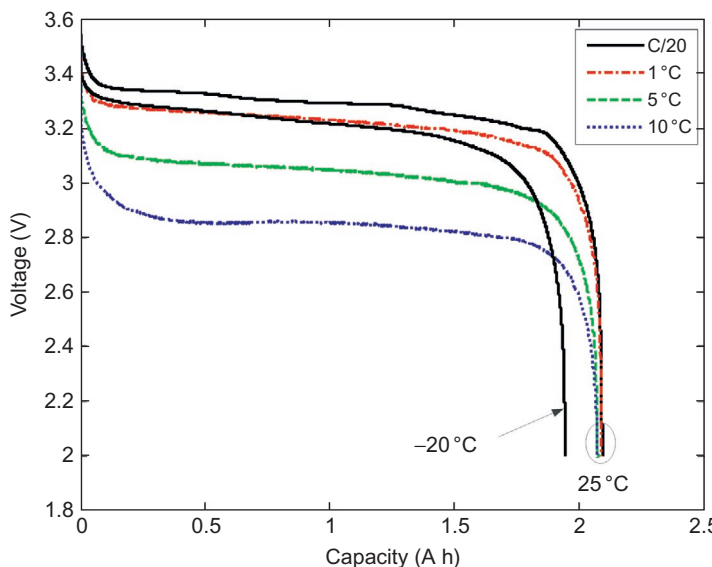


**Figure 10.1** Discharge capacities of a Li-ion battery at different current rates and temperatures.

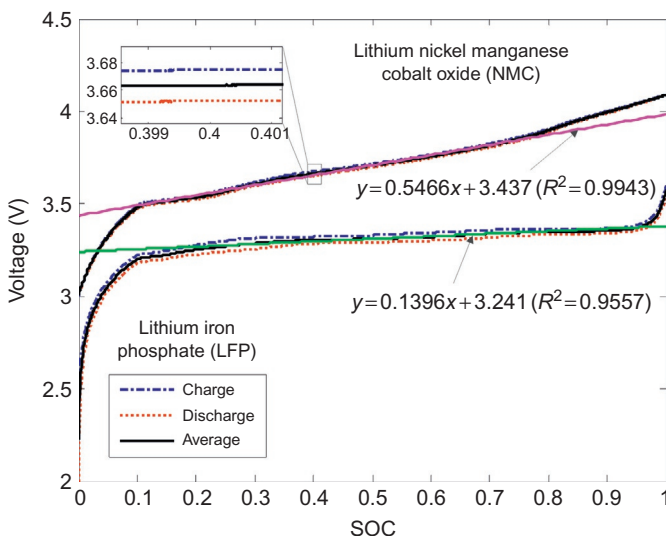


**Figure 10.2** Open circuit voltage of two batteries with different chemistries for positive electrode: lithium nickel manganese cobalt oxide and lithium iron phosphate.

interrupted to provide constant discharge current. Moreover, the one-to-one relationship cannot exist for discharge operation at high current rate. Additionally, including temperature dependence for SOC correction makes this estimation process more complicated and expensive than coulomb counting.

The second approach uses voltage measurement during voltage relaxation ( $I=0$ ) for SOC estimation. Because of zero current operation, this approach is named as open circuit voltage (OCV) inversion or electromotive force (EMF) method. The calculation of OCV is illustrated in Figure 10.2, where OCV is obtained by averaging terminal voltages during charging and discharging a battery with low current rate (e.g., C/20). This method is reliable due to the fact that the influences of temperature and aging on the SOC to OCV relationship are not significant [10]. Thus, the SOC–OCV relationship can be obtained by a lookup table or by inverting an analytic polynomial used to fit the SOC–OCV relationship.

$$\text{OCV} = g(\text{SOC}) \quad (10.5)$$

$$\text{SOC} = g^{-1}(\text{OCV}) \quad (10.6)$$

This method requires a long time to reach charge equilibrium or steady - state voltage. Moreover, for some chemistries such as lithium iron phosphate ( $\text{LiFePO}_4$ ), the SOC–OCV relationship is not well defined in the middle SOC range. Specifically, the slope  $\frac{d\text{OCV}}{d\text{SOC}}$  is very small; therefore, small errors in voltage measurement would lead to large errors in SOC estimation.

### 10.2.1.3 Model-based closed loop SOC estimation

To overcome the aforementioned drawbacks of coulomb counting and voltage inversion, or rather combine the good features of both techniques, various model-based methods have been developed for battery SOC estimation [6–9,11–15]. As illustrated in [Figure 10.3](#), the model-based method requires a battery model that can capture the dynamic evolution of the battery behavior. The battery models applicable for SOC estimation are:

- Equivalent circuit model [6,7,12].
- Electrochemical model [9,14,15].
- Artificial neural network model [8].
- Fuzzy logic model [13].
- Supporting vector machine model [11].

Various equivalent circuit models have been widely used in the form of the Thevenin model in the literature [6,7,16,17] for their simple structure and reasonable accuracy. Particularly, Hu *et al.* [16] have compared the accuracy of 12 different equivalent circuit models of Li-ion batteries.

For instance, the dynamics of a battery is expressed with the OCV–R–RC model with 100% coulomb efficiency as follows:

$$\frac{dSOC}{dt} = -\frac{I}{C_b} \quad (10.7)$$

$$\frac{dV_c}{dt} = -\frac{I}{R_c C_c} + \frac{I}{C_c} \quad (10.8)$$

$$V = OCV(SOC) - V_c - IR_s \quad (10.9)$$

Suppose that a battery in [Figure 10.2](#) is considered and the SOC range from 20% to 80% is of interest (e.g., hybrid electric vehicles). Within this SOC range, the SOC–OCV relationship can be reasonably approximated by a linear function:

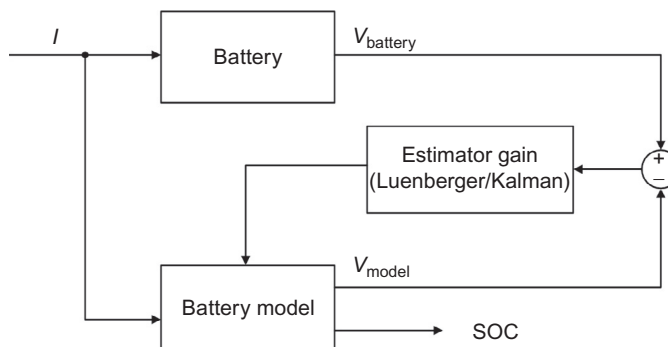


**Figure 10.3** A schematic of model-based closed loop SOC estimation.

$OCV = \alpha SOC + \beta$ . Then, the battery dynamics (open loop dynamics) can be expressed in state space representation as follows:

$$\begin{aligned}\dot{x} &= Ax + Bu \\ y &= Cx + Du + E\end{aligned}\quad (10.10)$$

where the states, input, and outputs are defined as  $x = [SOC \ V_c]^T$ ,  $u = I$ , and  $y = [SOC \ V]^T$ , respectively. System matrices,  $A, B, C, D$ , and  $E$ , are calculated by

$$A = \begin{bmatrix} 1 & 0 \\ 0 & \frac{-1}{R_c C_c} \end{bmatrix}, \quad B = \begin{bmatrix} -1 \\ \frac{C_b}{C_c} \end{bmatrix}, \quad C = \begin{bmatrix} 1 & 0 \\ \alpha & -1 \end{bmatrix}, \quad D = \begin{bmatrix} 0 \\ -R_s \end{bmatrix}, \quad E = \begin{bmatrix} 0 \\ \beta \end{bmatrix}. \quad (10.11)$$

To build a closed loop SOC estimator, the open loop dynamics are modified by adding a second input that is the product of the voltage prediction error,  $e$ , and an estimation gain,  $L$ , as shown in Figure 10.3. The estimated battery behavior is then given by

$$\begin{aligned}\dot{\hat{x}} &= A\hat{x} + Bu + Le \\ e &= y_2 - \hat{y}_2\end{aligned}\quad (10.12)$$

where the estimation gain  $L$  can be obtained through pole placement or Kalman filtering. More advanced techniques using sliding mode observer, extended Kalman filter, or unscented Kalman filter can be found in the literature [2,9,14,18]. As the parameters of a battery are influenced by operating conditions such as current rate and temperature, adaptive SOC estimators have been studied to identify those unknown parameters in real time [7,19].

### 10.2.2 SOP estimation

Battery SOP, or power capability, refers to the constant power that can be safely drawn from or provided to a battery over a finite window of time [20,21]. Information on the battery SOP is useful when making decisions for optimal power split in the core of hybrid power train systems [22,23]. Model-based methods to estimate battery SOP in real time have been addressed in the literature [7,15,24–26], wherein algorithms accounting for electrical constraints such as terminal voltage, battery SOC, surface concentration, and potential difference are developed.

Typically, battery SOP is obtained as follows:

$$P_{\max}^k(t) = I_{\max}^k(t)V_{\text{limit}}^k(t), \quad k \in \{\text{discharge, charge}\} \quad (10.13)$$

where  $P_{\max}$  and  $I_{\max}$  are the maximum allowable power and current of the battery, respectively. The manufacturer specified limit is usually used for voltage limit,  $V_{\text{limit}}$ . Therefore, battery SOP can be determined by estimating the maximum allowable current. The maximum allowable current,  $I_{\max}$ , can be computed using two techniques:

- A linearized model inversion.
- A nonlinear model-based numerical programming.

Moura *et al.* [25] compared two approaches to investigate a trade-off between computational time and constraint satisfaction. It was shown that the linear model-based approach is about four times faster than the nonlinear model-based one, at the expense of possible constraint dissatisfaction. It should be noted that electrical or electrochemical parameters of the battery are crucial information to estimate battery SOP. Thus, state and parameter identification is also an important topic in the BMS as discussed in the literature [7,19,24,27].

Battery SOP estimation is also important for battery thermal management for applications such as laptop computers, satellites, and mobile robots because of limited cooling for Li-ion batteries. Thus, Kim *et al.* [24] improved upon the state-of-the-art by accounting for the maximum operating temperature as a thermal constraint as well as electrical constraints so that none of these constraints violate the limit values as shown in Figure 10.4.

### 10.2.3 SOH estimation

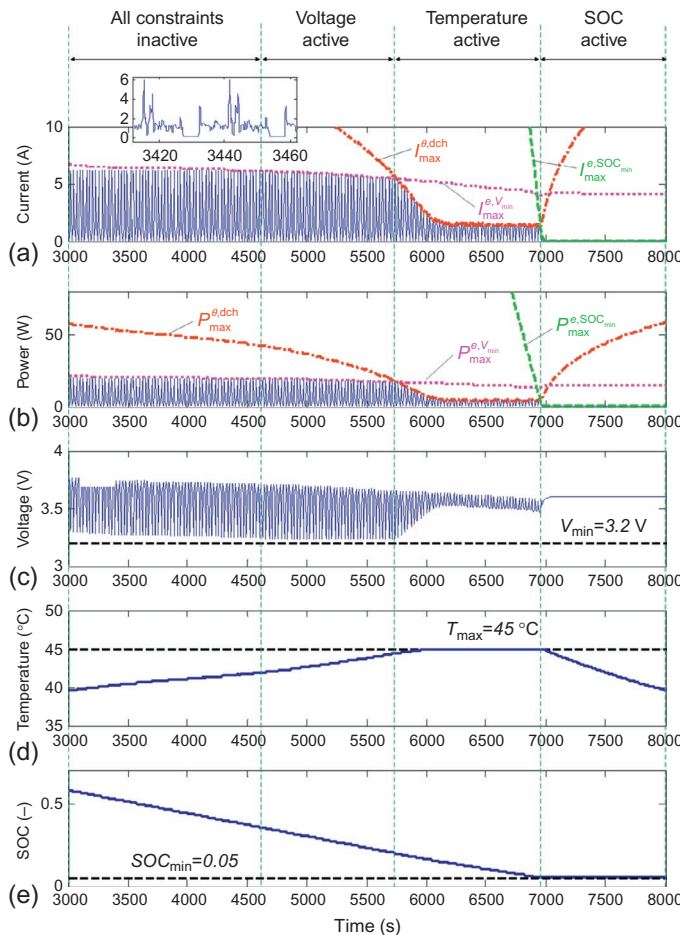
Battery SOH as an indicator of battery degradation defines the present performance of a battery relative to its fresh condition. The performance degradation of a battery may not be the result of a single mechanism but of several complicated mechanisms as studied in the literature [28–30]. Moreover, the degradation mechanisms may differ from one chemistry to another. Nonetheless, the consequences of degradation mechanisms can be observed as follows:

- A decrease in total available capacity [4,30–32].
- An increase in internal resistance or impedance [3,6,32–35].

Capacity loss, one of the consequences or phenomena, is illustrated in Figure 10.5. It is shown that the capacity of a battery is reduced as the number of cycles increases. Battery SOH is defined as the ratio between initial and nominal parameters, as follows:

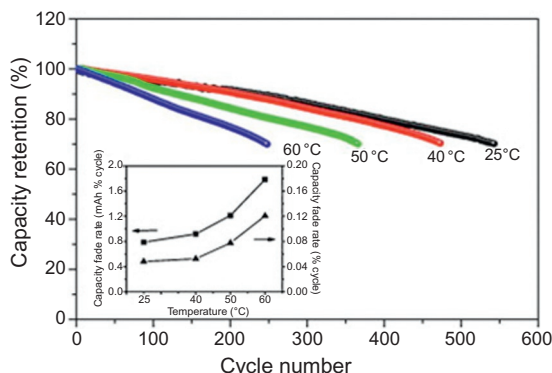
$$\text{SOH}(t) = \begin{cases} \frac{C_{b,\text{nominal}}(t, T)}{C_{b,\text{initial}}(T)} & \text{Based on capacity} \\ \frac{R_{\text{int,initial}}(T)}{R_{\text{int,nominal}}(t, T)} & \text{Based on internal resistance} \end{cases} \quad (10.14)$$

where  $C_b$  and  $R_{\text{int}}$  are the capacity and internal resistance of a battery, respectively. Battery SOH can be useful information in BMSs to detect battery end of life (EOL), which refers to the state when nominal capacity reaches 80% of the initial capacity of a battery. Ecker *et al.* [33] suggested that EOL is detected at the moment when internal resistance becomes two times larger than its initial resistance. The nominal capacity of a battery can be measured using coulomb counting during the constant current–constant voltage (CCCV) charging. This method however requires a considerable amount of time, which makes it difficult to use in real-time applications.



**Figure 10.4** Battery SOP estimation during battery operations at 30 °C ambient temperature with natural convection (6 W/m<sup>2</sup>/K): (a) current, (b) power, (c) terminal voltage, (d) temperature, and (e) SOC [24].

**Figure 10.5** Capacity retention vs. cycle number and the average capacity fade rate (inset) for the LFP/graphite cells cycled at different temperatures [31].



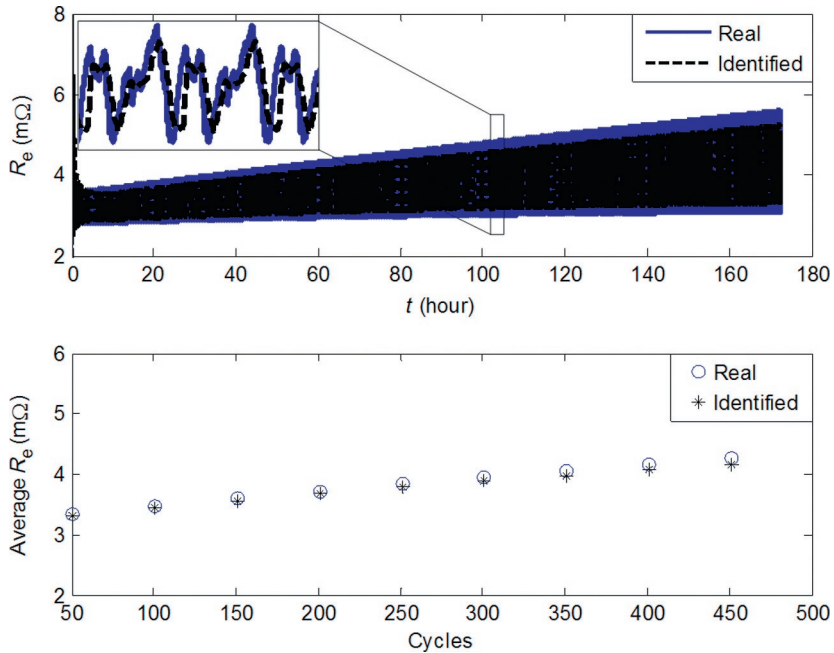


**Figure 10.6** Identification of internal resistance subject to battery degradation [34].

Therefore, various model-based estimation techniques have been developed to identify those parameters with voltage measurement: recursive least square method [6], particle filter [36], sliding-mode observer [2], and extended Kalman filter [3,70]. On the other hand, Lin *et al.* [34] developed an adaptive temperature estimator using a recursive least square regression and showed that surface temperature measurements can be used to identify the internal resistance of a battery. Figure 10.6 demonstrates how the online parameterization algorithm can monitor the gradual increase of internal resistance. The short-term variation of internal resistance is caused by changes in battery temperature.

### 10.3 Battery cell equalization

Applications that need high voltage levels, like hybrid electrical vehicles (HEV) usually employ large banks of series-connected cells to provide the power requested. Considering that Li-ion cells have low rated voltage (i.e., about 3.7 V), generally an HEV battery pack is composed of 200 or 300 individual cells. Aging, use, and calendar life lead to cell-to-cell variability. It is not, however, possible to substitute a single exhausted cell in a battery pack with a new one. Li-ion batteries need special protection from overcharge and overdischarge, because if the single cell voltage

becomes higher than 4.5 V, the production of carbon dioxide, ethylene, and other gases will increase temperature and internal pressure, causing severe battery damage or, in the worst case, cell explosion; while if the voltage goes below 2.4 V, internal chemical reactions cause the cell to irreversibly lose a large amount of its capacity [37,38]. So, it becomes clear that the SOH of the entire pack is equal to the SOH of the most damaged cell. Simply stopping the discharge when the unit with the least capacity is empty (or conversely during a charge when the most charged unit is full) will limit the use of the potential remaining pack energy.

In order to prolong the battery life cycle and increase the stack utilization, it is recommended that all the cells in a pack have the same SOC during battery operations. While different types of batteries are able to self-equalize by extended charging (i.e., trickle charging for lead acid batteries), Li-ion batteries cannot be overcharged, and so a BMS has to be used. Several equalization methods have been proposed in the literature [39,40]. They can be divided into two big categories, dissipative and nondissipative. The management systems of the first kind usually try to equalize the cells by extracting energy from the higher-charged ones and dissipating it on shunts or resistors [41], or selectively disconnecting imbalanced cells from the battery pack [42]. Even if such systems have high equalization speed, they will consume energy stored into the battery or lower the pack voltage too much causing power failure and so are not suited for HEV, where energy equals mileage.

Nondissipating methods can be divided into discharge equalizing systems, like multioutput transformers [43]; charge equalizing systems, like distributed the Cuk converter [44,45]; and bidirectional equalizing systems, like switched capacitor or inductor circuit [46]. Each one of those schemes has its advantages and drawbacks, in term of equalization speed, circuit complexity, number of parts needed, and rating of the part to be used, particularly the current rating of the switching components and the voltage rating of the diodes, but they all benefit from a good SOC estimation to perform equalization operation.

Usually, the SOC value used for control in those methods is often based only on the measured voltage differences between cells. This leads to a limited usefulness of the proposed solution in the case of Li-ion batteries that exhibit a flat voltage curve in the mid-SOC range. The voltage-driven cell equalization decisions could be influenced by voltage measurement noise, limiting the performance of a chosen solution to the performance of the sensor used to measure voltage. Other methods need a short rest of the battery in order to measure the voltage that could be approximately equal to the OCV, and then estimate the battery SOC from this value. An extensive review of such SOC estimation techniques can be found in Section 10.2.1. A different solution based on an EKF SOC estimator can be found in [9], where the battery model is mainly based on an equivalent circuit representation including terms that describe the dynamic contribution because of open-circuit voltage or temperature effects, while the closed loop feedback regulation provides root mean squared error lower than the quantization error expected on the sensor measurements. The solution proposed in [47] also uses an EKF SOC estimator in order to estimate remaining charge in all the cells and use the estimated value to control the operation of a simple bidirectional method based on charge shuttling. A capacitor will absorb energy from the whole battery, charging very fast and selectively discharging on the weakest cell in the pack.

## 10.4 Battery thermal management

Li-ion batteries' cycle life or capacity is considerably affected by operating temperature because of irreversible chemical reactions [48]. This phenomenon is also illustrated in Figure 10.5, where capacity loss is higher at higher operating temperature. If the battery temperature is not monitored and controlled, the battery could have a thermal runaway with the possible risk of explosion [49,50]. Moreover, nonuniform temperature distributions in the battery packs caused by poorly designed thermal systems can accelerate battery aging at the hottest spot (i.e., localized aging). Thus, the thermal management system is critical to maximize battery performance and durability. Toward this end, the thermal management system should have the capability of monitoring and maintaining battery operating temperatures within the range of optimum temperatures and minimizing temperature distributions inside the battery pack. The focus of this section is on the estimation of temperature and heating/cooling methods.

### 10.4.1 Temperature estimation

Temperature of a battery cell or a pack can be directly measured using thermocouples. Despite this simple principle, there are two major concerns about temperature monitoring:

- Whether the measured temperature can be representative of the whole cell?
- How many sensors are required to monitor all batteries inside a pack?

For a relatively small cell (e.g., 18650 type), the Biot number (Biot number,  $Bi$ , is the ratio of heat convected to the surroundings to heat conducted to the surface) of the battery cell is small ( $Bi \ll 0.1$ ), suggesting that the heat transfer at the surface is much smaller than the internal heat transfer by conduction. Hence, no significant temperature gradient inside the cell is expected, meaning that measured temperature can be considered as cell temperature. However, as reported in the literature [34,51,52], for a relatively large cylindrical battery (e.g., 26650 type), core temperature can be considerably higher than surface temperature. Figure 10.7 shows the maximum difference between measured surface and core temperatures of a 2.3 A h LFP battery by A123 is about 3.5 °C during an HEV operation. Debert *et al.* [53] have shown that the temperature of a prismatic cell can differ from the measured temperature by a thermistor mounted in an interstice of a module. These observations on thermal nonuniformity of a battery cell motivated them to develop a temperature estimator utilizing control-oriented battery thermal models such as a lumped parameter model [34,51,53] and a reduced order model [52]. Particularly, Lin *et al.* [34] and Kim *et al.* [52] have shown the capability of the estimator in detecting a gradual increase in internal resistance and malfunctioning of the cooling system, respectively.

In various applications, batteries are usually packed in modules to satisfy the energy and power demand. Lin *et al.* [54] built a thermal model for a battery cluster

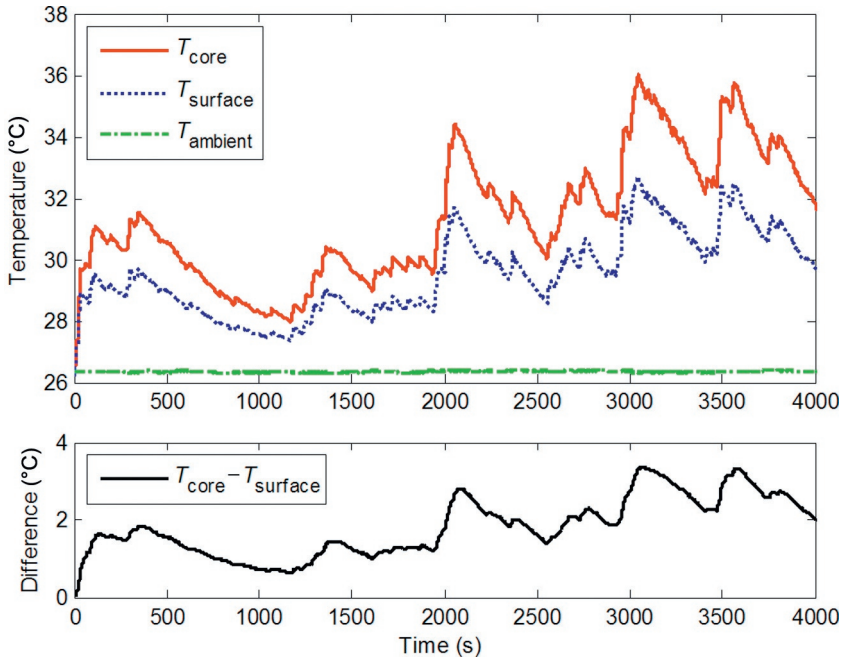


**Figure 10.7** Comparison between temperatures at core and surface of a battery under a certain duty cycle.

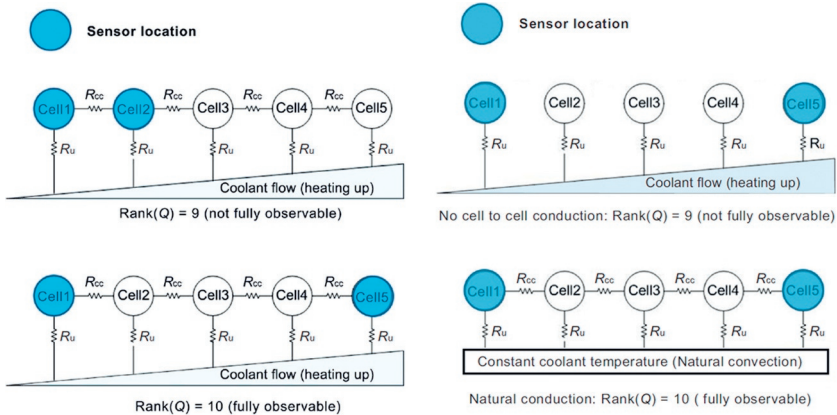


**Figure 10.8** Observability influenced by sensor locations and cooling conditions [54].

augmenting cell-to-cell heat conduction and convection by coolant flow. The observability of the cluster model was then investigated to guide pack sensor deployment. As shown in Figure 10.8, the sensor locations affect the observability of the cluster, and such impacts are different under various cluster constructions and cooling conditions.

## 10.4.2 Heating/cooling system

Thermal management for heating/cooling of Li-ion batteries can be passive or active, based on the existence of auxiliary systems to control the ambient temperature of the fluid [55]. Thermal management systems can be also categorized based on a medium, such as fluid (air or liquid) or solid (phase change material (PCM)). The ultimate goal of all these techniques is to control the convection coefficient.

### 10.4.2.1 Fluid medium (air/liquid)

Fluids such as air and liquid are commonly used as a heat transfer medium for thermal management. Table 10.1 illustrates electrified vehicles in the market and their cooling schemes. Air is in direct contact with modules for heat transfer, whereas liquid can be in either direct or indirect contact with modules; for example, submerging modules in a dielectric fluid [56] or placing a heat sink plate between the modules [57].

For instance, the convection coefficient for the battery module illustrated in Figure 10.9 is calculated by

$$h = \frac{C_L k_f \bar{N}u_D}{D} \quad (10.15)$$

where  $C_L$  is the correction factor depending on the number of cells in a row. Parameters  $k_f$  and  $\bar{N}u_D$  are the thermal conductivity and the Nusselt number of heat transfer fluid, respectively. Empirical correlation for the Nusselt number in various

**Table 10.1 Cooling systems for electrified vehicles**

Type	Brand name	Cell type	Pack capacity [kW h]	Cooling
EV	Tesla Roadster	Cylindrical	53	Liquid
	Tesla Model S	Cylindrical	40	Liquid
	Daimler Smart	Prismatic	17.6	Liquid/metal
	Nissan Leaf	Prismatic	24	Air
	Mitsubishi i-MiEV	Prismatic	16	Air
	Ford FOCUS	Prismatic	23	Liquid
PHEV	GM Volt	Prismatic	16	Liquid
	Fisker Karma	Prismatic	20	Liquid
	Hymotion PRIUS	Cylindrical	5.0	Air
	Ford C-MAX energi	Prismatic	7.6	Air
	Mercedez Benz S400	Cylindrical	0.9	Liquid
HEV	Ford C-MAX hybrid	Prismatic	1.4	Air

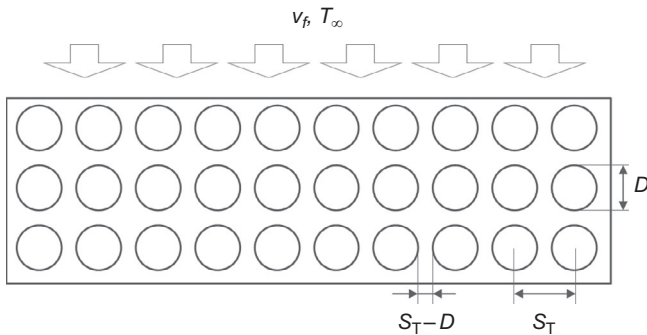


**Figure 10.9** Schematic of a module of cylindrical batteries: the batteries are aligned in the direction of the fluid.

designs can be found in the literature [58]. The power consumption by a fan or pump is calculated by

$$W_{\text{fan}} = \frac{\Delta P \dot{V}_f}{\eta_{\text{fan}}} \quad (10.16)$$

where  $\dot{V}_f$  is the volume flow rate of fluid and  $\eta_{\text{fan}}$  is the efficiency of the fan. The pressure drop across the battery pack  $\Delta P$  is calculated by

$$\Delta P = N_c \chi \left( \rho_f \frac{v_{f,\text{max}}^2}{2} \right) f_f \quad (10.17)$$

where  $N_c$  is the number of cells and the friction factor,  $f_f$ , and the correction factor,  $\chi$ , depends on the design configuration and air velocity as provided by Zukauskas [58]. The maximum fluid velocity is obtained from  $v_{f,\text{max}} = (S_T / (S_T - D)) v_f$  and thus  $v_f$  becomes an input for heating/cooling of the battery module. It can be found that there is a trade-off between the heat rejection and power consumption for cooling. Moreover, these performances are influenced by design factors such as the number of cells in series and parallel, gap between cells, and arrangements. Pesaran [55] and Park and Jung [59] investigated performance of air and liquid cooling systems and cooling schemes; namely, parallel and series cooling. Parallel cooling is advantageous to minimize cell-to-cell variations of temperature, temperature nonuniformity, which is important to minimize localized degradation in the module or pack. Toyota Prius and Ford Fusion use a parallel cooling for thermal management by supplying the conditioned air from the cabin [60]. Moreover, a parametric study has been conducted to optimize design parameters for both air and liquid cooling systems [59], wherein it was reported that a liquid cooling system consumes much less power compared with an air cooling system owing to better thermal properties of liquid and high heat exchange efficiency of the radiator. Nevertheless, air cooling involves simpler design,

lower cost, easier maintenance, and shorter warm-up period over liquid cooling. Mahamud and Park [61] proposed a method using reciprocating airflow to achieve uniform temperature distribution across a battery pack. It was shown that the reciprocating flow method can reduce the cell temperature difference of the battery system by about 4 °C (72% reduction) and the maximum cell temperature by 1.5 °C compared to the unidirectional flow case.

Despite the high rate of thermal rejection in the direct cooling system, the performance is limited for high viscosity of liquids and associated higher pumping power; that is, cooling performance is 1.5–3 times higher than that of air [55]. Thus, liquids with low viscosity and high thermal conductivity are used for heat pipe to cool the batteries without direct contact with them [62,63]. It was shown that the maximum temperature and temperature difference can be well controlled within the desirable range. However, a decrease in effectiveness owing to indirect contact needs to be considered because the heat must be transferred through the walls of the jacket/container or fins.

#### 10.4.2.2 *Phase change material*

PCM can be an alternative option for heat transfer material. This option is advantageous in terms of efficiency as parasitic power consumption can be removed by using the latent heat of phase change (solid/liquid) at constant temperature or the melting point. Al Hallaj and Selman [64] proposed placing batteries of a satellite in a PCM to regulate the temperature at which the efficiency of the battery is high during a sudden change in temperature. Khateeb *et al.* [65,66] have studied the design of Li-ion batteries with PCM for an electric scooter and their performance and experiments validated the efficacy of using the PCM, respectively. Even though this method is beneficial to obtain the minimum temperature distribution in a battery module or pack, there are several concerns associated with the increase of volume and weight of the system because of PCM [67]. Further temperature increases in the battery can be led by a large thermal resistance when the phase of the PCM is liquid only. Moreover, warm-up of the battery in cold temperature would be difficult because of the low thermal conductivity.

#### 10.4.3 *An example of thermal control in HEVs*

The thermostatic control, one of the heuristic or rule-based control techniques, has been widely employed for temperature regulation [60]. The basic idea of the thermostatic control is that cooling is applied when the measured temperature exceeds a target maximum temperature. The cooling control (fan-off or pump-off) is turned off when the measured temperature falls below another temperature threshold. This strategy is advantageous because of its ease of implementation and the effectiveness of temperature regulation.

Toyota's PRIUS is considered to be an example of a hybrid electric vehicle. A cylindrical Li-ion battery is used to provide similar performance compared to

**Table 10.2 Specifications of battery pack and cell**

Pack	Value
Number of module	6
Number of cells per module	30
Cell	Value
Heat capacity	77.7 J/K
Nominal electrical capacity	2.3 A h
Nominal voltage	3.3 V

nickel-metal hydride cells. The specifications for the battery pack under consideration are summarized in [Table 10.2](#). All cells in the battery module is connected in series to provide the nominal voltage for PRIUS. Thus, every cell in the battery module has the same current rate to each other. As suggested by Pesaran [55] and Park and Jung [59], a parallel (or large aspect ratio type) cooling scheme is favorable to minimize total power consumption in an air cooling system. As shown in [Figure 10.9](#), the battery module has 10 rows and 3 columns and the detailed design such as the gap between cells is adopted from the literature [59].

For simplicity, the energy balance equation in the cell with convection can be described by one bulk cell temperature,  $T_b$ , with heat capacity,  $C_p$ :

$$\begin{aligned} C_p \frac{dT_b}{dt} &= Q_{\text{gen}} + Q_{\text{rev}} + Q_{\text{rej}} \\ Q_{\text{gen}} &= I^2 R_{\text{int}} \\ Q_{\text{rev}} &= -IT_b \frac{\partial \text{OCV}}{\partial T} \\ Q_{\text{rej}} &= A_b h (T_\infty - T_b) \end{aligned} \tag{10.18}$$

where  $Q_{\text{gen}}$ ,  $Q_{\text{rev}}$ , and  $Q_{\text{rej}}$  represent joule heating, entropic heat generation, and heat rejection through convection, respectively. The internal resistance,  $R_{\text{int}}$ , lumps Ohmic, activation, and diffusion polarization resistances. The term  $\frac{\partial \text{OCV}}{\partial T}$  can be experimentally characterized as a function of battery SOC. The convection coefficient,  $h$ , and surface area of the battery,  $A_b$ , determine the convective thermal resistance. The ambient temperature is denoted by  $T_\infty$ .

The US06 Supplemental Federal Test Procedure (SFTP) cycle is selected because this cycle is aggressive compared to other federal cycles such as the Urban Dynamometer Driving Schedule (UDDS) and the Highway Fuel Economy Test (HWFET). The US06 cycle has average and maximum speeds of 48.4 mph (77.9 kph) and 80.3 mph (129.2 kph), respectively, as well as high acceleration/deceleration driving behavior. A single trip is short (8.03 mi) so that significant increase in temperature of each cell will not be observed. Thus, by following a similar test setup in the literature [60], 10 consecutive current profile over US06 is used. As shown in [Figure 10.10](#), the battery pack blower operates in predefined power levels such as off, low, medium, and high to reject heat from the batteries.

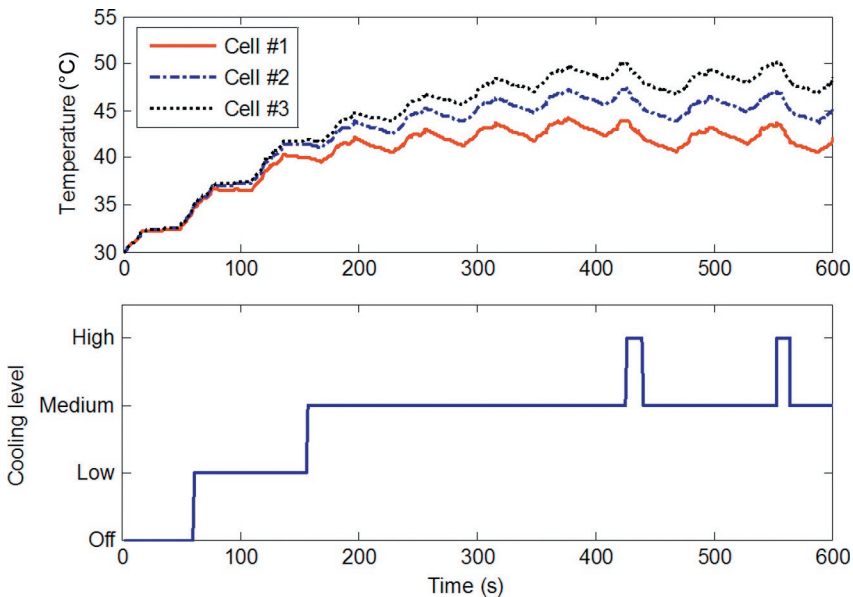


**Figure 10.10** Simulated temperature profiles during consecutive US06 cycles.

## 10.5 Conclusion

An overview of a system-level battery management that includes estimation of battery states and enforces electrical and thermal constraints has been given in this chapter. The concepts of battery states such as SOC, SOH, and SOP have been described in [Section 10.2](#). For battery SOC estimation, three methods such as coulomb counting, voltage inversion, and the model-based method have been discussed and a simple example for closed loop SOC estimation is given. Cell balancing is reviewed in [Section 10.3](#). The focus in [Section 10.4](#) has been on battery thermal management. Specifically, estimation methods for core temperature of a cell and a battery pack have been discussed. Cooling methods also have been discussed. An example for a HEV battery thermostatic cooling algorithm is provided for better understanding. These basic components of a BMS described in the above sections are found to be effective, but there are many opportunities for future improvements.

One such area of active investigation is an optimal warm-up strategy. Li-ion batteries are well known to suffer from poor performance at low temperatures. Specifically, the discharge capacity and available power of Li-ion batteries are substantially deteriorated below  $-20^{\circ}\text{C}$ . For a given design of Li-ion batteries, heating with current drawn from or applied to the battery can be a viable solution to exploit the thermal dynamics of the battery by generating heat inside a battery cell. In such a case, a hybrid energy storage system (HESS), for instance, a battery and a supercapacitor, is required for current shuttling. The optimal control algorithm and associated

hardware sizing are still under investigation for the battery warm-up problem that properly accounts for objectives (e.g., warm-up duration, efficiency, and battery SOH) and constraints (temperature, terminal voltage, and current).

Energy-efficient power/thermal management for an HESS is also an interesting topic. Because energy storage systems including a battery, a supercapacitor, and a fuel cell are different in terms of electrical and thermal characteristics, it is very important for a supervisory controller to distribute power demands among those energy storage systems.

Even though mechanical vibration of the battery pack seems to be more relevant to design for durability and longevity [68], it also needs to be taken into account for battery SOH estimation. As the pack system ages due to various reasons in addition to battery aging, maximum forced response levels for the system with and without parameter variations [69] may change.

Other important advances in estimation and control are needed in managing battery internal constraints such as distributed overpotential and mechanical stress. It is expected that the combination of advanced *in situ* sensing with model-based estimations will allow better battery management in the near future and consequently enable higher battery utilization and lower cost.

## References

- [1] M. Coleman, C.K. Lee, C. Zhu, W.G. Hurley, State-of-charge determination from EMF voltage estimation: using impedance, terminal voltage, and current for lead-acid and lithium-ion batteries, *IEEE Trans. Ind. Electron.* 54 (5) (2007) 2550–2557, <http://dx.doi.org/10.1109/TIE.2007.899926>.
- [2] I.-S. Kim, A technique for estimating the state of health of lithium batteries through a dual-sliding-mode observer, *IEEE Trans. Power Electron.* 25 (4) (2010) 1013–1022, <http://dx.doi.org/10.1109/TPEL.2009.2034966>.
- [3] J. Kim, B.H. Cho, State-of-charge estimation and state-of-health prediction of a Li-ion degraded battery based on an EKF combined with a per-unit system, *IEEE Trans. Veh. Technol.* 60 (9) (2011) 4249–4260, <http://dx.doi.org/10.1109/TVT.2011.2168987>.
- [4] K.S. Ng, C.-S. Moo, Y.-P. Chen, Y.-C. Hsieh, Enhanced coulomb counting method for estimating state-of-charge and state-of-health of lithium-ion batteries, *Appl. Energy* 86 (9) (2009) 1506–1511, <http://dx.doi.org/10.1016/j.apenergy.2008.11.021>.
- [5] V. Pop, H.J. Bergveld, P.H.L. Notten, P.P.L. Regtien, State-of-the-art of battery state-of-charge determination, *Meas. Sci. Technol.* 16 (12) (2005) R93–R110, <http://dx.doi.org/10.1088/0957-0233/16/12/R01>.
- [6] M. Verbrugge, E. Tate, Adaptive state of charge algorithm for nickel metal hydride batteries including hysteresis phenomena, *J. Power Sources* 126 (2004) 236–249, <http://dx.doi.org/10.1016/j.jpowsour.2003.08.042>.
- [7] G.L. Plett, High-performance battery-pack power estimation using a dynamic cell model, *IEEE Trans. Veh. Technol.* 53 (5) (2004) 1586–1593, <http://dx.doi.org/10.1109/TVT.2004.832408>.
- [8] M. Charkhgard, M. Farrokhi, State-of-charge estimation for lithium-ion batteries using neural networks and EKF, *IEEE Trans. Ind. Electron.* 57 (12) (2010) 4178–4187, <http://dx.doi.org/10.1109/TIE.2010.2043035>.

- [9] D. Di Domenico, A.G. Stefanopoulou, G. Fiengo, Lithium-ion battery state of charge and critical surface charge estimation using an electrochemical model-based extended Kalman filter, *J. Dyn. Syst. Meas. Control.* 132 (6) (2010) 061302, <http://dx.doi.org/10.1115/1.4002475>.
- [10] M. Dubarry, C. Truchot, B.Y. Liaw, K. Gering, S. Sazhin, D. Jamison, C. Michelbacher, Evaluation of commercial lithium-ion cells based on composite positive electrode for plug-in hybrid electric vehicle applications: III. Effect of thermal excursions without prolonged thermal aging, *J. Electrochem. Soc.* 160 (1) (2013) A191–A199, <http://dx.doi.org/10.1149/2.063301jes>.
- [11] T. Hansen, C.-J. Wang, Support vector based battery state of charge estimator, *J. Power Sources* 141 (2) (2005) 351–358, <http://dx.doi.org/10.1016/j.jpowsour.2004.09.020>.
- [12] S. Lee, J. Kim, J. Lee, B. Cho, State-of-charge and capacity estimation of lithium-ion battery using a new open-circuit voltage versus state-of-charge, *J. Power Sources* 185 (2) (2008) 1367–1373, <http://dx.doi.org/10.1016/j.jpowsour.2008.08.103>.
- [13] S. Malkhandi, Fuzzy logic-based learning system and estimation of state-of-charge of lead-acid battery, *Eng. Appl. Artif. Intell.* 19 (5) (2006) 479–485, <http://dx.doi.org/10.1016/j.engappai.2005.12.005>.
- [14] S.K. Rahimian, S. Rayman, R.E. White, State of charge and loss of active material estimation of a lithium ion cell under low earth orbit condition using Kalman filtering approaches, *J. Electrochem. Soc.* 159 (6) (2012) A860–A872, <http://dx.doi.org/10.1149/2.098206jes>.
- [15] K.A. Smith, C.D. Rahn, C.-Y. Wang, Model-based electrochemical estimation and constraint management for pulse operation of lithium ion batteries, *IEEE Trans. Control Syst. Technol.* 18 (3) (2010) 654–663, <http://dx.doi.org/10.1109/TCST.2009.2027023>.
- [16] X. Hu, S. Li, H. Peng, A comparative study of equivalent circuit models for Li-ion batteries, *J. Power Sources* 198 (2012) 359–367, <http://dx.doi.org/10.1016/j.jpowsour.2011.10.013>.
- [17] H.E. Perez, J.B. Siegel, X. Lin, A. Stefanopoulou, Y. Ding, M.P. Castanier, Parameterization and validation of an integrated electro-thermal LFP battery model, in: *ASME Dynamic Systems Control Conference*, Fort Lauderdale, Florida, USA, 2012.
- [18] G.L. Plett, Sigma-point Kalman filtering for battery management systems of LiPB-based HEV battery packs. Part 2: simultaneous state and parameter estimation, *J. Power Sources* 161 (2) (2006) 1369–1384, <http://dx.doi.org/10.1016/j.jpowsour.2006.06.004>.
- [19] R.D. Anderson, Y. Zhao, X. Wang, X.G. Yang, Y. Li, Real time battery power capability estimation, in: *Proceedings of the American Control Conference*, 2012, pp. 592–597.
- [20] M. Verbrugge, B. Koch, Generalized recursive algorithm for adaptive multiparameter regression: application to lead acid, nickel metal hydride, and lithium-ion batteries, *J. Electrochem. Soc.* 153 (1) (2006) A187–A201, <http://dx.doi.org/10.1149/1.2128096>.
- [21] S. Wang, M. Verbrugge, J.S. Wang, P. Liu, Multi-parameter battery state estimator based on the adaptive and direct solution of the governing differential equations, *J. Power Sources* 196 (20) (2011) 8735–8741, <http://dx.doi.org/10.1016/j.jpowsour.2011.06.078>.
- [22] C.-C. Lin, H. Peng, J. Grizzle, J.-M. Kang, Power management strategy for a parallel hybrid electric truck, *IEEE Trans. Control Syst. Technol.* 11 (6) (2003) 839–849, <http://dx.doi.org/10.1109/TCST.2003.815606>.
- [23] S.J. Moura, H.K. Fathy, D.S. Callaway, J.L. Stein, A stochastic optimal control approach for power management in plug-in hybrid electric vehicles, *IEEE Trans. Control Syst. Technol.* 19 (3) (2011) 545–555, <http://dx.doi.org/10.1109/TCST.2010.2043736>.
- [24] Y. Kim, S. Mohan, J.B. Siegel, A.G. Stefanopoulou, Maximum power estimation of lithium-ion batteries accounting for thermal and electrical constraints, in: *ASME Dynamic Systems Control Conference*, Palo Alto, California, USA, 2013.

- [25] S.J. Moura, N.A. Chaturvedi, M. Krstic, Constraint management in Li-ion batteries: a modified reference governor approach, in: Proceedings of the American Control Conferences, 2013, pp. 5332–5337.
- [26] R. Xiong, H. He, F. Sun, X. Liu, Z. Liu, Model-based state of charge and peak power capability joint estimation of lithium-ion battery in plug-in hybrid electric vehicles, *J. Power Sources* 229 (2013) 159–169, <http://dx.doi.org/10.1016/j.jpowsour.2012.12.003>.
- [27] T.-K. Lee, Y. Kim, A. Stefanopoulou, Z. Filipi, Hybrid electric vehicle supervisory control design reflecting estimated lithium-ion battery electrochemical dynamics, in: Proceedings of the American Control Conference, 2011, pp. 388–395.
- [28] D.P. Abraham, E.M. Reynolds, E. Sammann, A.N. Jansen, D.W. Dees, Aging characteristics of high-power lithium-ion cells with  $\text{LiNi}_{0.8}\text{Co}_{0.15}\text{Al}_{0.05}\text{O}_2$  and  $\text{Li}_{4/3}\text{Ti}_{5/3}\text{O}_4$  electrodes, *Electrochim. Acta* 51 (3) (2005) 502–510, <http://dx.doi.org/10.1016/j.electacta.2005.05.008>.
- [29] J. Li, E. Murphy, J. Winnick, P. Kohl, Studies on the cycle life of commercial lithium ion batteries during rapid charge–discharge cycling, *J. Power Sources* 102 (1–2) (2001) 294–301, [http://dx.doi.org/10.1016/S0378-7753\(01\)00821-7](http://dx.doi.org/10.1016/S0378-7753(01)00821-7).
- [30] Q. Zhang, R.E. White, Capacity fade analysis of a lithium ion cell, *J. Power Sources* 179 (2) (2008) 793–798, <http://dx.doi.org/10.1016/j.jpowsour.2008.01.028>.
- [31] L. Tan, L. Zhang, Q. Sun, M. Shen, Q. Qu, H. Zheng, Capacity loss induced by lithium deposition at graphite anode for  $\text{LiFePO}_4$ /graphite cell cycling at different temperatures, *Electrochim. Acta* 111 (2013) 802–808, <http://dx.doi.org/10.1016/j.electacta.2013.08.074>.
- [32] Y. Zhang, C.-Y. Wang, X. Tang, Cycling degradation of an automotive  $\text{LiFePO}_4$  lithium-ion battery, *J. Power Sources* 196 (3) (2011) 1513–1520, <http://dx.doi.org/10.1016/j.jpowsour.2010.08.070>.
- [33] M. Ecker, J.B. Gerschler, J. Vogel, S. Kabitz, F. Hust, P. Dechent, D.U. Sauer, Development of a lifetime prediction model for lithium-ion batteries based on extended accelerated aging test data, *J. Power Sources* 215 (2012) 248–257, <http://dx.doi.org/10.1016/j.jpowsour.2012.05.012>.
- [34] X. Lin, H.E. Perez, J.B. Siegel, A.G. Stefanopoulou, Y. Li, R.D. Anderson, Y. Ding, M. P. Castanier, Online parameterization of lumped thermal dynamics in cylindrical lithium ion batteries for core temperature estimation and health monitoring, *IEEE Trans. Control Syst. Technol.* 21 (5) (2013) 1745–1755, <http://dx.doi.org/10.1109/TCST.2012.2217143>.
- [35] U. Tröltzsch, O. Kanoun, H.-R. Tränkler, Characterizing aging effects of lithium ion batteries by impedance spectroscopy, *Electrochim. Acta* 51 (8–9) (2006) 1664–1672, <http://dx.doi.org/10.1016/j.electacta.2005.02.148>.
- [36] K. Goebel, B. Saha, A. Saxena, J. Celaya, J. Christophersen, Prognostics in battery health management, *Instrum. Meas. Mag. IEEE* 2008 (11) (2008) 33–40, <http://dx.doi.org/10.1109/MIM.2008.4579269>.
- [37] P.A. Cassani, S.S. Williamson, Significance of battery cell equalization and monitoring for practical commercialization of plug-in hybrid electric vehicles, in: Twenty-Fourth Annual IEEE Applied Power Electronics Conference and Exposition, 2009, pp. 465–471.
- [38] S.Y. Kan, M. Verwaal, H. Broekhuizen, The use of battery–capacitor combinations in photovoltaic powered products, *J. Power Sources* 162 (2) (2006) 971–974, <http://dx.doi.org/10.1016/j.jpowsour.2005.07.001>.
- [39] A. Baughman, M. Ferdowsi, Battery charge equalization-state of the art and future trends, 2005, SAE 2005-01-3474.
- [40] S. Moore, P. Schneider, A review of cell equalization methods for lithium ion and lithium polymer battery systems, 2001, SAE 2001-01-0959.

- [41] J.A. Asumadu, M. Haque, H. Vogel, C. Willards, Precision battery management system, in: Proceedings of the IEEE Instrumentation and Measurement Technology Conference, 2005, pp. 1317–1320.
- [42] H. Shibata, S. Taniguchi, K. Adachi, K. Yamasaki, G. Ariyoshi, K. Kawata, K. Nishijima, K. Harada, Management of serially-connected battery system using multiple switches, in: Proceedings of International Conference on Power Electronics and Drive Systems, 2001, pp. 508–511.
- [43] N. Kutkut, H.L.N. Wiegman, D. Divan, D. Novotny, Design considerations for charge equalization of an electric vehicle battery system, *IEEE Trans. Ind. Appl.* 35 (1) (1999) 28–35, <http://dx.doi.org/10.1109/28.740842>.
- [44] M. Chen, Z. Zhang, Z. Feng, J. Chen, Z. Qian, An improved control strategy for the charge equalization of lithium ion battery, in: Twenty-Fourth Annual IEEE Applied Power Electronics Conference and Exposition, 2009, pp. 186–189.
- [45] H.-S. Park, C.-E. Kim, C.-H. Kim, G.-W. Moon, J.-H. Lee, A modularized charge equalizer for an HEV lithium-ion battery string, *IEEE Trans. Ind. Electron.* 56 (5) (2009) 1464–1476, <http://dx.doi.org/10.1109/TIE.2009.2012456>.
- [46] C.S. Moo, Y.-C. Hsieh, I.S. Tsai, Charge equalization for series-connected batteries, *IEEE Trans. Aerosp. Electron. Syst.* 39 (2) (2003) 704–710, <http://dx.doi.org/10.1109/TAES.2003.1207276>.
- [47] C. Speltino, A. Stefanopoulou, G. Fiengo, Cell equalization in battery stacks through state of charge estimation polling, in: Proceedings of American Control Conference, 2010, pp. 5050–5055.
- [48] J. Shim, R. Kostecki, T. Richardson, X. Song, K. Striebel, Electrochemical analysis for cycle performance and capacity fading of a lithium-ion battery cycled at elevated temperature, *J. Power Sources* 112 (1) (2002) 222–230, [http://dx.doi.org/10.1016/S0378-7753\(02\)00363-4](http://dx.doi.org/10.1016/S0378-7753(02)00363-4).
- [49] R. Spotnitz, J. Franklin, Abuse behavior of high-power, lithium-ion cells, *J. Power Sources* 113 (1) (2003) 81–100, [http://dx.doi.org/10.1016/S0378-7753\(02\)00488-3](http://dx.doi.org/10.1016/S0378-7753(02)00488-3).
- [50] S. Tobishima, J. Yamaki, A consideration of lithium cell safety, *J. Power Sources* 81–82 (1999) 882–886, [http://dx.doi.org/10.1016/S0378-7753\(98\)00240-7](http://dx.doi.org/10.1016/S0378-7753(98)00240-7).
- [51] C. Forgez, D. Vinh Do, G. Friedrich, M. Morcrette, C. Delacourt, Thermal modeling of a cylindrical LiFePO<sub>4</sub>/graphite lithium-ion battery, *J. Power Sources* 195 (9) (2010) 2961–2968, <http://dx.doi.org/10.1016/j.jpowsour.2009.10.105>.
- [52] Y. Kim, S. Mohan, J.B. Siegel, A.G. Stefanopoulou, Y. Ding, The estimation of temperature distribution in cylindrical battery cells under unknown cooling conditions, *IEEE Trans. Control Syst. Technol.* (2014), <http://dx.doi.org/10.1109/TCST.2014.2309492>.
- [53] M. Debert, G. Colin, G. Bloch, Y. Chamaillard, An observer looks at the cell temperature in automotive battery packs, *Control Eng. Pract.* 21 (8) (2013) 1035–1042, <http://dx.doi.org/10.1016/j.conengprac.2013.03.001>.
- [54] X. Lin, H. Fu, H.E. Perez, J.B. Siegel, A.G. Stefanopoulou, Y. Ding, M.P. Castanier, Parameterization and observability analysis of scalable battery clusters for onboard thermal management, *Oil Gas Sci. Technol. Rev. IFP Energies nouvelles* 68 (1) (2013) 165–178, <http://dx.doi.org/10.2516/ogst/2012075>.
- [55] A.A. Pesaran, Battery thermal management in EVs and HEVs: issues and solutions, in: Advanced Automotive Battery Conference, Las Vegas, Nevada, USA, 2001.
- [56] M. Panao, A. Moreira, D. Durao, Intelligent thermal management for full electric vehicles, *Strojarstvo: J. Theory Appl. Mech.* 55 (1) (2013) 45–56.
- [57] A. Jarrett, I.Y. Kim, Design optimization of electric vehicle battery cooling plates for thermal performance, *J. Power Sources* 196 (23) (2011) 10359–10368, <http://dx.doi.org/10.1016/j.jpowsour.2011.06.090>.

- [58] A. Zukauskas, Heat transfer from tubes in crossflow, *Advances in Heat Transfer*, vol. 8, Academic Press, New York, 1972, 93–160.
- [59] S. Park, D. Jung, Battery cell arrangement and heat transfer fluid effects on the parasitic power consumption and the cell temperature distribution in a hybrid electric vehicle, *J. Power Sources* 227 (2013) 191–198, <http://dx.doi.org/10.1016/j.jpowsour.2012.11.039>.
- [60] M. Zolot, A.A. Pesaran, M. Mihalic, Thermal evaluation of Toyota Prius battery pack, (2002), SAE 2002-01-1962.
- [61] R. Mahamud, C. Park, Reciprocating air flow for Li-ion battery thermal management to improve temperature uniformity, *J. Power Sources* 196 (13) (2011) 5685–5696, <http://dx.doi.org/10.1016/j.jpowsour.2011.02.076>.
- [62] Y. Park, S. Jun, S. Kim, D.-H. Lee, Design optimization of a loop heat pipe to cool a lithium ion battery onboard a military aircraft, *J. Mech. Sci. Technol.* 24 (2) (2010) 609–618, <http://dx.doi.org/10.1007/s12206-009-1214-6>.
- [63] Z. Rao, S. Wang, M. Wu, Z. Lin, F. Li, Experimental investigation on thermal management of electric vehicle battery with heat pipe, *Energy Convers. Manag.* 65 (2013) 92–97, <http://dx.doi.org/10.1016/j.enconman.2012.08.014>.
- [64] S. Al Hallaj, J.R. Selman, A novel thermal management system for electric vehicle batteries using phase change material, *J. Electrochem. Soc.* 147 (9) (2000) 3231–3236, <http://dx.doi.org/10.1149/1.1393888>.
- [65] S.A. Khateeb, M.M. Farid, J. Selman, S. Al-Hallaj, Design and simulation of a lithium-ion battery with a phase change material thermal management system for an electric scooter, *J. Power Sources* 128 (2) (2004) 292–307, <http://dx.doi.org/10.1016/j.jpowsour.2003.09.070>.
- [66] S.A. Khateeb, S. Amiruddin, M. Farid, J.R. Selman, S. Al-Hallaj, Thermal management of Li-ion battery with phase change material for electric scooters: experimental validation, *J. Power Sources* 142 (1–2) (2005) 345–353, <http://dx.doi.org/10.1016/j.jpowsour.2004.09.033>.
- [67] T.M. Bandhauer, S. Garimella, T.F. Fuller, A critical review of thermal issues in lithium-ion batteries, *J. Electrochem. Soc.* 158 (3) (2011) R1–R25, <http://dx.doi.org/10.1149/1.3515880>.
- [68] J.-K. Lee, J.-S. Yeo, M.-C. Jang, J.-M. Yoon, D.M. Kang, Mechanical durability and electrical durability of an aluminum-laminated lithium-ion polymer battery pack for a hybrid electric vehicle, *Proc. Inst. Mech. Eng. D: J. Automob. Eng.* 224 (6) (2010) 765–773, <http://dx.doi.org/10.1243/09544070JAUTO1388>.
- [69] S.-K. Hong, B.I. Epureanu, M.P. Castanier, Reduced-order modeling method for fatigue life predictions of hybrid electric vehicle batteries, in: 2012 NDIA Ground Vehicle Systems Engineering and Technology Symposium, Troy, Michigan, USA, 2012.
- [70] G.L. Plett, Extended Kalman filtering for battery management systems of LiPB-based HEV battery packs: part 3. State and parameter estimation, *J. Power Sources* 134 (2004) 277–292, <http://dx.doi.org/10.1016/j.jpowsour.2004.02.033>.

# Environmental performance of lithium batteries: life cycle analysis

11

*M. Messagie, L. Oliveira, S. Rangaraju, J.S. Forner, M.H. Rivas*  
Vrije Universiteit Brussel, Brussels, Belgium

## 11.1 Introduction

Energy storage systems based on lithium-ion batteries have a wide range of sizes and usages. From small applications like portable batteries (cell phones, laptops, etc.) to bigger ones like batteries for electric mobility (bikes, electric vehicles (EVs), trains, etc.) to large battery groups for grid applications. Lithium rechargeable batteries provide energy devices as described above with capacities ranging from just a few watt hours to megawatt hours. Typical laptop batteries have a capacity rating from 45 Wh to roughly 100 Wh. Cell phone batteries are significantly smaller, and typical electrical vehicle applications have capacities in the range of dozens of kWh (while the Nissan Leaf has a 24 kWh, Tesla model S with variants ranging from 40 to 85 kWh) [1]. Electrical grid applications using large-scale lithium-ion battery systems have capacities on the megawatt scale.

The fact that lithium batteries have so many kinds of applications makes the technology development grow fast; especially in emerging applications such as electric mobility, where the demand for more efficient battery packs increases continuously in order to provide a competitive technology in terms of driving range and durability with internal combustion engine vehicles. The continuous growth of batteries for EVs is also associated with the enormous effort that governments from different countries have put into electric mobility in order to reduce emissions from road transport. Electricity as an energy vector for vehicle propulsion offers the possibility to substitute oil with a wide diversity of primary energy sources. This could ensure security of energy supply and a broad use of renewable and carbon-free energy sources in the transport sector, which could help to achieve targets on CO<sub>2</sub> emissions reduction (e.g., the Kyoto agreements on emissions targets by 2020). However, what is the environmental impact induced by these new battery developments?

Batteries are known for their large effect on the environment. However, is this also applicable for larger applications, maintained in a closed loop. This chapter focuses on the environmental impacts of two lithium batteries for EVs. How do you evaluate the environmental performance of two different lithium batteries? A good method to implement an environmental assessment of a product is with a life cycle approach; that is to say that all the life cycle stages of the product are considered. For that purpose there are well-developed methodologies such as life cycle assessment (LCA).

LCA is a tool that assists in identifying opportunities to improve the environmental performance of products at various points in their life cycle, and informing decision makers in industry, government, or nongovernment organizations on this matter [2]. The European Commission (EC) and others (member states, industry, consumer organizations, and environmental organizations) recognize LCA as “the best framework for assessing the potential environmental impact of products” [3]. LCA has a broad system perspective, it incorporates different life cycle stages (from raw material acquisition, overusage, to end of life strategies) and evaluates various impact categories (especially climate change (CC), toxicity, depletion, acidification, particle matter formation, etc.). This broad perspective is crucial, as optimizing a specific point in the life cycle of a product can induce new impacts elsewhere in the product chain. LCA enables mapping all these types of burden shifts.

## 11.2 Problem setting: environmental impacts and lithium resource availability

The role of lithium in electrochemical energy storage applications is gaining increasing attention. Lithium metal is taking an important share in the mobility sector, particularly for the manufacturing of batteries for both hybrid and full EVs. Accordingly, the study of the performance of this metal, from an environmental point of view, has great relevance in order to analyze, understand, and possibly avoid the environmental impacts associated with the Li-ion batteries industry, from the extraction of lithium to the final disposal of the vehicle batteries [4].

First, this chapter focuses on the study of the availability of lithium. Future expansion, expected to take place for the EVs industry in the coming years, has caused some questioning about whether the availability of lithium metal will be capable of meeting future demand. An analysis on this situation is conducted through a literature review regarding the different estimations of the current lithium resources and reserves present, worldwide. In addition, several models were designed to predict the growth of the EV industry and, therefore, the related future demand of lithium was analyzed and compared. These discussions concluded that lithium availability probably will not pose an obstacle for the EV industry. However, certain conditions have to be met in order to guarantee this situation. These conditions are explained in more detail in the following sections.

Second, a comprehensive LCA is performed, comparing two different Li-ion battery chemistries. For this LCA, lithium manganese oxide (LMO), and lithium iron phosphate (LFP) battery chemistries are selected. The objective of the study is to provide an insight, from a life cycle perspective, on which typical environmental impacts are generated by producing 1 kW of energy with these two types of battery chemistries. The assessment includes all life stages of a traction battery, including the extraction of raw materials, the manufacturing of the battery, the use of the vehicle, and the final disposal and recycling of the elements contained in the battery. Several locations are included in this study, according to where the different stages of the life cycle of

the battery take place. Locations like Asia and South America are more typical for extraction and production stages, while Europe is considered as the location for the use of the battery and its end of life disposal.

### 11.3 Depletion of metal resources: the case of lithium

Lithium metal is gaining importance in the batteries industry and particularly, as a component of EVs, due to high energy density by weight and behavior at temperature changes. In addition, for production volumes greater than 300,000 units per year, Li-ion batteries are projected to be less expensive [4], compared to nickel metal hydride batteries. These reasons make lithium a potential dominant option for the powering of EVs. Studying the availability of this resource is then important when speaking about the development of the EV industry. Many believe that it is just a matter of time before the availability of lithium supplies, and consequently the industries depending on this resource, may be threatened [5]. Therefore, reliable analyses are needed to make clear, to the extent possible, whether the availability of lithium will meet future requirements.

Several assessments on the presence of lithium on Earth, and its expected future demand, have been performed in the past. They are used in this chapter to shed some light on whether the amount of lithium mineral could possibly become an obstacle, and if the EV industry would just be replacing the depletion of fossil fuels by the depletion of another nonrenewable, insufficient resource.

Performing minerals availability assessments requires first clarifying the difference between “resources” and “reserves.” This classification is explained in broad terms as follows: resources are geologically assured quantities that are available for exploitation, and reserves are the quantity that is exploitable within current technical and socioeconomic conditions. There has been extensive research on the definitions and classifications of these two terms in the literature [6,7]. Several published studies of lithium availability, in the forms of world resources and reserves, are assessed in Refs. [3–12].

The range of lithium resources varies greatly from the lowest 19.2 Mt [5] to the highest 71.3 Mt [6]. These estimations vary mainly due to the number of deposits considered, how conservative the study is, the availability of information and its interpretation, and the discrepancies between authors on the definition of reserves and resources. At present, the global demand of lithium is distributed across end-use markets, and the battery market accounts for 22% [11]. Figure 11.1 shows how the current resources and reserves of lithium are distributed around the world.

Several studies calculated the future demand of lithium. The different strategies and assumptions used to predict demand deliver results that vary substantially [7,8,10]. However, the majority of the studies on this issue assume that large-scale recycling will take place, to relieve pressure from the extraction and production of primary lithium. Moreover, the studies suggest that the biggest source of lithium in the second part of the twenty-first century will come from recycling [12]. Nevertheless, at present, the development of technology and strategies for recycling are far from

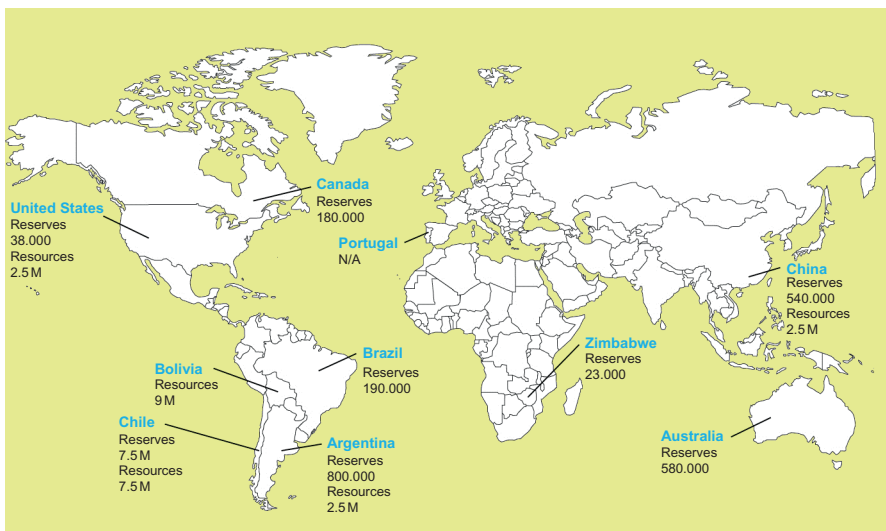


**Figure 11.1** World lithium resources and reserves in tons.

Data source: USGS 2010 [11].

reaching this situation. In addition, the studies suggest that the penetration of EVs will be significant (and predominant over other end uses) by the year 2050, reaching levels from 60% to 100% of either hybrid or fully EVs, which is a rather optimistic perspective. At the same time, there seems to be little agreement on which type of technology will be more widely used in the future, the evolution of the battery capacity in these technologies, and the required amount of lithium that will be needed for each battery.

Given the inherent uncertainties surrounding the future course of technological change and other determinants of mineral commodity prices, it is difficult to estimate with great accuracy how the demand will behave in future years. The development of technology may decrease the need for lithium in each battery, or it could make it less energy intensive to extract lithium from low-quality reservoirs, among others. On the other hand, population growth, changes in future consumer preferences, and other determinants governing how rapidly society will move toward EV, are factors that are difficult to predict. In addition, some critical information on mineral commodities is currently unavailable. For these reasons, it may be debated whether this kind of forecasting should be used for such long-term projections [8]. The actual demand for lithium in coming years can significantly differ from the predicted values, but at least the studies give a general impression of the situation of lithium depletion.

Nevertheless, when comparing the estimations on supply and demand it seems, at a first glance, that lithium shortage will not pose an obstacle for the EV industry. Certainly, the majority of the studies considered agree that lithium availability will not become a constraint for the EV industry.

While some authors [3,4,7] assure that depletion of lithium is not a serious threat, some emphasize the importance of the fast inclusion of recycling measures [6,8]. Others [8,9] state that availability is not assured, and that production rates may pose serious problems of competitiveness among the markets in need of lithium.

Given its criticality, it is necessary to take action today to achieve efficient and relatively low-cost lithium recycling from car batteries, once the batteries of all the vehicles that are massively entering the fleet arrive to the end of their expected lifetime. This could be done through the implementation of policies, or the reduction of the current high expenses associated with recycling through technology improvement [12]. In addition, research is still needed in order to find a potential substitute for lithium, to decrease the pressure of its depletion.

## 11.4 Methodology: life cycle assessment of batteries

A sound and solid LCA study has a series of defined stages that have to be followed and are described in ISO 14040 and 14044, which are explained in more detail in the ILCD Handbook [13].

The comparison between the two lithium battery technologies serves the purpose of assessing the environmental performance of different lithium-based battery systems. This will allow a ranking of the two chemistries addressed, LMO and LFP, in terms of environmental performance. The results should target individuals who are assembling systems that need a lithium-based energy source and want to take into account the environmental performance above other parameters that might be disregarded in the application. The selected functional unit used in the analysis is the delivery of 1 kWh of energy previously stored in the lithium battery.

The system boundaries comprise the mining and extraction of raw materials, their processing, the component manufacturing, battery production, use stage, and the end of life of the product through hydrometallurgical recycling. A schematic of the system boundaries can be observed in Figure 11.2. The quality of data is limited to the

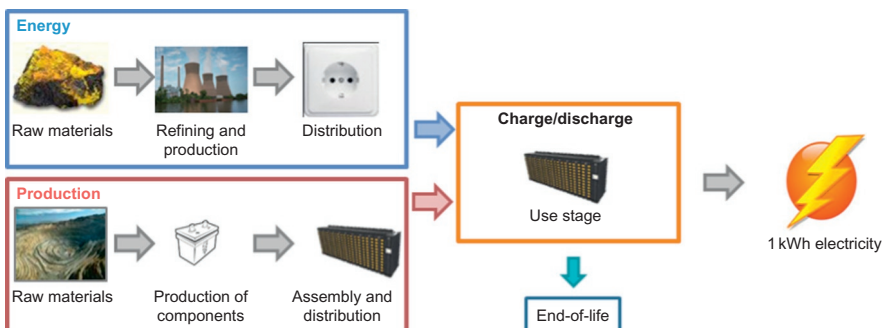


Figure 11.2 System boundaries and product stages.

inventories developed over the years, with the experience of several projects where the contact and input from battery manufacturers was paramount. Further laboratory analyses were conducted periodically as a control system to the provided inventory data.

The selected size for the storage is 1 kWh. Using an energy density of 125 Wh/kg [14] as a reference, a total battery size of 8 kg is modeled. As the functional unit is exactly the delivery of 1 kWh of energy stored, this will facilitate the impact assessment calculations and avoid further error propagation. The total number of cycles was assumed to be 4000 up to an end of life capacity of 30% [15]. The combination of these parameters leads to a total life cycle energy of 1400 kWh [16].

The manufacturing stage of the different lithium ion batteries includes the extraction of raw materials, their processing, and technological manipulation in order to produce the different components. The components that constitute the lithium battery chemistries addressed in the assessment are seen in [Table 11.1](#).

The components are accounted for in each of the chemistries, where transportation is included. Water consumption, heat, and assembly energies are taken into account during this stage. Both chemistries use the same components, although in different weight percentages and proportions.

The use stage is mostly dependent on the application that the battery systems are directed to. As a reference, the electricity mix for Belgium in the year 2011 is used. The environmental performance of this mix will be affected by the charge/discharge efficiency of the battery system. As an assumption, this efficiency is selected to be 95% [14]. The energy feedstocks on the Belgian electricity mix and their shares can be seen in [Table 11.2](#).

The end of life of both LMO and LFP battery systems includes their collection and processing. A hydrometallurgical method is used (as it is the standard in the recycling industry for these types of batteries) with recovery efficiencies of 100% for lithium and cobalt (almost negligible amounts), 75% for iron and steel, and 94% for the remaining nonferrous materials [15]. The inputs and outputs can be observed in [Table 11.3](#).

**Table 11.1 Lithium ion pack components**

Lithium iron phosphate (LFP)	Lithium manganese oxide (LMO)
Cell container	Cell container
Cell module and package	Cell module and package
Li-ion substrate (positive)	Li-ion substrate (positive)
Negative electrode	Negative electrode
Electrolyte	Electrolyte
Separator	Separator
Li-ion substrate (negative)	Li-ion substrate (negative)
Positive electrode	Positive electrode

**Table 11.2 Belgium electricity mix 2011, share of production per kWh**

BE mix 2011	
Coal and wood	4.60%
Fuel oil	0.02%
Gas	28.1%
Nuclear	59.2%
Pumped hydro	1.70%
Wind	1.10%
Solar	0.02%
Wood	0.60%
Industrial gas	2.30%
Municipal waste	2.36%

**Table 11.3 Inputs per kg of battery waste [15]**

Process	Amount	Unit
Waste batteries	1	kg
Reagent	0.025	kg
Electricity, national grid (France)	0.14	kWh
Industrial water	0.72	L
$H_2SO_4$ (92%)	0.23	kg
Lime	0.12	kg

## 11.5 Results: life cycle impact assessment

The life cycle impact assessment step of LCA aims at recounting the “environmental consequences” of the environmental loads gathered in the life cycle inventory analysis. This is done in order to make the inventory results more environmentally relevant and comprehensive, as well as to improve the communicability of the results. The impact assessment is done by classification and characterization of the quantified environmental loads into different impact categories. Classification is nothing but sorting and assigning of LCI parameters to different impact categories, based on their environmental effects. Categorization is a quantification step during which the total impact score for each impact category is obtained by multiplying the classified inventory parameters by their respective characterization factors.

The midpoint impact categories represent the environmental effects induced by the anthropogenic activities (e.g., CC, ozone layer depletion, resource depletion, etc.). These environmental effects create damage to areas that need to be protected (human health, ecosystem quality, natural resources) referred to as end point impact

categories. In general, the number of environmental load parameters of an LCI can vary from 50 to more than 300. Through LCIA, this vast number of environmental loads can be reduced to around 15 by grouping them into different midpoint impact categories. This number can further be reduced to approximately three by grouping the midpoint impacts into the following end point categories: damage to human health, damage to the ecosystem, and damage to resource availability. Through LCIA, it is also possible to obtain a single environmental score of a product by weighting and scoring across the impact categories. This will make comparison of two products easier.

In this study, the ReCiPe method has been employed to perform the life cycle impact assessment of the two battery technologies. Figure 11.3 illustrates the impact categories and environmental mechanism pathway used in the ReCiPe method.

Moving from an inventory model, the life cycle inventory results will appear in the form of elementary flows. These data are then used to calculate the different impact categories at midpoint level. Further up the process, the midpoint damages are compiled in three different end point categories such as damage to human health, damage to the ecosystem diversity, and resource availability.

Hereunder, the results of a life cycle impact assessment (midpoint categories) of LFP and LMO battery technologies are discussed briefly. Though there are 18 midpoint impact categories covered in the ReCiPe method, the focus of this study is on the

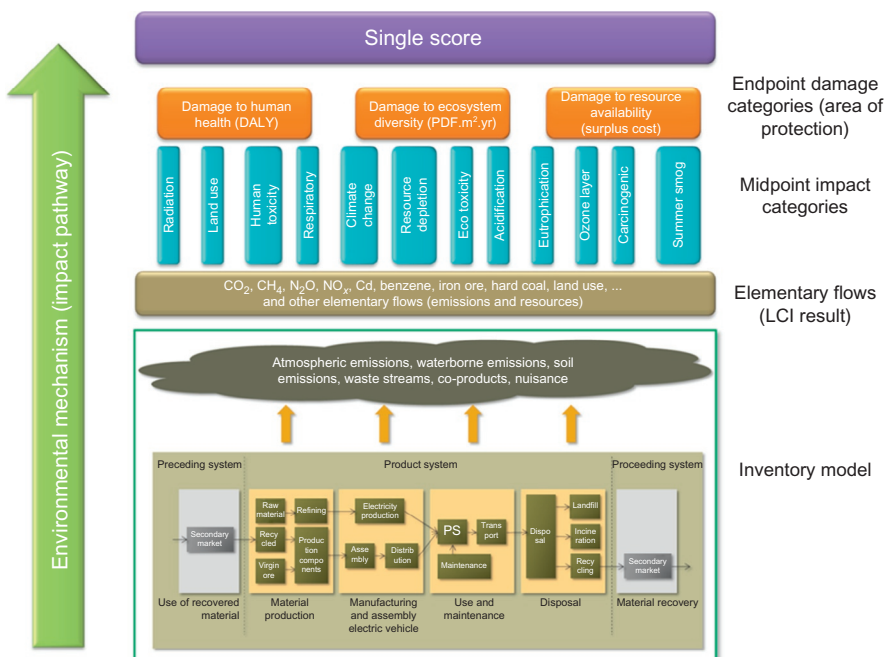


**Figure 11.3** Environmental impact pathway using ReCiPe methodology.

following four important categories: CC, human toxicity (HT), particulate matter formation (PMF), and metal depletion (MD).

### 11.5.1 Climate change

Man-made CC is caused by the emission of greenhouse gases (e.g., CO<sub>2</sub>, chlorofluorocarbons, etc.) from anthropogenic activities. Greenhouse gases are substances that are capable of absorbing infrared radiation from the earth (radiative forcing). Though there are many substances contributing to CC, carbon dioxide (CO<sub>2</sub>), methane (CH<sub>4</sub>), and dinitrogen monoxide (N<sub>2</sub>O) are the main contributing greenhouse gases. In the ReCiPe method, at the midpoint level, CC is expressed as the radiative forcing in the atmosphere of a substance relative to the radiative forcing of the reference greenhouse gas (CO<sub>2</sub>). CC is also known as the global warming potential (GWP) and is expressed in kg CO<sub>2</sub> equivalent. It has adverse effects on human health and ecosystem diversity.

Figure 11.4 compares the impact of the two battery models on CC. The LFP battery has higher CO<sub>2</sub> equivalent emissions per kWh than the LMO battery, because the use stages (i.e., efficiency) of these two batteries are exactly the same. The use stage emissions from charging electricity mix emanate mainly from natural gas (44%), coal (20%), and blast furnace gas (19%) power plants. Besides use stage emissions, the LFO battery has 26% and 24% of total CO<sub>2</sub> equivalent emissions from the manufacturing and recycling stages, respectively. On the other hand, the LMO battery has 14% and 11% of CO<sub>2</sub> emissions from the manufacturing and recycling stages, respectively.

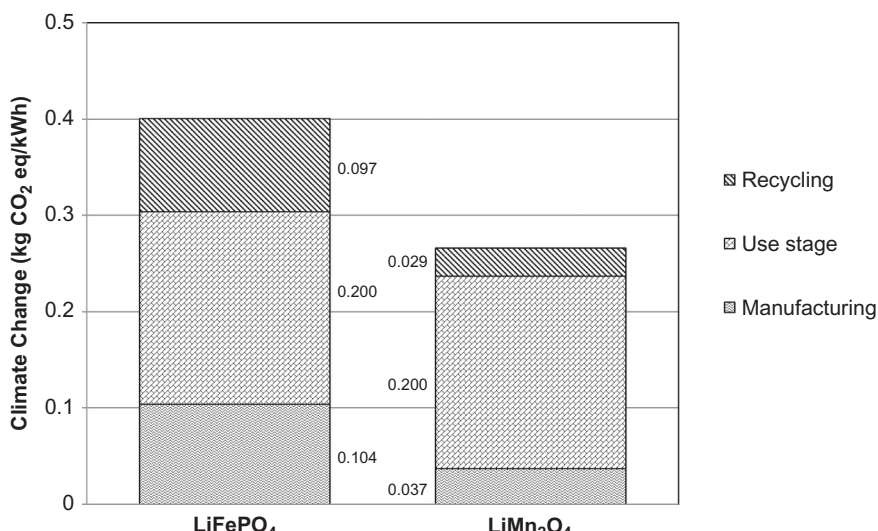


**Figure 11.4** Contribution to climate change (CC) from different product stages.

In the manufacturing stage of the LFP battery, production of materials (mainly tetrafluoroethylene and chlorodifluoromethane) for the electrodes contributes the most to the CC impact category. Next to that, a significant fraction of contribution originates from the use of electricity in the manufacturing process and the production of the cell container. In the LFP battery, the greenhouse gas emissions in the manufacturing stage originate primarily from the electricity used. Besides, production of electrodes and aluminum used in the LMO battery parts contribute a significant portion of the emissions in the manufacturing stage.

In the recycling process of both the batteries, emissions originate mainly from recycling of materials in the electrodes and the container, as well as from the electricity used in the recycling processes. There is a small benefit of greenhouse gas emissions from the recycling of aluminum metal in the cell container. However, this benefit is negligible when compared to the environmental burden caused by the materials and energy use in the recycling processes. The recycling process includes the collection of the batteries, its processing (energy and materials needed), and the resulting emissions. All the emissions and damages of this process are allocated to the battery system itself, as modeled.

### 11.5.2 Human toxicity

The HT midpoint category indicates the environmental persistence and accumulation of substances in the food chain together with the toxicity of the chemicals. In ReCiPe method, fate-exposure model has been used to describe the persistence and accumulation of toxic substances. It also considers the degradation half-lives and geographical conditions. The human exposure to toxic substances might take place through drinking, ingestion, inhalation, and so forth. The chemical 1,4-dichlorobenzene is used as a reference substance for this impact category.

Figure 11.5 illustrates the impact of LFP and LMO batteries on HT. It shows that the LMO battery has higher impact when compared to the LFP battery. This is mainly due to the fact that the environmental benefits for HT of recycling of the LFP battery is larger, compared to the benefits of recycling of the LMO battery. This means the emissions avoided due to the recycling of materials outweigh the emissions from the recycling process of the LFP battery. Hence, a big portion of the impact in the manufacturing stage of the LFP battery is balanced by the benefits of recycling. Secondly, the manufacturing process of the LFP battery has lower impact compared to the manufacturing of the LMO battery.

In both of the batteries, disposal of spoils from the mining of materials (e.g., lignite, sulfide, coal, copper, etc.) that are used in manufacturing and recycling are the main processes responsible for the HT impact in the manufacturing and recycling stages.

In both of the batteries, a major portion of contributions come from the use stage. These use stage emissions originate mainly from the disposals and tailings of wastes at the mining sites of uranium, coal, lignite, and copper.

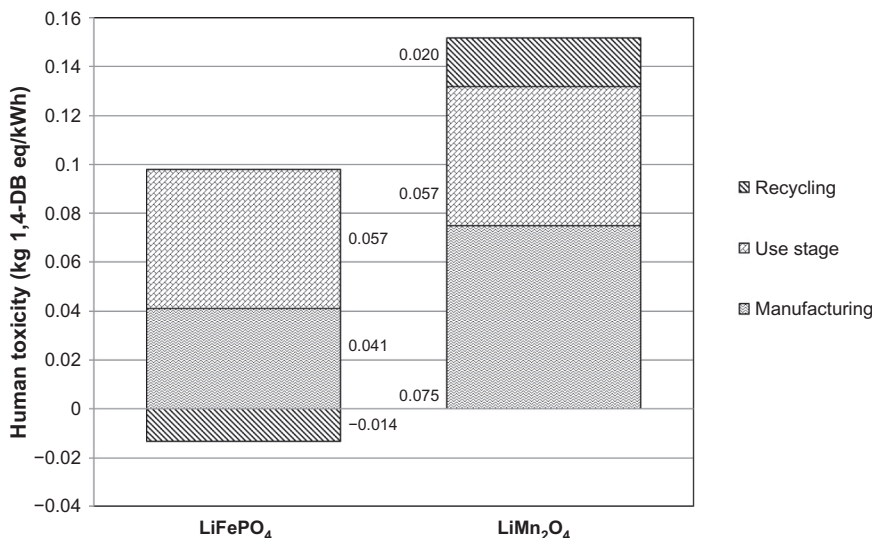


**Figure 11.5** Contribution to human toxicity (HT) from different product stages.

### 11.5.3 Particulate matter formation

Particulate matter (PM), also called *particle pollution*, is a mixture of very small airborne dust particles. Particle pollution might contain a number of components such as soil or dust, metal particles, organic chemicals, and acid (e.g., sulfates and nitrates). PM can be categorized as primary and secondary, based on the compounds and processes involved in its formation. Primary PM is discharged from the source as dust particles. In addition, sulfur dioxide (SO<sub>2</sub>), nitrogen oxides (NO<sub>x</sub>), and ammonia (NH<sub>3</sub>) emissions create PMs during their transformation in the atmosphere. This is called *secondary PM emissions*. Also, PM can be categorized based on the size of the particles (e.g., PM<sub>2.5</sub> and PM<sub>10</sub>). For instance, PM<sub>10</sub> denotes the airborne PM with a median diameter less than 10 µm. The impact category PMF aggregates primary and secondary forms of PM emissions under the unit PM<sub>10</sub> equivalent. This unit includes primary PMs up to 10 µm diameter, as well as the secondary PM emissions from SO<sub>2</sub>, NO<sub>x</sub>, and NH<sub>3</sub>.

Figure 11.6 describes the impact of LFP and LMO batteries on PMF. It shows that the LMO battery has slightly lower impact on the PMF category than the LFO battery. The dominance analysis shows that, in both the batteries, the largest portion of impact comes from the use stage (i.e., charging electricity mix). These use stage PM emissions originate mainly from coal, wood, and nuclear electricity generation. Coal and wood electricity have high PM emissions in the energy conversion stage, whereas PM emissions of nuclear energy originate mainly from the fuel production stage.

In both batteries, PM emissions at the manufacturing stage emanate primarily from the extraction of raw materials (mainly bauxite, aluminum, and copper) and electricity (mainly from coal) used for manufacturing.

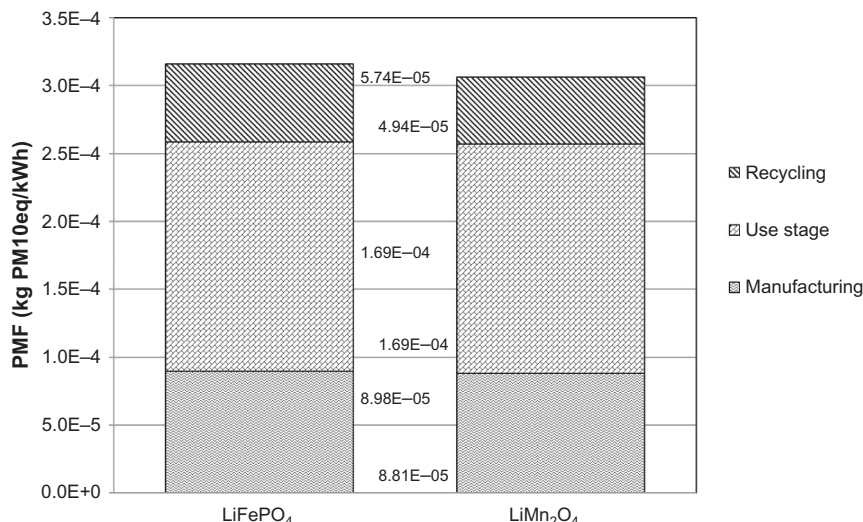


**Figure 11.6** Contribution to particulate matter formation (PMF) from different product stages.

In the recycling of the LFP battery, the emissions arise mainly from the recycling of the cell container and the electricity used in the process. Recycling of copper, aluminum, and steel has considerable fractions of benefits. In case of the LMO battery, recycling of electrodes and electrolyte (sulfuric acid) has greater impact than other processes. At the same time, there is a considerable amount of benefits from the recycling of manganese, aluminum, and copper metals.

#### 11.5.4 Metal depletion

Minerals or metals are nonrenewable resources, extracted from the natural deposits in mines. When the Earth was formed, geologic processes created areas in which minerals were deposited. The mineral resources depletion category focuses on the depletion of metals in these concentrated areas. Normally, usage of scarce metals leads to higher impact on the MD impact category. In the ReCiPe method, iron (Fe) has been taken as a reference material for the characterization factors.

Figure 11.7 compares the impact of the two battery technologies on the MD category. From the figure, it is apparent that the LMO battery has higher impact on MD when compared to the LFP battery. The material composition is almost the sole reason for this huge difference between the two batteries. The higher MD potential of manganese is the main reason for the LMO battery having higher impact on this impact category.

In the LFP battery, electrode substrates (copper) and the cell container (aluminum) are the main contributing system components for MD in the manufacturing stage. In case of the LMO battery, the positive electrode (manganese) and copper used for

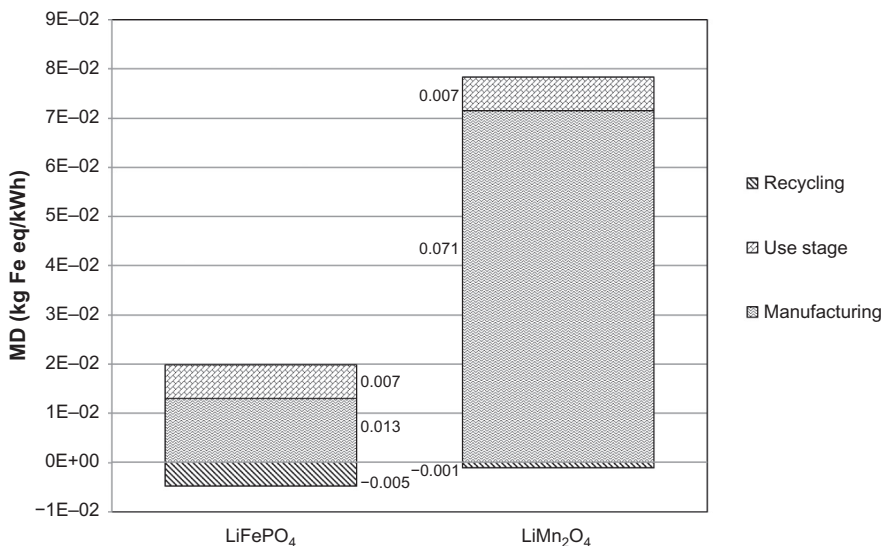


**Figure 11.7** Metal depletion (MD).

electrode substrates and wiring are the main components contributing to MD in the manufacturing stage.

In the LFP battery, materials used for the recycling of electrode substrates have a significant effect on MD. However, the benefits of recycling of copper and ferrous components prevail over the negative effect of the recycling process of the LFP battery. Similar to the LFP battery, recycling of electrodes is the main contributing process in the recycling stage of the LMO battery. Recycling of manganese, copper, and low-alloy steel has greater benefits by avoiding the extraction of virgin materials. Overall, in both the batteries, the benefit of recycling is greater than the environmental burden caused by the recycling processes.

In the use stage, the contribution for the MD category is mainly from the extraction of nuclear fuel (uranium) and the metals used in the transmission and distribution (steel, copper, and aluminum) infrastructures.

### 11.5.5 The influence of the electricity generation

Depending on the application of the Li-ion storage system, the environmental performance does vary through a very wide range. It is observable that the environmental ranking during the use stage is a function of the origin of electricity used (application). Using CC as an example of this hypothesis, Figure 11.8 shows a comparison of a LMO battery of 1 kWh under different energy mixes. The energy mix Union for the Co-ordination of Transmission of Electricity (UCTE) is now obsolete but quite descriptive of the average European energy feedstock provided by the network operators. This mix is mostly dependent on coal-fed plants and natural gas [14,15]. The environmental

### Infrastructure and use stage contributions to climate change

Various mixes

Unit: kg CO<sub>2</sub> equiv./kWh delivered

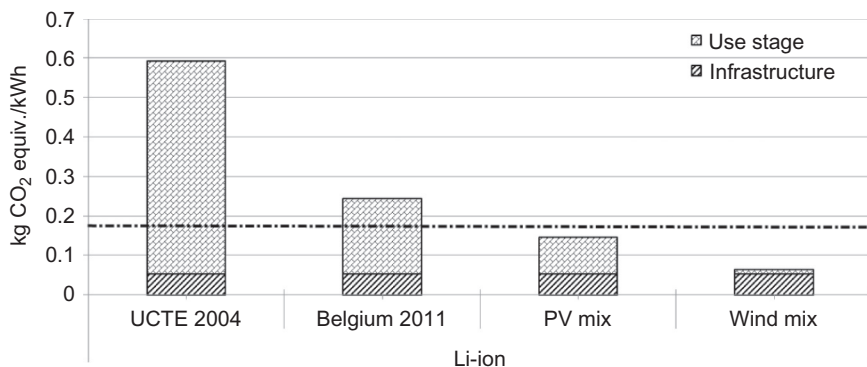


**Figure 11.8** Climate change contributions—LMO battery under different energy mixes.

performance concerning CC is 0.516 kg CO<sub>2</sub> equiv./kWh. The PV mix accounts for a feedstock totally dependent on photovoltaic energy supply (0.089 kg CO<sub>2</sub> equiv./kWh) and wind mix, for wind energy (0.0112 kg CO<sub>2</sub> equiv./kWh).

Being offset by the infrastructure contribution, the use stage damage score is a direct function of the efficiency multiplied by the baseline contribution of producing 1 kWh. The dashed line in Figure 11.8 shows the base load score for 1 kWh produced in Belgium for the year of 2011. The amount in kg of CO<sub>2</sub> equiv./kWh is of 183. The high efficiency is the responsible factor that determines the low damage. The infrastructure contribution is responsible for a significant share of the impact and is independent from the energy mix used in the use stage. It is not possible, now, to use any other energy mix different than the average for the country where the manufacturing stage takes place [15]. The low life cycle energy (number of cycles and capacity at EOL) is responsible for the high value of damages of this stage.

## 11.6 Conclusions

It is safe to say that the environmental performance of lithium battery storage systems is overall dependent on its efficiency and directly tied to the energy mixes associated with its use stage. When using renewable energy production mixes such as wind, the relevance of the use stage ceases to exist and the recycling and use stage become dominant. The LMO battery performs below threshold levels with a 100% wind electricity mix. In the case of CC, for example, the difference between the best and worst performer regarding CC would be close to 8%. Again, the impacts related to battery systems can be displayed with a temporal and geographical dimension as different components, and materials are extracted and produced in different places at different time frames.

When assessing the environmental impacts of the different chemistries of lithium batteries addressed here, differences can be seen mostly in the manufacturing and recycling stages. Depending on the impact category, the scores shift from both technologies. In the case of CC, producing an LFP battery causes more environmental burden than manufacturing an LMO pack. The LFP's score is roughly threefold higher. In terms of end of life, the proportion is similar, with a more penalizing score for LFP. HT damages are higher in the case of LMO for both manufacturing and end of life processes. In the case of LFP, an avoidance of the HT damage is observed by the negative (credit) score. PMF impacts are similar for both battery chemistries. No relevant differences are observed in this case. Material depletion shows a significant environmental impact of the manufacturing stage of the LMO battery pack. The resource availability issue in this case does not originate from the lithium itself but from manganese ore.

Environmentally, the inclusion of impacts on the selection of the lithium chemistry to be used in an application should be taken into account. The environmental impacts are spread through the two chemistries, with LMO favoring reductions on HT and MD and LFP, CC. PMF is similar in both cases.

## References

- [1] S. Vazquez, S.M. Lukic, E. Galvan, L.G. Franquelo, J.M. Carrasco, Energy storage systems for transport and grid applications. *IEEE Trans. Ind. Electr.* 57 (12) (2010) 3881–3895, <http://dx.doi.org/10.1109/TIE.2010.2076414>.
- [2] ISO 14040, Environmental management—life cycle assessment—principles and framework, first ed., 2006.
- [3] Communication from the Commission to the Council and the European Parliament (2003) Integrated product policy: building on environmental life-cycle thinking (COM (2003) 302); Brussels 2003.
- [4] P. Gruber, P. Medina, *Global Lithium Availability: A Constraint for Electric Vehicles?* University of Michigan, 2010.
- [5] A. Yaksic, J.E. Tilton, Using the cumulative availability curve to assess the threat of mineral depletion: the case of lithium, *Resour. Policy* 34 (2009) 185–194. <http://dx.doi.org/10.1016/j.resourpol.2009.05.002>.
- [6] S.H. Mohr, G.M. Mudd, D. Giurco, *Lithium resources and production: critical assessment and global projections*, *Minerals* 2 (2012) 65–84.
- [7] Keith Evans, An Abundance of Lithium Part Two, 2008. Retrieved from: [http://www.worldlithium.com/AN\\_ABUNDANCE\\_OF\\_LITHIUM\\_-Part\\_2.html](http://www.worldlithium.com/AN_ABUNDANCE_OF_LITHIUM_-Part_2.html). Last visited: 07-05-2014.
- [8] C. Grosjeana, P.H. Miranda, M. Perrin, P. Poggi, Assessment of world lithium resources and consequences of their geographic distribution on the expected development of the electric vehicle industry, *Renew. Sust. Energ. Rev.* 16 (2012) 1735–1744. <http://dx.doi.org/10.1016/j.rser.2011.11.023>.
- [9] H. Vikström, S. Davidsson, M. Höök, Lithium availability and future production outlooks, *Appl. Energy* 110 (2013) 252–266. <http://dx.doi.org/10.1016/j.apenergy.2013.04.005>.
- [10] W. Tahil, *The Trouble with Lithium—Implications of Future PHEV Production for Lithium Demand*, Meridian International Research, 2007.

- [11] USGS, Lithium Statistics and Information, 2014. Retrieved from: <http://minerals.usgs.gov/minerals/pubs/commodity/lithium/>, Last visited: 07-05-2014.
- [12] S.E. Kesler, P.W. Gruber, P.A. Medina, G.A. Keoleian, M.P. Everson, T.J. Wallington, Global lithium resources: relative importance of pegmatite, brine and other deposits, *Ore Geol. Rev.* 48 (2012) 55–69. <http://dx.doi.org/10.1016/j.oregeorev.2012.05.006>.
- [13] G. Majeau-Bettez, T.R. Hawkins, A.H. Strømman, Life cycle environmental assessment of lithium-ion and nickel metal hydride batteries for plug-in hybrid and battery electric vehicles, *Environ. Sci. Technol.* 45 (10) (2011) 4548–4550, <http://dx.doi.org/10.1021/es103607c>.
- [14] The International Reference Life Cycle Data System (ILCD) Handbook – Towards more sustainable production and consumption for a resource-efficient Europe – WOLF Marc-Andree; PANT Rana; CHOMKHAMSRI Kirana; SALA SERENELLA; PENNINGTON David, Publications Office of the European Union, 2012. <http://publications.jrc.ec.europa.eu/repository/handle/JRC66506>.
- [15] I. Hadjipaschalidis, A. Poullikkas, V. Efthimiou, Overview of current and future energy storage technologies for electric power applications, *Renew. Sustain. Energy Rev.* 13 (6–7) (2009) 1513–1522. <http://dx.doi.org/10.1016/j.rser.2008.09.028>.
- [16] H. Chen, T.N. Cong, W. Yang, C. Tan, Y. Li, Y. Ding, Progress in electrical energy storage system: a critical review, *Prog. Nat. Sci.* 19 (2009) 291–312. <http://dx.doi.org/10.1016/j.pnsc.2008.07.014>.

## Appendix: abbreviations

BE	Belgium
CC	climate change
CO <sub>2</sub>	carbon dioxide
EC	European Commission
EV	electric vehicle
GWP	global warming potential
HT	human toxicity
LCA	life cycle assessment
LCIA	life cycle impact assessment
LFP	lithium iron phosphate
Li-ion	lithium-ion
LMO	lithium manganese oxide
MD	metal depletion
PM	particulate matter
PMF	particulate matter formation
USGS	United States Geological Service

# Rechargeable lithium batteries for energy storage in smart grids

12

K. Zaghib<sup>1</sup>, A. Mauger<sup>2,3</sup>, C.M. Julien<sup>2,4</sup>

<sup>1</sup>Energy Storage and Conversion, Research Institute of Hydro-Québec, Varennes, QC, Canada;

<sup>2</sup>Sorbonne Universités, Paris, France; <sup>3</sup>IMPMC-Institut de Minéralogie, de Physique des Matériaux, et de Cosmochimie, Paris, France; <sup>4</sup>PHENIX-Laboratoire de Physicochimie des Electrolytes et Nanosystèmes Interfaciaux, Paris, France

## 12.1 Introduction

The rapid increase in electricity consumption imposes the integration of new primary sources, requiring more attention in the design, control, and management of the electric grid [1]. Wind is one of the renewable resources having advantages that separate it from other kinds of renewable energies [2]. First, wind is a primary resource that is abundant everywhere. Second, compared with other resources like solar energy, the investment cost in wind power is relatively low. In this case, the output power of wind turbine generators always fluctuates because of the random nature of the wind speed [3]. Traditional grids, which are not designed to meet these goals, are often unable to provide satisfactory performance, and recent studies have suggested that the grid can become unstable if power from these sources exceeds 20% of the whole generated power without adequate compensating measures, namely energy storage [4,5]. The traditional solution to smooth the fluctuations is to sell the surplus wind power on the competitive market or purchase traditional power to compensate the shortage of the wind power generation. The process, however, has some limits. The first one is response time. For instance, EPEX SPOT that operates short-term trading in power for Germany, Austria, France, and Switzerland, provides physical delivery of power for the next day. It also provides an intraday market for Germany and France, allowing participants to buy electricity up to 45 min before the specific hour [6]. This is the shortest time. In addition, this solution is not acceptable from two viewpoints: first, during the compensation process the bioenvironmental contamination increases by thermal units; second, purchasing with no anticipation causes extra costs [7]. Therefore, energy storage is mandatory, not only in developed countries [8] but also in developing countries as well [9,10]. A battery energy storage system can be an efficient way to smooth wind power fluctuation in spite of a little higher cost of batteries [11].

The grid-connected energy storage market will increase from 340 MW in 2013 to more than 6 GW in 2017, according to IHS [12] and Meza [13]. To satisfy this demand, a few different types of storage can assist the grid. It need high-energy short duration storage (like flywheels or supercapacitors) for power quality issues. It needs shorter duration, but high power (NaS, Li-ion, flow batteries, etc.), to support variability. It needs high-energy capacity systems (like pumped hydro and compressed air)

to support load leveling and transmission constraints. They are reviewed hereunder. The different processes are reviewed in this section. They are devoted to optimizing the supply of electricity at different scales, from pumped-storage hydroelectricity (PSH) that is devoted to deliver a typical power at 2000 MW and, thus, operate at the scale of a region, down to battery plants that deliver a power smaller than 50 MW and, thus, are intended to optimize electricity delivery at the scale between a town, or a house. So, these processes are not in competition, but instead should be considered as complementary. On the other hand, within a given process, such as batteries, several technologies are possible, and a comparison in terms of effectiveness and prices is given for each of them in order to help decision makers to make a choice, depending on the use that is planned.

## 12.2 Energy storage

### 12.2.1 Pumped-storage hydroelectricity (PSH)

This method stores energy in the form of potential energy of water, pumped from a lower elevation reservoir to a higher elevation. The scheme is illustrated in Figure 12.1. Low-cost off-peak electric power is used to run the pumps. During periods of high electrical demand, the stored water is released through turbines to produce electric power. This is the largest capacity form of grid energy storage available. The technique is currently the most cost-effective means of storing large amounts of electrical energy on an operating basis. A new use for pumped storage is to level the fluctuating output of intermittent energy sources. The pumped storage provides a load

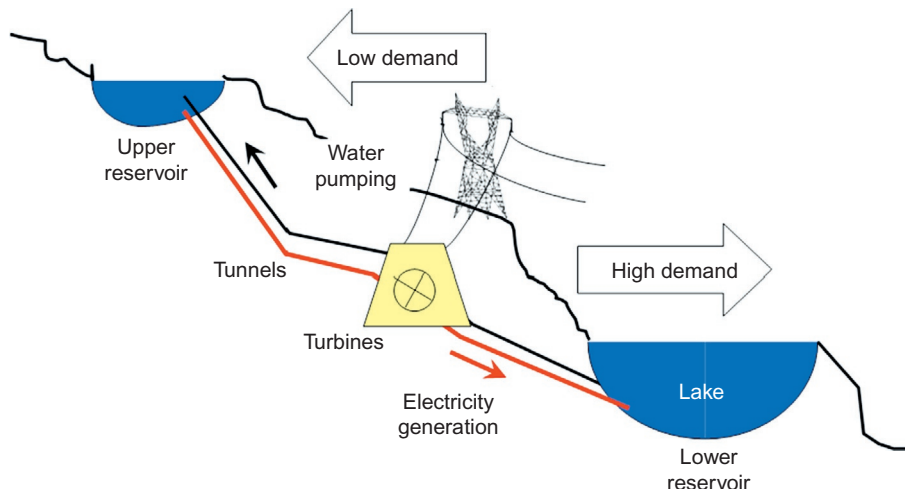


**Figure 12.1** Principle of the pumped-storage hydroelectricity. The pumped storage provides a load at times of high electricity output and low electricity demand, enabling additional system peak capacity.

**Table 12.1 The largest operational pumped-storage plants**

Station	Country	Power (MW)
Bath County Pumped-Storage Station	USA	3003
Guangdong Pumped-Storage Power Station	China	2400
Huizhou Pumped-Storage Power Station	China	2400
Okutataragi Pumped-Storage Power Station	Japan	1932
Ludington Pumped-Storage Power Plant	USA	1872
Grand Maison	France	1800

at times of high electricity output and low electricity demand, enabling additional system peak capacity. Along with energy management, pumped storage systems help control electrical network frequency and provide reserve generation. The big plants are listed in [Table 12.1](#) with their implementation and the power they deliver. The main advantages are (1) long lifetime (30–50 years) [\[14,15\]](#); (2) big capacities: power rating 10–1000 MW, energy rating 500–8000 MWh [\[15\]](#); (3) very good cycle capability of 20,000–30,000 cycles according to the Electricity Storage Association; and (4) fast response time: a reaction time as short as 10 min or less from complete shutdown (or from full reversal of operation) to full power. In addition, if kept on standby, full power can even be reached within 10–30 s according to [\[16\]](#).

There are, however, some drawbacks. First, taking into account evaporation losses from the exposed water surface and conversion losses, only 70–85% of the electrical energy used to pump the water into the elevated reservoir can be regained [\[17,18\]](#). Second, capital costs for purpose-built hydro-storage are relatively high (power capital costs of 500–1500 \$/kW and 10–20 \$/kWh) [\[14\]](#). It requires massive reservoirs that cost more than \$1 billion and take years to construct with ideal geography and abundant water resources. And, finally, the process requires important grid. This technology can be implemented only in regions that have the appropriate geology, because it cannot be implemented in flat regions for instance, and of course, it requires water resources. That pretty much rules out the arid southwestern United States, but also sub-Saharan Africa. Nevertheless, the technique is currently the most cost-effective means of storing large amounts of electrical energy on an operating basis where it can be implemented. As this technology is old (authors date the first use in the 1890s), we shall not discuss it any further, but this should not mask that it accounts for more than over 90 GW of pumped storage in operation worldwide, which is about 3% of global generation capacity, including 20 GW for the United States and 38 GW for Europe [\[19\]](#). It is the most used technique for power applications [\[20\]](#). The technology has also improved, with the use of wind turbines or solar power to drive water pumps directly, which is a useful tool to smooth out the variability of energy captured from the wind or sun [\[21,22\]](#). It is also expected to play an important role as a balance for photovoltaic generation at very large scale. Also, with the recent introduction of variable speed machines, PSH systems can now be used for frequency regulation in both pumping and generation modes. For these reasons, PSH is considered to be one of

the most well-suited storage systems in order to achieve high penetration levels of wind power in isolated systems [23–26].

### 12.2.2 Compressed air energy storage

In this process, illustrated in [Figure 12.2](#), the energy is stored in the form of compressed air in an underground storage cavern. When energy is required to be injected into the grid, the compressed air is drawn from the storage cavern, heated, and then expanded in a set of high- and low-pressure turbines, which convert most of the energy of the compressed air into rotational kinetic energy. While the turbines are connected to electrical generators in order to obtain electrical energy, the turbine exhaust is used to heat the cavern air. Two plants have been built: one in Germany (290 MW) and the other in the United States (110 MW) [20]. Among the biggest projects that have been carried out is the Iowa Stored Energy Park, with 2700 MW of turbine power.

In advanced adiabatic compressed air energy storage (CAES), the air is adiabatically compressed and then pumped into an underground cavern. RWE Power, General Electric (GE), Züblin, and DLR are investing in the ADELE adiabatic CAES project that will have a storage capacity of 360 MWh and an electric output of 90 MW. This enables ADELE-Stassfurt to provide substitute capacity on extremely short notice and replace up to 50 wind turbines of the type used in this region of Germany for a period of 4 h [28]. The project will run 3.5 years from 2013 and has an overall budget of some €40 million. The price is due to the heat exchangers, which are quite expensive. The effectiveness and the economics of these heat exchangers and the compressor and expander trains are the main concerns for the success of this technology. Joseph Simmons, director of the Arizona Research Institute for Solar Energy (azRISE), estimates a 10-kW compressed air storage system with a \$50,000 price tag can generate 30 kWh or 3 h of electricity at 33 €/kWh [29]. The main characteristics of CAES storage are (1) lifetime of 30–40 years [30,31], and cycling capability of 10,000–30,000 cycles [32], quite similar to PSH figures; (2) capital cost of 3–5 €/kWh [14],

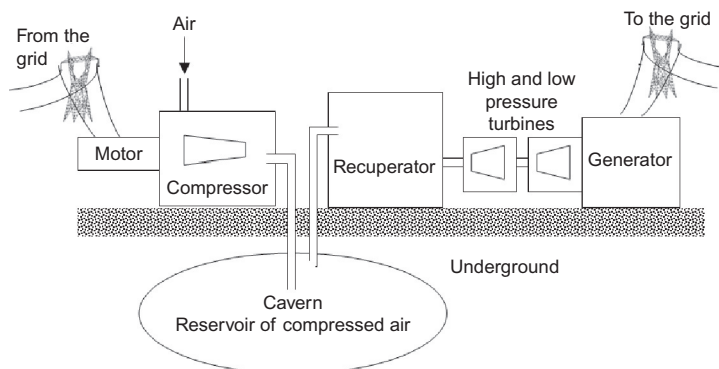


**Figure 12.2** Principle of the compressed air energy storage [27]. This technique uses an underground cavern as a reservoir of compressed air.

10–70 €/kWh [33]; (3) power rating of 50–300 MW [34,35] and energy rating of 580–2860 MWh [35]; (4) efficiency of 70–73% [20,30,34]; and (5) fast reaction time with plants usually able to go from 0% to 100% in less than 10 min, 10% to 100% in approximately 4 min, and 50% to 100% in less than 15 s. As a result, it is ideal for acting as a large sink for bulk energy supply and demand and, also, it is able to undertake frequent start-ups and shutdowns [36].

### 12.2.3 Flywheel energy storage

This storage, illustrated in Figure 12.3, works by accelerating to a very high speed a cylindrical assembly called a *rotor flywheel*, usually in carbon fiber [37,38], and by maintaining the energy in the system as rotational energy. The energy is converted back by slowing down the flywheel. The flywheel system itself is a kinetic, or mechanical battery, spinning at very high speeds to store energy that is instantly available when needed. The entire structure is placed in a vacuum to reduce wind shear [38–42]. The advantages of this technology are (1) high cycling capability using flywheels are designed for hundreds of thousands of charge–discharge cycles over their 20-year life; (2) almost no maintenance; and (3) very fast response so that it is well suited to dampen frequency variations and smooth the irregular electrical output. There are also disadvantages: (1) capital cost: 400–800 kWh [34,43]; (2) low energy rating: 0.0252 MWh [44], power rating 0.1–20 MW; (3) the output: the total system round-trip charge/discharge efficiency is 85% (to reduce the friction as much as possible, the recent rims are levitated on hybrid magnetic bearings operating in a near-frictionless vacuum-sealed environment [44]); and (4) the time storage is limited to 15 min. An example of this technology is Beacon Power's 20 MW Stephentown Advanced Energy Storage plant that provides about 10% of New York's overall frequency regulation needs. The rated capacity is 20 MW with 4 s' response time (5 MWh over 15 min).

We report in Figure 12.4a and b the comparison of the annual costs, in \$/kW-year, for a 1-h distributed generation application between different technologies, and the

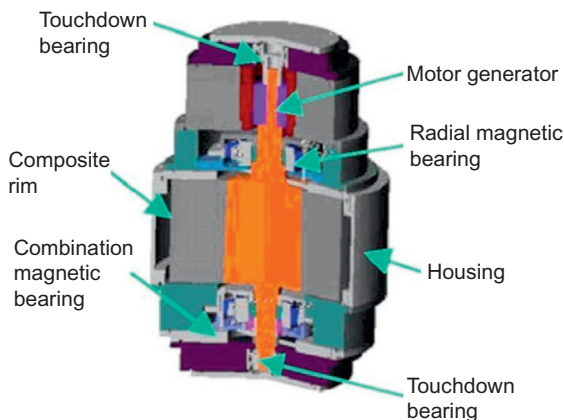


**Figure 12.3** Flywheel energy storage.

Source: Electric Power Research Institute.

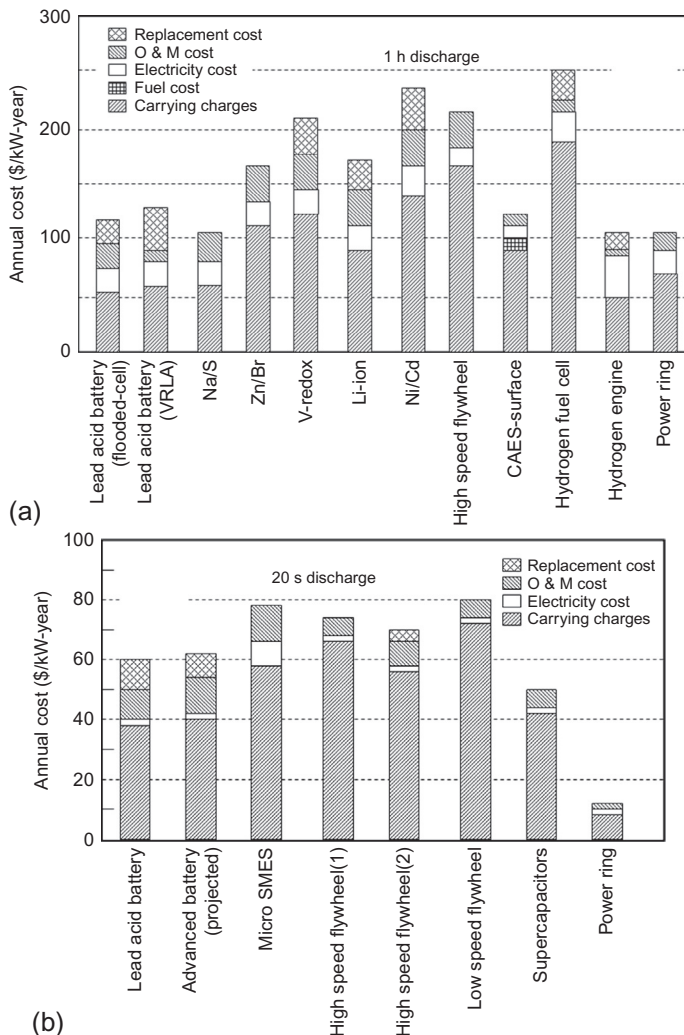


**Figure 12.4** Components of annual costs for distributed generation technologies [45].  
(a) One-hour discharge and (b) 20-s discharge.

same Figure 12.4a for a reduced storage duration of 14 s, both of these figures published by Schoenung [46]. An added column shows Power Ring costs, using the same methodology. Power Ring is a third generation flywheel that LaunchPoint Technologies is developing [45], using radial gap magnetic bearings to levitate thin-walled composite hoops rotated at high speed to store kinetic energy. The details of this technology are reported in this reference. The result assumes a 200 kW (Figure 12.4a), 1-h ring with an estimated price in high-volume production of \$120k, AC/DC converter included, resulting in costs of 6k\$/kWh or 6k\$/kW, and

a carrying charge of 72 \$/kW-year. In [Figure 12.4b](#), for the 20-s application, the result is for a 45 MW, 20-s ring with an estimated low-volume production price, including converter, of  $\sim$ 2.5 million (10k \$/kWh or 55.5 \$/kW), and a carrying charge of 6.67 \$/kW-year. [Figure 12.4a and b](#) illustrates that “Power Rings” will be even more cost effective as storage duration decreases. Power levels exceeding 50 MW and electricity storage capacities exceeding 5 MWh appear technically feasible and economically attractive.

### 12.2.4 Electrochemical batteries

Since the invention of the lead-acid battery by Planté in 1659, numerous electrochemical systems have been developed; schematics of three of these are shown in [Figure 12.5](#). Lead-based batteries (LBB) are the most used energy storage. For on-grid storage, they feature the following performance characteristics: (1) calendar life of 5–15 years [[34,47,48](#)]; (2) capital cost of 50–200 \$/kWh [[14,34](#)]; (3) energy rating of  $\leq$ 40 MWh (typically 40 Wh/l) and power rating of  $\leq$ 10 MW [[48](#)]; and (4) energy efficiency: of 75–80% [[14,49](#)]. LBBs are thus well suited for several on-grid applications [[50](#)]. They have some advantages such as (1) robust technology and less sensitivity to application conditions; (2) low self-discharge (0.1–0.2%) per day [[34,51,52](#)]; and (3) the possibility to connect in large battery arrangements without sophisticated management systems. The main advantage, with respect to Li-ion batteries (LiBs) in particular, is the low cost per kWh (typical about €120–200) to install and low cost per kWh electricity throughput (typical range of 0.1–0.15 €/kWh turnover for the battery only) [[53](#)]. The low cost, however, is not sufficient to win the market, as performance in terms of cycling life and specific density is far from the other batteries on the market. In particular, Texas-based startup Xtreme Power decided to sell off the factory where it makes its novel advanced lead-acid batteries earlier this year, to concentrate on the less capital-intensive business of energy storage management software. Indeed, these batteries also have the disadvantages of (1) low energy and power densities

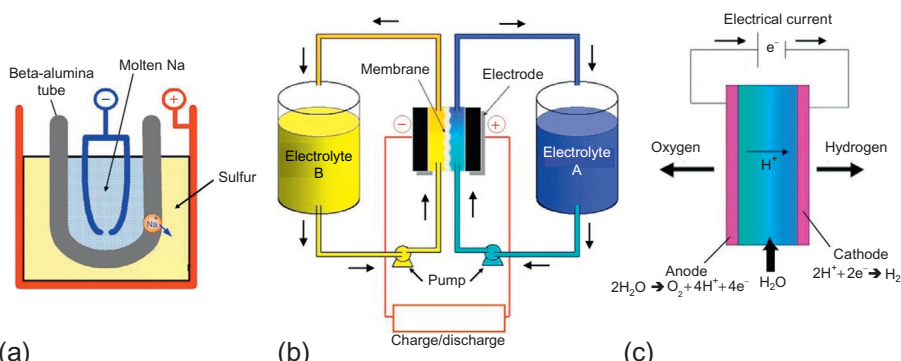


**Figure 12.5** Schematic representation of three electrochemical systems. Principle of NaS cell (a), flow battery (b), and fuel cell (c).

(30 Wh/kg and 180 W/kg, respectively); (2) low cycle life of 1800 cycles [34,49]; (3) they are very sensitive to temperature as a departure by 2 ° from the nominal temperature (25 °C) reduces the life by a factor 2 [36]. High operating temperatures (up to 45 °C) can improve battery performance in terms of higher capacity, but reduce the lifetime of the system; (4) the charge must be done at low rate; and (5) sulfation can lead to premature failure of the battery [48].

Sodium-based systems include two technologies: sodium–sulfur (NaS) and sodium–nickel–chloride batteries. A sodium–sulfur battery is constructed from liquid sodium and sulfur operating at high temperature (300–350 °C) [54]. Ceramic  $\beta$ -Al<sub>2</sub>O<sub>3</sub> acts as both the electrolyte and the separator simultaneously [55]. This scheme is shown in [Figure 12.5a](#). The main problem with this battery is safety, because the sodium is highly corrosive and burns spontaneously in contact with air and moisture. Even in sodium-ion batteries under investigation today as an alternative to Li-ion batteries in the future, it is generally accepted that sodium is too dangerous to be used as a negative electrode, and sodium intercalation compounds are preferred. Since 2008, only the consortium NGK Insulators Ltd and Tokyo Electric Power Co (TEPCO) have run the risk to manufacture the NaS battery. The implementation of NaS batteries, however, has been slowed down by the 2011 accident at the Tsukuba plant in Japan, where such batteries caught on fire. Nevertheless, NGK Insulators Ltd reports on its website ([www.ngk.co.jp/english/announce/111031\\_nas.html](http://www.ngk.co.jp/english/announce/111031_nas.html)) that it has commenced the production of new NaS batteries that have been modified to avoid the spread of fire by adding fuses between battery cells, insulating boards between blocks in battery modules, and antifire boards between battery modules. These efforts to develop this technology, despite the hazard it presents, are motivated by the fact that Na and S are cheap products, and abundant; in addition, the NaS battery has a high energy density (150 Wh/kg). Such a battery has been used as a demonstrator to supply electric power in the Space Shuttle, but in practice the safety concerns limit the use of the NaS battery to grid energy storage. The biggest NaS plant was built at Presidio (Texas) in 2010, just 1 year before the Tsukuba fire, to store up to 4 MW of power upon charging in 8 h, serving as an emergency backup to the outages caused by the line going down. This is an example of the use of battery technology to put off expensive upgrades for the power grid. Characteristics of NaS batteries include relative cost and efficiency. Presently, the approximate cost of a 1-MW, 6-h sodium–sulfur (NaS) battery is 3000\$/kW. That translates to a cost of 500\$/kWh (\$3000/6 h = \$500) [29]. This result compares well with another estimate of 450\$/kWh [56]. Energy density of 151 kWh/m<sup>3</sup> and efficiency of 85% have been found [15]. Back in 2009, GE launched its foray into the grid-scale energy storage business, announcing it was investing \$100 million in a plant to commercialize its sodium–nickel–chloride Durathon battery technology [57]. A variant on the high-temperature sodium–metal battery chemistries, GE’s Durathon batteries [58] were aimed at storing lots of energy for longer periods of time than competing lithium-ion technologies. However, with the new Li-ion technology that allows for cycling lives longer than 30,000 cycles, it remains to be seen how the markets will decide on Durathon. The characteristics of NaNiCl<sub>2</sub> batteries are [53] (1) calendar life > 10 years in stationary float applications and cycle life of 4500 cycles at 80% depth of discharge (DOD); (2) operating temperature range of –30 to +60 °C

without power reduction; (iii) energy density of 120 Wh/kg (140 Wh/l) at battery level; (iv) energy efficiency of 92% at C/4 rate; and (v) power rate up to the MW size and 3–6 h energy are being developed and are currently under test.

Nickel-based batteries (nickel–cadmium, nickel–metal hydride, nickel–hydrogen, and nickel–zinc) are the second most used electrochemical energy storage after LBB. They serve special markets where energy must be stored in an extreme climate; in particular, the operating temperature range extends down to  $-40^{\circ}\text{C}$ , while Li-ion batteries are not operating below  $-20^{\circ}\text{C}$ . Their characteristics are (1) capacity of 0.5–2000 Ah; (2) 20–80 Wh/kg (50–300 Wh/l) nominal energy density; (3) energy efficiency of  $>90\%$  (dependent on application); (4) calendar life of 25 years; and (5) cycle life of  $>3000$  cycles. Their costs range from 350 to 1400\$/kWh to install. The cycle life needs to be improved, and the cost needs to be reduced. Nickel–metal hydride (NiMH) can perform over extended periods of time in a wide operating range of  $-30$  to  $+65^{\circ}\text{C}$ , significantly reducing the complexity and cost of thermal management systems required for a utility-scale energy storage installation. This was the motivation for BASF to make investments in 2013 on this battery for backup grid applications [59]. Early cells were susceptible to memory effect and also suffered from high self-discharge, nearly 10 times worse than lead-acid or lithium batteries, but both of these weaknesses have been overcome and it is claimed that the most recent cells can hold their charge for a year. The active chemicals are inherently safer than lithium-based cells, and NiMH batteries don't need the complex battery monitoring system that is mandatory for Li-ion batteries. Nevertheless, because of potential pressure buildup due to gassing, they usually incorporate a resealable vent valve. With the improvement of the safety of LiFePO<sub>4</sub> positive electrodes of Li-ion batteries, however, the advantage of NiMH is reduced to the extended operating temperature range and the cost. Because NiMH batteries have much smaller energy density and power density than Li-ion batteries, and have lost their advantage with respect to Li-ion batteries that can be cycled 30,000 times at 100% charge–discharge within a minute, the future for Ni-based batteries in the coming years relies only on its lower price, and mostly for off-grid applications.

In a flow battery, two different aqueous electrolytic solutions, say A and B, are contained in separate tanks, as shown in Figure 12.5b. During normal operation of the battery, these aqueous solutions are pumped through the electrochemical cell where the electrochemical reactions occur [60,61]. During the charge process, the electrolyte A is oxidized at the anode, while the electrolyte B is reduced at the cathode. The discharge cycle consists of the reverse process. Like any battery, the flow batteries have in common that their energy is easily scalable as it depends on the volume of the stored electrolyte. But they have an advantage with respect to Li-ion batteries: their self-discharge rate is negligible because the electrolytes are stored in separate sealed tanks [62–64], while that of Li-ion batteries is typically 5% per month. On the other hand, the energy densities of flow batteries are low compared to Li-ion batteries. Some of them also show tolerance to overcharge/overdischarge, which is rarely the case with Li-ion batteries, except with the LiFePO<sub>4</sub> cathode. A review on the different flow batteries and their components has been published online, with a focus on understanding the underlying physical processes [65]. The detailed chemistry on the redox reactions and technical aspects has been reviewed in Ref. [66]. Attention, here, is

focused on the main three types of flow batteries that are used for grid applications. Commercial flow batteries use vanadium ions in the liquid on both sides of the barrier. But vanadium and the membranes are very expensive: the world's largest flow battery, installed at a wind farm in China, probably costs 1000\$/kWh [67]. This contradicts prior claims according to which the cost per kWh decreases as energy storage capacity increases, achieving costs as low as 150\$/kWh for 8 or more hours of storage devices [68]. It is even recommended to replace the membrane every 5 years [49], which enhances even more the cost of the kWh. A capital cost of 600\$/kWh has also been reported for these batteries [69]. These differences show that vanadium redox flow batteries (RFB), being still an emerging technology, have uncertain a precise cost right now. Nevertheless, the most authoritative studies estimate the cost of a VRFB system designed for frequency regulation is about 1460–1613\$/kW of rated power [70]. Li Hongfeng of Prudent Energy [71] described the tryout of the company's trademarked vanadium redox battery-energy storage system (VRB-ESS) vanadium redox flow battery (VRFB) in Germany where the grid is required to buy wind energy at 9€/kWh and photovoltaic energy at 20€/kWh (presumably in a feed-in tariff system). The objective was to determine whether the flow battery could help reduce the town's dependence on the grid and provide some support for it. VRB-ESS could yield revenue and improve grid performance [72]. Li Hongfeng reported that the optimal sizing of the system in a microgrid environment appears to be 3 MW of power and 4 h worth of energy storage. Germany's Bielefeld-based Gildemeister with a majority stake in Cellstrom, the Austrian-based maker of the CellCube VRFB system [73], has sold its CellCube devices in Europe and Asia. In particular, it received €29.2 million in December 2012 to supply a VRFB for the Smart Region Pellworm project of the energy supplier "E.on" [74]. With a capacity of 1.6 MWh, the CellCube stores energy from wind power and solar installations. The renewable energy is fed, according to consumption, into the regional electricity grid and ensures a self-sufficient base load supply for the third largest island in the Schleswig Holstein Wattenmeer national park [75]. The solar projects include a 6.5 MW solar farm in Italy and an 8 MW solar park in Romania. It is also working with partner Younicos to create "battery parks" meant to serve broad grid-balancing functions in Europe's increasingly renewable-energy-disrupted energy markets. American Vanadium, a Canadian mining company that is based in British Columbia and produces vanadium, has been Gildemeister's North American distribution partner since May 2013. It announced a potential milestone in the efforts to promote this technology, with the delivery of the first CellCube units for testing by the Department of Energy's National Renewable Energy Laboratory (NREL) in Golden, Colorado. That testing could be complete by this summer, at which point at least one US utility, as well as various integration partners, are interested in deploying it state-side [76]. The world's largest vanadium redox flow battery on line in 2012 is the 600 kW/3.6 MWh VRB® Energy Storage System used to expand onsite power generation at an agricultural processing facility in California owned by Gills Onions [77]. In May 2013, the State Grid Corporation of China has commissioned a 2 MW/8 MWh VRB-ESS battery system, as part of the Zhangbei National Wind/PV/Energy Storage and Transmission Joint Demonstration Project. On the other hand, huge projects, such as a project for 60 MWh in Alaska, or the outstanding 120 MWh for the Arnold Air

Force do not look reasonable [78], and seem to have been abandoned. The characteristics of the vanadium flow batteries are (1) an energy rating mostly in the range of the MWh [48]; (2) a power rating of 0.2–10 MW [48,79]; (3) cycling capability of 1000 [80] to 13,000 [81]; (4) life of 15–20 years [30,74,82]; and (5) energy efficiency of circa 75% [30,76,83,84] although rates up to 85% have been claimed [60]. In the case of the zinc–bromine flow battery, the two electrolytes are based on Zn and Br. During the discharge process, bromide ions  $\text{Br}^-$  are converted to bromine  $\text{Br}_3$  in the positive electrode. Meanwhile, in the negative electrode, positive zinc ions  $\text{Zn}^{2+}$  are converted to metallic Zn. This technology is now available in sizes of 1 MW/3 MWh for utility-scale applications [32], with the ability to provide its rated power for 2–10 h [85] without significant self-discharge [79]. The metal negative electrode allows for a compact electrode, thus increasing the energy density. In addition, the zinc/bromine system has a high cell voltage, good reversibility, and expectations of low material costs. However, the toxicity of  $\text{Br}_2$  and the highly complexing/corroding character of concentrated HBr are limitations. The toxicity of  $\text{Br}_2$  can be mitigated by the use of complexing agents [86], but the effect of complexing agents on kinetics has not been studied quantitatively. Material corrosion that limits the life and dendrite formation that limits the power density are also issues that limited the development. RedFlow Ltd (<http://www.redflow.com.au/>) successfully demonstrated a zinc/bromine RFB unit up to MW size with an energy efficiency of nearly 74% in Australia. The cell architecture was designed to optimize plating and deplating efficiency of zinc during charging and discharging operations. The characteristics for this technology are (1) a capital cost of 500\$/kWh [56] (according to the *EPRI-DOE Handbook of Energy Storage*, total system cost for a typical multifunctional application of a polysulfide bromide flow battery is 639\$/kW, with 60% of this attributable to the storage module); (2) an energy rating of 0.1–4 MWh [32,79,87–90]; (3) a power rating of 0.2–1 MW [32,79,87–90]; (4) a specific energy of 70–90 Wh/kg [60,91]; and (5) a specific power of 45 W/kg [44].

The bromine/polysulfide RFB was studied by Regenesys Technology until 2006 when it was acquired by VRB Power Systems [62]. In these batteries, the positive electrolyte is sodium bromide and the negative electrolyte is sodium polysulfide. The electrolytes are separated by a polymer membrane that only allows the interchange of positive sodium ions [19,30,85]. During the charge cycle, bromide ions ( $\text{Br}^-$ ) are transformed into  $\text{Br}^{3-}$  ions in the positive electrode of the cell. In the negative electrode, dissolved sodium particles ( $\text{S}_4^{2-}$ ) in the polysulfide electrolyte are reduced to sulfide ions ( $\text{S}_2^{2-}$ ). The discharge cycle consists of the reverse process. A commercial-size 15 MW system was successfully demonstrated. This plant used up to 120 modules, each of them having 100 kW of rated power, 200 bipolar electrodes with an energy storage capacity up to 120 MWh, and two 1800 m<sup>3</sup> electrolyte storage tanks [92]. It provides a duty cycle of 10 h [93]. The energy efficiency of the system is 75%, with a life of 15 years. The project budget was around \$250 million. Bromine–polysulfide batteries operate ideally between 20 and 40 °C, and the heat generated during operation must be removed by the use of a plate cooler. Regular maintenance includes a biweekly removal of sodium sulfate crystal by-products. Other maintenance tasks, including spent absorbent and replenishment and maintenance of the electrolytic solution, must be done quarterly [94]. The main characteristics are

(1) according to the *EPRI-DOE Handbook of Energy Storage*, total system cost for a typical multifunctional application of a polysulfide bromide flow battery are 1094\$/kW, with 80% of this attributable to the storage module, so that prior estimates were actually too optimistic [14,69,95]; (2) lifetime of 15 years [62]; and (3) energy efficiency of 60–65% [82] or 75% [62], depending on the system. Besides the maintenance already mentioned, the system has other disadvantages. It is prone to crossover and mixing of the electrolytes, which can lead to precipitation of sulfur species and the formation of  $H_2S$  and  $Br_2$ . Then, a tank failure would expel toxic bromine gas [41].

In hydrogen-based systems, a fuel cell takes a fuel (normally hydrogen) and an oxidant (typically air) and produces electricity and water. For a fuel cell, hydrogen oxidizes at the anode and oxygen reduces at the cathode (see [Figure 12.5c](#)). When the system acts in both the charge and discharge directions, a reversible or regenerative fuel cell is obtained [96–99]. The difference with the other redox flow batteries we have reviewed is that the reactants are in the gas phase and not the liquid phase and, thus, hydrogen compression or novel hydrogen storage materials are needed. Hydrogen can be stored in many forms, as gas in metal tanks at pressures up to 350 bar, or in metal hydrides [34,100,101]. Storing hydrogen in metal tanks may be suitable for large-volume applications for long-term storage (more than 30 h), while storing hydrogen in metal hydrides is suitable for storage periods longer than 3 h [102]. The sizing of the stack depends on the type of technology used, ranging from 100 kW for the polymer electrolyte membrane fuel cell, to 2 MW for the solid oxide fuel cell [22]. Their life is 15 years, and they can support 20,000 cycles at 100% DOD [20,91,102]. They have, however, dramatic disadvantages. First, the catalytic material is platinum, which is quite expensive; the oxygen reactions are known to be very sluggish and result in very large overpotentials [103]. Second, hydrogen impurities affect the life of the battery. Third, the energy efficiency is very small, about 42% [104], unless the wasted heat is used to heat a building in a cogeneration system [105]. Different investigations are currently being made to decrease the price, by looking at closed systems where the air is replaced by oxygen. To remedy the slow oxygen reaction, the difficulty associated with finding robust and effective oxygen reduction/evolution catalysts, different oxidants have been examined, including bromine and chlorine, both of which react rapidly on carbon surfaces [106–108]. Presently, the hydrogen-based storage technology is not economically viable. The economic evaluation of a hybrid wind/photovoltaic/hydrogen generation system shows a clear economic advantage of the traditional wind/PV/battery system over the wind/PV/hydrogen system [109]. However, this situation might change in the future due to the decrease in the cost of fuel cells and electrolyzers. Gas companies in Europe have made commitments to inject hydrogen in the pipes of gas circuits by 2050.

## 12.3 Lithium-ion batteries

In Li-ion batteries (LiBs),  $Li^+$  ions move from the positive electrode to the negative electrode upon charging, and reversely upon discharge, as shown in [Figure 12.6](#). The negative electrode is usually carbon-graphite ( $LiC_6$ ). On the other hand, there are

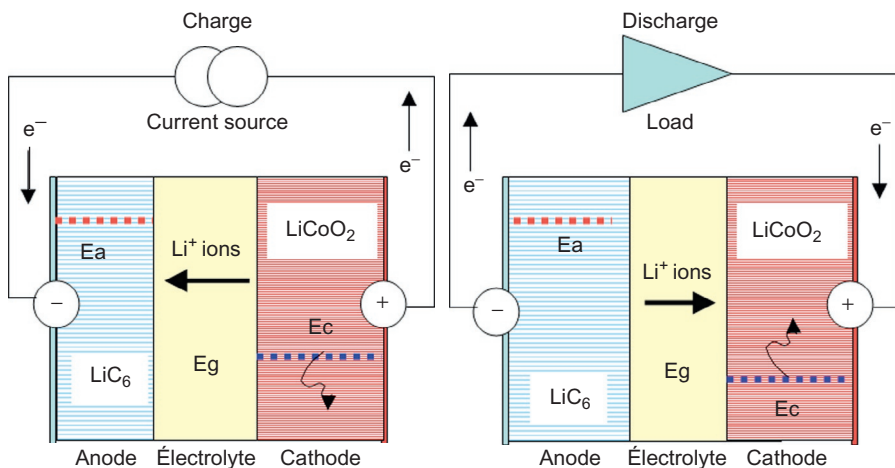


**Figure 12.6** Principle of Li-ion cell, with a graphite-based ( $\text{LiC}_6$ ) negative electrode and a  $\text{LiCoO}_2$  (LCO) positive electrode. Flow of ions and electrons are mentioned for charge and discharge process.

different kinds of positive electrodes that can be divided into three families of materials, identified by the lattice in which they crystallize: the lamellar compounds (archetype  $\text{LiCoO}_2$ ), the spinel compounds (archetype  $\text{LiMn}_2\text{O}_4$ ), and the olivine compounds ( $\text{LiFePO}_4$ ). The electrolyte is either liquid, made of carbonates plus a Li salt, or a solid (a conductive polymer). The choice or the liquid electrolyte allows for much greater power density because the carbonates are good ionic conductors. However, they boil at about  $90^\circ\text{C}$ , and in practice, these batteries can be operated in the temperature range of 20 to  $+60^\circ\text{C}$ . At higher temperatures the electrolyte deteriorates; at lower temperatures the conductivity is too small. On the other hand, with a solid-state battery, the conductivity of the electrolyte is small so that the battery must be heated to  $90^\circ\text{C}$ .

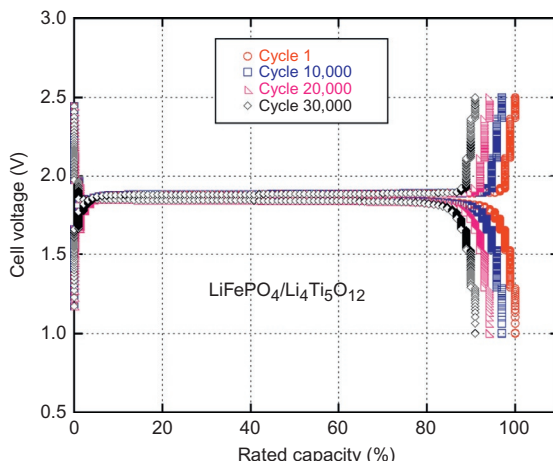
### 12.3.1 Electrochemical performance of the C/ $\text{LiFePO}_4$ cell

The performance of the battery depends very much on the choice of the positive electrode. We have already reported a comparative study of these different batteries in different review papers [110–113]. To summarize the results, the lamellar compounds have the highest energy density, but their thermal and structural instability is at the origin of battery fires. The safety problem for Li-ion batteries in which the active element of the cathode is a lamellar compound  $\text{LiMO}_2$  with M a mixture of Ni, Mn, and Co remains unsolved [114]. Doping with a foreign ion to stabilize the structure did not solve the problem either. Surface modifications of the active particles improved the situation, but still did not solve the problem [115]. Manganese spinel has much better thermal stability, but the manganese dissolves into the electrolyte, and the kinetics of this chemical reaction increases with temperature, destroying the battery. Therefore,

Li-ion batteries in which the active element of the cathode is the  $\text{LiMn}_2\text{O}_4$  spinel must be kept at a temperature close to room temperature. The success of  $\text{LiFePO}_4$  is due to the fact that this material avoids two problems: the iron of this olivine compound does not dissolve into the electrolyte and the material has a remarkable thermal stability. In addition, it is not toxic, and it can be prepared at an industrial level with a capacity of 160 mAh/g. The graphite anode has one disadvantage: it limits the power of the battery. The reason is that, when one tries to charge the battery too fast, lithium plating at the surface of the graphite is inevitable. To overcome the problem, a new anode has been proposed: the titanate  $\text{Li}_4\text{Ti}_5\text{O}_{12}$ . The advantage is that this compound does not change volume upon insertion or deinsertion of lithium, which avoids the strains that may shorten the calendar and cycling life of the battery. In addition, there is no formation of solid–electrolyte interface (SEI), that is, no formation of a resistive layer at the surface of the particles that limit the current density. This is why the combination of the  $\text{LiFePO}_4$  cathode with the  $\text{Li}_4\text{Ti}_5\text{O}_{12}$  anode gives a Li-ion battery that can be cycled within seconds, leading to very high power density. Another advantage is that, with this combination of  $\text{LiFePO}_4/\text{Li}_4\text{Ti}_5\text{O}_{12}$  (LFP/LTO) it is possible to get rid of the carbonate to replace them with other electrolytes that make the battery operational up to 90 °C [116]. In addition, these batteries can support 30,000 cycles at deep charge and discharge without capacity fading, as shown in Figure 12.7 [117]. The only drawback is the loss of potential, and thus of energy density, as the redox potential of the LTO with respect to  $\text{Li}^+/\text{Li}$  is 1.55 V, which must be subtracted from the redox potential of  $\text{Fe}^{2+}/\text{Fe}^{3+} = 3.45$  V, so that the cell delivers a discharge capacity 160 mAh/g under an operating voltage  $3.45 - 1.55 = 1.9$  V.

As has been pointed out, the  $\text{LiPF}_6$ -based electrolyte suffers above 30 °C, so Zaghib *et al.* have tested C-LFP/C-LTO cells with other electrolytes that are stable at higher temperatures [116]. The results are reported in Figure 12.8. At 25 °C (Figure 12.8a), the performance is nearly the same for the three electrolytes that have been considered. Note, however, that the  $\text{LiPF}_6$  in EC-DEC electrolyte limits the capacity at high C-rates ( $>10\text{C}$ ). On the other hand, at 60 °C (Figure 12.8b), a major

**Figure 12.7** Charge–discharge profiles of the  $\text{LiFePO}_4/\text{EC-DEC-1 mol L}^{-1} \text{LiPF}_6/\text{Li}_4\text{Ti}_5\text{O}_{12}$  (cycle charge rate is 15C, the discharge rate is 5C) [117].



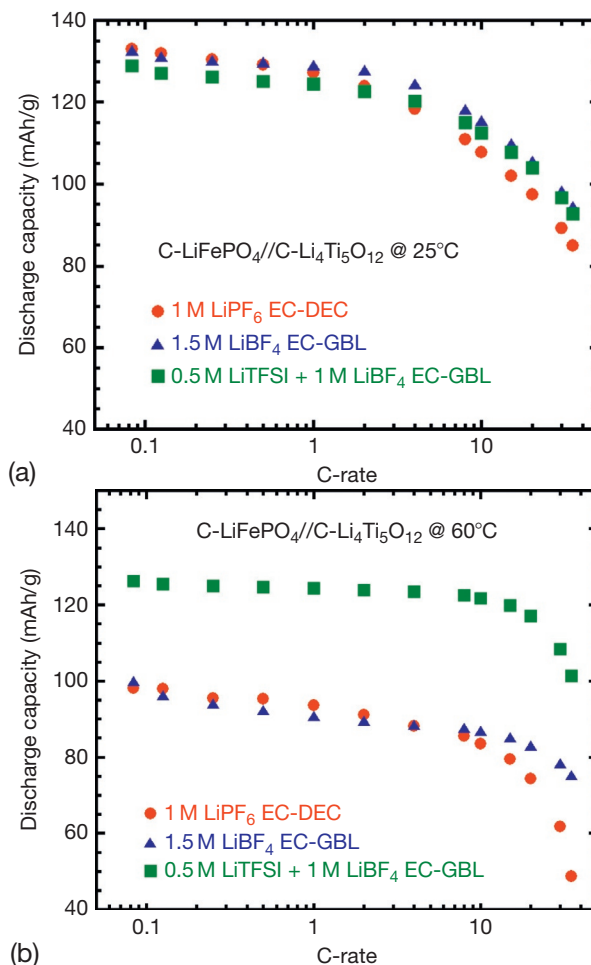


**Figure 12.8** Inverse modified Peukert plots at 25 °C (a) and 60 °C (b) of the C-LTO/C-LFP "18,650-type" cell with different electrolytes [116].

improvement has been achieved at any C-rate with the 0.5 mol/L LiTFSI + 1 mol/L LiBF<sub>4</sub> EC-GBL. At 40C (90 s discharge time), the capacity remains as high as 92 mAh/g, while it has dropped at 20 mAh/g with LiPF<sub>6</sub> in EC-DEC [116].

### 12.3.2 Li-ion battery performance at 60 °C

The impact of material optimization (i.e., impurity-free powders, quality of carbon coating) on the electrochemical properties has been reported elsewhere [113,118]. Electrochemical tests were conducted at 60 °C under various conditions to assess the influence of the electrolyte on stability and the influence of electrode processing.

Postmortem analysis after 200 charge–discharge cycles (i.e., inductively coupled plasma mass spectrometry, ICP; X-ray diffraction, XRD; scanning electron microscopy, SEM) showed that no iron species were detected at the separator-negative electrode interface in cells with lithium metal, graphite, and C-Li<sub>4</sub>Ti<sub>5</sub>O<sub>12</sub> (LTO) anodes. Figure 12.9a and b shows the cycling behavior of these cells cycled in the potential range 2.5–4.0 V. The

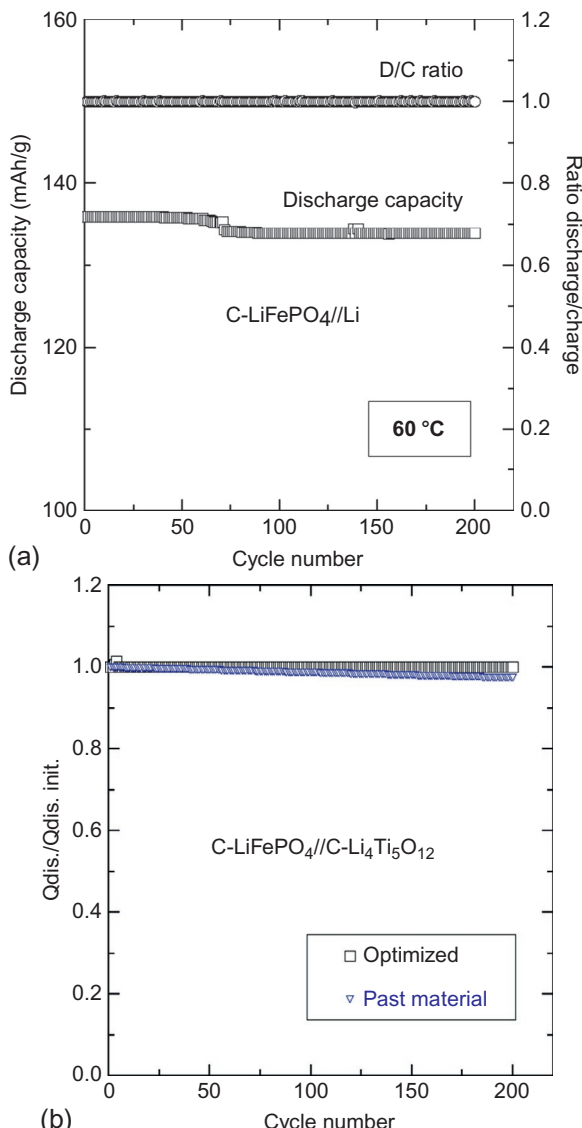


**Figure 12.9** (a) Discharge capacity and discharge/charge ratio (electrochemical utilization) vs. cycle number for C-LiFePO<sub>4</sub>/LiPF<sub>6</sub>-EC-DEC/Li cells at 60 °C. (b) Plot of the ratio between the current discharge capacity and the initial capacity vs. cycle number for Li-ion cells cycled at 60 °C with C-Li<sub>4</sub>Ti<sub>5</sub>O<sub>12</sub> anodes. Cells were discharged at 1C in the potential range 2.5–4.0 V.

discharge capacity and electrochemical utilization (i.e., the ratio discharge/charge) vs. cycle number are excellent for the C-LiFePO<sub>4</sub>/LiPF<sub>6</sub>-EC-DEC/Li cells discharged at 1C and charged at C/6 (Figure 12.9a). Similar results are shown for cells with graphite and C-Li<sub>4</sub>Ti<sub>5</sub>O<sub>12</sub> negative electrodes (Figure 12.9b). These Li-ion cells provide coulombic efficiencies of 99.9% and 100%, respectively. Plots of the ratio between the current discharge capacity and the initial capacity vs. cycle number indicate a constant capacity retention at 60 °C. No capacity fade was observed after 200 cycles with lithium, LTO, and graphite. These results have been attributed to the high quality of the “optimized” LiFePO<sub>4</sub>, impurity-free materials used as positive electrodes.

### 12.3.3 Safety issues

The carbon-coated LiFePO<sub>4</sub> Li-ion oxide cathode was studied for its electrochemical, thermal, and safety performance. This electrode exhibited a reversible capacity corresponding to more than 89% of the theoretical capacity when cycled between 2.5 and 4.0 V. Cylindrical 18,650 cells with carbon-coated LiFePO<sub>4</sub> also showed good capacity retention at higher discharge rates up to a 5C rate with 99.3% coulombic efficiency, implying that the carbon coating improves the electronic conductivity. A hybrid pulse power characterization test performed on the LiFePO<sub>4</sub> 18,650 cell indicated the suitability of this carbon-coated LiFePO<sub>4</sub> for high-power hybrid electric vehicles (HEV) applications. The heat generation during charge and discharge at a 0.5C rate, studied using an isothermal microcalorimeter, indicated cell temperature is maintained in near-ambient conditions in the absence of external cooling. Thermal studies were also investigated by differential scanning calorimeter (DSC) and accelerating rate calorimeter (ARC), which showed that LiFePO<sub>4</sub> is safer, upon thermal and electrochemical abuse, than the commonly used lithium metal oxide cathodes with layered and spinel structures. Safety tests, such as nail penetration and crush test, were performed on LiFePO<sub>4</sub> and LiCoO<sub>2</sub> cathode-based cells, to investigate on the safety hazards of the cells upon severe physical abuse and damage. Figure 12.10 shows the self-heat rate (SHR) released from the 18,650 cell (LiFePO<sub>4</sub>/graphite) fully charged to 1.42 Ah capacity, when heated up to 450 °C in ARC. The figure illustrates three different exothermic reactions. The first self-heat exotherm was observed between 90

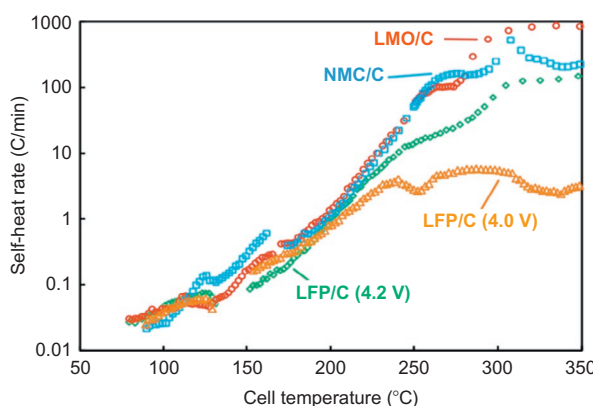


**Figure 12.10** Self-heat rates of fully charged 18,650 cells with spinel, layered, and olivine cathodes measured in ARC. Self-heat rates of olivine cathode overcharged to 4.0 and 4.2 V are also shown [114].

and 130 °C, and it is mainly attributed to the reaction of the carbonaceous material in combination with the electrolyte caused by the SEI layer decomposition [114]. At temperatures above 150 °C, which corresponds to the melting temperature of the separator, the second self-heat exotherm was initiated, causing the cathode to be exposed to reaction with electrolyte. Cathode was subsequently decomposed at temperatures higher than 245 °C and reacted with the electrolyte, releasing more heat and increasing the cell temperature further. At temperatures above 260 °C, the oxygen released from the composed cathode reacted with the organic solvents, initiating the third self-heat exotherm that corresponds to the beginning of the thermal runaway. However, the cell remained safe and did not explode for temperatures up to 450 °C, as the maximum SHR of the cell was found to be less than 6 °C/min only. It is deduced that the peak producing the maximum SHR of 6 °C/min at 286 °C corresponds to the major exothermic reaction as described in the DSC study. The SHR observed in the ARC study of LiFePO<sub>4</sub> cathode was significantly lower than the layered oxide and spinel cathodes, indicating the thermal stability of the olivine cathode. The onset temperature and maximum SHR for different cathode chemistries show that even an overcharged (to 4.2 V) LiFePO<sub>4</sub>/C cell showed only 158 °C/min maximum SHR, compared to 532 and 878 °C/min maximum SHR observed in layered and spinel oxide cathodes.

LiBs that are currently used for grid storage have the following advantages: (1) high energy density (150–200 kWh/m<sup>3</sup>, 140 kWh/ton at battery level); (2) high efficiency (near 100%); (3) long cycle life (>5000 cycles at 80% DOD) combined with long calendar life of 20 years; (4) maintenance-free design; and (5) versatility, where electrodes can be optimized for different power/energy patterns. LiB technology has taken huge advantage of the extensive research that has been done over the past three decades for use of LiBs in automotive applications and for portable use, including electric vehicles. Their price is still too high, but it is a promising solution for grid storage applications because the increasing demand from mass production should be accompanied by a decrease in the price. This progress in the technology will just increase what is already the major advantage of Li-ion technology, namely its versatility: highly scalable, it can be adapted to practically any voltage, power, and energy requirement, which may explain that, LiBs will account for 64% of energy storage installations between 2012 and 2017 [12]. This prediction, however, is subject to controversy. Lux Research [119] predicts that Li-ion batteries will only capture 13% of the demand by 2017 with the rest occupied by vanadium redox, sodium–sulfur, sodium–nickel–chloride, and zinc–bromine flow batteries at 33%, 19%, 15%, and 19%, respectively [120]. The reasons they cite are cheaper alternatives such as flow batteries coming onto the scene. Indeed, today's flow batteries are priced anywhere from 400 to 600\$/kWh, but at lower efficiencies. Lithium-ion batteries, on the other hand, cost 800–1000\$/kWh and up, although some Chinese Li-ion manufacturers are targeting 500\$/kWh. This implies a need for Li-ion battery manufacturers to reduce costs.

Table 12.2 lists the main examples of plants using Li-ion batteries for grid storage. About 100 MW of stationary Li-ion batteries are operating worldwide in grid-connected installations. Systems in association with distributed renewable generators from a few kW to several MW, as well as for grid support with voltages up to 6000 V

**Table 12.2 Some examples of grid storage solution using Li-ion battery systems**

Location	Energy storage (MWh)	Power (MW)	Application
Huntington Beach, CA	0.5	2	Frequency regulation
Los Andes, Northern Chile	4	12	Primary reserve
Auwahi, HI	11	4.4	Wind ramp management
Westover, NY	8	2	Frequency regulation
Laurel Mountain, WV	32	8	Frequency regulation
Angamos, Northern Chile	20	5	Primary reserve
Denmark	0.1	0.4	Wind ramp management
Westminster, CA	1	4	Frequency regulation
Molokai Island, HI	1	1	Peak shaving
Carmona, Spain	–	1	Frequency regulation
Rokkasho, Japan	34	51	Energy balancing
Nishisendai, Japan	20	–	Frequency regulation
Miyako Island, Japan	0.2	–	PV and wind generation
Abu Dhabi	48	8	Load leveling

have been designed and successfully tested. AES Energy Storage (<http://www.aesenergystorage.com>) is installing a 32-MW lithium-ion storage system to regulate the 100-MW Laurel Mountain Wind Farm in West Virginia. Since it was founded in 2007, AES Energy Storage has completed more than 32 MW of storage, and it claims to have 500 MW “in the pipeline.” PV inverter manufacturer Power One has proposed a new battery storage system called REACT (renewable energy accumulator and conversion technology), launched so far in Germany and Italy [121]. It consists of a 4.6 kW single-phase grid-connected inverter coupled with a lithium-ion battery. The PV inverter is matched with a 2-kWh battery [27]. According to Lancini [122], Power One’s product marketing manager for renewable energies, the battery is 2 kWh “effective” because the actual size of the battery is 2.6 kWh and only needs to be charged and discharged to 40%. The life cycle of the battery is the most critical and expensive component, so the life of the battery is protected as much as possible.

The battery will last 10,000 cycles. The choice of 2 kWh is a compromise due to the extremely high cost of the battery; a 10 kWh battery could cost €25,000. Under such conditions, the run of simulations with environmental predictions and load profile and the trade-off have shown that the optimum solution between the cost and the benefit is 2 kWh. However, it is possible to expand the battery pack by up to 6 kWh.

## 12.4 Supercapacitors

The supercapacitors are divided in two categories: electric double-layer (EDL) capacitors and pseudocapacitors. Like batteries, double-layer capacitors are based on electrochemical cells that contain two conductor electrodes, an electrolyte and a porous membrane, whereby ion transit between the two electrodes is permitted (Figure 12.11). However, no redox reactions occur in the cells: the electrostatic storage is achieved by separation of charge in a Helmholtz double layer at the interface between the surface of a conductive electrode and an electrolyte (ion adsorption). In Faradic pseudocapacitors, electrochemical storage with electron charge-transfer is achieved by redox reactions, intercalation, or electrosorption (surface redox reaction). Capacities of commercialized supercapacitors are as large as 5000 F. This result is obtained by increasing the effective surface between the electrolyte and the active particles of the electrodes. This has been achieved by using electrodes under the form of nanoparticles with a porous surface [123–125]. EDL supercapacitors are usually preferred, because their power density is larger. The power is actually the main advantage of supercapacitors.

Charge and discharge cycle times of the system are about 1–30 s at rated power, while the specific power is in the range 2000–5000 W/kg (20,000–30,000 W/m<sup>3</sup>). The cycle life depends on the type of supercapacitor. Pseudocapacitors using conducting polymers or metal oxides as electrode materials age upon cycling. EDL capacitors

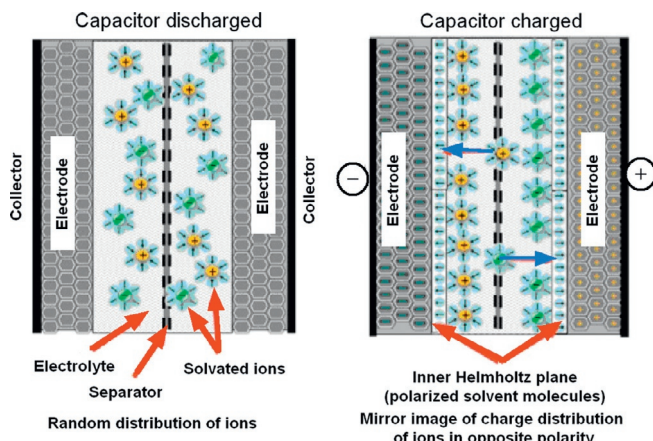


**Figure 12.11** Schematic representation of electric double-layer supercapacitor.

with porous carbon electrodes do not age upon cycling [126]. However, supercapacitors based on carbon nanotubes cannot exhibit good capacitive performance without adding a pseudocapacitive component [127].

The main disadvantages are the cost, estimated at 9500 \$/kWh [128], which is the major drawback of this system, and high self-discharge of the system, which can be 20% of its rated capacity in 12 h, due to the nonnegligible equivalent resistance of the contact between the electrolyte and the electrodes [84,129], which limits the grid applications to short timescale applications and short time responses. Commercialized supercapacitors usually have an energy density in the range of 3–5 Wh/kg [130,131], one or two orders of magnitude smaller than that of Li-ion batteries. However, better results can be obtained for graphene capacitors. Ideally, a monolayer of  $sp_2$  bonded carbon atoms can reach a specific capacitance up to  $\sim 550$  F/g as well as a high surface area of  $2675\text{ m}^2/\text{g}$ , which basically set the upper limits for all carbon materials. Gravimetric energy density values of graphene supercapacitors are between 20 and 90 Wh/kg at 1 A/g [132–135]. However, an energy density  $\sim 148$  Wh/kg (50,000 Wh/m<sup>3</sup>) at 1 A/g was achieved and has been reached with hydrogen-annealed graphene at room temperature [136]. Therefore, some progress is on the way to increase the energy density. At the same time, the combination of LiFePO<sub>4</sub> positive electrode with Li<sub>4</sub>Ti<sub>5</sub>O<sub>12</sub> provides us with a Li-ion battery that improves the power density by an order of magnitude, the gap in the energy and power densities between Li-ion batteries and supercapacitors is filled at the scale of the laboratory.

## 12.5 Vehicle-to-grid

Conventional electric-drive vehicles (EVs) are plugged to the grid for charging their batteries, while plug-in hybrid vehicles (PHVs) can generate electricity from fuel. One of the challenges of the electric car is what is called the vehicle-to-grid (V2G); i.e., the ability to inject electricity contained in the batteries of the car on the grid [137]. This is where the electric car is involved: its large storage capacity of electricity through the battery can smooth the energy grid. In fact, most cars are immobilized 90% of the time. One can imagine an electric car driver that uses the car in the morning to go to work, then branches it on a source of solar electricity to recharge the car during the day; then the driver returns home in the evening at 19:00 hours and branches it so that the car then provides electricity to the power grid to compensate for the peak consumption, and recharges later in the night with the wind or a hydraulic source. One can consider two categories of grid support for which V2G might be used: (1) meeting the demands of peak power and (2) providing an operating reserve in case of generator failure or any disruption to the electricity supply.

In the vehicle-to-grid technology or V2G introduced by AC Propulsion Inc., the electricity flows from the V2G [138]. This concept has been developed by the University of Delaware (UD) and NRG Energy as a set of interacting technologies, considering that energy source and power electronics of EVs and PHVs are capable of producing the 60 Hz AC electricity that can power homes. The amount of revenue

that the owner could expect for providing electricity to the grid was estimated to be \$400–5000 each year [139–141]. For testing and demonstrating, UD uses a fleet of V2G-enabled vehicles [142]. In March 2006, Kempton *et al.* gave a brief technical introduction to V2G as storage for wind power, analyzed the duration of low-wind events as a measure of storage needs, and compared national-level potential V2G power with average load in 11 countries [143–146]. An example of V2G architecture is depicted in Figure 12.12. In the V2G project, the EV or PHV contains a “vehicle smart link” (VSL) device implemented into the in-board computer. The VSL communicates with the “battery management system” (BMS) to control the charge and exchange with the grid.

In 2008, Udo mentioned the feasibility of V2G and power system/transportation synergies. This report explains the overall approach of using electric vehicles to support the power system. Also, reports have been made on the first successful dispatch of an electric vehicle from a real-time ISO signal. Several car manufacturers are working on the V2G system. Nissan announced the upcoming launch of its “LEAF to Home” system, explaining that the LEAF® battery can power a Japanese household electricity for 2 days. The same station is reversible and can recharge the car battery in less than 4 h. The final system should cost around \$4000. Toyota is working on a similar system and will start testing with rechargeable Prius hybrids in its Toyota City Project. Mitsubishi is also working on V2G.

Various automotive Li-ion battery packs with lithium-iron phosphate technology are available in the market. Figure 12.13 shows the schematic design of a pack composed of a battery module formed by the association of elementary cells that could be the safer LiFePO<sub>4</sub>/LiPF<sub>6</sub> in EC-DMC/Li<sub>4</sub>Ti<sub>5</sub>O<sub>12</sub> electrochemical systems. The battery pack is monitored by the BMS and TMS controllers. For instance, AMP20 Energy Module with a nominal voltage of 393 V delivers a nominal energy of 23 kWh composed of prismatic cells of nominal energy of 5.38 kWh per module. The battery pack powering the Chevrolet Volt has 9 modules and 288 cells. Tesla Motors (TSLA)

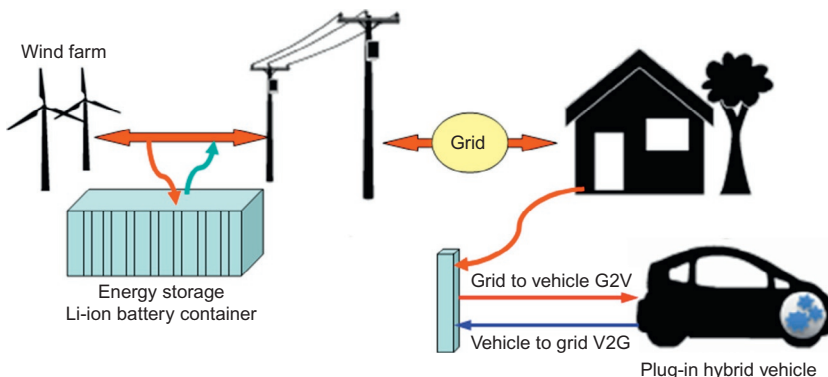


**Figure 12.12** Plug-in electric vehicle form of a distributed source of energy. The electricity is primarily injected into the grid by a renewable system such as a wind farm and stored in the energy storage battery container.

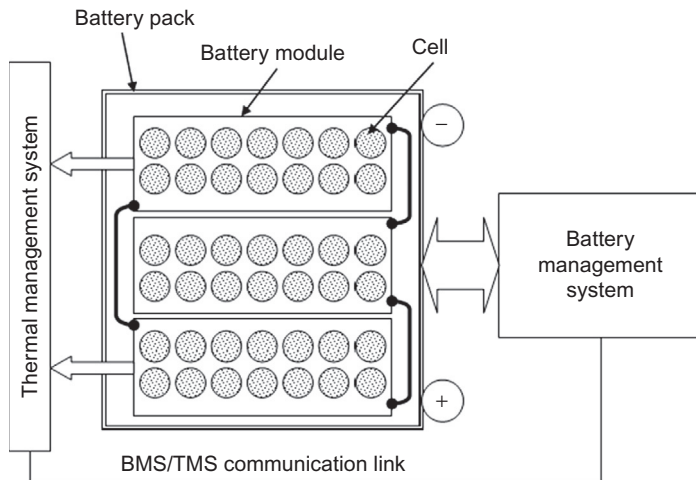


**Figure 12.13** Schematic representation of a battery pack for green transportation formed by the association of a battery module including the elementary Li-ion cell.

uses over 6000 Li-ion 18,650-type cells to power its Roadster (85-kWh battery pack) at high speed. The 24-kWh Li-ion battery of Nissan LEAF® stores its energy to power the 80 kW AC motors in 48 Li-ion modules; each module contains four Li-ion battery cells. Typical PHEV charge time of a 13-kWh battery at AC voltage 240 V rated current 32 A (6.5 kW) is 2 h, while using DC voltage 480 V rated current 85 A has been going on for 13 min. A recommended regime for the V2G evaluation is related to battery performance and impact testing: life-cycle impact from frequent charge/discharge operations and thermal impact from rapid charge/discharge rates.

## 12.6 Future trends

The portfolio of electricity storage technologies that have been reviewed here can provide a range of services to the electric grid to respond to the challenge that is posed by the increase of the grid-connected storage market that should explode from 340 MW in 2013 up to 6 GW in 2017, after IHS [13]. A detailed description of the different applications of these different energy storage technologies can be found in [21], which show that the addition of energy storage in electricity plants is determinant in the integration of intermittent sources such as wind and solar energy in the grid. For example, the purpose for using Li-ion technology is managed for either load leveling, energy storage, or frequency regulation. Presently, hybrid ancillary power units (i.e., battery-pack containers) of 2 MWh are commercially available in the market.

The main tasks of the electricity supplier are generating, transmitting, and distributing energy. Hydro-Québec (HQ), a major corporation in North America, conducts R&D in energy-related fields, including energy efficiency. The intelligent network of HQ is

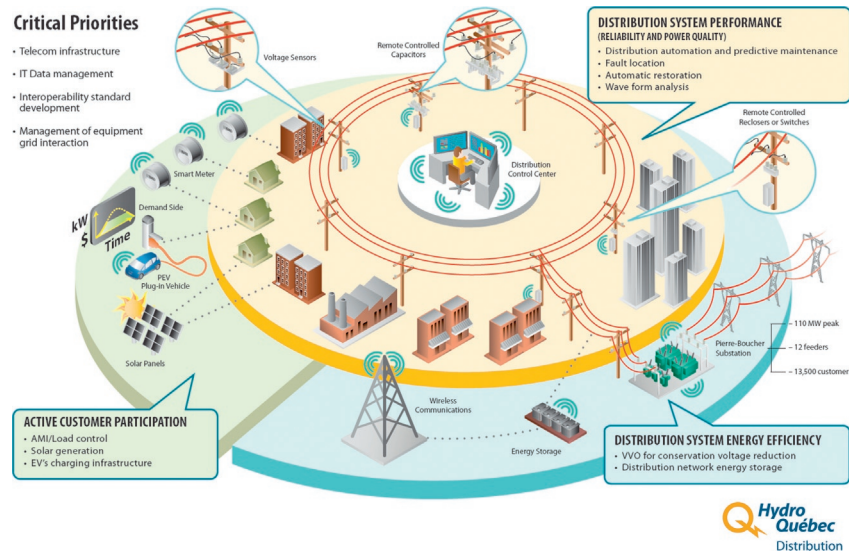


**Figure 12.14** Smart grid project at Hydro-Québec (Canada). The critical priorities are (i) telecom infrastructure, (ii) IT data management, (iii) interoperability standard development, and (iv) management of equipment grid interaction (with permission of HQ).

schematized in [Figure 12.14](#). In August 2002, HQ distribution produced an internal study on the future of distribution network automation including the development of smart grid with a \$25.5 million project [\[147\]](#). The project's goal is to validate that the systems of optimization of type Volt contributes to the reduction of the consumption of energy and the losses of the distributive network without damaging the quality of the energy distributed to the customers. It also aims at testing the performance, compatibility, and integration in the operations of all the tried technologies. For the DMS (distribution management system) integrating the advanced voltage control (CATVAR), a good modeling of the network is essential (characteristics of equipment, phasage, model of load). In particular, the imbalance of the tensions on a distributive network constitutes a real challenge when it comes time to optimize the level of tension to reduce the consumption of energy. Also, the measure of tension has to be made at the level of the customer for the calibration of the system. Finally, the collaboration with the transport system allows a better optimization of the reductions of energy.

The new capabilities of pumped hydro, through the use of variable-speed pumping, is opening up the potential for the provision of additional services that may be used to assist in the integration of variable generation sources. Projects may be practically sized up to 4000 MW and operate at about 76–85% efficiency. A CAES plant can enhance the grid to allow successful integration of significant amounts of renewable resources while enhancing the transmission system and providing grid stability during intermittent operations. It will also provide ancillary services such as regulation, capacity reserve, and reactive power for voltage support with the size and flexibility that will enable large amounts of energy to be stored and discharged for use to

maintain and improve the grid system reliability and relieving transmission congestion. However, both CAES and pumped hydro have very specific geographic requirements, making their installation site dependent. In contrast to the capabilities of these two technologies, various batteries and flywheels are positioned around lower power and shorter discharge times, ranging from a few seconds to 10 h, and these technologies can generally be built without specific geographical features at the site. Flywheels are currently commercially deployed primarily for frequency regulation, as they can ensure steady power (60 Hz) supplied to the grid. The interest in flow batteries primarily stems from the liquid suspension and separation of the chemical components that allow for full charge utilization with a high number of discharge cycles and extremely long unit life. Flow batteries have faced obstacles related to their low energy density and integrated design requirements that make it difficult to compete at sub-MW scale, but they are well suited to provide MW-scale storage capacity beyond the geographic constraints of hydroelectric facilities. Among other batteries, Li-ion batteries tend to be the best suited for relatively short discharges (under 2 h). Most of them do not handle deep discharges well, so these batteries are more suited to power management operations such as frequency regulation or as an uninterruptible power source (UPS). NaS batteries are somewhat behind Li-ion battery technology in terms of energy and power, but they can maintain longer discharges (4–8 h) and may be more suitable for load leveling and price arbitrage operations. Lead-acid batteries, a mature technology with good battery life, are relatively cheap; however, the low energy density and short cycle time are challenges to large-scale deployment. Supercapacitors can be useful in power-quality applications, such as frequency regulation and voltage stabilization. The devices may have longer useful lives as there is little breakdown in the capacitors' ability to store energy electrostatically. The current research results in an increase of the energy capability of the supercapacitors, and an increase of the power capability of the Li-ion batteries, so that the gap between the two technologies is decreasing, and the two technologies can be combined to fulfill multiple applications on the grid combining the power-management operations and the power quality applications above mentioned. Clearly, integrated supercapacitor/Li-ion battery backup are expected to make significant inroads in the near future, by combining high energy and high power. This combination is very well suited to maintain voltage and frequency quality during instabilities of base load generating sources. Another grid application is the generating braking system for light rail systems and reduce electrical usage and frequency variation on the overall regional grid due to frequent starts/stops of multiple trains [148]. UPSs used to protect expensive assets such as computer data centers and hospitals, representing an \$8 billion per year market, Li-ion batteries are in competition with lead batteries that are inferior performers, but also much cheaper, so that the reduction of the cost of Li-ion batteries will be critical to win this market. This is expected due to the increasing production of Li-ion batteries, boosted by the market of electric and hybrid vehicles and off-grid applications. Another technology in the demonstration/applied research phase is superconductive magnetic energy storage (SMES). Most SMES technologies currently have a high cycle life and power density, but low energy density and high cost that make them best suited for supplying short bursts of electricity into the energy

system. Superconductors currently have the highest round-trip efficiency of any storage device, though they are costly to manufacture and maintain and they have only a limited number of small demonstrations: The superconductor technology is still cost prohibitive. In addition, the increase in the price of liquid helium does not go in the right direction to facilitate the use of this technology in grid applications. High-Tc superconductors that would avoid cooling at liquid helium have still too low critical current densities despite intensive research. Hydrogen systems, as with the other storage technologies, require careful analysis to fully capture the value stream. Multiple components such as electrolyzers, fuel cells, or hydrogen oxygen turbines coupled with storage, either underground in geologic formations or above ground in hydrogen tanks, can be used in grid systems. Hydrogen can also allow for the decoupling of electricity production and storage resulting in flexible operation. While round-trip energy efficiencies might be at a level of 40%, this relatively low efficiency is balanced by energy storage potential that may last days, to weeks, or longer. New opportunities are opened by the progress in the technology of Li-ion batteries with the development of LiFePO<sub>4</sub> and Li<sub>4</sub>Ti<sub>5</sub>O<sub>12</sub> electrodes, and the progress in the technology of graphene-based supercapacitors. The main challenge of these technologies, as that of the hydrogen-based technologies, is now the uncertainty of their economic viability: Their future is dependent of the reduction of the capital cost and the cost of the products that are expected from their development at larger scale.

## References

- [1] E. Coster, J. Myrzik, B. Kruimer, W. Kling, Integration issues of distributed generation in distribution grids, *Proc. IEEE* 99, 2011, pp. 28–39.
- [2] Zh. Chen, F. Blaabjerg, Wind farm—a power source in future power systems, *Renew. Sustain. Energy Rev.* 13 (6) (2009) 1288–1300.
- [3] M.A. Abdullah, A.H.M. Yatim, C.W. Tan, R. Saidur, A review of maximum power point tracking algorithms for wind energy systems, *Renew. Sustain. Energy Rev.* 16 (2012) 3220–3227. <http://www.aesenergystorage.com/>.
- [4] M. Swierczynski, R. Teodorescu, C.N. Rasmussen, P. Rodriguez, H. Vikelgaard, Overview of the energy storage systems for wind power integration enhancement, in: *Proceedings of the IEEE International Symposium on Industrial Electronics (ISIE)*, 2010, pp. 3749–3756.
- [5] S. Vazquez, S. Lukic, E. Galvan, L.G. Franquelo, J.M. Carrasco, J.I. Leon, Recent advances on energy storage systems, in: *Proceedings of the IECON: 37th Annual Conference of the IEEE Industrial Electronics Society*, 2011, pp. 4636–4640.
- [6] Epexspot, <http://www.epexspot.com/en/>, 2014.
- [7] M. Jannati, S.H. Hosseiniyan, B. Vahidi, G.-J. Li, A survey on energy storage resources configurations in order to propose an optimum configuration for smoothing fluctuations of future large wind power plants, *Renew. Sustain. Energy Rev.* 29 (2014) 158–172.
- [8] M. Chebbo, Electricity networks of the future 2020 and beyond, in: *Framework ESG* (Ed.), *Proceedings of IEEE General Meeting Power Engineering Society*, 2007.
- [9] M. Fadaeenejad, A.M. Saberian, M. Fadaee, M.A.M. Radzi, H. Hizam, M.Z.A. AbKadir, The present and future of smart power grid in developing countries, *Renew. Sustain. Energy Rev.* 29 (2014) 828–834.

- [10] M. Welsch, M. Bazilian, M. Howells, D. Divan, D. Elzinga, G. Strbac, L. Jones, A. Keane, D. Gielen, V.S.K. Balijepalli, A. Brew-Hammond, K. Yumkella, Smart and just grids for sub-Saharan Africa: exploring options, *Renew. Sustain. Energy Rev.* 20 (2013) 336–352.
- [11] R.S. Bhatia, S.P. Jain, D.K. Jain, B. Singh, Battery energy storage system for power conditioning of renewable energy sources, in: *Proceedings of the Power Electronics and Drives Systems (PEDS) Conference*, vol. 1, 2006, pp. 501–506.
- [12] IHS, <http://www.ihs.com/index.aspx>, 2014.
- [13] E. Meza, Grid-connected storage market set to explode, *pv-magazine*, 2014. Available at: [http://www.pv-magazine.com/news/details/beitrag/grid-connected-storage-market-set-to-explode\\_100013945/#axzz2xusqeBB1](http://www.pv-magazine.com/news/details/beitrag/grid-connected-storage-market-set-to-explode_100013945/#axzz2xusqeBB1) (accessed 15.01.14).
- [14] J.K. Kaldellis, D. Zafirakis, Optimum energy storage techniques for the improvement of renewable energy sources-based electricity generation economic efficiency, *Energy* 32 (2007) 2295–2305.
- [15] J.S. Kazempour, M.P. Moghaddam, M.R. Haghifam, G.R. Yousefi, Electric energy storage systems in a market-based economy: comparison of emerging and traditional technologies, *Renew. Energy* 34 (2009) 2630–2639.
- [16] First Hydro Company website: [http://www.fhc.co.uk/pumped\\_storage.htm](http://www.fhc.co.uk/pumped_storage.htm).
- [17] T. Jacob, Stucky Consulting Engineers Ltd. Available from: [http://www.stucky.ch/en/contenu/pdf/Pumped\\_storage\\_in\\_Switzerland\\_Dr\\_Jacob.pdf](http://www.stucky.ch/en/contenu/pdf/Pumped_storage_in_Switzerland_Dr_Jacob.pdf) (accessed 29.03.10).
- [18] J.G. Levine, Pumped hydroelectric energy storage and spatial diversity of wind resources as methods of improving utilization of renewable energy sources, *MS Thesis*, University of Colorado, 2007.
- [19] R.L. Busby, *Wind Power: The Industry Grows Up*, PennWell Corporation, Tulsa, Oklahoma, 2012.
- [20] H. Ibrahim, A. Ilinca, J. Perron, Energy storage systems—characteristics and comparisons, *Renew. Sustain. Energy Rev.* 12 (2008) 1221–1250.
- [21] F. Díaz-González, A. Sumper, O. Gomis-Bellmunt, R. Villafáfila-Robles, A review of energy storage technologies for wind power applications, *Renew. Sustain. Energy Rev.* 16 (2012) 2154–2171.
- [22] M. Popp, Storage for a secure Power Supply from Wind and Sun, 2014. Available at: [http://poppware.de/Storage\\_for\\_a\\_secure\\_Power\\_Supply\\_from\\_Wind\\_and\\_Sun.pdf](http://poppware.de/Storage_for_a_secure_Power_Supply_from_Wind_and_Sun.pdf).
- [23] J.L. Bernal-Agustín, R. Dufo-López, Hourly energy management for grid-connected wind-hydrogen systems, *Int. J. Hydrol. Energy* 33 (2008) 6401–6413.
- [24] P.D. Brown, J.A. Peças Lopes, M.A. Matos, Optimization of pumped storage capacity in an isolated power system with large renewable penetration, *IEEE Trans. Power Syst.* 23 (2008) 523–531.
- [25] M. Kapsali, J.K. Kaldellis, Combining hydro and variable wind power generation by means of pumped-storage under economically viable terms, *Appl. Energy* 87 (2010) 3475–3485.
- [26] S. Papaefthimiou, E. Karamanou, S. Papathanassiou, M. Papadopoulos, Operating policies for wind-pumped storage hybrid power stations in island grids, *IET Renew. Power Gener.* 3 (2009) 293–303.
- [27] A. Colthorpe, Ecobuild: Power One's Energy Storage Vision for Next Step of PV Market, 2014. Available at: [http://www.solarpowerportal.co.uk/news/ecobuild\\_power\\_ones\\_energy\\_storage\\_vision\\_for\\_next\\_step\\_of\\_pv\\_market](http://www.solarpowerportal.co.uk/news/ecobuild_power_ones_energy_storage_vision_for_next_step_of_pv_market) (accessed 6.03.14).
- [28] P. Moser, Available from: RWE Corporate website: <https://www.rwe.com/web/cms/en/365478/rwe/innovation/projects-technologies/energy-storage/project-adele-adele-ing/> (accessed 22.11.10).

- [29] P. Crowe, <http://www.renewableenergyworld.com/rea/news/article/2011/08/energy-stor-age-industry-grows-to-integrate-wind-solar> (accessed 17.08.11).
- [30] P. Denholm, G.L. Kulcinski, Life cycle energy requirements and greenhouse gas emissions from large scale energy storage systems, *Energy Convers. Manage.* 45 (2004) 2153–2172.
- [31] H. Lund, G. Salgi, The role of compressed air energy storage (CAES) in future sustainable energy systems, *Energy Convers. Manage.* 50 (2009) 1172–1179.
- [32] Electricity Storage Association, <http://www.electricitystorage.org/>.
- [33] S. Faias, P. Santos, J. Sousa, R. Castro, An overview on short and long-term response energy storage devices for power systems applications, in: Proceedings of the International Conference on Renewable Energies and Power, Quality (ICREPQ'08), 2008, pp. 1–6.
- [34] I. Hadjipaschalidis, A. Poullikkas, V. Efthimiou, Overview of current and future energy storage technologies for electric power applications, *Renew. Sustain. Energy Rev.* 13 (2009) 1513–1522.
- [35] Ridge Energy Storage & Grid Services L.P. The economic impact of CAES on wind in TX, OK, and NM, [http://www.ridgeenergystorage.com/re\\_wind\\_projects-compressed2005.pdf](http://www.ridgeenergystorage.com/re_wind_projects-compressed2005.pdf) (accessed 27.06.05).
- [36] ScottMadden Management Consultants. Available from: [www.scottmadden.com/?a=strm&aid=259](http://www.scottmadden.com/?a=strm&aid=259), 2009.
- [37] S.R. Holm, H. Polinder, J.A. Ferreira, Analytical modeling of a permanent magnet synchronous machine in a flywheel, *IEEE Trans. Magn.* 43 (2007) 1955–1967.
- [38] H. Liu, J. Jiang, Flywheel energy storage—an upswing technology for energy sustainability, *Energy Build.* 39 (2007) 599–604.
- [39] B. Bolund, H. Bernhoff, M. Leijon, Flywheel energy and power storage systems, *Renew. Sustain. Energy Rev.* 11 (2007) 235–258.
- [40] X. Dai, Z. Deng, G. Liu, X. Tang, F. Zhang, Z. Deng, Review on advanced flywheel energy storage system with large scale, *Trans. China Electrotech. Soc.* 26 (2011) 133–140.
- [41] D. Yogi-Goswami, F. Kreith, *Energy Conversion*, CRC Press, Taylor & Francis Group, Abingdon, UK, 2007.
- [42] J. Zhang, Research on flywheel energy storage system using in power network, Conference on Power Electronics and Drive Systems (PEDS), vol. 2. Available at: <http://ieeexplore.ieee.org/xpl/mostRecentIssue.jsp?punumber=10774>, 2005.
- [43] A. Poullikkas, V. Efthimiou, Overview of current and future energy storage technologies for electric power applications, *Renew. Sustain. Energy Rev.* 13 (2009) 1513–1522.
- [44] Beacon Power, Beacon Power's "Smart Energy 25" flywheel. Available at: <http://www.beaconpower.com/products/smart-energy-25.asp> (accessed 03.06.11).
- [45] O.J. Fiske, M.R. Ricci, Third Generation Flywheels for High Power Electricity Storage. LaunchPoint Technologies, Inc., Goleta, California, 2006. Available at: [www.launchpnt.com/portals/53140/docs/002\\_Fiske\\_PowerRing.pdf](http://www.launchpnt.com/portals/53140/docs/002_Fiske_PowerRing.pdf).
- [46] S.M. Schoenung, Long- vs. short-term energy storage technologies analysis. Sandia Report SAND 2003-2783 (2003).
- [47] J.B. Greenblatt, S. Succar, D.C. Denkenberger, R.H. Williams, R.H. Socolow, Baseload wind energy: modeling the competition between gas turbines and compressed air energy storage for supplemental generation, *Energy Policy* 35 (2007) 1474–1492.
- [48] J. McDowall, Integrating energy storage with wind power in weak electricity grids, *J. Power Sources* 162 (2006) 959–964.

- [49] C.J. Rydh, Environmental assessment of vanadium redox and lead-acid batteries for stationary energy storage, *J. Power Sources* 80 (1999) 21–29.
- [50] IEEE Power and Energy Society, IEEE Recommended practice for the characterization and evaluation of emerging energy storage technologies in stationary applications, in: IEEE Std, 1679-2010, 2010.
- [51] K.E. Aifantis, S.A. Hackney, R. Vasant-Kumar, *High Energy Density Lithium Batteries*, Wiley-VCH, Weinheim, RFA, 2010.
- [52] W.F. Pickard, Q.A. Shen, N.J. Hansing, Parking the power: strategies and physical limitations for bulk energy storage in supply-demand matching on a grid whose input power is provided by intermittent sources, *Renew. Sustain. Energy Rev.* 13 (2009) 1934–1945.
- [53] EUROBAT, Association of European Automotive and Industrial Battery Manufacturers, (2013). [http://www.eurobat.org/sites/default/files/eurobat\\_smartgrid\\_publication\\_may\\_2013\\_0.pdf](http://www.eurobat.org/sites/default/files/eurobat_smartgrid_publication_may_2013_0.pdf).
- [54] M. Broussely, G. Pistoia, *Industrial Applications of Batteries. From Cars to Aerospace and Energy Storage*, Elsevier B.V., 2007.
- [55] Z. Wen, J. Cao, Z. Gu, X. Xu, F. Zhang, Z. Lin, Research on sodium sulfur battery for energy storage, *Solid State Ion.* 179 (2008) 1697–1701.
- [56] D.T. Ton, C.J. Hanley, G.H. Peek, J.D. Boyes, *Solar Energy Grid Integration Systems-Energy Storage (SEGIS-ES)*, 2008. Available at: <http://prod.sandia.gov/techlib/accesscontrol.cgi/2008/084247.pdf>.
- [57] J. Saint-John, General Electric's Slow Path to Grid-Scale Energy Storage, 2013. Available from: <http://www.greentechmedia.com/articles/read/general-electrics-slow-path-to-grid-scale-energy-storage> (accessed 06.11.13).
- [58] GE Energy Storage, Transforming grid operations through innovation. Available at: <http://geenergystorage.com/grid>.
- [59] M. Bartmann, BASF to Present New Developments in NiMH Batteries for Grid Energy Storage Applications at IRES 2013. <http://www.bASF.com/group/pressrelease/P-13-514> (accessed 11.11.13).
- [60] P.J. Hall, E.J. Bain, Energy-storage technologies and electricity generation, *Energy Policy* 36 (2008) 4352–4355.
- [61] D.P. Scamman, W.R. Gavin, E.P.L. Roberts, Numerical modelling of a bromidepolysulphide redox flow battery. Part 1: modelling approach and validation for a pilot-scale system, *J. Power Sources* 189 (2009) 1220–1230.
- [62] C. Ponce-de-Leon, A. Frías-Ferrer, J. González-García, D.A. Szánto, F.C. Walsh, Redox flow cells for energy conversion, *J. Power Sources* 160 (2006) 716–732.
- [63] Prudent Energy Corp., URL: <http://www.pdenergy.com/>.
- [64] Redflow Technologies Ltd., URL: <http://www.redflow.com.au/>.
- [65] A.Z. Weber, M.M. Mench, J.P. Meyers, P.N. Ross, J.T. Gostick, Q. Liu, Redox flow batteries: a review, *J. Appl. Electrochem.* 41 (2011) 1137–1154.
- [66] P.P. Alotto, M. Guarneri, F. Moro, Redox flow batteries for the storage of renewable energy: a review, *Renew. Sustain. Energy Rev.* 29 (2014) 325–335.
- [67] R. Van Noorden, A better battery, chemists are reinventing rechargeable cells to drive down costs and boost capacity, *Nature* 507 (2014) 26–28.
- [68] University of New South Wales, Vanadium Redox Battery. <http://www.ceic.unsw.edu.au/centers/vrb/Index.html>.
- [69] A. Barin, L.N. Canha, K. Magnago, A. Da-Rosa-Abaide, Fuzzy multi-sets and multi-rules: analysis of hybrid systems concerning renewable sources with conventional and flow batteries, in: 15th International Conference on Intelligent System Applications to Power Systems, 2009.

- [70] D. Wogan, <http://blogs.scientificamerican.com/plugged-in/2013/10/21/vanadium-flow-batteries-could-become-a-cost-effective-solution-for-balancing-texas-power-grid/>, 2013 (accessed 21.10.13).
- [71] H. Li, IEEE's Annual Innovative Smart Grid Technologies Conference (ISGT), 2013. <http://resourcecenter.ieee-pes.org/>.
- [72] B. Sweet, Vanadium redox gaining ground in energy storage, Spectrum, IEEE, 2013. Available at: <http://spectrum.ieee.org/energywise/energy/renewables/vanadium-redox-gaining-ground-in-energy-storage> (accessed 10.03.13).
- [73] Gildemeister energy solutions, Cell Cube FB 200 kW, <http://energy.gildemeister.com/de/speichern/cellcube-fb-200>.
- [74] E. On, Smart Grid and Innovative Energy-Storage Device Enter Service, Available at: <https://www.eon.com/en/media/news/press-releases/2013/9/9/smart-grid-and-innovative-energy-storage-device-enter-service.html> (accessed 09.09.13).
- [75] Gildemeister energy solutions receive storage and solar orders worth €29.2-million, *Energy Storage J.* Available at: <http://energystoragejournal.com/gildemeister-energy-solutions-receive-storage-and-solar-orders-worth-e29-2-million-2/> (accessed February 2013).
- [76] Greentech Media, <http://www.greentechmedia.com/articles/read/the-german-american-vanadium-flow-battery-connection> (accessed 15.03.13).
- [77] Prudent Energy Corp., World's largest vanadium flow battery goes on line in USA. Available at: <http://www.pdenergy.com/news-042612-battery.php> (accessed 26.04.12).
- [78] S. Van de Linden, Bulk energy storage potential in the USA, current developments and future prospects, *Energy* 31 (2006) 3446–3457.
- [79] Alaska Energy Authority Energy Storage Review, <http://www.aidea.org/aea/>; see Prudent Energy Corp. Website: <http://www.pdenergy.com/>.
- [80] F. Beck, P. Ruetschi, Rechargeable batteries with aqueous electrolytes, *Electrochim. Acta* 45 (2000) 2467–2482.
- [81] K.-L. Huang, X.-G. Li, S.-Q. Liu, N. Tan, L.-Q. Chen, Research progress of vanadium redox flow battery for energy storage in China, *Renew. Energy* 33 (2008) 186–192.
- [82] C.J. Rydh, B.A. Sandén, Energy analysis of batteries in photovoltaic systems. Part II: energy return factors and overall battery efficiencies, *Energy Convers. Manage.* 46 (2005) 1980–2000.
- [83] P. De-Boer, J. Raadschelders, 'Flow batteries' leonardo energy, briefing paper, <http://www.leonardo-energy.org/webfmsend/164> (2011) (accessed 20.04.11).
- [84] J. Kondoh, I. Ishii, H. Yamaguchi, A. Murata, K. Otani, K. Sakuta, N. Higuchi, S. Sekine, M. Kamimoto, Electrical energy storage systems for energy networks, *Energy Convers. Manage.* 41 (2000) 1863–1874.
- [85] P. Lex, B. Jonshagen, The zinc–bromine battery system for utility and remote area applications, *Power Eng.* 13 (1999) 142–148.
- [86] M. Hromadova, W. Ronald Fawcett, Studies of double-layer effects at single crystal gold electrodes II. The reduction kinetics of hexaaquairon(III) ion in aqueous solutions, *J. Phys. Chem. A* 105 (2001) 104–111.
- [87] M. Beaudin, H. Zareipour, A. Schellenbergblabe, W. Rosehart, Energy storage for mitigating the variability of renewable electricity sources: an updated review, *Energy Sustain. Dev.* 14 (2010) 302–314.
- [88] G.P. Corey, An assessment of the state of the zinc–bromine battery development effort, 2013. Available at: [www.redflow.com](http://www.redflow.com).
- [89] EPRI, Palo Alto, CA and the U.S. Department of Energy. EPRI-DOE handbook, supplement of energy storage for grid connected wind generation applications (2004).
- [90] Premium Power Corp., URL: <http://www.premiumpower.com/>.

- [91] W. Smith, The role of fuel cells in energy storage, *J. Power Sources* 86 (2000) 74–83.
- [92] A. Price, S. Bartley, S. Male, G. Cooley, A novel approach to utility scale energy storage [regenerative fuel cells], *Power Eng.* 13 (1999) 122–129.
- [93] A. Price, Technologies for energy storage—present and future: flow batteries, in: The Proceedings of IEEE Power Engineering Society Summer Meeting, 2000, pp. 1541–1545.
- [94] R. Baxter, *Energy Storage: A Non-Technical Guide*, PennWell Books, Tulsa, Oklahoma, USA, 2006.
- [95] K.C. Divya, J. Ostergaard, Battery energy storage technology for power systems—an overview, *Electr. Power Syst. Res.* 79 (2009) 511–520.
- [96] B.J. Chang, C.P. Garcia, D.W. Johnson, D.J. Bents, V.J. Scullin, I.J. Jakupca, Continuous operation of polymer electrolyte membrane regenerative fuel cell system for energy storage, *J. Fuel Cell Sci. Technol.* 4 (2007) 497–500.
- [97] S.A. Grigoriev, P. Millet, V.I. Porembsky, V.N. Fateev, Development and preliminary testing of a unitized regenerative fuel cell based on PEM technology, *Int. J. Hydrogen Energy* 36 (2011) 4164–4168.
- [98] X. Li, Y. Xiao, Z.G. Shao, B. Yi, Mass minimization of a discrete regenerative fuel cell (RFC) system for on-board energy storage, *J. Power Sources* 195 (2010) 4811–4815.
- [99] F. Mitlitsky, B. Myers, A.H. Weisberg, Regenerative fuel cell systems, *Energy Fuels* 12 (1998) 56–71.
- [100] M. Conte, A. Iacobazzi, M. Ronchetti, R. Vellone, Hydrogen economy for a sustainable development: state-of-the-art and technological perspectives, *J. Power Sources* 100 (2001) 171–187.
- [101] E. Varkaraki, N. Lymeropoulos, E. Zoulias, D. Guichardot, G. Poli, Hydrogen-based uninterruptible power supply, *Int. J. Hydrogen Energy* 32 (2007) 1589–1596.
- [102] C.J. Winter, Hydrogen energy—abundant, efficient, clean: a debate over the energy-system-of-change, *Int. J. Hydrogen Energy* 34 (2009) 1–52.
- [103] K.C. Neyerlin, W.B. Gu, J. Jorne, H.A. Gasteiger, Determination of catalyst unique parameters for the oxygen reduction reaction in a pemfc batteries, fuel cells, and energy conversion, *J. Electrochem. Soc.* 153 (2006) A1955–A1963.
- [104] P. Li, Energy storage is the core of renewable energy technologies, *IEEE Nanotechnol. Mag.* 2 (2008) 13–18.
- [105] US Department of Energy, Office of energy efficiency and renewable energy, Types of Fuel Cells, 2011. [http://www1.eere.energy.gov/hydrogenandfuelcells/fuelcells/fc\\_types.html](http://www1.eere.energy.gov/hydrogenandfuelcells/fuelcells/fc_types.html) (accessed 08.03.11).
- [106] J.T. Kim, J. Jorne, The kinetics of a chlorine graphite electrode in the zinc–chlorine battery, *J. Electrochem. Soc.* 124 (1977) 1473–1477.
- [107] J.A. Kosek, A.B. LaConti, Advanced hydrogen electrode for a hydrogen bromine battery, *J. Power Sources* 22 (1988) 293–300.
- [108] V. Livshits, A. Ulus, E. Peled, High-power H<sub>2</sub>/Br<sub>2</sub> fuel cell, *Electrochem. Commun.* 8 (2006) 1358–1362.
- [109] D.B. Nelson, M.H. Nehrir, C. Wang, Unit sizing and cost analysis of stand-alone hybrid wind/PV/fuel cell power generation systems, *Renew. Energy* 31 (2006) 1641–1656.
- [110] C.M. Julien, A. Mauger, Review of 5-V electrodes for Li-ion batteries: status and trends, *Ionics* 19 (2013) 951–988.
- [111] C.M. Julien, A. Mauger, K. Zaghib, H. Grout, Comparative issues for cathode materials for Li-ion batteries, *Inorganics* 2 (2014) 132–154.

[112] D. Liu, W. Zhu, J. Trottier, C. Cagnon, F. Baray, A. Guerfi, A. Mauger, H. Groult, C.M. Julien, J.B. Goodenough, Spinel materials for high-voltage cathodes in lithium-ion batteries, *RSC Adv.* 4 (2014) 154–167.

[113] K. Zaghib, A. Mauger, H. Groult, J.B. Goodenough, C.M. Julien, Advanced electrodes for high-power Li-ion batteries, *Materials* 6 (2013) 1028–1049. Available at: <http://www.mdpi.com/1996-1944/6/3/1028>.

[114] K. Zaghib, J. Dubé, A. Dallaire, K. Galoustov, A. Guerfi, M. Ramanathan, A. Benmayza, J. Prakash, A. Mauger, C.M. Julien, Intrinsic safety of high-power Li-ion batteries, in: G. Pistoia (Ed.), *Handbook on Lithium-Ion Batteries: Advances and Applications*, Elsevier, 2013b, pp. 437–480 (Chapter 19).

[115] A. Mauger, C.M. Julien, Surface modifications of electrode materials for lithium-ion batteries: status and trends, *Ionics* 20 (2014) 751–787.

[116] K. Zaghib, M. Dontigny, A. Guerfi, J. Trottier, J. Hamel-Paquet, V. Gariepy, K. Galoutov, P. Hovington, A. Mauger, H. Groult, C.M. Julien, An improved high-power battery with increased thermal operating range: C-LiFePO<sub>4</sub>/C-Li<sub>4</sub>Ti<sub>5</sub>O<sub>12</sub>, *J. Power Sources* 216 (2012) 192–200.

[117] K. Zaghib, M. Dontigny, A. Guerfi, P. Charest, I. Rodrigues, A. Mauger, C.M. Julien, Safe and fast-charging Li-ion battery with long shelf life for power applications, *J. Power Sources* 196 (2011) 3949–3954.

[118] K. Zaghib, N. Ravet, M. Gauthier, F. Gendron, A. Mauger, J.B. Goodenough, C. M. Julien, Optimized electrochemical performance at 60 °C of LiFePO<sub>4</sub> with purity controlled by SQUID magnetometry, *J. Power Sources* 163 (2006) 560–566.

[119] Lux Resaerch Inc.,: <http://www.luxresearchinc.com/>.

[120] A. Habib, A.-O. Shamsiah, Advancing Li-ion, 2012. Available at: [http://www.pv-magazine.com/archive/articles/beitrag/advancing-li-ion\\_100006681/501/#axzz2vx36ILCi](http://www.pv-magazine.com/archive/articles/beitrag/advancing-li-ion_100006681/501/#axzz2vx36ILCi) (accessed 01.05.12).

[121] Power One URL: <http://www.power-one.com>.

[122] SNEC, 8th International Photovoltaic Power Generation Conference ‘Power One: Energy storage is next step for PV market’. Available at: <http://www.s nec.org.cn/website/newsDetail.aspx?id=1158&lang=en>, 2014 (accessed 21.03.14).

[123] E.G. Bakhoun, New mega-farad ultracapacitors, *IEEE Trans. Ultrason. Ferroelectr. Freq. Control* 56 (2009) 14–34.

[124] Z. Dong, S.J. Kennedy, Y. Wu, Electrospinning materials for energy-related applications and devices, *J. Power Sources* 196 (2011) 4886–4904.

[125] P. Sharma, T.S. Bhatti, A review on electrochemical double-layer capacitors, *Energy Convers. Manage.* 51 (2010) 2901–2912.

[126] J.R. Miller, P. Simon, Electrochemical capacitors for energy management, *Science* 321 (2008) 651–652.

[127] H. Pan, J. Li, Y.P. Feng, Carbon nanotubes for supercapacitor, *Nanoscale Res. Lett.* 5 (2010) 654–668.

[128] A. Kusko, J. Dedad, Short-term and long-term energy storage methods for standby electric power systems, *IEEE Ind. Appl. Mag.* 66–72 (2007).

[129] O.C. Onar, M. Uzunoglu, M.S. Alam, Modeling, control and simulation of an autonomous wind turbine/photovoltaic/fuel cell/ultra-capacitor hybrid power system, *J. Power Sources* 185 (2008) 1273–1283.

[130] A. Burke, Ultracapacitors: why, how, and where is the technology, *J. Power Sources* 91 (2000) 37–50.

[131] P. Simon, Y. Gogotsi, Materials for electrochemical capacitors, *Nat. Mater.* 7 (2008) 845–854.

- [132] M.F. El-Kady, V. Strong, S. Dubin, R.B. Kaner, Laser scribing of high-performance and flexible graphene-based electrochemical capacitors, *Science* 335 (2012) 1326–1330.
- [133] C. Liu, Z. Yu, D. Neff, A. Zhamu, B.Z. Jang, Graphene-based supercapacitor with an ultrahigh energy density, *Nano Lett.* 10 (2010) 4863–4868.
- [134] X. Yang, C. Cheng, Y. Wang, L. Qiu, D. Li, Liquid-mediated dense integration of graphene materials for compact capacitive energy storage, *Science* 341 (2013) 534–537.
- [135] Y. Zhu, S. Murali, M.D. Stoller, K.J. Ganesh, W.W. Cai, P.J. Ferreira, A. Pirkle, R. M. Wallace, K.A. Cychosz, M. Thommes, D. Su, E.A. Stach, R.S. Ruoff, Carbon-based supercapacitors produced by activation of graphene, *Science* 332 (2011) 1537–1541.
- [136] H. Yang, S. Kannappan, A.S. Pandian, J.-H. Jang, Y.S. Lee, W. Lu, arXiv:1311.1413 [cond-mat.mtrl-sci, 6 nov. 2013].
- [137] H. Khayyam, H. Ranjbarzadeh, V. Marano, Intelligent control of vehicle to grid power, *J. Power Sources* 201 (2012) 1–9.
- [138] A. Emadi, *Handbook of Automotive Power Electronics and Motor Drives*, CRC Press, Abingdon, UK, 2005 p. 34.
- [139] M.K. Hirlue, G.R. Parsons, W. Kempton, M.P. Gardner, Willingness to pay for electric vehicles and their attributes, *Resour. Energy Econ.* 33 (2011) 686–705.
- [140] S. Kamboj, N. Pearre, W. Kempton, K. Decker, K. Trnka, C. Kern, Exploring the formation of electric vehicle coalitions for vehicle-to-grid power regulation, in: *Proceedings of 2010 AAMAS Workshop on Agent Technologies for Energy Systems*, 2010.
- [141] W. Kempton, F. Marra, P.B. Andersen, R. Garcia-Valle, Business models and control and management architectures for EV electrical grid integration, in: *3rd IEEE PES Innovative Smart Grid Technologies Europe (ISGT Europe)*, 2012.
- [142] W. Kempton, J. Tomic, Vehicle-to-grid power fundamentals: calculating capacity and net revenue, *J. Power Sources* 144 (2005) 268–279.
- [143] A. Briones, J. Francfort, P. Heitmann, M. Schey, S. Schey, J. Smart, Vehicle-to-grid (V2G). Power flow regulations and building codes, Review by AVTA, Idaho Nat. Lab. Report, Sept. 2012, INL/EXT-12-26853 (2012).
- [144] W. Kempton, A. Dhanju, Electric vehicles with V2G: storage for large-scale wind power, *Windtech Int.* 2 (2006) 18–21.
- [145] Y. Nussbaumer, Vehicle to grid: de la batterie vers le réseau électrique. In: *Energie, Voiture Electrique, Automobile Propre*. Available at: <http://www.automobile-propre.com/2012/06/07/vehicle-to-grid-de-la-batterie-vers-le-reseau-electrique/>, 2012 (accessed 07.06.12).
- [146] V. Udo, Proven at PJM: Vehicle to Grid (V2G) and Power System/Transportation Synergies, Pulse, Energy, 2008. Available at: [http://www.energypulse.net/centers/article/article\\_print.cfm?a\\_id=1878](http://www.energypulse.net/centers/article/article_print.cfm?a_id=1878) (accessed 17.11.08).
- [147] Hydro-Québec Report (2014), Démonstration d'une zone de réseau interactif, Hydro-Québec—Institut de recherche, <http://www.rncan.gc.ca/energie/financement/programmes-financement-actuels/fep/4958> (accessed 08.01.14).
- [148] NanoMarkets, Batteries and Ultra-capacitors for the Smart Power Grid, 2014, [www.nanomarkets.net](http://www.nanomarkets.net) (accessed 06.08.14).

# Rechargeable lithium batteries for medical applications

13

*M.J. Cleland*

University of Ottawa Heart Institute, Ottawa, ON, Canada

## 13.1 Introduction

The health care environment possesses several challenges to electromedical equipment manufacturers. The environment in which the equipment is employed is highly variable, ranging from a prehospital setting to a critical care unit. Challenges faced by emergency medical services (EMS) range from harsh environmental conditions to providing lifesaving treatments as the first responder. Their equipment must withstand the rigors of transportability while providing feedback and treatment via physiological monitors and defibrillators. The critical care environment relies on physiological monitoring and devices to monitor and maintain a patient's vital functions. Treatment and monitoring within critical care units often involves both invasive and noninvasive monitoring. Invasive monitoring procedures may range from indwelling pressure-monitoring catheters to mechanical circulatory assist devices. The electromedical equipment connected to patients in all of these environments employ batteries as a primary or secondary source of power. Increasingly, equipment manufacturers are selecting lithium-ion batteries to power their devices. It is the intention of this chapter to illustrate the importance of ensuring medical devices are in a state of readiness through a vigilant battery maintenance program.

## 13.2 Critical care and patient monitoring

Acutely ill patients require intensive treatments and monitoring of several physiological systems [1]. Frequently, when one system is compromised other systems are adversely affected. Throughout this chapter, the cardiac system will be discussed as our default example. The primary function of the cardiovascular system is to provide oxygenated blood to the body to meet its metabolic needs. Monitoring physiological parameters provides insight into the potential instabilities and responses to treatments. This level of care must be present within the critical care units and be fully transportable as intra-hospital transports to various diagnostic and treatment areas within the hospital.

### 13.2.1 History and philosophy of patient monitoring

Derived from the Latin word *monere*—to warn—and coupled with the concept of “how is the patient doing,” patient monitors are designed to caution, remind, or advise the health care provider on the patient's status. Utilizing the senses or by utilizing

instrumentation, monitoring and vigilance are interrelated. Monitoring provides information to enhance vigilance and facilitate therapeutic intervention. Some physiological parameters are monitored through several measurement modalities, so potentially more systems can alert the user to a problem making it more likely that appropriate therapeutic action will be taken. Monitoring information encompasses a variety of modalities from basic electrocardiographic, noninvasive blood pressure, pulse oximetry, and end-tidal carbon dioxide measurements to more sophisticated bispectral index and invasive pressure monitoring [2]. Invasive monitoring of the arterial pressures provides continuous observation of the waveform and associated pressure values. It is the gold standard of blood pressure measurement [1].

### **13.2.2 *Pulmonary artery catheter***

A flexible catheter capable of floating through the venous circulatory system has become one of the most important and valuable clinical tools for monitoring the critically ill patient. Invented by Dr Jeremy Swan and Dr William Ganz, the Swan–Ganz catheter provides clinicians with extensive hemodynamic information [3]. Pressure measurements obtained by the pulmonary artery (PA) catheter include: pulmonary artery pressure (PAP), pulmonary artery capillary wedge pressure (PACWP), and central venous pressure (CVP). In the 1970s a thermistor was added to the catheter, located at the tip of the catheter, in order to facilitate thermal dilution cardiac output measurements [4,5]. Further advancements included a fiber-optic bundle to allow light transmission, via an optical module, to allow continuous oxygen saturation of the venous system. Technological advances coupled with the values from direct pressure measures have allowed for derived calculations, which further defines cardiac performance. Information gathered by the PA catheter helps define various circulatory disease states in terms of pump failure, hypovolemia, as well as high or low resistance states. Referring back to Dr Casey Blitt's writings on how monitoring and vigilance are interrelated, the PA catheter provides hemodynamic information allowing clinicians to direct their treatment strategies with greater precision [1].

### **13.2.3 *Ventilators***

The lungs are complex organs whose primary function is gas exchange. Oxygen ( $O_2$ ) is drawn into the lung via the respiratory tract and delivered down to the alveoli where gas is exchanged with the capillary bed of blood vessels. Diffusion takes place as a result of differing partial pressures of gases between atmospheric concentrations and those within the pulmonary capillaries. The oxygen enters the blood stream while the carbon dioxide ( $CO_2$ ) is released into the lungs and exits the body. The process is defined through Fick's gas law. Properly functioning lungs are responsible for the regulation of the body's acid–base balance. Impairment of this process may be dealt with through mechanical ventilation. Mechanical ventilation will not cure any disease, but rather offer life-sustaining maintenance of this important physiological function. Thus, clinical goals of mechanical ventilation include relief of respiratory distresses and reversal of acute acid–base abnormalities [6].

Mechanical ventilators typically connect to two high-pressure sources of medical gas ( $O_2$  and air) and deliver a set concentration of gas to the patient. Gases are presented to the patient via an inspiratory module, generally comprised of internal pressure regulators, filters, and flow transducers. Oxygen concentration is controlled through a form of portioning circuitry, based on the operator's inspiratory  $O_2$  settings. The patient's exhaled breath returns to the ventilator through the exhalation module, which is comprised of a one-way valve, a heater to minimize humidity, a pressure transducer, and a flow sensor to provide readings for breath delivery calculations. Critical care ventilators also employ a battery pack, offering a secondary source of power in the event of unexpected power loss.

Breath delivery during mechanical ventilation occurs either by clinician-set volume or pressure. During volume-cycled ventilation, the inhalation phase proceeds until a set tidal volume (TV) is delivered. Constant inspiratory flow results in positive pressures applied to the airway, higher than the pressure required for normal lung distention. In this mode the delivered TV remains constant, the pressure applied to the airways will vary with changing pulmonary compliance and airway resistance. Volume-controlled ventilation is often the most common choice for initiation of mechanical ventilation. Monitoring airway pressures is vital to avoid barotrauma in patients. Pressure-cycled ventilation gained its popularity in the treatment of patients with acute respiratory distress syndrome (ARDS). An advantage of pressure-cycled ventilation is that the inspiratory flow profile decelerates as the lung inflates, thus creating a more homogeneous gas distribution throughout the lung. The limitation with this form of ventilation is the TV can vary with changes in pulmonary compliance and resistance; therefore, minute ventilation must be monitored to ensure an adequate amount of ventilation is being presented to the patient.

With great advancements in diagnostic imaging, including computed tomography (CT), magnetic resonance imaging (MRI), and angiography suites, increasingly, patients are being transported to other areas of the hospital for diagnostic procedures. Transporting ventilator dependent, critically ill patients is facilitated with sophisticated portable ventilators, but is not without risk [7–11]. These ventilators often alleviate the clinical challenge of maintaining the patient's respiratory and blood gas status during transport and, thereby, reduce the risk of hypotension and arrhythmias. Thus, portable ventilators have become the preferred method for transporting patients within the hospital. Employing high-energy lithium-ion battery technology, ventilator manufacturers are able to produce lightweight, highly sophisticated portable ventilators [12,13]. These ventilators offer both volume-controlled and pressure-cycled modes of delivery.

### 13.3 Defibrillation

Ventricular fibrillation (VF) is a potentially lethal cardiac arrhythmia in which the ventricle's muscle fibers randomly contract and relax without any form of synchronization. The heart is incapable of propelling blood out from the ventricles to the body.

This condition is the major cause of sudden death from a heart attack. It can be terminated with the passage of electrical current through the heart using electrodes applied to the chest wall. This technique is referred to a ventricular defibrillation [14]. In order for the defibrillator's shock to be effective it must depolarize a critical mass of the myocardium [15].

### 13.3.1 *Historical development of defibrillation*

The earliest notes on defibrillation back to 1898 when Prevost and Battelli applied strong currents directly to the heart to induce VF. In a footnote they mentioned, incidentally, that these electrical discharges were also capable of terminating the VF. It wasn't until the work of Kouwenhoven in the 1930s that showed 60 Hz alternating current (AC) applied directly to the heart could be used for defibrillation. Dr Paul Zoll reported the first closed chest, transthoracic, AC defibrillation in 1956 terminating the life-threatening VF [16]. In 1959, Dr Bernard Lown had a patient with a persistent ventricular tachycardia, a very rapid heart rate, requiring cardioversion. Knowing of Dr Zoll's success with terminating VF, Dr Lown recognized the only viable treatment would be to shock the patient with an AC defibrillatory shock. While unsure of the current settings, the procedure was performed and the patient responded well and was discharged from the hospital in normal sinus rhythm. Within two weeks the patient returned with a severe tachycardia. Again, Dr Lown used the AC defibrillator to cardiovert the patient; however, this time the postshock rhythm was VF. Unfortunately, they were unable to resuscitate the patient. Devastated with the result, Lown investigated the effects that AC defibrillation pulses had on the heart and found the technology they were using was very hazardous. With the aid of an engineer from the American Optical Company they started experimenting with direct current (DC) shocks. In 1961, Dr Lown was called to use his DC defibrillator on an elderly patient suffering ventricular tachycardia (VT), a very rapid heart rate creating an ineffective pumping action, as a result of an acute myocardial infarction. The VT was terminated with the first shock and the patient's rhythm and blood pressure went back to normal. This waveform, termed the *Lown waveform* was generated by charging a bank of capacitors to 1000 V, then discharging the capacitors through an inductor to a set of paddles to the patient's chest. The original machine weighed ~60 lbs. Refinement of the defibrillator has always been moving forward, thus reducing size and weight, but the damped sinusoidal waveform technology remained standard in most defibrillators for ~40 years. It has become the mainstay of resuscitation equipment throughout hospitals [17].

The 1970s brought forth improvements in battery technology that helped facilitate employing this lifesaving technology into the field through paramedic programs. Leading the push was Dr Mickey Eisenberg; his review of 39 EMS from 29 different locations helped illustrate the benefit of early CPR combined with early defibrillation [18]. This was adopted by the American Heart Association as a crucial link in the chain of survival. Not only an advocate for systematic improvement of prehospital defibrillation, Dr Eisenberg called for technological change pertaining to waveform technology [19]. The introduction of biphasic waveform technology brought forth smaller, lighter defibrillators. A bank of smaller capacitors replaced the larger storage

capacitors, the heavy wave-shaping coil inductor was eliminated, and display technology also contributed to making a smaller machine. Independent of the waveform evolution, miniaturization of electronic components reduced the number of circuit boards within the device. Automated VF detection algorithms coupled with treatment protocol voice prompts facilitated the development of automatic external defibrillators (AEDs). With the automation of built-in treatment protocols another tier was added to EMS [20,21]. Public access defibrillation programs were implemented to contribute to early defibrillation within communities.

Further advancements in battery technology have all manufacturers designing their defibrillators around lithium-ion chemistry. This is a welcomed change, as several reports illustrate defibrillator failure rates as high as 18%. Most failures involved the device's battery. Sealed lead-acid and nickel-cadmium were the chemistries most often involved. These reports emphasized the importance of regular device maintenance [22,23]. Battery maintenance is discussed later in this chapter.

Founded in 1980 by Dr Paul Zoll, the Zoll Medical Corporation has been one of the leaders in medical products, including defibrillation. Their latest models of defibrillators are powered by lithium-ion battery technology (Figure 13.1). The battery pack employs a fuel gage providing valuable feedback to the user pertaining to the amount of run time remaining.

## 13.4 Heart failure

Heart failure (HF) is a clinical syndrome in which the cardiac output is inadequate to meet the metabolic needs of the body as a result of an impaired pump. HF can be further classified into systolic or diastolic HF. In systolic HF, there is a reduction in the heart's contractility; thus, a lessened ability to eject blood out of the ventricle. In diastolic HF, there is impaired cardiac relaxation and abnormal ventricular filling.

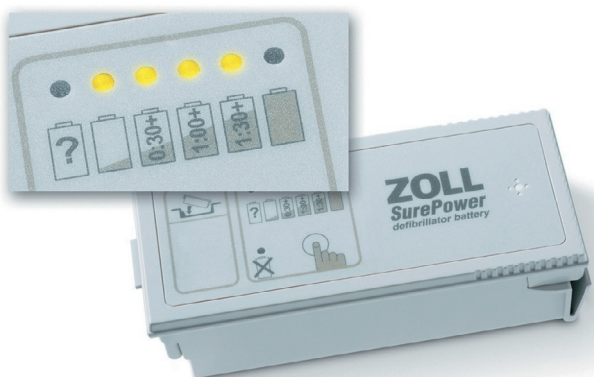


**Figure 13.1** SurePower rechargeable lithium-ion battery with fuel gage.  
Reproduced with permission from Zoll Medical Corporation.

Systolic dysfunction cases are most common and are usually a result of end-stage coronary artery disease, where there is a history of myocardial infarction or chronically under-perfused myocardium. Poor contractility is often associated with the ventricle wall becoming enlarged, resulting in a dilated cardiomyopathy. Diastolic dysfunction is an impairment of the ventricle's ability to relax usually related to chronic hypertension or ischemic heart disease. While HF is generally a left-sided (left ventricle) disease, the right ventricle (RV) may also suffer dysfunction as a result of RV infarction or pulmonary hypertension.

HF is a progressive disease with well-established classifications of various stages ([Table 13.1](#)).

Reportedly, there are in excess of 500,000 new cases of HF each year in the United States and over 275,000 deaths a year attributed to HF. Medical advancements in identifying and treating hypertension, have led to improved outcomes with HF [24,25]. However, patients suffering from Class IV symptoms for a prolonged period of time may stop responding to optimum medical therapy and face almost certain mortality [26,27]. Mechanical circulatory support or cardiac transplantation remain options for patients suffering from end-stage HF. Unfortunately, there are selection/inclusion criteria for each of those modalities as well. Although with the invention of cyclosporine, transplantation has seen a significant reduction in rejection, long-term immunosuppression is required for transplanted patients. A shortage of donor organs also poses a challenge to most transplant centers. Thus, many patients may die while awaiting transplantation.

## 13.5 Circulatory assist devices

Mechanical circulatory support got its start in 1934 when Dr Michael DeBakey developed the concept of a roller pump to facilitate blood transfusions. Twenty years later Dr John Gibbon, along with a team of five engineers from IBM, created the first

**Table 13.1 Progressive stages of heart failure based on New York Heart Association Functional Classification System**

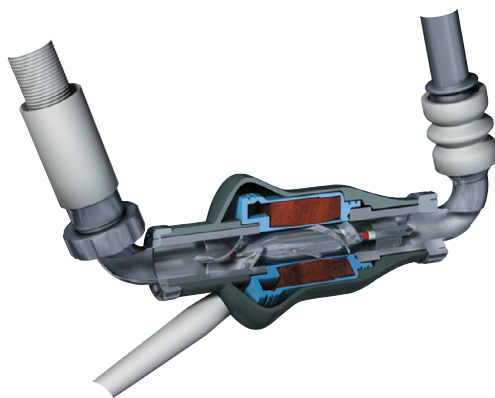
Class	Symptoms
Class I	Cardiac disease but no symptoms or limitation in ordinary physical activity such as walking
Class II	Mild symptoms such as shortness of breath with slight limitations during ordinary activity
Class III	Marked limitations in activity due to symptoms even during less than ordinary activities. Comfortable only at rest
Class IV	Severe limitations. Experiences symptoms even while at rest

cardiopulmonary bypass machine. In 1953, Dr Gibbon used the CPB machine to repair an atrial septal defect in an 18-year-old woman [28]. The use of this technology and its concept revolutionized cardiac surgery. In the years following this landmark surgery, the need for a device offering prolonged mechanical circulatory support was recognized. A mechanical device that could partially or completely replace the pumping action of the failing heart was pursued. In 1963, Dr DeBakey implanted the first successful ventricular assist device (VAD). The device was a double lumen tube, with a silastic inner tube acting as the blood chamber [29]. The device employed two Starr-Edwards ball valves to maintain a forward flow of blood out of the heart. The pumping mechanism was generated by a pneumatic source pressurizing the outer lumen, thus collapsing the blood chamber. A few years after Dr DeBakey's initial endeavor to provide mechanical circulatory support, Dr Kontrowitz developed the first concept of the artificial ventricle. In 1967, Dr Kontrowitz implanted his artificial ventricle in a patient who recovered sufficiently to be discharged home. The patient was supported for ~80 days. The biomedical and surgical worlds quickly went to work on variations of pulsatile VADs [28]. During the 1980s and 1990s it was becoming well defined that patients suffering from end-stage HF, who were no longer responding to optimum medical therapy, would benefit from a left ventricular assist device (LVAD). Mechanical unloading of the left ventricle and improved end-organ perfusion were quickly obtainable. The implanted devices ranged from intracorporeal to paracorporeal devices and had large drive consoles to power their device. Batteries provided a secondary source of power, but were limited to sealed lead-acid technology. Usage of the VAD was quickly evolving from its postsurgery support role.

Two primary treatment options for end-stage HF are pharmacological therapy and cardiac transplantation. Although advances in medical therapy have had important impacts on symptom status and short-term survival with patients suffering moderate to severe HF, they have only moderate success in patients with Class IV HF. Transplantation is limited by the complications of long-term immunosuppression, the shortage of donor organs, and coronary artery disease in the donor organ. Increasingly, centers were illustrating their LVAD program's ability to support failing circulation, and the bridge to transplant experience was growing [30–36]. One of the first clinical studies comparing medical management versus mechanical intervention for the treatment of end-stage HF was the Randomized Evaluation of Mechanical Assistance for the Treatment of Congestive Heart Failure (REMATCH) trial. The multicenter trial's inclusion criteria enrolled patients over 18 years of age, suffering Class IV HF, that were ineligible for transplant. In total, 129 patients met the inclusion criteria; they were randomized into two treatment groups. There were 68 patients entered the LVAD arm of the study and 61 patients were placed in the medical management arm of the study. The first year mortality rate of the medical therapy group was 75% compared to 48% in the LVAD group. The biggest contributor to death was left ventricular dysfunction in the medical therapy group and sepsis within the LVAD group. The study concluded that LVAD therapy is an acceptable alternative in patients and there was a meaningful survival benefit and an improved quality of life for those patients treated with LVAD insertion [37].

**Figure 13.2** Cutaway of an axial flow HeartMate II LVAD.

Reproduced with permission from Thoratec Corporation.



Since REMATCH, device technology has progressed to continuous flow employing axial and centrifugal flow characteristics [38,39]. This new style of device saw a great reduction in size of the implanted LVAD (Figure 13.2). Advances in battery technology have seen all devices employ lithium-ion as their choice of secondary power sources. Lithium-ion technology offers higher energy density per weight than any other battery, thus offering our patients prolonged battery life and more comfort, as the batteries are lightweight (Figure 13.3). Studies comparing pulsatile technology versus continuous flow technology have illustrated continuous flow devices significantly improve survival with reduced threat from disabling stroke over a two-year period [40–44].

Patients suffering from biventricular failure may require support for both the right and left ventricles. Like the LVAD, the biventricular assist devices (BIVADs) function in conjunction with the native heart. However, in this instance mechanical circulatory support is offered to both the pulmonary and systemic systems. Patients with biventricular failure coupled with aortic regurgitation, left ventricular thrombus, or have an aortic prosthesis, are not candidates for typical BIVAD support. An alternate form of biventricular support can also include replacing the native ventricles of the heart with the Total Artificial Heart (TAH) (Figure 13.4). Copeland *et al.* reported survival rates of 79% with 81 patients receiving the TAH as a bridge to transplant. Patients are able to ambulate well to a point where they are discharged home with the use of SynCardia's freedom pneumatic driver [45]. Improving the patient's quality of life, thus their ability to be discharged home from the hospital, places a huge demand on battery technology. Unexpected loss of power could severely compromise the patient's health and could even lead to death. The VAD and biomedical program ensures batteries are properly maintained and monitored. The patients are diligent, ensuring they always travel with a spare set of fully charged batteries. One of the continuous flow devices used within the VAD program at the University of Ottawa Heart Institute is the HeartMate II, manufactured by the Thoratec Corporation. Ancillary equipment for the LVAD includes a power module, battery charger, and battery clips. The power module provides power to the device while the patient is tethered to the unit via a patient cable, typically used at night while the patient is in bed. Batteries, seated

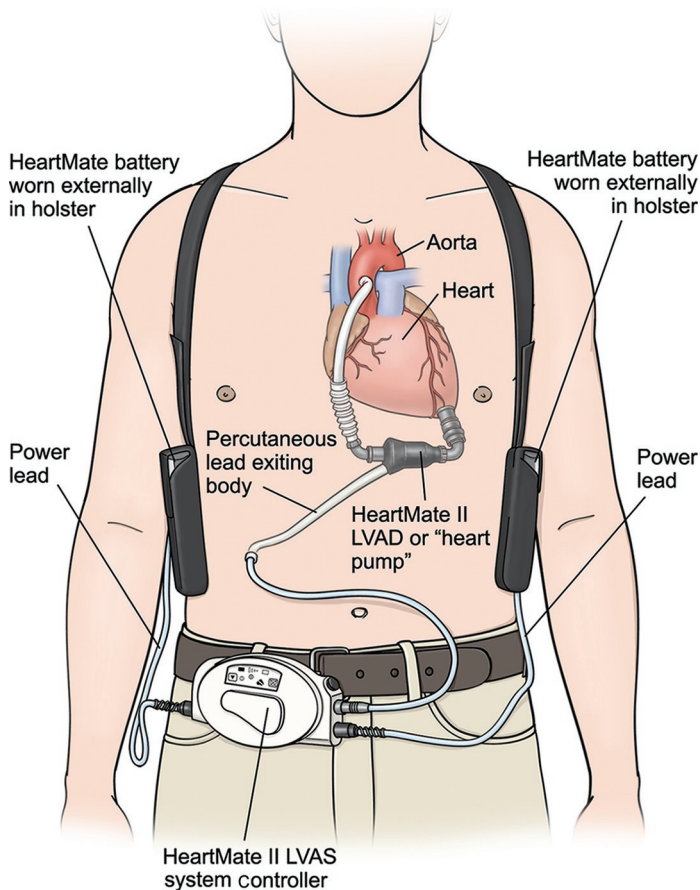


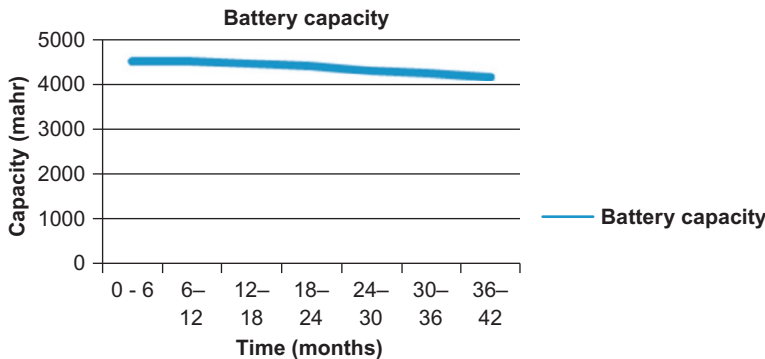
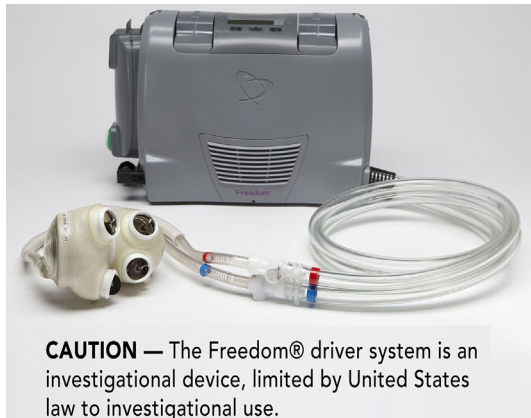
**Figure 13.3** HeartMate II LVAD system during battery powered operation.  
Reproduced with permission from Thoratec Corporation.

within battery clips, provide power to the device during times of ambulation. During the last four years, our program has implanted over 40 HeartMate II devices. The devices have been supported through 72 lithium-ion battery packs. A review of service history illustrates how well the batteries have been performing (see [Graph 13.1](#)). Over the four-year period there has only been an  $\sim 10\%$  loss of battery capacity.

## 13.6 Biomedical engineering

The grassroots of biomedical engineering (BME) can be traced back to the post-World War I era when a U.S. Army Surgeon General calls for a “central repair establishment within the medical department.” In the years following that statement, development of a medical maintenance shop and a 3-month training program were implemented within a

**Figure 13.4** Freedom driver system for the total artificial heart. Reproduced courtesy of [Syncardia.com](http://Syncardia.com).



**Graph 13.1** A plot of battery capacity vs. time.

medical army base in St. Louis. The combination of servicing medical devices and providing education, thus a liaison to bridge the technology gap among other health care professionals, are key elements within present day BME departments.

While BME departments have always played an integral role in delivering safe monitoring and care of patients through maintaining electromedical equipment within health care facilities. Patient safety has been at the forefront of clinical practice since the Institute of Medicine in the United States published the report “To Err Is Human: Building a Safer Health Care System” [46]. Establishing a risk-based maintenance program as well as technology assessment provides additional key elements in maintaining equipment in a state of readiness [47,48].

### 13.6.1 Asset management

A central feature of maintaining equipment in a state of readiness is the philosophy that batteries are treated no differently than other medical devices. Batteries are included in the medical equipment program. As with all medical devices, their asset

information is entered into the asset management program upon receipt into the organization. All batteries are entered into the preventative maintenance program for the equipment in which they are being used. A computerized asset management system contains information on purchasing, risk-based maintenance scheduling, and a maintenance history. Tracking service or product advisories are also facilitated through the asset management program. The current practice at our institution established by Zakutney and Cleland, has been recognized by the Ontario Hospital Association as a leading practice.

### 13.6.2 **Battery maintenance program**

Battery maintenance programs should consider the importance of end use, as described earlier within the risk-based maintenance program, as well as the characteristics of the battery pack itself and the usage profile. Uninterrupted operation of devices is paramount when delivering care to a patient. Their maintenance schedule should support this as well as establishing handling procedures for the staff pertaining to routine charging, including ensuring a fully charged battery is always on hand. Batteries play a key role in maintaining continuous monitoring and treatment to patients. The biggest demand on the equipment's battery comes during ambulation or transportation of a patient.

Battery capacity is a measurement of how much current can be delivered over a specified period of time [49]. The translation of this for clinicians is referred to as run time. Commercially available analyzers allow biomedical engineers to measure the battery's functional capacity; thus, the individual battery's capacity results can be monitored through the asset management program described above. Cadex Electronics is a Canadian company specializing in battery maintenance analyzers. Their analyzers (Figure 13.5) have been the cornerstone of our program and are utilized by many biomedical engineering departments. Various adapters allow testing of many commonly used battery chemistries. Their extended range series is capable of



**Figure 13.5** Cadex 7400ER battery analyzer.  
Reproduced with permission from Cadex Electronics.

handling 6 A per station with a battery voltage range of 1.2–36 V for lithium-ion battery packs.

A brief case report, illustrating the devastating effects of equipment-related failures within a critical care environment, follows below. While the technology in question was not a lithium-based battery, it does illustrate the importance of a battery maintenance program.

### 13.6.2.1 Case report

#### Introduction

This report arises from a patient incident that resulted in an adverse event caused by the failure of an infusion pump battery during transport of a patient from the cardiac operating room to the cardiac surgical intensive care unit (CSICU). The root-cause analysis arising from the incident lead to research on rechargeable batteries used to power infusion pumps when they are disconnected from the power supply.

#### Clinical background

The critical incident occurred in a patient who underwent an aortic valve replacement. Following cardiopulmonary bypass, the patient had a low cardiac output and low blood pressure requiring hemodynamic support with intravenous milrinone and norepinephrine. With the infusion of these two drugs, reasonable hemodynamic stability was achieved. After completion of the surgery, the patient was transported to the CSICU. The arterial blood pressure, pulse oximetry, and electrocardiogram were monitored throughout the transport. The infusion pumps that were being used to deliver the intravenous medications prior to transport were unplugged from the AC electrical source and immediately converted to battery power. The total transport distance was ~30 m with two 90° turns to negotiate. The usual time of transport is under 3 min. Approximately 30 s into the transport, the infusion pump that was delivering the norepinephrine stopped without warning. The arterial blood pressure very rapidly decreased to a systolic pressure of 60 mm Hg by the time the patient was in the CSICU. Within seconds of arrival, the patient developed VF and his sternum was reopened. A major resuscitative effort was required to restore the patient's hemodynamic stability.

A sentinel event review was undertaken that identified two root causes. These were complications related to transport of critically ill patients from the operating room to the CSICU and problems relating to the use of intravenous infusion pumps. Further inquiry was undertaken into the hazards inherent in the use of infusion pumps and a literature review showed that infusion pump hazards are commonplace and potentially life-threatening. Battery failure was recognized as a possible infusion pump hazard. Further inquiry of users of infusion pumps in the organization revealed that there were at least three similar incidents caused by battery failure with less devastating outcomes.

Several action plans were initiated to reduce the likelihood of hazards associated with the use of infusion pumps. These included a review of battery capacity and the development of a research-based battery management program for the organization.

## 13.7 Summary

The patient must always be the focus when dealing with medical equipment. Increasing reliability reduces the risk of equipment-related failures within the health care setting. Clearly establishing itself as the latest and greatest battery technology today, manufacturers of medical equipment are employing lithium-ion battery packs as their choice of battery technology. Lithium-ion batteries provide the largest energy density per weight, a flat discharge curve, and utilize stored power in a desirable voltage spectrum; all features that make this battery chemistry ideal for medical applications. Battery maintenance is an important component of the biomedical program and steps should be made at all centers to develop such programs, especially within a critical care setting.

## References

- [1] C.L. Lake, R.L. Hines, C.D. Blitt, *Clinical Monitoring: Practical Applications for Anesthesia and Critical Care*, W.B. Saunders Company, Philadelphia, 2001.
- [2] J. Truijen, et al., Noninvasive continuous hemodynamic monitoring, *J. Clin. Monit. Comput.* 26 (2012) 267–278.
- [3] N. Buchbinder, W. Ganz, Hemodynamic monitoring: invasive techniques, *Anesthesiology* 45 (2) (1976) 146–155.
- [4] H. Mehrnaz, M.R. Pinsky, Functional hemodynamic monitoring, *Curr. Opin. Crit. Care* 13 (3) (2007) 318–323.
- [5] M.R. Pinsky, Hemodynamic evaluation and monitoring in the ICU, *Chest* 132 (2007) 2020–2029.
- [6] R.P. Byrd Jr., et al., Mechanical ventilation, *Medscape* (2012).
- [7] J. Link, et al., Intrahospital transport of critically ill patients, *Crit. Care* 18 (12) (1990) 1427–1429.
- [8] U. Beckman, et al., Incidents relating to the intra-hospital transfer of critically ill patients, *Intensive Care Med.* 30 (2004) 1579–1585.
- [9] J. Warren, et al., Guidelines for inter- and intrahospital transport of critically ill patients, *Crit. Care Med.* 32 (1) (2004) 256–262.
- [10] M.J.G. Dunn, et al., Critical care in the emergency department: patient transfer, *Emerg. Med. J.* 24 (2007) 40–44.
- [11] J.M. Droog, et al., Inter-hospital transport of critically ill patients; expect surprises, *Crit. Care* 16 (2012) R26.
- [12] R.S. Campbell, et al., Battery duration of portable ventilators: effects of control variable, positive end-expiratory pressure, and inspired oxygen concentration, *Respir. Care* 47 (10) (2002) 1173.
- [13] T.C. Blakeman, et al., Battery performance of 4 intensive care ventilator models, *Respir. Care* 55 (3) (2010) 317–321.
- [14] R.E. Kerber, Electrical treatment of cardiac arrhythmias: defibrillation and cardioversion, *Ann. Emerg. Med.* 22 (2) (1993) 30–35.
- [15] R.E. Ideker, et al., Basic mechanisms of defibrillation, *J. Electrocardiol.* 23 (Suppl.) (1990) 36–38.
- [16] P.M. Zoll, A.J. Linenthal, Termination of refractory tachycardia by external countershock, *Circulation* 25 (1962) 596–603.

- [17] B. Lown, Defibrillation and cardioversion, *Cardiovasc. Res.* 55 (2002) 220–224.
- [18] M.S. Eisenberg, et al., Cardiac arrest and resuscitation: a tale of 29 cities, *Ann. Emerg. Med.* 19 (2) (1990) 179–186.
- [19] M.S. Eisenberg, The shocking state of external defibrillation, *Acad. Emerg. Med.* 2 (9) (1995) 761–762.
- [20] K.R. Stults, et al., Efficacy of an automated external defibrillator in the management of out-of-hospital cardiac arrest: validation of the diagnostic algorithm and initial clinical experience in a rural environment, *Circulation* 73 (4) (1986) 701–709.
- [21] R.O. Cummins, et al., Automatic external defibrillators used by emergency medical technicians. A controlled clinical trial, *JAMA* 257 (12) (1987) 1605–1610.
- [22] R.D. White, Maintenance of defibrillators in a state of readiness, *Ann. Emerg. Med.* 22 (2) (1993) 36–40.
- [23] E. Dyson, G.B. Smith, Common faults in resuscitation equipment—guidelines for checking equipment and drugs used in adult cardiopulmonary resuscitation, *Resuscitation* 55 (2002) 137–149.
- [24] E. Braunwald, Shattuck lecture—cardiovascular medicine at the turn of the millennium: triumphs, concerns, and opportunities, *N. Engl. J. Med.* 337 (19) (1997) 1360–1369.
- [25] D. Levy, et al., Long-term trends in the incident of and survival with heart failure, *N. Engl. J. Med.* 347 (18) (2002) 1397–1402.
- [26] J. Drazen, Heart failure—an epidemic of uncertain proportions, *N. Engl. J. Med.* 347 (18) (2002) 1442–1444.
- [27] P.A. McCullough, et al., Confirmation of a heart failure epidemic: findings from the resource utilization among congestive heart failure (REACH) study, *JACC* 39 (1) (2002) 60–69.
- [28] D.L. Joyce, L.D. Joyce, M. Loebe, *Mechanical Circulatory Support: Principles and Applications*, McGraw Hill, New York, 2012.
- [29] F. Gradel, et al., Successful hemodynamic results with a new u-shaped auxiliary ventricle, *ASAIO* 11 (1) (1965) 277–283.
- [30] D.J. Goldstein, C. Mehmet, E.A. Rose, Implantable left ventricular assist devices, *N. Engl. J. Med.* 339 (1998) 1522–1533.
- [31] O.H. Frazier, T.J. Myers, Left ventricular assist system as a bridge to myocardial recovery, *Ann. Thorac. Surg.* 68 (1999) 734–741.
- [32] K. Scherr, et al., Mechanical circulatory support as a bridge to cardiac transplantation: toward the 21st century, *Am. J. Crit. Care* 8 (5) (1999) 324–339.
- [33] E.A. Rose, et al., Long-term use of a left ventricular assist device for end-stage heart failure, *N. Engl. J. Med.* 345 (20) (2001) 1435–1443.
- [34] M. Haddad, et al., Ventricular assist devices as a bridge to cardiac transplantation: the Ottawa experience, *Artif. Organs* 28 (2) (2004) 136–141.
- [35] R.M. Lazar, et al., Neurological events during long-term mechanical circulatory support for heart failure: the randomized evaluation of mechanical assistance for the treatment of congestive heart failure (REMATCH) experience, *Circulation* 109 (2004) 2423–2427.
- [36] S.A. Hunt, Mechanical circulatory support: new data, old problems, *Circulation* 116 (2007) 461–462.
- [37] E.A. Rose, et al., The REMATCH trial: rational, design, and end points, *Ann. Thorac. Surg.* 67 (1999) 723–730.
- [38] M.S. Slaughter, et al., Advances heart failure treated with continuous-flow left ventricular assist device, *N. Engl. J. Med.* 361 (23) (2009) 2241–2251.
- [39] J.A. LaRose, et al., Design concepts and principle of operation of the heartware ventricular assist system, *ASAIO* 56 (4) (2010) 285–289.

- [40] A. Boyle, Current status of cardiac transplantation and mechanical circulatory support, *Curr. Heart Fail. Rep.* 6 (2009) 28–33.
- [41] J. Pepper, Update on mechanical circulatory support in heart failure, *Heart* 98 (2012) 663–669.
- [42] S. Lee, et al., Left ventricular assist devices: from the bench to the clinic, *Cardiology* 125 (2013) 1–12.
- [43] R.J. Gordon, et al., Prospective, multicenter study of ventricular assist device infections, *Circulation* 127 (2013) 691–702.
- [44] E.J. Molina, S.W. Boyce, Current status of left ventricular assist device technology, *Semin. Thorac. Cardiovasc. Surg.* 25 (1) (2013) 56–63.
- [45] J.G. Copeland, et al., Cardiac replacement with a total artificial heart as a bridge to transplantation, *N. Engl. J. Med.* 351 (9) (2004) 859–867.
- [46] H.T. Stelfox, et al., The “To Err is Human” report and the patient safety literature, *Qual. Saf. Health Care* 15 (2006) 174–178.
- [47] M. Capuano, S. Koritko, Risk-orientated maintenance, *Biomed. Instrum. Technol.* 30 (1) (1996) 25–37.
- [48] M.J. Cleland, et al., Ensuring equipment readiness: the role of checkout procedures, quality assurance programs, and preventive maintenance, *Prehosp. Emerg. Care* 2 (4) (1998) 336–337.
- [49] M.J. Cleland, et al., Relationship between battery capacity and the delivery of shocks in prehospital defibrillators, *Prehosp. Disaster Med.* 12 (2) (1997) 61–64.

# Rechargeable lithium batteries for aerospace applications

14

*W.Q. Walker*

National Aeronautics and Space Administration (NASA), Houston, TX, USA

## 14.1 Introduction

Energy storage systems developed for aerospace applications must meet extensive requirements to function with the widest array of storage and operating limits, need to exhibit the highest performance characteristics for their class, must maintain low mass and volume combinations, need to be safe and reliable, and must also be cost-effective. Energy storage systems are relied on in all areas of the aerospace industry as the only power available for these applications is maintained through limited fuel and primary–secondary energy storage and electrical systems. Battery chemical combinations are sought after to provide the highest performing energy density (W h/kg) to power density (W/kg) ratios, superior thermal performance, functionality in extreme environments, low mass and volume combinations, trustworthy control and monitoring systems, low maintenance requirements, and the highest reliability–safety margins available; for most aerospace applications, a failure in any one of these categories has the potential to induce a catastrophic event with the potential for the loss of life.

Lithium/lithium-ion (Li/Li-ion) batteries are an increasingly used battery type in aerospace as replacements to heavier and lesser-performing batteries such as nickel–cadmium (NiCd) and lead-acid (PbSO<sub>4</sub>) as they are uniquely qualified with superior performance characteristics, durability, and reliability through a wide range of operating and storage conditions, large life cycles, and low mass (Li is the lightest metal, with an atomic mass of 6.941) and volume combinations. A simple Ragone plot assessment from any source indicates that Li/Li-ion batteries offer more than double the energy and power densities of their NiCd and PbSO<sub>4</sub> counterparts. A few examples of popular lithium energy storage chemical compositions considered by modern aerospace are:

- Lithium cobalt oxide (LiCoO<sub>2</sub>),
- Lithium manganese oxide (LMO),
- Lithium sulfur (LiS),
- Lithium iron phosphate (LiFePO<sub>4</sub>),
- Lithium–air (Li–air).

These example Li/Li-ion batteries either currently maintain the general ability to meet industry requirements or exemplify strong promise to soon meet most requirements; only a few underlying concerns regarding safety and design maturity remain for most.

Even with room for improvement and maturity available, the chemical properties and current designs of these advanced energy storage devices enable them to power the largest of aircraft and the most complex of satellites in the most extreme of environments.

Primary aerospace applications of Li/Li-ion batteries are divided into three classifications: (1) commercial-grade and private aircraft main and auxiliary power supply; (2) military and defense vehicles, weapons, and satellites; and (3) space exploration vehicles, devices, and satellites. This chapter provides (i) an introduction to the use of Li/Li-ion batteries in these three aerospace classifications, (ii) a review of the primary applications for these energy storage devices, (iii) a discussion of recent aerospace-related Li/Li-ion battery failures, (iv) insight into potential future trends, and (v) sources for further information and advice. First, a discussion of the global aerospace market is provided through examination of some of the leading industrial grade Li/Li-ion battery developers and manufacturers and their respective products (Genzou Shimadzu Yuasa Li Power, Cell-Con, EnerSys, Quallion, and Eagle Picher Technologies). This discussion is followed by a provision of the drivers and barriers for the use of Li/Li-ion batteries considered by the aerospace industry.

### ***14.1.1 Global aerospace market***

The various classifications of Li/Li-ion batteries entertain a large multibillion United States dollar (USD) market in aerospace fields alone, consisting mainly of (a) commercial and private aircraft producers (e.g., Boeing, Gulfstream, and Cessna); (b) military and defense vehicle, weapons, and satellites developers [e.g., U.S. Air Force (USAF) and U.S. Navy (USN)]; and (c) government space exploration agencies [e.g., National Aeronautics and Space Administration (NASA), European Space Agency (ESA), Japanese Aerospace Exploration Agency (JAXA), Russian Federal Space Agency (RFSA), and the Canadian Space Agency (CSA)]. Frost & Sullivan, world-class providers of market research and growth strategies, report that just the Li-ion battery market alone in 2012 was \$11.7 billion USD globally (note that this estimation also includes Li-ion batteries for medical, consumer goods, and automobiles) [1]. Based on current and past market performance, Frost & Sullivan analysts predict that the total Li-ion battery market will double to \$22.5 billion USD by 2016 [1]. The growth of the lithium energy storage technology market (including both Li/Li-ion battery types) is exponential in all fields, including the aerospace sector, and as this energy technology rapidly matures it will quickly dominate the market for industrial-grade batteries.

### ***14.1.2 Primary manufacturers***

The developing market for lithium energy storage options in aerospace is competed by hundreds of manufacturers globally. Genzou Shimadzu (GS) Yuasa Lithium Power (GYLP) is an International Traffic in Arms Regulations (ITAR) compliant Japan-based corporation that develops advanced Li/Li-ion batteries for aerospace, industrial, military, and specialty markets [2]. Regarding aerospace, GYLP batteries provide power and storage for satellites, rockets, and aircraft around the globe and in space near-Earth-orbit (NEO). In 2017, GYLP batteries will be installed on the International Space Station (ISS) as part of updates to the orbital replacement units (ORUs) exterior to the

cabin in the vacuum of space (the ISS Li-ion battery ORU project is discussed in detail later in this chapter) [2]. GYLP is also the developer of the auxiliary power unit (APU) batteries for the Boeing 787-8 Dreamliner that received mass media attention in January 2013 when an APU Li-ion battery failed due to the damaged electrodes and caught fire. With respect to space exploration, GYLP reports energy systems relying on Li-ion cell power in 50 satellites that have accumulated more than 1,100,000 Watt-hours (W h) in orbit without failure (this is the equivalent of 37 million working cell hours). GYLP is considered the world leader for lithium energy storage classifications in space applications and reports a \$2.7 billion USD in total company sales for 2013 alone [2].

Based on Pennsylvania, Cell-Con is one of the leading battery designers and manufacturers in the United States for custom large-scale lithium battery systems (leading products include Li-ion varieties, Li-polymer, and LiFePO<sub>4</sub> compositions) and is also ITAR compliant [3]. Most Cell-Con customers are medical, military, or industrial. Overall, Cell-Con produces battery chargers, battery packs, custom chargers, and smart packs [3].

EnerSys is another leading manufacturer and provider of industrial batteries. EnerSys owns 15 companies globally that produce a variety of Li, Li-ion, and nickel (Ni) batteries for aerospace, military and defense, medical, automotive power, reserve power, space exploration, and specialty systems [4,5]. EnerSys owns Quallion, a leading US-operated battery developer based in Sylmar, California, which specializes in rechargeable Li/Li-ion battery technology. Quallion batteries are used in commercial airliners, military aircraft and weapons, the medical industry, and more. Quallion cells have provided 349,666 h of in-orbit operations time over the last 10 years [4-6]. Quallion's chemistry mix deals with Li-ion (LiCoO<sub>2</sub>, LiMnCo, and LiNiCoO), Li-polymer, Li-metal, and Li-air. Of notable mention, Quallion is the developer of the world's smallest Li-ion cell (a cylindrical 1.8 mA h cell), which is popular in the medical industry for use in various implant devices. Also, Quallion is considered the largest Li-ion cell manufacturer outside of Asia. Finally, Quallion is a developer of a Zero-Volt system of cells that "tolerate extended deep discharges with no impact on cycle life, capacity, or performance" [6].

EPT is another leading manufacturer in the lithium energy storage market for commercial airliners, military and defense vehicles, missiles, satellites, and for various medical applications [7]. Relevant battery systems produced by EPT are LiNiCoO and LiFePO<sub>4</sub> combined with a variety of lithium (Li), aluminum (Al), carbon (C), and graphite anodes [7]. Ten Li-ion batteries produced by EPT are currently in space NEO, and approximately 100 aircraft are equipped with backup stair actuator Li-ion batteries. Notable research by EPT delves into next-generation Li cells with high-low temperature and nonflammable electrolytes. In 2013, EPT exceeded two billion in-orbit Li-ion hours of operation without a failure [7].

#### **14.1.3 Drivers and barriers for use of Li/Li-ion batteries in aerospace**

Li/Li-ion batteries are attractive to the aerospace community because they are reliable, exhibit high energy (W h/kg) and power densities (W/kg), operate nominally in extreme environments (−40 to +60 °C in some cases), have long shelf lives, and exhibit a high number of life cycles when operated in nominal configurations. Of great

importance to the aerospace industry, lithium is the lightest of any known metal, which enables large reductions in mass associated with electrical and power management systems; Li batteries are generally one-half the mass of their NiCd and  $\text{PbSO}_4$  counterparts while offering double the performance [8]. Energy available to an aerospace system is either generated through limited fuel resources, stored in batteries, or first gathered through solar or mechanical means and then stored in batteries. Efficient energy storage is key to the longevity of flight for any aerospace system, and Li/Li-ion batteries provide the option to fly with safe and reliable systems for longer durations. Furthermore, aerospace environments range between  $-40$  and  $+200^\circ\text{C}$  at low to zero pressure external to the vehicle for high altitude and/or space traveling vehicles. These operating ranges are readily encompassed by the wide operating and storage limits of Li/Li-ion batteries with minimal need for complex, expensive, and cumbersome active thermal control systems.

Despite the numerous benefits associated with the use of Li/Li-ion batteries, these systems are not without faults—primarily in safety. The chemistry associated with this category of battery typically includes highly reactive electrode and electrolyte materials that are dangerous and/or explosive if not managed properly. Consider the catastrophic result if a Li-ion cell on an ORU installed exterior to the ISS experiences a system failure due to manufacturer defect that leads to a thermal runaway condition. Another barrier preventing the use of Li/Li-ion cells is associated with toxicity. Aside from the commonly discussed thermal concerns, the materials used for the electrodes and electrolytes of these batteries are extremely toxic (e.g., the organic electrolytes used in some Li/Li-ion batteries), which makes handling and materials processing hazardous if caution is not taken. These barriers and safety concerns repeatedly prevent the complete reliance on Li/Li-ion systems in aerospace due to the dangers and high costs that already exist in high altitude and NEO operations. Li/Li-ion battery safety problems can easily lead to disastrous events that would most certainly end with the loss of human life, and large safety risks must first be overcome before Li/Li-ion technologies can be fully incorporated into aerospace applications.

## 14.2 Primary aerospace applications

The primary aerospace classifications for Li/Li-ion batteries divide into (a) commercial-grade and private aircraft main and auxiliary power supply; (b) military and defense vehicles, weapons, and satellites; and (c) space exploration vehicles and satellites. Each classification is discussed in detail in this section.

### 14.2.1 *Commercial and private aircraft main and auxiliary power supply*

Rechargeable batteries are utilized by modern commercial and private aircraft to (a) provide power to a gas-turbine APU used to produce startup power to the engines (once the engines are running, power is provided through generators), (b) provide

power to the “main” power system that supplies power to the aircraft prior to starting the engines, and (c) provide backup power during flight in the event of an emergency; larger aircraft typically place the “main” power rechargeable battery toward the front of the pressurized cabin and the APU rechargeable battery in the mid-to-end section of the cabin nearest the engines [8]. Traditionally, heavy NiCd batteries are used (e.g., Boeing 777, 747, and MD-11) for auxiliary and main power supply, but replacement with Li/Li-ion battery technology (for Boeing, Li-ion) is under consideration.

French-based Airbus recently demonstrated a keen interest in incorporating Li/Li-ion technology into its aircraft, but has withdrawn its attention in light of the Boeing 787-8 Dreamliner incident in January 2013 (details are discussed in later sections of this chapter). In the private aircraft sector, both Cessna and Gulfstream still demonstrate interest in Li/Li-ion technology for the G650 and CJ4 aircraft, respectively, but as a result of the 787-8 incident have yet to directly incorporate the advanced batteries into their electrical systems [9]. However, despite the recent negative attention given to Li/Li-ion batteries, Embraer, another private aircraft company, continues its plans for using Li-ion cells for the Legacy 500 and 450 airliners that begin service between 2013 and 2014 [9]. For each of these commercial and private aircrafts, battery performance, reliability, and safety are key, which is why it is clear that Li/Li-ion batteries will soon dominate the industry once safety concerns are finally mitigated.

True Blue, a battery manufacturing company for private airliners, hopes to educate the public on the realities and benefits of Li/Li-ion batteries and to get their systems in the air despite all the negative media attention. True Blue has expressed the position that their 26.4–44.0 A h nanophosphate Li-ion battery systems for private airliners are significantly smaller and safer than the 787-8’s much larger 75 A h LiCoO<sub>2</sub> system [9]. In addition, True Blue boasts that all lessons learned from the 2013 787-8 event have been considered and implemented into the designs of their smaller battery systems [9].

#### 14.2.1.1 Boeing 787-8 dreamliner

Boeing is the world’s largest manufacturer of commercial and private aircrafts, space, and security systems, and has an overall 40 years of experience with airliner development. Boeing had an estimated 2013 revenue just under \$90 billion USD and is the most known for the following commercial, private, and military products: 737, 747, 767, 777, 787, F/A-18, CH-47 Chinook, and the 702 [10].

Boeing has invested an estimated \$32 billion USD since 2005 in the development of the 787-8 Dreamliner commercial airliner (displayed in Figure 14.1)—a vehicle that is the first and only one of its kind to boast the use of Li-ion battery technology for main and auxiliary power [8]. Boeing, in collaboration with GS Yuasa and Thales Alenia, is using Li-ion batteries (specifically the GS Yuasa LVP-10 and LVP-65) in the 787-8 Dreamliner for the aircraft’s electrical power conversion system (main power, APU startup power, and emergency backup power) [8]; GS Yuasa provides the batteries and Thales Alenia provides the system electronics and integration processes. The Li-ion batteries developed for the 787-8 systems charge from 0% to 90% in 75 min and utilize independent monitoring processes for system assurance



**Figure 14.1** Public access image taken by Dave Sizer of the Boeing 787-8 Dreamliner during its first flight on December 15, 2009.

and safety [8]. In general, the system is described directly by GS Yuasa with the following characteristics: “high energy density, excellent discharge characteristics, sealed structure, low self-discharge, and low maintenance” [2]. The specifications for the 787-8 batteries are the following: 75 A h nominal capacity, 29.6 total nominal voltage (3.7 V per cell), 20–32.2 operational voltage range (2.5–4.025 per cell), 28 kg total (2.72 kg per cell), and overall dimensions of  $27.7 \times 36.1 \times 21.6 \text{ cm}^3$  (individual cell dimensions of  $13.2 \times 5.1 \times 19.6 \text{ cm}^3$ ) [8]. The replacement of the traditional NiCd batteries enabled Boeing to exploit a lighter, smaller, and more powerful battery system, which enables a more efficient mass and volume-driven aerospace design.

#### 14.2.2 Military

EnerSys, one of the largest manufacturers, marketers, and distributors of industrial-grade primary and secondary batteries globally for over 100 years, discusses in a June 2014 investors presentation that the global market for aerospace and defense industrial-grade batteries alone was a \$1–2 billion USD market in 2012 [4,5]. Defense is considered the second primary classification for Li/Li-ion battery system use in aerospace largely because of their access to a nearly unlimited budget. Most military organizations operate with some type of aerospace application and are, therefore, becoming a major player in the growing Li/Li-ion battery market. Military reasons for selecting lithium batteries are the same as any other organization: superior performance characteristics, mass reduction, and efficiency.

Militaries and defense agencies and contractors are working with Li/Li-ion battery manufacturers to provide energy storage options for helicopters, aircraft (jets), unmanned vehicles (drones), surveillance and global positioning system (GPS) tracking satellites, and more. A highlight military and defense battery project is the General Electric Aviation \$6.5 million contract to develop a 28 V/270 V Lithium-ion system for Lockheed Martin’s F-35 Lightning II (see Figure 14.2) for the USAF; a 28 V system provides the APU start-up power while another 270 V system provides backup power for the “flight control surfaces” [11]. The F-35 Li-ion battery technology is also under consideration for the FA-18 and the T-45. The initial delivery of the F-35 battery systems



**Figure 14.2** Public access image displays the Lockheed Martin-developed F-35 Lightning II for the USAF during flight.

began in 2009 and models of the batteries can be seen on display at the Saft booth in the Paris Air Show [11]. Currently, the military works with Yardney Technical Products Incorporated for Li-ion battery outfitting of the B-2 Spirit Bomber (Northrop Grumman developed stealth attack vehicle, [Figure 14.3](#)) and the Global Hawk (Northrop Grumman developed unmanned surveillance aircraft, [Figure 14.4](#)) [11].

Military and defense contractors such as Northrop Grumman, Bell Helicopter, Sikorsky Helicopter, and Boeing are primary sources of information for technology development in this sector.



**Figure 14.3** Public access image displays the Northrup Grumman-developed B-2 Spirit Bomber during flight.



**Figure 14.4** Public access image displays the Northrup Grumman-developed Global Hawk during flight.

### 14.2.3 Space exploration applications

Energy storage and electrical systems have been used for energy storage in space vehicles and satellites since the inception of this industry; even the Wright brothers used startup electricity to start the engines of their aircraft [8]. Li/Li-ion cells are highly integrated in the space exploration market, an industry that is above all else driven by cost, efficiency, mass, and volume. Each year, numerous satellites and space vehicles are developed through government agencies such as NASA, ESA, CSA, JAXA, and RFSA and private companies such as Boeing, Orbital, SpaceX, Virgin Galactic, and Sierra Nevada. As with Earth-based aerospace applications, power and fuel are not readily available in space and are limited to what is brought from Earth and in what can be stored in rechargeable batteries—only at a much higher cost than with terrestrial applications. In addition, these vehicles and satellites orbit in and out of the Sun's view (or fly into deep space) where vacuum exists, and extreme thermal environments and radiation are constantly fluctuating (solar radiation, infrared flux, albedo, etc.). Therefore, the performance of Li/Li-ion batteries selected for space applications plays a direct role in the longevity and success of the mission.

#### 14.2.3.1 Satellites

Quallion develops large-scale satellite Li-ion battery materials through the Title III program awarded by the U.S. government in 2006, and as a result, cathode and anode materials manufacturing lines were established in the United States in 2013 [6]. Quallion battery systems for large-scale satellites maintain a long shelf life, Zero-Volt technology, SaFE-LYTE technology, and a primarily Lithium–polymer chemical makeup. Quallion Li-ion cells use calendar fade and self-discharge characteristics; these 15 A h cells have a 95% calendar life capacity after 500 days at room temperature (charged to 4.1 V each time they were placed in storage) [6]. The Zero-Volt technology allows the Quallion battery to remain for long storage periods in a discharged state

without a permanent capacity loss. Quallion's SaFE-LYTE technology enhances the battery's safety without degrading the electrochemical composition; SaFE-LYTE is a liquid halogen compound that is flame-retardant and immiscible to the electrolyte [6]. Though Quallion is not the only manufacturer of batteries utilized by satellites, they provide a great example of the advanced cells required to power satellite electrical systems.

#### 14.2.3.2 International space station

NASA, in collaboration with JAXA, works to utilize Li-ion battery technology for the ISS, shown in [Figure 14.5](#), where continuous manned presence in space over the last decade and groundbreaking research has been achieved. Li-ion batteries are in development for NASA by GS Yuasa, the developers of the Boeing 787-8 Dreamliner Li-ion batteries, to replace some of the nickel–hydrogen ( $\text{NiH}_2$ ) batteries that are part of the ORU systems; the project is conducted as a \$208.8 million USD contract through Boeing to deliver 27 Li-ion batteries in 2017 [10]. The ISS requires secondary batteries for constant energy storage; charging processes collect energy from the Sun through solar panels during insulation periods of orbit and discharging provides energy during out of sun periods of orbit [2]. The control systems for the batteries are developed by Rocketdyne, a California-based company [2]. This historic milestone of Li-ion battery utilization is only possible due to the collaboration and teamwork of NASA, Boeing, GS Yuasa, Rocketdyne, the ISS partners, and more.

#### 14.2.3.3 SpaceX dragon and NASA orion

Not many details are available for private sector space vehicle designs due to their proprietary nature, but it is well known that Elon Musk's SpaceX Dragon unmanned cargo carrying vehicle (see [Figure 14.6](#)) is integrated with Panasonic-developed Li-ion battery



**Figure 14.5** Public access image displays the completed ISS, which was finished in the late 2000s and will soon receive replacement Li-ion batteries in 2017 as part of the ORU systems currently utilizing nickel–hydrogen ( $\text{NiH}_2$ ) batteries.

**Figure 14.6** Public access image displays of Elon Musk's SpaceX Dragon unmanned cargo-carrying space flight vehicle that is launched from a Falcon rocket.



technology as part of its electrical system [12]. Though SpaceX does not provide much insight into the specifics regarding their designs, it is known that the Li-ion batteries meet NASA's "two fault tolerant" redundancy requirements for space-quality batteries [12]. It is also known that the SpaceX Dragon uses three battery packs that are similar to those used in Musk's Tesla (fully electric automobile). The cells are small in size (cylindrical design 1.8 cm in diameter and 6.5 cm in height) and controlled through SpaceX-developed circuitry [12]. Musk is noted for commenting that he believes the Boeing 787-8 Dreamliner batteries are experiencing problems due to their large size and that SpaceX/Tesla would be more than willing to assist in resolving the issue.

The Orion deep space exploration vehicle in development by NASA and Lockheed Martin is a similar classification of vehicle to the SpaceX Dragon. The capsule-type spacecraft, slated for its first test flight in December 2014, will take humans out of NEO, beyond the Moon, to asteroids, and 1 day to Mars. Orion makes use of x32 38 A h NCP25-5 Li-ion prismatic cells built by Yardney Technical Products configured for a nominal 120 V system [13]. The batteries will collect and store energy gained from Orion's solar panels. The Orion spacecraft is displayed in Figure 14.7.

#### 14.2.3.4 Unique solutions for space applications

Because of the complexities associated with operating in harsh space environments, unique solutions are often employed to ensure the success of a mission. Some researchers focus on advanced materials and chemical compositions, while others focus on the analysis techniques used during the design of a battery system.

High energy density batteries are desirable for space exploration, and a current solution is sought in sulfur compound electrodes. A recent study of liquid electrolyte lithium–sulfur (Li–S) combinations displayed that Li–S batteries have a 3–5 times higher theoretical energy density than the most advanced Li/Li-ion batteries used today [14]. The primary issues researchers work to overcome with Li–S batteries are short cycle



**Figure 14.7** Public access concept art image by NASA of the Orion vehicle in space.

life, low cycling efficiency, safety concerns, and high self-discharge rates [14]. The paradox is that the dissolution of the Li polysulfide is what enables this battery to be so powerful; however, it is this same dissolution that is the reason for the issues listed previously [14]. However, the excitement is that if these obstacles are overcome the scale of the performance of Li–S batteries will dwarf the modern Li/Li-ion cells today.

Effective thermal design is of the utmost importance for any space-bound Li/Li-ion battery, which is subject to the harshest thermal environments known to man. Some researchers seek to improve the thermal design of Li/Li-ion batteries by developing detailed thermoelectrochemical models of battery cells in specialized software (C&R Technology's Thermal Desktop SINDA-FLUINT) for orbital heat transfer analysis [15]. Techniques developed by Walker and Ardebili display that this type of software can accurately incorporate the highly complex heat generation rate equations of Li-ion batteries during charge–discharge processes into the FORTRAN code of Thermal Desktop for combination simulations of orbital heating loads and battery operating heat generation [15]. Incorporation of these types of analysis techniques in the battery development phase can lead to a more thermally stable system for an NEO-bound battery.

### 14.3 Recent aerospace-related lithium/lithium-ion (Li/Li-ion) battery failures

Lithium batteries, or more specifically Li-ion batteries, receive large amounts of technical and media attention with respect to safety; the primary example being the Boeing 787-8 APU battery failure that occurred in January 2013. As a result, not only are the large-scale Li/Li-ion systems under fire, but also even the rules associated with bringing devices containing small Li/Li-ion batteries (e.g., laptops) on commercial jetliners are also undergoing evaluation.

### 14.3.1 Boeing 787-8 dreamliner APU failure

The following facts are as reported by the National Transportation Safety Board (NTSB) in an incident report detailing the events of and the response to a failed APU LIB on a Boeing 787-8 Dreamliner in January 2013.

Around 10:20 a.m. Eastern Standard Time (EST) on January 7, 2013, on a Japan Airlines Boeing 787-8 (JA829J) parked at a gate at General Edward Lawrence Logan International Airport (BOS) in Boston, Massachusetts, maintenance personnel noticed that the APU providing power for the vehicle at the time automatically shut down; the APU LIB dropped from a full charge of 32–28 V, suddenly, 7 s before shutdown [16].

Following the system shutdown, the aft end electronic equipment bay was opened, where heavy smoke and fire coming from the front of the APU battery case was observed. Once on scene, firefighters used thermal imaging equipment to analyze the situation as the smoke intensity prevented any visibility [16]. A hot spot was observed at which point a “burst of Halotron” (a handheld portable fire extinguishing chemical) was used for 10–20 s. Following this activity, fans were placed to blow smoke out of the cabin for ventilation [16].

The battery case was then visible but still glowing, giving off the indication that it could be rekindling. This led to the incident commanding officer making the decision to remove the batteries [16]. Firefighters reported that the removal was difficult due to the damage of the unit, but finally the system was successfully removed at 11:57 a.m. EST and reported as controlled by 12:19 p.m. EST. The overall damage remained within 51 cm of the battery installation location and the primary structure of the aircraft had not been damaged. In all, this was a 1 h and 40 min event from the point of initial notification [16].

This GS YUASA-developed APU Li-ion battery had x8 3.7 V Li-ion cells ( $\text{LiCoO}_2$  chemical makeup inside a flammable electrolytic liquid) connected in series. The situation resulted in the FAA grounding of the 787-8 Dreamliner, apparently the first grounding of an aircraft since 1979 [16]. The aircraft in question had only logged 169 flight hours and 22 flight cycles at the time of the incident. Currently, it is thought that the cause of the incident was a damaged electrode, which triggered a short, which resulted in a thermal runaway situation; the battery is reported to have reached a temperature upwards of 260°C [16].

### 14.3.2 Other Li/Li-ion battery failures

The use of Li/Li-ion batteries in aerospace applications is still fairly new, and there aren't many other incidents that are the same magnitude of the Boeing Dreamliner 787-8 incident; however, there are numerous other lithium battery failures that are of high relevance to the aerospace community with respect to safety and reliability. Several cases each year occur where explosions or fires occur with automotive vehicles and portable devices utilizing Li/Li-ion technology. In 2013, Elon Musk's patented fully electric Tesla automobile hit metal debris in the road, which caused a fire that resulted in an explosion because of damage sustained by the battery system;

this was the third Tesla to catch fire [17]. Though this is not directly an aerospace incident, the same type of battery failure could occur in an aircraft.

Another recent incident occurred when a United Parcel Service (UPS) Boeing 747-44AF transporting thousands of lithium battery cells crashed in the United Arab Emirates (UAE) on September 3, 2010, because fire and smoke filled the cockpit [18]; a 322-page report by the UAE aviation authorities stated that the fire disabled the oxygen system in the smoke-filled cockpit within 3 min of the start of the incident. Both pilots were killed when the Boeing 747 crashed [18]. This is a prime example that casts light onto the fact that these types of batteries, though highly efficient and superior in performance, are made of highly flammable and unstable materials. The magnitude of effect of a Li/Li-ion battery failure of this type yields catastrophic impact. Therefore, the safety and control measures of any type of Li/Li-ion battery is of the utmost importance to the aerospace industry.

### **14.3.3 Trends for safer batteries**

Discussion on Li/Li-ion battery failures presents several questions:

- How are researchers maturing the design of these rechargeable systems?
- How can researchers design safer Li/Li-ion batteries?
- How can thermal runaway be avoided without restricting the performance of the system?

Currently, techniques are incorporated into modern battery designs to accurately monitor the status of the large-scale batteries (like the Boeing APU batteries) to trigger automatic shutdowns if necessary. Some batteries use a three-step approach for safety and thermal control: (1) high conductivity encasement to serve as a heat spreader; (2) incorporation of charge interruption devices (CIDS) that trigger shutdowns if the pressure inside the battery rises too high, which indicates a possibility for thermal runaway; and (3) venting, which allows gaseous buildup through charge–discharge cycles to leave the system safely. Advanced chemical compositions that experience less problems are explored (e.g., Li–S and Li–air batteries). A primary example of a battery that mitigates thermal propagation concerns is the LiFePO<sub>4</sub> battery that will not go into thermal runaway. Other examples of highly developed options incorporate polymer or ceramic-solid electrolytes, which are safer than standard organic electrolytes.

## **14.4 Future trends**

Li/Li-ion battery technology utilization increases in use in all forms of industry, including aerospace, which results in an exponentially growing world market. Boeing's success with the use of Li-ion technology in the 787-8 Dreamliner aircraft APU systems, regardless of the single failure experienced in 2013, and the interest of major companies such as Cessna and Gulfstream indicates that as lithium battery technology matures, the use in private and commercial aircrafts will increase. Clearly, the technology still needs to reach a level of maturity before it's completely implemented into all new aircraft, but

it is expected that as the aerospace community seeks lighter and smaller designs, Li/Li-ion batteries will continually step up as the answer to the call.

Military aircraft and unmanned vehicles are not excluded from consideration for the future of Li/Li-ion battery technology. Obviously, a market for these types of vehicles already exists and the framework and foundation for the use of Li/Li-ion batteries here is already laid (e.g., F-35, B-2, and Global Hawk). It's only a matter of time until rechargeable Li/Li-ion batteries are used in the majority of military aircraft. In addition to military unmanned vehicle applications, consider the actions and investments in this technology of powerful private companies like Amazon who are attempting to utilize unmanned aircraft for major-city product delivery. These unmanned drones, where weight and efficiency drive productivity, require the benefits of light weight and reliable Li/Li-ion batteries.

Li/Li-ion battery technology utilization increases yearly in the space industry. It's clear why these rechargeable systems are prime candidates for the government-managed space industry, but what also needs consideration is the massive growth of the private space sector through the 2000s. Historically, space exploration was controlled by government agencies such as NASA, ESA, RFSA, and JAXA. The permanent establishment of companies such as Boeing, SpaceX, Orbital, Virgin Galactic, and Sierra Nevada indicate that soon the private sector will dominate NEO space transportation. As the private sector grows, the costs of NEO space travel decreases, and as more vehicles and satellites are developed, the need for energy storage and power access will increase. Li/Li-ion technology will have matured by this point and will likely continue to be selected to provide energy storage. Whether through advanced compounds like the previously discussed Li-S battery or through increased safety and maturity for currently used compounds, Li/Li-ion systems will provide the solution to the needs of the space sector of the aerospace industry.

## 14.5 Sources of further information

The primary source of information for the latest news on aerospace Li/Li-ion batteries is found through accessing information and databases available on the world leaders in battery production: for example, GS YUASA, EnerSys, Cell-Con, Quallion, Eagle Picher, and others. The authors of this work can provide other useful information regarding questions about Li/Li-ion batteries. Also, the latest trends and research for Li/Li-ion batteries are discussed at various prominent international conferences and congresses and published in the respective proceedings (e.g., Lithium Battery Power Conference hosted by Knowledge Foundation, American Chemical Society Congress, International Conference on Lithium Batteries, etc.).

## References

[1] C. Carella, Frost and Sullivan: Global Lithium-Ion Market to Double Despite Recent Issues. Available at: [www.frost.com](http://www.frost.com), 2012 (accessed 01.06.14).

- [2] Genzou Shimadzu Yuasa, GS Yuasa Lithium Power. Available at: [www.gsyuasa-lp.com](http://www.gsyuasa-lp.com), 2013 (accessed 01.07.14).
- [3] Cell-Con, Cell-Con Battery and Charger Solutions. Available at: [www.cell-con.com](http://www.cell-con.com), 2014 (accessed 02.07.14).
- [4] EnerSys, EnerSys. Available at: [www.enersys.com](http://www.enersys.com), 2014 (accessed 10.06.14).
- [5] EnerSys, EnerSys Power/Full Solutions Investors Presentation, s.l. EnerSys, 2014.
- [6] Quallion, Quallion Technology: Batteries. Available at: <http://www.quallion.com>, 2014 (accessed 21.06.14).
- [7] Eagle Picher, Eagle Picher LLC. Available at: <http://www.eaglepicher.com>, 2014 (accessed 02.07.14).
- [8] Boeing, Boeing 787 Dreamliner Provides New Solutions for Airlines Passengers. Available at: [www.boeing.com](http://www.boeing.com), 2014 (accessed 30.06.14).
- [9] G. Norris, True Blue Launches Li-Ion GA Batteries. Available at: <http://aviationweek.com/business-aviation/true-blue-launches-lithium-ion-ga-batteries>, 2013 (accessed 04.09.14).
- [10] Boeing, Boeing in Brief. Available at: [www.boeing.com](http://www.boeing.com), 2013 (accessed 01.06.14).
- [11] J. Ledger, Saft Li-Ion Batteries Power F-35 Lighting II Joint Strike Fighter Through LRIP Programme. Available at: <http://www.saftbatteries.com>, 2009 (accessed 31.06.14).
- [12] SpaceX, SpaceX Dragon. Available at: <http://www.spacex.com>, 2014 (accessed 09.07.14).
- [13] **J. Walker, et al., Development of 120V batteries for the orion multi-purpose crew vehicle**, in: NASA Aerospace Battery Workshop, Huntsville, 2011.
- [14] **S. Zhang**, Liquid electrolyte lithium/sulfur battery: fundamental chemistry, problems, and solutions, *J. Power Sources* 231 (2013) 153–162.
- [15] **W. Walker, H. Ardebili**, Thermo-electrochemical analysis of lithium ion batteries for space applications using Thermal Desktop, *J. Power Sources* 269 (2014) 486–497.
- [16] **National Transportation Safety Board**, Interim Factural Report DCA13IA047, NTSB, Washington, 2014.
- [17] P. Valdes-Dapena, Third Tesla Model S Catches Fire after Crash. Available at: <http://money.cnn.com/2013/11/07/autos/tesla-fire/>, 2013 (accessed 05.09.14).
- [18] United Arab Emirates General Civil Aviation Authority, Boeing 747-44F report, s.l. GCAA, 2010.

# Index

*Note:* Page numbers followed by *f* indicate figures and *t* indicate tables.

## A

*Ab initio*-based theoretical modeling, 246, 255–256, 257  
Acoustic emission (AE), 203–204, 203*f*, 204*f*  
Activation polarization, 30  
Additives, 80–83, 81*f*, 81*t*, 87, 89*t*, 94–95, 94*t*  
Aerospace applications  
    battery failure, 380–381  
    future technology, 381–382  
    global battery market, 370  
    manufacturers, 370–371  
    operating/storage capacity, 371–372  
    power supply, 372–374  
    SaFE-LYTE technology, 376–377  
    space exploration applications, 376–379  
    SpaceX Dragon, 377–378, 378*f*  
    thermal design, 379  
    toxicity issues, 372  
Aging degradation  
    battery behavior, 268–271  
    calendar life, 264, 265*f*  
    capacity (*see* Capacity degradation)  
    HPPC, 264  
    model parameters (*see* FreedomCar  
        battery model)  
Air cathodes  
    battery test system, 42–44, 43*f*  
    carbon, 59–60, 61*f*, 62*f*, 62*t*, 65  
    catalysts for, 42–58, 46*t*, 52*f*, 62*t*  
    DACAPO-2.7 code, 55–56  
    DFT, 55–56  
    electrical efficiency, 64  
    material aspects, 64  
    MC simulations, 56–57  
    metal oxides, 61–63  
    micro–macro homogeneous model, 54–55  
    noncarbon supporting materials, 62*t*, 63–64, 63*f*

ORR and OER, 48–51, 53–54  
porous electrode, 65  
R&D for, 58  
solid matrix phases, 54–55  
spectroscopic techniques, 44  
three-electrode half-cell, 42–44, 43*f*  
Alkyl phosphates, 82  
Alkyl phosphonates, 82  
Aluminum bag, 184–185  
Aqueous electrolyte, 6*f*, 9–10  
Asset management program, 362–363

## B

Bader charge values, 248, 248*t*, 249, 252*t*  
Battery management program, 363–364  
Battery management system (BMS), 281  
Battery state estimation  
    SOC, 282–286, 283*f*, 284*f*, 285*f*  
    SOH, 287–289, 288*f*, 289*f*  
    SOP, 286–287, 288*f*  
Bifunctional catalysts, 48–51, 50*f*  
Biomedical engineering (BME)  
    asset management, 362–363  
    battery capacity, 363–364  
    Cadex battery analyzer, 363–364, 363*f*  
    infusion pump hazards, 364  
Biot number, 291  
Biventricular assist devices (BIVADs), 360–361  
Blends, 87, 89*t*  
Boeing 787-8 Dreamliner aircraft company, 373–374, 374*f*, 380  
Born–Oppenheimer (BO) approximation, 234–235  
Bromine/polysulfide RFB, 329–330  
Brunauer–Emmett–Teller (BET) surface area, 169–171  
B-2 Spirit Bomber company, 374–375, 375*f*, 376*f*

Bulk reaction mechanisms  
  acoustic emission (AE), 203–204,  
    203*f*, 204*f*  
  Mössbauer spectroscopy, 195, 196*f*  
  neutron diffraction, 188–195, 191*f*,  
    193*f*, 194*f*  
  NMR, 200–203, 201*f*, 202*f*  
  schematic of, 188, 188*f*  
  X-ray absorption spectroscopy, 196–198,  
    197*f*  
  X-ray diffraction, 188–195, 190*f*  
  X-ray tomography microscopy,  
    198–199, 199*f*

**C**

Cadex battery analyzer, 363–364, 363*f*  
CAES. *See* Compressed air energy storage (CAES)  
Capacity degradation  
  battery type, 267–268  
  capacity test, 264  
  SEI growth, 266–267  
  *vs.* storage time, 265–266, 266*f*, 267*f*  
Carbon  
  air cathodes, 59–60, 61*f*, 62*f*  
  material, 8  
Carbon nanofibers (CNFs), 122,  
  134–135  
Cardiopulmonary bypass machine (CPB),  
  358–359  
Catalysts, 42–58, 46*t*, 52*f*, 62*t*  
Cathode active material, 10  
Cathode material selection, 26–27, 27*f*  
CCCV. *See* Constant current-constant voltage (CCCV)  
Cell-Con company, 371  
Cell equalization, 289–290  
Ceramic solid-state electrolyte, 133  
Charge and discharge curves, 34–35, 34*f*  
Circulatory assist devices  
  artificial ventricle, 358–359  
  BIVADs, 360–361  
  CPB machine, 358–359  
  lithium-ion technology, 360, 362*f*  
  LVAD therapy, 360, 360*f*, 361*f*  
  REMATCH trial, 359  
  total artificial heart, 360–361, 362*f*  
  ventricular assist device, 358–359

Coffee bag design  
  definition, 184–185  
  *in situ/operando* electrochemical measurements, 186  
Mössbauer experiments, 195  
neutron imaging, 217, 218*f*  
NMR, 200, 201*f*  
schematic diagram, 185*f*  
UV/Vis spectroscopy, 221

Composite gel polymer electrolytes (CGPEs), 132–133

Composite polymer electrolyte, 132–133

Compressed air energy storage (CAES),  
  322–323, 322*f*, 342–344

COMSOL software, 54–55

Configuration interaction (CI) method,  
  235–236

Constant current-constant voltage (CCCV),  
  287–289

Costing, 6–8, 12

Coulomb counting, 282–283

Coupled cluster (CC) method, 235–236

CPB. *See* Cardiopulmonary bypass machine (CPB)

Cu<sub>3</sub>P electrode material, 200–203, 202*f*

Cyclic carbonates, 74–75

Cyclic voltammetry (CV) test, 33, 33*f*

**D**

Density functional theory (DFT)  
  air cathodes, 55–56  
  BO approximation, 234–235  
  GGA, 238, 239  
  HF method, 235–236  
  HK theorem, 236  
  KS equations, 236–237  
  LDA, 237  
  Li<sub>2</sub>O<sub>2</sub>/graphene interfaces, 255–256  
  Li/Sn surfaces, 251–255  
  many-body problem, 234  
  PBE approximation, 238, 239  
  Si/Li surfaces, 239–251

Diethylene glycol dibutyl ether (DEGDBE), 128

Differential electrochemical mass spectrometry (DEMS), 214–217,  
  215*f*, 216*f*

Differential electrochemical mass spectroscopy (DEMS), 159  
1,2-Dimethoxyethane (DME), 128, 129, 131  
1,3-Dioxolane (DOL), 128–129, 130  
DMMEMP, 82  
DMMP, 82  
Doping and surface coating, 25–26  
Double-phase boundaries (DPBs), 167  
Dry polymer electrolytes  
  additives, 94–95, 94*f*  
  conductivity, 94–95, 94*f*  
  polymeric host, 93, 94–95  
  salts, 93

**E**

Eagle Picher Technologies (EPT), 371  
EKF SOC estimator, 290  
Electric double-layer (EDL), 338–339  
Electricity, 303, 315–316  
Electric vehicles (EVs), 303, 339–340  
Electroactive materials, 191–193, 192*f*  
Electrochemical analysis  
  anodes, SEI, 162–163, 163*f*  
  assessment system, 176  
  bulk reaction mechanisms (*see* Bulk reaction mechanisms)  
  carbon surface, 171–172, 172*f*  
  cathodes (*see* Electrolytic manganese dioxide (EMD))  
  decomposition, 161–162, 162*f*  
  efficiency utilization, 174–176  
  electrolyte distribution, 173–174, 173*f*  
  energy density, 149, 150*f*  
  ex situ measurement, 184  
  freezing temperature, 166–167, 167*f*  
  in situ cell designs, 184–188  
  neutron tomographic imaging, 174–176, 175*f*  
  nonaqueous electrolyte (*see* Oxygen evolution reaction (OER); Oxygen reduction reaction (ORR))  
  operando measurements, 184  
  optical characterizations (*see* Optical characterizations)  
  reaction zone, 174–176  
  specific energy, 149–151, 150*f*  
  surface passivation, 167–171, 168*f*, 170*f*  
  surface properties of electrodes (*see* Surface characterizations)

Electrochemical impedance spectroscopy (EIS)  
  charge transfer, 268  
  electroactive surface area, 270–271  
  metal connectors, 268  
  Nyquist plot, 268–270, 268*f*, 269*f*, 270*f*  
  ohmic resistance, 268–270  
  storage temperature, 271

Electrochemical stability window (ESW), 86

Electrochemical tests, 333–335, 334*f*

Electrolyte additives, 133–134

Electrolytic manganese dioxide (EMD)  
  electrode performance, 163–164  
  graphene sheets, 164–166, 165*f*  
  hollow core microfibers, 164–166, 166*f*  
  novel 3-D electrode structures, 164–166, 164*f*, 165*f*

Electron–electron interaction energy, 236, 237

Electronic charge density, 248–249, 248*t*, 249*f*

Embraer aircraft company, 373

:Energy density trend, 3–4, 3*f*

Energy storage  
  CAES, 322–323, 322*f*  
  electrochemical batteries (*see* Lead-based batteries (LBB))  
  flywheel energy storage, 323–325, 323*f*, 324*f*  
  PSH systems, 320–322, 320*f*, 321*t*

::EnerSys company, 371, 374

Environmental impacts, 304–305

Ethylene carbonate (EC), 246, 247*f*, 248–251, 248*t*, 249*f*, 250*f*, 257

Exchange-correlation energy, 237, 238, 239

**F**

F-35 Lighting II, 374–375, 375*f*

Flow battery, 325–326, 325*f*, 327–330, 342–344

Fluids, 293–295, 293*t*, 294*f*

Fluorinated carbonates, 75–76

Fluorinated esters, 83

Flywheel energy storage, 323–325, 323*f*, 324*f*

FreedomCar battery model  
  calendar life, 271*f*, 275  
  first order model, 271, 271*f*

FreedomCar battery model (*Continued*)  
 HPPC test, 272–273, 272*f*  
 internal resistance *vs.* time, 272–273, 272*f*,  
 273*f*, 274*f*  
 lithium cobalt oxide, 274  
 lithium-ion loss, 274  
 MAS-NMR technique, 274  
 performance optimization, 275  
 SoC level, 272*f*, 273*f*, 274*f*, 275  
 storage temperature, 275–277, 276*f*  
 French-based Airbus, 373  
 Functionalized graphene-sulfur  
 nanocomposite (FGSS), 123

## G

Galvanostatic intermittent titration technique  
 (GITT), 35–37, 35*f*, 36*f*, 159  
 Gel polymer electrolytes, 132  
 strong gel electrolytes, 91–92  
 weak gel electrolytes, 92  
 Generalized gradient approximation  
 (GGA), 238  
 :Genzou Shimadzu (GS) Yuasa Lithium  
 Power (GYLP) batteries, 370–371  
 Graphite-based (LiC<sub>6</sub>) negative electrode,  
 330–331, 331*f*  
 Grid storage, LiBs, 336–338, 337*t*

## H

Hartree-Fock (HF) method, 235–236  
 Heart failure (HF)  
 diastolic dysfunction, 357–358  
 mechanical circulatory support  
 (*see* Circulatory assist devices)  
 stages of, 358, 358*t*  
 systolic dysfunction, 357–358  
 transplantation, 358, 359  
 HeartMate II LVAD system, 360, 360*f*, 361*f*  
 HESS. *See* Hybrid energy storage system  
 (HESS)  
 HEV. *See* Hybrid electrical vehicles (HEV)  
 High-Tc superconductors, 342–344  
 Hohenberg and Kohn (HK) theorem, 236  
 Hybrid electrical vehicles (HEV), 289–290  
 Hybrid energy storage system (HESS),  
 297–298  
 Hybrid pulse power characterization  
 (HPPC), 264, 272–273, 272*f*

Hydrofluoroethers (HFEs), 82  
 Hydro-Québec (HQ) smart grid project,  
 341–342, 342*f*

## I

International Space Station (ISS), 377, 377*f*  
 Ionically conducting membranes.  
*See* Polymer electrolytes  
 Ionic liquid electrolytes  
 blends, 87, 89*t*  
 cathodic and anodic potential values,  
 86, 87*t*  
 chemical structure, 83–84, 84*f*  
 ionic liquid–lithium salt electrolyte  
 mixtures, 84–86, 86*t*, 87*t*, 88*t*  
 ionic liquids (ILs), 83–84, 83*f*, 84*f*, 85*t*  
 transport properties, 87, 89*t*  
*vs.* organic electrolyte, 83*f*  
 weight loss, 88*t*  
 Ionic liquid–lithium salt electrolyte mixtures,  
 84–86, 86*t*, 87*t*, 88*t*

## K

Kapton foil, 184–185  
 Kapton window, 186  
 Kohn and Sham (KS) equations, 236–237

## L

Layered oxide materials, 22–23, 22*f*, 23*t*  
 LBB. *See* Lead-based batteries (LBB)  
 LCA. *See* Life cycle assessment (LCA)  
 LCIA. *See* Life cycle impact assessment  
 (LCIA)  
 Lead-based batteries (LBB)  
 flow battery, 325–326, 325*f*, 327–330  
 fuel cell, 325–326, 325*f*, 330  
 nickel-based batteries, 327  
 performance characteristics, 325–326  
 sodium–nickel–chloride battery, 326–327  
 sodium–sulfur battery, 325–327, 325*f*  
 LFP/LTO, 331–333, 332*f*, 333*f*  
 Li-air batteries, 255–256, 256*f*  
 LiBOB, 79–80, 80*t*  
 ::LiCoO<sub>2</sub> (LCO) positive electrode, 22–23,  
 22*f*, 330–331, 331*f*  
 LiDFOB salt, 80  
 Life cycle assessment (LCA)  
 Belgian electricity, 308, 309*t*

components, 308, 308*t*  
definition, 304  
environmental performance, 307  
inputs and outputs, 308, 309*t*  
system boundaries, 307–308, 307*f*

Life cycle impact assessment (LCIA)  
characterization, 309  
classification, 309  
climate change, 311–312, 311*f*  
electricity generation, 315–316, 316*f*  
end point impact, 309–310  
human toxicity, 312, 313*f*  
metal depletion, 314–315, 315*f*  
midpoint impact, 309–310  
particulate matter formation, 313–314,  
314*f*  
ReCiPe method, 310, 310*f*

LiFePO<sub>4</sub>, 24, 25*f*

Liquid plasticizers, 94

Lithium depletion, 305–307, 306*f*

Lithium intercalation mechanism  
activation polarization, 30  
charge and discharge curves, 34–35, 34*f*  
chemical potential, 27–28  
cyclic voltammetry (CV) test, 33, 33*f*  
free energy curves, 28–29, 28*f*  
galvanostatic intermittent titration (GITT),  
35–37, 35*f*, 36*f*  
lithium concentration profile, 29, 30*f*  
phase transformation, 31–32  
potentiostatic intermittent titration (PITT),  
35–37, 35*f*, 36*f*  
shrink-core model, 29, 29*f*

Lithium iron phosphate (LFP) battery, 311,  
312, 313, 314–315

Lithium manganese oxide (LMO), 311, 312,  
313, 314

Lithium resource availability, 304–305

Lithium-sulfur (Li-S) batteries  
battery design, 139  
binder-free cathode, 134–135  
carbon paper interlayer, 135–136, 136*f*  
electrolyte additives, 133–134  
ionic liquid electrolytes, 130–131  
lithium anode, 121  
lithium metal-free anodes, 136–137  
lithium polysulfides, redox shuttle of,  
119, 120*f*  
polymer binder, 125–126

polymer electrolytes, 131–133  
PS catholyte, 137–138  
S-C composites, 122–123  
self-discharge, 121  
solvent electrolytes, 128–130  
sulfur cathode, 117, 120, 138  
sulfur-graphene composite, 123  
sulfur-polymer composites, 123–125  
voltage characteristics, 118–119, 118*f*  
water-based binders, 126

Local density approximation (LDA), 237

Lockheed Martin F-35 Lighting II,  
374–375, 375*f*

**M**

Magic angle spinning (MAS), 274

Manganese-based nanocrystalline spinels, 49

Manganese oxides, 45–47, 48

Many-body Schrödinger equation, 234

Market position, 3–4

Material availability, 4–5

Mesocellular carbon foam (MCF-C),  
169–171

Metal catalysts, 44, 45*f*

Metal depletion (MD), 314–315, 315*f*

Metal-insulator-metal (MIM) model,  
167–169

Metal oxides  
air cathodes, 61–63  
cathode materials, 21–27

Micro–macro homogeneous model, 54–55

Military applications, 374–375

Model-based closed loop, SOC, 285–286,  
285*f*

Monte Carlo (MC) simulations, 56–57

Mössbauer spectroscopy, 195, 196*f*

Multiple redox reactions, 117

Multiwalled carbon nanotubes (MWNTs),  
122–124, 125

**N**

NASA orion, 377–378

Neutron diffraction, 188–195

Nickel-based batteries, 327

Nitriles, 78

Nonaqueous electrolyte, 8, 9

Novak’s group, 191

Nuclear magnetic resonance (NMR)  
spectroscopy, 200–203, 201*f*, 202*f*, 274

**O**

OCV. *See* Open circuit voltage (OCV)  
 OER. *See* Oxygen evolution reaction (OER)  
 :Olivine oxide materials, 24, 25*f*  
 Open circuit voltage (OCV), 26, 35–37, 284, 284*f*  
 Optical characterizations  
   AFM, 222–224, 222*f*, 223*f*  
   colorimetry, 218–219, 220*f*  
   electrochemical analysis, 217*f*  
   neutron imaging, 217–218, 218*f*, 219*f*  
   UV/Visible spectroscopy, 220–221, 221*f*  
 Organic electrolytes, 126–134  
 Organic liquid electrolytes  
   additives, 80–83, 81*f*, 81*t*  
   electrochemical stability, 75, 78*f*  
   ionic conductivity, 75, 77*t*  
   physicochemical properties, 74–75, 74*t*, 77*t*  
   salts, 79–80, 79*f*, 80*t*  
   standard solvent (*see* Solvents)  
 Organic solvents, 73–75  
 Orion space exploration, 378, 379*f*  
 ORR. *See* Oxygen reduction reaction (ORR)  
 Oxide catalysts, 45–48, 46*t*, 47*f*  
 Oxide electrolytes, 95  
 Oxygen evolution reaction (OER)  
   catalysts, 159–160  
   cathode materials, 160  
   charge curves, 158–159, 159*f*  
   DEMS, 159  
   discharge/charge rates, 159–160  
   electrolyte solution, 160–161, 160*f*, 161*f*  
   GITT, 159  
   mechanisms, 48–51, 53–54, 57–58  
   PITT, 159  
   SERS, 159  
 Oxygen reduction reaction (ORR)  
   acetonitrile solution, 152–153, 152*f*  
   aqueous solution, 151–152  
   cathode materials, 156–158, 157*f*  
   cyclic voltammogram, 153, 154–155, 154*f*  
   discharge process, 155–156  
   dismutation process, 153  
   electrolyte solution, 158  
   gas-diffusion electrode, 153, 154*f*  
   hanging meniscus configuration, 153, 154*f*  
   HSAB theory, 155, 155*f*  
   kinetic parameters, 156

mechanisms, 48–51, 53–54, 56, 57–58  
 moisture impurity, 153  
 peroxide anion reaction, 153  
 Raman and magnetic measurements, 155*f*, 156  
 Randles–Sevcik plots, 152*f*, 153  
 tetrabutylammonium  
   hexafluorophosphate, 152–153, 152*f*

**P**

Particulate matter formation (PMF), 313–314, 314*f*  
 Patient monitoring system  
   history and philosophy, 353–354  
   mechanical ventilators, 354–355  
   pulmonary artery catheter, 354  
 Pauli’s exclusion principle, 235–236  
 Pearson’s hard and soft acids and bases  
   (HSAB) theory, 155, 155*f*  
 Perdew–Burke–Ernzerhof (PBE)  
   approximation, 238, 239  
 Perfluoroalkylsulfonylimide, 84  
 Phase change material (PCM), 295  
 Phosphate solid electrolyte, 95–97  
 Phosphazenes, 82  
 Plug-in hybrid vehicles (PHVs), 339–340  
 Poly(vinylidene fluoride) (PVDF), 120, 125–126  
 Polyacrylonitrile (PAN), 123–124  
 Polyaniline (PANI), 125  
 Poly(ethylene oxide) (PEO) electrolytes, 92–95, 94*t*  
 Polyethylene glycol dimethyl ether (PEGDME), 128  
 Polyethylene oxide (PEO), 126, 131–132  
 Polymer electrolytes  
   ceramic solid-state electrolyte, 133  
   composite polymer electrolyte, 132–133  
   dry polymer electrolytes, 91*f*, 92–95  
   gel polymer electrolyte, 132  
   gel polymer electrolytes, 90*f*, 91–92  
   LiBOB, 134  
   LiNO<sub>3</sub>, 133–134  
   P<sub>2</sub>S<sub>5</sub>, 134  
   solid polymer electrolyte, 131–132  
 Polypyrrole (PPy), 124  
 Polythiophene (PTh), 125  
 Positive electrode materials. *See* Metal oxides, cathode materials

Potentiostatic intermittent titration (PITT), 35–37, 35*f*, 36*f*  
Potentiostatic intermittent titration technique (PITT), 159  
Power Ring flywheel, 323–325  
Pressure-cycled ventilation, 355  
Pseudocapacitors, 338–339  
Pt and Pt alloys, 44, 55–56  
Pt–Au system, 49  
Pulmonary artery catheter, 354  
Pumped-storage hydroelectricity (PSH) systems, 320–322, 320*f*, 321*t*  
Pushing mechanism, 243–244, 245–246, 256–257  
Pyrochlore  $Pb_2Ru_2O_{7-\delta}$  compound, 50  
Pyrolyzed PAN-sulfur-graphene nanosheet (pPAN-S-GNS) composite, 123–124, 124*f*

**Q**  
Quallion's SaFE-LYTE technology, 371, 376–377

**R**  
ReCiPe method, 310, 310*f*  
Reduced graphene oxide (RGO), 123  
Renewable energy accumulator and conversion technology (REACT), 336–338  
Rietveld method, 188–189, 193

**S**  
Safety, 6–8  
Salts, 79–80, 79*f*, 80*t*, 93  
Satellites, 376–377  
Scanning electron microscopy (SEM), 205–206, 205*f*, 206*f*  
Schrödinger equation, 234  
Self-heat rate (SHR), 335–336, 335*f*  
Si anodes, 239–251  
Sn anodes, 251–255  
Sodium–nickel–chloride battery, 326–327  
Sodium–sulfur (NaS) battery, 326–327  
Solid–electrolyte interphase (SEI) layer, 126–127, 128–129, 162–163, 163*f*, 246, 248, 257, 331–332  
Solid inorganic electrolytes  
  ionic conductivity, 95–97, 96*t*  
oxides, 95  
phosphates, 95–97  
sulfides, 97  
Solid polymer electrolyte, 131–132  
Solid-state electrolytes, 11  
Solvents  
  chemical structure, 74–75, 74*f*, 74*t*, 76*f*  
  flammability, 75  
  fluorinated carbonates, 75–76  
  nitriles, 78  
  oxidation stability, 75  
  physicochemical properties, 74–75, 74*t*, 77*t*  
  requirements, 73–74  
  sulfones, 77–78  
Space exploration applications, 376–379  
SpaceX Dragon, 377–378, 378*f*  
Spinel oxide materials, 23–24, 24*f*  
State of charge (SoC), 272*f*, 273*f*, 274*f*, 275, 282–286, 283*f*, 284*f*, 285*f*  
State of health (SOH), 287–289, 288*f*, 289*f*  
State of power (SOP), 286–287, 288*f*  
Strong gel polymer electrolytes, 91–92  
Sulfide solid electrolyte, 97  
Sulfones, 77–78  
Sulfur–carbon (S–C) composites, 122–123  
Sulfur–graphene composite, 123  
Sulfurized polyacrylonitrile (SPAN), 123–124  
Sulfur–polypyrrole (S–PPy) composite, 124, 124*f*  
Sulfur, properties of, 118  
Supercapacitors, 338–339, 338*f*, 342–344  
Superconductive magnetic energy storage (SMES), 342–344  
SurePower lithium-ion battery, 357, 357*f*  
Surface characterizations  
  DEMS, 214–217, 215*f*, 216*f*  
  FTIR and Raman spectroscopy, 211–214, 213*f*  
  SEM analysis, 205–206, 206*f*  
  transmission electron microscopy, 206–209, 207*f*, 208*f*  
  XPS, 209–211, 210*f*  
Surface-enhanced Raman spectroscopy (SERS), 159  
Surface passivation  
  BET surface area, 169–171  
  capacity limitation, 167–169

Surface passivation (*Continued*)

- DPBs, 167
- film growth, 167–169
- galvanostatic discharge, 167–169
- MCF-C, 169–171
- MIM model, 167–169
- pore blockage and clogging, 167, 168f
- pore size distribution, 169–171, 170f
- TPBs, 167

Swagelok design, 186

**T**

TAH. *See* Total artificial heart (TAH)

Technology Readiness Levels (TRLs), 1, 2t

Tetra(ethylene glycol)dimethyl ether (TEGDME), 128, 129, 130, 131, 132

Thermal management system

- heating/cooling system, 293–295, 293t, 294f
- temperature estimation, 291–292, 292f
- thermostatic control, 295–296, 296t, 297f

Thermal runaway, 22–23

TiN bifunctional catalyst, 51

Titanium, 191–193

Tomographic reconstruction algorithm, 198–199

Total artificial heart (TAH), 360–361, 362f

Transmission electron microscopy, 206–209, 207f, 208f

Triple-phase boundaries (TPBs), 167

True Blue battery manufacturing company, 373

**U**

US06 Supplemental Federal Test Procedure (SFTP) cycle, 296, 297f

**V**

VAD. *See* Ventricular assist device (VAD)

Vanadium redox flow batteries (VRFBs), 327–329

Vehicle smart link (VSL), 339–340

Vehicle-to-grid (V2G) technology, 339–341, 340f, 341f

Ventilators, 354–355

Ventricular assist device (VAD), 358–359

Ventricular defibrillators

- AC/DC defibrillation, 356
- battery technology, 357
- SurePower lithium-ion battery, 357, 357f
- waveform technology, 356–357

Voltage inversion method, 283–284, 283f, 284f

Volume-cycled ventilation, 355

VRB-ESS, 327–329

VRFBs. *See* Vanadium redox flow batteries (VRFBs)

VSL. *See* Vehicle smart link (VSL)

**W**

Weak gel polymer electrolytes, 92

**X**

X-ray absorption spectroscopy, 197f

X-ray photoelectron spectroscopy (XPS), 209–211, 210f

X-ray tomography microscopy, 198–199, 199f